Pattern Formation and Stress Propagation in Confined Colloidal Flows

Craig Andrew Hall

Submitted in accordance with the requirements
for the degree of Doctor of Philosophy

The University of Leeds

School of Mathematics

June 2015

To my parents, David and Brenda, and
my sister, Steph.

Acknowledgements

First and foremost I would like to thank my supervisor, Mike Evans, for: his supervision and guidance, being a constant source of inspiration and good ideas, giving my project clear direction and keeping me on track and for his constant interest and enthusiasm for my work. I would also like to thank Mike for inspiring me to study my PhD in the fascinating area of soft matter Physics after I worked with him on a summer project as an undergraduate.

I would like to thank the University of Leeds for providing me with an excellent place to study and for funding my project through a university research scholarship.

I would also like to thank: Patrick Warren for a very interesting and helpful discussion about simulation techniques for including many body hydrodynamic forces and for recommending the use of HYDROLIB for my simulations. Oliver Harlen for an interesting and useful discussion of simulation techniques for fluids. Rammile Ettelaie for a very interesting discussion about how hydrodynamic effects are relevant to food science, and in particular their potential relevance to gel formation. My first year assessors Peter Olmsted and Sarah Harris and my advisors Peter Hine and Sandro Azaele for their support, advice and guidance.

Thanks also to all of the wonderful friends I have made over the course of my studies, both within university and also at various conferences and summer schools, who have made my time as a PhD student an absolute pleasure. I would especially like to thank: John Williamson for helping me to settle in when I first started and for always showing an interest in my work, and Malcolm Cartwright for being a great friend and an excellent person with whom to share ideas.

I am also very grateful to Glenys Bowles, Faith Bonner and later on Jeanne Shuttleworth for helping me with the various administrative tasks that arose during my PhD, particularly those involved in moving departments.

Most of all I would like to thank my family: my sister Steph, for always being there with words of encouragement and a sense of humour and for being my very best friend, ever since childhood. And my parents, Brenda and David, for their constant support and encouragement, for their unwavering belief in me, for always being there when I need them, for being the best role models I could ever hope for, for helping me in more ways than I could express in a whole thesis, let alone this section.

Abstract

Particulate solutions exhibit many interesting and varied behaviours when driven out of equilibrium. Not least of which is their ability to form elaborate and intricate patterns when subject to gravity driven flow in the confined space between a substrate and the fluid-air interface of a thin film.

The present work presents results of investigations into some of the key physical processes within the fluid, that are thought to lead to the formation of patterns. These were performed using a range of simplified models and numerical simulations. The central theme of the work is a simplified two fluid model of the particle-laden fluid itself, the results of which reveal a novel pattern formation process, entirely distinct from the conventional instability driven process normally associated with patterning. This process involves the decay of fluctuations in the particle volume fraction in one direction while fluctuations in the other persist. Ultimately, however, it was found, using both simulations and analytical stability analysis, that the physical processes encompassed by this simple model are not sufficient to increase the intensity of the patterns.

As well as considering additions to the model; two more, in depth, studies of physical processes at the microscopic level, thought to be potentially important to the formation of patterns, were also carried out. These consisted of the formulation of a simple, analytical, constitutive relation and a particle scale simulation including full many body hydrodynamic interactions. These highlighted the importance of memory effects and, long range, hydrodynamic interactions as potentially important processes by which band patterns may grow and increase in intensity.

The whole issue of patterning on a surface also leads to the question of how these, two dimensional, patterns should be characterised and, to this end, a number of novel methods for calculating the complexity are also discussed.

Contents

Appendices

List of Figures

List of Flow Charts

List of Tables

Abbreviations and Conventions

Symbols

Below is a list of some of the most commonly used symbols within this work and their meanings. This table aims to serve as a reference for the most general meaning of these symbols; more specific meanings are attributed to these symbols and other symbols are defined at the point of use within the various sections.

Variables

$\dot{\gamma}$	Shear rate
δ	Rotation
$\dot{\epsilon}$	Strain rate
ζ	Friction coefficient/Drag coefficient
$\boldsymbol{\zeta}$	Friction matrix
η	Viscosity
κ	Deformation magnitude
π	Osmotic pressure
ρ	Density
$\boldsymbol{\Sigma}$	Microstuctural stress
ϕ	Particle volume fraction
C_{ICC}	Information based measure of complexity
C_{LMC}	López-Ruiz, Mancini, Calbet measure of complexity
$\mathcal{D}$	Diffusion coefficient
$\mathbf{f}$	Force
$\mathbf{F}$	Deformation gradient tensor
g	Two particle distribution function
$\mathbf{g}$	Acceleration due to gravity
$\mathbf{I}$	Identity matrix
$\mathbf{J}$	Jacobian
k_B	Boltzmann's constant
$\mathbf{K}$	Velocity gradient tensor
$\mathcal{M}$	Mobility
N	Number of particles/Number of states
p	Pressure
$\mathbf{r}$	Position vector/Separation vector
t	Time
T	Temperature
$\mathbf{u}$	Solvent velocity
U	Interaction potential
$\mathbf{v}$	Velocity
V	Volume

Functions

$\mathcal{F}\{\ldots\}$	Fourier transform operator
$\mathrm{Tr}\{\ldots\}$	Trace of a matrix
$\mathrm{diag}\{\ldots\}$	Place the elements of a vector along the leading diagonal of a matrix

Conventions

Throughout the present work the following conventions have been used:

- round, (), and square, [], brackets have been used to group mathematical qualities while curly braces, {}, have been used to identify the argument of a function.

- bold face symbols refer to vectors and tensors while those in standard text refer to scalars, with upper case characters typically, but not always, referring to matrices.
- the dot product, $\cdot$, notation has been used for all inner products between matrices and vectors; two or more of these objects displayed next to one anther without a dot is intended to imply their outer product.
- lower case subscript s and p characters have been used to identify symbols relating to properties of the solvent and particles, or particle fluid, respectively.
- the symbol δ preceding another symbol refers to a small change in that variable.
- hatted variables, $\hat{}$, correspond to non-dimensionalised versions of the original.
- variables with tildes above them, $\tilde{}$, refer to a truncated multipole expansion approximation to the original.
- dotted variables, $\dot{}$, refer to time derivatives.
- superscript numbers in round brackets, (), in the text pertain to footnotes, while those in square brackets, [], refer to references listed in the bibliography.

Chapter 1

Introduction

1.1 Background and Applications

Nature provides many examples of systems in which order can develop spontaneously without there being any indication of the system's final state when it started out. This phenomenon, of a state developing without being apparent in a system's initial description, is known as emergence[1]. Examples of these kinds of systems range from the structures formed by protein molecules, through the intricate patterns formed by growing bacteria and geological structures up to the structure of whole galaxies.

The focus of the present work is the emergence of the non-trivial patterns which form when a particle-laden solvent is flowing over a surface[2]. This particular kind of pattern formation occurs in many everyday fluids such as: sugar particles forming patterns around the top of a honey jar[2], fat particles in yoghurt or the dirt left behind on a window by rain water[3]. Figure 1.1 shows examples of some of the patterns found on the side of a bottle of salad cream.

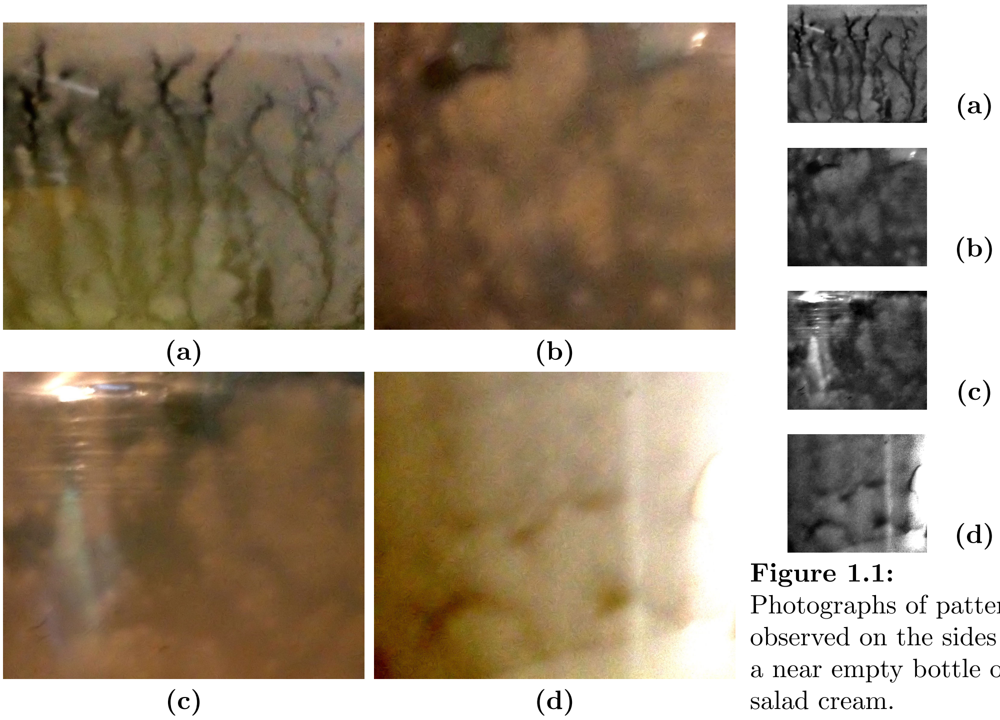

Figure 1.1: Photographs of patterns observed on the sides of a near empty bottle of salad cream.

Despite the range of systems involved there appear to be only two main types of pattern formed[2], one with channels parallel to the flow direction and the other with ridges perpendicular to the flow direction[2] .The former case is usually associated with smaller particles, where it is thought that attractive inter-particle interactions play an important role, forming aggregates which later go on to shear-thin, forming streams of fast flowing fluid which clears out a channel[2]. In the latter case attractive interactions are thought to be less important, for the larger particles; instead it is thought that the ridges form as streamlines in the fluid are pushed together to pass blockages caused by jamming of particles; these convergent streamlines push the particles together causing the jam to grow at the ends[2,3].

All of these systems have one thing in common: they are all comprised of a particle-laden solvent which forms a thin film as it drains over the substrate. This forms a gravity driven flow in a quasi-two dimensional geometry, in which the thickness of the film, perpendicular to the substrate, is negligible compared to the expanse of fluid in the other two directions[3].

Understanding of how these patterns come into being and what effects the properties of the fluid have on the resulting pattern could be applied to surface coatings, making it possible to tune properties of the bulk fluid in order to obtain a particular patterned surface. Perhaps the most valuable feature of these patterns, however, lies in their underlying physics[2,4–81]. The formation of patterns, in this and many other systems, is intrinsically a non-equilibrium process. In this particular case the physical processes occurring within the particle-laden fluid as it drains are closely linked to some of the most important phenomena in non-equilibrium physics, such as: many body hydrodynamic interactions[4–15], jamming[16–34], memory effects[35–39], non-Newtonian flow[4,5,35,38,40–64] and the effects of confinement[2,24,30].

In addition to the physical processes within the fluid the study of such a system also inevitably leads to the question of how one should go about characterising the patterns formed in a quantitative manner. In this respect the patterns formed by these thin draining films relate to a much wider discussion of whether or not it is possible to quantify the complexity[1,2,63,82–97] of such a pattern in any meaningful way. In itself complexity is a relatively poorly defined concept[1], with numerous conflicting descriptions, and two dimensional patterns provide an excellent example of why this is the case. The issue being that while one may be able to say, based upon intuition, that one pattern is more complex than another, it is much more difficult to say what it is about it that makes it more complex.

1.2 Outline of Thesis

The present work aims to demonstrate a number of ways in which the physical processes governing the flow of the colloidal particles, in their confined space between the substrate and the solvent-air interface, can lead to the formation of patterns as well as examining means by which the patterns themselves may be quantified and what one can learn from doing this.

At the heart of this work is a simplified, two dimensional, model of the draining colloidal fluid[3], which was investigated using numerical simulations. Essentially the model treats the system as two separate, yet interacting, fluids and reduces all of the interactions of the fluids with one another and the surface to friction constants [3]. Using this model as a starting point a number of additional features, such as: non-Newtonian behaviour [35,42,45,52,64], static friction [79], volume fraction dependent friction, diffusion and attractive inter-particle forces [16,55,80], were added to examine their effect on the pattern formation process.

Some of the key features of the flow, thought to be relevant to the pattern formation process [2], were also investigated. In part this was achieved through the creation of a first principles constitutive relation [35], based upon the virial theorem [98], to investigate the stress-strain relationship obeyed by the particles and consider what ramifications memory effects [35] had for the flow of the colloidal fluid in two dimensions. The effect of hydrodynamic interactions [4,5,8,9] between the spherical particles in a number of flow scenarios relevant to the draining film system [2] were also probed using a particle scale simulation, which accounted for full many body hydrodynamic effects [4,5,8,9]. These investigations yielded a deeper understanding of these specific aspects of the flow and produced results that could be fed back in to the simulation of the draining particle-laden fluid to better inform the modelling of the additional features, as well as illustrating other possible mechanisms for the pattern formation process, inaccessible to the simple particle-laden fluid model [3].

The following chapter in this thesis gives an overview of the current literature on the topics relevant to the current work. This includes: a discussion of the literature relating to the concepts of complexity [1,63,83–94,97,99] and emergence [1,100], and how they relate to pattern formation [2,78,84–86,90], similar pattern formation processes in fluids [2,78], several of the physical processes [2,4–81] relevant to pattern formation [2,78] and the other models [73,78,101] presented here and a survey of the numerical methods [102–115] relevant to the simulations performed as part of this work. Chapter 3 then describes the models used in the present work in a fairly abstract sense, paying attention to the theory behind all of the different aspects of each of the models and calculations, with the intention of giving a sound theoretical understanding of the physics upon which the simulations are based and motivating a mathematical framework for the complexity measures used. Chapter 4 leads on from this going into more detail about the practicalities of how the simulations were performed and complexity measures calculated, including the numerical methods and algorithms used. The results obtained from the various simulations are then presented and discussed in chapter 5. The results of each of the models are presented in individual sections, with a discussion of what can be learnt about the pattern formation process from each and how the models relate to one another. Finally chapter 6 draws together the main points and summarises the key results.

Chapter 2

Literature

There are two important aspects to understanding the nature of pattern formation [2,78] in the flow of a particle-laden fluid.

Firstly there are the underlying physical processes [2,4–81] taking place within the fluid as it flows, which lead to the formation of patterns and determine their features. These include things like: the inter-particle interactions, interactions between the solvent and the particles, interactions between the fluid and the substrate and the rheological properties of the fluid.

Secondly one must also consider the means by which the patterns may be classified and described in a quantitative manner. To this end it is informative to consider the concepts of emergence [1] and complexity. However, these terms can be poorly defined in general, as their meanings are often dependent on the context in which they are used [1], so it is worth considering what exactly would make an appropriate definition for these in terms of two dimensional patterns [82,84,85,90].

Finally this chapter shall conclude with a brief survey of some of the numerical procedures [102–116] relevant to the simulation of particle-laden fluids and the analysis of the resulting patterns.

2.1 Emergence and Complexity

Complexity is a fairly intuitive concept [1]. It is easy to say whether or not a pattern is complex or even whether one pattern is more complex than another. It is not easy, however, to say exactly how complex a pattern is, as one would need to be much more precise about what is meant by complexity, and this of course depends on the context [1]. To this end a mathematical definition can be very useful, but there is no universal, formal, definition of complexity. Instead one must formulate a definition suitable to the system in question. Broadly speaking there are three possible classes of definition [91]:

(a) a monotonic function of the amount of disorder, with the minimum complexity for a perfectly ordered state and the maximum complexity for a completely random state [85,91,93],

(b) a monotonic function of the amount of order in the system, with the minimum complexity for a completely random state and the maximum for a perfectly ordered state [63,91,99],

(c) a convex function of order or disorder, with minimal complexity for both completely random and perfectly ordered states and the maximum somewhere in between [1,63,83,87,91,92].

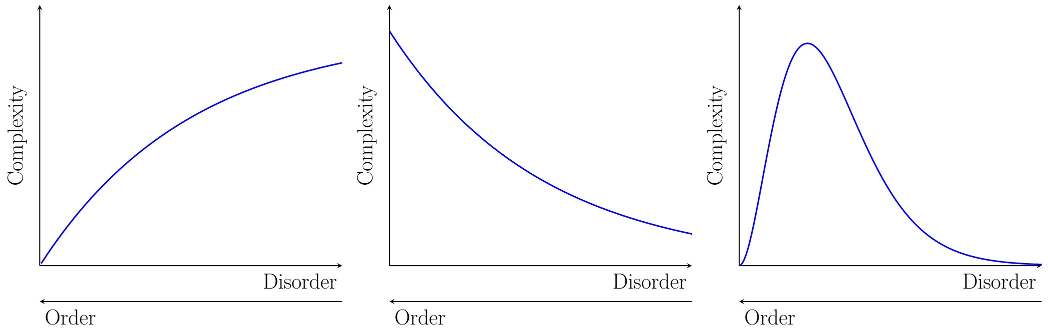

(a) Increasing with disorder. **(b)** Increasing with order. **(c)** Convex function.

Figure 2.1: Sketches of the three classes of complexity measure, in terms of the amount of order and disorder in the system.

Of course the most appropriate choice of measure depends on the system in question [1] and what one hopes to learn by calculating its complexity. For example when considering spatial patterns [82,84–86,90] the third definition [1,63,83,87,91,92] has the desirable property of attributing zero complexity to both a perfectly ordered and a completely disordered system [91], which is in tune with what one's intuition may tell one. While one may be far more interested in the other two classes of measure when considering the amount of information [88,89,99] stored in a given system, since the first would give an indication of how much storage space would be required and the second would give some impression as to the maximum possible compression ratio.

These two examples typify one of the main problems in arriving at a single universal definition of complexity, since the first definition tends to dominate the discussion in areas of computer science [88,89,99], relating to information processing, algorithm design and cryptography, where one is most interested in the amount of information to be processed and the number of steps involved in the most efficient processing route, or how best to compress information for storage or transmission. A good example of how complexity can be used in this area comes from considering storing the pixels of a simple image file; the only way of reproducing a completely random array of pixels is to store each and every one, hence this could be said to have maximum complexity as it requires the largest possible amount of storage space. By contrast an image consisting of just a block of one colour could easily be compressed, requiring only the size and colour of the block, and thus would be thought of as having minimal complexity. Of course switching to the second definition means that the complexity is essentially a measure of how much compression is possible which may also be a useful quantity to calculate. In this field the concept of complexity is also commonly applied to algorithms themselves, where again measures that fall into the first class are used to assess how many levels of recursion are necessary in the optimal algorithm for a particular task. Here tasks with high complexity are typically associated with large computational costs. By contrast those interested in characterising physical systems or patterns tend to favour the third definition [1,63,83,87,91,92] as this leads to both extremes being characterised as minimal complexity states, which tends to agree with human intuition. For example as far as structure and dynamics go ordered crystals and disordered, ideal, gasses are very well understood and can be described with relatively simple equations, hence they are not complex. Liquids on the other hand may exhibit some short range order, or order in a particular direction, but also contain a certain amount of disorder and usually exhibit a wider range of behaviours, making them much more difficult to describe theoretically, hence they are considered complex. Similarly one is unlikely to say that a regular repeat pattern or a random array is particularly complex, while one is far more likely to consider a mixture of ordered and disordered regions, or an unusual shape, as being complex[1,83].

As well as there being important differences in the uses of the different complexity measures there are also some important differences in the source data required by the different measures. Many of the measures in the literature rely on knowledge of a probability distribution[1,63,83,87,90–92] which characterises the data. Of course precisely which probability distribution[90] this is, is another important decision one must make when considering what one hopes to learn from the calculation and will be discussed in detail later on in this section. While probability distributions are key to a great many complexity measures there are some notable exceptions, such as the algorithmic complexity[88] which falls into the first of the above classes and can be calculated directly from strings of data by splitting them into sections and searching for repeat units[88]. A convenient way to examine the differences in how these measures work is to consider how the complexity of a string of characters making up a sentence would be calculated[90]. A probability based measure, also falling into the first class, would arrive at a value based upon the frequency at which each letter appeared whereas the algorithmic measure would arrive at a value based upon the size and the number of repeat units. Clearly one would expect a certain level of disagreement between these two measures for any given sentence, but that is not to say that one or other of the measures is wrong, simply that they are sensitive to different qualities of the data and as such provide different perspectives. Thus it may be informative to calculate both and compare the results. Here again, as with the way in which the measure scale with order and disorder, the choice of which approach to use really comes down to the context[1,91] and what one hopes to learn. While probability based measures are commonly used in many fields measures, like the algorithmic complexity, which search for repeat units, tend to be most heavily used in in the context of data processing and transmission.

The idea of emergence[1] is closely related to that of complexity, in that the two generally coincide. The presence of emergent properties generally relies on a system having many degrees of freedom or being described by non-linear equations, and as such these systems are likely to be considered complex. Or one may observe a complex state emerging from a relatively simple system, such as the self assembly of a non-trivial structure from a uniform fluid.

As with complexity there exists no unambiguous definition of emergence or of how to measure how "emergent" something is[1]. Unlike complexity, however, it is often more difficult to get an intuitive feeling about whether a property should be considered emergent or not, or even when an emergent property has emerged. This is due to the fact that it is open to interpretation whether a particular property emerged unexpectedly or whether it was in the system definition from the outset.

Consider, for example, self assembly of amphiphilic molecules[36]; the individual units may be relatively simple and have a relatively simple interaction potential and yet, given the right conditions, they can form extremely elaborate structures, such as: spherical and cylindrical micelles, vesicles, bilayers and hexapods[36]. So one could justifiably say that these structure are emergent, there was certainly no hint of them in the initial state, but the physics has not changed, the units of the structure are exactly the same units that made up the uniform state, they formed the only state they could given their own initial properties, and thus one could equally justifiably say that the final structure was in the initial description of the system and is not emergent at all. If one chooses to take the point of view that this is indeed an emergent property one is then left with the problem of when exactly the unexpected state emerged. In other words the point at which it became apparent that the system was going to settle in a state far from the one that was expected. Clearly this must have happened by the time the system reached its steady state, but could not have happened immediately, as this would mean that the property would not be emergent. The only way one can hope to pin down a time is if they can say exactly what initial state the system would be in for them to conclude, with their definition of emergence, that the final state was not an emergent state given this initial one, for example when an order parameter of the system exceeds some critical value. Then once such a state appears the system could be said to be in the emergent state.

It is not only the physical states of a system that have this property, it can also be extended to far more abstract and fundamental concepts[1]. One such concept is that of the entropy of a gas, nothing about the particle interactions or conservation of momentum suggests that entropy should be maximised and yet when one considers a large enough number of particles this becomes abundantly clear, which might lead one to the conclusion that the tendency of a system to maximise its entropy is an emergent property. However, the counter-argument, that the maximum entropy is achieved through a series of collisions which obey the system's initial description, is equally valid.

2.2 Pattern Formation Processes

Patterns are a very common sight in nature and arise from a wide variety of physical processes[2,73,78,101,117,118]. Even if one restricts oneself to only considering pattern formation processes in fluids there are still a huge range of systems[2,73,78,101] where patterns can occur, and just as wide a range of underlying physical processes.

In bulk colloidal solutions interactions between the particles can lead to phase separation[36,78,118], which is a common source of patterns as the two phases emerge from the uniform mixture[36,78,118] . Here the balance between the energy gained from the attractive inter-particle forces and the cost of creating a particle-solvent interfaces means that fluctuations on a certain length scale grow preferentially[36] and the result is a macroscopic pattern. This kind of pattern formation process, referred to as spinodal decomposition[36], is often modelled using the Cahn-Hilliard equation[36,118],

$$\frac{\partial \phi}{\partial t} = \boldsymbol{\nabla} \cdot \left[\mathcal{M} \boldsymbol{\nabla} \left(\frac{\partial f}{\partial \phi} - \kappa_S \nabla^2 \phi \right) \right], \tag{2.1}$$

where ϕ is the volume fraction, t is time, $\mathcal{M}$ is the mobility of the particles, which may be a function of the volume fraction, f is the bulk free energy density of the particles and κ_S is a constant related to the surface free energy. Here one can clearly see how the interplay between the competing effects of the surface tension in the interface and the attractive nature of the interaction affects the spatial distribution of the particles over time[36,118].

As well as forming in the bulk in system that do not experience an imposed flow, patterns are also commonly observed in draining films[2], where the fluid is confined in one of the spacial dimensions, between a substrate and the air, and gravity acts to produce a net flow down the surface[2]. Of particular relevance to the present work are the results presented in reference 2, which describes the patterns formed when a suspension is allowed to drain down the side of its container. In these experiments two very distinct patterns are observed depending upon the relative concentrations of different sized particles suspended within the solvent. Reference 2 reports that a system made up of predominantly small particles will produce a pattern consisting of narrow channel regions, devoid of particles, running vertically down the side of the container, between particle rich regions. By contrast fluids carrying predominately large, granular, particles produce a band pattern perpendicular to the flow direction, with horizontal ridges made up of particles, with a smooth transition in between, in which patterns exhibit some elements of each. The explanation given in reference 2 for these observations is that: because the small particles, which experience van der Waals' forces, are prone to gel formation, and as such exhibit shear thinning behaviour, an environment is formed where any increase in the flow rate will result in a proportionately smaller resistance to further flow. This coupled with the fact that the, porous, gel structure impedes the solvent's flow, as well as that of the particles, means that any region where the flow rate is slightly enhanced due to inhomogeneities will experience less resistance[2]. Due to the incompressibility of the combined fluid this region will then fill with solvent from the surrounding area, which is prevented from bringing particles with it by the attractive forces which hold the gel network together. This solvent then proceeds rapidly down the channel washing away any loose particles in its path[2]. By contrast the large particles which do not form aggregates and, in fact, offer little resistance to redistribution within the solvent, unless driven to high concentration, may become pinned to the substrate by the solvent-air interface, due to their size. For whatever reason a particle becomes pinned, once stationary, it forms an obstruction which the solvent and other particles must flow around[2,3]. This results in convergence of the stream lines in the direction perpendicular to the flow[3]. This means that the separation between particles, still travelling with the solvent at this point, is reduced in this direction which can lead to them jamming[25] at the site of the obstruction and thus creating a larger obstruction. This process then repeats and the band grows in the horizontal direction. A sketch illustrating this behaviour is given in figure 2.2.

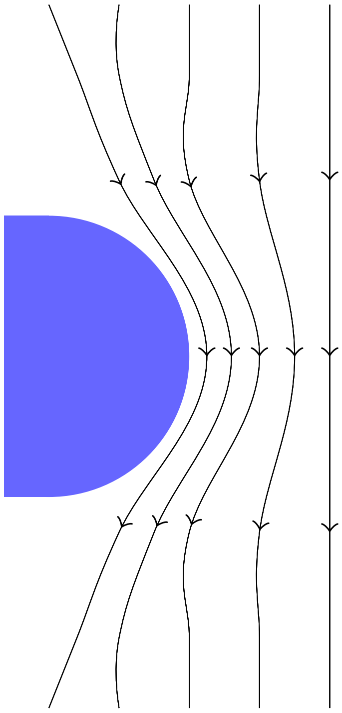

Figure 2.2: Sketch of the streamlines of the flow around an obstruction, thought[3] to be relevant to the growth of band patterns in draining thin films of colloidal suspension.

Once a band reaches a significant size it is able to act as a filter allowing solvent through while particles pile up behind. This creates regions of high concentration behind and low concentration in front.

The idea of the surface pinning the particles, due to capillary action, is also discussed in reference 78, in which a solvent carrying particles fills half of a rotating cylinder while the particles coat the other half. Here it is proposed that the effect of the free surfaces pinning the particles in the top half of the cylinder can be well modelled using an equation[78] very similar to the Cahn-Hilliard equation[78,118] and that the resulting patterns possess many of the characteristics of those produced by spinodal decomposition in a bulk fluid.

Less relevant to the present work, but also of interest, with regard to pattern formation in draining thin films, are experiments of the type presented in references 73 and 101. In these experiments a uniform suspension flows down an inclined substrate producing either a jagged ridged leading edge or finger like projections to the leading edged of the flow as the suspension wets the substrate, but unlike the two fluid systems discussed here this suspension remains uniform and the pattern only exists at the leading edge of the fluid and does not remain in steady state[73,101]. Though the present work only considers systems where the fluid covers all of the surfaces from the outset it is, nevertheless, worth mentioning these systems here as it serves as another example of a system where flow confined in one direction leads to a pattern forming instability.

2.3 Constitutive Relations for Colloidal Dispersions

Unlike many simple fluids, such as water and oil, where the stress remains proportional to the strain rate across a very broad range of strain rates, complex fluids, such as: polymer solutions, colloidal dispersions, liquid crystals and surfactants, which have a non-trivial microstructure, can exhibit a variety of different flow behaviours, depending on the particular nature of the flow field and the magnitude of the strain rate. Colloidal dispersion[43,61,80,119], granular systems[19,62,67,71,95,120] and emulsions[64] exhibit many, varied, flow behaviours and are well studied experimentally [18,22–25,27–30,34,45,53,69,76,119], yet, compared with other complex fluids such as polymer solutions [37,39] and liquid crystals [121], there are relatively few first principles constitutive relations to provide a theoretical framework within which their behaviour may be understood. One important reason for this is the fact that their flow is heavily influenced by many body interactions, such as long range hydrodynamic forces [4,5,8] and many particle contacts [19,23–25] at high volume fraction. Attractive interactions [16,44,66,122], such as van der Waals' forces can also lead to the formation of aggregates and fractal gel networks [16,44,66,122], which are able to support stresses [16,44,66,122], but may also collapse [44]. These complex interactions often mean the flow response depends on both the strain rate as well as the concentration of particles in the fluid.

Because the flow is heavily influenced by the particles it is useful, especially for theoretical work, to define the rate of flow in terms of the time scale relevant to the particles. Thus one often finds the flow rate quoted in terms of the, dimensionless, Péclet number [35],

$$Pe = \frac{\dot{\epsilon} a^2}{\mathcal{D}} \tag{2.2}$$

where a is the particle radius, $\dot{\epsilon}$ is the rate of strain and $\mathcal{D}$ is the particle diffusion coefficient. This provides a convenient means by which one can compare the rate of flow to the rate at which rearrangements occur in the microstructure at equilibrium and so gain an insight into how much the imposed flow is deforming and rearranging the structure itself.

It is difficult to make generalisations about the flow response of this class of fluids due to the large variety of different types of particle it encompasses. There are many different, some times seemingly contradictory, results in the literature [18,22–25,27–30,34,45,53,69,76,119] concerning flow behaviour, since the results of experiments [18,22–25,27–30,34,45,53,69,76,119] often depend on the precise nature of the interactions between the particular types of particles being used. Clearly one would not expect an emulsion of soft particle [22,64] to have exactly the same rheological behaviour as a suspension of hard spheres [24,52,123]. As such there are many different relationships [42,51,64] which aim to fit the stress-strain data of the different experiments [40,45,124].

One of the most straightforward ways of doing this is with a simple power law expression,

$$\sigma \propto \dot{\epsilon}^a, \tag{2.3}$$

where σ is the stress, $\dot{\epsilon}$ is the strain rate and a is a constant, which can be fitted to the experimental data. One of the main advantages of this, empirical, formalism is that it allows one to say immediately whether a fluid is shear thickening, shear thinning or Newtonian simply from the exponent; if $a < 1$ then the effective viscosity(1),

$$\eta \propto \dot{\epsilon}^{a-1}, \tag{2.4}$$

falls as the strain rate is increased and the fluid is said to be shear thinning, if $a > 1$ then it rises and the fluid is described as shear thickening, and of course $a = 1$ leads to

---

(1) In the sense that it is the local gradient of the stress with respect to the strain rate. In the strictest sense the concept of viscosity only applies to a Newtonian fluid.

$\sigma \propto \dot{\epsilon}$ which is the definition of Newtonian flow. While equation 2.3 may be convenient there are very few fluids for which it holds over a broad range of strain rates and, other than allowing one to identify shear thickening or shear thinning behaviour, it offers no real insight into the physical mechanisms responsible for the flow from a microscopic point of view.

One common approach to overcoming the problem of the range where equation 2.3 is applicable is to simply make use of a piecewise function[64] made up of several copies of equation 2.3, each with a different value of a. In this context one may then refer to different regimes in the fluid's constitutive relation. Though this does not address the second problem it is still a very useful concept, even when considering the behaviour of microscopic models, because it allows one to get an intuitive feeling about the fluid's response at different strain rates and make meaningful comparisons with experiments.

Overcoming the second problem and producing a constitutive relation from a microscopic theory is very difficult for colloidal fluids since there are many factors affecting their motion, not least the presence of all of the other particles, which they cannot pass through. As a result there are relatively few first principles constitutive relations[35] for these fluids. Those that do exist are mostly based on mode-coupling theory[33,35,74], which provides a means of incorporating the many body interactions that arises as a result of steric hindrance in a crowded system[35]. Aside from the complexity of the calculation involved in establishing the constitutive relation by this method one runs into major difficulties in trying to establish the effects of certain approximations[74], which must be made in order that the equations be tractable, and whether or not they are valid in certain situations. This is an important drawback because, while this is a genuinely microscopic theory, the amount one can learn about the effect the structure has on the flow behaviour is, to some extent, limited by the fact that the approximations are not well controlled[74]. That said mode coupling theory does provide useful insight into many aspects of the behaviour of colloidal dispersions[33,35,74], not just their rheology, and as reference 35 shows can be used to make meaningful predictions about the stress-strain relationship in such fluids. The essence of the model described in reference 35 is to consider the evolution of a probability distribution associated with the relative positions of the particles(2). From this distribution one can then calculate the fluctuations in the density of particles and, in turn, the structure factor, from which the stress can be obtained. In reference 35 these equations are then solved numerically to yield a stress-strain relationship with three distinct regimes: a Newtonian regime at low strain rates followed by a strongly shear thinning regime and then a weaker shear thinning regime at higher strain rates. These regimes are reported to be qualitatively very similar in both planar extension and simple shear flow, though they occur at slightly different strain rates in the two flow protocols. This is in good agreement with the results of the simulations of reference 5 at low and intermediate strain rates, but not at very high strain rates.

The explanation offered in reference 5 is that while the Brownian motion of the particles is responsible for the shear thinning at low strain rates it is hydrodynamic interactions that are responsible for the shear thickening at higher strain rates. It is also clear from the results of several other similar works[38,45,53,58,125,126] that this behaviour is much more

---

(2) The constitutive relation presented here in section 3.4 takes a very similar starting point.

pronounced at high volume fraction [38,45,53,58,125,126]. With this explanation in mind it is hardly surprising that the constitutive relation of reference 35 lacks this shear thickening behaviour as hydrodynamic effects are not included in the calculation. With the hydrodynamic effects included one finds very good agreement with experimental results [45,125,126] for hard sphere colloids, which suggest a general tendency to exhibit four regimes at high volume fraction: Newtonian flow, at very low Péclet numbers, followed by shear thinning, followed by another Newtonian region finally ending with shear thickening at very high Péclet numbers [5]. At intermediate volume fractions one tends not to see the final regime and only observes the shear thinning and Newtonian regimes [5,45,125], while at very low volume fractions one only finds the Newtonian regime, which is, of course, to be expected since the solvent by itself is Newtonian [5,45,125]. Of course all of this is consistent with the explanation given in reference 5 that the Brownian forces are responsible for the shear thinning since they are bound to dominate when the Péclet number is small. Once there are a sufficient number of particles for the microstructure to play a significant role, these forces help to rearrange the structure and in doing so reduce the stress. Furthermore at high volume fractions when the particles are close together the hydrodynamic lubrication forces result in a strong resistance to relative motion of the particles [5]. This coupled with the fact that there is little time for the Brownian forces to rearrange the structure when the Péclet number is high(3) leads to the observed shear thickening.

Because colloidal dispersions have well defined microstructures [35], they are also capable of exhibiting memory effects [35,37] and by extension viscoelastic behaviour in response to flow [35]. This arises because the microstructure takes a certain amount of time to return to its equilibrium form after a deformation is imposed, so the stress does not decay immediately after the force which caused the deformation is removed and thus inter-particle forces drive the structure back towards its original state. These memory effects also mean that stress builds up in a fluid as it begins to flow [37], rather than immediately reaching its steady state value as it does in simple, Newtonian, fluids. One can again think of this in terms of the microstructure, since it takes a certain amount of time before the structure is deformed to the extent that it is in steady state, there are relatively few particles in close contact at the onset of the flow, but as the flow field brings more and more particles together the stress in the microstructure, due to these contacts, builds up until the steady state is reached. Of course the Brownian motion of the particles also rearranges the structure and helps to relax some of the stress [5,35,37] so the macroscopic fluid is unable to return completely to its original state. Since the relaxation of the particles is, in part, due to diffusion, a strain with a high Péclet number is likely to result in an elastic response [37] from the microstructure as it is unable to rearrange itself on the time scale of the deformation. Meanwhile a deformation with a very low Péclet number allows plenty of time for Brownian motion to continually rearrange the structure and so a viscous response is observed. This kind of behaviour is particularly important when one flow protocol follows another within the time scale of the relaxation, since one cannot expect the stress in the second flow field to build up in the same way as it would if the fluid had initially been in its equilibrium state [3]. Importantly this can lead to a higher than expected stress or

---

(3) Meaning that their contribution is small compared with the contribution of the hydrodynamic forces.

unexpectedly low flow rate.

Another important feature that sets the flow behaviour of colloidal dispersions apart from that of simple Newtonian fluids is the fact that they produce a non-zero normal stress difference when subjected to shear flow. In colloidal fluids this, first, normal stress difference is usually positive[5,47,48,57]. It is relatively straightforward to see how this arises when one thinks in terms of the microstructure of the fluid. A very simplistic view of shear flow is to think of slabs of fluid in the gradient direction moving past one another at different rates. This causes tension in the stream lines and results in the particles being pulled together[57], resulting in the measurement of a positive normal stress difference.

2.4 Structural Arrest in Complex Fluids

As well as the equilibrium crystal and gas phases[36] colloidal dispersions can enter a number of other non-equilibrium phases as a result of many particle specific factors, such as: shape, size and the type of inter-particle interactions they experience, as well as factors affecting the fluid as a whole, such as the temperature, or the presence of an external flow field. While these phases are not equilibrium phases, by virtue of the fact that they do not adhere to the ergodic hypothesis, they are often very stable and exist for prolonged periods of time. Two very important phases, which are thought to be relevant to the pattern formation process, are those of the amorphous solid[23,24,29,66,74,123,127] and colloidal gel[44,55,80,122,128,129].

While these two phases differ significantly in terms of the volume fraction and particle interactions that lead to their emergence, they also bear some striking similarities[70], not least of which is that they both result in a state which has all of the mechanical properties of a solid(4), but a structure that is more akin to a liquid[70], in its lack of any kind of periodic ordering. Another important similarity is the nature of the transition between the fluid and the solid like, glass or gel state, with both occurring as a result of kinetic rather than thermodynamic reasons[70].

2.4.1 Jamming and Crowding

The phenomena of jamming and the glass transition in colloids and granular materials are a source of tremendous research interest and have received a great deal of attention in the literature[17,22–24,28,29,70,123,127]. However, they are not restricted to colloidal solutions alone, in fact the processes are completely independent of the particle size, shape[95] or even the extent to which they can be deformed[22]. The phenomenon of jamming is purely due to the volume available to the particles and affects systems as diverse as large boulders rolling down the sides of mountains, gravel, sand or powder in a hopper[95], latex beads in a solvent, emulsions and even bubbles[22]. While jamming and the glass transition themselves remain something of an open question[17,22,24], with much debate about the nature and even the precise location of the glass transition[123], there exist a number of commonly used theories[19,22,23,33] about how the flow properties of particle fluids change as the jamming transition is approached[19,22,23,33,123]. In the present work the word jamming will be used to refer to the process by which particles form an amorphous solid due to

---

(4) At least for strains in a certain range.

the nature of their flow[24], while the word glass shall be reserved for the amorphous solid formed in the absence of flow for purely geometric reasons(5).

As far as colloidal suspensions are concerned; one very important example is that of hard spheres[24,45,123]. Though this is an idealised model its flow behaviour is far from simplistic with rich phase behaviour. At volume fractions below $\phi \approx 0.49$[130] the system is generally considered to be in its liquid state, with: a coexistence region, between $\phi \approx 0.49$ and $\phi \approx 0.55$[130], a glass transition commonly thought to be at $\phi \approx 0.58$[130], though this is disputed[123], and finally forming a FCC crystal at $\phi \approx 0.74$[130]. The phase diagram for the two dimensional equivalent, hard disks, is not nearly as well studied thought there is commonly accepted to be a glass transition in the region of $\phi \approx 0.85$[31] and a crystal structure at $\phi \approx 0.92$[131]

The infinite nature of the hard sphere interaction potential places an absolute limit on how close two particles may approach one another; once a contact is made the particles in question must find another path if flow is to continue. At low concentration the vast majority of collisions involve only a small number of particles so many such paths are available. These typically lead to particles rolling over or sliding past one another causing a slight increase in the fluid's resistance to the imposed flow due to friction between the particle or increased drag with the solvent. As long as the volume fraction remains low this increase in the viscosity is well modelled by a small parameter expansion in terms of the volume fraction, ϕ[42,51,64],

$$\hat{\eta} \approx 1 + [\eta]\,\phi, \tag{2.5}$$

where $\hat{\eta} = \frac{\eta_p}{\eta_s}$ is the ratio of the viscosities, η_p and η_s, of the particle fluid and solvent respectively and $[\eta]$ is the intrinsic viscosity, which has a been shown to take the value $\frac{5}{2}$ for all hard sphere fluids, regardless of particle size and polydispersity[51].

As the volume fraction is increased the frequency of multi-particle collisions also increases meaning that the number of routes that particles may take to pass one another is reduced due to the presence of other particles. This slows down the rearrangements in the microstructure since many more particles have to move around in order that two may pass each other. This leads to an increase in the stress as the contact points between the particles all carry stresses which cannot be released[19,23,95]. Ultimately as the volume fraction approaches the glass transition these stress networks[19,23,95], made up of particles that are unable to move due to steric hindrance can propagate through significant proportions of the system and the support enormous stresses[19,23,95], rendering the fluid unable to flow. Thus once the volume fraction approaches this point the effective viscosity diverges[42,51] towards infinity since the strain rate possible from any finite stress is essentially zero. Naturally the fact that interactions in this regime involve a significant proportion of the total number of particles in the system makes them incredibly difficult to model theoretically since one requires knowledge of the exact location of every particle in the stress network[19,23,95]. Though the understanding of how the applied stress propagates though these networks and what consequences this has for the flow behaviour is a huge area of research in itself, from the point of view motivating an model of how the volume fraction affects the effective viscosity of the fluid it is perhaps sufficient to simply

---

(5) Though various different conventions are used in the literature.

say that one requires a model with two features: that the viscosity ratio, $\hat{\eta}$, increases linearly from one at low volume fractions[42,51], with a constant of proportionality equal to the intrinsic viscosity and that this ratio diverges[42,51] as the volume fraction approaches the glass transition.

Over the years a great deal of experimental[18,22,24,30,123] and theoretical[23,29,33,42,51] work has been devoted to the pursuit of this function and, unsurprisingly, many different functions have been proposed. In the present work the popular semi-continuum model proposed by Krieger and Dougherty in reference 42 shall be used as many works have shown this to be in excellent agreement with experimental measurements[18,49,53,62,76,124], on a wide range of colloidal fluids[42]. Like many other semi-continuum models[42,51] this model is derived by considering what effect adding particles in two stages has on the viscosity of the fluid and insisting that this gives the same result as adding all of the particles at once. Insisting further, that one must re-derive equation 2.5 in the low volume fraction limit then prescribes a unique equation[42]. The key difference between the models of this type lies in their treatment of crowding effects[42]. If one neglects these altogether then one obtains[42]

$$\hat{\eta} = e^{[\eta]\phi}, \tag{2.6}$$

which performs well at low and intermediate volume fractions, but fails to diverge as one approaches the jamming transition[42]. This failure at high volume fractions is hardly surprising given that the model assumes that the second group of particles is added into the same amount of space as the first group was. One improves the situation, obtaining[42]

$$\hat{\eta} = \left(1 - \frac{\phi}{\phi_{max}}\right)^{-[\eta]\phi}, \tag{2.7}$$

by reducing the amount of volume available to the second group of particles by a factor related to the volume fraction of the first and a crowding factor, while allowing the first group of particles to take up the full volume[42]. As is clear from equation 2.7 making this adjustment produces the desired property that the viscosity ratio will diverge at a given volume fraction, ϕ_{max}.

As well as undergoing structural arrest at the glass transition colloidal fluids and granular systems can also jam at lower volume fractions as a result of particles being forced into close proximity by particular flow fields, for example as they flow through a constriction such as the neck of a syringe[24]. This kind of behaviour has been observed in colloidal dispersions in the experiments printed in references 24 and 30 and is a common problem in industrial applications involving granular systems, such as powders[95]. Here particles are forced together as the fluid approaches the constriction and a significant number of them come into contact; some of these will simply roll over one anther or drift apart an instant later, but given the right local environment some will seed the formation of a stress network which propagates rapidly through the fluid leading to a macroscopic cessation of the flow. These networks can be observed visually in experiments as arcs propagating into the bulk fluid from the neck of the syringe[24,30]. One particularly interesting feature of these jammed states is that, while they may remain indefinitely whilst under the action of the force that created them they soon break apart and disperse once this force is removed. This is due to the fact that there are no attractive forces between the particles, the only time they feel any kind of interaction with the other particles in the system is when they are in contact with them(6). Thus with the contacts released the particles are once again free to move locally and the microstructure is able to relax and undergo rearrangement[24]. Because there are no attractive forces holding the network together, even a slight change to the force, in the right place can cause the network to collapse and allow flow to resume[24]. Hence the reason why these system are some times referred to as forming "fragile matter"[26].

As well as potentially undergoing many jamming and unjamming transitions during flow these fluids may also undergo a process known as "self filtration"[30], which can lead to problems in experiments since one cannot necessarily say, with confidence, that the volume fraction in a sample taken from a bulk solution is the same as in the bulk solution itself[24,30,132]. The reason for this is that while the system is in its jammed state very few particles are entering the sampling vessel, but because there are gaps in the structure this does not stop the solvent from entering. Hence while the vessel is filling up with liquid, this liquid may contain a disproportionate amount of solvent[24].

The wide range of systems that exhibit a tendency to form fragile solids under flow, and the number of open questions relating to understanding how this phenomenon occurs, have prompted a great deal of research into the topic[24,30,132]. One important avenue of investigation, as far as industrial applications relating to the processing of colloids and granular materials goes, is the search for effective methods of breaking up the jammed network and restoring flow[32,79]. As described above this can be done by making perturbations to the forces as this leads to buckling within the stress network. A natural choice of method for producing such perturbations is to introduce vibrations[32,79] into the steady flow. These have been shown to significantly increase the number of avalanche events observed in the flow of powder in a silo, leading to an increase in the flux[32,79]. Another method that leads to the collapse of the stress-bearing arcs is the introduction of vortices to the flow field. Such a phenomenon is described in reference 24, where it is demonstrated that the stop-start motion associated with the creation and destruction of fragile solids in a colloidal suspension flowing into a capillary tube ceases above a certain pressure drop and is replaced by steady flow. This is observed to coincide with the formation of vortices either side of the mouth of the tube[24], leading to the collision that these vortices break up fragile solids before the stress network is able to propagate[24]. Rotational motion of the particles has also been shown to be an important factor in the break up of the fragile solid, as this allows for a plastic response at the level of the microstructure even when there isn't enough room for the particles to move past one another. It has also been reported that confinement can play a key roll[67] in jamming and un-jamming processes, and perhaps surprisingly flows in channels less than about twenty particle diameters wide have been reported to jam and unjam in a periodic manner[67].

2.4.2 Gel Formation

At the opposite end of the spectrum, at relatively low concentrations[16,70], small particles that experience strong, short range, attractive interactions, can form another kind of non-ergodic state which has huge implications for their flow behaviour[70]. The relatively

---

(6) Neglecting hydrodynamic interactions, of course.

small size of the particles means that their movement is affected significantly by thermal fluctuations in the solvent. This means, in the absence of a flow field, they explore space as a result of Brownian motion, until they pass another particle within the range of the interaction, at which point the strength of the interaction potential means that they become irreversibly stuck together[128]. This process is repeated with other particles adding to the cluster and forming clusters of their own eventually leading to a fractal gel network which spans the entire system[55,128]. Because the magnitude of the interaction potential is large compared with the thermal energy it is very unlikely that the bonds holding this network together will break so the particles are unable to explore phase space and find their equilibrium, crystal, structure for a very long time[80]. In fluids where the interaction is slightly weaker the gel phase can be observed to form and then coarsen, before eventually collapsing[44], as rare bond breaking and reforming events occur[44].

Unlike the "fragile"[26] jammed phase[16,28,66,70,127] the attractive forces between these particles enable the gel network[16,55,66,70,128] to support forces from any direction[16]. However, in this case the magnitude of the force plays a key role in determining the flow response. If the force is small, and not strong enough to over come the attractive inter-particle forces[16], then the gel network responds in much the same way as a cross-linked polymer network and undergoes an elastic deformation. If, however, the force is large and breaks the inter-particle bonds, then sections of the network move as the bonds continually break and reform[44,80], leading to an overall plastic deformation. As a result these fluids often exhibit shear thinning behaviour[2,80] since the stronger flow fields are able to break the bonds more readily.

An important consequence of the fact that the fractal gel structure is able to support some stress[16] without breaking is that it allows the fluid to exhibit "memory effects"[37] and means that, as with many polymer solutions, the flow response is viscoelastic[37], possessing both solid and liquid properties depending on the strain rate[37].

Like the jammed phase the existence of the gel phase depends heavily on the precise nature of the flow field. However, this time it is the rate, and not the direction[16], of flow that is important for maintaining the structure. Also in similarity with the jammed phase, the fractal gel network can act as a filter, trapping particles and allowing the solvent to pass through the gaps[2].

2.4.3 Intermediate States

As a sweeping generalisation one can say that, as far as colloidal dispersions are concerned, large particles, which are relatively immune to the effects of Brownian motion and van der Waals' forces, only interacting through steric hindrance, typically jam at high concentrations and can for a fragile solid when forced into high concentration by the flow field. While small particles, whose motion is dominated by Brownian forces and strong attractive interactions at short range, form gels at low concentrations. Yet nothing has been said of systems made up of particles of intermediate size[16], small particles, with attractive interactions, at high volume fraction[16] or polydisperse[17] systems, as this region of the phase diagram is not fully understood[17]. Of course all particles, even soft ones, can jam so one can say with confidence that there must be a jamming transition for small and polydisperse particles[17]. However the nature of this transition and the structure formed is significantly different from that of the classic hard sphere. For one thing polydisperse systems[17] can reach much higher volume fractions in a random closed packed structure than particles of identical size can, but to some extent this relies on the smaller particles being able to find the gaps[17], which they may not be able to do if the larger particles rapidly form a fragile solid at a constriction. Furthermore small particles with attractive interactions have been observed to aggregate into clusters which later jam as though they were large particles[70]. On the scale of the aggregates this forms a similar structure to the fragile solid, but with the attractive forces of the small particles this structure is far less fragile and responds to changes in the applied force in a manner more akin to the gel[70].

2.5 Hydrodynamic Interactions Between Particles

In many simplified physical simulations of particles, hydrodynamic interactions are one of the very first phenomena to be coarse grained out and replaced with a constant drag coefficient. Though there are many good physical reasons for doing this, as there are many systems where their effects are small, there is one very clear practical advantage of removing hydrodynamic interactions from simulations where they are not absolutely necessary in that they are incredibly complicated and time consuming to calculate[4,5,12,68,133,134], restricting the simulation size severely. There are, however, many physical systems where hydrodynamic interactions are very important, these include many biological systems[6,11,124] and systems relevant to food science[50,129]. The massive increase in computational power seen over the past few decades has made accurate simulation of these systems much more feasible and is even leading to questions about whether hydrodynamics do play a significant role in systems where they have previously been ignored, out of necessity[135].

Another important consideration regarding the relevance of hydrodynamic forces in simulations of physical systems is how much detail one must retain[12,134]. In some situations, where particles are tightly packed, or there is a strong external flow field, one need only consider lubrication forces[6,13] and alleviate the need to calculate the full many body interactions.

Even for two identical spheres, in the low Reynolds' number limit, the calculation of exact hydrodynamic forces is very non-trivial[68] since one must solve the Stokes equation for the solvent applying the appropriate, non-slip, boundary conditions for each particle. Though this can be done analytically in the case of two particles[68] one must turn to numerics in order to perform the calculation if there are any more[4,5,7,12,68]. This is made all the more complicated by the fact that, unlike many particle-particle interactions, hydrodynamic interactions cannot be calculated in a pairwise manner[4,4,5,7,12,68,133], since every particle interacts with the solvent and the interactions from each particle affects the way it interacts with all of the others. This is the reason why hydrodynamic interactions are referred to as many body interactions[4,4,5,7,12,68,133]. In addition to this hydrodynamic interactions are long range, falling away like the reciprocal of the particle separation[68], so one cannot, realistically, reduce the size of the calculation by defining a cut-off radius and only considering a particles near neighbours.

Over the years many approaches to overcoming the problem of calculating these hydrodynamic forces correctly have been proposed in the literature[4,4,5,7,12,68,133,136,137]. For the purposes of giving a brief overview, these typically fall into two classes: those which consider the system to be one continuous fluid with highly viscous pockets [136,137], which are thought of as modelling the particles, and those which focus on the forces experienced by the particles, treating the solvent implicitly and never actually calculating the full flow field [4,4,5,7,12,68].

Two key advantages of the first method are that it provides information about the entire flow field, including the behaviour of the solvent, and it can be used with particles of any shape and size since the shape of the particles has no effect on the size or difficulty of the calculation. However, while it may treat the particles as being much more viscous than the solvent, real, hard, particles have an infinite viscosity and cannot be deformed(7), in particular this leads to problems defining the edges of the particles [137]. A second draw back comes in terms of the size of the system for which simulations are, realistically, possible since the computational effort involved in solving the Stokes equation for a reasonable mesh size is much larger than that required to merely calculate the forces acting on the same arrangement of particles. Meanwhile the latter class of method, commonly referred to as Stokesian dynamics simulations [4,5,133], permit many more particles, as it is significantly faster [4,5], and does treat the particles correctly but, it does not allow for calculation of the solvent's behaviour [4,5,68] and, in order to achieve the greatest performance increase, one must restrict themselves to spherical particles which are all the same size as one another [68].

Since the method used in the present work falls into the second class, the remainder of this section shall, for the most part, be devoted to examining this class of methods in more detail, with details of the exact method used appearing in section 3.3. For this class of methods the key to the calculation of the hydrodynamic forces is finding a means of calculating one of two matrices, known as the friction(8) and mobility matrices, each being the inverse of the other [68,133]. The elements of which summarise the six components of the interaction between each pair of particles, with three for the three components of the force and three for the three components of the torque, in three dimensional space [68,133]. The mobility matrix can then be used to calculate the steady state velocities of the particles given the forces acting upon on them, or, its inverse, the friction matrix [68], can be used to calculate the forces acting on the particles given their velocities relative to the solvent. In the presence of gradients in the external flow field one also requires a further, third rank, tensor coupling the particles to the external flow field [133]. Thus the total hydrodynamic force, including all torques, for all particles is summarised in the $6N$ dimensional vector [4,133]

$$\mathbf{f}_H = -\mathbf{R}_{FU} \cdot (\mathbf{u} - \mathbf{u}_s) + \mathbf{R}_{FE} : \mathbf{E}, \tag{2.8}$$

where $\mathbf{R}_{FU}$ is the friction matrix, $\mathbf{u}$ is the $6N$ dimensional velocity vector, describing the velocity each particle relative to the velocity of the solvent at the location of the particle, $\mathbf{u}_s$ is the net solvent velocity evaluated at infinity, $\mathbf{R}_{FE}$ is the tensor coupling the forces on the particles to the external flow field, $\mathbf{E}$ is the symmetric part of the velocity gradient tensor of the solvent, evaluated at infinity, and N is the number of particles. In the

---

(7) While it is a drawback in the case of hard particles this is clearly an advantage if one is interested in simulating soft particles.

(8) Commonly referred to in the literature as the resistance matrix.

literature the two resistance matrices, $\mathbf{R}_{FU}$ and $\mathbf{R}_{FE}$, are commonly thought of as being part of a larger matrix[133],

$$\mathscr{R} = \begin{pmatrix} \mathbf{R}_{FU} & \mathbf{R}_{FE} \\ \mathbf{R}_{SU} & \mathbf{R}_{SE} \end{pmatrix}, \tag{2.9}$$

known as the grand resistance matrix. Thus this matrix relates the force and the symmetric first moment of the surface stress, or stresslet, exerted on the fluid by the flow field to the flow field itself, by[133]

$$\begin{pmatrix} \mathbf{F} \\ \mathbf{S} \end{pmatrix} = \mathscr{R} \cdot \begin{pmatrix} \mathbf{u}_s - \mathbf{u} \\ \mathbf{E} \end{pmatrix}. \tag{2.10}$$

The advantage of this formalism is that the grand resistance matrix may be inverted to form the grand mobility matrix allowing for one to move easily between the two representations. This is key to the solution of the problem since one can approximate the solution of the far field problem using a multipole expansion at the surface of each particle to obtain the elements of the grand resistance matrix[133]. In the far field limit this expansion may be truncated at relatively low order, since the higher order moments fall away rapidly as the separation between the particles increases. While the mobility matrix has the desirable property of being pairwise additive[4,133], the process of inverting it solves the many body problem and thus, at the level of the forces and stresslets, the grand resistance matrix describes the full many body interaction, in the far field limit[133].

To obtain the correct lubrication force from the near field interaction, using this method one would need to include an infinite number of terms in the multipole expansion. Fortunately, however, since these forces are short range, its possible to combine them in a pairwise manner in the representation involving the grand resistance matrix[133]. Thus one may obtain a good estimate, valid at all length scales, by adding the lubrication correction, calculated in the resistance matrix formalism, to the inverse of the mobility matrix and remembering to subtract off the two particle contribution calculated from the multipole expansion[4,12,133].

Of course these matrices become very large very quickly as the number of particles increases and, in order to preserve the full formalism, one can expend a great deal of computational effort calculating matrix elements that are not required, especially, if one is only interested in the forces acting on the particles in situations where there are no gradients in the flow field. In this situation, which is of most relevance to the present work, one only requires the friction matrix[4,122], $\mathbf{R}_{FU}$, thus it makes sense to calculate this directly, rather than forming and then inverting an much larger matrix. For the most part this is done in a similar way, using a multipole expansion[4,122] to create a one particle friction matrix for each particle and combining these in a pairwise additive manner[4,12]. This is where the two methods differ since the one particle friction matrix created up to this point does not treat the many body interactions correctly as the inverse of the grand mobility matrix did. There is, however, a relationship between this matrix and the full friction matrix, $\boldsymbol{\zeta} = \mathbf{R}_{FU}$(9), in terms of an multipole expansion to the Oseen tensor[4,12].

---

(9) Although these two matrices are equivalent up to the level of approximation of the multipole expansion, they are not strictly equivalent. The reasons for the change of notation are two fold; firstly to highlight the difference in the two different methods and secondly to try and remain consistent with the notation widely used in the literature on both topics.

The exact method shall not be covered in too much detail here, since the full relationship and accompanying derivation are given in section 3.3.2, suffice to say that the bulk of the computational work goes into the calculation of the Oseen tensor [4,12].

Numerous examples in the literature [4,4,5,47,59,133] have shown these multipole methods, Stokesian dynamics in particular, to be extremely accurate and reliable as well as being efficient [4,5,47,59,133]. These typically include calculations of well established quantities, such as: long and short time diffusion coefficients and the two particle distribution function, for which there is very good agreement with experimental results [126] even with relatively few particles [5]. This, impressive, agreement coupled with the fact that this class of methods is much more computationally efficient than those that attempt to solve for the full flow field, allowing for several hundred particles to be simulated in a reasonable time scale [12], make them very popular in the simulation of systems in which a correct treatment of hydrodynamic forces is necessary, and is also the reason for the choice of method here.

Often to simulate physical systems one does not wish to consider hydrodynamic forces in isolation and instead one needs to combine them with other forces such as: other interparticle interactions, like van der Waals' forces or electrostatic interactions, external fields, like gravity or imposed electric or magnetic fields, or Brownian forces [4–6,8,9]. Of course forces are additive, so in many cases this is not a problem, however, Brownian forces are an important exception, where hydrodynamics is concerned [4–6,8,9], since obeying the fluctuation-dissipation theorem [113] requires that the magnitudes of the Brownian forces scale with the particle-solvent friction coefficient [4,113]. However, when hydrodynamic forces are dealt with correctly, this is different for each particle, leading one to the question of which drag coefficient to use. It is relatively straightforward to show(10) the answer to this question is to use the Cholesky decomposition of the friction matrix and scale the force individually for each particle [4], as this means the force is scaled correctly for the particle in its own environment within the solvent.

2.6 Numerical Simulation Techniques for Fluids

The simulation of fluids is a huge area of research [2,5,12,104,108,113–115,136–150], and is used extensively in academic research [4,5,148], engineering [102,136,137,139,141,144,146,148,150] and even video game development [114,138,142]. In order to satisfy the needs of such a variety of applications a wide range of simulation methods have been employed.

2.6.1 Discretisation of Space

Typically the first decision one has to make about a simulation is whether to use the Eulerian [142,143,150] frame of reference, which consists of a fixed grid of points over which the fluid flows [142,143,150], or the Lagrangian [102,136,139,146,150] frame of reference, in which the grid flows with the fluid and the matter inside each cell is conserved [139]. The Eulerian approach generally yields much simpler equations of motion [139,141,142], which is an important consideration in terms of computational effort, but the fixed grid can potentially lead

---

(10) A first principle derivation is given in section 3.3.3.

to issues with numerical diffusion and the method is generally regarded as poor at dealing with elastic behaviour and history dependence[137,141,144]. The Lagrangian method is much more suited to this kind of behaviour, but falls down when is comes to turbulent flow as the mesh can become tangled[137,141,144], this can be rectified by re-meshing[137,141,144], but this coupled with the more complicated equations of motion can result in a very high computational cost. Of course the key to making a good choice is knowledge of the expected behaviour. The Eulerian method is generally regarded as better for high Reynolds' number fluids which experience turbulent flow while the Lagrangian method is usually chosen for solid like materials which exhibit elastic behaviour. However, the situation need not be as simple as a single fluid; hybrid methods[137,141,144,148], which model different regions of space according to the different models, can be employed. These methods, however, require careful treatment of the boundary between the two meshes. Multigrid[108,136] methods are also employed in a number of simulations in order to increase the rate of convergence of solutions and reduce numerical rounding errors and instabilities associated with the discretisation of space. These work by making a number of identical copies of the system at each point in time and then using a different sized mesh on each[108], the solutions are then mapped onto each other to produce the final solution which benefits from both the precision of the smallest and the fluctuation decay rate of the largest[108].

Another important question concerning a discretised model of space is how one should take spatial derivatives. An obvious choice is a simple finite difference method, but a choice must be made between symmetrical differencing which has second order precision and doesn't bias any particular direction, but can lead to a checker-board instability[151], or asymmetrical differencing which is only first order and introduces a bias[151], but removes the risk of the checker-board instability appearing. A rather elegant alternative, for systems with periodic boundaries, is to use a spectral method[114] which takes advantage of the fact that

$$\frac{d}{dx}f = \mathcal{F}^{-1}\left\{iq_x\mathcal{F}\left\{f\right\}\right\}, \tag{2.11}$$

where $\mathcal{F}$ denotes the Fourier transform, to produce derivatives which are both symmetrical and are influenced by cells on all length scales. Though this may appear more costly than a simple finite difference method in some circumstances it can greatly simplify the problem and the fast Fourier transform algorithm[114] can be used to further reduce cost, if the grid size permits it.

2.6.2 Matrix Manipulation

Solving the equations of motion for a continuum model of a fluid on a grid usually involves several matrix operations. These operations can be very costly in terms of computational effort, since the standard[151] algorithms for performing common matrix operations typically scale rather poorly with the matrix size[151]. The worst of which being inversion, or decomposition[151], and multiplication[151] which all scale with the cube of the matrix size[151]. However, many techniques[106,110–112,114,138,142,143,151] for reducing this work load have been devised for use in numerous situations. The choice of which method is most appropriate typically depends on the matrices in question. If there are relatively few non-zero elements in the matrix then the use of a sparse methods[106,152] can be advantageous. These methods save time and achieve improved scaling, with respect to the size of the matrix, by only performing calculations on the non-zero elements and avoiding the zeros[106,152]. However, keeping track of the positions of these non-zero elements introduces and additional overhead to the calculation[106]. Thus the use of such methods on matrices which contain more than a certain proportion of non-zero elements can in fact result in inferior performance relative to standard methods. Even when there are a sufficient number of zeros reducing the overhead as far as possible, whilst retaining the information about the location of the non-zero elements, in both the input and output matrices is still very important. One way of achieving this, which is commonly used in many such matrix algorithms, is to store the non-zero elements of the matrix in compressed column format[106]. This compresses a matrix into, essentially three vectors: one containing a cumulative count of non-zero elements at the beginning of each row of the matrix, one containing the column numbers and one containing the values of any non-zero elements[106]. Compressing sparse matrices in this way saves a great deal of memory and allows algorithms devoted to performing operations on such matrices to function more efficiently[106].

Though sparse methods exist for most common matrix operations, inversion, or decomposition, and multiplication offer arguably the greatest performance boost, since the standard, dense, methods for these operations typically scale very poorly[151], with execution times proportional to the cube[151] of the matrix size. While multiplication is relatively straightforward, as it is for dense matrices, decomposition can be much more involved and there are a wide range of different approaches to achieving the greatest performance. There are essentially two, common, approaches[106], which are both based on Gaussian elimination, these are referred to in the literature as left looking[106,152] and right looking, or multi-frontal, methods[106]. The left looking class of methods[106,152], like the one provided in the CSparse[106] library and used in some of the simulations presented here, is generally considered the simpler of the two as it treats each column in turn and only relies on the information available from previous calculations[106]. By contrast right looking and multi-frontal methods use graphs determined from the non-zero pattern of the matrix[106] to establish the interdependence between the different elements. While this results in a more complicated algorithm it does allow for one to make better decisions about which elements to use as pivots and, because the dependence of each element on all of the others is known upfront these methods can often be parallelised[106].

Ignoring the fact that the algorithm uses compressed column format to store the matrices, the essence of the left looking method is essentially the same as that of normal, dense, LU-decomposition, with full pivoting[106], except that the pivot is chosen as a compromise between the largest element and the one that minimises the number of new elements that will be added to the matrix at each step[106,152]. Like the standard LU-decomposition algorithm, this method starts with the left most column and moves to the right treating each column in turn, each time selecting from the remaining columns a pivot that is both large enough to maintain stability and limits the number of new elements that must be added. This is done using the Markowitz criteria[152] which state that the element, a^*, chosen from the unprocessed part of the matrix, at step k, is the one that minimises the product[152]

$$\mathcal{P}_{ij} = (R_i - 1)(C_j - 1) \qquad i \wedge j \geq k, \tag{2.12}$$

where R_i and C_j are the number of non-zero elements in row i and column j of the unprocessed part of the matrix, while satisfying

$$|a^*| \geq \alpha \, |a_{ik}| \qquad \forall i \geq k, \tag{2.13}$$

where $0 \leq \alpha \leq 1$ is a constant used to set the balance between reducing the number of elements added[152] and the stability of the algorithm(11). Typically $\alpha = 0.1$ is used as a compromise.

Of course, one may also ask the question of whether anything can be done to speed up these two key operations when the matrix, or matrices, in question are dense. Surprisingly, perhaps, it is indeed possible to increase the speed and improve the scaling in many cases[110–112]. This is done using a set of algorithms proposed by Strassen[110], which, successively, divide the matrices into smaller and smaller sub-matrices to perform the calculation and then recombine them at the end[110–112]. Though Strassen's original methods[110] only worked for matrices which could be divided into four, subsequent studies[153,154] have proposed methods that work with some other numbers, so unless the dimensionality of a given matrix is a prime number there is a good chance that one or a combination of these methods will be applicable. The fundamental theory underpinning these methods is rooted in the fact that while the multiplication of two matrices

$$\mathbf{X} = \begin{pmatrix} \mathbf{X}_{11} & \mathbf{X}_{12} \\ \mathbf{X}_{21} & \mathbf{X}_{22} \end{pmatrix} \quad (2.14a) \qquad \mathbf{Y} = \begin{pmatrix} \mathbf{Y}_{11} & \mathbf{Y}_{12} \\ \mathbf{Y}_{21} & \mathbf{Y}_{22} \end{pmatrix}, \quad (2.14b)$$

whose elements are themselves matrices, by the conventional method takes eight multiplication operations, it is possible, by reordering the steps to obtain the product, $\mathbf{X} \cdot \mathbf{Y}$, with just seven multiplication operations[110–112]:

$$\mathbf{Z}_1 = \mathbf{X}_{22} \cdot (\mathbf{Y}_{21} - \mathbf{Y}_{11}) \tag{2.15a}$$

$$\mathbf{Z}_2 = \mathbf{X}_{11} \cdot (\mathbf{Y}_{12} - \mathbf{Y}_{22}) \tag{2.15b}$$

$$\mathbf{Z}_3 = (\mathbf{X}_{21} + \mathbf{X}_{22}) \cdot \mathbf{Y}_{11} \tag{2.15c}$$

$$\mathbf{Z}_4 = (\mathbf{X}_{11} + \mathbf{X}_{12}) \cdot \mathbf{Y}_{22} \tag{2.15d}$$

$$\mathbf{Z}_5 = (\mathbf{X}_{11} + \mathbf{X}_{22}) \cdot (\mathbf{Y}_{11} + \mathbf{Y}_{22}) \tag{2.15e}$$

$$\mathbf{Z}_6 = (\mathbf{X}_{21} - \mathbf{X}_{11}) \cdot (\mathbf{Y}_{11} + \mathbf{Y}_{12}) \tag{2.15f}$$

$$\mathbf{Z}_7 = (\mathbf{X}_{12} - \mathbf{X}_{22}) \cdot (\mathbf{Y}_{21} + \mathbf{Y}_{22}) \tag{2.15g}$$

The product itself is then given by

$$\mathbf{X} \cdot \mathbf{Y} = \begin{pmatrix} \mathbf{Z}_1 - \mathbf{Z}_4 + \mathbf{Z}_5 + \mathbf{Z}_7 & \mathbf{Z}_2 + \mathbf{Z}_4 \\ \mathbf{Z}_1 + \mathbf{Z}_3 & \mathbf{Z}_2 - \mathbf{Z}_3 + \mathbf{Z}_5 + \mathbf{Z}_6 \end{pmatrix}. \tag{2.16}$$

Here the fact that this strategy contains many more addition operations is irrelevant, provided that the matrices are large enough, since these operations only scale with the square of the matrix size while multiplication operations scale with the cube. Of course, if the size of the original matrix allows, it is possible to apply the same procedure to

---

(11) Setting $\alpha = 1$ essentially makes the algorithm revert back to the standard LU-decomposition algorithm.

equation set 2.15 as well, using the method recursively[110–112], up to the point where the matrix size is no longer a multiple of two, or it becomes inefficient to increase the number of addition operations because the matrices involved are so small. Thus for a sufficiently large matrix, of dimension n, the dominant scaling factor is $n^{\log_2\{7\}}$[110]. Furthermore, because the method splits the matrices into sub-matrices it lends itself well to parallelisation, which can further boost the speed of the operation.

In addition to this method Strassen[110] also proposed a method of matrix inversion using the same principle. Following this method one may invert the matrix $\mathbf{X}$, from equation 2.14a, using the following steps[110–112]:

$$\mathbf{Z}'_1 = \mathbf{X}_{11}^{-1} \tag{2.17a}$$
$$\mathbf{Z}'_2 = \mathbf{X}_{21} \cdot \mathbf{Z}'_1 \tag{2.17b}$$
$$\mathbf{Z}'_3 = \mathbf{Z}'_1 \cdot \mathbf{X}_{12} \tag{2.17c}$$
$$\mathbf{Z}'_4 = \mathbf{X}_{21} \cdot \mathbf{Z}'_3 \tag{2.17d}$$
$$\mathbf{Z}'_5 = \mathbf{Z}'_4 - \mathbf{X}_{22} \tag{2.17e}$$
$$\mathbf{Z}'_6 = \mathbf{Z}'^{-1}_5 \tag{2.17f}$$
$$\mathbf{Z}'_7 = \mathbf{Z}'_6 \cdot \mathbf{Z}'_2 \tag{2.17g}$$

giving

$$\mathbf{X}^{-1} = \begin{pmatrix} \mathbf{Z}'_1 - \mathbf{Z}'_3 \cdot \mathbf{Z}'_7 & \mathbf{Z}'_3 \cdot \mathbf{Z}'_6 \\ \mathbf{Z}'_7 & -\mathbf{Z}'_6 \end{pmatrix}. \tag{2.18}$$

Unfortunately, while this method offers better scaling than standard methods, such as LU-decomposition and Gaussian elimination, it is not as stable[112], since the fact that $\mathbf{X}$ is well conditioned does not necessarily mean that $\mathbf{X}_{11}$ is[112] which can lead to poor accuracy. This can, of course, be improved by pivoting[112], but this requires the calculation of the determinants of the sub-matrices[112], which incurs an additional computational cost. In many cases, and especially where the simulation of fluids is concerned, one is only interested in the inverse of a matrix as a means of solving a set of linear equations. This can also be split into smaller operations using a similar method, provided that there are an even number of equations so they can be written in the form[112]

$$\begin{pmatrix} \mathbf{X}_{11} & \mathbf{X}_{12} \\ \mathbf{X}_{21} & \mathbf{X}_{22} \end{pmatrix} \cdot \begin{pmatrix} \mathbf{x}_1 \\ \mathbf{x}_2 \end{pmatrix} = \begin{pmatrix} \mathbf{y}_1 \\ \mathbf{y}_2 \end{pmatrix}, \tag{2.19}$$

where x_i is a sub-vector of the unknowns and y_i is a sub-vector containing the, known, right hand sides of the equations. Rearranging equation 2.19 then provides a means of finding half of the solutions immediately, as follows[112]:

$$\mathbf{x}_1 = \mathbf{X}_{11}^{-1} \cdot (\mathbf{y}_1 - \mathbf{X}_{12} \cdot \mathbf{x}_2) \tag{2.20a}$$
$$\big(\mathbf{X}_{22} - \mathbf{X}_{21} \cdot \mathbf{X}_{11}^{-1} \cdot \mathbf{X}_{12}\big) \cdot \mathbf{x}_2 = \mathbf{y}_2 - \mathbf{X}_{21} \cdot \mathbf{X}_{11}^{-1} \cdot \mathbf{y}_1, \tag{2.20b}$$

while the other half may be found by recursive application of the same algorithm. Provided $\mathbf{X}_{11}$ is reasonably well conditioned, this provides a very efficient means of solving a large set of equations, since one can make use of Strassen's multiplication and inversion algorithms[110–112] to improve the scaling of the most computationally intensive tasks[112]. The multiplication steps also offer the possibility of an even greater boost in the speed thanks to the fact that they can be run in parallel, though one must take care here since many of the steps in the matrix inversion must be performed in a specific order, making this harder to parallelise[112].

Before concluding this section it is also worth mentioning some of the iterative methods[109,114,138,142,155] that may be employed to solve sets of linear equations. The key advantage of these methods is that they are very simple to parallelise and can be run on massively parallel systems[138] with very little over head. Another advantage is that one can specify the required level of accuracy and have the iteration stop once it is attained, rather than relying on pivoting to produce reasonable accuracy. The draw back is that, while the direct methods, such as LU-decomposition and the methods described above, guarantee that a solution will be found, provided that the matrix is non-singular, iterative methods will only converge if the matrix has certain properties or the initial trial solution is reasonably close to the actual solution[155]. That said they are commonly used in the solution of the equations of motion describing fluids. Three of the most common algorithms in use are: Jacobi[109,114,138,142,155] iteration, Gauss-Seidel iteration[155] and Successive over relaxation[109,155]. All of these methods use essentially the same principle, though differ in terms of their update schemes. In each method the matrix equation[155]

$$\mathbf{X} \cdot \mathbf{x} = \mathbf{y} \tag{2.21}$$

is solved iteratively by using a rearrangement of each of the equations to make the solution, x_i, the subject of equation i. Thus the improved solutions, at step k, in the Jacobi scheme, are given by[155]

$$x_i^k = \frac{1}{X_{ii}} \left(y_i - \sum_{\substack{i=1 \\ i \neq j}}^{N} X_{ij} x_j^{k-1} \right), \tag{2.22}$$

where N is the number of equations. Both Gauss-Seidel[155] and Successive over relaxation[109,155] iteration schemes proceed in a similar fashion, except that Gauss-Seidel uses the results from previous solutions from the same iteration where ever possible, thus[155]

$$x_i^k = \frac{1}{X_{ii}} \left(y_i - \sum_{i=1}^{j-1} X_{ij} x_j^k - \sum_{i=j+1}^{N} X_{ij} x_j^{k-1} \right), \tag{2.23}$$

while successive over relaxation[109,155] uses a weighted average of the two[109,155]. If the weighting is correct this can lead to much faster convergence, but there is no rigorous method for choosing the weighting factor so one runs the risk of reducing the rate of convergence as well[109]. As mentioned previously the key down fall of all of these methods is that they only guarantee convergence if the matrix meets certain criteria[109,155]. In the case of the Jacobi method the matrix must be strongly diagonally dominant, on a row by row basis[155], meaning that the magnitude of the diagonal elements must be greater than the sum of the magnitudes of all of the other elements in that row. The other two methods require that the matrix is symmetric and positive definite[155].

As a final point in this section it is worth pointing out the massive performance boost which can be offered by parallelisation and the use of modern programmable graphics hardware[114,138,142,156,157], containing hundreds of cores[157]. A key difficulty here, however, is the fact that most fluid simulations, at some stage, involve solving a set of linear equations and the standard, direct, methods of doing this are not parallelisable. In order to avoid this, iterative methods, such as Jacobi [109,114,138,142,155] and Gauss-Seidel [155] iteration are commonly used. This is an area, however, where Strassen's method [110–112] of solving the set of equations could be of significant use as it has been shown to be faster than the fastest conventional method, LU-decomposition, when used recursively and is highly paramellisable [112].

In terms of the problem being dealt with in the present work, however, it was found that, since most of the matrices were dominated by zeros, the sparse methods [106,152] of multiplication and LU-decomposition out performed all of the others(12).

2.6.3 Time Integration

Of course, the purpose of any dynamical simulation is to advance the state of the system in a way that is both efficient and remains faithful to the true dynamics of the system. Thus the choice of integration scheme is key to the success of any simulation and there are many schemes available [108,115,116,146,151] each with its own set of advantages and disadvantages. One of the key difficulties specific to time integration is the fact that it is difficult to take a properly centred time derivative since one cannot say, beforehand, what the future state will be. This problem can lead to instabilities in explicit methods [115,151], which use the information from the previous and current states to evolve to the next state, which results in a divergence from the true solution. Though there are a wide variety of explicit methods [115,151], with various stability criteria [151], which are commonly used in simulations [5,114,133,138,142,146], there are also a range of implicit methods [108,116,158] which offer unconditional stability and guarantee that, while the solution may not capture the true dynamics correctly, it will be physically realistic for the given equations of motion [108,116,158].

In order to explain how these implicit methods work it is worth considering an example in the form of the implicit Euler [108,158] method(13). In the standard Euler method the state of the system evolves from step i to $i + 1$ according to [151]

$$f_{i+1} = f_i + \delta t \left. \frac{\partial f}{\partial t} \right|_i , \tag{2.24}$$

where t is the time, δt is the size of the time step and f is an arbitrary function of time. In the implicit, or backwards, Euler method the system is evolved according to [108,158]

$$f_{i+1} = f_i + \delta t \left. \frac{\partial f}{\partial t} \right|_{i+1} . \tag{2.25}$$

While this change is subtle it has huge ramifications for both the stability of the integration scheme and the approach one must take to obtaining the new state, f_{i+1}. Unlike equation 2.24, where all of the terms on the right hand side of the equation are known, with equation 2.25 one must find the solution, f_{i+1}, for which the equation holds given f_i and the function, or functions, that determine $\frac{\partial f}{\partial t}$ [108,158]. Naturally this comes at a

---

(12) Full details of the methods used are given in section 4.1.5.

(13) This method was used in the present work in the simulation of the particle-laden fluid described in section 3.1.

significant increase to computational cost since these solutions typically involve matrix inversion if the system of equations is linear or iteration if it is non-linear, but precisely because of this one can say with absolute confidence that the new state is a solution of the equations regardless of how large the time step is, whereas the forward method can make no such guarantee and one must rely on a sufficiently small time step to keep f_{i+1} close to the true solution. Thus it is possible to offset the cost of having to solve equation 2.25 by using a much larger time step. This is especially useful in situations where one is willing to sacrifice some short time resolution in order to access long time dynamics.

Another slightly more sophisticated method in this class is the Crank-Nicolson [108,116] method, which has similar properties to the implicit Euler method, but improves on it by using a half time step so that the time derivative can be properly centred [116]. While this improves the accuracy of the method, once again it increases the complexity of the algorithm and the computational cost.

2.6.4 Simulation of Particles

One very important aspect of colloidal flow is the microstructure formed by the particles. If one wishes to go beyond continuum models and resolve this structure then one must consider how best to simulate the particles themselves. Here it is difficult to make use of implicit methods since one usually wishes to deal with the particles one at a time rather than trying to solve for the structure as a whole, meaning one has little choice other than using forward iteration methods. One, particularly good and widely used, algorithm for this is the velocity Verlet algorithm [113,115,146], which offers a number of advantages over the simple Euler method [113,146,151] while only slightly increasing the work load at each time step. One such advantage is that, in its basic form, the velocity Velret algorithm is time reversal symmetric, which means that it conserves the average energy exactly [115]. The essential feature of the algorithm that gives it this very desirable property is that it calculates the velocity in a manner that is properly centred with respect to the time step, by updating using the average of the acceleration calculated from the updated positions and that calculated at the previous time step [115]. This is in addition to including the acceleration in the position update to make the method second order accurate [115]. Mathematically speaking one can summarise the method in the following two steps [115].

$$\mathbf{r}_{t+\delta t} \approx \mathbf{r}_t + \delta t \left(\mathbf{u}_t + \frac{1}{2m} \delta t \mathbf{f}_t \right) \tag{2.26a}$$

$$\mathbf{u}_{t+\delta t} \approx \mathbf{u}_{t+\frac{1}{2}\delta t} + \frac{1}{2m} \delta t \left(\mathbf{f}_t + \mathbf{f}_{t+\delta t} \right), \tag{2.26b}$$

where $\mathbf{r}$ is the particle's position, $\mathbf{u}$ is its velocity, $\mathbf{f}$ is the force acting upon it, m is its mass(14), t is the current time and δt is the size of the time step.

Of course there are many situations, the present work being one example, where one needs to include velocity dependent forces. This is especially true when particles are immersed in a viscous solvent. Fortunately a straightforward modification to the velocity

---

(14) In the hydrodynamics simulations presented in the present work the particles are assumed to have a mass, despite the solvent being assumed to be in the low Reynolds' number limit, as a means of rationalising the relationship between the forces calculated and the motion of the particles. This is discussed further in section 4.3.4.

Verlet algorithm was proposed by Groot and Warren in reference 113 for precisely this purpose. Essentially this algorithm makes a prediction about the velocity in order to calculate the force and then later corrects it using the equivalent of equation 2.26b before moving on to the next step(15). While this algorithm loses the exact energy conservation properties of the conventional velocity Verlet algorithm[113] it retains many of its other desirable properties and has been shown to perform very well in practice[113].

---

(15) Full details of the algorithm will be given in section 4.3.4.

Chapter 3

Theoretical Background

3.1 A Two Dimensional Model of a Particle-Laden Fluid

In order to try to extract the essential physics involved in the formation of patterns when a particle-laden solvent flows over a surface a very simple model[3] of the fluid was devised. The fact that the model is simple has three major advantages over an exact description of such a fluid. Firstly it exposes which physical processes need to be present in order for pattern formation to take place and what effect different processes have[3]. Secondly by being more abstract, and only taking account of the essential features of the physical processes involved in the fluid flow, this model is very general and can be used to draw very broad conclusions that may be applicable to a whole range of different fluids rather than being a precise description of a very narrow class of fluids[3].

Although this approach has the distinct disadvantage that it cannot provide quantitative information about any given system it actually makes it possible to learn much more about the general process than an exact model ever could because in an exact model, where many of the properties are interrelated it would not be possible to identify which physical feature, or features, of the system were responsible for the pattern formation. One could only conclude whether or not that precise system formed patterns. Furthermore this knowledge could not be used to make predictions about other systems.

The final major advantage of using a simplified model is the ease of the implementation; the model that will be described in this section can be written in terms of a closed set of four differential equations[3] which are well suited to numerical solution. Furthermore the various equations used to determine the coefficients are all simple, closed, analytical expressions which can be evaluated quickly and efficiently. This meant that it was possible to run simulations with many different parameters relatively quickly even for reasonably large grid sizes. The simplicity of the model also made the implementation straightforward in the sense that it made it easy to add new features and isolate different terms due to the fact that the various coefficients, for properties such as the effective viscosity of the particles and friction coefficients, could be tuned independently of one another.

3.1.1 Basic Model

A simple model of a particle-laden fluid draining over a surface was created by treating the system as two interacting fluids as first proposed by Evans[3], one being the solvent and the other being a fluid of particles. In order to try to demonstrate how the model relates to the microscopic properties of the fluids this section shall provide a slightly different derivation to that provided in reference 3.

By treating the particles as a fluid all of the microscopic interactions between particles are effectively coarse grained out. This assumption is valid in the limit where the length scales under consideration are much larger than the typical sizes of the particles and the length scale of any interactions between them. All of the information about the particle-particle interactions was then assumed to be accounted for by macroscopic properties[3] of the fluid such as the viscosity and the osmotic pressure. While this principle of assuming a significantly large number of particles to behave as a fluid is commonly used in two fluid models described in the literature[159] the treatment here is slightly different; firstly because one aims to crate a two dimensional model and secondly, and more significantly because this particular model[3] aims to be as simple as possible[3]. One particular significant difference that arises in meeting both of these requirements is the coarse graining of all of the hydrodynamic interactions between the particles and the solvent and the particles and the surface into constant friction coefficients.

Since the draining process is quite slow in the fluids of interest it was assumed that both the particle fluid and the solvent were in the low Reynolds' number limit and thus both fluids must, independently, obey the Stokes equation[160],

$$-\boldsymbol{\nabla} p + \boldsymbol{\nabla} \cdot \boldsymbol{\sigma} + \mathbf{f}^{ext} = \mathbf{0}, \tag{3.1}$$

where p is the total pressure, $\mathbf{f}^{ext}$ is the sum of all external forces acting on the fluid, per unit volume, and $\boldsymbol{\sigma}$ is the symmetric part of the stress tensor, given by[160]

$$\boldsymbol{\sigma} = \eta \left[\boldsymbol{\nabla} \mathbf{v} + (\boldsymbol{\nabla} \mathbf{v})^T \right], \tag{3.2}$$

where η is the viscosity and $\mathbf{v}$ is the velocity field of the fluid in question. In the first instance both fluids were assumed to exhibit Newtonian flow behaviour, so η is constant for each fluid. Furthermore because the model is two dimensional the gradient operators here are assumed to act in the two dimensions parallel to the surface and the fluid us assumed to be uniform in the third. In section 3.1.2 the viscosity of the particle fluid will be generalised to be a function of strain rate.

In order to model the interactions between the two fluids and the interaction between the fluids and the substrate a number of external forces were added to the model. All of the forces acting on a fluid element are shown in figure 3.1.

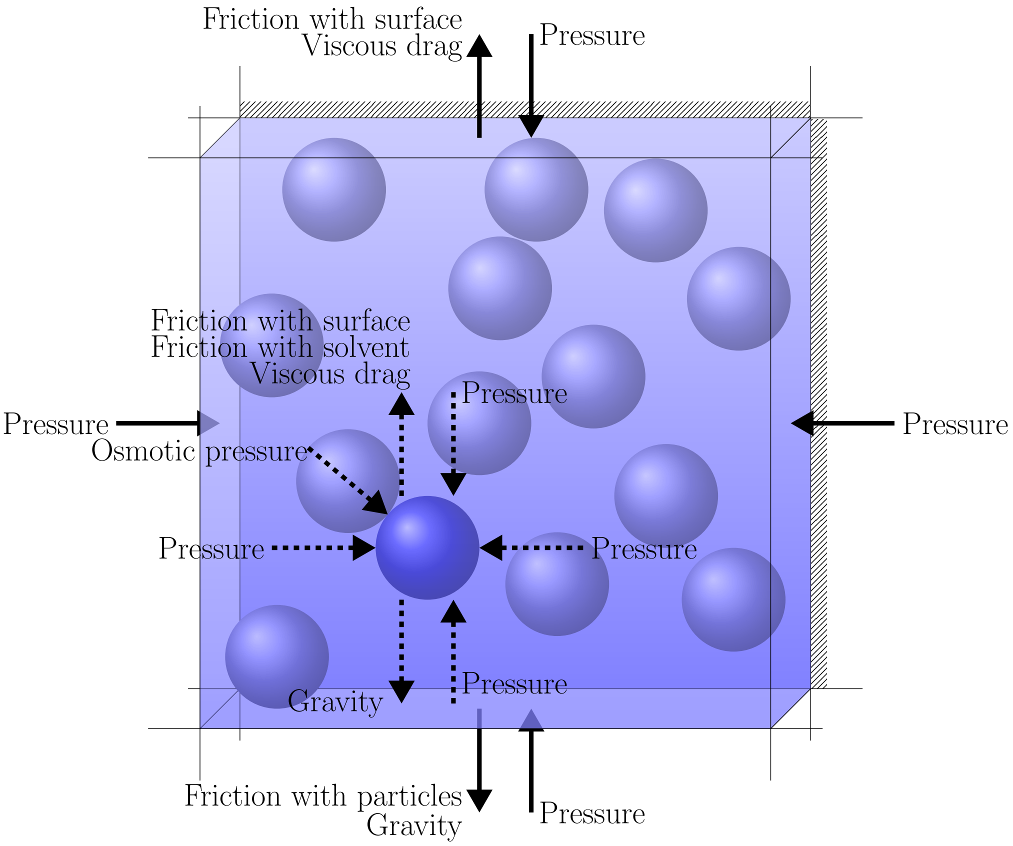

Figure 3.1: Schematic showing a small region of colloidal dispersion and the relevant forces. Here the dashed arrows correspond to forces on the particles while the solid arrows correspond to forces on the solvent.

In the particle fluid each particle feels a force due to gravity$^{(1)}$ which is proportional to the mass of the particle $\rho_{pi} V_{pi}$ and the acceleration $\mathbf{g}$. Thus the force on a fluid element is given by

$$\delta \mathbf{F}^{ext}_{acc} = \mathbf{g} \sum_{i=0}^{N\{\delta V\}} \rho_{pi} V_{pi}, \tag{3.3}$$

where N is the number of particles in the element of fluid, with volume δV, which is a function of the volume fraction of the particles and the volume of the fluid element. Now if one replaces ρ_{pi} and V_{pi} with average quantities, $\rho_p{}^{(2)}$ and V_p, and assumes that the region of fluid under consideration is large enough that it contains a sufficient number of particles such that they can be considered representative of the fluid as a whole, then the summation is trivial and one finds

$$\delta \mathbf{F}^{ext}_{acc} = \rho_p \mathbf{g} V_p N \left\{\delta V\right\}. \tag{3.4}$$

Each small element of the particle fluid, of volume δV, also feels a force due to friction with the surface. This is modelled simply as the negative of the force that would be felt by a rigid body moving in a viscous fluid, ignoring, for the sake of simplicity, any gradients within the flow perpendicular to the surface, and is proportional to the velocity of the

---

(1) Or acceleration of the whole system due to any external influence.

(2) Here buoyancy can be accounted for by replacing ρ_p with the difference between the density of the particles and the solvent.

fluid relative to the surface, $\mathbf{v}_p$,

$$\delta \mathbf{F}_{frp}^{ext} = -\zeta_p \mathbf{v}_p \delta V. \tag{3.5}$$

Here the constant of proportionality, ζ_p, is assumed to be the average friction constant describing all of the hydrodynamic lubrication interactions between the particles and the surface, and in the basic model is assumed constant. Naturally each small element of the particle fluid also experiences friction with the solvent which is proportional to the difference in the absolute velocities of the particles, $\mathbf{v}_p$, and of the solvent $\mathbf{v}_s$,

$$\delta \mathbf{F}_{frsp}^{ext} = -\zeta_{sp} \left(\mathbf{v}_p - \mathbf{v}_s\right) \delta V. \tag{3.6}$$

Again all of the hydrodynamic interactions are coarse grained into a single friction constant ζ_{sp}.

In order to calculate the total force on the particle fluid, $\delta \mathbf{F}_p$ one must combine these forces in a way that accounts for the fact that the fluid in any given region is a mixture of particle fluid and solvent. In some sense the force due to friction with the surface can be thought of as the force that would be felt by the pure particle fluid. However, since the fluid is not pure the force must be weighted to take account of what volume of particle fluid, NV_p exists in the total volume, δV of the fluid element. In a similar way the frictional force between the particles and the solvent depends on both the volume of particles and the volume of solvent in the region, δV. Thus the combined force due to all three contributions is

$$\delta \mathbf{F}_p^{ext} = \rho_p \mathbf{g} \frac{NV_p}{\delta V} \delta V - \zeta_p \mathbf{v}_p \frac{NV_p}{\delta V} \delta V - \zeta_{sp} \left(\mathbf{v}_p - \mathbf{v}_s\right) \frac{\delta V - NV_p}{\delta V} \frac{NV_p}{\delta V} \delta V. \tag{3.7}$$

Since the combined fluid is, in general, not homogeneous then in order to obtain the total force one must take the limit $\delta V \to 0$ and integrate over the entire fluid volume. Before doing this, however, it is worth noting that the weighting factor that has been used in equation 3.7 is in fact, by definition, the volume fraction of the particle fluid, $\phi = \frac{NV_p}{\delta V}$. Thus

$$\mathbf{F}_p^{ext} = \int \rho_p \mathbf{g} \phi - \zeta_p \mathbf{v}_p \phi - \zeta_{sp} \left(\mathbf{v}_p - \mathbf{v}_s\right) (1 - \phi)\, \phi dV. \tag{3.8}$$

Finally, in addition to these body forces, the particle fluid also experiences internal forces due to interactions between particles, such as particles colliding with, rolling over or sliding past other particles. These forces act at the surface of the element of fluid and produce stresses, which account for the first two terms in equation 3.1. In order to successfully combine these internal forces with the external forces already discussed one must define the total stress tensor, $\boldsymbol{\tau}$ such that $\delta \mathbf{F}_p^{int} = \hat{\mathbf{n}} \cdot \boldsymbol{\tau}$, where $\mathbf{F}_p^{int}$ is the sum of the internal forces and $\hat{\mathbf{n}}$ is the normal to the surface[39]. Then make use of the divergence theorem, resulting in

$$\mathbf{F}_p^{int} = \int \boldsymbol{\nabla} \cdot \boldsymbol{\tau} dV. \tag{3.9}$$

At this point it is convenient to separate the total stress into an isotropic pressure, p^{tot}, and an extra stress, $\boldsymbol{\sigma}$ which is proportional to the irrotational part of the flow field,

$$\boldsymbol{\sigma} = \eta_p \left[\boldsymbol{\nabla} \mathbf{v}_p + \left(\boldsymbol{\nabla} \mathbf{v}_p \right)^T \right]. \tag{3.10}$$

Here the viscosity, η_p, is the macroscopic, coarse grained, quantity that accounts for the resistance due to all sliding and rolling interactions. In the case of the particle fluid it is then convenient to subdivide the isotropic pressure, p^{tot}, even further to discriminate between the pressure in the combined fluid due to the fact that it is incompressible, p, and the osmotic pressure in the particle fluid due to particle collisions, π, this will be discussed in more detail in section 3.1.1.1. As with the external force one must take care to weight the force according to the proportion of the particle fluid in the volume element under consideration. This means that the extra stress, $\boldsymbol{\sigma}$, and the pressure due to the incompressibility of the combined fluid, p, must be multiplied by ϕ. However since the osmotic pressure is only felt by the particle fluid and is itself a function of ϕ this does not need to be weighted. Making the substitution

$$\boldsymbol{\tau} = -\left(p + \pi\right) \mathbf{I} + \eta_p \left[\boldsymbol{\nabla} \mathbf{v}_p + \left(\boldsymbol{\nabla} \mathbf{v}_p \right)^T \right] \tag{3.11}$$

into equation 3.9 and weighting the forces results in

$$\mathbf{F}_p^{int} = \int -\phi \boldsymbol{\nabla} p + \boldsymbol{\nabla} \pi + \phi \boldsymbol{\nabla} \cdot \left(\eta_p \left[\boldsymbol{\nabla} \mathbf{v}_p + \left(\boldsymbol{\nabla} \mathbf{v}_p \right)^T \right] \right) dV. \tag{3.12}$$

Now by combining equations 3.12 and 3.13, for the external and internal forces respectively, one finds that the total force on the particle fluid is given by

$$\mathbf{F}_p = \int \phi \left[\rho_p \mathbf{g} - \zeta_p \mathbf{v}_p - \zeta_{sp} (1-\phi)(\mathbf{v}_p - \mathbf{v}_s) - \boldsymbol{\nabla} p + \frac{1}{\phi} \boldsymbol{\nabla} \pi + \boldsymbol{\nabla} \cdot \left(\eta_p \left[\boldsymbol{\nabla} \mathbf{v}_p + \left(\boldsymbol{\nabla} \mathbf{v}_p \right)^T \right] \right) \right] dV. \tag{3.13}$$

As with the particle fluid the solvent also feels a force due to gravity, or acceleration of the system, and a force due the friction with the surface, and, naturally, the negative of the force felt by the particles due to friction with the solvent. These is also stress due to viscous forces and pressure due to the fact that the combined fluid is incompressible. As before, in order to obtain the total force one must multiply the sum of these forces by the volume fraction of solvent, $1 - \phi$. By doing so one obtains

$$\mathbf{F}_s = \int (1-\phi) \left[\rho_s \mathbf{g} - \zeta_s \mathbf{v}_s - \zeta_{sp} \phi \left(\mathbf{v}_s - \mathbf{v}_p \right) - \boldsymbol{\nabla} p + \boldsymbol{\nabla} \cdot \left(\eta_s \left[\boldsymbol{\nabla} \mathbf{v}_s + \left(\boldsymbol{\nabla} \mathbf{v}_s \right)^T \right] \right) \right] dV \tag{3.14}$$

for the total force acting on the solvent, where ρ_s is the density of the solvent and ζ_s is the friction constant which accounts for the interactions between the solvent and the surface. In terms of the forces at work on their respective fluids, equations 3.13 and 3.14 are identical except for the fact that the solvent experiences no osmotic pressure.

In the low Reynolds' number limit, where there are no inertial forces and the fluid is always in steady flow, $\mathbf{F}_p = \mathbf{F}_s = \mathbf{0}$. Therefore, since the volume of fluid being considered is arbitrary, the integrands of equations 3.13 and 3.14 must be zero. Hence dividing through by the volume fraction of the fluid in question results in two coupled, vector, equations describing force balance in the two fluid system [3]:

$$\rho_p \mathbf{g} - \zeta_p \mathbf{v}_p - \zeta_{sp} (1-\phi)(\mathbf{v}_p - \mathbf{v}_s) - \boldsymbol{\nabla} p - \frac{1}{\phi}\boldsymbol{\nabla}\pi + \boldsymbol{\nabla}\cdot\left(\eta_p\left[\boldsymbol{\nabla}\mathbf{v}_p + (\boldsymbol{\nabla}\mathbf{v}_p)^T\right]\right) = \mathbf{0} \tag{3.15a}$$

$$\rho_s \mathbf{g} - \zeta_s \mathbf{v}_s - \zeta_{sp} \phi (\mathbf{v}_s - \mathbf{v}_p) - \boldsymbol{\nabla} p + \boldsymbol{\nabla}\cdot\left(\eta_s\left[\boldsymbol{\nabla}\mathbf{v}_s + (\boldsymbol{\nabla}\mathbf{v}_s)^T\right]\right) = \mathbf{0}. \tag{3.15b}$$

In two dimensions these provide four equations for the six unknowns, $\mathbf{v}_p$, $\mathbf{v}_s$, p and ϕ. As is common practice for solving the Stokes equation these are complemented by an equation which enforces incompressibility. In this case, where there are two fluids, this condition must be treated with care. While it is true that the combination of the two fluids is incompressible it is certainly not true that each fluid is incompressible since it is possible for one of the fluids to expand provided that the other fills the vacant space. Thus the incompressibility condition states that any flux of one fluid out of a region must be matched by an equal flux of the other fluid into that region, meaning the net flux is zero. This can be expressed mathematically as

$$\boldsymbol{\nabla}\cdot\left[\phi\mathbf{v}_p + (1-\phi)\,\mathbf{v}_s\right] = 0. \tag{3.16}$$

The final equation of this model can be derived by enforcing the conservation of particles which simply states that the rate of increase of the volume fraction, $\frac{\partial\phi}{\partial t}$, in a region of fluid must be equal to the net flux of particles into that region, $-\boldsymbol{\nabla}\cdot(\phi\mathbf{v}_p)$. This can be expressed as

$$\frac{\partial\phi}{\partial t} + \boldsymbol{\nabla}\cdot(\phi\mathbf{v}_p) = 0. \tag{3.17}$$

It is worth noting that there is no similar equation for the solvent as conservation of solvent is implied by the combination of equations 3.16 and 3.17. This can be seen immediately by substituting equation 3.17 into equation 3.16.

Taking all of this into consideration one finally arrives at a closed system of equations forming Evans' original model(3) of a particle-laden solvent [3]:

$$\rho_p \mathbf{g} - \zeta_p \mathbf{v}_p - \zeta_{sp} (1-\phi)(\mathbf{v}_p - \mathbf{v}_s) - \boldsymbol{\nabla} p - \frac{1}{\phi}\boldsymbol{\nabla}\pi + \boldsymbol{\nabla}\cdot\left(\eta_p\left[\boldsymbol{\nabla}\mathbf{v}_p + (\boldsymbol{\nabla}\mathbf{v}_p)^T\right]\right) = \mathbf{0} \tag{3.18a}$$

$$\rho_s \mathbf{g} - \zeta_s \mathbf{v}_s - \zeta_{sp} \phi (\mathbf{v}_s - \mathbf{v}_p) - \boldsymbol{\nabla} p + \boldsymbol{\nabla}\cdot\left(\eta_s\left[\boldsymbol{\nabla}\mathbf{v}_s + (\boldsymbol{\nabla}\mathbf{v}_s)^T\right]\right) = \mathbf{0} \tag{3.18b}$$

$$\boldsymbol{\nabla}\cdot\left[\phi\mathbf{v}_p + (1-\phi)\,\mathbf{v}_s\right] = 0 \tag{3.18c}$$

$$\frac{\partial\phi}{\partial t} + \boldsymbol{\nabla}\cdot(\phi\mathbf{v}_p) = 0. \tag{3.18d}$$

Like Stokes' equations for a simple incompressible fluid these equations only depend on the derivatives of the pressure. Thus it is only possible to solve for the pressure up to the addition of a constant reference pressure [3]. This will be discussed in more detail in section 4.1.3.1 in relation to solving a discrete version of equation set 3.18.

It is worth noting at this point that these equations couple together the velocities of the two fluids with the particle volume fraction. The origin of this coupling goes back to

---

(3) The following sections will go on to describe how this model was adapted to suit the present work as well as the additions that were made to the model.

the fact that the force that each fluid contributes to the overall force must be weighted by the amount of that fluid in any given volume fraction, and similarly to the important point that the incompressibility condition relates to the combined fluid and not to its constituent parts.

3.1.1.1 Modelling the Osmotic Pressure

In the most basic version of the model the various constants are taken to be intrinsic properties of the particular system in question and as such these can be tuned to model specific fluids, meaning that the only function which requires a mathematical description is the osmotic pressure, π. As was previously stated this is the macroscopic quantity that models the collisions between particles. Since this model is concerned with a macroscopic description of the fluid the osmotic pressure can be thought of as being a thermodynamic quantity, namely the pressure in a "gas" of colloidal particles. For particles whose only interaction is steric repulsion the free energy density, f, at low volume fractions is that of an ideal gas, $f \propto \phi \ln \phi$, and must diverge as the volume fraction reaches the limit of random close packing[36]. Thus the free energy density must be of the form show in figure 3.2.

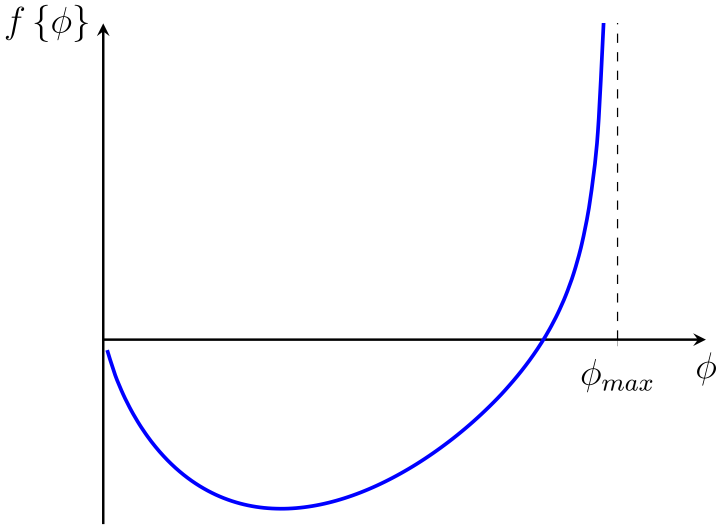

Figure 3.2: Sketch of the free energy density as a function of volume fraction for a gas of colloidal particles that interact by steric repulsion only.

Since the pressure is defined as

$$p = -\frac{\partial F}{\partial V} \tag{3.19}$$

then the osmotic pressure is given by

$$\pi = \phi \frac{\partial f}{\partial \phi} - f. \tag{3.20}$$

This implies that it must be negative for small volume fractions, and tend to zero at $\phi = 0$, and be positive for large volume fractions, and diverge at $\phi = \phi_{max}$. However this lower limit presents a problem computationally since it does not guard against the possibility of negative volume fractions, for this reason a function that diverges at $\phi = 0$ was used. In effect this function guarantees that particles will be drawn in to a region of very low concentration from the surrounding area, which is achieved by diffusion in real systems(4).

---

(4) Diffusion will be discussed in more detail later in this section.

A simple function which possesses these properties is a piecewise combination of power laws,

$$\pi = \begin{cases} -\left(\frac{1}{\phi} - \frac{1}{\phi_l}\right)^2 & \phi < \phi_l \\ 0 & \phi_l \leq \phi \leq \phi_u \\ \left(\frac{1}{\phi_{max} - \phi} - \frac{1}{\phi_{max} - \phi_u}\right)^2 & \phi > \phi_u \end{cases}, \tag{3.21}$$

where ϕ_u and ϕ_l define the upper and lower points at which the osmotic pressure is non-zero respectively. Figure 3.3 shows a sketch of this function.

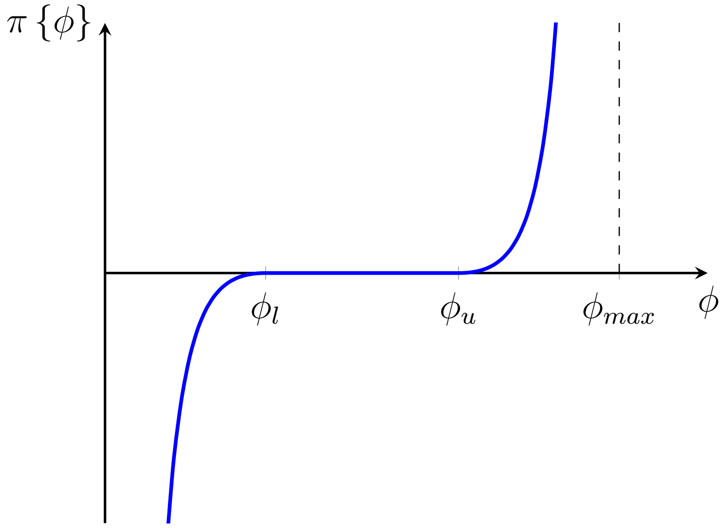

Figure 3.3: Sketch of the osmotic pressure, used in the model of a particle-laden fluid, as a function of volume fraction.

Here the power of two is used to ensure that the derivative of the function goes to zero at the cut-off points to prevent a sharp change. Although the exact form of this function has no real physical motivation, it does have all of the desired physical properties and has the added advantage of been relatively efficient to evaluate computationally[3]. Furthermore the two tuneable parameters, ϕ_l and ϕ_u, provide a simple means of modelling different types of particles, since the point at which the osmotic pressure begins to increase can be thought of as being related to the rigidity of the particles. Using this form of the osmotic pressure one is essentially limited to considering granular media, which have no attractive interactions and are too large to be affected by Brownian forces. This is the motivation behind the flat region of the osmotic pressure curve, since having an osmotic pressure with a positive gradient across the whole range would effectively model a diffusion process, where the pressure is high in regions of high volume fraction. This will be discussed further in section 3.1.2.5.

3.1.2 Additional Features

3.1.2.1 Non-Newtonian Viscosity

Colloidal fluids are observed to exhibit a wide variety of flow behaviours[64] including: shear thinning, shear thickening and Newtonian flow. They are also know to change their flow response as a function of shear rate. In order to try to capture the essence of this rich variety of different responses in this simple model the shear dependent particle viscosity,

$\eta_{\dot\gamma}$, was defined as a piecewise combination of power laws[64],

$$\eta_{\dot\gamma} = \begin{cases} 1 & \dot\gamma < \dot\gamma_A \\ \eta_A \dot\gamma^{-a} & \dot\gamma_A \leq \dot\gamma < \dot\gamma_B \\ \eta_B & \dot\gamma_B \leq \dot\gamma < \dot\gamma_C \\ \eta_C \dot\gamma^{b} & \dot\gamma_C \leq \dot\gamma < \dot\gamma_D \\ \eta_D \dot\gamma^{-c} & \dot\gamma_D \leq \dot\gamma \end{cases}, \tag{3.22}$$

where a, b and c are the constant exponents which determine the extent to which the fluid shear thins or shear thickens, $\dot\gamma_A$, $\dot\gamma_B$, $\dot\gamma_C$ and $\dot\gamma_D$ are the shear rates at which the system changes from one regime to another and η_A, η_B, η_C and η_D are constants which determine the relative magnitude of the viscosity in each regime, these are not free parameters, however, as they must be chosen such that the different regimes join together smoothly. In order to achieve this one requires that $\eta_A = \dot\gamma_A^a$, $\eta_B = \dot\gamma_A^a \dot\gamma_B^{-a}$, $\eta_C = \dot\gamma_A^a \dot\gamma_B^{-a} \dot\gamma_C^{-b}$ and $\eta_D = \dot\gamma_A^a \dot\gamma_B^{-a} \dot\gamma_C^{-b} \dot\gamma_D^{b+c}$. It is worth pointing out that in equation 3.22 the signs of the exponents have been chosen in order to agree with the flow profiles described in references 64 and 69, but a, b and c can, in principle, take any value. The form of this function[64], when a, b and c take positive values, is given in figure 3.4.

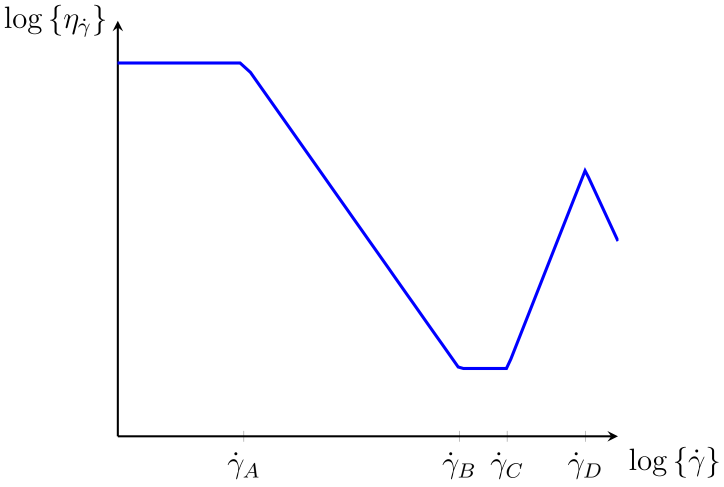

Figure 3.4: Sketch of the shear rate dependent viscosity as a function of the shear rate for the model described in equation 3.22.

Section 3.4 describes a constitutive relation which provides microscopic motivation for some of the features of this figure.

In equation 3.22 the function is normalised such that the zero shear rate viscosity is one. This means it can be combined with other functions which describe the behaviour of the viscosity, for example the volume fraction dependent viscosity, η_ϕ, as discussed in section 3.1.2.2, in a multiplicative way and then the total combined viscosity can be scaled by a constant which is a well defined quantity, the zero shear rate viscosity, η_0. This means that, ultimately, the particle viscosity, η_p, is given by

$$\eta_p = \eta_0 \eta_{\dot\gamma} \eta_\phi. \tag{3.23}$$

As with the osmotic pressure, described in section 3.1.1.1, this function has not been chosen for strict adherence to a well established physical model, but rather because it is relatively simple, computationally inexpensive to evaluate and flexible whilst still capturing all the essential features which are commonly observed for the flow behaviour of colloidal dispersions. As section 5.1.2 will show despite its rather simple nature this expression can be easily adapted to model the flow behaviour predicted by a physically motivated model of the microscopic interactions at the particle level.

Due to the fact that the model described in section 3.1.1 aims to describe a thin film the shear rate, $\dot{\gamma}$, in equation 3.22 is assumed to be dominated by the contribution whose gradient direction is perpendicular to the plane as this will have the smallest length scale and so the greatest velocity gradient[3]. Thus

$$\dot{\gamma} \approx \frac{|\mathbf{v}_p|}{\tau}, \tag{3.24}$$

where τ is the film thickness, which is assumed to be constant throughout the fluid. Strictly speaking the value used for $\dot{\gamma}$ should include contributions from velocity gradients in all directions, which could be achieved by taking the determinant of the velocity gradient tensor, however, this would be costly computationally and would be unnecessary since this model seeks only to capture the essential, qualitative, features of the flow, which it can do comfortably with only an approximation of the magnitude of the shear rate, and not calculate exact numerical values. Thus, in summary, while the viscous forces are calculated using gradients in the two directions parallel to the plane(5) the shear rate used in the calculation of the viscosity itself is that which has its gradient direction perpendicular to the plane.

It is also worth pointing out here that, in practice, limits were set on the viscosity to allow for parameters to be chosen such that a wide range of viscocities were explored within the typical range of velocities without allowing extreme cases to destabilise the numerical algorithm used to simulate the flow.

3.1.2.2 Volume Fraction Dependent Viscosity

As well as having shear rate dependence the flow properties of colloidal dispersions also depend heavily on their volume fraction, ϕ. Section 2.4 covered a range of different models which have been proposed in the literature to account for this phenomenon. However, in this simple model the semi-continuum[42] form proposed in reference 42,

$$\eta_\phi = \left(1 - \frac{\phi}{\phi_{max}}\right)^{-[\eta]\phi_{max}}, \tag{3.25}$$

shall be used. In equation 3.25 $[\eta]$ is the intrinsic viscosity, typically $[\eta] \approx 2.5$ and ϕ_{max} denotes the volume fraction at which the viscosity diverges, in practice this was typically taken to be the same value as the volume fraction at which the osmotic pressure diverges, but could in general take a different value, usually that of the glass transition[33,42,123].

As with the other functions used in this model equation 3.25 is a semi-empirical equation, which was chosen because it is relatively simple and inexpensive to evaluate whilst retaining the essential features of increasing slowly at low concentrations before diverging at the maximum volume fraction possible in the system. The form of the function is shown in figure 3.5.

---

(5) The resistance to flow due to gradients perpendicular to the plane is already accounted for by the fraction coefficients of the respective fluids.

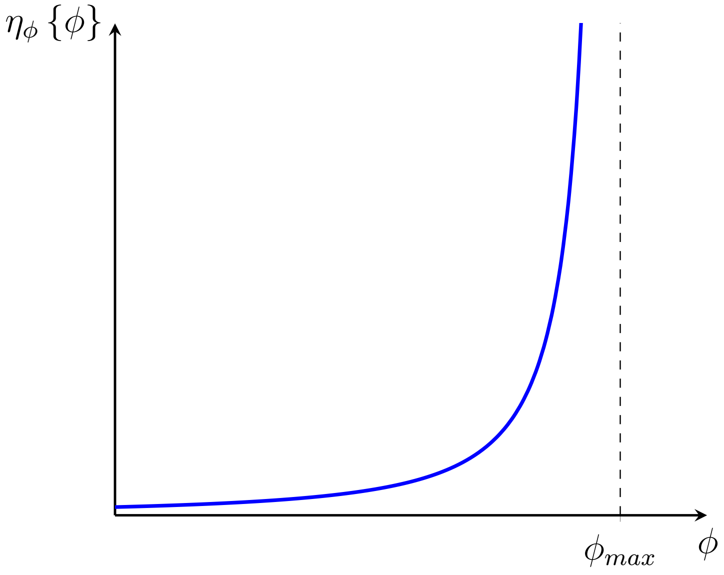

Figure 3.5: Sketch of the volume fraction dependent viscosity as a function of the volume fraction for the model described in equation 3.25.

3.1.2.3 Static Friction

Although spherical particles can roll[67], sliding is an important part of the particle motion when considering a particle-laden fluid draining over a surface. Firstly because the particles need not be perfectly spherical and thus sliding may occur in preference to rolling, friction with the solvent may add resistance or prevent particles from rolling altogether and also, as discussed in section 3.1.2.4, rolling may not be possible, even for spherical particles, if the volume fraction is sufficiently high that many of the particles are in contact with others.

In section 3.1.1 the friction coefficient describing the interaction between the particles and the surface is assumed constant. However, this would not be the case in a real system firstly because of the complex hydrodynamic interactions between the particles and the surface, which is beyond the scope of this model(6), but also due to the fact that the particles are constantly stopping and starting as they travel over the surface[79]. This means that at any one time there are a certain number of particles which experience the, higher, static friction[79] coefficient while the rest experience the dynamic friction coefficient.

At the individual particle level[79] the transition between static and dynamic friction is discontinuous[79]. However it is reasonable to assume that the net, effective, friction coefficient for a given volume of the particle fluid will be a continuous function of the proportion of particles which are at rest with respect to the surface. This in turn will be related to the average velocity of the particle fluid in that region. When the fluid as a whole is at rest on the surface it is likely that the vast majority of the particles in it will be at rest as well and thus the contribution from the static friction coefficient will dominate. Whereas when the fluid velocity is large most of the particles will be moving over the surface and thus the dominant contribution to the overall friction coefficient will come from dynamic friction, with a smooth transition between the two as more and more particles begin to move.

---

(6) And hence why the resistance due to particles rolling within the solvent is not considered here.

A simple mathematical model of this was created using a translated Gaussian function of the form

$$\zeta_{p\mathbf{v}_p} = (\zeta_0 - \zeta_\infty)\, e^{-\left(\frac{|\mathbf{v}_p|}{v^*}\right)^2} + \zeta_\infty, \tag{3.26}$$

where ζ_0 is the coefficient of static friction between the particles and the surface, ζ_∞ is the coefficient of dynamic friction and v^* is a constant which characterises the velocity scale over which the change occurs. Consequently, as a measure of the width of the distribution, v^* can be thought of as a means of quantifying the typical fluid velocity required to force a static particle to begin sliding, since in essence it represents the velocity above which more than a certain proportion of the particles are moving. The features of equation 3.26 can be seen in figure 3.6.

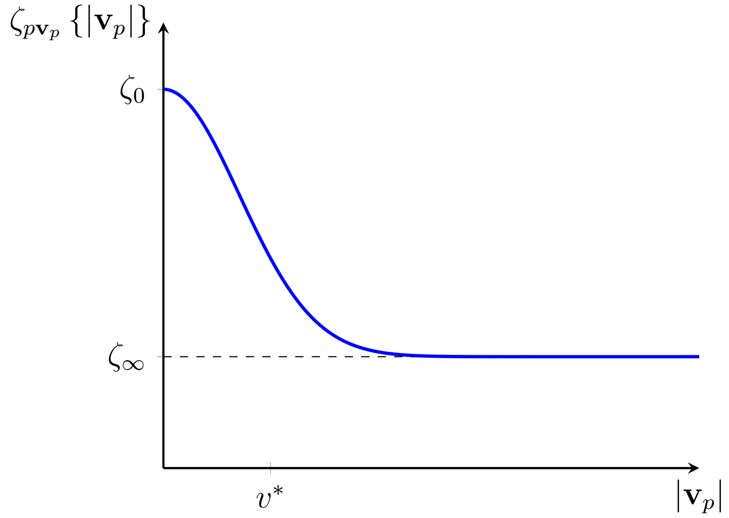

Figure 3.6: Sketch of the velocity dependent friction coefficient as a function of the magnitude of the particle velocity for the model described in equation 3.26.

As with the rest of this model the function described by equation 3.26 is purely empirical and was chosen simply for the fact that it provides a smooth transition between the two extreme cases and a tuneable characteristic length scale for that transition. Although the use of a friction coefficient makes little sense in the description of the discontinuous transition between dynamic and static friction at the individual particle level, on the scale of a fluid element containing a significant number of particles the product of the fluid velocity with an friction coefficient that increases rapidly as the velocity of that element tends to zero does have the desired phenomenological behaviour, in that it produces a disproportionally large resistive force at low velocities.

3.1.2.4 Volume Fraction Dependent Friction

If the particles can roll to reduce their effective friction coefficient then contact between particles can significantly increase the effective friction coefficient because the friction at the contact point either introduces a new source of friction or if it is strong enough can inhibit the motion of the particles and stop them rolling[67] altogether, forcing them to slide as a cluster rather than roll as they would as individuals. These different scenarios are shown in figure 3.7.

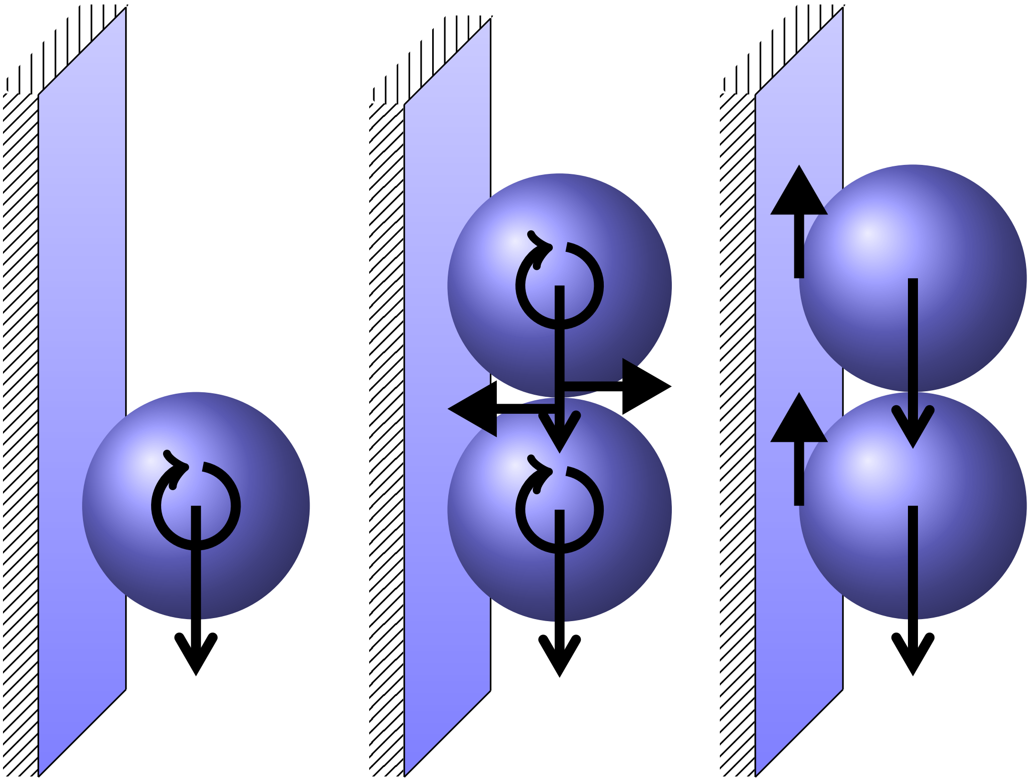

(a) Particle freely rolling over the surface.

(b) Two particles in contact rolling over the surface causing friction at the point of contact.

(c) Two particles in contact sliding over the surface.

Figure 3.7: Sketches showing the frictional forces, translational and rotational velocities for particles moving over the surface in different scenarios. Here the open headed straight arrows represent the translational velocity, the curved arrows represent the rotational velocity and the triangular headed arrows represent the forces due to friction.

Clearly as the volume fraction increases the number of particles that cannot roll due to contact with other particles will increase. Hence the effective friction constant describing the interaction between the particles and the surface must also increase. In order to model this the total friction coefficient for the particle surface interaction was taken to be the product of the velocity dependent friction coefficient, $\zeta_{p\mathbf{v}_p}$, given by equation 3.26, and the volume fraction, ϕ.

$$\zeta_p = \phi \zeta_{p\mathbf{v}_p}. \tag{3.27}$$

This makes good sense at low volume fraction since if one considers any given particle and asks how likely it is to be in contact with another particle this is simply proportional to the number of other particles in the region and hence ϕ. At high volume fraction of course there is the potential for multi-particle contacts, which complicates matters somewhat. However, because of the complicated nature of these interactions, a full treatment would not be in keeping with the simplicity of the original model.

3.1.2.5 Diffusion

As mentioned in section 3.1.1.1 the basic model of the particle-laden fluid is in essence a model of granular particles, which do not experience Brownian forces, in a solvent. At the macroscopic level Brownian forces manifest themselves by causing diffusion[36]. Therefore in order to expand the basic model to include smaller particles, like those that form gels[2,44,70,80,122], one must add diffusion. This can be done simply by changing the form of the function used to model the osmotic pressure.

In order to motivate this model physically one may think of the particles as an ideal gas with a certain amount of thermal energy, k_BT. Then simply by replacing the pressure in the ideal gas equation with the osmotic pressure one arrives at

$$\pi_D \propto \phi k_B T, \tag{3.28}$$

where π_D denotes the diffusive contribution to the osmotic pressure. This can then be added to the contribution due to entropy and steric hindrance, modelled by equation 3.21. Figure 3.8 gives a graphical representation of the osmotic pressure when diffusion is included.

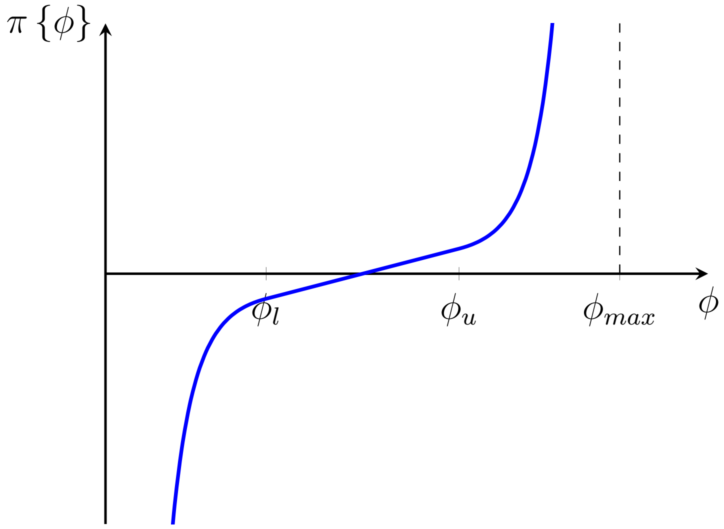

Figure 3.8: Sketch of the osmotic pressure as a function of volume fraction used in the model of a particle-laden fluid where the particles are able to diffuse.

3.1.2.6 Attractive Inter-Particle Forces

Many colloidal particles experience attractive inter-particle forces which can arise from any number of different sources such as: charges on their surfaces, depletion interactions and Van der Waals' forces[36]. An effective attractive force may also be caused by the surface tension in the solvent at the free surface[73,101], due to the fact that clusters of particles cause less curvature of the solvent-air interface than the same number of particles would if they were spread out. In order to keep the model simple and in-keeping with the models presented thus far for the properties of the particle-laden fluid all attractive forces will be treated in the same, phenomenological, way, irrespective of their origin. In section 3.1.2.5 the ideal gas equation was used to model the effect of diffusive processes on the osmotic pressure in the particle fluid. In order to include attractive interactions in the model one can simply replace equation 3.28 with the Van der Waals' equation.

$$\left(\pi_A + a_{vdW}\phi^2\right) \propto \frac{\phi}{1 - b_{vdW}\phi} k_B T, \tag{3.29}$$

where a_{vdW} is a measure of the attractive forces, b_{vdW} is a measure of the volume occupied by each particle and π_A is the osmotic pressure due to particles with attractive forces. Since this model already includes a contribution to the osmotic pressure due to excluded volume, and in order to keep the expression simple, b_{vdW} was fixed at zero, essentially modelling point like particles. Thus equation 3.29 can be rewritten as

$$\pi_A \propto \phi k_B T - a_{vdW}\phi^2. \tag{3.30}$$

The form of this function, both with and without the diffusive contribution is shown in figure 3.9.

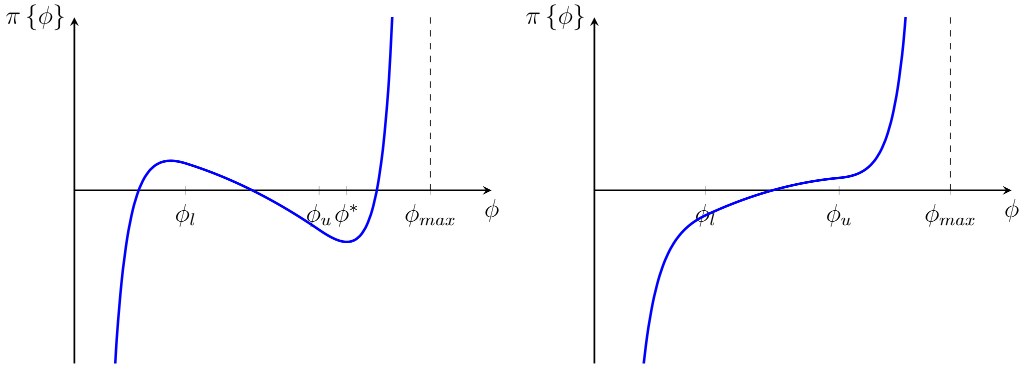

(a) Low temperature.

(b) High temperature.

Figure 3.9: Sketches showing the osmotic pressure as a function of volume fraction used in the model of the of the particle-laden fluid where the particles experience attractive inter-particle forces.

It is worth noting that by comparing figures 3.9a and 3.9b one can see that there is a phase transition as a function of temperature. In figure 3.9a where the temperature is low and the attractive interactions dominate there is a preferred volume fraction ϕ^* where the osmotic pressure is minimised. This turing point in the osmotic pressure curve implies the possibility of a region in the equilibrium phase diagram where phase separation occurs, as a means of minimising the global free energy, whereas at high temperatures the diffusive contribution dominates and the osmotic pressure increases monotonically with volume fraction, essentially approaching the ideal gas limit.

In systems with no external driving force, **g**, the presence of attractive forces between the particles can lead to phase separation, by spinodal decomposition[36,78,118]. Here the presence of the interface between the two phases incurs a free energy cost which is modelled by the addition of a term proportional to the square of the gradient of the volume fraction and the surface energy[36,78,118]. By using equation 3.19 one finds that the same effect can be achieved by adding a term proportional to $\phi\nabla^2\phi$ to the osmotic pressure, making the total contribution to the osmotic pressure from attractive interactions

$$\pi_A \propto \phi k_B T - a_{vdW}\phi^2 - \kappa_S\phi\nabla^2\phi, \tag{3.31}$$

where κ_S is a constant that is related to the surface free energy for the particular phases in question(7).

---

(7) It is worth noting that in this simple phenomenological model a_{vdW} and κ_S are merely used to control the relative contributions of the different forces and as such other constants, such as constant factors and the volume of the particles, have been absorbed into them. Thus they scale with, but are not necessarily equal to, the physical parameters they represent.

3.2 Complexity Measures

As described in section 2.1 many different kinds of complexity measure have been proposed in the literature, for many different and varied purposes. Of the three classes [91] of measure described in section 2.1 the measures which are most relevant to two dimensional patterns, like those produced by the particle-laden fluid, are convex measures [1,63,83,87,91,92] which treat both highly ordered and highly disordered states as having low values of complexity. The rationale for this goes back to one's intuitive impression of what should be considered complex in terms of visual appearance. Typically one would not consider a checker board pattern very complex nor would one consider a totally random pattern complex, but one might attribute a higher value of complexity to something in-between, perhaps where there was clearly some long range structure, but not an obvious repeat unit. In terms of physical systems this means that both a perfect crystal and an ideal gas would be attributed very low values of complexity while something like a fractal gel network or the nematic phase of liquid crystals would be attributed a very high value. As well as agreeing with intuition about the visual appearance of these patterns such a measure also agrees well with how one might perceive a model of the underlying physics behind such a system. The physics behind the shapes of simple crystals, where the bonds between the constituent particles determine the shape, and ideal gases, where the particle position is entirely random, is well understood. Conversely the physics of systems such as gels, where thermal and inter-particle forces are comparable, and liquid crystals where there is direction dependent order is far more complex and requires far more sophisticated modelling.

One theme which appears regularly in discussions of complexity, especially relating to physical systems is that of order and disorder, in fact this has played an important role in the examples discussed above. A natural approach for calculating the complexity of a system then is to consider the entropy of the system as this too provides a measure of the disorder. Entropy is well defined in a thermodynamic sense, in terms of the number of states available to the system. However, the same argument can be generalised to consider the information content of a system by using the measure proposed by Shannon in reference 99. The Shannon entropy, H is given by [99]

$$H = -K \sum_{i=1}^{N} p_i \log \{p_i\}, \tag{3.32}$$

where p_i is the probability of finding the system in state i if there are N possible states and K is a positive constant(8). As well as being closely related to the thermodynamic definition of entropy, the Shannon entropy [99] has three important features [99] that make it the natural choice for a description of the amount of information in a system. It is continuous in p_i, as it must be since p_i could take any value [99]. If all the probabilities, p_i, are equal then it increases monotonically as a function of the number of states [99], this means that systems with more available states have a greater amount of disorder, which agrees well with intuition. Finally if the system must pass through one state to reach

---

(8) If one considers a thermodynamic system where the probability represents the probability of finding the system in a given state, the constant K takes on the value of Boltzmann's constant and H is exactly equivalent to the Gibbs' entropy.

another and this process is broken down into separate processes then the value of H in the final state must be equivalent to the weighted sum of its values in the states of the multi-stage process[99].

It is clear from looking at equation 3.32 that the Shannon entropy alone is not the kind of convex measure required in the analysis of two dimensional patterns, as it increases monotonically with the amount of disorder in the system[99]. However, it does form a crucial part of both of the measures of complexity which will be discussed here[83,99]. Thus understanding its properties is vital in understanding the properties of the two convex complexity measures used. One of the key features of the Shannon entropy is that it depends on a probability distribution, p_i[99]. This means that in order to evaluate the complexity one must summarise the pattern in terms of a probability distribution[90]. Three different methods of doing this were explored in the present work and these will be presented later in this section. It is also worth noting that by choosing the Shannon entropy one is making a further choice about which sub category of complexity measure to use. That is to say there are other ways of calculating complexity that do not involve probability distributions. One such example is the algorithmic complexity[88], described in section 2.1. The reason for the choice of a measure based on a probability distribution here is that the Shannon entropy itself is well physically motivated and has strong links with one's intuition about order and disorder in the system, whereas the choice of a repeat unit, especially in more than one dimension, is somewhat arbitrary, particularly when one factors in the tolerances that would have to be applied to obtain anything meaningful from a model where continuous variables are being assessed. Furthermore using a probability distribution which depends upon the entire system is far less susceptible to the influence of extreme values, for example two regions which happen to be exactly the same in an otherwise random distribution implying the presence of some significant structure when there is none.

The Shannon entropy provides an excellent starting point for deriving a complexity measure that is applicable to the probability distributions that characterise two dimensional patterns, but it cannot be used in isolation as it increases with the amount of disorder in the system and so attributes a very high value to random distributions which is not desirable, as discussed earlier. In order to resolve this one requires another quantity which decreases with the amount of disorder in the system. Two such choices shall be considered here and these will result in two different complexity measures. Firstly if one follows the description of the Shannon entropy given in reference 99 in terms of the amount of information in the system then one can, in a similar way to reference 99, arrive at a measure of the amount of redundant information, R, in the system,

$$R = 1 - \frac{H}{H_m}, \tag{3.33}$$

where H_m is the maximum entropy that could be obtained from the N possible states(9). Clearly this quantity has the required property that it decreases as the system becomes more disordered. Reference 99 explains this in terms of the number of characters in a string of text that can be inferred from the other characters and a knowledge of the

---

(9) Clearly the maximum entropy state occurs when all the probabilities are equal, $p_i = \frac{1}{N}, \forall i$.

language. For example in English the letter Q is nearly always followed by a U, hence the U is redundant information. Thus in essence it is a measure of how much the information about the system could be compressed without loss. These two quantities can be combined in a multiplicative way to produce a convex complexity measure[91], which shall hereafter be referred to as the information compressibility measure, or information measure, C_{ICC}, given by

$$C_{ICC} = -K\left(1 + \frac{1}{\log\{N\}}\sum_{i=1}^{N} p_i \log\{p_i\}\right)\sum_{i=1}^{N} p_i \log\{p_i\}\,. \tag{3.34}$$

It is clear when one considers the two extreme cases that multiplication is indeed the correct means of combining these two quantities into a meaningful measure of complexity since the complexity must be zero at both extremes. Furthermore one can see from the form of the equation 3.34 that this is clearly a parabolic function of the Shannon entropy and hence the amount of disorder.

Another popular measure of complexity used in the literature is the measure proposed by López-Ruiz, Mancini and Calbet[83]. As with the information compressibility measure this measure, known as the LMC measure, is comprised of the Shannon entropy multiplied by a quantity which decreases with the amount of disorder in the system. In the LMC measure this quantity, referred to as the disequilibrium, D, is defined as[83].

$$D = \sum_{i=1}^{N}\left(p_i - \frac{1}{N}\right)^2 . \tag{3.35}$$

As one can see from equation 3.35 this is essentially a measure of how far the probability distribution is from uniformity. Clearly the quantity in the summation must be squared otherwise D would always be zero. As with the redundancy in the information compressibility measure the disequilibrium multiplies the Shannon entropy to form the LMC complexity measure.

$$C_{LMC} = -K\left(\sum_{i=1}^{N}\left[p_i - \frac{1}{N}\right]^2\right)\left(\sum_{i=1}^{N} p_i \log\{p_i\}\right). \tag{3.36}$$

At this point it is worth considering the relationship between the two measures presented here; clearly since both make use of the Shannon entropy all the differences in their behaviour stem from the difference between the redundancy and the disequilibrium as measures of order in the system[91]. It makes sense then that in a highly disordered state the two measures should tend towards giving the same result[91]. This becomes clear if one expands R about the uniform state[91]

$$R \approx \left(\frac{1}{\log\{N\}} + 1\right)\sum_{i=1}^{N}\left(p_i - \frac{1}{N}\right) + \frac{1}{2}\frac{N}{\log N}\sum_{i=1}^{N}\left(p_i - \frac{1}{N}\right)^2 , \tag{3.37}$$

where the summation in the first term is clearly zero leaving

$$R \approx \frac{1}{2}\frac{N}{\log N} D. \tag{3.38}$$

Finally since the base of the logarithm is arbitrary it could, in principle, be chosen such that the constant of proportionality in equation 3.38 is unity for a given value of N.

3.2.1 Creating a Probability Distribution from Two Dimensional Patterns

Since both of the complexity measures used in this work depend upon probability distributions one requires a means of summarising a two dimensional pattern in terms of a probability distribution which characterises its appearance[90]. The first step towards tackling this problem is to identify a well defined mathematical quantity which can be thought of as characterising the appearance of a pattern. An obvious choice for this is the grey scale value of each pixel of the image. In the case of the model of the particle-laden fluid the volume fraction of particles in each cell was used(10). However this alone does not provide a useful probability distribution, firstly because the values are continuous so there would be an infinite number of possible states, but secondly, and arguably more importantly, the values are local so they give no information about the spatial distribution or the shape of the pattern. A checker board pattern would have exactly the same distribution as a large white rectangle, or any other shape formed from just two grey values for that matter; all of the images in figure 3.10 have the same value of complexity according to this probability distribution.

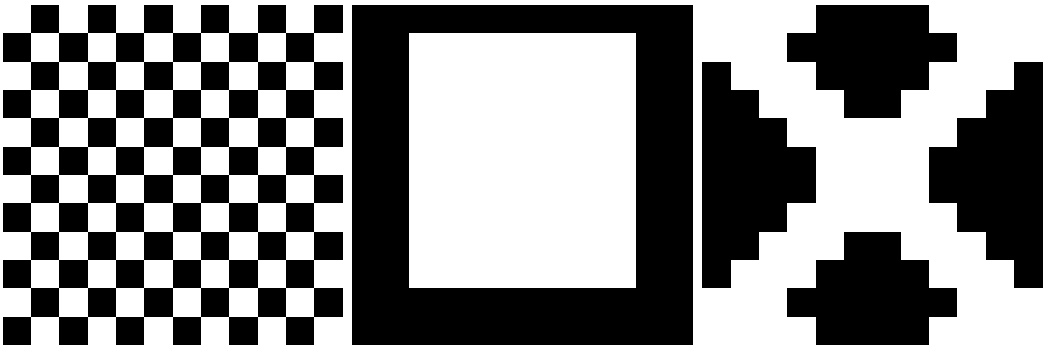
(a) Checker board. **(b)** Rectangle. **(c)** Capital X.

Figure 3.10: Examples of different images which all have the same number of black and white squares and hence would have the same value of complexity were grey scale values to be be used as the probability distribution.

Hence one requires non-local measurements that take into account the shape of the structures in the pattern. Three such measurements are described below with details of how their respective probability distributions are generated.

3.2.1.1 Gaussian Curvature

A fairly straightforward way to characterise the shape on the local scale(11) is to consider the Gaussian curvature[90] of an imaginary surface whose height, z, is given by the grey scale value, ϕ_i(12), of cell i. At each point on the surface the Gaussian curvature, K_G, is

---

(10) For this reason black is defended as having the highest value and white zero in order to be consistent.

(11) Local in the sense that the surrounding cells are involved in the calculation. The quantity is non-local, but the calculation does not include all of the cells so cannot be considered global.

(12) ϕ is used here for the grey scale value to be general, but in practice this is the value of the volume fraction when considering patterns generated by the particle-laden fluid, hence the use of the same symbol.

defined as

$$K_G = \frac{1}{r_1}\frac{1}{r_2}, \tag{3.39}$$

where r_1 and r_2 are the two principle radii of curvature at a given point in space. In principle this construction allows for any variable to be treated as the z coordinate of the surface so the complexity could be calculated for any quantity which varies on a two dimensional grid. The reason for the choice of ϕ in this case is that it is the quantity which is most readily observed simply by looking at the patterns and hence provides a visual representation. However, because the z coordinate is not the true height of a real surface in three dimensional space one must take care to understand what information the Gaussian curvature really holds about the system. In essence this measurement provides information about how quickly the value of whichever variable is chosen is changing in two dimensional space at a particular location, rather than what one might think of in a geometric sense. Nevertheless it is still useful to consider the value of interest playing the role of the z coordinate in the calculation of the curvature as it helps to make the ideas less abstract.

Using this description it is possible to avoid an explicit calculation of the Gaussian curvature and instead calculate the closely related excess angle [90], Θ_i, defined, for the eight nearest neighbours on a two dimensional grid of rectangles, by [90,161]

$$\Theta_i = 2\pi - \sum_{j=1}^{8} \theta_{ij}, \tag{3.40}$$

where θ_{ij} is the angle at the vertex in cell i of a triangle that is made up of straight lines joining the surface at the centre of cell i with the surface at the centre of its neighbour j and its neighbour, $j+1$, which is the next cell going anticlockwise around the centre of i from j. This is shown in figure 3.11a. Clearly on a grid of rectangles each cell makes contact with eight others, four at its edges and four at it's vertices, thus there are eight such triangles making up the excess angle measured in each cell, i, these are shown in figure 3.11b.

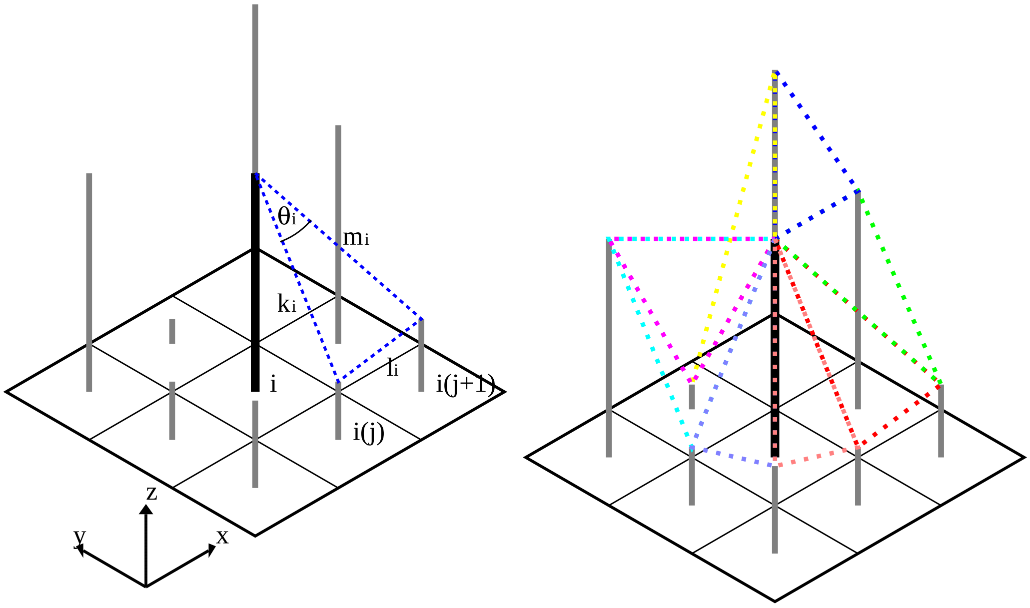

(a) Diagram showing how each component of the excess angle was calculated.

(b) Diagram showing each of the eight different triangles that make up the excess angle calculation.

Figure 3.11: Diagrams showing the steps involved in calculating the excess angle at each point in space. Here the height of the bars signifies the volume fraction, ϕ, in each of the cells and the black bar indicates the cell, i, for which the curvature is being calculated while the grey bars are its immediate neighbours. k, l and m are the lengths of the dashed lines, θ is the angle the two dashed line make at the centre of cell i and $i\,(j)$ refers to neighbour j of cell i where the convection is to increase j moving anticlockwise as viewed from above.

From inspection of the diagrams in figure 3.11 one can see qualitatively how the excess angle is linked to the Gaussian curvature in that by finding the angles on the surface around the centre of cell i and subtracting their sum from 2π one is in essence measuring how far the surface is from being flat.

Once the Gaussian curvature, or excess angle, has been found for each cell it is then possible to bin the resulting angles and use the frequency of occurrence of angles in each range to form a probability distribution[90] from which the complexity can be calculated and since the Gaussian curvature takes account of the shape of the pattern, at least on a regional scale, one is left with a complexity measure which is sensitive to non-local order within the system. Clearly a periodic structure, such as a checker board, would only have one value of curvature, which would be the same for all cells, and hence zero complexity as required. Similarly a random array would have all possible curvature values with equal probability and so, again, zero complexity. By contrast, however, an arrangement of differently shaped structures would have a range of curvature where some were more prevalent than others and therefore would be attributed a high value of complexity by the measures outlined above.

3.2.1.2 Mean Curvature

Another, closely related, means of quantifying the shape of a pattern is the mean curvature, K_M. This is defined as

$$K_M = \frac{1}{2}\left(\frac{1}{r_1} + \frac{1}{r_2}\right), \tag{3.41}$$

where, for the purposes of generating a measure that was consistent across all patters, r_1 and r_2 are the orthogonal axes of the coordinate system. Unlike the Gaussian curvature, which is an intrinsic measure of curvature[162], the mean curvature is an extrinsic measure[162]. This means that the mean curvature can be non-zero even when the geodesics of the surface remain parallel, hence the mean curvature of a corrugated sheet would be non-zero whereas the Gaussian curvature would be zero. Another way to think of this is to say that it is possible to detect intrinsic curvature using purely two dimensional data about the surface, whereas extrinsic measures require data from the third dimension. This is why it was possible to characterise the Gaussian curvature in terms of the excess angle. Whether these properties are an advantage or disadvantage when trying to characterise the complexity of patterns is unclear, since it depends heavily on the pattern, as will be demonstrated in section 5.3. The main advantage, however, is that by comparing both measures one is able to build up a picture of what a pattern might look like given the complexity values alone.

When calculating the mean curvature the principle radii of curvature, r_1 and r_2 were calculated directly by joining the two points on the surface at the centres of the two cells either side of cell i to the point on the surface at the centre of cell i with a circle and calculating its radius for each of the two principle radii of curvature. In essence using the three data points to determine the three parameters: α, β and r in the general equation of a circle

$$r^2 = (x - \alpha)^2 + (y - \beta)^2 . \tag{3.42}$$

Figure 3.12 shows how this was done for one of the principle radii of curvature, r, on a one dimensional slice through the pattern.

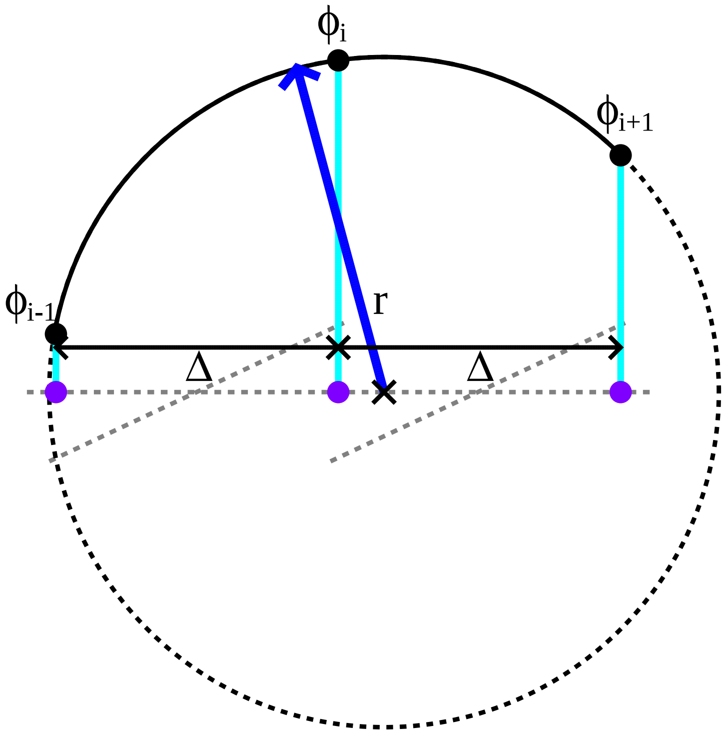

Figure 3.12: Sketch showing how one of the principle radii of curvature, r, used in the calculation of the mean curvature was calculated. Here Δ represents the distance between the centres of the two cells, represented by the purple dots and the centre of the circle is represented by the cross.

Since each of the cells has eight neighbouring cells on a rectangular grid there are potentially two values for the mean curvature, one from the cells that share edges with the central cell and the other from those that share vertices with it. One must make a choice about which version to use. In the present work the mean curvature has always been calculated using the values in the cells that share edges, since this makes the calculation slightly easier.

3.2.1.3 Two Dimensional Correlation Function

One of the main disadvantages of curvature based measures is that they are only sensitive to one particular length scale, namely the cell and its immediate neighbours, and cannot take account of the global structure of the pattern as a whole. By contrast the density-density correlation function takes account of order on all length scales. On a two dimensional N by N grid the density-density correlation function, $g_{ij}^{\phi\phi}$ in a cell at position i,j is defined as

$$g_{ij}^{\phi\phi} = \frac{1}{N^2} \sum_{k=-\frac{1}{2}N}^{\frac{1}{2}N} \sum_{l=-\frac{1}{2}N}^{\frac{1}{2}N} \phi_{k-i,l-j} \phi_{k,l} - \phi_0^2, \tag{3.43}$$

where $\phi_{i,j}$ is the grey scale value, or volume fraction, in the cell at position i,j(13) and ϕ_0 is the average of this quantity. Because of the symmetry associated with the definition of $g^{\phi\phi}$ in equation 3.43(14) one finds that a reflected copy of the correlation function is produced in each of the four quadrants of the two dimensional plane containing i and j. In order to prevent this from affecting the value of the complexity the data was compressed on to the first quadrant, such that i and j were both positive, by performing successive reflections of the data in the other quadrants and adding it to the data in the first, this is shown graphically in figure 3.13.

---

(13) The definition given in equation 3.43 is in fact most appropriate for systems with periodic boundary conditions, the reason for this choice, which will be explained in more detail in section 5.3.4, is that the focus of the present work is to examine patterns produced by bulk systems such as particle-laden fluids. In order to deal with systems where the boundaries are not periodic one would need to change the limits on the summations to take account of the position of the boundary relative to the cell in question.

(14) Again this argument would differ slightly for a system with non-periodic boundaries.

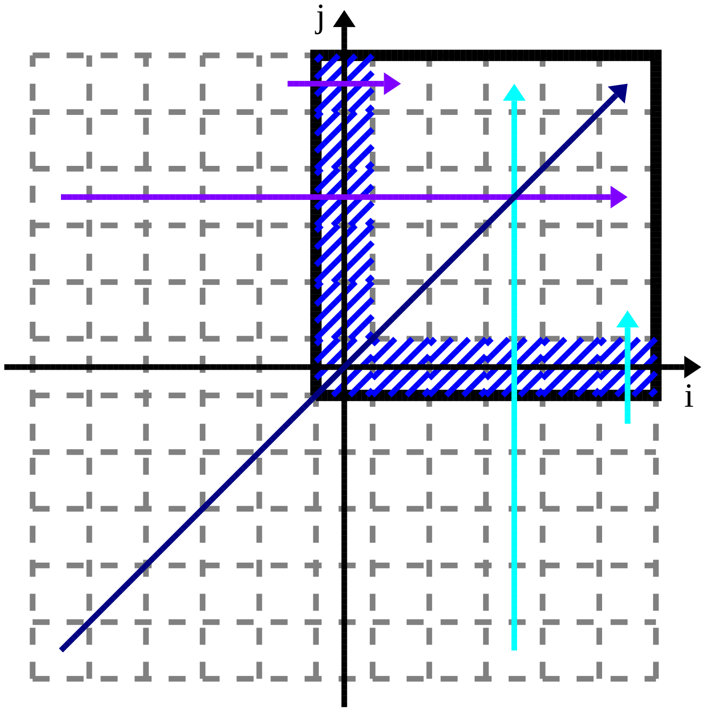

Figure 3.13: Sketch showing how the correlation function was compressed into the first quadrant. The arrows show where the data in each cell of each quadrant was moved to in the first quadrant, the thick black line represents the boundary of the region used in the calculation of the complexity and the blue shaded cells are the cells which correspond to self correlations, these had to be treated differently; the cells along the i axis were only copied in the i direction, not both directions and likewise for the cells on the j axis.

This was done to all cells with the exception of those on the lines $i = 0$ and $j = 0$. This produced a two dimensional grid of probabilities which was half of the system size in both directions which was then normalised and used as the probability distribution in the complexity measures.

In terms of what the correlation function means for the complexity one can think of a system with a high value of complexity as one which has order on multiple, but not all, length scales and ideally different strengths of correlation at different length scales. This, however, presents an immediate problem because a repeated pattern like a crystal, for which it has already been argued, the complexity should be zero does have order on many length scales, at multiples of the size of the repeat unit, so the correlation function does indeed show multiple strong correlations, and hence the complexity value would be high. This problem is avoided by means of a simple alteration to the definition of the Shannon entropy, given in equation 3.32, to give

$$H = -K \sum_{i=1}^{N} p_i \log \left\{ \frac{p_i}{p_i^*} \right\} . \tag{3.44}$$

By dividing the probability distribution in the logarithm by a prior probability distribution[3], p_i^* which is the correlation function generated by a perfect crystal, one removes the false impression of disorder given by the fact that there are multiple peaks in the probability distribution and restores the Shannon entropy to zero. Of course the draw back of this method is that there are many possible crystal structures so in theory the Shannon entropy should be calculated using the correlation function of each one as the prior and then the minimum value chosen. After examining the results of several test cases it was decided that a checker-board pattern should be used as a prior for all of the patterns examined here, for consistency, such that direct comparison could be drawn between all of the patterns considered.

3.3 Brownian Hydrodynamics of Identical Spheres

In order to complement the understanding gained by using the simplified phenomenological models described in section 3.1 a model of the particle scale behaviour, including the full many body hydrodynamic effects, was created in the hope that this would reveal more about how microscopic interactions affected the flow. Here the situations of most interest are those where the many body interactions between the particles affect their flow around obstacles or following a change in the direction of the flow. These effects are not only relevant in the sense that they go some way towards informing the choice of effective particle viscosity used in the model of the particle-laden fluid, but also because they allow one to learn a great deal about the flow behaviour of particle-laden fluids at the microscopic level, which is not accessible to the model described in section 3.1.

Many ways of dealing with hydrodynamic interactions are discussed in the literature. The derivation given in the following two sections closely follows that given in reference 68, but also draws on reference 12, as these describes the method used by HYDROLIB [12]. Section 3.3.3 presents a first principles derivation, using elements of reference 163, of the formula for quoted in reference 4 for the correct calculation of the Brownian forces in a system with hydrodynamic forces, that complements the method outlined in the following.

3.3.1 Many Body Hydrodynamic Forces

For a system of particles dispersed in an incompressible solvent at low Reynolds' number the flow field of the solvent, $\mathbf{v}_s$, is described by the incompressible Stokes' equations [160]

$$-\boldsymbol{\nabla} p + \eta \nabla^2 \mathbf{v}_s = \mathbf{0}, \tag{3.45a}$$

$$\boldsymbol{\nabla} \cdot \mathbf{v}_s = 0, \tag{3.45b}$$

where p is the pressure and η is the viscosity of the solvent. In principle, given appropriate boundary conditions on the surfaces of the particles and the container(15), this equation could be solved to give the velocity field of the solvent at every point in space. However, if one is only interested in the motion of the particles this is unnecessary since the forces which act on them due to the flow of the solvent can be determined directly from their motion relative to the solvent and the friction matrix, $\boldsymbol{\zeta}$ using the equation [12,68]

$$\mathbf{f}_H = \boldsymbol{\zeta} \cdot \mathbf{u}, \tag{3.46}$$

where, for N particles, $\mathbf{f}_H$ is a, $6N$ dimensional, vector that contains the components of the forces and torques that act on each particle and $\mathbf{u}$ is a, $6N$ dimensional, vector that contains all of the translational and rotational components of the particles' velocities relative to the net motion of the solvent [12]. The aim in any simulation of particles with hydrodynamic interactions to obtain this friction matrix, or its inverse, the mobility matrix. In the case of a solitary spherical particle, of radius a, in an infinite solvent this matrix reduces to a scalar, the familiar Stokes' drag coefficient, $\zeta_1 = 6\pi\eta a$ [160], but when many particles are considered $\boldsymbol{\zeta}$ becomes much more difficult to calculate. There are three key reasons for

---

(15) In the case of the present work non-slip boundary conditions are used on the surfaces of the particles and the system is either assumed to have periodic boundaries or be in an infinite solvent.

this. Firstly hydrodynamic interactions depend on the positions and locations of all of the particles in the system; they are not pairwise additive[68] like many other interactions. One can convince oneself of this simply by considering three particles arranged in a horizontal line, as shown in figure 3.14.

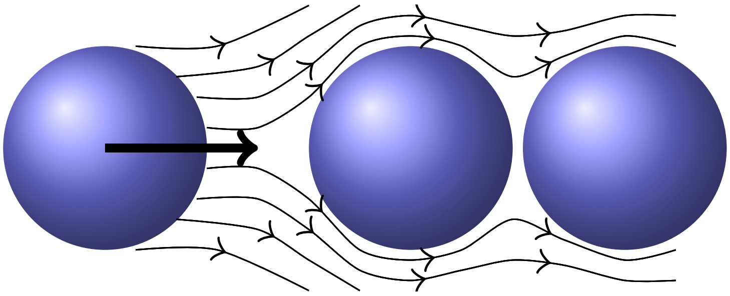

Figure 3.14: Sketch showing the approximate flow field around two static particles, on the right, due to the motion of a third, on the left.

If the particle on the left starts to move right it sets up a flow field in the solvent, also moving to the right, this in turn exerts a force on the particle in the centre, but the particle on the right will feel a weaker force because it is, to some extent, shielded from the flow field by the particle in the centre. Secondly because these forces arise due to the flow field they are very long range, decaying like the inverse of the particle separation. This is clear from the form of the Oseen tensor[68],

$$\mathbf{T} = \frac{1}{8\pi\eta\left|\mathbf{r}\right|}\left(\mathbf{I} + \hat{\mathbf{r}}\hat{\mathbf{r}}\right), \tag{3.47}$$

which is the Green's function of equation set 3.45[68] for the velocity field at point $\mathbf{r}$ when there is a point force at the origin. This means that it is not possible to define a cut-off separation where the interactions are neglected, meaning that where periodic boundary conditions are used one must correct for the contributions from all periodic images[12]. Finally the forces diverge at very small separations and become singular at the point of contact when non-slip boundary conditions are used. Clearly if the friction coefficient on the particle surface is assumed infinite, in the case of non-slip boundary conditions, then the force resisting relative, shear, motion of particles in contact must also be infinite.

Fortunately there are a range of libraries available for calculating many body hydrodynamic forces. The present work made use of the HYDROLIB library, detailed in reference 12. This was used to provide the hydrodynamic friction matrix for a given particle arrangement. Section 3.3.2 details the approximation scheme used by HYDROLIB[12].

3.3.2 Calculation of the Friction Matrix By Multipole Expansion

By performing a multipole expansion[12,68] in terms of the angular dependence of the flow field around a spherical particle, of radius a centred at the origin one can express the force on it in terms of the force multipole tensor, $\boldsymbol{\mathcal{F}}$, given by

$$\mathcal{F}_{\alpha}^{(p)} = \frac{1}{(p-1)!}\int_{|\mathbf{r}|=a}^{|\mathbf{r}|=\infty} r_{\alpha}^{p-1}\tilde{f}_{H,\beta}\left\{\mathbf{r}\right\} d\mathbf{r}, \tag{3.48}$$

where p is the multipole order and also the rank of the tensor $\boldsymbol{\mathcal{F}}$ and $\tilde{\mathbf{f}}_H$ is the multipole moment of the force[68]. In the case of the exact solution this is an infinite dimensional vector with a block structure of three sub-vectors, of which two are the force and torque acting on the particle and the other is made up of higher order terms, but in practice in the implementation of HYDROLIB the multipole expansion, and by extension the vector $\tilde{\mathbf{f}}_H$, is truncated at low order[68]. In a similar manner another vector, $\tilde{\mathbf{u}}$, with the same dimensionality as $\tilde{\mathbf{f}}_H$, can be created for the components of the particle velocity relative to the solvent. Thus[68]

$$\tilde{\mathbf{f}}_H = \begin{pmatrix} \mathbf{F}_H \\ \boldsymbol{\tau}_H \\ \vdots \end{pmatrix} \tag{3.49a}$$

$$\tilde{\mathbf{u}} = \begin{pmatrix} \mathbf{U} - \mathbf{v}_s|_{\mathbf{0}} \\ \boldsymbol{\Omega} - \frac{1}{2}\left(\boldsymbol{\nabla} \times \mathbf{v}_s\right)|_{\mathbf{0}} \\ \vdots \end{pmatrix} \tag{3.49b}$$

where $\mathbf{F}_H$ and $\boldsymbol{\tau}_H$ are the force and torque respectively, $\mathbf{U}$ and $\boldsymbol{\Omega}$ are the absolute translational and rotational velocities of the particle respectively and all quantities relating to the flow field are evaluated at the particle centre. Thanks to the block structure of these vectors it is possible to summaries the velocities and forces acting on all N particles in the system simply by concatenating the vectors with individual components for each particle. Thus $\tilde{\mathbf{f}}_H$ can be thought of as a $6N$ dimensional vector containing the forces and torques on all N particles, and likewise with $\tilde{\mathbf{u}}$ for the components of their velocity. Using these definitions one can write the multipole expansion equivalent of equation 3.46, for the whole system[68],

$$\tilde{f}_{H,\alpha} = \tilde{\zeta}_{0,\alpha\beta}\tilde{u}_{\beta}, \tag{3.50}$$

where $\tilde{\boldsymbol{\zeta}}_0$ is a block diagonal matrix made up of repeat units of the one particle friction matrix.

At this stage it is convenient to split the particle velocity, $\tilde{\mathbf{u}}$ into two terms; one which is due to the absolute velocity of the particles, $\tilde{\mathbf{u}}_a$, and the other due to the flow field induced in the solvent by the other particles, $\tilde{\mathbf{u}}_s$. Thus[68]

$$\tilde{\mathbf{u}} = \tilde{\mathbf{u}}_a - \tilde{\mathbf{u}}_s, \tag{3.51}$$

where

$$\tilde{\mathbf{u}}_a = \begin{pmatrix} \mathbf{U} \\ \boldsymbol{\Omega} \\ \vdots \end{pmatrix} \tag{3.52a}$$

$$\tilde{\mathbf{u}}_s = \begin{pmatrix} \mathbf{v}_s|_{\mathbf{0}} \\ \frac{1}{2}\left(\boldsymbol{\nabla} \times \mathbf{v}_s\right)|_{\mathbf{0}} \\ \vdots \end{pmatrix} \tag{3.52b}$$

and hence[68]

$$\tilde{f}_{H,\alpha} = \tilde{\zeta}_{0,\alpha\beta}\left(\tilde{\mathbf{u}}_a - \tilde{\mathbf{u}}_s\right)_{\beta}. \tag{3.53}$$

But the component of the velocity vector that is due to the flow field created by the other particles can be written, approximately, in terms of the multipole version of the Oseen tensor, $\tilde{\mathbf{T}}$, which has the form of equation 3.47, but the dimensionality of $\tilde{f}_H$ and $\tilde{u}$, and the force vector giving[68]

$$\tilde{f}_{H,\alpha} = \tilde{\zeta}_{0,\alpha\beta}\left(\tilde{\mathbf{u}}_a - \tilde{\mathbf{T}} \cdot \tilde{\mathbf{f}}_H\right)_{\beta}. \tag{3.54}$$

Solving equation 3.53 for $\tilde{\mathbf{f}}_H$ results in

$$\tilde{f}_{H,\alpha} = \left(\mathbf{I} + \tilde{\boldsymbol{\zeta}}_0 \cdot \tilde{\mathbf{T}}\right)^{-1}_{\alpha\beta}\tilde{\zeta}_{0,\beta\gamma}\tilde{u}_{a,\gamma}. \tag{3.55}$$

Now by comparing equations 3.46 and 3.55 one is able to identify the friction matrix[68],

$$\zeta_{\alpha\beta} = \left(\mathbf{I} + \tilde{\boldsymbol{\zeta}}_0 \cdot \tilde{\mathbf{T}}\right)^{-1}_{\alpha\gamma} \tilde{\zeta}_{0,\gamma\beta}. \tag{3.56}$$

In the limit of an infinite number of multipole moments equation 3.56 is exact[68] and one can apply this friction matrix to obtain the exact values of the forces due to the full, many body hydrodynamic interactions, at all length scales[68]. However, if one truncates the expansion to order L then one finds that the friction matrix for the many body interactions in the far field limit converges very rapidly as a function of L[68]. However, due to the fact that the, near field, lubrication forces diverge at very small separations obtaining a reasonable approximation of these requires many more terms[68]. This would incur a huge computational cost since the number of elements in the vectors and matrices, which must be dealt with in order to obtain the friction matrix, increases rapidly with the order of the multipole expansion[12,134]. Fortunately, however, because of its short range nature the lubrication force acting on a given particle, i, is dominated by the particles closest to it and is not strongly influenced by the positions of the other particles. As such the lubrication interaction can be treated in a pairwise manner[68].

With all of this considered it becomes clear that the most efficient means of calculating a good approximation of the friction matrix is to use the multipole expansion up to a small value of L to obtain a matrix $\tilde{\boldsymbol{\zeta}}^L$, which is reasonably accurate in the far field. Then use an expansion of the exact solution(16) for the two particle lubrication interaction at small separations, $\boldsymbol{\zeta}_2$, treating each pair as though they were the only particles in the system, and combine the forces in a pairwise additive manner in the near field[68]. Thus the near field friction matrix, $\boldsymbol{\zeta}_{near}$, is given by[68]

$$\boldsymbol{\zeta}_{near} = \sum_{i}^{N} \sum_{j}^{M\{i\}} \boldsymbol{\zeta}_{2,ij}, \tag{3.57}$$

where the inner summation is the sum over all the particles within a given cut-off radius of particle i and it is understood that $\boldsymbol{\zeta}_2$ is a $6N \times 6N$ matrix with zeros everywhere except in the block matrix at i, j relating to particles within the cut off radius. At this stage one must subtract the equivalent sum of two particle interactions[68] given by the truncated multipole expansion of the friction matrix,

$$\tilde{\boldsymbol{\zeta}}^L_{near} = \sum_{i}^{N} \sum_{j}^{M\{i\}} \tilde{\boldsymbol{\zeta}}^L_{2,ij}. \tag{3.58}$$

Thus the final friction matrix, which is calculated by HYDROLIB, is given by[12,68]

$$\boldsymbol{\zeta} \approx \tilde{\boldsymbol{\zeta}}^L + \boldsymbol{\zeta}_{near} - \tilde{\boldsymbol{\zeta}}^L_{near}. \tag{3.59}$$

With the friction matrix in place it is possible to calculate the forces acting on a given arrangement for particles from their known velocities, or conversely invert the matrix to

---

(16) This will be presented in more detail in section 3.3.2.1.

discover the velocities of the same agreement of particles subject to given forces(17). The present work made use of the former.

3.3.2.1 Lubrication Correction

For two particles in an infinite solvent three contributions can be identified as being responsible for the full hydrodynamic interaction between them. These are due to the three possible relative motions, summarised in figure 3.15: translational motion along the line connecting the centres, shear due to translational motion perpendicular to the line connecting the centres and shear due to relative rotation[68].

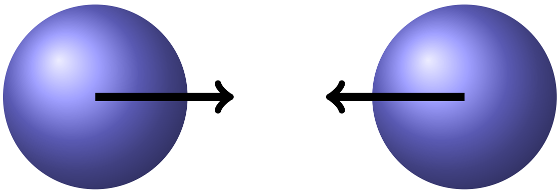

(a) Translational motion along the line connecting the centres.

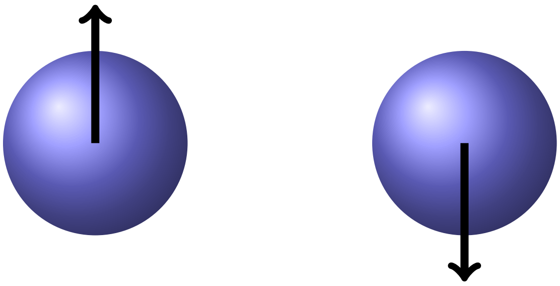

(b) Translational motion perpendicular to the line connecting the centres.

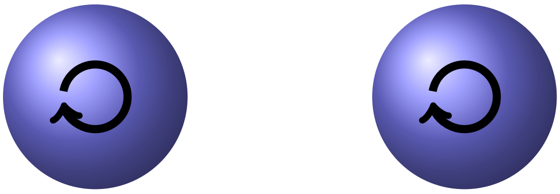

(c) Rotational motion.

Figure 3.15: Sketches showing the three relative motions that result in lubrication forces between two particles.

Since the multipole expansion, already discussed, gives an excellent approximation to the hydrodynamic force at reasonably large separations one is only concerned with the lubrication correction when the separation between the closest points on the surface, ϵ, is small compared with the sizes of the particles, $\epsilon \ll 1$. For any two particle, both of radius a, at positions $\mathbf{r}_1$ and $\mathbf{r}_2$

$$\epsilon = \frac{|\mathbf{r}_1 - \mathbf{r}_2|}{a} - 2. \tag{3.60}$$

In this limit the dominant term in the force acting on the particles due to translational motion along the line connecting the centres of the particles is of order $\frac{1}{\epsilon}$ while the dominant term due to both kinds of shearing motion is of order $\ln\{\epsilon\}$[68]. Thus considering all of these interactions together, and retaining terms up to order $\epsilon \ln\{\epsilon\}$(18), one finds that

---

(17) Though for piratical reasons this is not the most efficient means of performing the latter operation.

(18) This is the level of accuracy used by HYDROLIB[134].

the fiction matrix $\boldsymbol{\zeta}_2$ for two particles are $\mathbf{r}_1$ and $\mathbf{r}_2$ is given, approximately, by[68]

$$\boldsymbol{\zeta}_2 \approx \frac{1}{\epsilon}\mathbf{K}_1 + \ln\{\epsilon\}\,\mathbf{K}_2 + \mathbf{K}_3 + \epsilon\ln\{\epsilon\}\,\mathbf{K}_4, \tag{3.61}$$

where the various constant matrices, $\mathbf{K}_i$, are determined by the properties of the fluid and the particular geometry of the situation under consideration[68] and are independent of the movement of the particles. The full expressions for these matrices, along with a more detailed discussion of their derivation, are given in reference 68.

3.3.3 Preserving Detailed Balance

Thus far in the discussion of hydrodynamic interactions the method implemented in HYDROLIB[12] for calculating the friction matrix for a system of N particles has been described. The resulting friction matrix forms a proportionality between the viscous forces felt by the particles and their velocity relative to the net velocity of the solvent[12]. However, nothing has been said of the Brownian forces, felt by the particles due to the finite temperature of the system, or of any other external forces for that matter. Thus what has been presented so far is, in essence, a means of calculating the forces on granular particles, which do not feel Brownian forces, in the absence of any inter-particle interactions or external forces.

Fortunately due to the fact that forces are additive one can write the total force acting on any particle, $\mathbf{f}$, as[4,6]

$$\mathbf{f} = \mathbf{f}_H + \mathbf{f}_B + \mathbf{f}_E, \tag{3.62}$$

where $\mathbf{f}_H$, $\mathbf{f}_B$ and $\mathbf{f}_E$ are $6N$ dimensional vectors containing all of the translational forces and torques acting on all N particles from the hydrodynamic interactions, Brownian forces and external forces respectively.

Since the Brownian forces are random they are characterised by a Gaussian probability distribution the first moment of which can be characterised by appealing to conservation of momentum. Because Brownian forces arise from collisions between the particles of the solvent and the particles suspended in it the forces felt by individual particles do not need to be momentum conserving as the solvent will account for any differences. However there can be no net change, over a significant period of time, in the momentum of the centre of mass of the particle ensemble as this would require a change in the momentum of the fluid as a whole. If one considers the change in the velocities of all of the particles due to Brownian forces alone,

$$m\frac{\partial \mathbf{u}}{\partial t} = \mathbf{f}_B, \tag{3.63}$$

and then takes a thermal average, over many replicas of the system, and insists that the average change in the momentum of the centre of mass, $m\left\langle \frac{\partial \mathbf{u}}{\partial t}\right\rangle$, is zero one finds

$$\langle \mathbf{f}_B \rangle = \mathbf{0}. \tag{3.64}$$

In order for the particles to be in thermal equilibrium with the solvent the Brownian forces must obey the principle of detailed balance. As such the rate at which they acquire energy from the solvent must be, exactly, matched by the rate at which this energy is returned to the solvent by the dissipative hydrodynamic forces when a thermodynamic average is taken.

According to kinetic theory, for a thermal system which experiences only Brownian and hydrodynamic forces, one expects

$$\frac{1}{2}m\left\langle \mathbf{u}\mathbf{u}\right\rangle = \frac{1}{2}k_BT\mathbf{I}, \tag{3.65}$$

where $\mathbf{I}$ is the identity matrix, m is the mass of the particles, assumed to be the same for all, T is the temperature of the system and $\langle \mathbf{u}\mathbf{u}\rangle$ denotes a thermal average of the outer product of the velocity, over many duplicates of the system. Furthermore, neglecting any external forces, the velocity must obey

$$m\frac{\partial \mathbf{u}}{\partial t} = \mathbf{f}_B + \mathbf{f}_H. \tag{3.66}$$

After substituting equation 3.46 for the hydrodynamic force and solving the resulting equation one finds that the velocity of the particles after a short period of time, δt, is given by[163]

$$\mathbf{u}\left\{\delta t\right\} = \mathbf{u}\left\{0\right\}e^{-\frac{\zeta}{m}\delta t} + \frac{1}{m}\int_0^{\delta t}\mathbf{f}_B e^{-\frac{\zeta}{m}(\delta t - s)}ds, \tag{3.67}$$

where $t = 0$ denotes the last known state of the system(19). Taking the outer product of $\mathbf{u}\left\{\delta t\right\}$ with itself and averaging, remembering that the Brownian force is random and so uncorrelated with the velocity one obtains[163]

$$\left\langle \mathbf{u}\left\{\delta t\right\}\mathbf{u}\left\{\delta t\right\}\right\rangle = \left\langle \mathbf{u}\left\{0\right\}\mathbf{u}\left\{0\right\}\right\rangle e^{-2\frac{\zeta}{m}\delta t} + \frac{1}{m^2}\int_0^{\delta t}\int_0^{\delta t}\left\langle \mathbf{f}_B\left\{s\right\}\mathbf{f}_B\left\{s'\right\}\right\rangle e^{-\frac{\zeta}{m}(2\delta t - s - s')}ds ds'. \tag{3.68}$$

Now using equation 3.65 to replace the velocities with the thermal energy and once again appealing to the fact that the Brownian force is random and so uncorrelated in time, hence $\left\langle \mathbf{f}_B\left\{s\right\}\mathbf{f}_B\left\{s'\right\}\right\rangle = 0$ for $s' \neq s$, one can reduce equation 3.68 to[163]

$$k_BT\mathbf{I} = k_BT\mathbf{I}e^{-2\frac{\zeta}{m}\delta t} + \frac{1}{m}\int_0^{\delta t}\left\langle \mathbf{f}_B\left\{s\right\}\mathbf{f}_B\left\{s\right\}\right\rangle e^{-2\frac{\zeta}{m}(\delta t - s)}ds. \tag{3.69}$$

Finally by evaluating the integral on the right hand side of equation 3.69 and rearranging one discovers the second moment of the probability distribution,

$$\left\langle \mathbf{f}_B\mathbf{f}_B\right\rangle = 2k_BT\delta\left\{t - t'\right\}\boldsymbol{\zeta}, \tag{3.70}$$

where t and t' are two instants in time and δ is the Kronecker delta function.

Due to the fact that the Brownian forces are normally distributed it makes sense to model them as a Wiener process, $d\mathbf{W}$, with zero mean and unit standard deviation, and then weight the values accordingly in order to satisfy equation 3.70. Due to local differences in the effective drag coefficient, however, it is not sufficient to use a scalar weighting parameter. Instead this parameter must be a matrix, $\mathbf{Q}$, which has the same

---

(19) The time here is arbitrary, $t = 0$ is chosen for notational simplicity.

dimensions as the friction matrix, $\boldsymbol{\zeta}$. This is written mathematically as

$$\mathbf{f}_B = \mathbf{Q} \cdot d\mathbf{W}. \tag{3.71}$$

In order to discover the relationship between $\mathbf{Q}$ and $\boldsymbol{\zeta}$ one must rewrite equation 3.70 with the Brownian force written explicitly[4],

$$\langle \mathbf{Q} \cdot d\mathbf{W}\mathbf{Q} \cdot d\mathbf{W} \rangle = 2k_B T \delta \left\{ t - t' \right\} \boldsymbol{\zeta}. \tag{3.72}$$

After a simple rearrangement and the use of the fact that the Wiener processes for different particles are uncorrelated, while the Wiener process for each scales like $d\mathbf{W} = \sqrt{\delta t}$, for a finite time step, one is left with

$$\mathbf{Q} \cdot \mathbf{Q}^T = \frac{2k_B T}{\delta t} \boldsymbol{\zeta}. \tag{3.73}$$

Thus from equation 3.73 one concludes that an appropriate weighting matrix, $\mathbf{Q}$ is the Cholesky decomposition of the friction matrix[4] multiplied by $\sqrt{\frac{2k_B T}{\delta t}}$.

3.4 A Constitutive Relation for Interacting Colloidal Fluids

In contrast with polymeric solutions[37,39] there are relatively few constitutive relations for colloidal dispersions which are based on the microscopic properties of the fluid. Many of those that do exist are based on mode coupling theory[33,35,74]. One of the drawbacks of this is that it is not possible to evaluate what effects the approximations made in mode coupling theory will have on the final solution at the time that they are made[74]. This means that it does not have the desirable property, which was also sought in the model of the particle-laden fluid, that the different features of the model can be directly related to their effect on the results. Furthermore the complexity of mode coupling theory means that there is no closed analytical expression for the effective viscosity as a function of strain rate.

In this section a simple model, which is valid at low particle concentrations, will be presented. Due to its simplicity this model has the desirable properties that: the approximations are well controlled and their consequences for the final result and physical interpretations are clear. It is general and the results are applicable to a wide range of fluids and, in many cases, it is possible to write simple analytical expressions that fully describe the steady state stress-strain relationship. Although this model does not have the same range in terms of concentration of particles as models derived from mode coupling theory do it does produce results which are in reasonable qualitative agreement with other models[5,35,42,47,51,52,58,75] and with experimental data[10,20,40,49,76,126,164] for a wide range of strain rates. And, because of its simplicity, it is able to give an indication as to the effects of the different microscopic properties on the stresses felt in the bulk fluid.

One of the key motivations behind the derivation of this model is that its results could be used to inform the function used to calculate the effective particle viscosity in the model of the particle-laden fluid. This meant that as well as understanding the origins of the non-Newtonian flow behaviour used in the model the relationship used to calculate the viscosity was well motivated and could be related to the microscopic properties of the particles. In practice, because the model detailed in section 3.1.2.1 was so flexible this simply meant adjusting the parameters used to describe the flow curve so that it was a good fit for the data produced by the constitutive relation which shall be described in this section.

This section shall be devoted to the deviation of the model in an abstract sense, then in section 4.4.1 the model cast into cartesian coordinates for evaluation. First of all the equations of motion are derived from first principles and used within a thermal average to discover the dynamics of the two particle distribution function. This derivation proceeds in much the same way as that presented in reference 39 for the dumbbell model of polymers[39]. Then the virial equation[165] is used to formulate an equation for the stress and its rate of change in terms of the two particle distribution function and the equation describing its dynamics. A number of assumptions are then made about the nature of the flow field and the symmetry properties of the stress tensor in order to make analytical solutions possible. Finally this section concludes with a discussion of how the model can be simplified by assuming the overall deformation of the two particle distribution function to be small.

3.4.1 Derivation of the Equations of Motion

If one considers two massless particles interacting through a pair potential, $U\left\{\mathbf{r}\right\}$, immersed in a solvent at temperature T and with drag coefficient ζ_{sp} then, by balancing the drag force with the forces arising from the inter-particle interactions and Brownian motion, and considering an infinitesimal amount of time, one can obtain the equations of motion[39]

$$\zeta_{sp}\left(d\mathbf{r}_1 - \mathbf{u}\left\{\mathbf{r}_1\right\}dt\right) = \boldsymbol{\nabla} U\left\{\left|\mathbf{r}_2 - \mathbf{r}_1\right|\right\}dt + \nu d\mathbf{W}_1 \tag{3.74a}$$

$$\zeta_{sp}\left(d\mathbf{r}_2 - \mathbf{u}\left\{\mathbf{r}_2\right\}dt\right) = -\boldsymbol{\nabla} U\left\{\left|\mathbf{r}_2 - \mathbf{r}_1\right|\right\}dt + \nu d\mathbf{W}_2, \tag{3.74b}$$

where $\mathbf{r}_i$ is the absolute position of particle i, $\mathbf{u}$ is the velocity of the solvent at position $\mathbf{r}_i$, $\nu = \sqrt{2k_BT\zeta_{sp}}$ and $d\mathbf{W}_i$ is a Wiener process acting on particle i.

It is worth noting at this point that by using the pair interaction potential, U, all multi-particle interactions are being neglected. This means that this model is unable to deal with phenomena such as jamming and buckling which are attributed to such multi-particle interactions. However, in the low volume fraction limit, situations where the interaction between two particles is significantly affected by the presence of one or more other particles, such as a three particle collision, will be very rare. Thus it is reasonable to assume that the bulk behaviour is described, to a very good approximation, by considering interactions at the two particle level only. Furthermore it has been assumed that there is always a finite amount of solvent between any two particles as inter-particle friction has been ignored. This complements both the assumptions that the particles are point like and that they are at low concentration. The use of the constant friction coefficient here represents another important approximation. It implies the lack of hydrodynamic interactions. As with the approximation relating to the interaction potential this approximation is also valid in the low volume fraction limit where the particles are typically far apart and unable to influence the solvent around another particle significantly, meaning that, aside from the pair interaction, the particles move independently of each other. Finally it is worth pointing out that having massless particles complements the assumption that was made in section 3.1.1 that the fluid is in the limit of zero Reynolds' number, where the effects of inertia may be ignored.

Subtracting equation 3.74a from equation 3.74b gives

$$\zeta_{sp}\left(d\mathbf{r} - \mathbf{u}\left\{\mathbf{r}_1\right\}dt + \mathbf{u}\left\{\mathbf{r}_2\right\}dt\right) = -2\boldsymbol{\nabla}U\left\{\mathbf{r}\right\}dt + \nu d\mathbf{W}, \tag{3.75}$$

where $\mathbf{r} \equiv \mathbf{r}_2 - \mathbf{r}_1$ and $d\mathbf{W} \equiv d\mathbf{W}_2 - d\mathbf{W}_1$. Since the gradients in the flow field will be small on the length scale of the particles $\mathbf{u}\left\{\mathbf{r}_2\right\} - \mathbf{u}\left\{\mathbf{r}_1\right\} \approx \mathbf{K}\cdot\mathbf{r}$, where

$$\mathbf{K}_{ij} = \frac{\partial \mathbf{u}_i}{\partial \mathbf{r}_j} \tag{3.76}$$

is the velocity gradient tensor. Thus

$$d\mathbf{r} = \mathbf{K}\cdot\mathbf{r}dt - \frac{2}{\zeta_{sp}}\boldsymbol{\nabla}U\left\{\mathbf{r}\right\}dt + \frac{\nu}{\zeta_{sp}}d\mathbf{W}. \tag{3.77}$$

Now by applying the properties of the Wiener process, $\langle d\mathbf{W}\rangle = \mathbf{0}$ and $\langle d\mathbf{W}_i d\mathbf{W}_j\rangle = \delta_{ij}$, remembering that $d\mathbf{W}$ is the difference of two Wiener processes and removing all terms of order dt^2 and higher one obtains equations of motion for the average particle to particle vector and the average of its square magnitude

$$\langle d\mathbf{r}\rangle = \left\langle \mathbf{K}\cdot\mathbf{r} - \frac{2}{\zeta_{sp}}\boldsymbol{\nabla}U\left\{\mathbf{r}\right\}\right\rangle dt \tag{3.78a}$$

$$\left\langle \left|d\mathbf{r}\right|^2\right\rangle = 2\frac{\nu^2}{\zeta_{sp}^2}ddt, \tag{3.78b}$$

where d is the number of spatial dimensions. These equations form the basis for the calculation of all of the other relevant system averaged quantities and in doing so form the link between the microscopic description of the particles and the macroscopic, observable, properties of the fluid.

In order to proceed with the derivation of an equation of motion for any average quantity which relates to this system one must consider how a general, scalar, function $F\left\{\mathbf{r}\right\}$ varies in time. This can be done by considering an infinitesimal change in the function defined by

$$dF = F\left\{t + dt\right\} - F\left\{t\right\}. \tag{3.79}$$

One can also obtain the change in the average of this quantity simply by averaging both sides of equation 3.79. Furthermore it is clear that, since F is a function of $\mathbf{r}$ only, any change in F must be due to a change in $\mathbf{r}$. Thus

$$\langle dF\rangle = \left\langle F\left\{\mathbf{r} + d\mathbf{r}\right\} - F\left\{\mathbf{r}\right\}\right\rangle. \tag{3.80}$$

Now by using the fact that $d\mathbf{r}$ is small and applying the Taylor expansion

$$F\left\{\mathbf{r} + d\mathbf{r}\right\} \approx F\left\{\mathbf{r}\right\} + d\mathbf{r}\cdot\boldsymbol{\nabla}F\left\{\mathbf{r}\right\} + \frac{1}{2}\left|d\mathbf{r}\right|^2\nabla^2 F\left\{\mathbf{r}\right\}, \tag{3.81}$$

and using equation set 3.78, remembering that $d\mathbf{r}$ and $F\{\mathbf{r}\}$ are uncorrelated(20) and taking the limit of an infinitely small time step, $dt \to 0$, one obtains the expression

$$\frac{\partial}{\partial t}\langle F\rangle = \left\langle \mathbf{K}\cdot\mathbf{r} - \frac{2}{\zeta_{sp}}\boldsymbol{\nabla}U\{\mathbf{r}\}\right\rangle \cdot \langle \boldsymbol{\nabla}F\{\mathbf{r}\}\rangle + \frac{\nu^2 d}{\zeta_{sp}^2}\left\langle \nabla^2 F\{\mathbf{r}\}\right\rangle \tag{3.82}$$

for the average change in F.

Alternatively one may wish to approach this problem from a macroscopic point of view by considering $\psi\{\mathbf{r},t\}$ to be the probability of finding two particles with a separation $\mathbf{r}$ at time t. Then by integrating over the whole system one obtains:

$$\langle F\rangle = \int_{-\infty}^{\infty} F\{\mathbf{r}\}\,\psi\{\mathbf{r},t\}\,dV. \tag{3.83}$$

Differentiating both sides with respect to time and remembering that F is a function of $\mathbf{r}$ only gives

$$\frac{\partial}{\partial t}\langle F\rangle = \int_{-\infty}^{\infty} F\frac{\partial\psi}{\partial t}dV, \tag{3.84}$$

but this must be equivalent to equation 3.82 and hence,

$$\left\langle \left(\mathbf{K}\cdot\mathbf{r} - \frac{2}{\zeta_{sp}}\boldsymbol{\nabla}U\right)\cdot\boldsymbol{\nabla}F + \frac{\nu d}{2\zeta_{sp}}\nabla^2 F\right\rangle = \int_{-\infty}^{\infty} F\frac{\partial\psi}{\partial t}dV. \tag{3.85}$$

Replacing the left hand side of equation 3.85 with the definition of the volume average and integrating by parts twice, assuming that ψ and all of its derivatives are zero on the boundary surface, one obtains

$$\int_{-\infty}^{\infty}\left[\frac{\partial\psi}{\partial t} + \boldsymbol{\nabla}\cdot\left[\left(\mathbf{K}\cdot\mathbf{r} - \frac{2}{\zeta_{sp}}\boldsymbol{\nabla}U\right)\psi\right] - \frac{\nu^2 d}{\zeta_{sp}^2}\nabla^2\psi\right]F dV = 0. \tag{3.86}$$

Clearly since F can be any function of $\mathbf{r}$ this implies

$$\frac{\partial\psi}{\partial t} = \boldsymbol{\nabla}\cdot\left[\left(\frac{\nu^2 d}{\zeta_{sp}^2}\boldsymbol{\nabla} + \frac{2}{\zeta_{sp}}\boldsymbol{\nabla}U - \mathbf{K}\cdot\mathbf{r}\right)\psi\right]. \tag{3.87}$$

Using the fact that, for two interacting particles, the two particle distribution function, g, is essentially proportional to ψ, up to the addition of a constant, applying the Einstein relation and defining the mobility as $\mathcal{M} \equiv \frac{1}{\zeta_{sp}}$, one obtains

$$\frac{\partial g}{\partial t} = \boldsymbol{\nabla}\cdot\left[\left(2d\mathcal{D}\boldsymbol{\nabla} + 2\mathcal{M}\boldsymbol{\nabla}U - \mathbf{K}\cdot\mathbf{r}\right)g\right]. \tag{3.88}$$

Finally for notational convenience the factors of two and d will be absorbed into the constants. Thus[35,56]

$$\frac{\partial g}{\partial t} = \boldsymbol{\nabla}\cdot\left[\left(\mathcal{D}\boldsymbol{\nabla} + \mathcal{M}\boldsymbol{\nabla}U - \mathbf{K}\cdot\mathbf{r}\right)g\right]. \tag{3.89}$$

Although equation 3.89 has been derived by considering two isolated particles it can easily be applied, to a very good approximation, to systems of any number of particles at low concentration simply by using the average two particle distribution function for that sys-

---

(20) This means that $\langle d\mathbf{r}\cdot\boldsymbol{\nabla}F\rangle = \langle d\mathbf{r}\rangle\cdot\langle\boldsymbol{\nabla}F\rangle$ and $\left\langle |d\mathbf{r}|^2\,\nabla^2 F\{\mathbf{r}\}\right\rangle = \left\langle |d\mathbf{r}|^2\right\rangle\left\langle\nabla^2 F\{\mathbf{r}\}\right\rangle$.

tem and arguing that, because the concentration is low, the dynamics will be dominated by pair interactions as situations where the interactions are affected significantly by other particles will be extremely rare.

The real significance of equation 3.89 is that in describing the dynamics of the two particle distribution function it describes how the distribution of length scales in the system changes over time. This in turn provides all of the information necessary to calculate the stress tensor at any given time, since all of the stresses in the system must come from the inter-particle interactions as the particles are assumed to be massless.

3.4.1.1 Equilibrium Solution

Although the equilibrium solution of equation 3.89 is fairly trivial to obtain it is of great physical significance and crucial to the calculation of stresses. At equilibrium there is, by definition, no external flow field, therefore $\mathbf{K} = \mathbf{0}$, and the two particle correlation function is constant, meaning $\frac{\partial g}{\partial t} = 0$. Thus equation 3.89 reduces to

$$\boldsymbol{\nabla} \cdot \left[\left(\mathcal{D} \boldsymbol{\nabla} + \mathcal{M} \boldsymbol{\nabla} U \right) g \right] = 0 \tag{3.90}$$

which can be solved immediately to obtain

$$g_e = e^{-\beta U}, \tag{3.91}$$

where $\beta = \frac{1}{k_B T}$ and the constant of integration has been set to zero since the probability of finding two particles at a separation where the potential is infinite must be zero at any finite temperature. Clearly this is exactly the function one would expect from the definition of the two particle correlation function.

3.4.2 The Virial Equation

For a fluid of massless particles, like those described in section 3.4.1, the stress tensor, ignoring any contribution from the solvent, can be defined as[165]

$$\tau_{\alpha\beta} = \frac{1}{V} \sum_{i=1}^{N-1} \sum_{j=i+1}^{N} r_{ij,\alpha} f_{ij,\beta}, \tag{3.92}$$

where N is the number of particles, V is the system volume, $\mathbf{r}_{ij} = \mathbf{r}_j - \mathbf{r}_i$ and f_{ij} is the force exerted on particle i by particle j. However, this double sum can be rewritten as an integral over all particle separations, $\mathbf{r}_{ij}$, or equivalently an integral over the whole volume. In this case the force must be multiplied by the number of particles at that separation, $N^2 g \left\{ \mathbf{r} \right\}$,

$$\tau_{\alpha\beta} = \frac{1}{2} \frac{N^2}{V^2} \int_{-\infty}^{\infty} r_\alpha f_\beta g dV, \tag{3.93}$$

here dividing by a factor of $2V$ accounts for the double counting which has been introduced by considering all pairings, not just those with $j > i$, and normalises the volume integral. By remembering the definition of the volume fraction, $\phi = \frac{N}{V} V_p$, where V_p is the average volume of the particles, and separating the product of the separation vector and force into its magnitude and direction, remembering that the force is purely radial, one obtains the stress in a more convenient form, where the different components can be easily separated,

$$\tau_{\alpha\beta} = \frac{1}{2}\frac{\phi^2}{V_p^2}\int_{-\infty}^{\infty} \hat{r}_\alpha \hat{r}_\beta r_\gamma f_\gamma g dV. \tag{3.94}$$

Here $\hat{\mathbf{r}}$ is the unit vector pointing along the line passing through the two particle centres. This is also the direction of the force, since it is purely radial. Finally the contribution to the stress due to the microstructure can be separated from the isotropic pressure using

$$\mathbf{\Sigma} = \boldsymbol{\tau} - \frac{d-1}{d} p\mathbf{I}, \tag{3.95}$$

where p is the isotropic pressure, d is the number of spatial dimensions and $\mathbf{I}$ is the identity matrix. This means the microstructural stress, $\mathbf{\Sigma}$, is given by

$$\Sigma_{\alpha\beta} = \frac{1}{2}\frac{\phi^2}{V_p^2}\int_{-\infty}^{\infty} \left(\hat{\mathbf{r}}\hat{\mathbf{r}} - \frac{d-1}{d}\mathbf{I}\right)_{\alpha\beta} r_\gamma \boldsymbol{\nabla}_\gamma U g dV, \tag{3.96}$$

where the force has been rewritten as the gradient of the inter-particle, pair, interaction potential. Writing the force in this form is essentially making the same approximation as the model in section 3.4.1 as it neglects any multi-particle interactions.

For notational convenience and clarity the matrix

$$\mathbf{N} = \frac{1}{2}\frac{\phi^2}{V_p^2}\left(\hat{\mathbf{r}}\hat{\mathbf{r}} - \frac{d-1}{d}\mathbf{I}\right) \tag{3.97}$$

shall be defined, with the caveat that the remainder of the calculation must be performed on each element individually(21). This can be thought of as a means of discriminating between the different components of the stress tensor, since it is a function of the relative directions of the force and separation of the particles. It also accounts for the overall scaling of the stress with the volume fraction of particles and the particle size, which will be assumed to be constant in all further calculations since the fluid as a whole will be assumed to be incompressible, the motivation for this will be discussed in more detail in section 3.4.4.1. Thus equation 3.96 can be written, in a more compact form, as

$$\Sigma_{\alpha\beta} = \int_{-\infty}^{\infty} N_{\alpha\beta} r_\gamma \boldsymbol{\nabla}_\gamma U g dV. \tag{3.98}$$

With the definition of the microstructural stress given in equation 3.94 it is possible to obtain the rate of change of the stress simply by differentiating with respect to time and remembering that for an incompressible fluid $\mathbf{N}$ is constant(22). Doing so gives

$$\dot{\Sigma}_{\alpha\beta} = \int_{-\infty}^{\infty} N_{\alpha\beta} r_\gamma \boldsymbol{\nabla}_\gamma U \frac{\partial g}{\partial t} dV. \tag{3.99}$$

---

(21) That is to say $\Sigma_{ij} = \int_{-\infty}^{\infty} N_{ij}\mathbf{r}\cdot(\boldsymbol{\nabla}U)\, gdV$ and not $\Sigma_{ij} = \left(\int_{-\infty}^{\infty} \mathbf{N}\mathbf{r}\cdot(\boldsymbol{\nabla}U)\, gdV\right)_{ij}$. Thus retaining the mapping between the directions of the inter-particle forces and the stress tensor.

(22) To account for compressible flow one would merely require the addition of the term $2\frac{\dot{\phi}}{\phi}\mathbf{\Sigma}$ to account for the change in the volume fraction. However since incompressible flow will be assumed in section 3.4.4.1 this term has been neglected.

It is then possible to substitute equation 3.89 into equation 3.99 and obtain

$$\dot{\Sigma}_{\alpha\beta} = \int_{-\infty}^{\infty} N_{\alpha\beta}\boldsymbol{\nabla}_{\gamma}\left[\left(\mathcal{D}\boldsymbol{\nabla}_{\gamma} + \mathcal{M}\boldsymbol{\nabla}_{\gamma}U - K_{\gamma\delta}r_{\delta}\right)g\right]r_{\epsilon}\boldsymbol{\nabla}_{\epsilon}U dV. \tag{3.100}$$

Since it is reasonable to assume that, for any physically realistic interaction potential, either: the potential itself will be zero at infinitely large separations, or, if the potential is finite, the two particle distribution function will tend to zero as the separation tends to infinity, this ensures that the integrand of equation 3.100 will be zero everywhere on the boundary surface, provided the relevant quantity tends to zero sufficiently quickly(23). Hence one can integrate by parts and obtain(24)

$$\begin{aligned}\dot{\Sigma}_{\alpha\beta} = -\mathcal{D}\int_{-\infty}^{\infty}\boldsymbol{\nabla}_{\gamma}\left[N_{\alpha\beta}r_{\delta}\boldsymbol{\nabla}_{\delta}U\right]\boldsymbol{\nabla}_{\gamma}g dV - \mathcal{M}\int_{-\infty}^{\infty} g\boldsymbol{\nabla}_{\gamma}\left[N_{\alpha\beta}r_{\delta}\boldsymbol{\nabla}_{\delta}U\right]\boldsymbol{\nabla}_{\gamma}U dV \\ + \int_{-\infty}^{\infty} g\boldsymbol{\nabla}_{\gamma}\left[N_{\alpha\beta}r_{\delta}\boldsymbol{\nabla}_{\delta}U\right]K_{\gamma\epsilon}r_{\epsilon}dV.\end{aligned} \tag{3.101}$$

Integrating the first term by parts once again, using the same assumptions as before, yields

$$\begin{aligned}\dot{\boldsymbol{\Sigma}}_{\alpha\beta} = \mathcal{D}\int_{-\infty}^{\infty} g\nabla^{2}\left[N_{\alpha\beta}r_{\gamma}\boldsymbol{\nabla}_{\gamma}U\right]dV - \mathcal{M}\int_{-\infty}^{\infty} g\boldsymbol{\nabla}_{\gamma}\left[N_{\alpha\beta}r_{\delta}\boldsymbol{\nabla}_{\delta}U\right]\boldsymbol{\nabla}_{\gamma}U dV \\ + \int_{-\infty}^{\infty} g\boldsymbol{\nabla}_{\gamma}\left[N_{\alpha\beta}r_{\delta}\boldsymbol{\nabla}_{\delta}U\right]K_{\gamma\epsilon}r_{\epsilon}dV.\end{aligned} \tag{3.102}$$

Here the first term in the expression for $\dot{\boldsymbol{\Sigma}}$ corresponds to the relaxation of stress arising from diffusion rearranging the microstructure. The second term pertains to the rearrangements driven by the inter-particle force and the last term accounts for the influence of the flow.

In principle the result in equation 3.102 along with equation 3.98 form a closed set of equations for the stress at any given time. However, in practice, one needs to make further assumptions in order to evaluate the integrals analytically.

3.4.3 Affine Deformations

In order to proceed one must make the assumption that the two particle distribution function, evolving according to equation 3.89, remains an affine transformation of the equilibrium distribution function, g_e. While this may not be valid in all flow situations it is nevertheless a necessary assumption to make in order to proceed with the analytical treatment.

If the fluid is deformed by an arbitrary deformation, represented by the deformation gradient tensor,

$$\mathbf{F}_{ij} = \frac{\partial \mathbf{r}'_i}{\partial \mathbf{r}_j}, \tag{3.103}$$

$\mathbf{r}'$ being the vector after the deformation, then the two particle distribution function will

---

(23) In fact it can be shown that this is a safe assumption for all the potentials of interest here. This will be proven in appendix B.1.

(24) At this stage it is especially important to remember that $\mathbf{N}$ must be split into component form before any operators act, as they must act on each element individually, not the whole matrix.

change according to

$$g\left\{\mathbf{r}\right\} \rightarrow g\left\{\mathbf{F}\cdot\mathbf{r}\right\}. \tag{3.104}$$

In two dimensions this can be thought of in terms of the deformation of an initially circular equiprobability contour of g. An example of a general deformation is shown in figure 3.16.

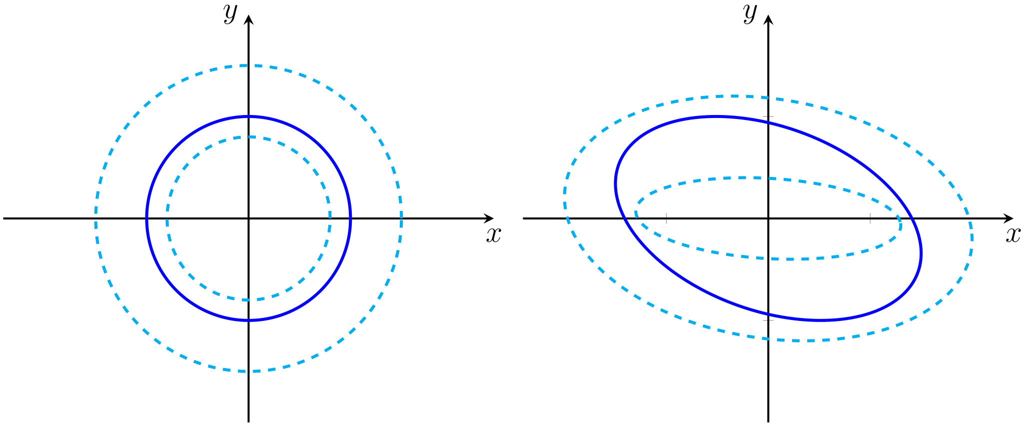

(a) Equilibrium, isotropic, two particle distribution function.

(b) Two particle distribution function following an arbitrary deformation.

Figure 3.16: Sketches of some of the equiprobability contours of the two particle distribution function before a deformation, in (a) and after a deformation, in (b).

In most cases applying the transformation given in equation 3.104 would make it impossible to evaluate the integrals in equations 3.96 and 3.102 analytically, as the possibility of $\mathbf{F}$ depending on $\mathbf{r}$ would mean that g would become a very complicated function of position. However, if the deformation is assumed to be affine, this provides a means of eliminating g and replacing it with the equilibrium two particle distribution function, g_e, discussed in section 3.4.1.1, which is a function of $|\mathbf{r}|$ only. Consequently one need only ever consider one of the probability contours of the two particle distribution function since all of the other contours will undergo exactly the same deformation. While this assumption may not hold in all flow situations it is necessary in order to make progress with the analytical treatment of the model and one may safely assume that this holds to a good approximation whenever a single power of r dominates equation 3.89. This occurs in the limits of both low and high Péclet number.

Physically the assumption that the deformation is affine requires that the ratios of the deformed to undeformed lengths are the same on all length scales. This to some extent implies that the particles are themselves deformable, however, as long as the typical distance between the particles is much greater than the typical particle size, as it will be in the dilute limit, the fact that the particles are not deformable can be safely ignored. It is worth noting that this assumption is somewhat complementary to the assumptions of low volume fraction made in sections 3.4.1 and 3.4.2.

The key to this method is that by assuming the deformation to be affine one ensures that $\mathbf{F}$ is independent of $\mathbf{r}$. This means that the coordinate transformation, F^{-1} can be applied to the integrands of equations 3.96 and 3.102 without any great difficulty, and effectively represents the deformation as a rescaling and rotation of coordinate axes while g remains constant. If, in addition to this, the interaction potential can be written as a sum of power laws in $|\mathbf{r}|^{(25)}$,

$$U = \sum_{i=1}^{O} U_i r^{p_i}, \tag{3.105}$$

where p_i and U_i are constants for the specific interaction, then the part of the integrand upon which $\mathbf{F}^{-1}$ acts is nothing more than a power law in $|\mathbf{r}|$. This means that it is possible to evaluate all of the necessary integrals analytically.

3.4.4 Constraints

3.4.4.1 Incompressible Flow

Although the assumption that the flow is incompressible has no significant effect on the ease with which the expressions for the microstructural stress and its rate of change can be formulated; it is an incredibly important assumption, both with regard to solving equations 3.98 and 3.102 for the stress as a function of time and in terms of the range of systems for which the model is valid.

Firstly, and most importantly, the assumption that the flow is incompressible means that the model is relevant for liquid suspensions, where the solvent provides an isotropic pressure to maintain incompressibility. This means that it relates to the kind of colloidal suspensions which are of interest in the model of the particle-laden fluid, described in section 3.1, as well as many other examples of colloid-liquid dispersion. Secondly it provides an additional constraint to reduce the number of unknowns in equations 3.98 and 3.102. This condition can be represented mathematically as

$$\|\mathbf{F}\| = 1, \tag{3.106}$$

which states that the determinant of the deformation gradient tensor, $\mathbf{F}$, must be unity. Physically speaking this can be thought of as a conservation of volume.

In addition to providing a constraint on the deformation gradient tensor, $\mathbf{F}$, demanding that the flow is incompressible also provides a constraint for the velocity gradient tensor, $\mathbf{K}$. This comes directly from the condition for incompressibility which normally complements Stokes' equations, described in section 3.1, namely

$$\boldsymbol{\nabla} \cdot \mathbf{v} = 0. \tag{3.107}$$

This is equivalent to

$$\mathrm{Tr}\{\mathbf{K}\} = 0. \tag{3.108}$$

3.4.4.2 Symmetry of the Stress Tensor

The intrinsic symmetry of this model is less a constraint and more a consequence of the way the stress tensor itself is formulated, owing to the fact that the isotropic pressure has been subtracted. This may also be thought of in terms of the two particle distribution

---

(25) This will be possible for any interaction since theoretically the sum can be infinite. However, realistically it is only possible to obtain meaningful expressions when the sum can be truncated after a small number of terms. Also it is worth bearing in mind that in a very limited number of cases the integrals will diverge.

function, g. By its definition this must also be invariant under the transformation $\mathbf{r} \to -\mathbf{r}$ and therefore has d, orthogonal, axes of symmetry, where d is the number of spatial dimensions. This leads to a number of important symmetries in the system, not least of which is the way the deformation may be represented. Though they are not technically constraints these symmetries are incredibly important in terms of reducing the number of free parameters in the system.

3.4.5 Small Strains

Up to this point all of the integrals in this model have been exact and can be solved analytically for any affine deformation, provided that the interaction potential can be written as the sum of a small number of power laws. However, the resulting equations for $\mathbf{\Sigma}$ and $\dot{\mathbf{\Sigma}}$ typically contain non-linear functions of the deformation gradient tensor, $\mathbf{F}$ and as such it is not possible to obtain an analytical expression for the stress as a function of time. Section 4.4.4 will describe the numerical methods used to evolve these equations forward in time and obtain the time dependence of the stress tensor in a given flow field. Furthermore, if the interaction potential is a complicated function of r and the summation cannot be truncated to only a small number of terms then the integrals themselves quickly become very complicated.

It is possible however to obtain an, approximate, analytical solution, for any interaction potential(26), provided that the total deformation, at any given time, is small. Mathematically this means that the deformation gradient tensor, $\mathbf{F}$ is close to the identity matrix, $\mathbf{I}$. Thus

$$\mathbf{F} \approx \mathbf{I} + \delta\mathbf{F}, \tag{3.109}$$

where $\delta\mathbf{F}$ is a small perturbation, $\delta F_{ij} \ll 1,\ \forall \{i, j\}$. When this is the case it is possible to expand the two particle distribution function about its equilibrium form in terms of $\delta\mathbf{F} \cdot \mathbf{r}$. Retaining only terms of order $\delta\mathbf{F} \cdot \mathbf{r}$ and lower results in

$$g\left\{\mathbf{F} \cdot \mathbf{r}\right\} \approx g_e\left\{\mathbf{r}\right\} + \mathbf{r} \cdot \delta\mathbf{F} \cdot \boldsymbol{\nabla} g_e\left\{\mathbf{r}\right\}. \tag{3.110}$$

Here the underling symmetries of the system have been used to write the last term in equation 3.110 in a slightly more convenient form. Substituting equation 3.110 into equations 3.98 and 3.102, and remembering that when the two particle distribution function takes its equilibrium form, as in the zeroth order term, there will be no contribution to the stress or the two relaxation terms in equation 3.102, gives

$$\mathbf{\Sigma} = \int_{-\infty}^{\infty} \left(\mathbf{r} \cdot \delta\mathbf{F} \cdot \boldsymbol{\nabla} g_e\right) \mathbf{N}\mathbf{r} \cdot \left(\boldsymbol{\nabla} U\right) dV \tag{3.111}$$

---

(26) Provided that it satisfies the conditions necessary for the integrands of the equations for $\mathbf{\Sigma}$ and $\dot{\mathbf{\Sigma}}$ to go to zero as $|\mathbf{r}| \to \infty$, as required in section 3.4.2.

and

$$\begin{aligned}\dot{\mathbf{\Sigma}} =&\mathcal{D}\int_{-\infty}^{\infty}\left(\mathbf{r}\cdot\delta\mathbf{F}\cdot\boldsymbol{\nabla}g_e\right)\nabla^2\left[\mathbf{N}\mathbf{r}\cdot\boldsymbol{\nabla}U\right]dV-\mathcal{M}\int_{-\infty}^{\infty}\left(\mathbf{r}\cdot\delta\mathbf{F}\cdot\boldsymbol{\nabla}g_e\right)\boldsymbol{\nabla}\left[\mathbf{N}\mathbf{r}\cdot\boldsymbol{\nabla}U\right]\cdot\boldsymbol{\nabla}UdV\\&+\int_{-\infty}^{\infty}\left(\mathbf{r}\cdot\delta\mathbf{F}\cdot\boldsymbol{\nabla}g_e\right)\boldsymbol{\nabla}\left[\mathbf{N}\mathbf{r}\cdot\boldsymbol{\nabla}U\right]\cdot\mathbf{K}\cdot\mathbf{r}dV+\int_{-\infty}^{\infty}g_e\boldsymbol{\nabla}\left[\mathbf{N}\mathbf{r}\cdot\boldsymbol{\nabla}U\right]\cdot\mathbf{K}\cdot\mathbf{r}dV.\end{aligned} \tag{3.112}$$

Since both g_e and the interaction potential, U, depend only on the magnitude of the separation then it makes sense to evaluate the integrals in spherical polar coordinates. This can be done, without loss of generality with respect to the coordinate system in which the stress and strain rate tensors exist, by applying the matrix transformation $\mathbf{M}$, which performs the appropriate transformation of the tensors to make them compatible with the spherical polar integrals$^{(27)}$. Thus

$$\mathbf{\Sigma}=\int_{-\infty}^{\infty}\left(\mathbf{r}\cdot\mathbf{M}\cdot\delta\mathbf{F}\cdot\mathbf{M}^T\cdot\boldsymbol{\nabla}g_e\right)\mathbf{N}\mathbf{r}\cdot\left(\boldsymbol{\nabla}U\right)dV \tag{3.113}$$

and

$$\begin{aligned}\dot{\mathbf{\Sigma}} =&\int_{-\infty}^{\infty}g_e\boldsymbol{\nabla}[\mathbf{N}\mathbf{r}\cdot\boldsymbol{\nabla}U]\cdot\mathbf{M}\cdot\mathbf{K}\cdot\mathbf{M}^T\cdot\mathbf{r}dV+\mathcal{D}\int_{-\infty}^{\infty}(\mathbf{r}\cdot\mathbf{M}\cdot\delta\mathbf{F}\cdot\mathbf{M}^T\cdot\boldsymbol{\nabla}g_e)\nabla^2[\mathbf{N}\mathbf{r}\cdot\boldsymbol{\nabla}U]dV\\&-\mathcal{M}\int_{-\infty}^{\infty}(\mathbf{r}\cdot\mathbf{M}\cdot\delta\mathbf{F}\cdot\mathbf{M}^T\cdot\boldsymbol{\nabla}g_e)\boldsymbol{\nabla}[\mathbf{N}\mathbf{r}\cdot\boldsymbol{\nabla}U]\cdot\boldsymbol{\nabla}UdV\\&+\int_{-\infty}^{\infty}(\mathbf{r}\cdot\mathbf{M}\cdot\delta\mathbf{F}\cdot\mathbf{M}^T\cdot\boldsymbol{\nabla}g_e)\boldsymbol{\nabla}[\mathbf{N}\mathbf{r}\cdot\boldsymbol{\nabla}U]\cdot\mathbf{M}\cdot\mathbf{K}\cdot\mathbf{M}^T\cdot\mathbf{r}dV.\end{aligned} \tag{3.114}$$

Using the symmetry properties of the matrices involved it is possible rearrange equations 3.113 and 3.114 to

$$\mathbf{\Sigma}=\delta\mathbf{F}:\mathbf{A} \tag{3.115}$$

and

$$\dot{\mathbf{\Sigma}}=\mathbf{K}:\mathbf{B}+\delta\mathbf{F}:\mathbf{C}+\mathbf{K}:\delta\mathbf{F}:\mathbf{D}, \tag{3.116}$$

where $\mathbf{A}$, $\mathbf{B}$, $\mathbf{C}$ and $\mathbf{D}$ are constants defiend as:

$$\mathbf{A}\equiv\int_{-\infty}^{\infty}\mathbf{r}\cdot\mathbf{M}\mathbf{M}^T\cdot\left(\boldsymbol{\nabla}g_e\right)\mathbf{N}\mathbf{r}\cdot\left(\boldsymbol{\nabla}U\right)dV \tag{3.117a}$$

$$\mathbf{B}\equiv\int_{-\infty}^{\infty}g_e\boldsymbol{\nabla}\left[\mathbf{N}\mathbf{r}\cdot\boldsymbol{\nabla}U\right]\cdot\mathbf{M}\mathbf{M}^T\cdot\mathbf{r}dV \tag{3.117b}$$

$$\begin{aligned}\mathbf{C}\equiv&\mathcal{D}\int_{-\infty}^{\infty}\mathbf{r}\cdot\mathbf{M}\mathbf{M}^T\cdot\left(\boldsymbol{\nabla}g_e\right)\nabla^2\left[\mathbf{N}\mathbf{r}\cdot\boldsymbol{\nabla}U\right]dV\\&-\mathcal{M}\int_{-\infty}^{\infty}\mathbf{r}\cdot\mathbf{M}\mathbf{M}^T\cdot\left(\boldsymbol{\nabla}g_e\right)\boldsymbol{\nabla}\left[\mathbf{N}\mathbf{r}\cdot\boldsymbol{\nabla}U\right]\cdot\boldsymbol{\nabla}UdV\end{aligned} \tag{3.117c}$$

$$\mathbf{D}\equiv\int_{-\infty}^{\infty}\left(\mathbf{r}\cdot\mathbf{M}\mathbf{M}^T\cdot\boldsymbol{\nabla}g_e\right)\boldsymbol{\nabla}\left[\mathbf{N}\mathbf{r}\cdot\boldsymbol{\nabla}U\right]\cdot\mathbf{M}\mathbf{M}^T\cdot\mathbf{r}dV \tag{3.117d}$$

and depend only on the choice of the coordinate system, interaction potential and volume

---

(27) The matrix, $\mathbf{N}$, which discriminates between the components of the stress tensor must also be written in spherical polar coordinates.

fraction of particles. Thus, given the constraints already discussed in section 3.4.4(28) , equations 3.115 and 3.116 form a closed set of linear differential equations for the two unknowns, $\delta\mathbf{F}$ and $\mathbf{\Sigma}$.

3.4.5.1 Potentials of Mean Force

The fact that the constitutive relation becomes much simpler in the limit of small strains allows one to obtain results for systems with much more complicated interaction potentials. This is of particular interest in the case where one wishes to simulate the effects of including many particle interactions whilst retaining the simplicity of the theory based upon pair interactions. This can be done by first obtaining the radial distribution function for a system of particles which includes higher order interactions and then using equation 3.91 to obtain the pairwise interaction which would produce the same, equilibrium, radial distribution function. This potential is referred to as the potential of mean force, U_{mf}.

One approach to obtaining such a radial distribution function is to use the Ornstein-Zernike equation[98],

$$h = c + \rho \int ch d\mathbf{r} \tag{3.118}$$

where $h = g_e - 1$ and c is the direct correlation function, which can be thought of as a simplified, short range, version of the true correlation function. Although the Ornstein-Zernike equation is exact this is only the case because it essentially defines c. In order to solve for h, and c, one requires a closure condition relating h and c[98]. There are several such equations commonly used in the literature[98,166]. One particularly popular closure condition is the Percus-Yevick approximation[166] which produces results which are valid for hard spheres[98,166].

---

(28) It is worth noting here that in order to enforce incompressibility, and satisfy equation 3.106, in a way that is consistent with the fact that the strain is small, one requires $\mathrm{Tr}\{\delta\mathbf{F}\} = 0$, not $\|\delta\mathbf{F}\| = 1$ as one might expect. This is perhaps best illustrated with an example. Consider the case of two dimensional Cartesian coordinates. One requires $1 = \|\mathbf{F}\| = \left\| \begin{smallmatrix} 1+\delta F_{xx} & \delta F_{xy} \\ \delta F_{yx} & 1+\delta F_{yy} \end{smallmatrix} \right\| = 1 + \delta F_{xx} + \delta F_{yy} + \delta F_{xx}\delta F_{yy} - \delta F_{xy}\delta F_{yx}$. Thus remembering that all of the elements of $\delta\mathbf{F}$ are small and retaining only first order terms one obtains $\delta F_{yy} = -\delta F_{xx}$, hence $\mathrm{Tr}\{\delta\mathbf{F}\} = 0$.

Chapter 4

Methods

4.1 Simulation of a Particle-Laden Fluid

4.1.1 Rescaling of the Equations of Motion

Before any simulations were performed the equations of motion for the two fluid model, given in equation set 3.18, were rescaled in order to reduce the number of free parameters and make discussion in terms of the relative sizes of the parameters easer.

In order to obtain the appropriate coordinate transformations one must first write the unknowns in a form where the rescaling factors appear explicitly;

$$\mathbf{r} = r_0\hat{\mathbf{r}} \qquad (4.1a)$$

$$\mathbf{v} = v_0\hat{\mathbf{v}} \qquad (4.1b)$$

$$\mathbf{g} = g_0\hat{\mathbf{g}} \qquad (4.1c)$$

$$p = p_0\hat{p} \qquad (4.1d)$$

$$t = t_0\hat{t}. \qquad (4.1e)$$

where $\hat{\mathbf{r}}$, $\hat{\mathbf{v}}$, $\hat{\mathbf{g}}$, $\hat{p}$ and $\hat{t}$ are the rescaled length, velocity, acceleration, pressure and time respectively. Since there are three basic units in the system: length, time and mass, then one is free to choose three of the scaling factors by setting three units and the remaining two will follow. Substituting these values into equation set 3.18 yields

$$\rho_p g_0\hat{\mathbf{g}}-\zeta_p v_0\hat{\mathbf{v}}_p-\zeta_{sp}v_0(1-\phi)(\hat{\mathbf{v}}_p-\hat{\mathbf{v}}_s)-\frac{p_0}{r_0}\hat{\boldsymbol{\nabla}}\hat{p}-\frac{1}{\phi}\frac{p_0}{r_0}\hat{\boldsymbol{\nabla}}\hat{\pi}+\frac{v_0}{r_0^2}\hat{\boldsymbol{\nabla}}\cdot\left(\eta_p\left[\hat{\boldsymbol{\nabla}}\hat{\mathbf{v}}_p+\left(\hat{\boldsymbol{\nabla}}\hat{\mathbf{v}}_p\right)^T\right]\right)=\mathbf{0} \qquad (4.2a)$$

$$\rho_s g_0\hat{\mathbf{g}}-\zeta_s v_0\hat{\mathbf{v}}_s-\zeta_{sp}v_0\phi(\hat{\mathbf{v}}_s-\hat{\mathbf{v}}_p)-\frac{p_0}{r_0}\hat{\boldsymbol{\nabla}}p+\frac{v_0}{r_0^2}\hat{\boldsymbol{\nabla}}\cdot\left(\eta_s\left[\hat{\boldsymbol{\nabla}}\hat{\mathbf{v}}_s+\left(\hat{\boldsymbol{\nabla}}\hat{\mathbf{v}}_s\right)^T\right]\right)=\mathbf{0} \qquad (4.2b)$$

$$\frac{v_0}{r_0}\hat{\boldsymbol{\nabla}}\cdot[\phi\hat{\mathbf{v}}_p+(1-\phi)\hat{\mathbf{v}}_s]=0 \qquad (4.2c)$$

$$\frac{1}{t_0}\frac{\partial\phi}{\partial\hat{t}}+\frac{v_0}{r_0}\hat{\boldsymbol{\nabla}}\cdot(\phi\hat{\mathbf{v}}_p)=0. \qquad (4.2d)$$

It its clear from equation set 4.2 that three of the free parameters can be removed by careful choice of the scale factors. For the purposes of the present work ζ_{sp}, η_s and ρ_s shall be removed, in essence rewriting all of the particle fluid's properties such that they are represented relative to the solvent's properties. To this end $r_0 = \sqrt{\frac{\eta_s}{\zeta_{sp}}}$, $t_0 = \frac{\rho_s}{\zeta_{sp}}$, $v_0 = \frac{\sqrt{\eta_s\zeta_{sp}}}{\rho_s}$, $g_0 = \frac{\zeta_{sp}}{\rho_s^2}\sqrt{\eta_s\zeta_{sp}}$ and $p_0 = \frac{\eta_s\zeta_{sp}}{\rho_s}$. Making these substitutions simplifies equation set 4.2 to

$$\frac{\rho_p}{\rho_s}\hat{\mathbf{g}} - \frac{\zeta_p}{\zeta_{sp}}\hat{\mathbf{v}}_p - (1-\phi)\left(\hat{\mathbf{v}}_p - \hat{\mathbf{v}}_s\right) - \hat{\boldsymbol{\nabla}}\hat{p} - \frac{1}{\phi}\hat{\boldsymbol{\nabla}}\hat{\pi} + \hat{\boldsymbol{\nabla}}\cdot\left(\frac{\eta_p}{\eta_s}\left[\hat{\boldsymbol{\nabla}}\hat{\mathbf{v}}_p + \left(\hat{\boldsymbol{\nabla}}\hat{\mathbf{v}}_p\right)^T\right]\right) = \mathbf{0} \tag{4.3a}$$

$$\hat{\mathbf{g}} - \frac{\zeta_s}{\zeta_{sp}}\hat{\mathbf{v}}_s - \phi\left(\hat{\mathbf{v}}_s - \hat{\mathbf{v}}_p\right) - \hat{\boldsymbol{\nabla}}p + \hat{\boldsymbol{\nabla}}\cdot\left[\hat{\boldsymbol{\nabla}}\hat{\mathbf{v}}_s + \left(\hat{\boldsymbol{\nabla}}\hat{\mathbf{v}}_s\right)^T\right] = \mathbf{0} \tag{4.3b}$$

$$\hat{\boldsymbol{\nabla}}\cdot\left[\phi\hat{\mathbf{v}}_p + (1-\phi)\,\hat{\mathbf{v}}_s\right] = 0 \tag{4.3c}$$

$$\frac{\partial\phi}{\partial\hat{t}} + \hat{\boldsymbol{\nabla}}\cdot\left(\phi\hat{\mathbf{v}}_p\right) = 0. \tag{4.3d}$$

Finally making the definitions:

$$\hat{\zeta}_p \equiv \frac{\zeta_p}{\zeta_{sp}} \tag{4.4a}$$

$$\hat{\zeta}_s \equiv \frac{\zeta_s}{\zeta_{sp}} \tag{4.4b}$$

$$\hat{\rho} \equiv \frac{\rho_p}{\rho_s} \tag{4.4c}$$

$$\hat{\eta} \equiv \frac{\eta_p}{\eta_s}, \tag{4.4d}$$

removed all of the dimensional parameters from equation set 3.18 reducing the equations of motion for the model to[3]

$$\hat{\rho}\hat{\mathbf{g}} - \hat{\zeta}_p\hat{\mathbf{v}}_p - (1-\phi)\left(\hat{\mathbf{v}}_p - \hat{\mathbf{v}}_s\right) - \hat{\boldsymbol{\nabla}}\hat{p} - \frac{1}{\phi}\hat{\boldsymbol{\nabla}}\hat{\pi} + \hat{\boldsymbol{\nabla}}\cdot\left(\hat{\eta}\left[\hat{\boldsymbol{\nabla}}\hat{\mathbf{v}}_p + \left(\hat{\boldsymbol{\nabla}}\hat{\mathbf{v}}_p\right)^T\right]\right) = \mathbf{0} \tag{4.5a}$$

$$\hat{\mathbf{g}} - \hat{\zeta}_s\hat{\mathbf{v}}_s - \phi\left(\hat{\mathbf{v}}_s - \hat{\mathbf{v}}_p\right) - \hat{\boldsymbol{\nabla}}p + \hat{\boldsymbol{\nabla}}\cdot\left[\hat{\boldsymbol{\nabla}}\hat{\mathbf{v}}_s + \left(\hat{\boldsymbol{\nabla}}\hat{\mathbf{v}}_s\right)^T\right] = \mathbf{0} \tag{4.5b}$$

$$\hat{\boldsymbol{\nabla}}\cdot\left[\phi\hat{\mathbf{v}}_p + (1-\phi)\,\hat{\mathbf{v}}_s\right] = 0 \tag{4.5c}$$

$$\frac{\partial\phi}{\partial\hat{t}} + \hat{\boldsymbol{\nabla}}\cdot\left(\phi\hat{\mathbf{v}}_p\right) = 0. \tag{4.5d}$$

Here one can interpret the two drag coefficients, $\hat{\zeta}_p$ and $\hat{\zeta}_s$ as being the magnitudes of the particle-surface and solvent-surface drag coefficients relative to the drag coefficient for the particle-solvent interaction, respectively, the density, $\hat{\rho}$, as the density of the particles relative to the solvent and the viscosity, $\hat{\eta}$, as the viscosity of the particles relative to the viscosity of the solvent. There is one, perhaps subtle, point worth making at this stage in that some of the scaling factors have implicitly been assumed constant across the whole system because they have been placed in front of the derivatives which operate on their respective variables. Hence one reason why they have been chosen to be properties of the solvent as they are invariant even in the more sophisticated models, introduced in section 3.1.2, which all alter properties of the particle fluid. Of course another good reason for this choice is that the solvent provides a natural benchmark for the properties of the particle fluid in general and helps to give one a physical intuition of what to expect from the flow behaviour.

4.1.2 Moving Into a Co-moving Frame

In an attempt to reduce the amount of numerical diffusion and make patterns appear static[3] so that they were easier to identify the simulation was performed in a frame that was co-moving with the particle velocity of a uniform mixture of fluid with the given system parameters, hereafter referred to as the particle drift velocity, $\mathbf{v}_{pd}$. This was chosen as the zero of velocity since it was thought that this would reduce numerical diffusion to the greatest extent since it reduced the net flux of the volume fraction, ϕ, between cells to just that which was due to inhomogeneity in the fluid.

In order to obtain the particle drift velocity one must solve equation set 4.5 for uniform steady flow. In this case, by definition, all of the derivatives, including the time derivative, must be zero leaving just the two vector equations

$$\hat{\rho}\hat{\mathbf{g}} - \hat{\zeta}_p\hat{\mathbf{v}}_{pd} - (1-\phi_0)\left(\hat{\mathbf{v}}_{pd} - \hat{\mathbf{v}}_{sd}\right) = \mathbf{0} \tag{4.6a}$$

$$\hat{\mathbf{g}} - \hat{\zeta}_s\hat{\mathbf{v}}_{sd} - \phi_0\left(\hat{\mathbf{v}}_{sd} - \hat{\mathbf{v}}_{pd}\right) = \mathbf{0}, \tag{4.6b}$$

where $\hat{\mathbf{v}}_{sd}$ is the solvent drift velocity and ϕ_0 is the volume fraction in the homogeneous fluid, equivalent to the average volume fraction of the same fluid in an inhomogeneous state. Since equation set 4.6 consists of two, linear, equations for the two unknowns, $\hat{\mathbf{v}}_{sd}$ and $\hat{\mathbf{v}}_{pd}$, they can be readly solved to obtain⁽¹⁾

$$\hat{\mathbf{v}}_{pd} = \frac{1 + \hat{\zeta}_s\hat{\rho} + \phi_0\left(\hat{\rho} - 1\right)}{\hat{\zeta}_s\hat{\zeta}_p + \phi_0\hat{\zeta}_p + \hat{\zeta}_s\left(1 - \phi_0\right)}\hat{\mathbf{g}}. \tag{4.7}$$

One can then transform equation set 4.5 in to the co-moving frame by applying the transformations

$$\hat{\mathbf{v}}_p \rightarrow \hat{\mathbf{v}}_p - \hat{\mathbf{v}}_{pd} \tag{4.8a}$$

$$\hat{\mathbf{v}}_s \rightarrow \hat{\mathbf{v}}_s - \hat{\mathbf{v}}_{pd} \tag{4.8b}$$

and remembering that the time derivative must be replaced with the Lagrangian derivative,

$$\frac{\partial}{\partial\hat{t}} \rightarrow \frac{\partial}{\partial\hat{t}} + \hat{\mathbf{v}}_{pd}\cdot\hat{\boldsymbol{\nabla}}, \tag{4.9}$$

to obtain

$$\hat{\rho}\hat{\mathbf{g}} - \hat{\zeta}_p\hat{\mathbf{v}}_{pd} - \hat{\zeta}_p\hat{\mathbf{v}}_p - (1-\phi)\left(\hat{\mathbf{v}}_p - \hat{\mathbf{v}}_s\right) - \hat{\boldsymbol{\nabla}}\hat{p} - \frac{1}{\phi}\hat{\boldsymbol{\nabla}}\hat{\pi} + \hat{\boldsymbol{\nabla}}\cdot\left(\hat{\eta}\left[\hat{\boldsymbol{\nabla}}\hat{\mathbf{v}}_p + \left(\hat{\boldsymbol{\nabla}}\hat{\mathbf{v}}_p\right)^T\right]\right) = \mathbf{0} \tag{4.10a}$$

$$\hat{\mathbf{g}} - \hat{\zeta}_s\hat{\mathbf{v}}_{pd} - \hat{\zeta}_s\hat{\mathbf{v}}_s - \phi\left(\hat{\mathbf{v}}_s - \hat{\mathbf{v}}_p\right) - \hat{\boldsymbol{\nabla}}p + \hat{\boldsymbol{\nabla}}\cdot\left[\hat{\boldsymbol{\nabla}}\hat{\mathbf{v}}_s + \left(\hat{\boldsymbol{\nabla}}\hat{\mathbf{v}}_s\right)^T\right] = \mathbf{0} \tag{4.10b}$$

$$\hat{\boldsymbol{\nabla}}\cdot\left[\phi\hat{\mathbf{v}}_p + (1-\phi)\,\hat{\mathbf{v}}_s\right] = 0 \tag{4.10c}$$

$$\frac{\partial\phi}{\partial\hat{t}} + \hat{\boldsymbol{\nabla}}\cdot\left(\phi\hat{\mathbf{v}}_p\right) = 0. \tag{4.10d}$$

It is worth noting here that one could obtain a set of equations identical to equation set 4.5 simply by redefining $\hat{\mathbf{g}}$ and $\hat{\rho}$ as

$$\hat{\rho} \rightarrow \frac{\hat{\rho}\hat{\mathbf{g}} + \hat{\zeta}_p\hat{\mathbf{v}}_{pd}}{\hat{\mathbf{g}} + \hat{\zeta}_s\hat{\mathbf{v}}_{pd}} \tag{4.11a}$$

$$\hat{\mathbf{g}} \rightarrow \hat{\mathbf{g}} + \hat{\zeta}_s\hat{\mathbf{v}}_{pd}. \tag{4.11b}$$

---

(1) For completeness $\hat{\mathbf{v}}_{sd} = \dfrac{1 + \hat{\zeta}_p + \phi_0\left(\hat{\rho} - 1\right)}{\hat{\zeta}_s\hat{\zeta}_p + \phi_0\hat{\zeta}_p + \hat{\zeta}_s\left(1 - \phi_0\right)}\hat{\mathbf{g}}$, though this was not used.

4.1.3 Equations of Motion in Matrix Form

With the equations of motion in their final state it was then necessary to discretise the system so that numerical solutions could be found. There are several important elements to this procedure. Firstly, since the model is two dimensional, one requires a two dimensional grid of cells, where each cell is assumed to be small enough such that the quantities inside it may be considered constant across the entire area of the cell. Figure 4.1 shows a 5 by 5 example of the kind of grid used in simulations.

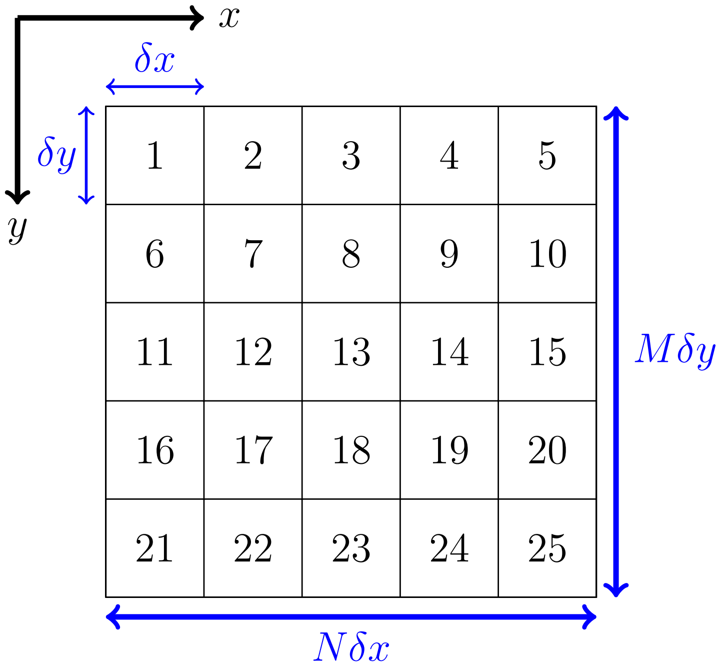

Figure 4.1: Diagram of a 5 by 5 grid of the kind used in the simulation of the particle-laden fluid. Here δx and δy are the lengths of the edges of the cell and N and M are the number of cells in the x and y directions respectively, here $N = M = 5$. The numbers in the cells represent the positions at which the values in those cells appear in the vectors describing the system.

Here the numbers in the cells correspond to the positions at which the quantities appear in the various vectors describing the system(2). Although this choice was entirely arbitrary it cannot be overemphasised as it was crucial in determining the structure of the matrices and vectors which were used to describe the discrete model.

With this coordinate system in place it was then possible to write the, continuous, equations of motion, given in equation set 4.10, in discrete form. This was done firstly by separating the two vector equations into orthogonal components, on a Cartesian grid like the one shown in figure 4.1, to give a total of six, scalar, equations for the six unknowns, $\hat{v}_{px}$, $\hat{v}_{py}$, $\hat{v}_{sx}$, $\hat{v}_{sy}$, $\hat{p}$ and ϕ. These equations were then discretised such that the six unknowns referred to their respective quantities in a given cell. This resulted in a set of $6NM$ equations with six unknowns for each of the NM cells in the grid. This set of equations can be represented in matrix-vector form as follows:

---

(2) This is known as row major ordering.

$$[2\mathbf{\Delta}_x\cdot\mathbf{H}\cdot\mathbf{\Delta}_x+\mathbf{\Delta}_y\cdot\mathbf{H}\cdot\mathbf{\Delta}_y-(\mathbf{I}-\mathbf{\Phi})-\mathbf{Z}_p]\cdot\mathbf{v}_{px}+\mathbf{\Delta}_y\cdot\mathbf{H}\cdot\mathbf{\Delta}_x\cdot\mathbf{v}_{py}+(\mathbf{I}-\mathbf{\Phi})\cdot\mathbf{v}_{sx}-\mathbf{\Delta}_x\cdot\mathbf{p} \\ -\mathbf{\Phi}^{-1}\cdot\mathbf{\Delta}_x\cdot\boldsymbol{\pi}=\mathbf{0} \tag{4.12a}$$

$$\mathbf{R}\cdot\mathbf{g}+[2\mathbf{\Delta}_y\cdot\mathbf{H}\cdot\mathbf{\Delta}_y+\mathbf{\Delta}_x\cdot\mathbf{H}\cdot\mathbf{\Delta}_x-(\mathbf{I}-\mathbf{\Phi})-\mathbf{Z}_p]\cdot\mathbf{v}_{py}+\mathbf{\Delta}_x\cdot\mathbf{H}\cdot\mathbf{\Delta}_y\cdot\mathbf{v}_{px}+(\mathbf{I}-\mathbf{\Phi})\cdot\mathbf{v}_{sy} \\ -\mathbf{\Delta}_y\cdot\mathbf{p}-\mathbf{\Phi}^{-1}\cdot\mathbf{\Delta}_y\cdot\boldsymbol{\pi}=\mathbf{0} \tag{4.12b}$$

$$\left[2\mathbf{\Delta}_x^2+\mathbf{\Delta}_y^2-\mathbf{Z}_s-\mathbf{\Phi}\right]\cdot\mathbf{v}_{sx}+\mathbf{\Delta}_x\cdot\mathbf{\Delta}_y\cdot\mathbf{v}_{sy}+\mathbf{\Phi}\cdot\mathbf{v}_{px}-\mathbf{\Delta}_x\cdot\mathbf{p}=\mathbf{0} \tag{4.12c}$$

$$\mathbf{g}+\left[\mathbf{\Delta}_x^2+2\mathbf{\Delta}_y^2-\mathbf{Z}_s-\mathbf{\Phi}\right]\cdot\mathbf{v}_{sy}+\mathbf{\Delta}_x\cdot\mathbf{\Delta}_y\cdot\mathbf{v}_{sx}+\mathbf{\Phi}\cdot\mathbf{v}_{py}-\mathbf{\Delta}_y\cdot\mathbf{p}=\mathbf{0} \tag{4.12d}$$

$$\mathbf{\Delta}_x\cdot\mathbf{\Phi}\cdot\mathbf{v}_{px}+\mathbf{\Delta}_x\cdot(\mathbf{I}-\mathbf{\Phi})\cdot\mathbf{v}_{sx}+\mathbf{\Delta}_y\cdot\mathbf{\Phi}\cdot\mathbf{v}_{py}+\mathbf{\Delta}_y\cdot(\mathbf{I}-\mathbf{\Phi})\cdot\mathbf{v}_{sy}=\mathbf{0} \tag{4.12e}$$

$$\mathbf{\Delta}_t\cdot(\phi-\phi_{old})+\mathbf{\Delta}_x\cdot\mathbf{\Phi}\cdot\mathbf{v}_{px}+\mathbf{\Delta}_y\cdot\mathbf{\Phi}\cdot\mathbf{v}_{py}=\mathbf{0}. \tag{4.12f}$$

Here the lower case letters represent NM dimensional column vectors which are made up of the values of their respective quantities in each cell of the grid, where the position of the quantity in the vector corresponds to the cell number using the row major [151] numbering system demonstrated in figure 4.1, while the upper case letters represent square matrices of dimension NM. With the exception of the spatial derivatives, $\mathbf{\Delta}_x$ and $\mathbf{\Delta}_y$, these are all diagonal matrices which contain the values corresponding to each cell on their leading diagonal, using the same numbering system as that used for the vectors. This formulation means that the matrix-vector scalar products result in a vector which contains, for each cell, the product of the two given quantities from that cell and the spatial derivatives act in a very similar way producing a vector which contains the approximate value of the derivative of a given quantity at that point in space. More detail on exactly how $\mathbf{\Delta}_x$ and $\mathbf{\Delta}_y$ were formulated in order that they possess this property is given in section 4.1.3.2. Thanks to the properties of matrix multiplication it is possible to act with multiple matrices on one vector simply by repeatedly multiplying from the left. This means that taking the derivative of a product, for example, works in exactly the same way as one would expect from the continuum equations.

The meanings of all of the symbols used in equation set 4.12 are given in table 4.1.

$\mathbf{v}_{px}$,$\mathbf{V}_{px}$	Vector/Matrix containing the x component of the particle fluid velocity, $\hat{\mathbf{v}}_p \cdot \hat{\mathbf{x}}$, in each cell.
$\mathbf{v}_{py}$,$\mathbf{V}_{py}$	Vector/Matrix containing the y component of the particle fluid velocity, $\hat{\mathbf{v}}_p \cdot \hat{\mathbf{y}}$, in each cell.
$\mathbf{v}_{sx}$,$\mathbf{V}_{sx}$	Vector/Matrix containing the x component of the solvent velocity, $\hat{\mathbf{v}}_s \cdot \hat{\mathbf{x}}$, in each cell.
$\mathbf{v}_{sy}$,$\mathbf{V}_{sy}$	Vector/Matrix containing the y component of the solvent velocity, $\hat{\mathbf{v}}_s \cdot \hat{\mathbf{y}}$, in each cell.
$\mathbf{p}$,$\mathbf{P}$	Vector/Matrix containing the pressure, $\hat{p}$, in each cell.
$\boldsymbol{\phi}$,$\boldsymbol{\Phi}$	Vector/Matrix containing the volume fraction, ϕ, in each cell.
$\boldsymbol{\pi}$,$\boldsymbol{\Pi}$	Vector/Matrix containing the osmotic pressure, $\hat{\pi}$, in each cell.
$\mathbf{g}$,$\mathbf{G}$	Vector/Matrix containing the acceleration due to gravity in the co-moving frame, $\hat{\mathbf{g}} - \hat{\zeta}_s \hat{\mathbf{v}}_{pd}$, in each cell.
$\boldsymbol{\rho}$,$\mathbf{R}$	Vector/Matrix containing the relative density in the co-moving frame, $\frac{\hat{\zeta}_p \hat{\mathbf{v}}_{pd} - \hat{\rho}\hat{\mathbf{g}}}{\hat{\zeta}_s \hat{\mathbf{v}}_{pd} - \hat{\mathbf{g}}}$, in each cell.
$\boldsymbol{\eta}$,$\mathbf{H}$	Vector/Matrix containing the relative viscosity, $\hat{\eta}$, in each cell.
$\boldsymbol{\zeta}_p$,$\mathbf{Z}_p$	Vector/Matrix containing the relative drag coefficient for the particle fluid, $\hat{\zeta}_p$, in each cell.
$\boldsymbol{\zeta}_s$,$\mathbf{Z}_s$	Vector/Matrix containing the relative drag coefficient for the solvent, $\hat{\zeta}_s$, in each cell.
$\boldsymbol{\Delta}_x$	Matrix operator to produce a vector of x derivatives of the vector to its right.
$\boldsymbol{\Delta}_y$	Matrix operator to produce a vector of y derivatives of the vector to its right.
$\boldsymbol{\Delta}_t$	Matrix operator to divide all elements of the vector to its right by the size of the time step.

Table 4.1: Table of the symbols used in the discretised version of the model of the particle-laden fluid and their physical meaning.

4.1.3.1 Boundary Conditions

Since the aim of the present work is to simulate the flow of a bulk fluid draining over a surface one wishes to approximate bulk behaviour in the directions parallel to the surface[3]. These are the dimensions of this two dimensional model, the third dimension, normal to the surface, is neglected[3] and it is assumed that variations are trivial in this dimension as the film is thin. In order to achieve this using a finite grid periodic boundary conditions[3,115] were implemented in both the x and y directions. This means that whenever information was needed about the right hand neighbour of a cell on the far right, in order to take the x derivative for example, the information from the cell on the far left was used and vice-versa, and similarly for the top and bottom. In essence this is equivalent to surrounding the grid with identical copies of itself⁽³⁾.

This meant that there were no edge effects and thus every cell on this grid appeared as if it were in a bulk fluid. However, the use of periodic boundaries meant that care needed to be taken to make sure that the grid was much larger than the length scale of any correlations within the system or any structures which were likely to form so that the order forced upon the system by the periodic boundaries did not affect the results.

In addition to the spatial boundary conditions one must specify the zero of pressure, since none of the equations of motion depend on the absolute value of pressure, only its derivatives, hence the pressure in each cell is only defined by equation set 4.12 up to the addition of a constant. Furthermore since matter is conserved by equation 4.12f enforcing incompressibility in $NM-1$ cells automatically enforces incompressibility in the remaining cell so equation set 4.12 is in fact degenerate because one of the rows of equation 4.12e is implied by all of the others. The resolution to both of these problems⁽⁴⁾ is not to apply equation 4.12e to one of the cells⁽⁵⁾ and instead demand that the pressure in this cell is zero thus removing the degeneracy from equation set 4.12 by replacing the duplicate and introducing a new independent equation.

4.1.3.2 Spectral Derivatives

As mentioned previously one wishes to choose the entries of the matrices $\mathbf{\Delta}_x$ and $\mathbf{\Delta}_y$ such that when they act upon a vector from the left they produce a vector which is its x or y derivative respectively. Although the aim here is to obtain matrices capable of performing these operations on a two dimensional grid it makes sense to begin by considering how to approach the problem in one dimension. An example of such a grid is given in figure 4.2.

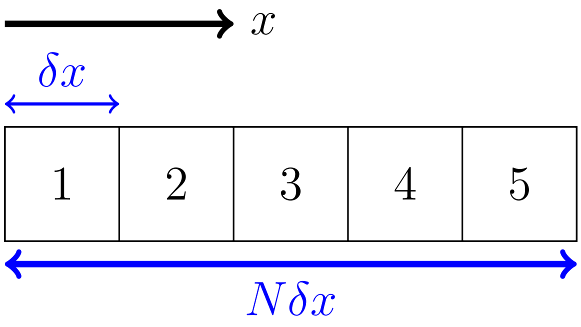

Figure 4.2: Diagram of a one dimensional grid with 5 cells.

As a first approach one might consider a simple differencing method for taking the derivative. In this one is presented with a choice of whether to take the derivatives in a symmetrical way,

$$\left.\frac{\partial f}{\partial x}\right|_{x=i\delta x} \approx \frac{1}{2\delta x}\left(f_{i+1} - f_{i-1}\right), \tag{4.13}$$

or one of two asymmetric ways,

$$\left.\frac{\partial f}{\partial x}\right|_{x=i\delta x} \approx \mp\frac{1}{\delta x}\left(f_i - f_{i\pm1}\right), \tag{4.14}$$

---

(3) Equivalently the grid may also be thought of as being on the surface of a tours, neglecting the curvature of course.

(4) Technically these are not two separate problems they are simply two manifestations of the same underlying issue.

(5) Typically the cell in the centre was used although the choice is entirely arbitrary.

where f is an arbitrary, continuous, function of x and δx is the size of each grid cell. The advantage of the symmetric method is that it produces a derivative which is centred at position i and has no bias toward either direction. However the symmetric method has the distinct disadvantage that the odd and even numbered cells are only coupled to one another through the periodic boundaries, and not at all if there is an even number of cells in the grid[151]. This is known as a checker board instability[151] and essentially means that, in the extreme case, one is simulating two grids which are interwoven, but do not interact with each other at all. The asymmetric method does not have this weakness and couples all of the cells in the grid[151]. The major disadvantages of this method are that the derivative used is technically the derivative at $x = i\left(\delta x \pm \frac{1}{2}\right)$ and one is forced to bias one direction[151] or another simply by choosing which direction to take the derivative in.

Fortunately, because the boundaries are periodic, it was possible to take the derivatives using a spectral method[114], which had the advantage of being symmetrical and coupling all of the cells in the grid. Because this method accounted for the values in all of the cells it in some sense gave a better approximation of the derivative and was far less susceptible to extreme values. In the case of the present work the spectral method did come with a slight additional computational cost, which will be discussed in more detail in section 4.1.5.3, but it was deemed worthwhile because of the improvements it made to the accuracy of the derivatives(6). The basis for this method is the fact that, in wave-vector space, one can obtain the real-space derivative simply by multiplying by the wave-vector itself and then transforming back[114],

$$\frac{\partial f}{\partial x} = \mathcal{F}^{-1}\left\{-2\pi \mathrm{i} q_x \mathcal{F}\left\{f\right\}\right\}, \tag{4.15}$$

where f is any continuous periodic function in one dimensional real space, parametrised by x, q_x is the wave-vector and $\mathcal{F}$ and $\mathcal{F}^{-1}$ denote the Fourier transform and its inverse respectively(7).

A computationally efficient way of using this method to calculate the derivative would be to use a fast-Fourier-transform algorithm to perform both the forward and inverse Fourier transforms[114]. However, this is not compatible with the matrix formalism of the rest of the model as it would only produce a vector containing the derivative and hence there would be no straightforward means of solving equation set 4.12, as section 4.1.4 describes one requires the full Jacobian to solve the equations. For this reason the standard discrete Fourier transform was used as it is possible to create a matrix that performs

---

(6) Tests were performed using the other two methods and it was found that this system was very susceptible to checker-board type instabilities and there was a bias introduce by the asymmetric method.

(7) Here the factors of 2π are neglected from the transform and its inverse in order to keep the matrices, used later, since as simple as possible. The factor of 2π in equation 4.15 accounts for this and results in a derivative with the correct scaling.

exactly the same operation as the summation,

$$\mathcal{F}\left\{f\right\} \approx \frac{1}{N}\sum_{m=0}^{N} f|_m \, e^{\frac{2\pi\mathrm{i}qm}{N}} = \frac{1}{N}\begin{pmatrix} 1 & 1 & 1 & \dots & 1 \\ 1 & e^{\frac{2\pi\mathrm{i}}{N}} & e^{\frac{4\pi\mathrm{i}}{N}} & \dots & e^{\frac{2(N\text{-}1)\pi\mathrm{i}}{N}} \\ 1 & e^{\frac{4\pi\mathrm{i}}{N}} & e^{\frac{8\pi\mathrm{i}}{N}} & \dots & e^{\frac{4(N\text{-}1)\pi\mathrm{i}}{N}} \\ \vdots & \vdots & \vdots & \ddots & \vdots \\ 1 & e^{\frac{2(N\text{-}1)\pi\mathrm{i}}{N}} & e^{\frac{4(N\text{-}1)\pi\mathrm{i}}{N}} & \dots & e^{\frac{2(N\text{-}1)^2\pi\mathrm{i}}{N}} \end{pmatrix} \cdot \begin{pmatrix} f|_0 \\ f|_1 \\ f|_2 \\ \vdots \\ f|_N \end{pmatrix}, \tag{4.16}$$

where N is the number of cells in the one dimensional grid. Clearly the inverse Fourier transform can be obtained by taking the inverse, or in this case the Hermitian conjugate(8), of the matrix in equation 4.16. However, before this can be applied one must first act on the vector containing the Fourier transform of f with a diagonal matrix, $\mathbf{Q}_x$, that multiplies each term by the correct wave-vector,

$$\mathbf{Q}_x = \frac{1}{\delta x}\begin{pmatrix} 0 & 0 & 0 & \dots & 0 \\ 0 & 1 & 0 & \dots & 0 \\ 0 & 0 & 2 & \dots & 0 \\ \vdots & \vdots & \vdots & \ddots & \vdots \\ 0 & 0 & 0 & \dots & N-1 \end{pmatrix}. \tag{4.17}$$

Multiplying equation 4.16 from the left by $-2\pi\mathrm{i}\mathbf{Q}_x$ and then the Hermitian conjugate of the matrix that performs the Fourier transform, one obtains the operator, $\mathbf{\Delta}$, that produces a vector of estimates to the derivatives of the function, $f\left\{x\right\}$ on a finite grid,

$$\mathbf{\Delta} = \frac{-2\pi\mathrm{i}}{\delta x N^2}\begin{pmatrix} \sum\limits_{m=1}^{N} m & \sum\limits_{m=1}^{N} m e^{\frac{2m\pi\mathrm{i}}{N}} & \sum\limits_{m=1}^{N} m e^{\frac{4m\pi\mathrm{i}}{N}} & \dots & \sum\limits_{m=1}^{N} m e^{\frac{2(N\text{-}1)m\pi\mathrm{i}}{N}} \\ \sum\limits_{m=1}^{N} m e^{\frac{\text{-}2m\pi\mathrm{i}}{N}} & \sum\limits_{m=1}^{N} m & \sum\limits_{m=1}^{N} m e^{\frac{2m\pi\mathrm{i}}{N}} & \dots & \sum\limits_{m=1}^{N} m e^{\frac{2(N\text{-}2)m\pi\mathrm{i}}{N}} \\ \sum\limits_{m=1}^{N} m e^{\frac{\text{-}4m\pi\mathrm{i}}{N}} & \sum\limits_{m=1}^{N} m e^{\frac{\text{-}2m\pi\mathrm{i}}{N}} & \sum\limits_{m=1}^{N} m & \dots & \sum\limits_{m=1}^{N} m e^{\frac{2(N\text{-}3)m\pi\mathrm{i}}{N}} \\ \vdots & \vdots & \vdots & \ddots & \vdots \\ \sum\limits_{m=1}^{N} m e^{\frac{\text{-}2(N\text{-}1)m\pi\mathrm{i}}{N}} & \sum\limits_{m=1}^{N} m e^{\frac{\text{-}2(N\text{-}2)m\pi\mathrm{i}}{N}} & \sum\limits_{m=1}^{N} m e^{\frac{\text{-}2(N\text{-}3)m\pi\mathrm{i}}{N}} & \dots & \sum\limits_{m=1}^{N} m \end{pmatrix}. \tag{4.18}$$

Clearly all higher derivatives can be generated simply by applying $\mathbf{\Delta}$ multiple times. However, there is a more computationally efficient way to achieve this: if one simply acts with $-2\pi\mathrm{i}\boldsymbol{Q}_x$ n times before applying the inverse transform then one obtains a generalisation of $\mathbf{\Delta}$,

$$\mathbf{\Delta}^n = \left(\frac{-2\pi\mathrm{i}}{\delta x N}\right)^n \frac{1}{N}\begin{pmatrix} \sum\limits_{m=1}^{N} m^n & \sum\limits_{m=1}^{N} m^n e^{\frac{2m\pi\mathrm{i}}{N}} & \dots & \sum\limits_{m=1}^{N} m^n e^{\frac{2(N\text{-}1)m\pi\mathrm{i}}{N}} \\ \sum\limits_{m=1}^{N} m^n e^{\frac{\text{-}2m\pi\mathrm{i}}{N}} & \sum\limits_{m=1}^{N} m^n & \dots & \sum\limits_{m=1}^{N} m^n e^{\frac{2(N\text{-}2)m\pi\mathrm{i}}{N}} \\ \vdots & \vdots & \ddots & \vdots \\ \sum\limits_{m=1}^{N} m^n e^{\frac{\text{-}2(N\text{-}1)m\pi\mathrm{i}}{N}} & \sum\limits_{m=1}^{N} m^n e^{\frac{\text{-}2(N\text{-}2)m\pi\mathrm{i}}{N}} & \dots & \sum\limits_{m=1}^{N} m^n \end{pmatrix}, \tag{4.19}$$

---

(8) The Hermitian conjugate is identical to the inverse for the matrix in equation 4.16 thanks to the symmetry of the Fourier transform.

which produces the n^{th} derivative of the vector it acts upon. Finally in the case where f is a purely real function of x, as it is in the present work, equation 4.19 can be simplified slightly, such that all of the entries in the matrix will be real. This is achieved by applying Euler's formula to the complex exponentials, remembering that the function f is periodic, and then retaining only the odd terms if the derivative, n, is odd and even terms if n is even. Finally it is worth noting, though the fact was not used in the simulation, that the inverse of $\boldsymbol{\Delta}$, as one might expect, produces an estimate of the integral of the function over the width of the grid.

In order to test the performance of this method, compared to the simple differencing methods, the derivatives of several different functions were taken. Examples of some of these are shown in figure 4.3.

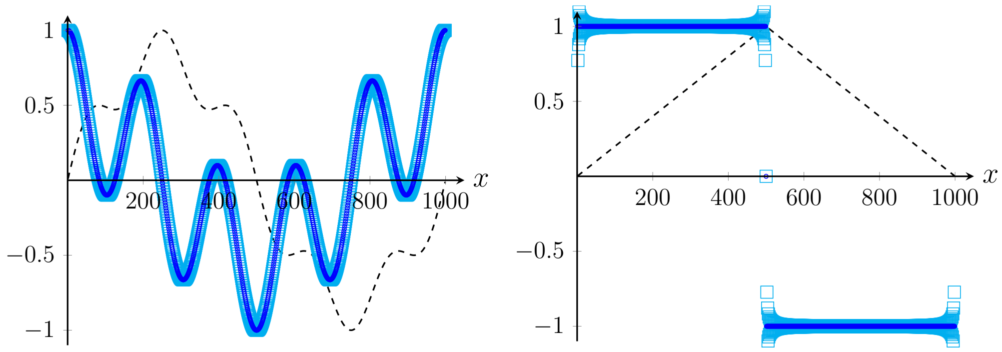

(a) A superposition of sinusoids.

(b) A piecewise function with a discontinuous derivative.

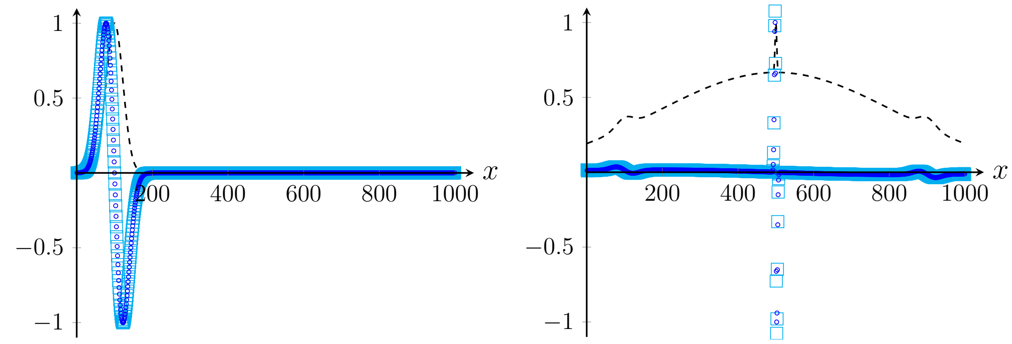

(c) An asymmetric function made from a Gaussian.

(d) A superposition of Gaussian functions with a sharp peak in the centre.

Figure 4.3: Plots showing examples of derivatives taken with both symmetric finite difference and spectral methods for a range of different functions on finite grids, for which $N = 1000$ and $\delta x = 1$. The cyan squares (□) indicate the values obtained from the spectral method while the blue circles (∘) are the values obtained from the symmetric differencing method. The dashed lines (- - -) show the forms of the original functions.

It is clear from figure 4.3 that the spectral method performs at least as well as the symmetric differencing on all of the smooth functions. However, as figure 4.3b shows it does not capture discontinuous features quite as well, this is clear from the slight smearing out of the step function close to the discontinuity. However, it was thought that this would not be a problem in the simulation of the particle-laden fluid as none of the variables are expected to contain discontinuities. On a coarse grid it was found that the spectral method out performs the symmetric differencing method, this is demonstrated in figure 4.4, where it is clear that the results of the spectral method are much closer to the analytical derivative of the function.

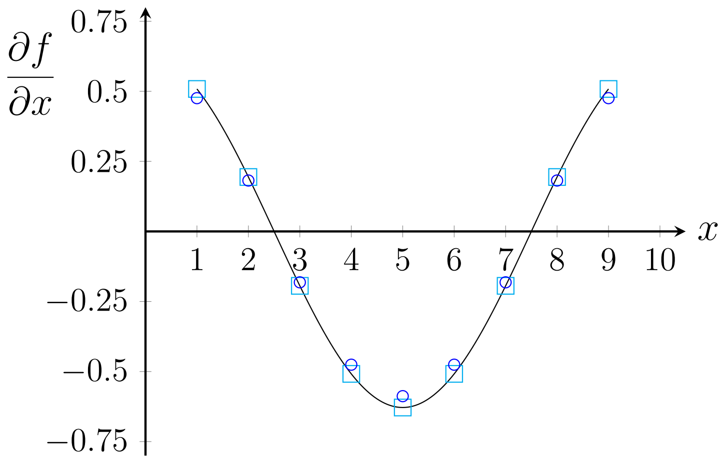

Figure 4.4: Plot of the derivatives of the function $f = \sin\left\{\frac{2\pi}{10}x\right\}$ obtained by both symmetric differencing, shown by the blue circles (○), and the spectral methods, shown by the cyan squares (□). The black line (——) shows the analytical solution, $\frac{\partial f}{\partial x} = \frac{2\pi}{10}\cos\left\{\frac{2\pi}{10}x\right\}$.

This is perhaps unsurprising since the spectral method can be thought of as a higher order approximation, using information from beyond the two nearest neighbours. In fact it is this property that produces the smearing out of the discontinuity seen in figure 4.3b.

The final step in incorporating this spectral method in to the simulation of the particle-laden fluid was to generalise the matrix, $\mathbf{\Delta}^n$ that performed the derivative in one dimension to two different matrices, $\mathbf{\Delta}_x$ and $\mathbf{\Delta}_y$, which performed the x and y derivatives, respectively, in a two dimensional system represented on a grid like that shown in figure 4.1. The vector formalism for the quantities in each grid cell makes this very straightforward since taking the derivative along any row or column is simply a matter of working out which cells are involved and placing the appropriate terms from $\mathbf{\Delta}$ into a square matrix of dimension NM and skipping the rest by padding the matrix with zeros. For example if one wishes to obtain the x derivative for the first row then one requires a NM dimensional square matrix with the matrix $\mathbf{\Delta}$ in the top left hand corner and zeros everywhere else. It is clear from figure 4.1 that in the case of a 5 by 5 grid this would correctly include entries from cells one to five only. The x derivative from any other row may be obtained equally well simply by moving the matrix $\mathbf{\Delta}$ down and to the right by an amount N within the larger matrix. Thus the overall x derivative, for the whole grid, can be obtained from a matrix, $\mathbf{\Delta}_x$, which is the sum of all such matrices, for all M, rows. The equivalent procedure for the y derivatives is perhaps less apparent. Here one wishes to skip all but one entry from every row so one needs to place the elements of $\mathbf{\Delta}$ such that they fall in every N^{th} row and N^{th} column. The derivative of the column to the left can then be obtained by moving these down and to the right by one and, as with $\mathbf{\Delta}_x$. One can then obtain the total y derivative by adding the matrices which perform this operation on each of the N rows together. As an example the full matrices for a 3 by 3 grid are as follows:

$$\mathbf{\Delta}_x^{3\times3} = \begin{pmatrix} \Delta_{11} & \Delta_{12} & \Delta_{13} & 0 & 0 & 0 & 0 & 0 & 0 \\ \Delta_{21} & \Delta_{22} & \Delta_{23} & 0 & 0 & 0 & 0 & 0 & 0 \\ \Delta_{31} & \Delta_{32} & \Delta_{33} & 0 & 0 & 0 & 0 & 0 & 0 \\ 0 & 0 & 0 & \Delta_{11} & \Delta_{12} & \Delta_{13} & 0 & 0 & 0 \\ 0 & 0 & 0 & \Delta_{21} & \Delta_{22} & \Delta_{23} & 0 & 0 & 0 \\ 0 & 0 & 0 & \Delta_{31} & \Delta_{32} & \Delta_{33} & 0 & 0 & 0 \\ 0 & 0 & 0 & 0 & 0 & 0 & \Delta_{11} & \Delta_{12} & \Delta_{13} \\ 0 & 0 & 0 & 0 & 0 & 0 & \Delta_{21} & \Delta_{22} & \Delta_{23} \\ 0 & 0 & 0 & 0 & 0 & 0 & \Delta_{31} & \Delta_{32} & \Delta_{33} \end{pmatrix}, \tag{4.20a}$$

$$\mathbf{\Delta}_y^{3\times3} = \begin{pmatrix} \Delta_{11} & 0 & 0 & \Delta_{12} & 0 & 0 & \Delta_{13} & 0 & 0 \\ 0 & \Delta_{11} & 0 & 0 & \Delta_{12} & 0 & 0 & \Delta_{13} & 0 \\ 0 & 0 & \Delta_{11} & 0 & 0 & \Delta_{12} & 0 & 0 & \Delta_{13} \\ \Delta_{21} & 0 & 0 & \Delta_{22} & 0 & 0 & \Delta_{23} & 0 & 0 \\ 0 & \Delta_{21} & 0 & 0 & \Delta_{22} & 0 & 0 & \Delta_{23} & 0 \\ 0 & 0 & \Delta_{21} & 0 & 0 & \Delta_{22} & 0 & 0 & \Delta_{23} \\ \Delta_{31} & 0 & 0 & \Delta_{32} & 0 & 0 & \Delta_{33} & 0 & 0 \\ 0 & \Delta_{31} & 0 & 0 & \Delta_{32} & 0 & 0 & \Delta_{33} & 0 \\ 0 & 0 & \Delta_{31} & 0 & 0 & \Delta_{32} & 0 & 0 & \Delta_{33} \end{pmatrix}. \tag{4.20b}$$

Clearly if the grid were not square then the dimensions of the one dimensional derivative matrix, $\boldsymbol{\Delta}$, would differ. Namely the x derivative would require an N dimensional matrix while the y derivative required an M dimensional matrix. Furthermore the cells of the grid need not be square either this would merely require a change of δx value in equation 4.19 to δy for the y derivative. With the exception of a small number of test cases to makes sure the meshing of the grid was not having a significant effect on the results, simulations were typically performed on square grids of square cells, as this made analysis slightly easier. Furthermore grids with an odd number of cells were always used as this meant that the diagonal terms in the one dimensional derivative matrix were always zero allowing for better performance optimisation, as is discussed in more detail in section 4.1.5.

4.1.3.3 Time Integration

Of course the central goal of the simulation was to integrate equation set 4.12 forwards in time. This was done using the backwards Euler method[108,158] . There were several reasons for this choice.

Firstly the implicit nature of the method means that, unlike forward integration schemes, which usually rely on a stability condition[151], this method is unconditionally stable[108,158] in terms of the size of the times step used(9). This is extremely important as it allowed for the use of significantly larger time steps and guaranteed that the numerical solution would remain physically realistic and not diverge from the true solution as the simulation time increased.

Secondly this relatively simple implicit method was much more straightforward to integrate into the equations of motion than a more sophisticated implicit scheme, such as the Crank-Nicholson method[108,116] which would have made equation set 4.12 significantly more complicated and increased computational costs both in terms of time and memory and although it offers second order accuracy it offers no improvement in the stability. Since the present work is mostly concerned with the formation of patterns, which occurs on long time scales relative to the motion of the fluids, it was thought at there would be no great benefit from obtaining high resolution on short time scales.

In terms of computational effort, for equations of the type presented here, this reverse Euler scheme is surprisingly efficient, even when compared with, the more common, forward Euler method. This is because the equations are non-linear. Because equation 4.12f is the only equation that contains a time derivative in a conventional, forward time integration, scheme one could reduce the size of the matrix making up equation set 4.12 from one with dimensions of $6NM$ to one with dimensions of $5NM$. This would speed up the simulation by a factor of no more than $\left(\frac{6}{5}\right)^{3}$(10). However, if decoupling ϕ had made equations 4.12a to 4.12e linear in the remaining variables this would have represented a significant saving, since it would have meant that the remaining five equations could have

---

(9) Though that is not to say that a solution will always be found when the time step is large, since solving the equations relies on an iterative scheme, discussed in section 4.1.4, that relies on the values at the previous time step as an initial guess.

(10) Assuming that the matrix inversion is carried out using a Gaussian elimination type method, such as LU-decomposition, which scales like the cube of the matrix dimension. In practice the sparse method[152], described in section 4.1.5.3 was used and since equations 4.12a to 4.12d account for the majority of the non-zero terms the saving for this method is likely to be much less.

been solved directly, with a single matrix decomposition rather than iteratively. Since this was not the case it was thought that the increased computational cost of $\left(\frac{6}{5}\right)^3$ for using the implicit method and solving all six equations together was easily outweighed by the potential to greatly increase the size of the time step without risking the simulation becoming unstable.

In order to implement the backwards Euler method the time derivative in equation 4.12f was written as the difference between the current, unknown, value of ϕ and the value of ϕ at the previous time step, ϕ_{old}, divided by the size of the time step[108,158]. Hence the term

$$\boldsymbol{\Delta}_t \cdot (\boldsymbol{\phi} - \boldsymbol{\phi}_{old}) \tag{4.21}$$

appears in equation 4.12f. All of the other values in this and the other equations of equation set 4.12 represent the values of variables at the current time step which were to be determined by solving the equations. This is how the method guarantees stability[108,158] since the values found will always be solutions to the equations(11) regardless of whether they accurately represent the progression of the solution in time.

In order to obtain the best compromise between accuracy and speed the size of the time step was set dynamically. Physically there are two key considerations here: the distance one is prepared to let the fastest fluid element in the system traverse during one time step and the change in osmotic pressure one is prepared to accept. It makes good sense to choose the time step such that at most the fastest fluid element in the system, be it solvent or particles, can traverse no more than one cell(12). In this way one avoids cells been skipped and giving the impression that the fluid disappears on one side of a cell and reappears on the other. With this model one must also consider the osmotic pressure as this can become very large quickly and sudden jumps in the pressure are best avoided. For this reason the current maximum osmotic pressure in the system was also taken into account when choosing the time step as more care needed to be taken when the osmotic pressure was high. Thus the time step was chosen according to

$$\delta t = \begin{cases} \dfrac{\delta l}{v_{max}} \delta_{max} & \pi_{max} \leq 1 \\ \dfrac{\delta l}{v_{max} \pi_{max}} \delta_{max} & \pi_{max} > 1 \end{cases}, \tag{4.22}$$

where δl is the smaller of the two cell dimensions, δn and δm, v_{max} is the maximum velocity in the system, for either fluid in either direction, π_{max} is the maximum magnitude of the osmotic pressure anywhere in the system and δ_{max} is a scale factor which controls how many cells can be traversed by the fastest fluid element when the osmotic pressure is less than one. This is set along with the other free parameters as a means of controlling the precision of the time evolution. It is worth noting that this physical argument is not the only factor that determines the most appropriate choice of time step. Another important consideration is the fact that equation set 4.12 must be solved by iterative means, using the method discussed in section 4.1.4, which means that one has to provide an initial guess as to the correct solution. For all time steps, except at $t = 0$, the state at the

---

(11) And hence physically realistic.

(12) Or the shortest of the two cell edge lengths if the cells are not square.

previous time was used as this initial guess, which meant that a careful choice of δ_{max} could greatly improve the ratio of the progression in time to the number of iterations. If δ_{max} was set too high then this initial guess would be very poor and the iteration may take a long time to converge, if it was able to converge at all. By contrast if δ_{max} was set too low then although the iteration would converge quickly little progress would have been made in terms of evolving the system to a new state. For these reasons δ_{max} was set much lower than one(13) as this meant that relatively few iterations were required to update the system to the correct state at the following time step and meant that overall the system time progressed faster with less computational effort. Of course this came with the additional advantage of improving the precision of the time propagation, despite the fact that this was not the original goal. Finally to ensure that the simulation could not get stuck at one time step for too long a clause was added such that if convergence had not been achieved after a set number of iterations then the previous state would be restored and the algorithm would try to evolve the system forwards with a smaller time step, hence improving the initial guess as to the future state(14).

4.1.4 Newton-Raphson Iteration

Due to the fact that the equations of equation set 4.12 are non-linear a direct solution was not possible and hence an iterative approach[151] to obtaining the solution at each time step was required. The Newton-Raphson method[151] lends it self well to this kind of situation, where there are many coupled non-linear equations. Although the method is fairly simple it is very powerful offering rapid convergence in the region of a solution[151]. The key drawback is that it is not globally convergent[151], however this property was not required for the present work as it was safe to assume that, if the time step was small enough, the previous state of the system would provide a reasonable starting point from which the method could obtain the solution at the current time.

The basis of this method is that, provided there are no turning points between the initial guess and the solution, the x intercept of the tangent to a non-linear function at the initial x value will be closer to the root than the initial value was. Hence by repeatedly updating this value one approaches the correct solution. This process can be expressed mathematically, for any arbitrary function, $f\left\{x\right\}$, as[151]

$$x_{n+1} = x_n - \frac{f\left\{x_n\right\}}{f'\left\{x_n\right\}}, \tag{4.23}$$

where $f'\left\{x_n\right\} = \frac{\partial f}{\partial x}$.

Since there are $6NM$ equations in equation set 4.12 one requires a matrix that contains the derivative of every equation with respect to every variable. This is the Jacobian

---

(13) Meaning that the fastest fluid element traversed less than one cell per time step.

(14) This clause was rarely needed, but has proven effective on the occasions where it was used.

matrix[151], $\mathbf{J}$, defined by

$$\mathbf{J} = \begin{pmatrix} \frac{\partial f_1}{\partial x_1} & \frac{\partial f_1}{\partial x_2} & \cdots & \frac{\partial f_1}{\partial x_{6NM}} \\ \frac{\partial f_2}{\partial x_1} & \frac{\partial f_2}{\partial x_2} & \cdots & \frac{\partial f_2}{\partial x_{6NM}} \\ \vdots & \vdots & \ddots & \vdots \\ \frac{\partial f_{6NM}}{\partial x_1} & \frac{\partial f_{6NM}}{\partial x_2} & \cdots & \frac{\partial f_{6NM}}{\partial x_{6NM}} \end{pmatrix}. \tag{4.24}$$

Thus one may obtain a vector, $\mathbf{x}_{n+1}$, of dimension $6NM$, containing the updated solutions to the equations from a vector containing the solutions at the previous iteration, $\mathbf{x}_n$, the equations evaluated for the previous iteration, $\mathbf{f}_n$, and the Jacobian, evaluated using the previous solutions, $\mathbf{J}_n$ by applying

$$\mathbf{x}_{n+1} = \mathbf{x}_n - \mathbf{J}_n^{-1} \cdot \mathbf{f}_n. \tag{4.25}$$

Hence the iteration scheme amounts to nothing more than repeated application of equation 4.25.

With equation set 4.12 there are six different matrix equations, each of dimension NM. Thus it makes sense to derive the Jacobian of the whole system by treating it as a 6 by 6 matrix, where each element is itself an NM dimensional square matrix. The reason for this is that it is far more convenient to deal with the different equations and variables separately, remembering that each matrix equation in fact represents NM copies of the same equation applied to each cell, than it would be to deal with all $6NM$ equations at once, since some require different operations to others. Thus the Jacobian may be broken down such that

$$\mathbf{J} = \begin{pmatrix} \mathbf{J}_{11} & \mathbf{J}_{12} & \mathbf{J}_{13} & \mathbf{J}_{14} & \mathbf{J}_{15} & \mathbf{J}_{16} \\ \mathbf{J}_{21} & \mathbf{J}_{22} & \mathbf{J}_{23} & \mathbf{J}_{24} & \mathbf{J}_{25} & \mathbf{J}_{26} \\ \mathbf{J}_{31} & \mathbf{J}_{32} & \mathbf{J}_{33} & \mathbf{J}_{34} & \mathbf{J}_{35} & \mathbf{J}_{36} \\ \mathbf{J}_{41} & \mathbf{J}_{42} & \mathbf{J}_{43} & \mathbf{J}_{44} & \mathbf{J}_{45} & \mathbf{J}_{46} \\ \mathbf{J}_{51} & \mathbf{J}_{52} & \mathbf{J}_{53} & \mathbf{J}_{54} & \mathbf{J}_{55} & \mathbf{J}_{56} \\ \mathbf{J}_{61} & \mathbf{J}_{62} & \mathbf{J}_{63} & \mathbf{J}_{64} & \mathbf{J}_{65} & \mathbf{J}_{66} \end{pmatrix}, \tag{4.26}$$

where, for the most general model,

$$\begin{aligned} J_{11} =& 2\boldsymbol{\Delta}_x \cdot \mathbf{H} \cdot \boldsymbol{\Delta}_x + \boldsymbol{\Delta}_y \cdot \mathbf{H} \cdot \boldsymbol{\Delta}_y - \mathbf{I} - \boldsymbol{\Phi} + \mathbf{Z}_p + \mathrm{diag}\left(\left(2\boldsymbol{\Delta}_x \cdot \frac{\partial \mathbf{H}}{\partial \mathbf{V}_{px}} \cdot \boldsymbol{\Delta}_x + \boldsymbol{\Delta}_y \cdot \frac{\partial \mathbf{H}}{\partial \mathbf{V}_{px}} \cdot \boldsymbol{\Delta}_y + \frac{\partial \mathbf{Z}_p}{\partial \mathbf{V}_{px}}\right) \cdot \mathbf{v}_{px}\right) \\ & + \mathrm{diag}\left(\boldsymbol{\Delta}_y \cdot \frac{\partial \mathbf{H}}{\partial \mathbf{V}_{px}} \cdot \boldsymbol{\Delta}_x \cdot \mathbf{v}_{py}\right) \end{aligned} \tag{4.27[11]}$$

$$\begin{aligned} J_{12} =& \boldsymbol{\Delta}_y \cdot \mathbf{H} \cdot \boldsymbol{\Delta}_x + \mathrm{diag}\left(\left(2\boldsymbol{\Delta}_x \cdot \frac{\partial \mathbf{H}}{\partial \mathbf{V}_{py}} \cdot \boldsymbol{\Delta}_x + \boldsymbol{\Delta}_y \cdot \frac{\partial \mathbf{H}}{\partial \mathbf{V}_{py}} \cdot \boldsymbol{\Delta}_y + \frac{\partial \mathbf{Z}_p}{\partial \mathbf{V}_{py}}\right) \cdot \mathbf{v}_{px}\right) \\ & + \mathrm{diag}\left(\boldsymbol{\Delta}_y \cdot \frac{\partial \mathbf{H}}{\partial \mathbf{V}_{py}} \cdot \boldsymbol{\Delta}_x \cdot \mathbf{v}_{py}\right) \end{aligned} \tag{4.27[12]}$$

$$J_{13} = \mathbf{I} - \boldsymbol{\Phi} \tag{4.27[13]}$$

$$J_{14} = \mathbf{0} \tag{4.27[14]}$$

$$J_{15} = -\boldsymbol{\Delta}_x \tag{4.27[15]}$$

$$\begin{aligned} J_{16} =& \mathbf{V}_{px} - \mathbf{V}_{sx} + \boldsymbol{\Phi}^{-1} \cdot \boldsymbol{\Phi}^{-1} \cdot \boldsymbol{\Delta}_x \cdot \boldsymbol{\Pi} + \mathrm{diag}\left(\left(2\boldsymbol{\Delta}_x \cdot \frac{\partial \mathbf{H}}{\partial \boldsymbol{\Phi}} \cdot \boldsymbol{\Delta}_x + \boldsymbol{\Delta}_y \cdot \frac{\partial \mathbf{H}}{\partial \boldsymbol{\Phi}} \cdot \boldsymbol{\Delta}_y + \frac{\partial \mathbf{Z}_p}{\partial \boldsymbol{\Phi}}\right) \cdot \mathbf{v}_{px}\right) \\ & + \mathrm{diag}\left(\left(\boldsymbol{\Delta}_y \cdot \frac{\partial \mathbf{H}}{\partial \boldsymbol{\Phi}} \cdot \boldsymbol{\Delta}_x + \frac{\partial \mathbf{Z}_p}{\partial \boldsymbol{\Phi}}\right) \cdot \mathbf{v}_{py}\right) - \boldsymbol{\Phi}^{-1} \cdot \boldsymbol{\Delta}_x \cdot \frac{\partial \boldsymbol{\Pi}}{\partial \boldsymbol{\Phi}} \end{aligned} \tag{4.27[16]}$$

$$\begin{aligned} J_{21} =& \boldsymbol{\Delta}_x \cdot \mathbf{H} \cdot \boldsymbol{\Delta}_y + \mathrm{diag}\left(\left(2\boldsymbol{\Delta}_y \cdot \frac{\partial \mathbf{H}}{\partial \mathbf{V}_{px}} \cdot \boldsymbol{\Delta}_y + \boldsymbol{\Delta}_x \cdot \frac{\partial \mathbf{H}}{\partial \mathbf{V}_{px}} \cdot \boldsymbol{\Delta}_x + \frac{\partial \mathbf{Z}_p}{\partial \mathbf{V}_{px}}\right) \cdot \mathbf{v}_{py}\right) \\ & + \mathrm{diag}\left(\boldsymbol{\Delta}_x \cdot \frac{\partial \mathbf{H}}{\partial \mathbf{V}_{px}} \cdot \boldsymbol{\Delta}_y \cdot \mathbf{v}_{px}\right) \end{aligned} \tag{4.27[21]}$$

$$J_{22}{=}2\boldsymbol{\Delta}_y{\cdot}\mathbf{H}{\cdot}\boldsymbol{\Delta}_y{+}\boldsymbol{\Delta}_x{\cdot}\mathbf{H}{\cdot}\boldsymbol{\Delta}_x{-}\mathbf{I}{-}\boldsymbol{\Phi}{+}\mathbf{Z}_p{+}\mathrm{diag}\Big(\Big(2\boldsymbol{\Delta}_y{\cdot}\tfrac{\partial\mathbf{H}}{\partial\mathbf{V}_{py}}{\cdot}\boldsymbol{\Delta}_y{+}\boldsymbol{\Delta}_x{\cdot}\tfrac{\partial\mathbf{H}}{\partial\mathbf{V}_{py}}{\cdot}\boldsymbol{\Delta}_x{+}\tfrac{\partial\mathbf{Z}_p}{\partial\mathbf{V}_{py}}\Big){\cdot}\mathbf{v}_{py}\Big) \\ {+}\mathrm{diag}\Big(\boldsymbol{\Delta}_x{\cdot}\tfrac{\partial\mathbf{H}}{\partial\mathbf{V}_{py}}{\cdot}\boldsymbol{\Delta}_y{\cdot}\mathbf{v}_{px}\Big) \tag{4.27[22]}$$

$$J_{23}{=}\mathbf{0} \tag{4.27[23]}$$

$$J_{24}{=}\mathbf{I}{-}\boldsymbol{\Phi} \tag{4.27[24]}$$

$$J_{25}{=}{-}\boldsymbol{\Delta}_y \tag{4.27[25]}$$

$$J_{26}{=}\mathbf{V}_{py}{-}\mathbf{V}_{sy}{+}\boldsymbol{\Phi}^{-1}{\cdot}\boldsymbol{\Phi}^{-1}{\cdot}\boldsymbol{\Delta}_y{\cdot}\boldsymbol{\Pi}{+}\mathrm{diag}\Big(\Big(2\boldsymbol{\Delta}_y{\cdot}\tfrac{\partial\mathbf{H}}{\partial\boldsymbol{\Phi}}{\cdot}\boldsymbol{\Delta}_y{+}\boldsymbol{\Delta}_x{\cdot}\tfrac{\partial\mathbf{H}}{\partial\boldsymbol{\Phi}}{\cdot}\boldsymbol{\Delta}_x{+}\tfrac{\partial\mathbf{Z}_p}{\partial\boldsymbol{\Phi}}\Big){\cdot}\mathbf{v}_{py}\Big) \\ {+}\mathrm{diag}\Big(\Big(\boldsymbol{\Delta}_x{\cdot}\tfrac{\partial\mathbf{H}}{\partial\boldsymbol{\Phi}}{\cdot}\boldsymbol{\Delta}_y{+}\tfrac{\partial\mathbf{Z}_p}{\partial\boldsymbol{\Phi}}\Big){\cdot}\mathbf{v}_{px}\Big){-}\boldsymbol{\Phi}^{-1}{\cdot}\boldsymbol{\Delta}_y{\cdot}\tfrac{\partial\boldsymbol{\Pi}}{\partial\boldsymbol{\Phi}} \tag{4.27[26]}$$

$$J_{31}{=}\boldsymbol{\Phi} \tag{4.27[31]}$$

$$J_{32}{=}\mathbf{0} \tag{4.27[32]}$$

$$J_{33}{=}2\boldsymbol{\Delta}_x^2{+}\boldsymbol{\Delta}_y^2{-}\mathbf{Z}_s{+}\boldsymbol{\Phi} \tag{4.27[33]}$$

$$J_{34}{=}\boldsymbol{\Delta}_x{\cdot}\boldsymbol{\Delta}_y \tag{4.27[34]}$$

$$J_{35}{=}{-}\boldsymbol{\Delta}_x \tag{4.27[35]}$$

$$J_{36}{=}\mathbf{V}_{px}{-}\mathbf{V}_{sx} \tag{4.27[36]}$$

$$J_{41}{=}\mathbf{0} \tag{4.27[41]}$$

$$J_{42}{=}\boldsymbol{\Phi} \tag{4.27[42]}$$

$$J_{43}{=}\boldsymbol{\Delta}_x{\cdot}\boldsymbol{\Delta}_y \tag{4.27[43]}$$

$$J_{44}{=}\boldsymbol{\Delta}_x^2{+}2\boldsymbol{\Delta}_y^2{-}\mathbf{Z}_s{+}\boldsymbol{\Phi} \tag{4.27[44]}$$

$$J_{45}{=}{-}\boldsymbol{\Delta}_y \tag{4.27[45]}$$

$$J_{46}{=}\mathbf{V}_{py}{-}\mathbf{V}_{sy} \tag{4.27[46]}$$

$$J_{51}{=}\boldsymbol{\Delta}_x{\cdot}\boldsymbol{\Phi} \tag{4.27[51]}$$

$$J_{52}{=}\boldsymbol{\Delta}_y{\cdot}\boldsymbol{\Phi} \tag{4.27[52]}$$

$$J_{53}{=}\boldsymbol{\Delta}_x{\cdot}(\mathbf{I}{-}\boldsymbol{\Phi}) \tag{4.27[53]}$$

$$J_{54}{=}\boldsymbol{\Delta}_y{\cdot}(\mathbf{I}{-}\boldsymbol{\Phi}) \tag{4.27[54]}$$

$$J_{55}{=}\mathbf{0} \tag{4.27[55]}$$

$$J_{56}{=}\boldsymbol{\Delta}_x{\cdot}(\mathbf{V}_{px}{-}\mathbf{V}_{sx}){+}\boldsymbol{\Delta}_y{\cdot}(\mathbf{V}_{py}{-}\mathbf{V}_{sy}) \tag{4.27[56]}$$

$$J_{61}{=}\boldsymbol{\Delta}_x{\cdot}\boldsymbol{\Phi} \tag{4.27[61]}$$

$$J_{62}{=}\boldsymbol{\Delta}_y{\cdot}\boldsymbol{\Phi} \tag{4.27[62]}$$

$$J_{63}{=}\mathbf{0} \tag{4.27[63]}$$

$$J_{64}{=}\mathbf{0} \tag{4.27[64]}$$

$$J_{65}{=}\mathbf{0} \tag{4.27[65]}$$

$$J_{66}{=}\boldsymbol{\Delta}_t{+}\boldsymbol{\Delta}_x{\cdot}\mathbf{V}_{px}{+}\boldsymbol{\Delta}_y{\cdot}\mathbf{V}_{py}. \tag{4.27[66]}$$

Here the meanings of the variables are those given in table 4.1, where the capital letters represent NM dimensional square matrices and the lowercase letters represent NM dimensional vectors. The derivatives of the functions, such as the viscosity and osmotic pressure, with respect to the variables they depend upon are written in the form $\frac{\partial\mathbf{A}}{\partial\mathbf{B}}$, which refers to a matrix with diagonal elements, ii, equal to $\frac{\partial\mathbf{A}_{ii}}{\partial\mathbf{B}_{ii}}$ and zeros everywhere else, these were typically analytical functions derived from differentiation of the original function with respect to the appropriate variable and as such were known exactly.

Once the elements of equation set 4.27 had been calculated using the current state(15) they were then added to the appropriate place in the Jacobian and equation 4.25 was used to update the state. The process was then repeated until the desired level of accuracy had been achieved. This was measured by evaluating equation set 4.12 with each set of values and then testing to see how many of the equations evaluated to zero within the specified

---

(15) Starting with an initial guess consisting of the state at the previous time step. Since it is assumed that the state will not have changed dramatically since the previous time step.

accuracy. Once all of the equations evaluated to zero, within the required accuracy, then the iteration was deemed to have converged and the simulation moved on to the next time step and the process was repeated there. Flow chart 4.1 summarises the algorithm used.

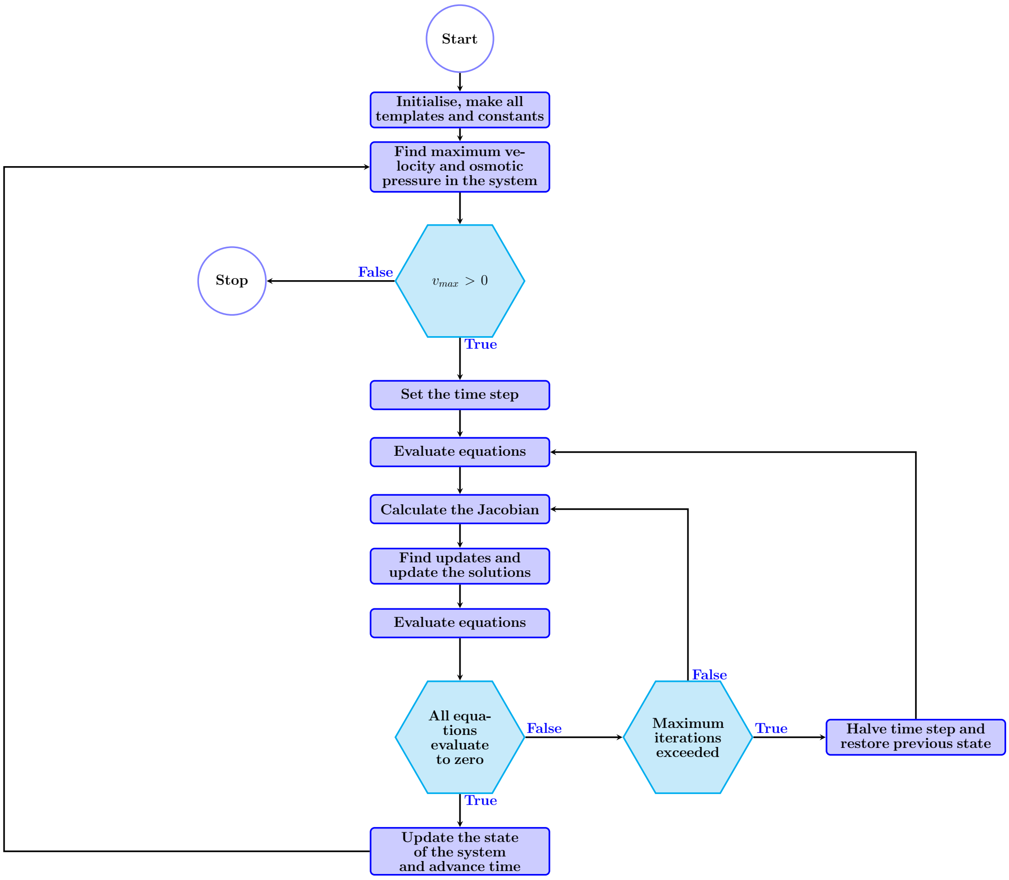

Flow Chart 4.1: Flow chart showing the main steps in the algorithm used to simulate a particle-laden fluid.

The only exception to this is the state of the system at $t = 0$ where there is no previous state to use as an initial guess so the uniform state with $\phi = \phi_{old}$ was used.

4.1.5 Sparse Matrix Methods

Since the vast majority of the computational workload involved in the simulation of the particle-laden fluid consists of manipulating matrices it makes sense that these operations should be the main focus of optimisation efforts. Even when optimised, profiling of the simulation revealed that matrix operations account for more than 99.9%(16) of the total CPU time used during a simulation for any reasonably large grid.

When one considers the matrices that make up both equation set 4.12 and the elements of the Jacobian it becomes clear that many of these matrices are sparse, containing mostly zeros, as is the Jacobian itself. This means that if one was to proceed using standard matrix methods a great deal of time would be spent dealing with the zeros. Hence it is preferable, where possible, to avoid this especially when one considers how standard matrix methods scale with the size of the matrices involved. For this simulation in particular matrix size is an important factor to consider since the simulation algorithm has to deal with matrices

---

(16) This value was obtained by using the GNU profiling tool, gprof.

of two different sizes; the matrices which have to be added and multiplied together to form the equations of motion and the elements of the Jacobin have dimensions of NM while the Jacobian itself, which only has to be inverted has dimensions of $6NM$. Clearly while operations on the smaller matrices will be faster(17) there are many more operations to do so optimisation is still very important.

It is worth pointing out that the discussion of sparse matrices in this section is limited to cases where all of the matrices involved are non-diagonal matrices. Calculations involving diagonal matrices were treated differently in order to optimise even further for the regular non-zero pattern possessed by such matrices. This is discussed further in section 4.1.6.

4.1.5.1 Addition and Subtraction

The number of operations involved in the addition or subtraction of matrices scales with the square of the dimensions of the matrices involved. Hence it is significantly faster than multiplication and LU-decomposition when large matrices are involved; and therefore only accounts for a small proportion of the time taken to perform the whole calculation. Furthermore by performing tests on matrices filled with random numbers at random locations it was found that, unless the matrices were very sparse, the overhead involved in skipping the zeros outweighed the gains made by avoiding them for matrices of all sizes that might be relevant to this simulation. The results of this testing can be seen in figure 4.5, which clearly shows that the sparse method is significantly slower than the standard method unless over 90% of the elements of the matrices are zeros(18).

---

(17) LU-Decomposition or multiplication of the smaller matrices would be 216 times faster than for the Jacobian as they both scale with the cube of the matrix's dimensions, while addition or subtraction would be 36 times faster as they scale with the square of the dimensions of the matrices involved.

(18) This is considerable for some of the matrices needed for the simulation of the particle-laden fluid, but would require the system to be quite large. In this case addition and subtraction would account for such a small fraction of the total computation time it was not deemed worthwhile implementing this method.

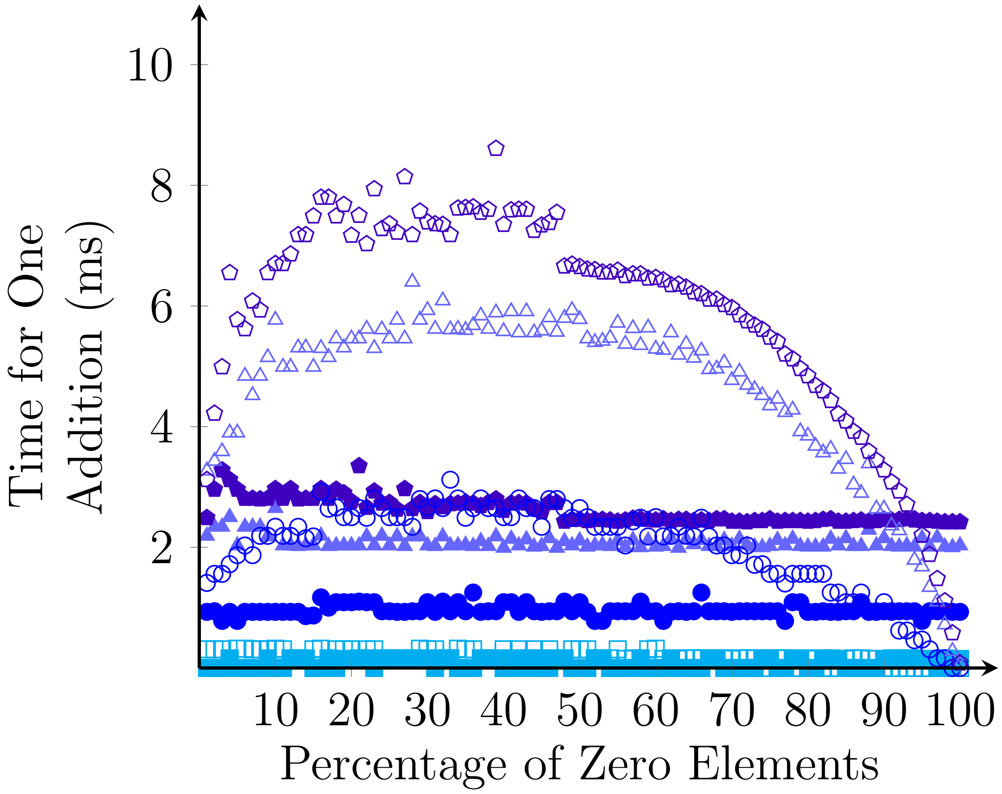

Figure 4.5: Plot of the average time taken to perform one addition of two square matrices, as a function the percentage of elements that are zero. Here the solid shapes (■,●,▲,⬟) mark the data for the standard, dense, method while the hollow shapes (□,○,△,⬠) mark the results for the sparse method, where a template was used to avoid the zeros where possible. Four different sized matrices were tested: 225 by 225 marked by the cyan squares (■,□), 400 by 400 marked by the blue circles (●,○), 600 by 600 marked by the light purple triangles (▲,△) and 700 by 700 marked by the dark purple pentagons (⬟,⬠).

Another important factor in the decision not to use a sparse method for addition and subtraction was the fact that, with the standard method, many additions and subtractions can be performed in one step without the need to store the results and read them back. This represents another potential saving in that it reduces the number of memory operations required. The cost associated with reading the locations of the non-zero elements from memory individually as opposed to in an optimised loop can be seen clearly in figure 4.5 as the time taken for the sparse method starts to increase with the proportion of zeros when the total number of zeros is small, this is likely to be due to the fact that the matrices are no longer compatible with the optimised loop structure provided by the compiler and so elements are having to be read from memory individually, increasing the overhead.

4.1.5.2 Multiplication

From equation sets 4.12 and 4.27 it is clear that each iteration consists of many matrix multiplications(19), this represents a substantial amount of computational effort. However, in practice much of this was avoided simply by exploiting the structure of the matrices involved.

---

(19) For the full version of the model, with all the additions discussed in section 3.1.2 there are 73 unique matrix multiplications to be performed.

Firstly many of the matrices were diagonal so it made sense to treat them differently from full matrices both in terms of the way they were stored and the way they operated on other matrices and vectors. Since diagonal matrices have the same number of non-zero entries as vectors of the same dimension it made sense to store them as if they were vectors, since this saved a great deal of memory and allowed for greater optimisation of the process of reading and writing the arrays. This storage method was especially useful since the majority of the diagonal matrices used in this algorithm had the same entries as their corresponding vectors so there was no need to store them both and spend time copying the entries from one form to another; it was simply possible to use the same object in different ways. Another property of diagonal matrices that was exploited was the way in which they act upon or are acted upon by other matrices. When a non-diagonal matrix, $\mathbf{M}$, is multiplied from the left by a diagonal matrix, $\mathbf{D}$, the result is that all entries, j, on row i of the non-diagonal matrix are multiplied by the element ii of the diagonal matrix,

$$(\mathbf{D} \cdot \mathbf{M})_{ij} = D_{ii} M_{ij}. \tag{4.28}$$

Similarly if a non-diagonal matrix is multiplied from the right by a diagonal matrix the result is that all entries, i, in column j of the non-diagonal matrix are multiplied by the element jj of the diagonal matrix,

$$(\mathbf{M} \cdot \mathbf{D})_{ij} = M_{ij} D_{jj}. \tag{4.29}$$

This property meant that multiplications involving a mixture of diagonal and non-diagonal matrices could be carried out in a way that scaled with the square of the dimensions of the matrices rather than its cube. Of course the product of two diagonal matrices scaled linearly with their dimensions since this was simply a matter of taking the product of each pair of diagonal elements, ii,

$$\left(\mathbf{D}' \cdot \mathbf{D}\right)_{ii} = D'_{ii} D_{ii}. \tag{4.30}$$

This is also true of the product between a diagonal matrix and a vector, where the each element, i, in the resulting vector is the product of the corresponding element in the original vector, $\mathbf{v}$, and the element of the diagonal matrix with which it shares a row,

$$(\mathbf{D} \cdot \mathbf{v})_i = D_{ii} v_i. \tag{4.31}$$

Secondly despite the fact that the derivative matrices, $\mathbf{\Delta}_x$ and $\mathbf{\Delta}_y$, were non-diagonal they were still relatively sparse, especially for large systems. This offered perhaps the most significant saving as far as matrix multiplication was concerned, because the standard method of multiplication for such matrices scales with the cube of the dimensions of the matrices and these matrices are involved in many of the terms of equation sets 4.12 and 4.27. A number of approaches were considered as potential means of optimising multiplications involving these matrices. These included using templates, which listed the positions of the non-zero elements so that only they were considered in the calculation, Strassen's method[110], which offered better scaling than the standard dense method by dividing the matrices into blocks of half the original size, and a combination of the two. The plots in figure 4.6 show how the time taken for each of these methods scaled with the proportion of zeros in the matrix, for matrices of a number of sizes.

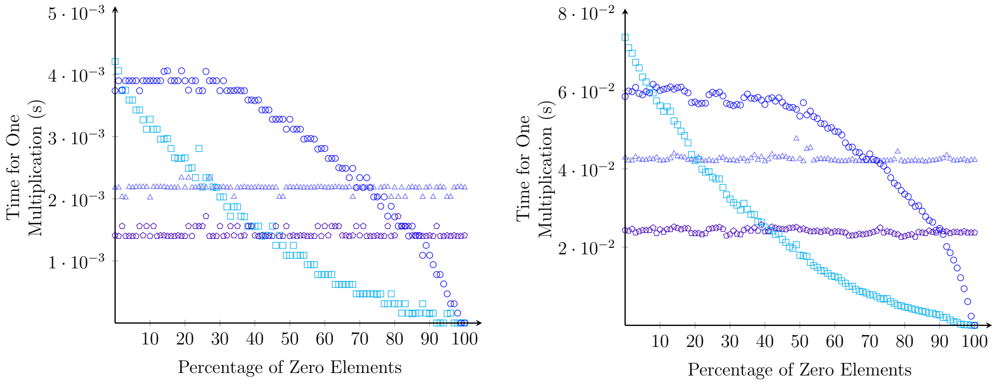

(a) 100 by 100. **(b)** 256 by 256.

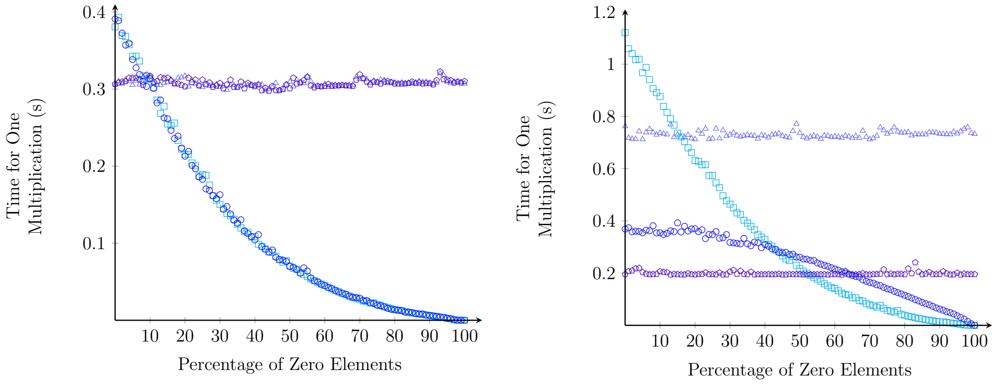

(c) 389 by 389. **(d)** 500 by 500.

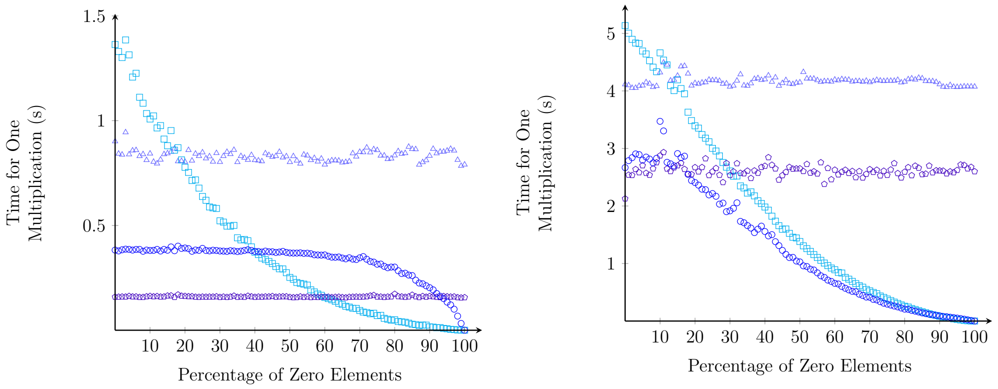

(e) 512 by 512. **(f)** 750 by 750.

Figure 4.6: Plots showing the results of timing different matrix multiplication schemes, for a range of different matrix sizes, as a function of the number zeros in the matrix. Here the times taken by the standard dense matrix multiplication algorithm are marked by the light purple triangles (△), the standard sparse, method with the zeros avoided, with cyan squares (□), Strassen's method with dark purple pentagons (⬠) and Strassen's method modified to avoid the zeros with blue circles (○).

As these plots show the methods which avoid the zeros in the matrices significantly out perform the dense methods once the proportion of zeros exceeds around 50% and that Strassen's method performs consistently better than the standard dense method, with the most extreme differences when the matrix size is a power of two, as one might expect(20). Despite the fact that the dense version of Strassen's method[110] outperforms the dense version of the normal method the same cannot be said of the sparse methods unless the

---

(20) Clear if the matrix size is not even then Strassen's method is identical to the standard method, as the matrix cannot be subdivided, this can be seen in figure 4.6c.

matrices are very large(21). For this reason(22) the standard sparse method was used for all of the non-diagonal matrix multiplications which needed to be performed in equation sets 4.12 and 4.27 and a similar method was used to save even more time during multiplications between diagonal and non-diagonal matrices, by avoiding the zeros within the non-diagonal matrix when applying equations 4.28 and 4.29.

The method used stored the whole matrix, including the zeros, and a separate template, which was used to keep track of the positions of the non-zero elements in the result as well as the elements that each depended on from the original matrix, for each product in equation sets 4.12 and 4.27 that involved two non-diagonal matrices. These templates were independent of the state of the system and only depended on the system size and so as a result could be calculated during initialisation and used repeatedly throughout the simulation without needing to be recalculated. Clearly the situation where a product contained one diagonal and one non-diagonal matrix was much simpler as this time the template only needed to hold the information about the location of the non-zero elements in the non-diagonal matrix, and the situation where one element in the final matrix depended on multiple elements of the initial matrices did not arise. However this sparse method still offered a significant speed increase over simply applying equation 4.28 or equation 4.29. This was also true of multiplication between non-diagonal matrices and vectors, where an identical template, was used.

The net effect of these sparse multiplication methods was that far from being the dominant factor in determining the overall speed of the simulation, which it could have been given the number of multiplications that needed to be performed, multiplication only accounted for between 2% and 5% of the CPU time per iteration, with almost all of the rest being attributed to LU-decomposition.

4.1.5.3 LU-Decomposition

As one might expect, since the Jacobian is the largest matrix used in the simulation, the majority of the simulation time was spent performing the LU-decomposition necessary to obtain the vector $\mathbf{J}_n^{-1}\cdot\mathbf{f}_n$, containing the update to the previous solution, $\mathbf{x}_n$, in the iterative scheme. This is the reason for the need to optimise this part of the algorithm as much as possible. Like the other matrices involved in the calculation the Jacobian is fairly sparse, with only around 13-15% of its values being non-zero, for the size of system typically used in simulations. For this reason it was decided that a sparse LU-decomposition scheme should be used to obtain the corrections to the solutions during each iteration. Here the left-looking scheme[106] provided in the CSparse library, described in reference 106, was used as it was fairly straightforward to incorporate into the existing program and came with less overhead than more complicated right-looking or multi-frontal[106] methods(23). As figure 4.7 shows this sparse method offered a significant performance increase compared with the standard, dense, method of LU-decomposition as well as better scaling with system size. This meant that large systems sizes were accessible to the simulation as well

---

(21) Typically in simulations gird sizes of 21 by 21 or less were used so the matrices used in equation sets 4.12 and 4.27 were never large enough of the sparse version of Strassen's method to be optimal.

(22) This method also required significantly less memory than either variation of Strassen's method.

(23) Though these methods can be faster and lend themselves more easily to parallelisation they were thought to be unnecessarily complicated for this situation.

as vastly reducing the run time for smaller systems.

The principle behind the left-looking sparse method is that, when choosing an element from the unprocessed part of the matrix as a pivot, the standard LU-decomposition attempts to use the largest value possible, while this method attempts to find a compromise between using an element with a large value and one which will result in the smallest possible number of new non-zero elements being added to the upper and lower triangular matrices of the decomposition[152]. A simple means of predicting the number of insertions is to use the Markowitz criteria[152] which selects the pivot as the element in the remaining unprocessed matrix that minimises the product between the number of non-zero elements with which it shares a row and the number with which it shares a column(24). In practice the routines from CSparse[106], used to solve the equations, achieve this compromise by first permuting the columns to reduce the number of insertions and then permuting the row as the algorithm progresses to select the largest possible pivot at each stage. In order to aid this process and improve performance the library keeps the matrix in compressed column format[106], where only the non-zero elements are stored and the matrix is accompanied by lists which indicate the positions in the full matrix which these values occupy. This formatting needed to be given careful consideration when the Jacobian was being formed from the sub-matrices of equation set 4.27 as it made sense to save both time and memory and copy the elements directly into the compressed version of the Jacobian rather than create an uncompressed version and compress it. This process was achieved through the use of a template, which was created when the simulation started up and stored for use at each time step. This mapped the locations in the full Jacobian to the corresponding locations in the compressed one(25).

Since the choice of the route that the decomposition takes depends heavily on the structure of the matrix it was not possible to assess the performance of this method using random matrices as in sections 4.1.5.1 and 4.1.5.2. Instead the tests were performed on the real Jacobian for the system, given in equation 4.26 and equation set 4.27. This was done by running the simulation as normal and adding a small amount of extra code to time the routine used to solve for the updates in the iterative scheme. The results of this timing for a number of system sizes are shown in figure 4.7.

---

(24) Of course for the sake of stability this element is only suitable if it is also a significant size compared to the largest element in the remaining matrix.

(25) The fact that smaller matrices of equation set 4.27 were not kept in compressed column format made no difference to this process as they were not the same size as the Jacobian so their elements would have had to have been added one by one regardless of the format of either matrix.

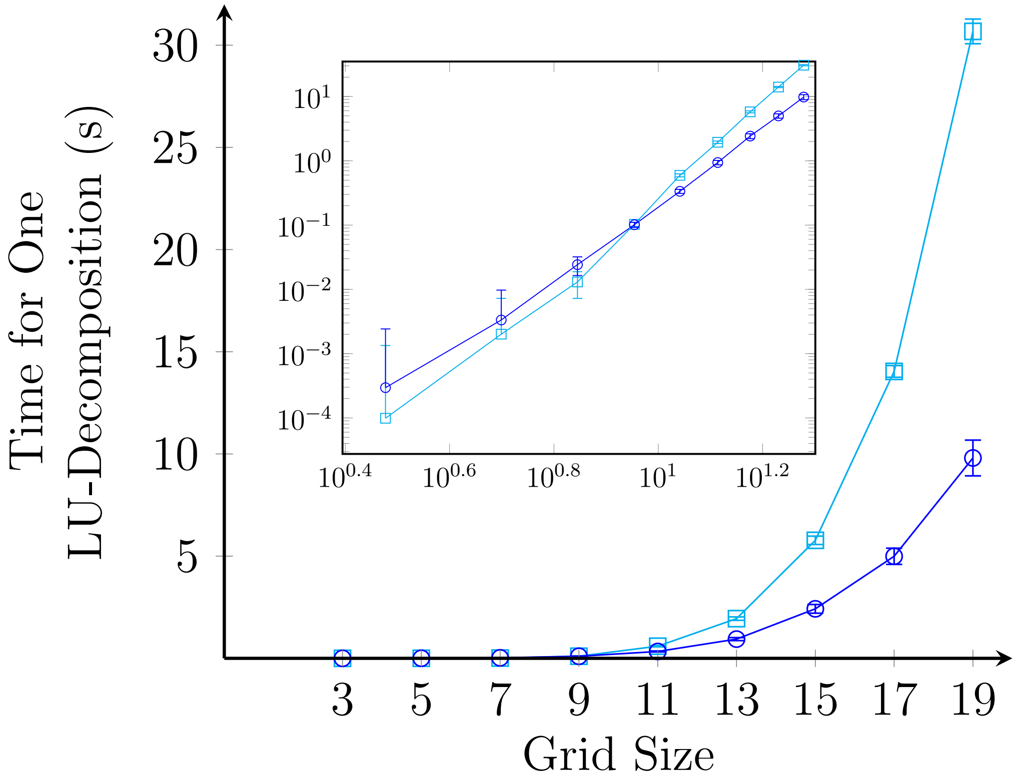

Figure 4.7: Plot showing the time taken to perform one LU-decomposition of the Jacobian for the particle-laden fluid model, as described in section 4.1.4, using two different algorithms, as a function of grid size on a two dimensional square grid. The insert shows the same data on a logarithmic scale. The cyan lines marked with squares (—□—) are the results for the dense matrix method while the blue lines marked with circles (—○—) are the results for the left-looking sparse method provided in the CSparse library. The results presented here are the average times taken after performing many runs and account for the time taken by the LU-decomposition part of the simulation only. The error bars shown represent one standard deviation from the mean value.

A further performance boost from the sparse method was achieved by removing small elements from the Jacobian for iteration steps early on in the scheme as the accuracy of the corrections was less important far from the solution, these were then reinstated just before the convergence criteria were reached to make the final solution as accurate as possible.

In addition to the two direct methods discussed in this section a number of iterative methods of obtaining the updates to the solutions, such as Jacobi iteration, GaussSeidel iteration and successive over relaxation, were tested, in the hope that these could exploit the sparse multiplication method. However, it was found that, for this system, these converged far too slowly to be competitive with the direct methods.

4.1.6 Optimisation

As described in section 4.1.5 almost all of the computational effort involved in the simulations of the particle-laden fluid was concerned with matrix operations. While things like the LU-decomposition step, necessary to find the updates to the solutions at each step of the iteration, were unavoidable and could not be optimised beyond the use of specialist libraries there were significant savings to be made in avoiding unnecessary matrix operations during the process of building up the Jacobian. Although individually these operations were relatively fast compared with the LU-decomposition step they were still fairly computationally expensive when the system size was large and there were many more of them.

Careful inspection of equation sets 4.12 and 4.27 reveals the fact that many of the terms are repeated and thus the potential saving to be had by storing the results and reusing them rather than recalculating every time the term appears. For example the combination $\mathbf{\Delta}_x \cdot \mathbf{H} \cdot \mathbf{\Delta}_x$ appears in equations 4.12a, 4.12b, 4.27[22] and 4.27[11] while $\mathbf{H} \cdot \mathbf{\Delta}_x$ appears in all of these terms as well as those involving $\mathbf{\Delta}_y \cdot \mathbf{H} \cdot \mathbf{\Delta}_x$.

Since many of the equations in equation sets 4.12 and 4.27 are quite complicated and contain many levels of multiplication, addition and subtraction it would have been very difficult to obtain the optimum performance by deciding which terms could be stored and which terms needed to be calculated manually. Furthermore any change to the system of equations, such as the additions to the model described in section 3.1.2 would have potentially meant starting the process from scratch. For these reasons a program was written to examine the equations of the model and calculate only the first instance of each combination, store it and then replace all other identical instances with the stored result. Of course examining the equations at every time step would have incurred a cost to computational time in itself so this program was not included into the main simulation and instead outputted the code for the necessary operations which was then compiled into the main simulation. This avoided the overhead altogether and meant that the optimisation was achieved a zero computational cost. Once provided with the equations showing how the matrices were to be grouped the algorithm proceeded to allocate a variable to each combination and then replace those matrices in the equations by that variable. This is done successively for each level of operation, starting with the inner most groups, like $\mathbf{H} \cdot \mathbf{\Delta}_x$, and then the next level, where the groups that were previously replaced were operated on, as in $\mathbf{\Delta}_x \cdot (\mathbf{H} \cdot \mathbf{\Delta}_x)$, and so on until all of the groups of variables had been stored. This essentially breaks down the complicated equations of equation sets 4.12 and 4.27 into a sequence of much simpler ones. These operations were then analysed and code to call the appropriate function was generated, based on what types of matrices were involved in the operations. This meant that the matrices that make up equations of motion and the Jacobian were calculated with the least number of matrix operations possible and that the operations were performed in the most efficient way possible given the matrices that were involved. Furthermore because the process was automated it was very easy to make changes to the equations of motion and still produce optimised code.

In addition to storing combinations of matrices after they were evaluated at each iteration it was also possible to store some combinations for the duration of the simulation as they were guaranteed not to change. For example the combination $\mathbf{\Delta}_x \cdot \mathbf{\Delta}_y$ remains constant once the simulation grid has been defined. Although there are relatively few such combinations in the full model they do typically involve the densest matrices in the system so performing them when the simulation initialises and storing the result to use at every subsequent time step does represent a worthwhile saving.

4.1.7 Linear Stability Analysis

In order to assess whether or not the equations of motion for the particle-laden fluid had a predisposition towards forming patterns, from an analytical point of view, linear stability analysis was performed on the equations of motion to assess whether the uniform state of the system was stable[3]. This was done by perturbing the parameters, $\hat{\mathbf{v}}_p$, $\hat{\mathbf{v}}_s$, $\hat{p}$ and ϕ, slightly about the uniform state. Thus

$$\hat{\mathbf{v}}_p = \hat{\mathbf{v}}_{pd} + \boldsymbol{\alpha} \quad (4.32a) \qquad \hat{p} = \hat{p}_0 + \gamma \quad (4.32c)$$

$$\hat{\mathbf{v}}_s = \hat{\mathbf{v}}_{sd} + \boldsymbol{\beta} \quad (4.32b) \qquad \phi = \phi_0 + \delta, \quad (4.32d)$$

where $\boldsymbol{\alpha}$, $\boldsymbol{\beta}$, γ and δ are small perturbations about the uniform state, $\hat{\mathbf{v}}_{pd}$ and $\hat{\mathbf{v}}_{sd}$ are the particle and solvent drift velocities, described in section 4.1.2, respectively and p_0 and ϕ_0 are the average pressure and volume fraction respectively. Substituting the perturbed variables in equation set 4.32 into equation set 4.5 yields

$$\begin{aligned}\hat{\rho}\hat{\mathbf{g}} - \hat{\zeta}_p\left(\hat{\mathbf{v}}_{pd} + \boldsymbol{\alpha}\right) + \left[1 - \left(\phi_0 + \delta\right)\right]\left[\left(\hat{\mathbf{v}}_{sd} + \boldsymbol{\beta}\right) - \left(\hat{\mathbf{v}}_{pd} + \boldsymbol{\alpha}\right)\right] - \hat{\boldsymbol{\nabla}}\left(\hat{p}_0 + \gamma\right) - \frac{1}{\phi_0 + \delta}\hat{\boldsymbol{\nabla}}\hat{\pi} \\ + \hat{\boldsymbol{\nabla}} \cdot \left[\hat{\eta}\left(\hat{\boldsymbol{\nabla}}\left(\hat{\mathbf{v}}_{pd} + \boldsymbol{\alpha}\right) + \left[\hat{\boldsymbol{\nabla}}\left(\hat{\mathbf{v}}_{pd} + \boldsymbol{\alpha}\right)\right]^T\right)\right] = \mathbf{0}\end{aligned} \quad (4.33a)$$

$$\begin{aligned}\hat{\mathbf{g}} - \hat{\zeta}_s\left(\hat{\mathbf{v}}_{sd} + \boldsymbol{\beta}\right) - \left(\phi_0 + \delta\right)\left[\left(\hat{\mathbf{v}}_{sd} + \boldsymbol{\beta}\right) - \left(\hat{\mathbf{v}}_{pd} + \boldsymbol{\alpha}\right)\right] - \hat{\boldsymbol{\nabla}}\left(\hat{p}_0 + \gamma\right) \\ + \hat{\boldsymbol{\nabla}} \cdot \left(\hat{\boldsymbol{\nabla}}\left(\hat{\mathbf{v}}_{sd} + \boldsymbol{\beta}\right) + \left[\hat{\boldsymbol{\nabla}}\left(\hat{\mathbf{v}}_{sd} + \boldsymbol{\beta}\right)\right]^T\right) = \mathbf{0}\end{aligned} \quad (4.33b)$$

$$\hat{\boldsymbol{\nabla}} \cdot \left[\left(\phi_0 + \delta\right)\left(\hat{\mathbf{v}}_{pd} + \boldsymbol{\alpha}\right) + \left[1 - \left(\phi_0 + \delta\right)\right]\left(\hat{\mathbf{v}}_{sd} + \boldsymbol{\beta}\right)\right] = 0 \quad (4.33c)$$

$$\frac{\partial}{\partial \hat{t}}\left(\phi_0 + \delta\right) + \hat{\boldsymbol{\nabla}} \cdot \left[\left(\phi_0 + \delta\right)\left(\hat{\mathbf{v}}_{pd} + \boldsymbol{\alpha}\right)\right] = 0. \quad (4.33d)$$

In order to obtain an, approximate, analytical solution to equation set 4.33 one must use the fact the perturbations, $\boldsymbol{\alpha}$, $\boldsymbol{\beta}$, γ and δ, are small and eliminate all terms higher than first order in these variables. This means that those parameters, such as the osmotic pressure, that are functions of these variables(26) must be expanded, to first order, about the uniform state. The necessary expansions are

$$\frac{1}{\phi_0 + \delta} \approx \frac{1}{\phi_0} - \frac{\delta}{\phi_0^2} \quad (4.34a) \qquad \hat{\eta} \approx \hat{\eta}\big|_{un} + \delta\left.\frac{\partial \hat{\eta}}{\partial \phi}\right|_{un} + \boldsymbol{\alpha} \cdot \left.\frac{\partial \hat{\eta}}{\partial \hat{\mathbf{v}}_p}\right|_{un} \quad (4.34c)$$

$$\hat{\pi} \approx \hat{\pi}\big|_{un} + \delta\left.\frac{\partial \hat{\pi}}{\partial \phi}\right|_{un} \quad (4.34b) \qquad \hat{\zeta}_p \approx \hat{\zeta}_p\Big|_{un} + \delta\left.\frac{\partial \hat{\zeta}_p}{\partial \phi}\right|_{un} + \boldsymbol{\alpha} \cdot \left.\frac{\partial \hat{\zeta}_p}{\partial \hat{\mathbf{v}}_p}\right|_{un}, \quad (4.34d)$$

where $f|_{un}$ denotes the function f evaluated with all of its arguments taking the values that they would have in the uniform state, $\hat{\mathbf{v}}_p = \hat{\mathbf{v}}_{pd}$, $\hat{\mathbf{v}}_s = \hat{\mathbf{v}}_{sd}$, $\hat{p} = \hat{p}_0$ and $\phi = \phi_0$.

Substituting these expansions into equation set 4.33 and removing all terms higher

---

(26) For the purposes of the linear stability analysis it shall be assumed that all of the generalisations to the basic model, discussed in section 3.1.2, are implemented and the effects of removing each will be discussed once the solution has been found. In this way one avoids repeating the same steps for each case.

than first order in the perturbations gives

$$\hat{\rho}\hat{\mathbf{g}}-\hat{\zeta}_p\Big|_{un}\hat{\mathbf{v}}_{pd}+(1-\phi_0)(\hat{\mathbf{v}}_{sd}-\hat{\mathbf{v}}_{pd})-\hat{\zeta}_p\Big|_{un}\boldsymbol{\alpha}-\hat{\mathbf{v}}_{pd}\left(\delta\left.\frac{\partial\hat{\zeta}_p}{\partial\phi}\right|_{un}+\boldsymbol{\alpha}\cdot\left.\frac{\partial\hat{\zeta}_p}{\partial\hat{\mathbf{v}}_p}\right|_{un}\right)+\delta(\hat{\mathbf{v}}_{sd}-\hat{\mathbf{v}}_{pd})$$
$$+(1-\phi_0)(\boldsymbol{\beta}-\boldsymbol{\alpha})-\hat{\boldsymbol{\nabla}}\gamma-\frac{1}{\phi_0}\left.\frac{\partial\hat{\pi}}{\partial\phi}\right|_{un}\hat{\boldsymbol{\nabla}}\delta+\hat{\boldsymbol{\nabla}}\cdot\left(\hat{\eta}|_{un}\left[\hat{\boldsymbol{\nabla}}\boldsymbol{\alpha}+\left(\hat{\boldsymbol{\nabla}}\boldsymbol{\alpha}\right)^T\right]\right)=\mathbf{0} \tag{4.35a}$$

$$\hat{\mathbf{g}}-\hat{\zeta}_s\Big|_{un}\hat{\mathbf{v}}_{sd}-\phi_0\left(\hat{\mathbf{v}}_{sd}-\hat{\mathbf{v}}_{pd}\right)-\hat{\zeta}_s\Big|_{un}\boldsymbol{\beta}-\hat{\mathbf{v}}_{sd}\delta\left.\frac{\partial\hat{\zeta}_s}{\partial\phi}\right|_{un}-\delta\left(\hat{\mathbf{v}}_{sd}-\hat{\mathbf{v}}_{pd}\right)-\phi_0\left(\boldsymbol{\beta}-\boldsymbol{\alpha}\right)$$
$$-\hat{\boldsymbol{\nabla}}\gamma+\hat{\boldsymbol{\nabla}}\cdot\left[\hat{\boldsymbol{\nabla}}\boldsymbol{\beta}+\left(\hat{\boldsymbol{\nabla}}\boldsymbol{\beta}\right)^T\right]=\mathbf{0} \tag{4.35b}$$

$$\phi_0\hat{\boldsymbol{\nabla}}\cdot\boldsymbol{\alpha}+(1-\phi_0)\,\hat{\boldsymbol{\nabla}}\cdot\boldsymbol{\beta}+(\hat{\mathbf{v}}_{pd}-\hat{\mathbf{v}}_{sd})\cdot\hat{\boldsymbol{\nabla}}\delta=0 \tag{4.35c}$$
$$\frac{\partial\delta}{\partial\hat{t}}+\phi_0\hat{\boldsymbol{\nabla}}\cdot\boldsymbol{\alpha}+\hat{\mathbf{v}}_{pd}\cdot\hat{\boldsymbol{\nabla}}\delta=0 \tag{4.35d}$$

Since these equations are now linear in the four unknowns, $\boldsymbol{\alpha}$, $\boldsymbol{\beta}$, γ and δ, they can be solved analytically. This was done, without loss of generality, by writing the unknowns as the sum of an infinite number of Fourier modes[3],

$$\boldsymbol{\alpha}=\sum_{\mathbf{q}=-\infty}^{\infty}\mathbf{A}_{\mathbf{q}}e^{\mathrm{i}\mathbf{q}\cdot\mathbf{r}} \tag{4.36a}$$
$$\gamma=\sum_{\mathbf{q}=-\infty}^{\infty}C_{\mathbf{q}}e^{\mathrm{i}\mathbf{q}\cdot\mathbf{r}} \tag{4.36c}$$
$$\boldsymbol{\beta}=\sum_{\mathbf{q}=-\infty}^{\infty}\mathbf{B}_{\mathbf{q}}e^{\mathrm{i}\mathbf{q}\cdot\mathbf{r}} \tag{4.36b}$$
$$\delta=\sum_{\mathbf{q}=-\infty}^{\infty}D_{\mathbf{q}}e^{\mathrm{i}\mathbf{q}\cdot\mathbf{r}}, \tag{4.36d}$$

where $\mathbf{r}$ is the position vector, $\mathbf{q}$ is the wave-vector and $\mathbf{A}_{\mathbf{q}}$, $\mathbf{B}_{\mathbf{q}}$, $C_{\mathbf{q}}$ and $D_{\mathbf{q}}$ are the amplitudes of each mode, the time evolution of which is the property of interest here.

Now by decoupling the different modes one obtains a set of four equations for each, non-zero mode(27),

$$-\hat{\zeta}_p\Big|_{un}\mathbf{A}_{\mathbf{q}}-\hat{\mathbf{v}}_{pd}\left(\left.\frac{\partial\hat{\zeta}_p}{\partial\phi}\right|_{un}D_{\mathbf{q}}+\left.\frac{\partial\hat{\zeta}_p}{\partial\hat{\mathbf{v}}_p}\right|_{un}\cdot\mathbf{A}_{\mathbf{q}}\right)+(\hat{\mathbf{v}}_{sd}-\hat{\mathbf{v}}_{pd})D_{\mathbf{q}}+(1-\phi_0)(\mathbf{B}_{\mathbf{q}}-\mathbf{A}_{\mathbf{q}})$$
$$-\mathrm{i}\mathbf{q}C_{\mathbf{q}}-\mathrm{i}\mathbf{q}\frac{1}{\phi_0}\left.\frac{\partial\hat{\pi}}{\partial\phi}\right|_{un}D_{\mathbf{q}}-\hat{\eta}|_{un}\left(\mathbf{q}\cdot\mathbf{A}_{\mathbf{q}}\mathbf{q}+q^2\mathbf{A}_{\mathbf{q}}\right)=\mathbf{0} \tag{4.37a}$$

$$-\hat{\zeta}_s\Big|_{un}\mathbf{B}_{\mathbf{q}}-\hat{\mathbf{v}}_{sd}\left.\frac{\partial\hat{\zeta}_s}{\partial\phi}\right|_{un}D_{\mathbf{q}}-(\hat{\mathbf{v}}_{sd}-\hat{\mathbf{v}}_{pd})D_{\mathbf{q}}-\phi_0(\mathbf{B}_{\mathbf{q}}-\mathbf{A}_{\mathbf{q}})-\mathrm{i}\mathbf{q}C_{\mathbf{q}}-\mathbf{q}\cdot\mathbf{B}_{\mathbf{q}}\mathbf{q}-q^2\mathbf{B}_{\mathbf{q}}=\mathbf{0} \tag{4.37b}$$

$$\phi_0\mathbf{q}\cdot\mathbf{A}_{\mathbf{q}}+(1-\phi_0)\mathbf{q}\cdot\mathbf{B}_{\mathbf{q}}+(\hat{\mathbf{v}}_{pd}-\hat{\mathbf{v}}_{sd})\cdot\mathbf{q}D_{\mathbf{q}}=0 \tag{4.37c}$$
$$\frac{\partial D_{\mathbf{q}}}{\partial\hat{t}}+\mathrm{i}\phi_0\mathbf{q}\cdot\mathbf{A}_{\mathbf{q}}+\mathrm{i}\hat{\mathbf{v}}_{pd}\cdot\mathbf{q}D_{\mathbf{q}}=0. \tag{4.37d}$$

Though it would have been possible, in principle, to solve equation set 4.37 to obtain the full time evolution for all of the modes of all of the variables this was not necessary since

---

(27) In the case of $\mathbf{q}=\mathbf{0}$, which corresponds to a constant term with no spatial fluctuations, one can see immediately from equations 4.35d and 4.37d that this mode is stable, since it is trivial to obtain $\frac{\partial D_{\mathbf{0}}}{\partial\hat{t}}=0$.

the aim of this linear stability analysis was merely to establish the conditions necessary for fluctuations to grow. Hence it was sufficient to obtain the imaginary part of $\mathbf{q} \cdot \mathbf{A_q}$(28) from equations 4.37a to 4.37c in terms of D_q and substitute it into equation 4.37d to investigate whether or not fluctuations in the volume fraction, which would lead to visible patterns, would grow or decay for a given set of parameters.

4.2 Complexity Measures

4.2.1 Calculation of Probability Distributions

4.2.1.1 Binning of Curvature Measurements

The exact form of the probability distribution that is used to summarise a given pattern has very important consequences for the complexity value calculated from it. Thus for the Gaussian and mean curvature approaches to producing a probability distribution, which required the data to be binned, the choice of the binning algorithm played a crucial role in the calculation of the complexity measure. If too many small bins, or too few large bins, had been used then the complexity measures would not have been very sensitive.

In order to make the complexity measures as sensitive as possible the binning algorithm was tuned carefully, using a number of test cases, to try to find a sensible compromise between having multiple entries in each bin, and having as many bins as possible. Of course this is an important consideration as one ideally wishes to use the same binning algorithm, with the same number of bins and bin sizes, for all patterns to be considered such that fair comparisons can be made between the patterns. Furthermore since all of the probabilities in the complexity measures discussed in section 3.2 are given equal weighting the bins needed to be of the same size so as to avoid biasing the measures. Since the aim here was to produce a discrete probability distribution from a continuous variable, namely the volume fraction in the case of the particle-laden fluid, it is important to realise that the bin size essentially represented the upper bound in terms of the sensitivity of the probability distribution to small changes in this variable. Thus dividing the range of values into smaller bins increased this precision, but, because there were only a finite number of cells in the grid, reduced the frequency expected in each cell; meaning that the situation approached the limit where each bin contained at most one value, again rendering the complexity value meaningless. As a compromise it was thought that a value of the order of the square root of the number of cells would be a good choice since this guaranteed that the frequency must be greater than one in at least one of the bins, while being large enough to obtain reasonable resolution. In order to obtain the optimum value for the number of bins the complexity values for a number of test cases(29) were evaluated with a range of different bin widths. In practice 25 bins were found to generate a reasonable distribution offering a wide range of complexity values. As such this value was used to generate all of the probability distributions used to characterise the complexity of these test cases and the patterns produced by the model of the particle-laden fluid. The typical

---

(28) Only the imaginary part was needed here since it is clear from equation 4.37d that it will be the real part of $\frac{\partial D_{\mathbf{q}}}{\partial \hat{t}}$ that determines the stability and $\mathbf{q} \cdot \mathbf{A_q}$ is multiplied by i in equation 4.37d.

(29) These are described in more detail in section 5.3.1, where they are presented along with the values of complexity obtained.

grid size in this case was between 121 and 361 cells.

In order to ensure a fair comparison between patterns all of the values to be analysed, whether they be volume fraction or any other measurements, were normalised, such that they ranged between zero and one. This ensured that the complexity measures were sensitive to the shapes and structures in the pattern rather than the intensity of the variations in the quantity being measured. This was very important in the case of the model of the particle-laden fluid, where the volume fraction varied as a function of time, as it meant that even in situations where the variations in the volume fraction were decreasing in magnitude the complexity measures treated each pattern individually, based purely upon the structures involved, and were unaffected by the overall magnitude of the variations.

Similarly, another important factor in ensuring that the measures of complexity lent themselves to a fair comparison was making sure that the probability distributions had upper and lower bounds that included all of the possible values that their respective measures of curvature could take and that these remained constant across all of the patterns being compared, despite the values that actually occurred in each case. Of course normalising the value from which the curvature was calculated made this process much more straightforward. It is worth noting at this stage, as it has a significant bearing on the maximum and minimum possible values for the curvature, that for the present work it was decided that only grids with square cells would be considered, regardless of the dimensions of the cells used in simulations, since it was felt that this better complemented how one might perceive the patterns visually. Since the forms taken by the two curvature measures are very different one would expect that they operate within a different range of possible values and this is indeed the case.

Due to its extrinsic nature[162], the upper and lower limits of the mean curvature are arguably easier to visualise than those of the Gaussian measure[90], which is based on the excess angle[90,161]. These both occur when the cell in the centre takes one extreme value while all of the cells around it take the other, as depicted in figure 4.8(30).

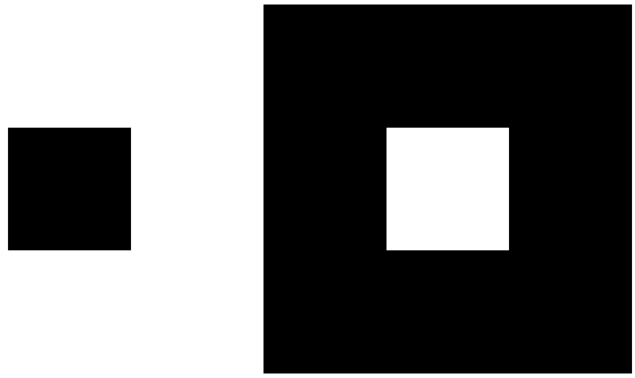

(a) Maximum mean curvature. **(b)** Minimum mean curvature.

Figure 4.8: Examples of regions of patterns where the mean curvature would take its extreme values.

Thus, when the values of the quantity whose complexity is to be evaluated range from zero to one,

$$K_M^{max} = \frac{4}{1+\Delta^2} \qquad (4.38a) \qquad\qquad K_M^{min} = -\frac{4}{1+\Delta^2}, \qquad (4.38b)$$

---

(30) The corner cells are shown in figure 4.8, but these do not affect the mean curvature.

where Δ is the size of the grid cells. This simplicity, however, presents a problem in terms of characterising the complexity of patterns since it is the relationship between the value of a particular quantity in a given cell relative to its value in the cells around it that this of interest here, so one could argue that figures 4.8a and 4.8b are, in fact, the same in this regard. If one imagines the pattern as a surface in three dimensions this is essentially the same as saying that it is the same pattern whether viewed from above or underneath. In addition to this it is clear that preserving the sign of the mean curvature would be a mistake when one considers what curvature values would be returned for a checker-board pattern, since there would be two occupied bins rather than the one required to obtain zero for the complexity value. Thus it was decided that only the magnitude of the mean curvature should be considered implying that the minimum possible mean curvature value is zero for a completely uniform surface. Thus, in practice, the probability distribution was generated based upon the values

$$K_M^{max} = \frac{4}{1+\Delta^2} \quad (4.39a) \qquad K_M^{min} = 0. \quad (4.39b)$$

For the Gaussian measure[90] the solution is, perhaps, less intuitive since one must consider how to find the extreme values of the excess angle[90,161], given by equation 3.40. Here, in order to minimise the excess angle one must try to create a shape with the largest possible perimeter, this happens when the cell in the centre has a value exactly half way between the two extremes and the cells around it alternate, as a function of the angle about the centre, from one extreme to the other, as depicted in figure 4.9b. Similarly the maximum excess angle is obtained when the perimeter of the shape formed is minimised, this is achieved by forming a cone, with the maximum possible value at the centre and the minimum possible value in the cells all around it, as shown in figure 4.9a.

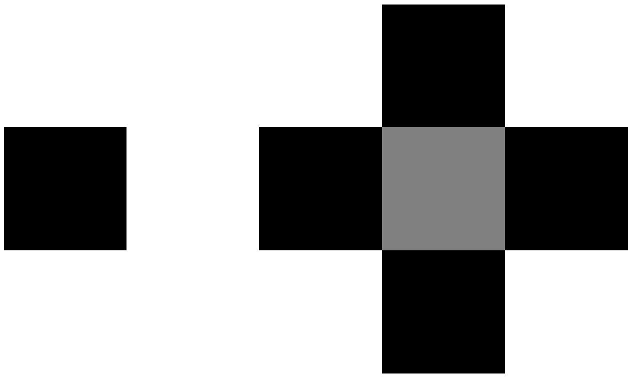

(a) Maximum Gaussian curvature.

(b) Minimum Gaussian curvature.

Figure 4.9: Examples of regions of patterns where the Gaussian curvature would take its extreme values.

Applying equation 3.40 to the pattern fragments shown in figure 4.9 one obtains

$$\Theta^{max} = 2\pi - 8\cos^{-1}\left\{\sqrt{\frac{1+\Delta^2}{1+2\Delta^2}}\right\} \qquad (4.40a)$$

$$\Theta^{min} = 2\pi - 8\cos^{-1}\left\{\frac{\Delta^2-1}{\sqrt{1+3\Delta^2+2\Delta^4}}\right\} \qquad (4.40b)$$

for values normalised between zero and one on a grid of square cells of size Δ.

4.2.1.2 Generating the Correlation Function

Unlike the curvature based measures, where a probability distribution needed to be generated by binning the data, the measures based on the correlation function already had a probability distribution associated with them and so did not require any binning of data. However, careful consideration did need to be given to the calculation of the correlation function itself. As patterns themselves were summarised in terms of a continuous variable, the volume fraction, distributed across a discrete grid the data lent itself well to calculation of the structure factor, and by extension the correlation function, by discrete Fourier transform,

$$\mathcal{F}_{ij}\left\{\phi_{kl}\right\} = \frac{1}{N} \sum_{k=-\frac{1}{2}N}^{\frac{1}{2}N} \sum_{l=-\frac{1}{2}N}^{\frac{1}{2}N} \phi_{k,l} e^{\frac{2\pi \mathrm{i}}{N}(ik+jl)}, \tag{4.41}$$

where N is the length of a square grid, of N^2 square cells. Since the sizes of the grids typically used in the simulation of the particle-laden fluid were relatively small and usually contained an odd number of cells, it was decided that it would be better to apply equation 4.41 directly to obtain the Fourier transform and inverse transform, necessary for the calculation of the correlation function, instead of using the fast Fourier transform. As the fast Fourier transform would require zero padding, in order to make the number of cells a power of two, which would introduce an additional error into the calculation. It was thought that because the grid size was relatively small this error could be quite large by comparison and also that the performance increase would be relatively small since the grid size would have had to be rounded up to the nearest power of two anyway.

4.2.2 Maximal Complexity Patterns

In order to try to better understand the different complexity measures introduced in section 3.2, Monte-Carlo simulations were run in order to find the pattern that maximised the complexity in each case[3]. These started from an initially uniform state and used a variant of the the Metropolis method[115] to update the pattern at each iteration. Here two cells in the grid were chosen at random and then a random amount of material was moved from one cell to the other. Provided that this did not leave either cell in a situation where it contained an unphysical amount of material(31) the move was accepted according to a set of rules, similar to the Metropolis Monte-Carlo method, using the complexity in the place of the negative of the energy in the standard algorithm. Hence all moves that increased the complexity were accepted unconditionally while those moves that reduced the complexity were accepted with a probability related to the Boltzmann factor for the change in the complexity. Here another uniform random number, $0 \leq \mathcal{R} \leq 1$, was chosen and the move was accepted if and only if

$$\mathcal{R} < e^{-\alpha\left(\frac{C_0 - C}{C_0}\right)^2}, \tag{4.42}$$

where C is the complexity of the proposed new state, C_0 is the complexity of the current state and α is a constant of proportionality which determines how likely it is that a state

---

(31) The normalised value of the volume fraction was still between zero and one.

of lower complexity will be accepted. In terms of the standard algorithm this can be thought of as the reciprocal of the thermal energy. Dividing the factor in the exponent by the current complexity ensured a fair comparison between the magnitudes of the changes at different iterations, since using the current value of the complexity meant that a small change when the complexity was small was given the same chance of been accepted as a large change when the complexity was large. The main reason for the choice of this Metropolis like method here is that it allows some states that lower the complexity and in doing so allows the system to explore more possible states and thus gave a better chance of finding the global maximum. The power of two was added to make the method less sensitive to small changes, so allowing the system to explore more states, of roughly equal complexity, whilst penalising large reductions in complexity more severely than the standard Metropolis method would do. This was important because the fact that random amounts of material were being moved between random cells meant that, in the absence of such a factor, it would be very likely that the system would move toward a highly disordered state and once in this state it would be very unlikely that it would find an ordered state again. Thus while it was important to allow the system to explore many different states, it was also important that it was not allowed to reduce its complexity too much early on as the chances of a high complexity state being proposed later, once the disorder had been established, would be very small.

In order to give the algorithm the best possible chance of finding the global maximum simulated annealing[3] was used, so that the system could explore many more states early on in the simulation, but would become less and less likely to accept a state of low complexity as the simulation went on. The effect of cooling the system, and making complexity reducing changes less likely to be accepted, was achieved by increasing the value of α, in equation 4.42, at a constant rate. Due to the diverse way in which the complexity measures responded to changes in the patterns this rate was set individually for each of the measures in order to obtain the best compromise between allowing the system to explore the widest possible variety of states while still honing in on the maximum complexity state in the shortest possible time and ensuring that the complexity was not allowed to fall too far in the early stages of the simulation as it would have taken a very long time to recover from this. Typically an increase in the region of 10^4 per cycle was used(32). The optimal rate was found by examining the behaviour of the complexity as a function of time in the early stages of the simulation.

Finally by choosing two cells at random and moving material between them one automatically conserves material[3], which means that the patterns formed are much more physically realistic, since they remain at the volume fraction specified at the start of the simulation, and also prevents the algorithm from becoming trapped in a state where most of the proposed moves are automatically rejected due to the fact that they result in a cell having a volume fraction outside of the prescribed limits because the mean is very close to one of those limits.

This method was applied to both of the complexity measures using all of the different methods to obtaining a probability distribution. In order to obtain detailed patterns

---

(32) While this value may seem rather large it is important to remember that the changes in the complexity can be very small, especially on a large grid.

slightly larger grids than those in the model of the particle-laden fluid were used. By extension this meant that more bins were used for binning the curvature data as this was better suited to the larger grids and gave better resolution. Of course, as described in section 4.2.1 this meant that care had to be taken when drawing comparisons, but since the aim of this work was to understand the behaviour of the complexity measures in a generic way and not to draw comparisons between the exact forms of individual patterns it was not important that the patterns were measured in exactly the same way. Ultimately the grid sizes used were chosen as a compromise between the maximum possible detail and allowing for the complexity values to be evaluated sufficiently quickly that a large number of Monte-Carlo steps could be taken in a reasonable amount of time to allow the system to explore as many states as possible.

Flow chart 4.2 gives a summary of the algorithm used.

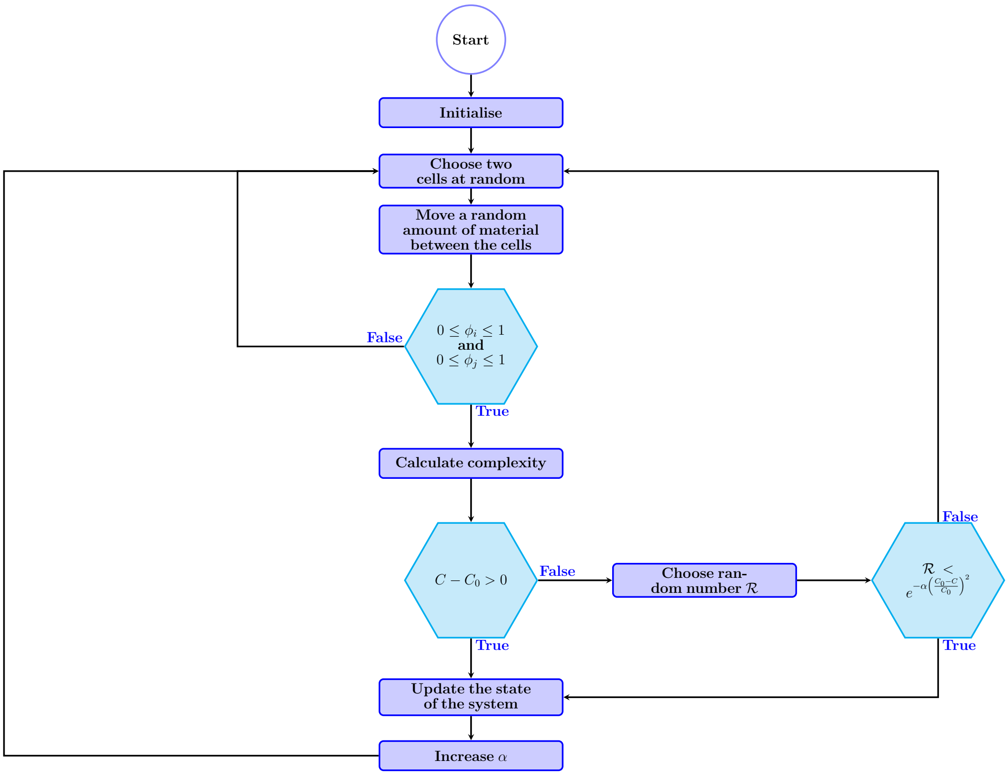

Flow Chart 4.2: Flow chart showing the main steps in the algorithm used to find the maximum complexity patterns.

4.3 Hydrodynamics Simulations

4.3.1 Non-Dimensionalisation

The calculation of the friction matrix, performed by HYDROLIB[12,134], assumed that the units were chosen such that the radii of all particles were unity, hence $a = 1$, and the viscosity of the solvent was always $\eta_s = \frac{1}{4\pi}$[134]. This left one unit undetermined and since one calculates forces from the hydrodynamics, but requires accelerations to update the positions and velocities of the particles, and since all of the particles were identical in size, it was decided that a convenient choice would be to set the mass of the particles to unity, such that the force and linear acceleration were interchangeable.

4.3.2 Rigid Bodies

As described in section 3.3 the HYDROLIB library[12,134] provided a convenient means of obtaining the friction matrix for a given arrangement of particles. It also provides a means of dealing with particles that are in contact separately and treats them as a rigid body, where the particles are unable to move relative to one another[134]. For normal, free, particles contact is forbidden. However, defining two particles as part of the same rigid body allowed for them to come into contact as HYDROLIB did not perform the lubrication correction for these particles. Thus the entries in the friction matrix corresponding to the movement of two particles, which were rigidly joined, were not infinite as one might expect and thus the numerical calculation was able to proceed. It may not be immediately apparent there is a sound physical motivation for this; although the entries in the friction matrix that correspond to the relative motion of these particles are wrong the particles are forbidden from performing any relative motion so the force generated will be zero as required.

This treatment of rigid bodies by the HYDROLIB library is intended to provide a means of simulating free particles that come into contact for a given period of time and move as a rigid body[134]. However, in the present work it was used to a somewhat different end, namely for providing the ability to insert large driven objects into the system, such as plates to shear the particles or obstacles for the flow field to traverse. Because hydrodynamic interactions between objects with arbitrary shapes are so complicated HYDROLIB only provides the routines for identical spherical particles[12,134], thus all of these rigid bodies had to be made from arrangements of particles connected by rigid connections(33). Doing this efficiently meant making a slight alteration to the way HYDROLIB calculates the final friction matrix. In its original state HYDROLIB performs the multipole expansion described in section 3.3.2 to obtain the friction matrix and then, at great expense in terms of CPU time, reduces the elements corresponding to the constituent particles of the rigid bodies to produce elements which correspond to the rigid body as a whole. Since, in this case, the rigid bodies were to be driven at a predetermined velocity the forces they felt were of little consequence and so an option was added to force HYDROLIB to skip this section to improve performance. Fortunately by virtue of the vector formalism defined by HYDROLIB these meaningless entries were automatically avoided and did not affect the forces felt by the free particles. In practice in simulations these rigid bodies were moved at a constant velocity and the hydrodynamic interactions, arising from the particles that were not moving as part of the same rigid body, were calculated.

4.3.3 Hydrodynamic Interactions and Brownian Forces

Since HYDROLIB only calculates hydrodynamic interactions at a given instant and does not deal with Brownian motion[12,134] the Brownian forces[4] had to be added separately. In order to preserve detailed balance this was done using equation 3.71, which meant that the weighting matrix $\mathbf{Q}$ had to be calculated. This was done simply by taking the Cholesky decomposition of the friction matrix[4], $\boldsymbol{\zeta}$, produced by HYDROLIB and then multiplying by $\sqrt{\frac{2k_BT}{\delta t}}$, where T is the temperature and δt is the size of the time step, in order to

---

(33) These will be discussed in later sections in the context of the specific structures used.

satisfy equation 3.73. For the purposes of the simulation the Gaussian noise, represented by the time step independent part of the Wiener process, $d\mathbf{W}$, in equation 3.71[4], was generated using the Box-Muller algorithm[167], for normally distributed random numbers, of unit standard deviation and zero mean, provided by the randgen.f random number library[167].

As well as the ability to deal with rigid body particles separately HYDROLIB also provides a means of controlling the order of the multipole expansion that is used[12,134]. This allowed for a compromise to be reached between accuracy and performance. In the present work, with the exception of performance testing, the multipole expansion always retained terms up to order three which, according to the HYDROLIB documentation, produces a friction matrix which is accurate to within 1%[134].

Another feature of HYDROLIB which was exploited in this work was its ability to deal with periodic boundary conditions[12,134], as well as those for an infinite solvent[12,134], and correct the friction matrix accordingly. This is incredibly important as the hydrodynamic forces decay so slowly and it is not possible to define a reasonable cut-off radius or only take the force calculated from the nearest periodic image. One slight draw back of the particular implementation used by HYDROLIB is that it only allows for a cubic unit cell[134] and does not allow for mixed periodic and infinite boundaries which meant some approximations had to be used to get the desired results. These will be discussed in more detail in the relevant results sections.

4.3.4 Velocity Verlet Algorithm

By far the most computationally expensive part of the simulation of particles with full hydrodynamic interactions was the calculation of the friction matrix from the arrangement of particles, which was performed by the HYDROLIB library[12,134]. This meant that the part of the simulation responsible for evolving the state of the system in time had to do so with the minimum possible number of evaluations of the friction matrix. Thus the algorithm used had to allow for as large a time step as possible while maintaining stability, and could not rely on multiple evolutions of the friction matrix during one time step.

In the present work a variant of the velocity Verlet algorithm was used[113]. This offered the advantage of being more stable than the simple Euler method as well as being based on an algorithm with the useful property of time reversal symmetry[115] and only requiring one evaluation of the forces per time step, thus making the relative increase in computational cost negligible, unlike the Runge-Kutta[151] methods which require multiple evaluations of the forces, implying multiple evaluations of the friction matrix. While the standard Verlet algorithm[115] does not calculate the velocities directly, making the calculation of velocity dependent forces difficult and potentially inaccurate, the velocity Verlet algorithm treats the velocities in a much more rigorous manner[115] meaning that, by extension, the hydrodynamic forces could be calculated in a simple and accurate manner. Since the forces here depend on the velocities of the particles as well as their positions[113] the algorithm used was a modified version of the velocity Verlet algorithm taken from reference 113. In this algorithm the forces were calculated by making an estimate of what the velocity would be in the middle of the time step, at $t + \frac{1}{2}\delta t$, and then correcting it once the forces were known to obtain the value at the end of the time step. This is the reason why this version of the algorithm was used for the hydrodynamic forces which clearly depend on the velocities of the particles.

The algorithm itself proceeds by evaluating the following four steps[113] in sequence.

$$\mathbf{r}_{t+\delta t} \approx \mathbf{r}_t + \delta t \left(\mathbf{u}_t + \frac{1}{2}\delta t \mathbf{f}_t \right) \tag{4.43a}$$

$$\mathbf{u}_{t+\frac{1}{2}\delta t} \approx \mathbf{u}_t + \frac{1}{2}\delta t \mathbf{f}_t \tag{4.43b}$$

$$\mathbf{f}_{t+\delta t} \approx \mathbf{f} \left\{ \mathbf{r}_{t+\delta t}, \mathbf{u}_{t+\frac{1}{2}\delta t} \right\} \tag{4.43c}$$

$$\mathbf{u}_{t+\delta t} \approx \mathbf{u}_{t+\frac{1}{2}\delta t} + \frac{1}{2}\delta t \mathbf{f}_{t+\delta t}, \tag{4.43d}$$

where $\mathbf{u}$ and $\mathbf{f}$ are the $6N$ dimensional vectors described in section 3.3.2, corresponding to the velocities and forces acting on all N particles, $\mathbf{r}$ is a $3N$ dimensional vector that corresponds to the positions of all of the particles, δt is the size of the time step and t is the current time, for which all variables are known.

For a relatively straightforward and compact algorithm this variant of the velocity Verlet algorithm[113] offers excellent stability[113] and energy and momentum conservation properties(34) as well as being fourth order accurate[115] in the position update(35). Another useful property of the standard Verlet algorithms is that the equations for the trajectories are properly centred, meaning the algorithm exactly obeys time reversal symmetry[115], though the fact that the forces depend on the velocity estimates means that this is only approximately true here[113]. All of these properties meant that it was possible to obtain reliable and stable results even with a large time step[113], reducing the number of times the friction matrix needed to be evaluated.

It is worth noting that although HYDROLIB implicitly assumes the solvent to be in the low Reynolds' number limit the particles are attributed a mass and so experience inertia, to some extent. This is done primarily as a means of rationalising the relationship between the forces produced by the hydrodynamic calculations and Brownian motion in terms of the motion of the particles. However, it is not expected to have a significant effect on the physics of the their motion as they may still be thought of as being at low Reynolds' number, since their velocity decays quickly compared with other relevant time scales in the system.

4.3.5 Collision Handling

Due to the fact that the hydrodynamic lubrication force diverges when two particles come into contact[12], contact between the particles needed to be avoided at all costs. Even a close approach, without contact, can generate very large forces which would have presented a problem numerically. For this reason the hard sphere radius, r_H, which determined the smallest possible distance between two particle centres, was always defined to be larger than the hydrodynamic radius of the spheres, a, as used to calculate the hydrodynamic forces. In essence this meant that the algorithm used to handle the collisions perceived

---

(34) For purely conservative forces it can be shown that this algorithm conserves momentum exactly[115].

(35) Strictly the algorithm is only fourth order accurate for deterministic systems. The order is unclear when stochastic processes are involved[113].

all of the particles to be slightly larger than HYDROLIB did[134]. When coupled with the finite time step this essentially amounts to adjusting the times of the collisions such that they never occur exactly between two steps and always occur just before the end of a step, while the hydrodynamic interactions are always calculated between the time steps. This means that the hydrodynamic interactions are never calculated at the point of contact, by the time this calculation is performed the two particles which were about to collide are moving apart again. This is shown in figure 4.10.

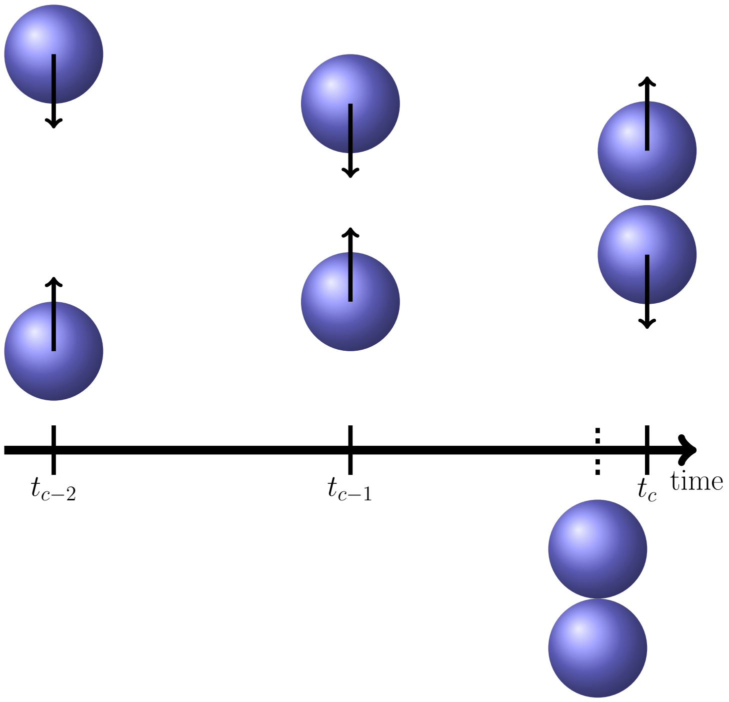

Figure 4.10: Schematic showing a simple collision between two particles. The particle positions and velocities, indicated by the arrows, are shown at each time step before the time step t_c, when the true collision, at a centre to centre distance of $2a$, would occur. However, using the slightly larger effective radius, r_H, for handling the collision essentially models the same collision happening at the slightly earlier time indicated by the dashed line.

Physically using a larger radius in the collision handling part of the algorithm to a certain extent means that this simulation was essentially a simulation of sterically stabilised colloids[168], which are coated in a thin layer of polymer molecules that have little effect on the drag coefficient, but stop the particles coming into direct contact(36).

In order to avoid very small time steps occurring in succession when many particles were simulated a third measure of the, effective, particle radius, r_S, was introduced to the collision handling scheme, such that $r_S \geq r_H > a$(37). This can be thought of as a "soft" radius where collisions may occur, but closer approach is not forbidden. If the centres of two particles were found to have a separation, r, of $r_H < r < r_S$ they were deemed to have collided and their velocities were altered accordingly. This avoids having to deal with another collision a very short time in the future and makes a much larger time step possible. Again this behaviour matches up well with how one might expect sterically stabilised colloids to behave[3]. These radii and their effect on how collisions were handled are shown in figures 4.11 and 4.12 respectively.

---

(36) In experiments these particles are often used in preference to hard colloids as the polymers prevent the colloids from sticking together, but here they merely provide a good example of a physical system that exhibits this kind of behaviour.

(37) For most of the simulations presented in the present work these values were set at $r_H = 1.025a$ and $r_S = 1.05a$.

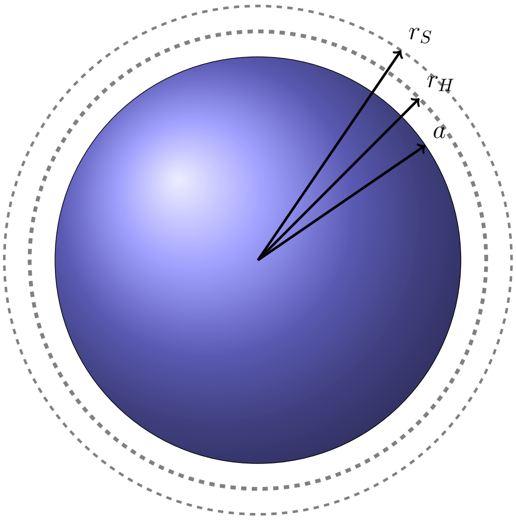

Figure 4.11: Diagram showing the different sphere radii used in the hydrodynamics simulation. a is the radius used in the calculation of the hydrodynamic interactions, r_H is the radius that no other particle can enter, used by the collision handling scheme, and r_S is the radius within which a collision will be deemed to have occurred. All particles which have centre to centre distances greater than $2r_S$ are unaltered by the collision handling scheme.

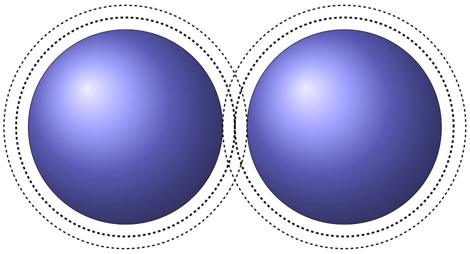

(a) Collision occurs because the centre to centre distance is $2r_H$. The time step would have been set to avoid these particles getting any closer than this.

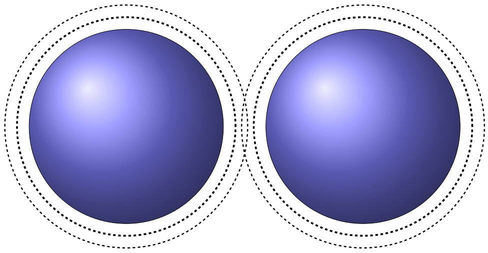

(b) Collision occurs because the centre to centre distance is less than $2r_S$.

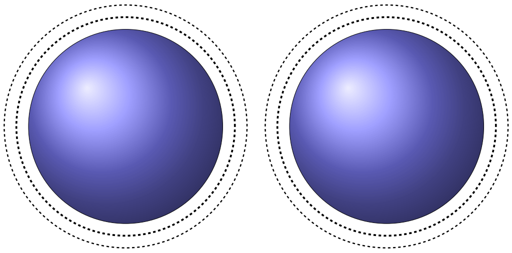

(c) No collision.

Figure 4.12: Sketches showing the three different collision scenarios. Here it is assumed that the particles are moving towards each other in each case, but the arrows are not shown in order to keep the diagrams simple.

Using this scheme gave a good approximation of the collisions between rigid particles while allowing for reasonable performance in terms of the sizes of the time steps which were possible. The key advantages of this scheme over the use of a potential that diverges on contact are: that it allows for perfectly elastic collisions, there is no risk of it affecting the behaviour of particles at separations greater than r_S, as an interaction potential might due to its long range, and one can say with certainty that no two particle centres come closer than $2r_H$(38).

The collisions themselves were treated as momentum conserving hard sphere collisions and dissipation due to the solvent or deformation of the particles was neglected, since the dissipation due to the solvent was already dealt with correctly in the calculation of the hydrodynamic interactions and as such treating it here as well would have been un-physical. Likewise the particles had to be assumed to be un-deformable since the hydrodynamic interactions could only be calculated for perfect spheres. Thus the post

---

(38) Of course this assumes that the time of the collision could be calculated accuratly, which was not the case in practice once Brownian forces were included. Hence extra checks had to be made to make sure no particles had a centre to centre distance less than $2r_H$. This is discussed in more detail in section 4.3.7.

collision velocities, $\mathbf{v}_i$ and $\mathbf{v}_j$, of the two particles, i and $j^{(39)}$, are given by

$$\mathbf{v}_i = \mathbf{v}_i^0 + J\hat{\mathbf{n}} \tag{4.44a}$$

$$\mathbf{v}_j = \mathbf{v}_j^0 - J\hat{\mathbf{n}}, \tag{4.44b}$$

where $\mathbf{v}_i^0$ and $\mathbf{v}_j^0$, are the incident velocities of the two particles, J is the magnitude of the component of the impulse that points along $\hat{\mathbf{n}}$, given by

$$J = -\left(\mathbf{v}_i^0 - \mathbf{v}_j^0\right) \cdot \hat{\mathbf{n}}, \tag{4.45}$$

and $\hat{\mathbf{n}}$ is a unit vector that points along the line connecting the centres, from particle i to particle j, given by

$$\hat{\mathbf{n}} = -\frac{\mathbf{r}_i - \mathbf{r}_j}{|\mathbf{r}_i - \mathbf{r}_j|}. \tag{4.46}$$

The fact that these collisions are momentum conserving may, at first sight, seem somewhat at odds with the nature of the dissipative hydrodynamic interactions, however it is important to remember that all of the particles not undergoing a collision travel ballistically between time steps and the dissipation is handled at the end of each time step. Thus it would be inconstant to attempt to correct for dissipation in the collision as this would, in essence, mean that the particles undergoing collisions would be treat differently to those that weren't.

4.3.6 Pair Interactions

In addition to the hydrodynamic interactions and collision handling the simulation was also designed to be able to deal with simple pair interactions such as: electrostatic or van der Waals' forces.

This addition yielded three important benefits: firstly it allowed for the simulation of particles which have such interactions in reality, such as those described in appendix A.2, secondly it provided a convenient additional means of testing the simulation to make sure the Brownian forces obeyed detailed balance, by means of calculating the distribution of separations for a bead and spring system, and finally, and most importantly, short range pair iterations provide a convenient means of preventing two particles which were being forced together from touching without decreasing the time step. This final property was used extensively in simulations at high particle concentrations.

In this case one requires a potential which is strong enough to counteract any external force which the particles are likely to experience, but falls away rapidly as the separation of the particles increases so it does not interfere with the bulk dynamics of the system. Another desirable property for this potential is that it should grow smoothly from zero such that it can match, exactly, any applied force without producing an unphysical imbalance which sends the particle back along its original trajectory. To achieve this a soft repulsive potential was used when the particles were close together, with a cut off when the centre to centre distance,

$$\varepsilon = |\mathbf{r}_i - \mathbf{r}_j|, \tag{4.47}$$

---

(39) To avoid considering collisions unnecessarily only combinations where $i < j$ were considered.

was greater than a given separation, r_0, typically taken to be the radius at which particles where deemed close enough to collide, r_S. This meant that particles that were being forced together by an external force could find a separation at which the interaction potential balanced the external force so that they could remain at rest with respect to one another at a small separation for an arbitrary amount of time without influencing the size of the time step. Meanwhile the cutoff meant that the potential could not influence interactions between particles over a significant distance and hence had a limited effect on the physics of the system as desired. Finally in order to make sure the potential was continuous as a function of the centre to centre distance the value of the potential at $\varepsilon = r_0$ was subtracted. Mathematically the potential used here can be expressed as[3]

$$U = \begin{cases} E_0\left[\left(\frac{\sigma}{\varepsilon-2r_\infty}\right)^4 - \left(\frac{\sigma}{\varepsilon-2r_\infty}\right)^2 - \left(\frac{\sigma}{2r_0-2r_\infty}\right)^4 + \left(\frac{\sigma}{2r_0-2r_\infty}\right)^2\right] & \varepsilon < 2r_0 \\ 0 & \varepsilon \geq 2r_0 \end{cases}. \tag{4.48}$$

Here r_0 is the radius at which the potential goes to zero, r_∞ is the radius at which the potential diverges, typically taken to be the hydrodynamic radius of the particles, a. While σ controls the relative magnitude of the attractive and repulsive terms, and was used to tune the shape of the potential, and E_0 controls the overall magnitude of the potential. Typically E_0 was chosen so that the potential could match the magnitude of the forces which were likely to occur in the given system. It is worth mentioning that there are, in principle, five radii at work in this simulation, although in actuality $r_\infty = r_H$ and $r_0 = r_S$ were used throughout, such that the potential only operated with the range where collisions were deemed to occur. Hence there are a total three pertinent length scales: $2r_S$, the separation at which particles do not interact except through hydrodynamic interactions, $2r_H$ the smallest possible separation and a the hydrodynamic radius. Of course for the purposes of preventing particles from getting too close to one another σ was always set such that the potential was purely repulsive. A sketch of the form of the potential typically used in simulations is given in figure 4.13.

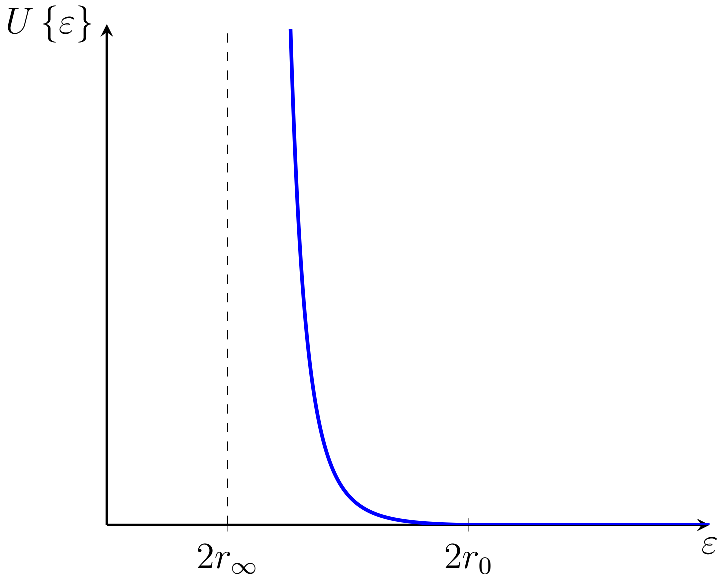

Figure 4.13: Sketch of the repulsive interaction potential, used to stabilise particles being forced together and so allow for larger time steps, as a function of particle centre to centre distance.

An example of a situation where this kind of interaction is useful is where a stream of particles are falling, due to gravity, at zero temperature towards an obstacle. If the particles are aligned in the vertical direction then they will stack up on top of the obstacle and gravity plays the part of the external force, that is pushing them together. Simulations were performed on two identical versions of this system, one with and one without the interaction potential described by equation 4.48 to demonstrate its effect⁽⁴⁰⁾. Figure 4.14 shows snapshots of the state of the system taken at different times for the two simulations and figure 4.15 shows a plot of the size of the time step as a function of time in the each simulation as well as the moving average of this quantity.

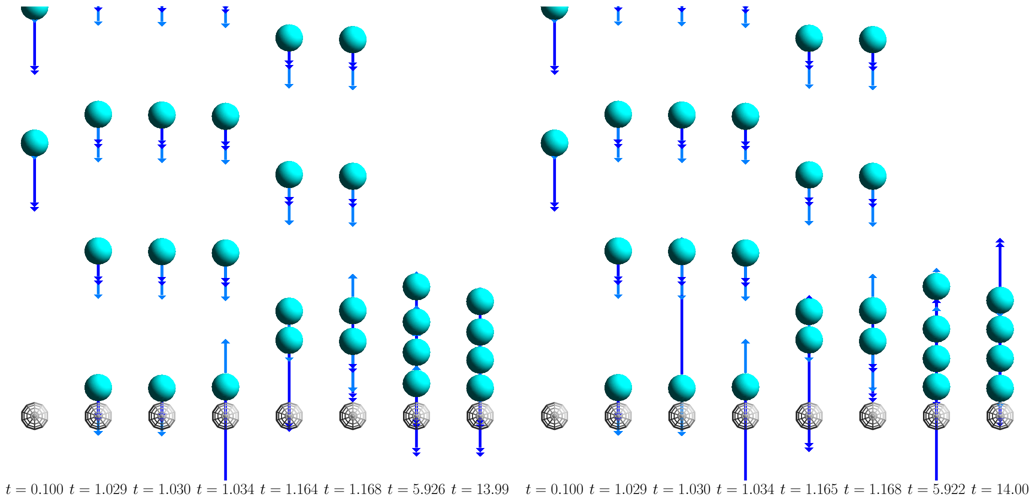

(a) Without interactions. **(b)** With interactions.

Figure 4.14: Snapshots of a simulation of a system of four free particles ,at zero temperature, falling, towards a fifth which is fixed. In the simulation with interactions the interaction potential used was that described in equation 4.48 with $E_0 = 0.5$, $\sigma = 0.1$, $r_0 = 1.05$ and $r_\infty = 1$. In both simulations the gravitation field strength was set at 50 in non-dimensional units and points vertically downwards in the above diagrams. Here the fixed particle is drawn as a grey wire framed sphere (◍) to distinguish it from the free particles which are drawn as solid cyan spheres (●), the velocity is shown by light blue, single headed, arrows (⟶) and the acceleration is shown by the dark blue, double headed, arrows (↠), the lengths of the arrows correspond to the relative magnitudes of the vectors they represent.

---

(40) In order to make the results as clear as possible the many body hydrodynamic friction matrix was replaced with a constant drag coefficient in these simulations.

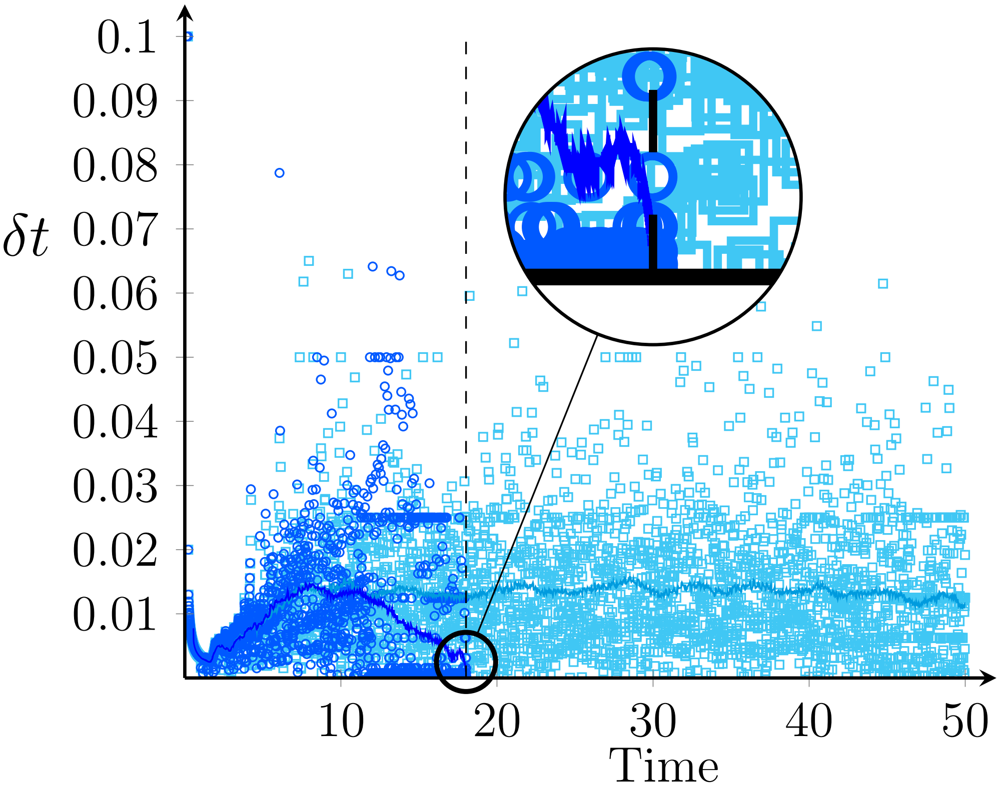

Figure 4.15: Plot showing the sizes of the dynamic time step as a function of time for an example system of four particles falling towards a fifth which is fixed at the origin. The blue circles (∘) correspond to the simulation that was run with no pair interactions while the cyan squares (▫) correspond to the simulation that was run with the repulsive interaction potential described in equation 4.48 with $E_0 = 0.5$, $\sigma = 0.1$, $r_0 = 1.05$ and $r_\infty = 1$. The solid coloured lines show a 99 point moving average of their respective data sets, cyan (——) for the simulation with pair interactions and blue (——) for the simulation without.

Figure 4.15 clearly shows that the interaction potential has the desired effect of preventing the time step from getting too small. The moving averages of both sets of data fall rapidly at first as the particles accelerate and rise again while the particles are bouncing, the average time step for the simulation with the interaction potential remains stable at a reasonable value as the particles come to rest in a column while the time steps in the simulation without the interaction become vanishingly small, as the algorithm successively reduces the size of the time step to avoid overlaps, up to the point where even the minimum allowed time step is too large and the simulation has to exit, at $t \approx 18.0$. It is also clear, by comparing figures 4.14a and 4.14b, that the interaction potential has little effect on the motion of the particles on long time scales or long length scales, as required. These figures do, however, highlight the draw back of this approach in that, instantaneously at the time of the collision, energy is not strictly conserved since the particles receive an additional momentum boost due to the interaction potential when they collide. This is clear from examining the acceleration vector of the free particle colliding with the fixed one in the third snapshot of figure 4.14b. Here the momentum conserving collision has occurred as normal, but the particle has received an additional impulse pointing away from the fixed particle due to the interaction potential which means it leaves with more kinetic energy than it started with. While this is clearly un-physical it does not represent a major problem since this high energy state is relatively short lived and the energy is soon dissipated by the viscous forces(41) and, as figures 4.14a and 4.14b, show has little effect on the long time dynamics. However, it is still worth bearing in mind when interpreting results where an interaction potential of this type has been used and a good reason to make the potential as weak as possible.

4.3.7 Dynamic Time Step

In order to obtain the maximum length of simulation time with the minimum number of evaluations of the friction matrix and to make sure particles never touched or overlapped a dynamic time step was used. This meant that when the particles were far apart and moving slowly the time could be advanced quickly at minimal computational expense while the time step could be reduced for careful treatment of collisions and fast moving particles.

Because the size of the time step depended on several factors and was key, not only to advancing the positions and velocities, but also to the magnitude of the Brownian forces, it required very careful treatment.

Firstly the algorithm found the particle whose velocity had the greatest magnitude, then calculated how long it would take for this particle to cover a predefined distance(42) and proposed that as the time step.

Secondly the time of the next collision was predicted based on the assumption that the particles, i and j(43), were traveling ballistically, as this made finding the solution easier(44). Thus, if two particles are travelling ballistically, their positions, $\mathbf{r}_i$ and $\mathbf{r}_j$, at any time, δt, after they are in initial positions, $\mathbf{r}_i^0$ and $\mathbf{r}_j^0$, can be written as

$$\mathbf{r}_i = \mathbf{r}_i^0 + \delta t \mathbf{v}_i^0 \tag{4.49a}$$

$$\mathbf{r}_j = \mathbf{r}_j^0 + \delta t \mathbf{v}_j^0, \tag{4.49b}$$

where $\mathbf{v}_i^0$ and $\mathbf{v}_j^0$ are the velocities of the two particles(45). For two finite particles of radius

---

(41) In the non-dimensional units used here the decay constant for the velocity of a free particle coming to rest in the solvent is one time unit while the behaviour of interest in the shear experiments at high volume fraction, where this interaction potential was used, has a time scale of tens to hundreds of time units.

(42) This was typically taken to be between 10% and 50% of a particle radius, a.

(43) To avoid considering collisions unnecessarily only combinations where $i < j$ were considered. As this automatically included the reverse case.

(44) A version of this algorithm which accounted for acceleration was tested, but was not found to be significantly more reliable at predicting collisions than the method that assumed ballistic motion. The likely course of this is that the formulas for the roots were far more complicated and introduced more rounding errors. Furthermore this method had the added disadvantage that there was not straightforward way of knowing which root would give the smallest positive result without simply calculating them all and comparing them.

(45) The assumption that the motion is ballistic means that the time at which the velocity is evaluated is irrelevant, but the superscript zeros are included here since, in practice, the values used for the initial state were those at the end of the previous time step, thus the zero is retained to make it clear that $\mathbf{r}^0$ and $\mathbf{v}^0$ are evaluated at the same time.

r_H[46] a collision must occur at the time when

$$|\mathbf{r}_i - \mathbf{r}_j| = 2r_H. \tag{4.50}$$

Thus, by substituting equations 4.49a and 4.49b into equation 4.50 and solving for δt, assuming there is a collision and assuming further that the angle between the vectors $\mathbf{r}_i^0 - \mathbf{r}_j^0$ and $\mathbf{v}_i^0 - \mathbf{v}_j^0$ is small, to simplify the solution[47], one obtains

$$\delta t \approx \frac{-\left(\mathbf{r}_i^0 - \mathbf{r}_j^0\right) \cdot \left(\mathbf{v}_i^0 - \mathbf{v}_j^0\right) \pm 2r_H \left|\mathbf{v}_i^0 - \mathbf{v}_j^0\right|}{\left|\mathbf{v}_i^0 - \mathbf{v}_j^0\right|^2} \tag{4.51}$$

for the times at which the condition in equation 4.50 is fulfilled. The first thing to note about equation 4.51 is that there are, potentially, two solutions corresponding to the time at which the particles first make contact and the time where they would break contact if they were able to pass through one another. There may also be negative roots corresponding to previous contacts. Clearly for the present algorithm one requires the smallest positive root. This is easily obtained by considering the condition necessary for a collision to occur at all, namely that the difference in the velocities must be of opposite sign to the difference in the positions, mathematically speaking one requires

$$\left(\mathbf{r}_i^0 - \mathbf{r}_j^0\right) \cdot \left(\mathbf{v}_i^0 - \mathbf{v}_j^0\right) < 0. \tag{4.52}$$

This automatically implies then that the smallest positive time is obtained when the second term on the top of the fraction in equation 4.51 is negative. Thus, using this method one obtains

$$\delta t \approx \frac{-\left(\mathbf{r}_i^0 - \mathbf{r}_j^0\right) \cdot \left(\mathbf{v}_i^0 - \mathbf{v}_j^0\right) - 2r_H \left|\mathbf{v}_i^0 - \mathbf{v}_j^0\right|}{\left|\mathbf{v}_i^0 - \mathbf{v}_j^0\right|^2} \tag{4.53}$$

as a sensible approximation as to the maximum time step possible without missing a collision or allowing overlaps or contact.

The final choice of time step was then taken to be the smaller of the time taken for the fastest particle in the system to traverse a given distance, the time until the next collision and, to ensure no loss of accuracy due to extremely large steps, a predefined maximum time step.

Finally, because the estimate of the time at which the next collision would occur did not include the effect of acceleration on the position of the particle and contacts needed to be avoided at all costs a final check was added after the full position update had been

---

[46] Since the goal of this calculation is to obtain the maximum time step possible without missing a collision the hard sphere radius, which no other particle can come within, was used as the particle size. Of course, as described in section 4.3.5 collisions may be deemed to occur at slightly larger distances within r_S, but this does not represent the maximum possible time between collisions so the choice of r_S did not influence this calculation.

[47] Although this may not always be the case, especially when the particles are close together, one only requires an estimate of the collision time and this cannot result is particle overlaps as this time will always be shorter that the actual time before the particles make contact. It is worth remembering also that even with an exact formula this procedure can only ever serve as an estimate since the Brownian forces are not accounted for here.

carried out, but before the forces were calculated, to make sure there were in fact no overlaps between particles. If such overlaps were found(48) the previous state, before the position update, was restored and the time step halved, in the hope that the state would be accepted at the next attempt. Since this was all done before the forces, and hence the friction matrix, were evaluated the computational cost of any failed attempts was negligible, especially compared to the potential gains of using the largest possible time step in situations where correcting for the acceleration did not lead to overlaps.

4.3.7.1 Correcting the Brownian Forces

In section 3.3.3 it was proven that the magnitude of the Brownian forces[4] must scale with $\delta t^{\frac{1}{2}}$[113], as stated in equation 3.73, if detailed balance is to be preserved. This is another reason why the dynamic time step must be treated with extreme care since these forces must be rescaled every time the size of the time step changes. As is clear from equation set 4.43 the force is calculated after the position update, so the time step is liable to change before the positions are updated again. If this is the case then the Brownian forces calculated at the previous time step no longer have the correct scaling to be used in the position update, or estimate of the velocity(49), in the current time step and need to be rescaled by,

$$\xi = \sqrt{\frac{\delta t^0}{\delta t}}. \tag{4.54}$$

where δt^0 is the size of the last time step used and δt is the size of the current time step. Unfortunately, however, because there are other forces, in addition to the Brownian forces, that do not scale with the size of the time step one cannot simply scale the total force and one must instead subtract off the old Brownian force while adding the rescaled one. The correct force to use at each time step, therefore, is

$$\mathbf{f} = \mathbf{f}^0 + (\xi - 1)\,\mathbf{f}_B^0, \tag{4.55}$$

where $\mathbf{f}_B$ is the purely Brownian contribution to the force. Here the superscript zeros denote the uncorrected values left at the end of the previous iteration of the velocity Verlet algorithm.

4.3.8 Algorithm Structure

With all of the components described in sections 4.3.4 to 4.3.7 in place an important consideration was how best to incorporate the elements specific to this simulation into the modified velocity Verlet algorithm, in a way that made the simulation as physically realistic as possible, but also as efficient as possible. Firstly it was important that any impending collisions were dealt with before particles overlapped. These changes would also affect the

---

(48) This did occur on rare occasions where there were strong forces, forcing the particles together, since the method used to estimate the time of the next collision would underestimate the distance the particles would move toward each other in the given time step.

(49) If one considers what would happen if a very long time step immediately followed a very short one; it is clear that this would course unphysical behaviour since it would result in a very large change in position and velocity due to the fact that the force, calculated in the previous time step, when δt was small, would be very large.

size of the next time step, which needed to be calculated before any of the particles were moved. With the time step set the Brownian forces were rescaled in preparation for the first step of the velocity Verlet algorithm, given by equation 4.43a. Once the move had taken place a final check was performed to make sure none of the particles were touching or overlapping as this would have caused the calculation of the friction matrix to fail. If overlaps or touching particles were found the algorithm tried to advance the state with a smaller time step. If the configuration was accepted the new hydrodynamic and Brownian forces were calculated and the velocity was corrected. The process was then repeated for another time step. The main points of the algorithm described here are summarised in flow chart 4.3.

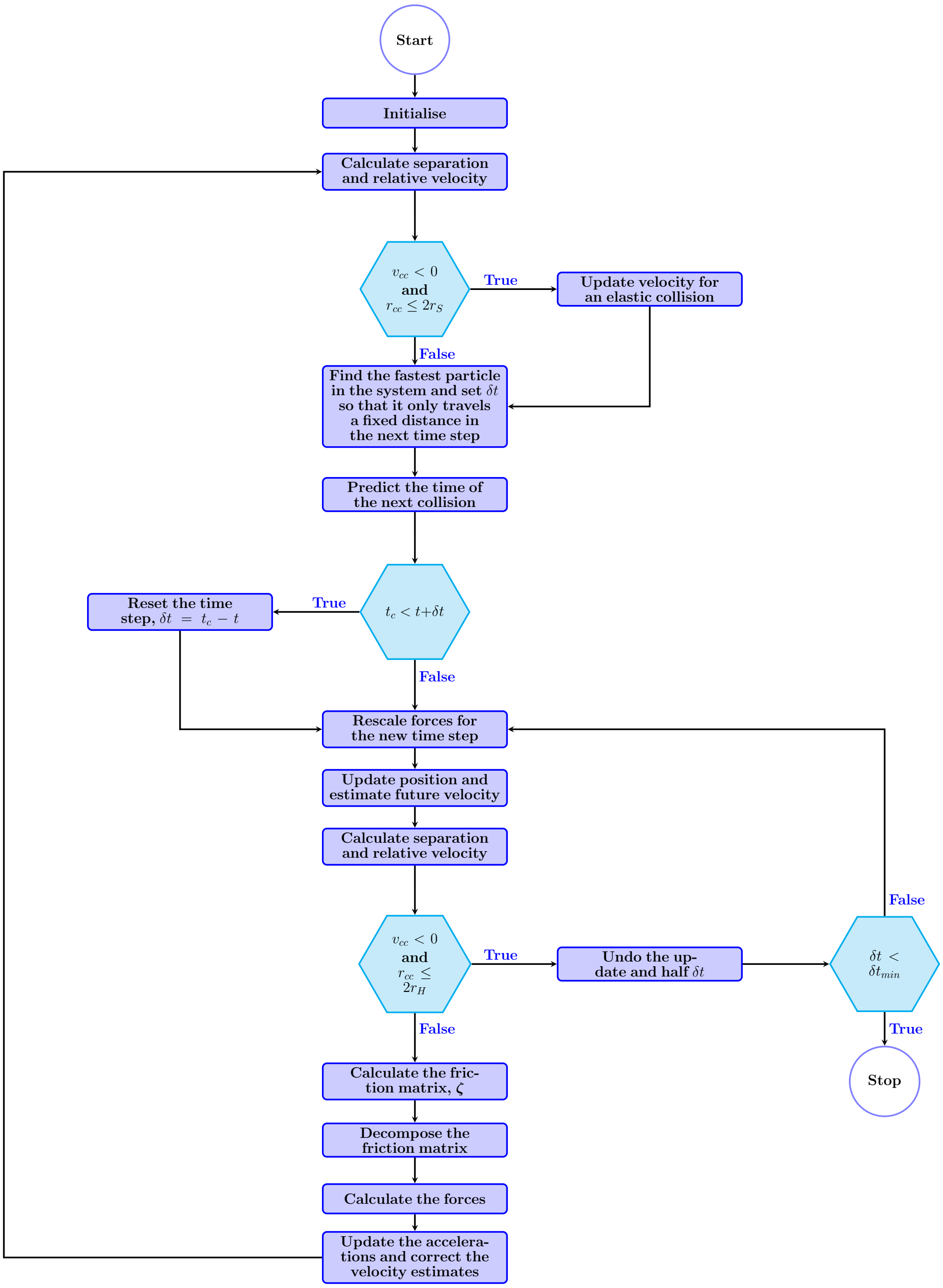

Flow Chart 4.3: Flow chart showing the main steps in the algorithm used in the simulation of Brownian particles with hydrodynamic interactions.

4.3.9 Optimisation

Due to the sizes of the matrices involved in the multipole calculation of the hydrodynamic forces, optimisation of any other part of the code made almost no difference to the overall runtime, as well over 99.9%(50) of the run time was spent in the HYDROLIB routines used to calculate the friction matrix for any system with more than a few particles. Hence this was the focus of optimisation efforts.

HYDROLIB relies on the BLAS and LAPACK libraries for performing all of the necessary matrix operations so a significant speed up was obtained simply by swapping the standard versions of the routines from these libraries, which were supplied with HYDROLIB, for the optimised versions provided in the OpenBLAS[169] library(51). As well as being noticeably faster when run in series these also had the capability to perform the calculations in parallel. Unfortunately, because of the many body nature of the problem, these calculations did not lend themselves particularly well to parallel computation and care needed to be taken to choose the optimum number of threads so as to obtain minimum run time for the simulation, by finding a compromise between having as many cores as possible working on the problem whilst minimising the overhead involved in communication between the cores and the time the cores spent waiting to access memory. To this end several test simulations were run to try to establish how long the calculation of the friction matrix took as a function of the number of particles and the number of cores working on the problem. The results of this testing, at the three of the levels of accuracy offered by HYDROLIB, are shown in figure 4.16.

---

(50) This value was obtained by using the GNU profiling tool, gprof.

(51) Because of the many body nature of the hydrodynamic interactions the matrices involved were far too dense for a sparse matrix solver, like that used in the simulation of the particle-laden fluid described in section 4.1, to be an option.

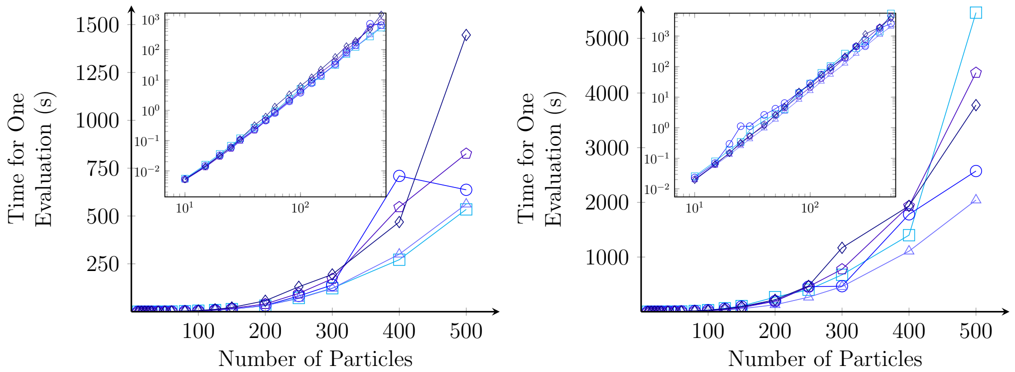

(a) Multipole expansion truncated after second order.

(b) Multipole expansion truncated after third order.

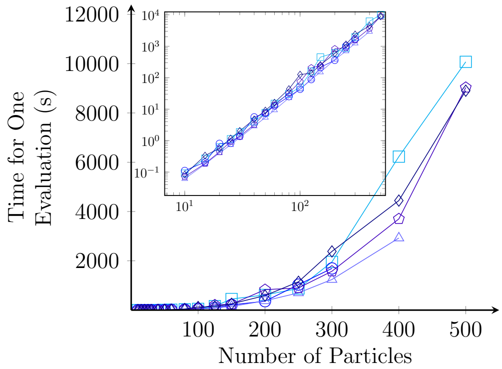

(c) Multipole expansion truncated after fourth order.

Figure 4.16: Plots showing the average time taken to evaluate the friction matrix once as a function of the number of particles and the number of cores used. The cyan squares (□) mark the data for one core, blue circles (○) two cores, light purple triangles (△) three cores, dark purple pentagons (⬠) four cores and dark blue diamonds (◇) eight cores. The inserts show the same data on a logarithmic scale.

It is clear from comparison of the plots in figure 4.16 that the dependence of the time taken to evaluate the friction matrix on the number of cores used is very complicated, as the data suggests that when the total problem size(52) is small using more cores actually reduces the speed at which HYDROLIB is able to evaluate the friction matrix. However, as the problem becomes larger, either by increasing the number of particles or the order of the multipole expansion, one begins to see a definite benefit from the extra cores. However, from this data it would appear that increasing the number of cores has no significant effect on how the problem scales and can even reduce the simulation speed, due to the additional overhead incurred. For reasonably sized systems, of a few hundred particles with the multipole expansion truncated after third order terms, it would appear that sharing the load between three cores does provide a noticeable increase in speed compared with one core.

Since HYDROLIB itself was not written to be run in parallel it was thought that parallelisation of some of the longest loops would reduce the amount of time cores hung, waiting for the master thread to execute the loops, and potentially increase the speed or make it efficient to use more cores. This was achieved by collapsing loops which contained many iterations using OpenMP. The results of timing the evaluation of the friction matrix are shown in figure 4.17 as a function of the number of particles in the system and the number of cores used. The results presented in figure 4.17 are for a system where the multipole expansion was truncated after third order, as this was the level of accuracy used in practice, but the qualitative results were the same at all orders.

---

(52) Here the problem size refers to the total size of the matrix used in the multipole expansion, which depends on the number of particles and the order of the multipole expansion itself.

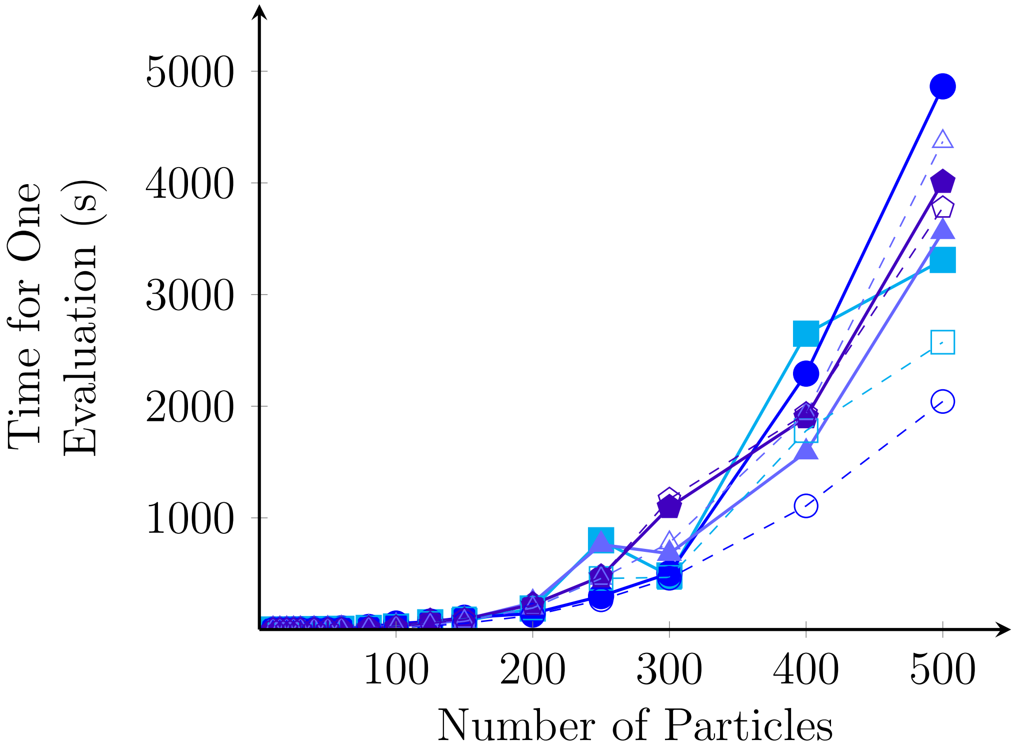

Figure 4.17: Plots showing the time taken to evaluate the friction matrix with and without parallelisation of the HYDROLIB routines. The solid symbols (—■—, —●—, —▲—, —⬟—) mark data with additional parallelisation, while the open symbols (-□-, -○-, -△-, -⬠-) make data with just the BLAS and LAPACK routines parellelised. The cyan squares (—■—, -□-), blue circles (—●—, -○-), light purple triangles (—▲—, -△-) and dark purple pentagons (—⬟—, -⬠-) correspond to: two, three, four and eight cores respectively.

As figure 4.17 shows this did prove slightly more efficient when four cores were used, but was significantly slower when fewer cores were used and slightly slower when more than four cores were used, probably due to the increased overhead. This suggests that for a larger system size, where more cores offered the fastest run time, this would have offered a slight saving. However, for the system sizes of interest here, it did not change the fact that using three cores, with only the BLAS and LAPACK routines parallelised, still appeared to offer the fastest evaluation time. Hence in practice the serial version of HYDROLIB was used alongside the parallel versions of BLAS and LAPACK, as this offered the fastest evaluation of the friction matrix overall.

Finally figure 4.18 demonstrates how the time taken to evaluate the friction matrix scales with the order at which the multipole expansion is truncated.

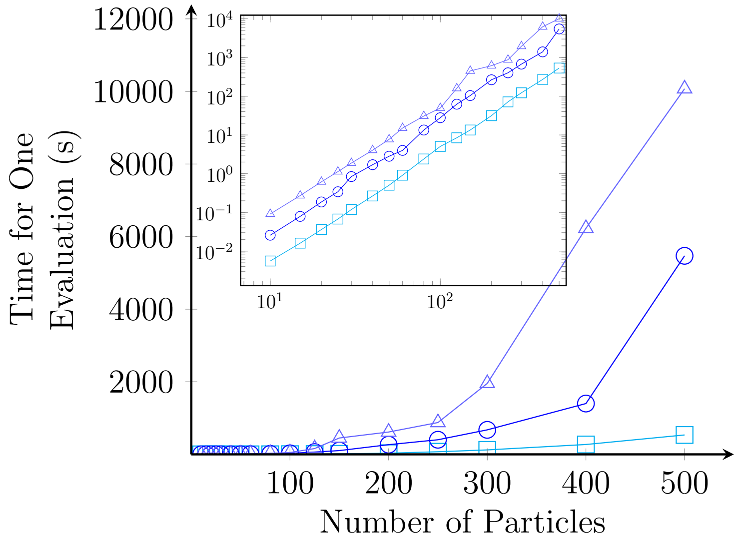

Figure 4.18: Plot showing the effect of changing the order of the multipole expansion on the time taken to evaluate the friction matrix, using one core. The cyan squares (—□—) correspond to truncating the expansion after second order, the blue circles (—○—) third order and the light purple trinagles (—△—) fourth order.

Here it is clear that while all of the different levels of accuracy have the same scaling with the number of particles, as one would expect since they change the size of the matrix by a constant, multiplicative, factor, there is a significant increase in the time taken to evaluate the friction matrix when the accuracy is increased. According to the HYDROLIB documentation the friction matrix calculated with the multipole expansion truncated after third order is accurate to within 1% hence it was decided that this would be the best compromise between speed and accuracy as it was thought that the higher resolution offered by including another term was not worth the additional computational cost, while it was also thought the higher uncertainty, of between 1% and 5%, offered by truncating after second order was too high, especially when large numbers of particles were to be used.

4.3.10 Obtaining Amorphous States at High Volume Fraction

At low volume fraction amorphous initial states were generated simply by placing the centres of the spheres at random locations in the system and then checking for overlaps and repositioning those that caused a problem. However, when higher volume fractions were required this method failed to find a suitable configuration in a reasonable amount of time. For this reason the more sophisticated method proposed by Evans[3] was employed. This method effectively began with point like particles and gradually increased their radii until the desired size was reached. This was combined with a Monte-Carlo style update scheme[3] for the particle positions, $\mathbf{r}$, which attempted to move one, randomly chosen, particle at a time. In order to decide whether or not the move allowed for the optimum growth[3] of the particles a simple, long range, repulsive interaction of the form[3]

$$U_{ij} = \frac{2r_0}{|\mathbf{r}_i - \mathbf{r}_j| - 2r_0}, \tag{4.56}$$

was used, where r_0 is the current particle radius. The moves were then accepted or rejected using the Metropolis algorithm, where moves that reduced the energy of the whole system were automatically accepted, but moves that increase the energy were accepted at a rate proportional to the exponential of the energy change relative to the thermal energy[3]. The move was accepted if and only if a uniform random number, $0 \leq \mathcal{R} \leq 1$, fulfilled the criterion[3]

$$\mathcal{R} < e^{-\beta(E-E_0)}, \tag{4.57}$$

where[3]

$$E = \sum_{i=1}^{N} \sum_{\substack{j=1 \\ j \neq i}}^{N} U_{ij}, \tag{4.58}$$

E_0 is the total energy of the previous configuration and β is the thermal energy.

After a certain number of moves the radius of all of the particles was increased to the average of the former radius and the minimum centre to centre distance in the system. If this value was greater than or equal to the target radius then the algorithm stopped with the current configuration[3]. In order to achieve optimum performance the thermal energy and the distance each particle was allowed to move were tuned at regular intervals to ensure a reasonable number of moves were being accepted, with smaller moves being taken as random close packing was approached.

4.4 Constitutive Relation for Interacting Colloidal Dispersions

4.4.1 Formulation in Two Dimensional Cartesian Coordinates

In order to examine the flow behaviour predicted by the constitutive model derived in section 3.4 one must consider a specific flow geometry. In principle this choice is arbitrary, but for the purposes of the present work two dimensional Cartesian coordinates were used. The main reason for this choice here is that it means that the results are directly compatible with the model of the particle-laden fluid as this is also formulated in two dimensional Cartesian coordinates. An additional advantage of restricting oneself to two dimensions is that it reduces the number of free parameters and equations and means that no further constrains, other than incompressibility and the symmetries already present in the system, needed to be added to describe the deformation.

In a two dimensional Cartesian reference frame the stress tensor, $\mathbf{\Sigma}$ and deformation gradient tensor, $\mathbf{F}$, can be written as

$$\mathbf{\Sigma} = \begin{pmatrix} \Sigma_{xx} & \Sigma_{xy} \\ \Sigma_{yx} & \Sigma_{yy} \end{pmatrix} \tag{4.59a}$$

$$\mathbf{F} = \begin{pmatrix} F_{xx} & F_{xy} \\ F_{yx} & F_{yy} \end{pmatrix} \tag{4.59b}$$

respectively. However since the stress tensor must be symmetric, $\Sigma_{xy} = \Sigma_{yx}$. Since the flow is incompressible and the isotropic pressure was subtracted in equation 3.95, the stress tensor must have the property $\Sigma_{yy} = -\Sigma_{xx}$ and the determinant of the deformation gradient tensor must be unity, $F_{yy} = \frac{1+F_{xy}^2}{F_{xx}}$. This, in addition to the symmetries within the two particle distribution function, reduces the original model to one in which there are only two free parameters. In the case of the stress tensor one, $\Sigma_{aa} = 2\frac{V_p^2}{\phi^2}\Sigma_{xx} = -2\frac{V_p^2}{\phi^2}\Sigma_{yy}$, describes the normal forces and the other, $\Sigma_{ab} = 2\frac{V_p^2}{\phi^2}\Sigma_{xy} = 2\frac{V_p^2}{\phi^2}\Sigma_{yx}$, describes the shear forces[53]. For the stress tensor these symmetries were also apparent in equations 3.98 and 3.102 once the unit vectors are entered.

Although one wishes to evaluate the stress in the Cartesian reference frame it still makes sense to perform the integrals of equations 3.98 and 3.102 in polar coordinate as these provide a more convenient form given the symmetries of the two particle distribution function, g, and the interaction potential, U. Thus the Cartesian unit vectors, needed to discriminate between the different components of the stress tensor, must be written in their polar form, $\hat{\mathbf{r}}_x = \cos\{\theta\}$ and $\hat{\mathbf{r}}_y = \sin\{\theta\}$. Thus the equations for the two independent components of the stress become

$$\Sigma_{aa} = \int_0^{2\pi} \cos\{2\theta\} \int_0^{\infty} g r^2 \frac{\partial U}{\partial r} dr d\theta, \tag{4.60a}$$

$$\Sigma_{ab} = \int_0^{2\pi} \sin\{2\theta\} \int_0^{\infty} g r^2 \frac{\partial U}{\partial r} dr d\theta. \tag{4.60b}$$

And similarly for the rate of change of these two components

$$\begin{aligned}\dot{\Sigma}_{aa} =& \frac{1}{2}\mathcal{D}\int_0^{2\pi} \cos\{2\theta\} \int_0^{\infty} g\left(5r\frac{\partial^2 U}{\partial r^2} + r^2\frac{\partial^3 U}{\partial r^3}\right) dr d\theta \\ &- \frac{1}{2}\mathcal{M}\int_0^{2\pi} \cos\{2\theta\} \int_0^{\infty} g\frac{\partial U}{\partial r}\left(2r\frac{\partial U}{\partial r} + r^2\frac{\partial^2 U}{\partial r^2}\right) dr d\theta \\ &+ \frac{1}{2}\int_0^{2\pi} \left(\hat{\mathbf{r}}\cdot\mathbf{K}\cdot\hat{\mathbf{r}}\right)\cos\{2\theta\} \int_0^{\infty} g\left(2r^2\frac{\partial U}{\partial r} + r^3\frac{\partial^2 U}{\partial r^2}\right) dr d\theta \\ &- \int_0^{2\pi} \left(\hat{\mathbf{r}}\cdot\mathbf{K}\cdot\hat{\boldsymbol{\theta}}\right)\sin\{2\theta\} \int_0^{\infty} g\left(r^2\frac{\partial U}{\partial r}\right) dr d\theta\end{aligned} \tag{4.61a}$$

$$\begin{aligned}\dot{\Sigma}_{ab} =& \frac{1}{2}\mathcal{D}\int_0^{2\pi} \sin\{2\theta\} \int_0^{\infty} g\left(5r\frac{\partial^2 U}{\partial r^2} + r^2\frac{\partial^3 U}{\partial r^3}\right) dr d\theta \\ &- \frac{1}{2}\mathcal{M}\int_0^{2\pi} \sin\{2\theta\} \int_0^{\infty} g\frac{\partial U}{\partial r}\left(2r\frac{\partial U}{\partial r} + r^2\frac{\partial^2 U}{\partial r^2}\right) dr d\theta \\ &+ \frac{1}{2}\int_0^{2\pi} \left(\hat{\mathbf{r}}\cdot\mathbf{K}\cdot\hat{\mathbf{r}}\right)\sin\{2\theta\} \int_0^{\infty} g\left(2r^2\frac{\partial U}{\partial r} + r^3\frac{\partial^2 U}{\partial r^2}\right) dr d\theta \\ &+ \int_0^{2\pi} \left(\hat{\mathbf{r}}\cdot\mathbf{K}\cdot\hat{\boldsymbol{\theta}}\right)\cos\{2\theta\} \int_0^{\infty} g\left(r^2\frac{\partial U}{\partial r}\right) dr d\theta.\end{aligned} \tag{4.61b}$$

If, like $\boldsymbol{\Sigma}$, $\mathbf{K}$ is represented in Cartesian coordinates it must be translated into polar coordinates within the integrals. This is done by applying the transformation

$$\mathbf{K}_p = \mathbf{M}\cdot\mathbf{K}_c\cdot\mathbf{M}^T, \tag{4.62}$$

where $\mathbf{M}$ performs a rotation of the basis vectors such that the Cartesian unit vectors upon which $\mathbf{K}$ was originally defined align with the polar unit vectors which are used to

---

(53) Here the pre-factor, $2\frac{V_p^2}{\phi^2}$, is added to the definition for notational convenience, to cancel out the pre-factor, $\frac{1}{2}\frac{\phi^2}{V_p^2}$ in the definition of $\mathbf{N}$ in equation 3.97.

extract the relevant components of **K** in the polar integrals$^{(54)}$.

$$\mathbf{M} = \begin{pmatrix} \cos\{\theta\} & -\sin\{\theta\} \\ \sin\{\theta\} & \cos\{\theta\} \end{pmatrix}, \tag{4.63}$$

which results in

$$\mathbf{K} = \begin{pmatrix} K_{xx}\mathrm{c}^2 + K_{yy}\mathrm{s}^2 - (K_{xy} + K_{yx})\,\mathrm{sc} & K_{xy}\mathrm{c}^2 - K_{yx}\mathrm{s}^2 + (K_{xx} - K_{yy})\,\mathrm{sc} \\ K_{yx}\mathrm{c}^2 - K_{xy}\mathrm{s}^2 + (K_{xx} - K_{yy})\,\mathrm{sc} & K_{yy}\mathrm{c}^2 + K_{xx}\mathrm{s}^2 + (K_{xy} + K_{yx})\,\mathrm{sc} \end{pmatrix}, \tag{4.64}$$

where $\mathrm{s} = \sin\{\theta\}$ and $\mathrm{c} = \cos\{\theta\}$. Although the constraints upon the flow field, discussed in section 3.4.4, will be imposed in this model it is more convenient to treat these at the end and keep **K** general for this stage of the derivation.

In order to make progress with evaluating the necessary integrals in equation sets 4.60 and 4.61 one needs to think about the geometric meaning of the deformation gradient tensor, **F**. This, along with the constraints already discussed and the fact that the deformation shall be considered affine, leads to a more convenient representation of the remaining free parameters of the deformation. Firstly consider a single equiprobability contour of g, as shown in figure 4.19a.

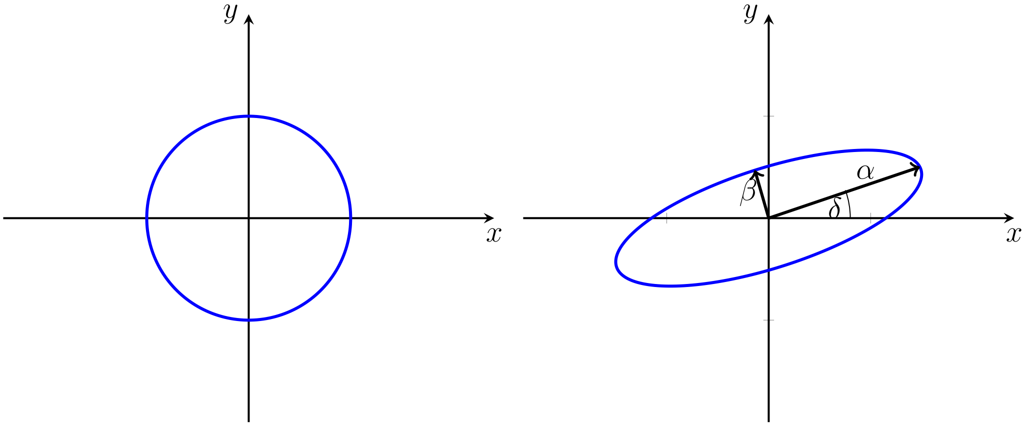

(a) Equilibrium two particle distribution function.

(b) Two particle distribution following volume conserving deformation. Here α and β are the lengths of the semi-major and semi-minor axes of the ellipse respectively and δ is the angle of rotation.

Figure 4.19: Sketches of an equiprobability contour of the two particle distribution function before deformation, in (a), and after a deformation, in (b).

If the system is deformed, by a volume conserving deformation, then the circular contour becomes an ellipse with the same area, as shown in figure 4.19b. This may also be rotated, through an angle θ, by the deformation. However, the symmetry of the deformed contour is guaranteed by the definition of the two particle distribution function itself. Hence a rotated ellipse is the most general form possible. Furthermore since the deformation is affine then all such contours are deformed in exactly the same way so all of the information

---

(54) This is not the same as performing a coordinate transformation on **K**; one does not wish to obtain the polar velocity gradient tensor which describes the same flow field, this would be far more difficult as the gradient operator is different in the two coordinate systems. One only wishes to establish the velocity gradient in the direction of the polar unit vectors for a given value of θ. Since these are merely a rotated version of the Cartesian unit vectors then it follows that rotating the flow field has an equivalent effect.

about the deformation is contained in the equation of the ellipse for one contour. This means that any allowed deformation can be summarised in terms of just two parameters: $\kappa = \frac{\alpha^2}{\beta^2}$ which is the square of the ratio of the length of the semi-major axis, α, to that of the semi-minor axis, β, and the angle, δ, between the semi-major axis and the x axis of the coordinate system⁽⁵⁵⁾. In polar coordinates the equation of the deformed contour may be written as

$$r = \sqrt{\frac{\kappa}{1 + (\kappa^2 - 1)\sin^2\{\theta - \delta\}}}. \tag{4.65}$$

Since g is the only function in equation sets 4.60 and 4.61 that is affected by the deformation then the argument of g must be multiplied by the right hand side of equation 4.65 while the other functions remain unchanged. However, if the interaction potential can be written as a sum of power laws, as previously discussed in section 3.4.3, then g is the only function in any of the integrands that is a function of θ and is not just a simple power law in r and yet it is the most complicated function. Thus it makes sense to make the coordinate transformation $r \to f\{\theta\} r$, where

$$f \equiv \sqrt{\frac{1 + (\kappa^2 - 1)\sin^2\{\theta - \delta\}}{\kappa}}. \tag{4.66}$$

Once this coordinate transformation has been performed then the deformed two particle distribution function can be replaced with its equilibrium form, g_e⁽⁵⁶⁾. Moreover the two integrals over the two coordinates can now be separated to give the product of two independent integrals over just one coordinate; the integral over r being constant for all deformations. After some rearrangement the entire problem reduces to solving integrals of the form

$$\mathcal{I}_{a,b} \equiv \int_0^{2\pi} \cos^{2a}\{\theta\} f^{-b-2} d\theta \int_0^{\infty} g_e r^{b+1} dr, \tag{4.67a}$$

$$\mathcal{I}'_{a,b} \equiv \int_0^{2\pi} \sin\{\theta\} \cos^{2a+1}\{\theta\} f^{-b-2} d\theta \int_0^{\infty} g_e r^{b+1} dr, \tag{4.67b}$$

where a and b are integer constants which are determined by the precise integral in question. Once the constants have been entered it is possible to solve the integrals analytically using reduction formulas. A proof of this is given in appendix B.2.

Finally, using the above definitions, if one restricts the flow field to be that of an incompressible fluid and asserts that there are no stresses produced due to rotational flow, as discussed in section 3.4.4.1 and section 3.4.4.2 respectively. Then the remaining,

---

(55) These definitions are used here because they fit more naturally into the polar coordinate system used in the rest of the calculation, and as such portray more clearly what form the two particle distribution function takes. However, the definition κ is rather awkward when it comes to numerical calculations since it can become very large, thus for the purposes of the numerical calculations the slightly different definitions, $\kappa' \equiv \frac{1}{\kappa}$ and $\delta' \equiv \frac{\pi}{2} - \delta$, were used such that $0 < \kappa' \leq 1$. This is equivalent to rotating the stress tensor by $\frac{\pi}{2}$ or arguing that value calculated for Σ_{aa} corresponds to the Σ_{yy} component of the stress tensor rather than the Σ_{xx} component. Of course this makes no difference to the final results, but simply required careful treatment of the solutions found.

(56) This follows on naturally, without further approximation, from the assumption that the deformation is affine. Since this already implies that the deformation affects the system in a identical way at all length scales, hence there must be a single coordinate transformation mapping g_e to g at any time. In this case this is exactly the transformation given in equation 4.65.

two, independent flow field parameters can be written in terms of an elongation rate, $\dot{\epsilon} = K_{xx} - K_{yy}$, and a shear rate, $\dot{\gamma} = K_{xy} + K_{yx}$. This results in the following equations for the normal and shear stresses and their respective rates of change.

$$\Sigma_{aa} = \frac{1}{2}\sum_{i=1}^{O} U_i p_i \left[2\mathcal{I}_{1,p_i} - \mathcal{I}_{0,p_i}\right], \tag{4.68a}$$

$$\Sigma_{ab} = \sum_{i=1}^{O} U_i p_i \mathcal{I}'_{0,p_i}, \tag{4.68b}$$

where U_i and p_i defined in equation 3.105,

$$\begin{aligned}\dot{\Sigma}_{aa}=&\frac{1}{2}\mathcal{D}\sum_{i=1}^{O}U_i p_i(p_i-1)(p_i+3)[2\mathcal{I}_{1,p_i-2}-\mathcal{I}_{0,p_i-2}]\\&-\frac{1}{2}\mathcal{M}\sum_{i=1}^{O}\sum_{j=1}^{O}U_iU_jp_ip_j(p_i+1)\left[2\mathcal{I}_{1,p_i+p_j-2}-\mathcal{I}_{0,p_i+p_j-2}\right]\\&+\frac{1}{4}\dot{\epsilon}\sum_{i=1}^{O}U_ip_i[4(p_i+3)(\mathcal{I}_{2,p_i}-\mathcal{I}_{1,p_i})+(p_i+1)\mathcal{I}_{0,p_i}]+\frac{1}{2}\dot{\gamma}\sum_{i=1}^{O}U_ip_i(p_i+3)\left[2\mathcal{I}'_{1,p_i}-\mathcal{I}'_{0,p_i}\right],\end{aligned} \tag{4.69a}$$

$$\begin{aligned}\dot{\Sigma}_{ab} =&\mathcal{D}\sum_{i=1}^{O}U_ip_i\left(p_i-1\right)\left(p_i+3\right)\mathcal{I}'_{0,p_i-2}-\mathcal{M}\sum_{i=1}^{O}\sum_{j=1}^{O}U_iU_jp_ip_j\left(p_i+1\right)\mathcal{I}'_{0,p_i+p_j-2}\\&+\frac{1}{2}\dot{\epsilon}\sum_{i=1}^{O}U_ip_i\left(p_i+3\right)\left[2\mathcal{I}'_{1,p_i}-\mathcal{I}'_{0,p_i}\right]+\frac{1}{2}\dot{\gamma}\sum_{i=1}^{O}U_ip_i\left[2\left(p_i+3\right)\left(\mathcal{I}_{2,p_i}-\mathcal{I}_{1,p_i}\right)-\mathcal{I}_{0,p_i}\right],\end{aligned} \tag{4.69b}$$

where O is the number of terms in the equation for the interaction potential.

Once the integrals within equation sets 4.68 and 4.69 have been evaluated, for a particular interaction potential, one is left with equations for the stress and its rate of change in terms of the parameters describing the deformation, κ and δ. These were used to investigate both the dynamics of the flow and the steady state stress-strain relationship.

4.4.1.1 Exact Steady State Solutions

With equation sets 4.68 and 4.69 evaluated obtaining steady state solutions in parametric form was relatively straightforward. This is simply a matter of setting $\dot{\Sigma}_{aa} = \dot{\Sigma}_{ab} = 0$ and solving equations 4.69a and 4.69b for $\dot{\epsilon}$ and $\dot{\gamma}$ in terms of the parameters describing the deformation.

However, since one wishes to investigate the response to a predefined flow geometry it is often more convenient to specify a relationship between $\dot{\epsilon}$ and $\dot{\gamma}$ and use either equation 4.69a or equation 4.69b to reduce the number of free parameters describing the deformation to one. Since κ describes the magnitude of the deformation this must be retained, however, it is possible to write δ as a function of κ(57).

In the case of purely extensional flow one can set $\dot{\gamma} = 0$ and use the remaining equa-

---

(57) This was done in order to obtain the stress-strain relationship predicted for simple shear flow.

tion(58) to discover $\delta = 0$. As one might expect this implies that there is no rotational motion of the fluid in extensional flow. Furthermore since a pure shearing flow is essentially a $\delta = \pm\frac{\pi}{4}$ rotation of this flow field setting $\delta = \pm\frac{\pi}{4}$ results in exactly the same solution except that the stress tensor has been rotated by $\pm\frac{\pi}{4}$. Thanks to the simplicity of this flow geometry it is possible to write the parametric form of the solution, for a general power law interaction, as

$$\Sigma_{aa} = \frac{1}{2}\sum_{i=1}^{O} U_i p_i \mathcal{I}'_{0,p_i}, \tag{4.70a}$$

$$\dot{\epsilon} = \frac{2\mathcal{M}\sum_{i=1}^{O}\sum_{j=1}^{O} U_i U_j p_i p_j \left(p_i+1\right)\mathcal{I}'_{0,p_i+p_j-2} - 2\mathcal{D}\sum_{i=1}^{O} U_i p_i \left(p_i-1\right)\left(p_i+3\right)\mathcal{I}'_{0,p_i-2}}{\sum_{i=1}^{O} U_i p_i \left[2\left(p_i+3\right)\left(\mathcal{I}_{2,p_i}-\mathcal{I}_{1,p_i}\right)-\mathcal{I}_{0,p_i}\right]}, \tag{4.70b}$$

where $\delta = \frac{\pi}{4}$(59).

4.4.1.2 Numerical Solutions for Time Dependent Equations

Although all of the integrals required to formulate the constitutive relation described in this section can be evaluated analytically for an arbitrary power law interaction potential the resulting set of equations for the stress as a function of time cannot typically be solved by analytical means. This is because they are made up of polynomial functions of κ and trigonometric functions of δ. Although the trigonometric functions are not necessarily a problem it is not always possible to solve a high order polynomial and even if the polynomials could be solved the function would be very expensive to evaluate and it is unlikely that the resulting differential equation could be solved analytically. For these reasons it was decided that a numerical solution should be sought.

The fact that the differential equation for the rate of change of the stress is a relatively straightforward function of the deformation parameter renders it suitable for integration by a simple Euler scheme

$$\Sigma_{aa}^{t+\delta t} \approx \Sigma_{aa}^{t} + \dot{\Sigma}_{aa}\left\{\kappa^t, \delta^t\right\}\delta t, \tag{4.71a}$$

$$\Sigma_{ab}^{t+\delta t} \approx \Sigma_{ab}^{t} + \dot{\Sigma}_{ab}\left\{\kappa^t, \delta^t\right\}\delta t, \tag{4.71b}$$

where the superscripts indicate the times at which the values are to be calculated. The Euler scheme was chosen here simply because the nature of the equations for $\boldsymbol{\Sigma}$ and $\dot{\boldsymbol{\Sigma}}$ means that it is relatively inexpensive computationally to evaluate the functions themselves whilst it is incredibly costly to find roots and this scheme only requires information from the previous time step and as such minimises the number of root finding steps, albeit

---

(58) Either equation 4.69a or equation 4.69b

(59) Although the obvious choice for finding the normal stress difference as a function of the extension rate is to use $\delta = 0$; the rotated versions of the equations have been used here. This is because they happen to take a slightly simpler form when the integrals are left unevaluated and so have been used here in the place of the more natural choice, since they are exactly equivalent once evaluated.

at the expense of requiring a smaller time step. Furthermore since the steady state of the system is well defined stability is not a serious issue as the system will tend towards this steady state for any reasonable parameter choice. The bulk of the workload in this algorithm is inverting the equations for the stress to discover the values of $\kappa^{t+\delta t}$ and $\delta^{t+\delta t}$ once the stress components have been found,

$$\kappa^{t+\delta t}, \delta^{t+\delta t} = \mathrm{root}\left\{\Sigma_{aa}\left\{\kappa, \delta\right\} = \Sigma_{aa}^{t+\delta t}, \Sigma_{ab}\left\{\kappa, \delta\right\} = \Sigma_{ab}^{t+\delta t}\right\}. \tag{4.72}$$

In practice this was done using Mathematica's multi-dimensional root finding algorithm with the values from the previous time step as the initial guess. This was found to be very effective for relatively small time steps, and hence complemented the Euler scheme well. Of course one of the key advantages of this method over attempting to find analytical solutions is that one does not have to make a choice about which solution to use, and the potential jumps in the solution that go along with it, since the root finding method guarantees to return the root that is closest to the previous value.

Here the integration scheme is started by specifying the values of κ^0 and δ^0 for the initial state. As such one can specify an initial state with any amount of deformation. In practice this provided a simple means of changing the flow field simply by taking the final state reached, at a given time, with one flow field and inserting it as the initial state for a simulation with another flow field. Concatenating the data then gave the impression of an instantaneous change in the flow field.

4.4.2 Non-Dimensionalisation

Thus far the model has been presented in terms of dimensional quantities, these make it easer to identify the terms with their physical origins. However, non-dimensionalising at this stage means that the results will be independent of the units belonging to the various physical constants and as such will be more general. The use of non-dimensional quantities also makes it easier to identify which process, or processes, are dominating the dynamics and has the additional advantage of reducing the number of free parameters, meaning that the behaviour of the system could be fully examined with fewer evaluations of the equations of motion. This section describes how this was done for the equations of motion in two dimensional Cartesian coordinates, as formulated in section 4.4.1, as these were the equations from which the results presented in the present work were derived, however, the same method could be applied in any reference frame and one would obtain very similar scaling.

Firstly, to aid clarity, the various quantities may be written in a form where all of the dimensional quantities are written explicitly. This means that the polynomial interaction potential of equation 3.105 becomes

$$U = U_0 k_B T \sum_{i=1}^{O} \hat{U}_i \left(\frac{r}{a}\right)^{p_i}, \tag{4.73}$$

this is equivalent to defining $U_i \equiv U_0 \hat{U}_i a^{-p_i} k_B T$. Here U_0 is the overall magnitude of the potential in units of the thermal energy, $k_B T$, at a temperature, T, and a is a length scale yet to be defined. Because $U_0 k_B T$ sets the magnitude of the interaction potential and $\hat{U}_i$

only determines the relative importance of the different powers it make sense to define $\hat{U}_i$ by demanding

$$\sum_{i=1}^{O}\left|\hat{U}_i\right| = 1. \tag{4.74}$$

This definition of U in turn means that the equilibrium two particle distribution function, given in equation 3.91, becomes

$$g_e = e^{U_0 \sum_{i=1}^{O} \hat{U}_i \left(\frac{r}{a}\right)^{p_i}}. \tag{4.75}$$

Before moving on to the equations of motion it makes sense, for notational simplicity, to make a change of variables, $\hat{r} = \frac{r}{a}$. Finally the velocity gradient tensor, $\mathbf{K}$, may be rewritten as

$$\mathbf{K} = \dot{\epsilon}\hat{\mathbf{K}}, \tag{4.76}$$

such that the magnitude of the velocity gradient is accounted for by $\dot{\epsilon}$ while $\left\|\hat{\mathbf{K}}\right\| = 1$

With all of this considered equation sets 4.60 and 4.61 become

$$\Sigma_{aa} = \frac{1}{2}k_B T U_0 a^2 \sum_{i=1}^{N} \hat{U}_i p_i \int_0^{2\pi} \cos\{2\theta\} f^{-p_i-2} d\theta \int_0^{\infty} g\hat{r}^{p_i+1} d\hat{r}, \tag{4.77a}$$

$$\Sigma_{ab} = \frac{1}{2}k_B T U_0 a^2 \sum_{i=1}^{N} \hat{U}_i p_i \int_0^{2\pi} \sin\{2\theta\} f^{-p_i-2} d\theta \int_0^{\infty} g\hat{r}^{p_i+1} d\hat{r} \tag{4.77b}$$

and

$$\begin{aligned}\dot{\Sigma}_{aa} =& \frac{1}{2}\mathcal{D}k_B T U_0 \sum_{i=1}^{N} \hat{U}_i p_i \left(p_i-1\right)\left(p_i+3\right) \int_0^{2\pi} \cos\{2\theta\} f^{-p_i} d\theta \int_0^{\infty} g_e \hat{r}^{p_i-1} d\hat{r} \\ &- \frac{1}{2}\mathcal{M}\left(k_B T\right)^2 U_0^2 \sum_{i=1}^{N}\sum_{j=1}^{N} \hat{U}_i \hat{U}_j p_i p_j \left(p_i+1\right) \int_0^{2\pi} \cos\{2\theta\} f^{-p_i-p_j} d\theta \int_0^{\infty} g_e \hat{r}^{p_i+p_j-1} d\hat{r} \\ &+ \frac{1}{2}\dot{\epsilon}k_B T U_0 a^2 \sum_{i=1}^{N} \hat{U}_i p_i \left(p_i+1\right) \int_0^{2\pi} \left(\hat{\mathbf{r}}\cdot\hat{\mathbf{K}}\cdot\hat{\mathbf{r}}\right) \cos\{2\theta\} f^{-p_i-2} d\theta \int_0^{\infty} g_e \hat{r}^{p_i+1} d\hat{r} \\ &- \dot{\epsilon}k_B T U_0 a^2 \sum_{i=1}^{N} \hat{U}_i p_i \int_0^{2\pi} \left(\hat{\mathbf{r}}\cdot\hat{\mathbf{K}}\cdot\hat{\boldsymbol{\theta}}\right) \sin\{2\theta\} f^{-p_i-2} d\theta \int_0^{\infty} g_e \hat{r}^{p_i+1} d\hat{r},\end{aligned} \tag{4.78a}$$

$$\begin{aligned}\dot{\Sigma}_{ab} =& \frac{1}{2}\mathcal{D}k_B T U_0 \sum_{i=1}^{N} \hat{U}_i p_i \left(p_i-1\right)\left(p_i+3\right) \int_0^{2\pi} \sin\{2\theta\} f^{p_i} d\theta \int_0^{\infty} g_e \hat{r}^{p_i-1} d\hat{r} \\ &- \frac{1}{2}\mathcal{M}\left(k_B T\right)^2 U_0^2 \sum_{i=1}^{N}\sum_{j=1}^{N} \hat{U}_i \hat{U}_j p_i p_j \left(p_i+1\right) \int_0^{2\pi} \sin\{2\theta\} f^{-p_i-p_j} d\theta \int_0^{\infty} g_e \hat{r}^{p_i+p_j-1} d\hat{r} \\ &+ \frac{1}{2}\dot{\epsilon}k_B T U_0 a^2 \sum_{i=1}^{N} \hat{U}_i p_i \left(p_i+1\right) \int_0^{2\pi} \left(\hat{\mathbf{r}}\cdot\hat{\mathbf{K}}\cdot\hat{\mathbf{r}}\right) \sin\{2\theta\} f^{-p_i-2} d\theta \int_0^{\infty} g_e \hat{r}^{p_i+1} d\hat{r} \\ &+ \dot{\epsilon}k_B T U_0 a^2 \sum_{i=1}^{N} \hat{U}_i p_i \int_0^{2\pi} \left(\hat{\mathbf{r}}\cdot\hat{\mathbf{K}}\cdot\hat{\boldsymbol{\theta}}\right) \cos\{2\theta\} f^{-p_i-2} d\theta \int_0^{\infty} g_e \hat{r}^{p_i+1} d\hat{r}.\end{aligned} \tag{4.78b}$$

By applying the Einstein relation,

$$\mathcal{D} = k_B T \mathcal{M}, \tag{4.79}$$

and defining the units of time, $\hat{t}$, in terms of the characteristic diffusion time

$$t = \frac{\mathcal{D}}{a^2}\hat{t}, \tag{4.80}$$

which implies

$$\frac{\partial}{\partial t} = \frac{\mathcal{D}}{a^2}\frac{\partial}{\partial \hat{t}}. \tag{4.81}$$

One notices that the pre-factor $\frac{1}{2}k_B T U_0 a^2$ appears in all four equations of equation sets 4.77 and 4.78. Thus it makes sense to define the units of stress in terms of this quantity,

$$\mathbf{\Sigma} = \frac{1}{2}k_B T U_0 a^2 \hat{\mathbf{\Sigma}}. \tag{4.82}$$

Finally since a, the only length scale in the system, is still undefined it is possible to remove one constant from equation sets 4.77 and 4.78 by defining the units of length such that a is the smallest value of r at which the magnitude of the interaction potential is equal to the thermal energy, $k_B T$, and thus $U_0 = 1$. Applying these changes reduces equation sets 4.77 and 4.78 to

$$\hat{\Sigma}_{aa} = \sum_{i=1}^{N} \hat{U}_i p_i \int_0^{2\pi} \cos\{2\theta\}\, f^{-p_i-2} d\theta \int_0^{\infty} g \hat{r}^{p_i+1} d\hat{r}, \tag{4.83a}$$

$$\hat{\Sigma}_{ab} = \sum_{i=1}^{N} \hat{U}_i p_i \int_0^{2\pi} \sin\{2\theta\}\, f^{-p_i-2} d\theta \int_0^{\infty} g \hat{r}^{p_i+1} d\hat{r} \tag{4.83b}$$

and

$$\begin{aligned}\dot{\hat{\Sigma}}_{aa} =& \sum_{i=1}^{N} \hat{U}_i p_i (p_i-1)(p_i+3) \int_0^{2\pi} \cos\{2\theta\} f^{-p_i} d\theta \int_0^{\infty} g_e \hat{r}^{p_i-1} d\hat{r} \\ & - \sum_{i=1}^{N}\sum_{j=1}^{N} \hat{U}_i \hat{U}_j p_i p_j (p_i+1) \int_0^{2\pi} \cos\{2\theta\} f^{-p_i-p_j} d\theta \int_0^{\infty} g_e \hat{r}^{p_i+p_j-1} d\hat{r} \\ & + \dot{\epsilon} \sum_{i=1}^{N} \hat{U}_i p_i \int_0^{2\pi} \left[(p_i+1)\left(\hat{\mathbf{r}}\cdot\hat{\mathbf{K}}\cdot\hat{\mathbf{r}}\right)\cos\{2\theta\} - 2\left(\hat{\mathbf{r}}\cdot\hat{\mathbf{K}}\cdot\hat{\boldsymbol{\theta}}\right)\sin\{2\theta\}\right] f^{-p_i-2} d\theta \int_0^{\infty} g_e \hat{r}^{p_i+1} d\hat{r},\end{aligned} \tag{4.84a}$$

$$\begin{aligned}\dot{\hat{\Sigma}}_{ab} =& \sum_{i=1}^{N} \hat{U}_i p_i (p_i-1)(p_i+3) \int_0^{2\pi} \sin\{2\theta\} f^{p_i} d\theta \int_0^{\infty} g_e \hat{r}^{p_i-1} d\hat{r} \\ & - \sum_{i=1}^{N}\sum_{j=1}^{N} \hat{U}_i \hat{U}_j p_i p_j (p_i+1) \int_0^{2\pi} \sin\{2\theta\} f^{-p_i-p_j} d\theta \int_0^{\infty} g_e \hat{r}^{p_i+p_j-1} d\hat{r} \\ & + \dot{\epsilon} \sum_{i=1}^{N} \hat{U}_i p_i \int_0^{2\pi} \left[(p_i+1)\left(\hat{\mathbf{r}}\cdot\hat{\mathbf{K}}\cdot\hat{\mathbf{r}}\right)\sin\{2\theta\} + 2\left(\hat{\mathbf{r}}\cdot\hat{\mathbf{K}}\cdot\hat{\boldsymbol{\theta}}\right)\cos\{2\theta\}\right] f^{-p_i-2} d\theta \int_0^{\infty} g_e \hat{r}^{p_i+1} d\hat{r}\end{aligned} \tag{4.84b}$$

respectively.

Physically, in these units, one can identify the non-dimensional quantity $\dot{\epsilon}$ as the Péclet number which defines the ratio of the strain rate to the diffusion time. Aside from the geometry of the flow field this is now the only free parameter in the system. As such this provides a useful means for one to access the stress-strain relationship for a given interaction potential in a way that is independent of the units of measurement.

4.4.3 Low Strain Approximation With Potentials of Mean Force

Unlike the full constitutive relation, described in section 3.4, which relies on the interaction potential between the particles being a relatively short power series, the low strain approximation, of section 3.4.5 admits a potential which can be any function of the particle separation, r. In particular this allows for the use of a potential of mean force, U_{mf}, generated from the equilibrium two particle distribution function, g_e, for a more realistic particle configuration simply by inverting equation 3.91 to give

$$U_{mf} = -\beta \ln \{g_e\}, \tag{4.85}$$

where β is the reciprocal of the thermal energy. Extracting the stress evolution in the low strain limit was then simply a matter of numerically evaluating the constant matrices, **A**, **B**, **C** and **D**, given in equation set 3.117 and solving equation 3.116 for the given geometry. In order to make the numerical calculation more robust and flexible data points were taken from the full form of the two particle distribution function and fitted with an interpolating function which was used in place of the two particle distribution function itself when numerically evaluating the integrals in equation set 3.117, as this was much faster to evaluate and the fact that the function was smooth and continuous allowed for the integration points to be taken anywhere within the bounds. In practice the most important part of the calculation was generating a suitable equilibrium two particle distribution function to work from.

4.4.3.1 The Percus-Yevick Approximation

For hard spheres, in three dimensions, one, relatively popular, closure condition for the Ornstein-Zernike equation[166] is the Percus-Yevick approximation[166], which results in a closed set of equations for the two particle distribution function, g_e[166],

$$g_e\{r\} = \sum_{i=1}^{\infty} \mathrm{H}\left\{\tfrac{1}{2}r - i\right\} g_i\{r\} \tag{4.86a}$$

$$g_i\{r\} = \frac{2(-12\phi)^{i-1}}{r(i-1)!} \sum_{j=0}^{2} \lim_{t\to t_j} \left(\frac{\partial^{i-1}}{\partial t^{i-1}}\left[(t-t_j)^i\, t \left(\frac{L\{t\}}{S\{t\}}\right)^i e^{t\left(\frac{1}{2}r-i\right)}\right]\right) \tag{4.86b}$$

$$S\{t\} = (1-\phi)^2 t^3 + 6\phi(1-\phi)t^2 + 18\phi^2 t - 12\phi(1+2\phi) \tag{4.86c}$$

$$L\{t\} = \left(1+\tfrac{1}{2}\phi\right)t + 1 + 2\phi, \tag{4.86d}$$

where, ϕ is the volume fraction, r is the particle separation, t_j is the j^{th} root of the three roots of the function $S\{t\}$ and $\mathrm{H}\{x\}$ is the Heaviside step function. While in theory the summation in equation 4.86a runs over an infinite number of terms a good approximation was obtained by truncating the series after between four and eight terms. In practice, in order to avoid unphysical singularities in the two particle distribution function due to the fact that the series was truncated, the function was cutoff above a certain value of r, typically $r = 10$, and a constant value of unity used, as the two particle distribution function is known to approach this value at large separations.

Of course because this theory relates to spheres in three dimensional space one must be very careful when combining it with the two dimensional theory presented here. There is, however, one particular geometry where this radial distribution function can be uses correctly in the two dimensional coordinate system for which the calculations in section 4.4.1 are valid. Fortunately this is also the relevant coordinate system for the model of the particle-laden fluid, described in section 3.1. In this case, to combine the radial distribution function calculated from the Percus-Yevick approximation with a two dimensional coordinate system successfully, one requires that there are no deformations in one of the directions such that the model may be solved in three dimensions using a purely two dimensional flow field and deformation gradient tensor, thus eliminating the need for any further constraints that would be required to model the flow in the third dimension. A suitable flow might be generated in a Hele-Shaw cell[73], where the third dimension is very thin compared with the other two and the flow in this direction is neglected, as in the draining particle-laden fluid described in section 3.1.

4.4.3.2 Numerically Generated Two Particle Distribution Functions

While the Percus-Yevick approximation is a commonly used method of generating the two particle distribution function for hard spheres in three dimensional space[166] much of the work on this constitutive relation has been done on two dimensional systems and unfortunately there is no two dimensional analogue of equation set 4.86. However, since the low strain rate model only requires data points from the two particle distribution function it was possible to generate it numerically using a slightly modified(60) version of the sphere packing algorithm described in section 4.3.10[3]. The two particle distribution function was then calculated by measuring, and then binning, the centre to centre distances between the particles, within a system of periodic boundaries to simulate the bulk(61). Of course the two particle distribution function created by this method was only valid up to the length of the shortest edge of the simulation cell and so, in a similar way to the result of the Percus-Yevick approximation this function was cutoff at this length and a constant value of unity was used for all larger separations.

4.4.4 Numerical Simulations

In addition to calculating the evolution of the stress analytically, the equations of motion, given in equation 3.74a, were also time stepped numerically using a simple Euler method. This was done simply by rearranging equation 3.74a to obtain the positions of particle i at a time δt in the future using the state of the system at the current time. This can be

---

(60) The modifications were simply a matter of fixing the z coordinates of all of the spheres so as to make the simulation cell effectively two dimensional.

(61) The centre to centre distances were measured as the distance between particle i and the closest image of particle j.

expressed mathematically as

$$\mathbf{r}_i^{t+\delta t} \approx \mathbf{r}_i^t + \frac{1}{\zeta_{sp}} \left[\zeta_{sp} \mathbf{u} \left\{ \mathbf{r}_i^t \right\} \delta t + \sum_{j=1}^{N} \boldsymbol{\nabla} U \left\{ \left| \mathbf{r}_j^t - \mathbf{r}_i^t \right| \right\} \delta t + \nu d\mathbf{W}_i \right], \tag{4.87}$$

where $\mathbf{r}_i$ refers to the position of particle i, U is the interaction potential, ζ_{sp} is the drag coefficient between the particles and the solvent, $\mathbf{u}\{\mathbf{r}\}$ is the velocity of the solvent at position $\mathbf{r}$, $d\mathbf{W}$ is a Wiener process, to simulate Gaussian noise, and ν is the amplitude of the Brownian forces. Here the subscripts refer to the different particles while the superscripts refer to the times at which the various quantities are evaluated.

The Euler method was chosen here because it lent itself well to a simple rearrangement of the equations of motion, which meant that each iteration could be performed at relatively little computational cost, outweighing the fact that a smaller time step would be required to obtain reasonable stability. Because this method only required information about the past state of the system it lent itself well to simulations involving very large numbers of particles since the equations were not coupled together in any way(62).

While equation 4.87 provides information about the evolution of the particle positions in time it is the evolution of the stress that is of most interest here. Thus it was necessary to convert the known positions and interaction potential into values for the components of the stress tensor, $\boldsymbol{\tau}$ at each time. This was done using equation 4.88[165],

$$\boldsymbol{\tau} = \frac{1}{V} \sum_{i=1}^{N-1} \sum_{j=i+1}^{N} \left(\mathbf{r}_i - \mathbf{r}_j \right) \boldsymbol{\nabla} U \left\{ \left| \mathbf{r}_j - \mathbf{r}_i \right| \right\}, \tag{4.88}$$

where N is the number of particles and the inner summation only runs from i to N to avoid double counting the interactions, and hence save time. At first sight one might expect to see a momentum term in equation 4.88, but this is not the case here since the particles have already been assumed to be massless in the derivation of equation set 3.74, and therefore have no momentum. Since the definition of zero pressure was arbitrary, as it generally is in incompressible Stokes' flow, it was decided that half of the trace of the stress tensor should be subtracted to leave the pressure-free stress tensor,

$$\boldsymbol{\Sigma} = \boldsymbol{\tau} - \frac{1}{2} \operatorname{Tr} \left\{ \boldsymbol{\tau} \right\} \mathbf{I}. \tag{4.89}$$

In keeping with the majority of the analytical work done on this model these simulations were performed on a two dimensional system of particles with periodic boundaries in both direction, as these made it possible to simulate bulk flow and prevented particles from leaving the simulation region. Because the particles had no momentum these periodic boundaries were implemented simply by taking a particle that had left one side of the simulation cell and putting it back on the other, there was no need to make any corrections for the velocity even in the presence of an external flow field. The flow field itself, however, was somewhat limited since it would have been relatively complicated to implement any general flow field whilst upholding incompressibility within the periodic

---

(62) For example an implicit method would have lead to the necessity of a very large matrix inversion since the force on each particle depends on the positions of all of the other particles.

system. In practice the simulation was restricted to a simple shear flow as this worked well with the periodic boundary conditions.

The direct simulation of the basic equation of motion provided an interesting comparison to the dynamics calculated using equation 4.72 since it did not contain any of the approximations that had to be made in oder to make analytical solutions possible and used the actual positions of the particles rather than the two particle distribution function. This make it possible to gain some insight into what effect these assumptions had on the results. Also because the process was entirely numerical the exact form of the interaction potential had little effect on the time taken for the results to be obtained meaning that it was possible to obtain the dynamics of the model for any pair interaction, no matter how complicated a function of separation it was. Of course one of the drawbacks of this method relative to the analytical method, which was the main focus of this work, is that it only provided information on the state of a given system and could not be used to make predictions based on the form of the equations.

Chapter 5

Results and Discussion

5.1 A Constitutive Relation for Colloidal Dispersions

5.1.1 Dynamics

Using equation 4.72 it was possible to advance the state of the system forwards in time to discover the dynamics predicted by the model, and several scenarios were investigated. Figure 5.1 shows how the two particle distribution function evolved as a function of time when the system was relaxing after an initial step extensional strain, for a fluid with a repulsive interaction potential acting between the particles.

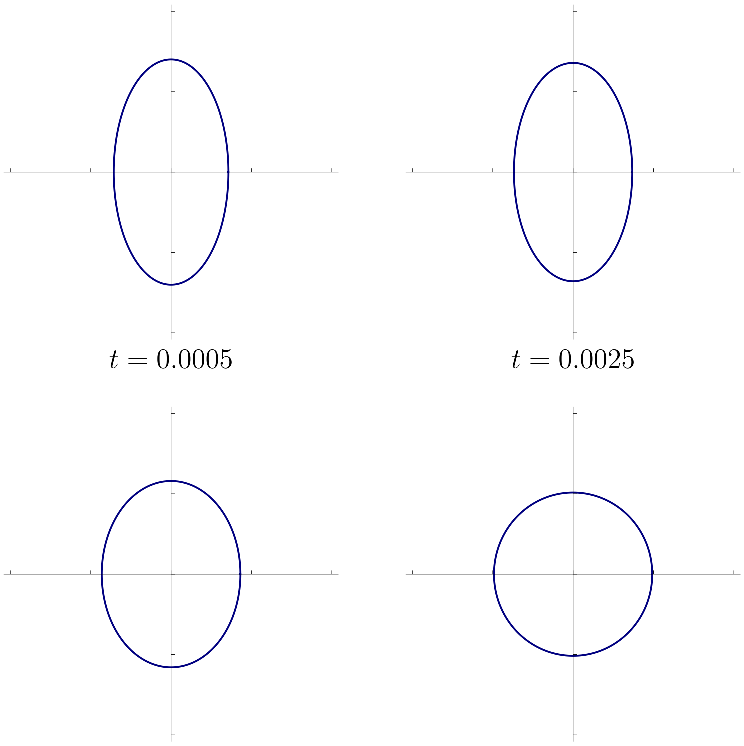

$t = 0.0005$ $t = 0.0025$

$t = 0.0250$ $t = 0.1250$

Figure 5.1: Diagrams showing how a contour of the two particle distribution function evolves with time when the system is relaxing back to its equilibrium state after a step strain, $\kappa = 2$. Here the tick marks on the axes correspond to integer multiples of the radius of the same contour in the equilibrium two particle distribution function. This example was generated using an interaction potential of $U = r^{-4}$.

Here it is clear that the system does not relax straight away, rather the deformation of the structure is still clear even after a significant amount of time. This is caused by the fact that it takes a finite time for the particles to rearrange themselves back into an equilibrium configuration after the strain has been applied. In the absence of an external flow field this process relies on diffusion and thus the most relevant time scale here is the diffusion time. When the two particle distribution function is anisotropic, as it is shortly after the deformation in figure 5.1, the inter-particle force will produce a stress beyond that of the isotropic pressure, in accordance with equation set 4.68. In this case the stress is solely in the normal direction, since the axes of the deformed two particle distribution function are aligned with the coordinate axes. The evolution of the normal and shear stresses, Σ_{aa} and Σ_{ab} respectively, as a function of time for the scenario shown in figure 5.1 is shown in figure 5.2

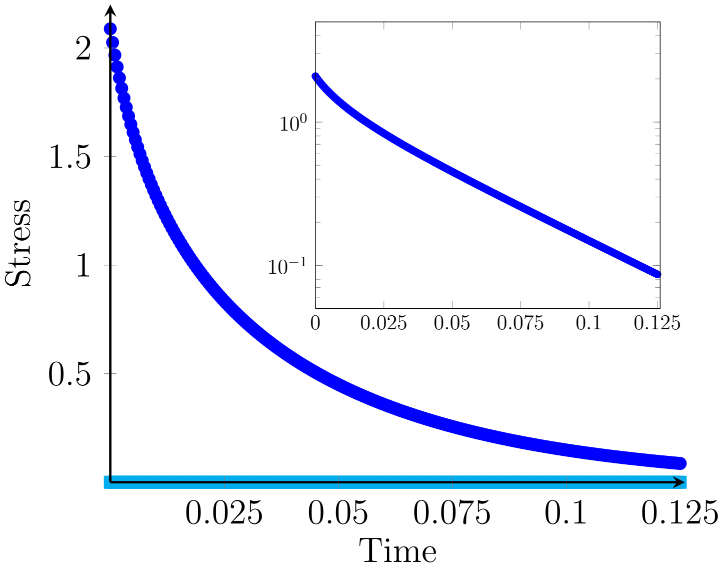

Figure 5.2: Plot showing how the stress evolves with time for a system relaxing back to its equilibrium state after undergoing a step strain, as in figure 5.1. Here the blue circles (—●—) mark the normal component of the stress while the cyan squares (—■—) mark the shear component. The insert shows the same data with a logarithmic scale on the y axis. In this example $U = r^{-4}$.

Here the positive normal stress corresponds to a force pushing out in the x direction accompanied by a force, of equal magnitude pulling inwards, in the y direction(1), which is consistent with what one would expect from the form of the two particle distribution function shown in figure 5.1. In a Newtonian fluid the stress would fall to zero at the instant the strain rate reached zero and not fall away smoothly as the structure relaxes, as the stress does here. One can think of the relaxation process here as being due to diffusion, by which the system "forgets" its initial configuration, and the two particle distribution function relaxes without any change in the shape of an element of the fluid. At the same time, the inter-particle force, which causes an elastic response in the fluid element, attempts to restore the original shape of the element. Thus while the fluid is held in its deformed state the two particle distribution function returns to its equilibrium shape, as it would for any fluid, but while this process is taking place the fluid is under stress due to the anisotropy in the forces arising from the microstructure. This kind of behaviour is commonly seen in viscoelastic materials[39]. Before leaving this example it is worth noting that, to a very good approximation, at later times, when the total deformation of the microstructure is small, the stress decays exponentially. This point will be relevant to the discussion in section 5.1.3.

Another way of observing the viscoelastic nature of this model is by examining how the stress builds up, and how the two particle distribution function changes, as the system is driven out of its equilibrium state by an imposed flow field. Figure 5.3 shows how the shape of the two particle distribution function evolves with time during volume conserving uniaxial extension, as indicated by the light blue arrows, while figure 5.4 shows how the stress evolves in this flow field.

---

(1) This convention follows naturally from the definitions given in section 4.4 and shall be used throughout.

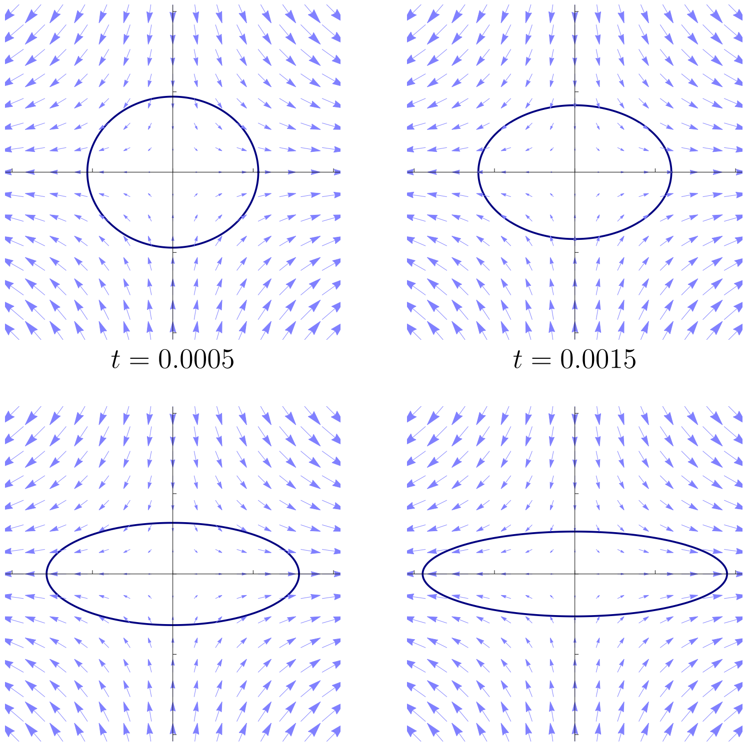

$t = 0.0005$ $t = 0.0015$

$t = 0.0040$ $t = 0.0250$

Figure 5.3: Diagrams showing how a contour of the two particle distribution function evolves with time when a system initially at equilibrium undergoes uniaxial extension. Here the light blue arrows (⟶) point in the direction of the flow field and the sizes of the arrow heads correspond to the magnitude of the fluid's velocity. The tick marks on the axes correspond to integer multiples of the radius of the contour in the equilibrium two particle distribution function. In this example $U = r^{-4}$ and $\dot{\epsilon} = 50$.

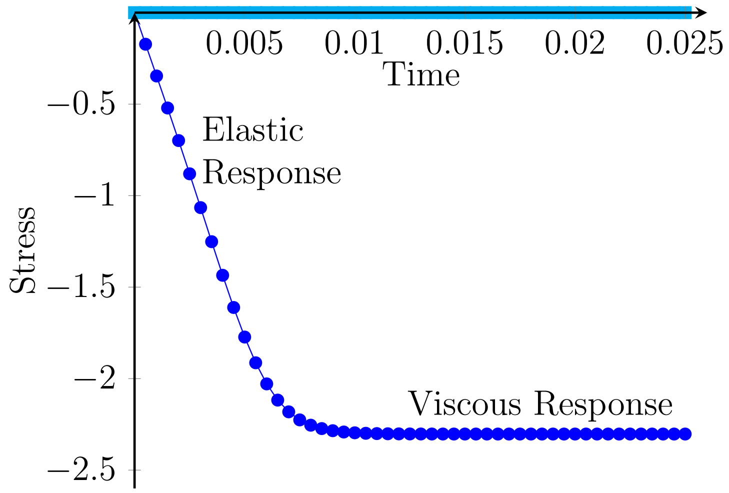

Figure 5.4: Plot showing how the shear and normal stresses, evolve with time for a system undergoing uniaxial extension after initially being in its equilibrium state. Here the blue circles (—●—) mark the normal component of the stress while the cyan squares (—■—) mark the shear component. In this example $U = r^{-4}$ and $\dot{\epsilon} = 50$.

Figure 5.4 shows the separate viscous and elastic responses very clearly. Here the elastic response manifests itself in the linear increase in the stress at short times. During this phase of the motion there is very little rearrangement of the microstructure, because there hasn't been sufficient time for the particles to move, so the deformation is met with resistance from the inter-particle forces which act to restore its shape, and thus the stress scales linearly with the amount of deformation. After a very long time, the system has forgotten its equilibrium configuration and the stress reaches a steady state, where the rate at which the flow field is deforming the fluid is matched by the rate at which it is undergoing structural rearrangements. This is more akin to the response of a viscous, Newtonian fluid. Here both the diffusion time and the flow rate are relevant time scales in the approach to steady state. In figure 5.3 one can see how the two particle distribution function reaches its steady state. Initially it expands rapidly along the x axis while being compressed by the flow field in the y direction, this means that the characteristic separation between the particles is decreasing in the y direction causing the net force pushing outwards in this direction, while the particles are spreading out in the x direction lowering the net force in this direction below the isotropic pressure, at equilibrium. Once these length scales reach the point where these forces balance the forces exerted by the flow field the system reaches a steady state, where the two particle distribution function will remain in its deformed state indefinitely. For this particular fluid and flow field this is shown in the bottom left of figure 5.3. Another important feature to notice from comparison of figures 5.2 and 5.4 is the fact that as well as deforming the structure, the flow field also drives rearrangements and hence the reason why the steady state is reached much faster when there is a non-zero flow field imposed on the system. As with the relaxation event, shown in figure 5.1, the axes of symmetry of the two particle distribution function shown in figure 5.3 are aligned with the coordinate axes throughout the deformation, thus the shear component of the stress tensor, shown in figure 5.4, remains at zero.

In cases where the axes of the two particle distribution function are not aligned with the coordinate axes, as is the case at the beginning of the scenario shown in figure 5.5, where the system has been subject to an arbitrary strain prior to the onset of the flow, one would expect there to be an non-zero shear stress, at least for a short time.

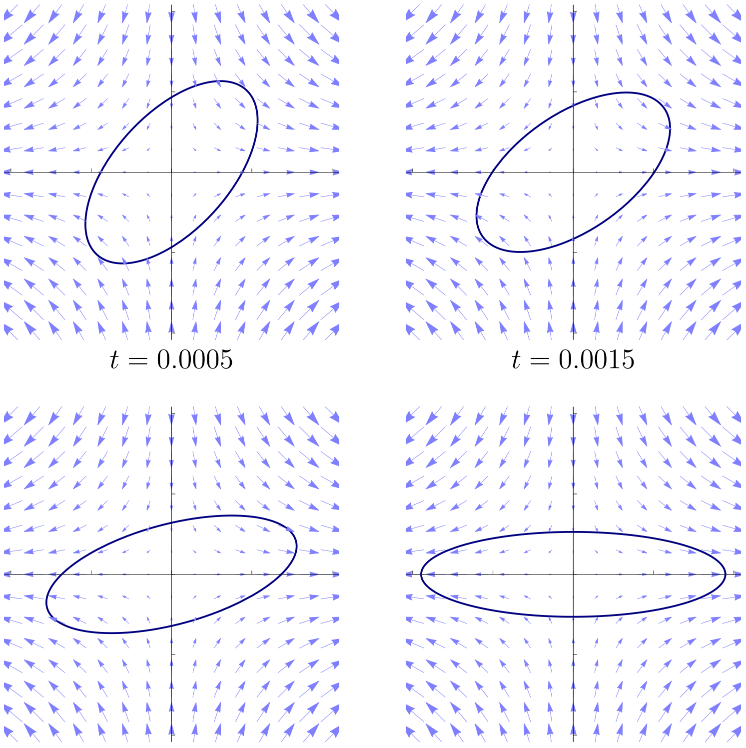
$t = 0.0005$ $t = 0.0015$
$t = 0.0040$ $t = 0.0250$

Figure 5.5: Diagrams showing how a contour of the two particle distribution function evolves with time when the system undergoes the same uniaxial extension as in figure 5.3, but starting from an initially deformed state, $\kappa = 2$ and $\delta = \frac{\pi}{4}$. The light blue arrows (⟶) point in the direction of the fluid's velocity and the sizes of their heads correspond to its magnitude. The tick marks on the axes are integer multiples of the radius of the contour at equilibrium. In this example $U = r^{-4}$ and $\dot{\epsilon} = 50$

This is indeed the case as figure 5.6 shows.

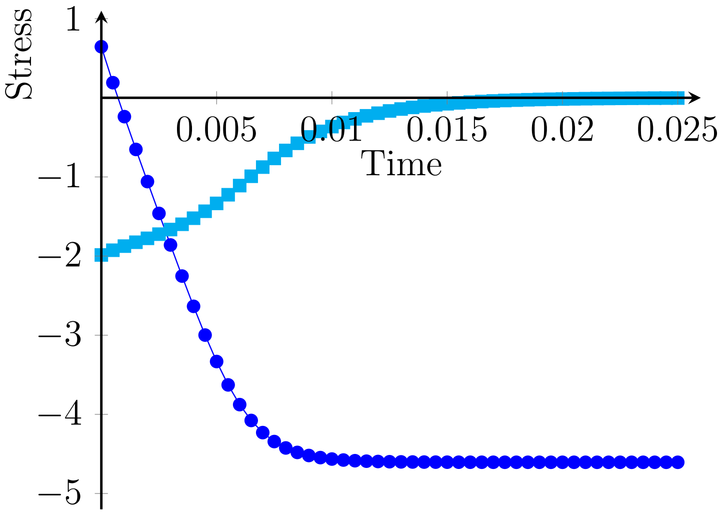

Figure 5.6: Plot showing how the shear and normal stresses evolve with time for an initially strained system undergoing uixaial extension, as shown in figure 5.5. Here the blue circles (—●—) mark the normal component of the stress while the cyan squares (—■—) mark the shear component. The parameters used in this example were $U = r^{-4}$ and $\dot{\epsilon} = 50$

Here the normal component of the stress evolves in much the same way as before, except, of course, for the fact that it starts from a non-zero value. The most interesting feature in figure 5.6 is the shear stress, which decays to zero in a non-linear way as the two particle distribution function first rotates into alignment with the axes of symmetry defined by the flow field and then stretches along the x axis until the normal stresses balance the forces imposed by the flow field. Since there is no resistance to a solid body rotation of the structure then this process happens relatively quickly compared to the deformation of the structure which must overcome the inter-particle forces. This is the reason why the initial growth of the normal stress is coupled to the decay of the shear component as the two particle distribution function rotates at roughly constant deformation before deforming to reach the stress required at steady state. This can be seen in the first two snapshots shown in figure 5.5 and the increasing rate at which the shear component of the stress tensor decays at short times in figure 5.6.

Thus far nothing has been said of the effect that the interaction potential has on the dynamics of the fluid and the corresponding response of the stress. In order to investigate this the relaxation experiment was repeated with a range of fluids with different single power law interaction potentials. Figures 5.7 and 5.8 show how the shape of the two particle distribution function and normal stress, respectively, change with time during this relaxation event for three different interaction potentials.

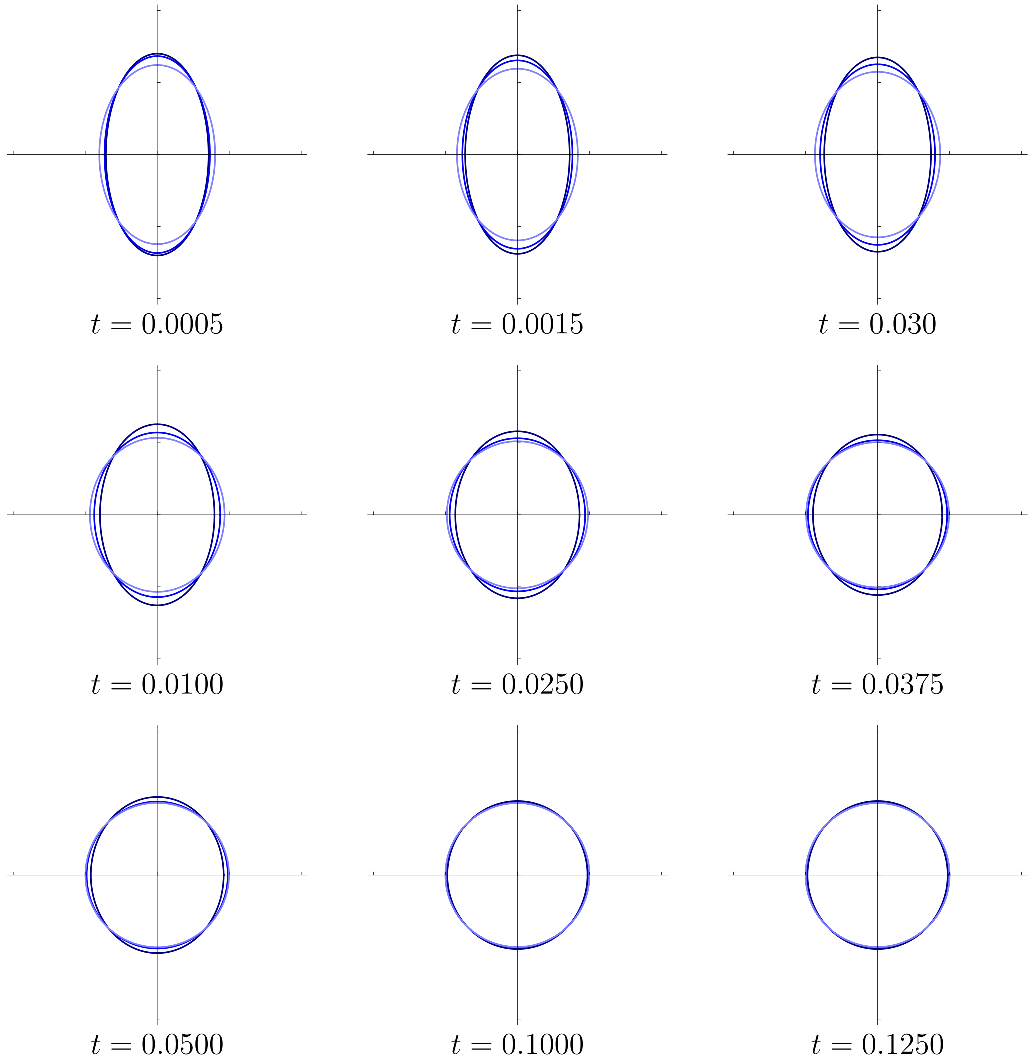
$t = 0.0005$ $t = 0.0015$ $t = 0.030$

$t = 0.0100$ $t = 0.0250$ $t = 0.0375$

$t = 0.0500$ $t = 0.1000$ $t = 0.1250$

Figure 5.7: Diagrams showing how a contour of the two particle distribution function evolves with time, for a range of fluids with single power law interaction potentials, when the system is relaxing back to its equilibrium state after an initial step strain, $\kappa = 2$. The dark blue line (—) corresponds to the contour for a fluid with an iteration potential of $U = r^{-4}$, the intermediate shade of blue (—) corresponds to $U = r^{-6}$ and the light blue line (—) to $U = r^{-8}$. All of the contours shown here had the same radius at equilibrium. Here the tick marks on the axes correspond to integer multiples of the radius of the same contour in the equilibrium two particle distribution function.

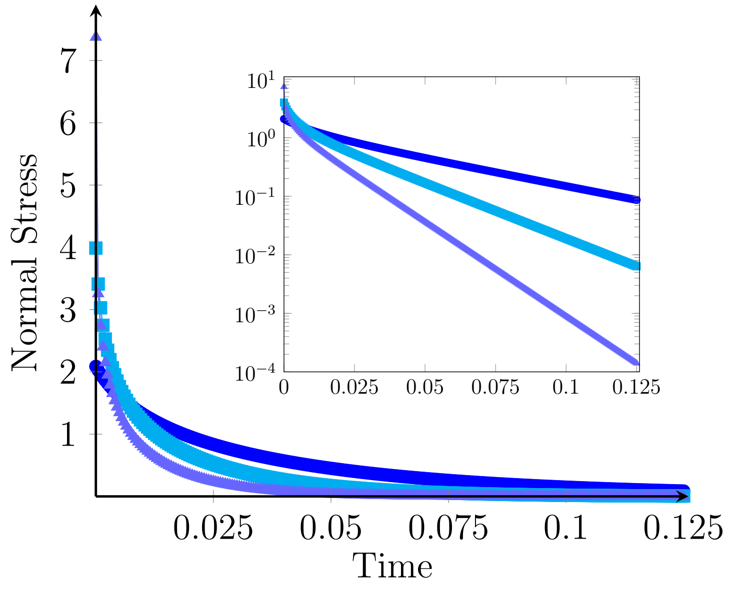

Figure 5.8: Plot showing how the magnitude of the normal stress decays, for fluids with different interaction potentials, when the system is relaxing after a step strain. The blue circles (—●—) correspond to an iteration potential of $U = r^4$, the cyan squares (—■—) to $U = r^{-6}$ and the light purple triangles (—▲—) to $U = r^{-8}$. The insert shows the same data plotted on a scale with a logarithmic y axis.

It is perhaps worth pointing out here that, for the purposes of this example, all of the fluids have been initialised with the same amount of strain, and not the same amount of stress, to ensure a fair comparison in terms of the rate at which the two particle distribution function changes. With this in mind one can see immediately from figure 5.7 that the fluids with the steeper interaction potentials relax much faster than those with shallower potentials. The reason for this is apparent in figure 5.8 in that the initial stress is much greater in the fluids with the steeper interaction potentials due to the fact that the particles are experiencing a greater increase in repulsive force for the same difference in characteristic separation. The origin of this higher stress is rooted in the higher order deformation terms in the equations for the stress, and by extension its rate of change, which come about due to the higher exponent in the interaction potential. This enhanced rate of relaxation, seen in the dynamics of the two particle distribution function, also extends to the relaxation of the stress, this is very clear from figure 5.8 where it is clear that the fluids with steeper potentials, which initially experience a greater stress, quickly relax and the stress in these fluids falls below the stress in the fluids with shallower potentials. Figure 5.8 also shows that, with the exception of the relaxation shortly after the original deformation, the stress in all of the fluids decays roughly exponentially, with the fluids with the steepest interaction potentials experiencing the highest decay rate. As before much of the later part of the decay process, where the total strain is small, is well approximated by this exponential decay, but it is worth noting that the higher stress experienced by the fluids with the steeper interaction potentials means that the initial decay that is not well approximated by this function is more pronounced.

Naturally the interaction potential also has an effect in the presence of a flow field, but the issue of most interest in this case is not the effect it has on the dynamics, but rather the effect it has on the steady state structure, and by extension the steady state stress. This is discussed in section 5.1.2.

5.1.1.1 Shear Flow Following Step Strain

One case of particular relevance to the notion of flow induced jamming [24,25] and to the formation of patterns in particle-laden fluids [2,3] is when shear flow immediately follows a compression in the shear gradient direction [3] as the fact that the particles are in close proximity to one another in the gradient direction means that it is more difficult for them to move past one another at the onset of the shear motion. Macroscopically this kind of behaviour would manifest itself in the form of an unexpectedly large value of the shear stress at the onset of shear flow, which would decay over time to the expected steady state value. Of course jamming [24,25] is the extreme limit of this, but it is not too difficult for one to imagine how this mechanism could lead to extremely large shear stress in dense suspensions of hard particles. This is not the limit of interest here since the approximations made in section 3.4 mean that this constitutive relation is only valid at low volume fractions.

While flow history dependence in colloidal dispersions is well documented in the rheology literature [170,171], with clear evidence that the stress at startup is significantly higher than the steady state stress [170], many experiments endeavour to avoid the situation of interest here by allowing the fluid to settle in the rheometer before the commencement of shearing[170]. In principle the situation of relevance to the problem of flow induced jamming, and to the present work, is an experiment in which the plates of the rheometer are pressed together before immediate commencement of the shear flow.

The effect of prior elongation on the stress during shear flow in this model was investigated by studying the dynamics of both of the independent components of the stress tensor, Σ_{aa} and Σ_{ab}, and the form of the two particle distribution function during start up shear with different initial conditions, which represented the state after some prior flow had ended at $t = 0$. Three cases were considered here: the first being a volume conserving elongation in the gradient direction coupled with compression in the flow direction, the second being the opposite to this, elongation in the flow direction and compression in the gradient direction, and the third, and final, test case was that of an isotropic fluid in its equilibrium state. Figures 5.9a to 5.9c show how the shape of the contours of the two particle distribution function evolved in time, from the point where the previous flow ceased to just before the steady state was reached in shear flow.

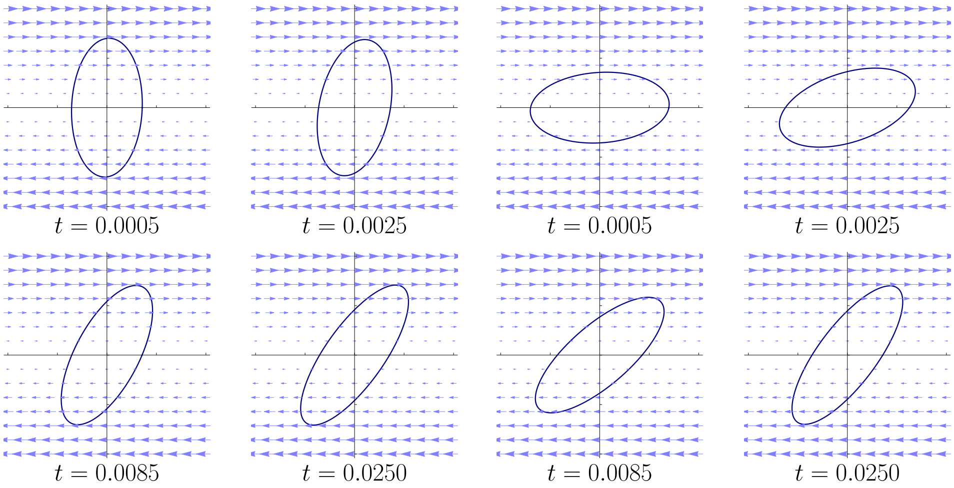

(a) Perpendicular elongation.

(b) Parallel elongation.

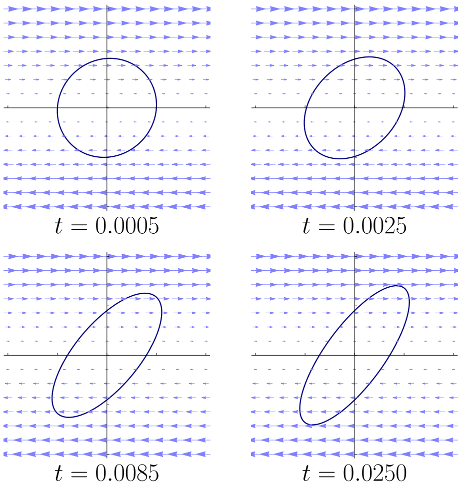

(c) Unstressed.

Figure 5.9: Diagrams showing how a contour of the two particle distribution function evolves with time in simple shear flow, given three different initial states. The light blue arrows (⟶) point in the direction of the flow field and their size corresponds to the magnitude of the fluid's velocity. The tick marks on the axes correspond to integer multiples of the radius of the equilibrium two particle distribution function. Here a fluid with an interaction potential of $U = r^{-4}$ and a Péclet number of 50 was used. Where initial strains were applied an initial stain of $\kappa = 2$ was used.

As the images in figure 5.9 show, the different initial conditions mean that the structure of the fluid takes different routes to the steady state structure. There is clear evidence that in the two pre-stressed states the two particle distribution function remains deformed and rotates into its final position, as in figure 5.5, while in the unstressed case it deforms slowly along the axis prescribed by the flow field and there is no rotation.

While figure 5.9 provides an insight into the dynamics of the underlying structure of the fluid it is the shear stress that is of most interest here as this gives an indication of whether or not the flow history limits the fluids ability to be sheared. The time evolution of both the shear stress, Σ_{ab}, and the normal stress, Σ_{aa}, for the three flow scenarios shown in figure 5.9 is plotted as a function of time in figure 5.10.

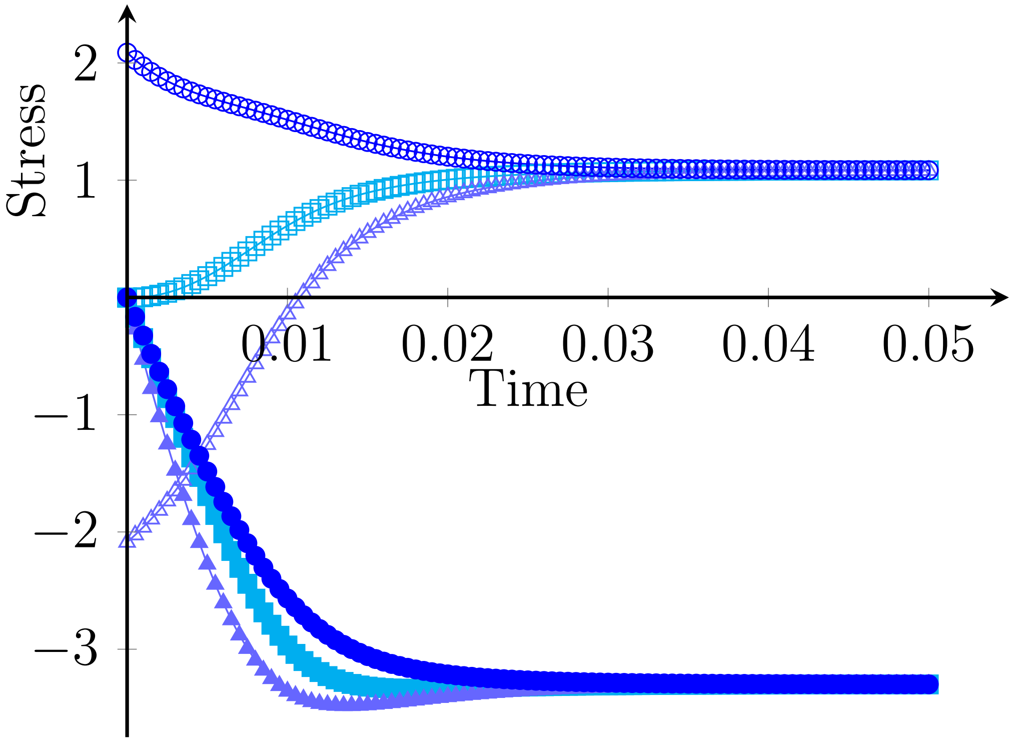

Figure 5.10: Plot showing the stress as a function of time for simple shear with three different stating conditions. The cyan squares (—■—, —□—) correspond to an unstressed initial state, shown in figure 5.9c, the blue circles (—●—, —○—) correspond to the shear flow following an elongation perpendicular to the direction of shear, as in figure 5.9a, and the light purple triangles (—▲—, —△—) correspond to an elongation parallel to the flow direction, as shown in figure 5.9b. The solid shapes (—■—, —▲—, —●—) mark the shear component of the stress tensor and the open shapes (—□—, —△—, —○—) mark the normal component of the stress tensor. Here a fluid with a power law interaction potential of $U = r^{-4}$ and a Péclet number of 50 was used.

There are several points to take from the data presented in figure 5.10. Firstly, and perhaps unsurprisingly, it is clear that all three scenarios result in the same steady state, since this is determined entirely by the properties of the shear flow and does not depend on the flow history. This is however important as it demonstrates the model's ability to "forget" its initial state, which is an important feature of any model of fluid flow.

Secondly, and most importantly, figure 5.10 shows clear evidence that the shear stress rises faster and reaches a higher peak value in the case shown in figure 5.9b, where the fluid has been compressed in the gradient direction. This is a very important result as it shows that even this relatively simple model is able to capture, to some extent, this essential feature of flow induced jamming[24,25]. However, the magnitude of this difference is relatively small, compared to the magnitude of the stress itself, and is by no means the divergence one would require to say definitively that the system was jammed, it does point toward the fact that, for fluids obeying this kind of constitutive relation, past flow events can reduce the flow rate of the fluid if the stress is fixed. The fact that the magnitude of the difference is small is hardly surprising since this model uses a soft potential and assumes low volume fractions so one would not expect there to be a dramatic difference in the stress, and certainly not the divergence seen in experiments[24,30] with hard particles at very high volume fractions.

Figure 5.10 also demonstrates how the shear stress builds up smoothly from zero. The fact that the stress builds over time further demonstrates the dependence of the stress on the flow history.

Another interesting feature of figure 5.10 is that there is a slight peak in the shear stress even when the system is initially isotropic, this is a manifestation of the relationship between the elastic and viscous nature of the fluid. Over short time scales the stress in the fluid builds due to the elastic response, which can be thought of in terms of the particles being forced together and increasing their potential energy. At later times rearrangement of the structure leads to a reduction in the stress as the particles reduce their potential energy. This leads to an initially enhanced shear stress that relaxes back to its steady state value.

It is also worth noting as an extension to this point that the scenario where an elongation in the gradient direction has occurred before the onset of shear flow provides the route to the steady state with by far the lowest start-up stress since the increased separation in the gradient direction means that the particles moving at different flow rates, as a consequence of the shear gradient, can pass each other with far less resistance.

Finally it is worth examining the dynamics of the normal stress, Σ_{aa}. This indicates, in a much clearer way than the shear stress, the separate effects of the rotation and deformation of the structure. These are clearly seen in the curve for the scenario where the fluid has undergone an elongation in the gradient direction, where the initial rapid decrease can be attributed to rotation, which happens quickly due to the fact that there is no resistance to rotational motion, followed by relaxation which happens more slowly. It is also worth noting that the normal stress difference, $2\Sigma_{aa}$, is initially negative and hence implies a force pushing the particles apart[47,57] in the gradient direction when there is initially a compression in this direction. This is important as it is this force that contributes to the increased shear stress once rotated by the flow field. The fact that the normal stress difference then becomes positive, in steady state, which implies that there is a force pulling particles towards the centre[47,57] in the gradient direction and expelling them out along the flow direction, can be thought of as being due to the tension in the stream lines[57] caused by the shear flow, resulting in particles migrating towards the centre. On the macroscopic scale this kind of behaviour would be detectable in the form of a force pulling the plates of the rheometer together.

The consequence of all of this for the formation of patterns in particle-laden flows is that this kind of history dependent flow may be a contributing factor to the formation of striped patterns perpendicular to the flow direction[2,3], which are observed in flows of large granular particles[2]. The idea behind this scenario is that, as the solvent flows around the end of a growing band the stream lines converge[2,3], as depicted in figure 2.2, and the solvent velocity increases; the structure of the particle fluid is drawn out in the flow direction and compressed perpendicular to this, thus by the time that element of the particle fluid passes the end of the growing band and is sheared it has been stretched in the flow direction, as in figure 5.9b, and thus, as figure 5.10 clearly shows, there is an increased resistance to the flow of the particles which would reduce the flux and may course them to jam and thus add to the end of the band. Also the fact that the steady state normal stress in figure 5.10 is positive implies that there is a force in the gradient direction pulling the stream of particles together[47,57] and thus increasing the chances of them colliding with one another and jamming. Also since the obstruction is fixed, but the stream of particles is free to move, this force may result in the particles being pulled toward the end of the obstruction, where they are likely to collide with the obstruction itself and jam. Another important manifestation of the presence of a positive normal stress difference as far as pattern formation is concerned is that in the case of a draining film there is a shear gradient normal to the surface and since the surface cannot move the force pulling particles inwards is effectively also pulling the air-solvent interface towards the fixed surface and the thinner the film gets the greater the effective shear rate becomes, increasing the magnitude of the effect, essentially causing an instability, which could result in regions of solvent that are too thin for large particles to inhabit and thus also contribute to the formation of patterns.

It is also worth noting the effect of the interaction potential on this behaviour. All of the examples shown here have used a fairly soft power law interaction, $U = r^{-4}$. However, tests with steeper interaction potentials revealed the same qualitative behaviour, in that the shear stress was always increased following an elongation in the flow direction an reduced following elongation in the gradient direction. The main difference is that the steeper potentials lead to faster relaxations and to a steady state where the two particle distribution function was less deformed(2). These properties can be seen in figure 5.7 and will be discussed further in due course.

The dependence of this behaviour on the Péclet number is somewhat more interesting, however. This is illustrated in figure 5.11.

---

(2) Except when the Pélet number is very large, where shear thinning leads to fluids with steeper interaction potentials having lower viscosities, this property is discussed in section 5.1.2.

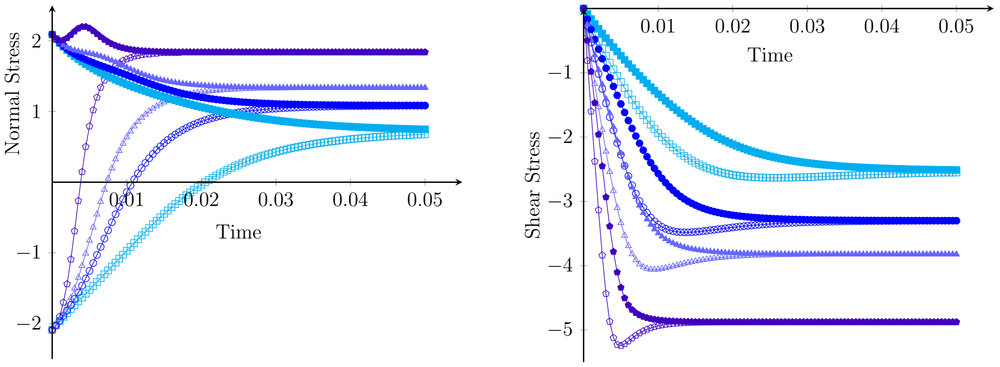

(a) Normal stress. **(b)** Shear stress.

Figure 5.11: Plots show how the normal and shear stresses evolve in a system undergoing simple shear, at a range of different Péclet numbers, following an initial step strain in two different directions. Here the solid shapes (—■—, —●—, —▲—, —⬟—) mark the data for the situation where the initial elongation is in the gradient direction, as shown in figure 5.9a, while the open shapes (—□—, —○—, —△—, —⬠—) mark the data for the situation where the system is initially elongated along the flow direction, as in figure 5.9b. The cyan squares (—■—, —□—) correspond to a flow with a Péclet number of 25, the blue circles (—●—, —○—) to a Péclet number of 50, the light purple triangles (—▲—, —△—) to a Péclet number of 75 and the dark purple pentagons (—⬟—, —⬠—) to a Péclet number of 150.

The first point to make here is that, in all cases, one sees the same qualitative difference between the start up shear stress in the systems that have been prepared in a state with an initial elongation parallel to the flow direction and those where this elongation is in the gradient direction. It is clear that where there is an elongation in the flow direction the start up shear stress will always increase faster and peak before relaxing to the steady state value, while an elongation in the gradient direction always provides the route to the steady state with the lowest shear stress. Despite this it is interesting to note that there are some clear general trends in figure 5.11b in terms of what effect the magnitude of the shear rate has on this behaviour. It is clear from figure 5.11b, and perhaps unsurprising, that the steady state and the peak stress are reached much faster when the Péclet number is higher. This is simply because the higher rate of flow changes the structure of the fluid much more rapidly. It is also worth noting though that the peaks, in the case where the system has been compressed in the gradient direction, are much sharper and deviate further from the steady state stress when the shear rate is higher. One can understand this by thinking in terms of how much of the stress stored in the fluid from the initial deformation remains in the structure as it is rotated to align with the flow field and so contributes to the shear stress. Clearly this rotation will occur more rapidly in a faster flow and thus there is more stress to contribute to the shear stress. In terms of the particles themselves one can think of this in much the same way: at high shear rates, the flow field is forcing the particles to pass close to one another as the particles near the edges travel faster than those near the centre, if they are already close to one another in the gradient direction and do not have time to rearrange and spread out in this direction before a fast moving particle, from near the edge, passes them then it is forced to pass much closer and thus there is a greater resistance to its motion. Returning to the point about the sharpness of the peaks it is worth pointing out that at higher strain rates these peaks begin to look much more like the kind of spikes one would expect to see in the stress profile of a granular system which is constantly jamming and unjamming as it flows, and remembering the results shown in figures 5.7 and 5.8, which demonstrated that the stresses are higher and relax faster in fluids with steeper interaction potentials, it is perhaps not unreasonable to consider this kind of behaviour as a slightly smoother version of such a phenomenon. Indeed if the stress were constant and the flow rate allowed to vary one would certainly see a pronounced drop in the flux of particles following a compression in the gradient direction. Thus, as mention before, it may be this kind of behaviour, that is lacking in the very simple model of the particle-laden fluid, that leads to the formation of the band structures observed in real[2] draining films of granular suspensions.

5.1.2 Steady State Solutions

One of the key advantages of using such a simple constitutive relation is that it was possible to extract analytical expressions for the steady state behaviour. This was done by solving equation set 4.69, with the rate of change of the stress set to zero, for the strain rate and coupling the solutions with equation set 4.68 to obtain the stress-strain relationship in parametric form. For uniaxial extension this results in equation set 4.70 for the general case. While equation set 4.70 has the distinct advantage of being completely general with regard to the form of the interaction potential it is very difficult to examine the flow behaviour it predicts while the integrals remain unevaluated. The aim of this section is to examine the results obtained for steady state flow for a number of specific interaction potentials, in both extensional and simple shear flow fields.

5.1.2.1 Uniaxial Extension

Perhaps the simplest interaction potential to be examined is that of a single, repulsive, power law. Despite the simplicity these interaction potentials are very important, and as they are very commonly used[115] to, crudely, model the hard sphere interaction in computer simulations of particles, like the one described in section 4.3, and because they are simple they are able to reveal much more about how the model works. As they are the basis for all of the interactions permitted in this model one can use the results obtained with such interaction potentials to make predictions about the effects of the component terms in much more complicated interaction potentials. Here several examples, of varying steepness were examined, these ranged from the shallowest potential permitted by the conditions for convergence of the integrals, $U = r^{-4}$, to the relatively steep $U = r^{-16}$. Here only the results for even exponents are presented since most physical interaction potentials of this type use even powers(3) and also because while it was possible to extract the solutions for odd powers this produced significantly more complicated expressions, which were much slower to evaluate computationally(4), without introducing any significant change in the physics. It is also worth noting, though it has not been the focus of this work, that this model is also defined for potentials with positive exponents, most notably it can be shown that $U = r^2$ reproduces the same stress-strain relationship as the dumbbell model[39], $\Sigma_{aa} \propto \kappa$.

---

(3) Such as the very popular Lennard-Jones interaction and van der Waals' forces.

(4) This is because the most basic integrals in the reduction formulae are elliptic integrals of the first or second kind, rather than constants as they are when the exponent in the interaction potential is even.

To give an impression of the form taken by the parametric functions, once evaluated. Table 5.1 shows the solutions for the three shallowest potentials with even powers⁽⁵⁾.

Potential	Strain Rate And Normal Stress
$U = r^{-4}$	$\dot{\epsilon}=\frac{-21\kappa^6+25\kappa^4-25\kappa^2+21}{10\pi^{\frac{1}{2}}\kappa^3}$ $\Sigma_{aa}=-\frac{\pi^{\frac{3}{2}}-\pi^{\frac{3}{2}}\kappa^2}{4\kappa}$
$U = r^{-6}$	$\dot{\epsilon}=\frac{-1485\kappa^{12}-540\kappa^{10}+1260\kappa^9-255\kappa^8+252\kappa^7-252\kappa^5+225\kappa^4-1260\kappa^3+540\kappa^2+1485}{360\Gamma\{\frac{2}{3}\}\kappa^8+176\Gamma\{\frac{2}{3}\}\kappa^6+360\Gamma\{\frac{2}{3}\}\kappa^4}$ $\Sigma_{aa}=-\frac{\pi\Gamma\{\frac{2}{3}\}-\pi\Gamma\{\frac{2}{3}\}\kappa^4}{4\kappa^2}$
$U = r^{-8}$	$\dot{\epsilon}=\frac{-5005\kappa^{14}+3003\kappa^{12}+959\kappa^{10}-9\kappa^8+9\kappa^6-959\kappa^4-3003\kappa^2+5005}{840\Gamma\{\frac{3}{4}\}\kappa^9-528\Gamma\{\frac{3}{4}\}\kappa^7+840\Gamma\{\frac{3}{4}\}\kappa^5}$ $\Sigma_{aa}=-\frac{-15\pi\Gamma\{\frac{3}{4}\}\kappa^6-3\pi\Gamma\{\frac{3}{4}\}\kappa^4+3\pi\Gamma\{\frac{3}{4}\}\kappa^2+15\pi\Gamma\{\frac{3}{4}\}}{64\kappa^3}$

Table 5.1: Table of the parametric equations for the steady state stress and strain rate predicted by the constitutive relation described in section 3.4 for a fluid undergoing uniaxial extension evaluated for three different, single power law, repulsive interaction potentials. Here the parameter κ corresponds to the square of the ratio of the lengths of the semi-minor to semi-minor axis of the, elliptical, two particle distribution function.

Here the fact that the flow geometry is fixed meant that it was possible to eliminate one of the two free parameters, in this case the rotation of the deformed two particle distribution function was chosen as it makes much better physical sense to retain the magnitude of the deformation. Hence the expressions in table 5.1 are functions of one parameter only, κ, which corresponds to the square of the ratio of the semi-major axis of the two particle distribution function to its semi-minor axis, and hence this describes the magnitude of the deformation. Thus the equations in table 5.1 may be thought of as describing the Péclet number necessary to obtain a given deformation at steady state during uniaxial extension and the stress that results from this flow. There is a general tendency for the expressions for the stress to become more and more complicated as the potential becomes steeper, this is simply because one requires more cycles of the reduction formulae in order to evaluate the integrals in equation 4.70a. While this is also true of the equations describing the strain rate it is less obvious at first sight since equation 4.70b contains many more terms and there is a certain amount of cancellation when the exponent of the potential is a multiple of four. It is perhaps unsurprising, since this model demands that the particle interactions obey a power law, that the resulting expressions are themselves power laws in terms of the deformation parameter, κ. It is worth noting, however, that the coefficients of these expressions mean that there are no turning points in any of the expressions within the domain of allowed values of $1 < \kappa < \infty$. This is in good agreement with how one might expect a viscoelastic fluid to behave, in that the stress increases monotonically with the magnitude of the rate of deformation; one would not expect a more rapidly deforming state to reduce the total stress. The fact that this property extends to the Péclet number⁽⁶⁾ required to attain that stress implies that the stress-strain relationship will also

---

(5) Solutions for steeper potentials are straightforward to obtain in a similar fashion, but have not been included here because there are too many terms in the equations for displaying the full form to be practical.

(6) Here the Péclet number and the strain rate are essentially interchangeable if one assumes that the temperature, and length scale are being held constant.

be monotonic and thus rules out the possibility of phenomena like strain localisation. Though it is unclear from equation set 4.70 whether or not this will aways be the case, the results obtained for the interaction potentials investigated here all suggest a monotonic relationship.

The exact nature of the stress-strain relationship predicted by this model for a fluid undergoing uniaxial extension is perhaps best expressed graphically, as in figure 5.12.

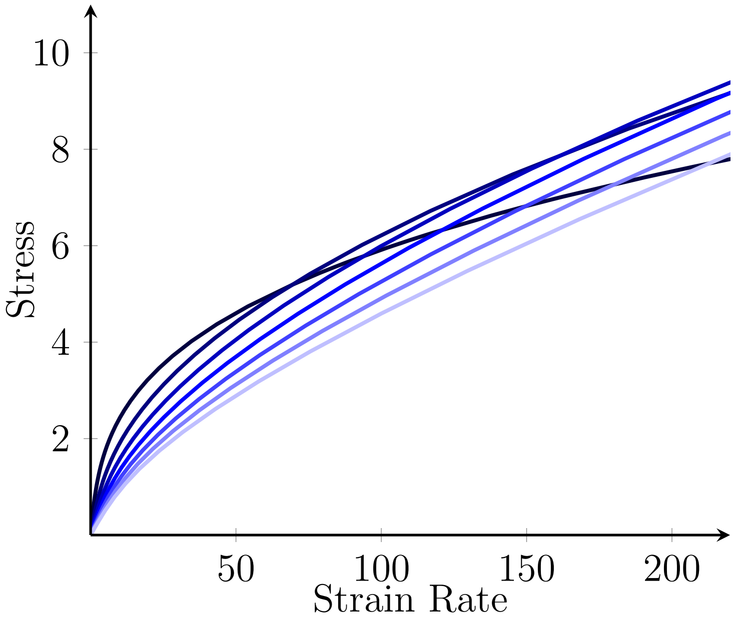

Figure 5.12: Plot showing the magnitude of the steady state normal stress as a function of elongation rate for a system undergoing steady elongational flow, like that shown in figures 5.3 and 5.5. The different coloured lines show the relationship for fluids with different, repulsive, power law interaction potentials, ranging from $U = r^{-16}$, in palest blue, to $U = r^{-4}$, in darkest blue, in steps of two.

In figure 5.12 the first thing to notice is that the stress-strain rate relationship is in fact monotonic and that the model predicts shear thinning behaviour for all of the power law interactions tested over a large range of strain rates. This behaviour is also clear in figure 5.13, which shows how the extensional viscosity varies with the rate of strain.

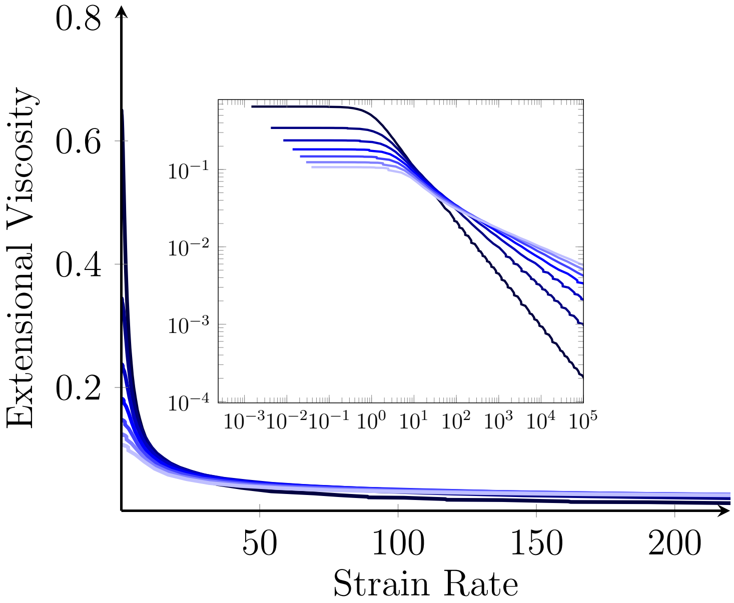

Figure 5.13: Plot showing the extensional viscosity as a function of elongation rate for a system undergoing steady elongational flow. The different coloured lines show the relationship for fluids with different, repulsive, power law interaction potentials, ranging from $U = r^{-16}$, in palest blue, to $U = r^{-4}$, in darkest blue, in steps of two. The insert shows the same data on a logarithmic scale.

This kind of shear thinning behaviour is commonly seen in colloidal suspensions and emulsions[64] at low and intermediate strain rates and is in good agreement with the theoretical results from mode coupling theory, presented in reference 35, as well as experiments[34,49,76,126,164], for low and intermediate strain rates. When the potential is steep the model even shows a weakening in the shear thinning behaviour, like that present in the results of the mode coupling theory presented in reference 35. However, this is not nearly as pronounced for the potentials used here as it is for the hard spheres described in the reference. This is hardly surprising since mode coupling theory is designed to deal with systems at much higher concentrations than the present model and attempts to take account of[35] many particle interactions, which can lead to phenomena like jamming, which do not fall within the scope of this model. While the switch from Newtonian behaviour to shear thinning, which is clear in figure 5.13, is in good agreement with the results of many other works[5,34,35,49,61,64,76,126,164] it is some what at odds with the experimental results of reference 69 which show a certain amount of shear thickening at low strain rates followed by shear thinning. This again is likely to be down to the fact that many body interactions have been neglected here, or may be due to the fact that the particles have been assumed to be massless in this model, as they are in the mode coupling model presented in reference 35, which also lacks this behaviour. Another effect missing from this model, that is also absent in the model presented in reference 35, is the shear thickening observed in hard sphere systems at high concentrations and high Péclet numbers[5,34,126]. It is particularly interesting to think of the results presented here in the context of the conclusions made in reference 5, which concludes that, while Brownian forces are responsible for shear thinning, it is hydrodynamic interactions that lead to shear thickening behaviour. This certainly goes some way towards explaining why the present model lacks such an effect. In the model presented here the origin of the shear thinning behaviour is likely to be the fact that the flow field drives rearrangements in the microstructure as well as causing the initial deformation, this much is clear from the last two terms of equations 4.69a and 4.69b, which illustrate the dependence of the rate of change of stress on the strain rate for an arbitrary flow field. This implies that the Newtonian region is the region where the strain rate is sufficient to deform the structure, but not sufficient to drive relaxation events which make a significant effect, beyond that of diffusion.

Another feature of note in these results is the dependence of the viscosity on the interaction potential used; here the shallower interaction potentials result in a higher initial viscosity which then decays at a higher rate as the strain rate increases. This can be seen in both figure 5.12, where the gradients of the curves corresponding to the shallowest potentials are greatest at low strain rates and become shallower rapidly, and figure 5.13, where these effects can be seen very clearly on the logarithmic scale. Both of these effects appear to diminish as the potentials become steeper, with the most noticeable difference being between $U = r^{-4}$ and $U = r^{-6}$. The increased low strain rate viscosity for the shallower potentials is likely to be due to the fact that they have a longer range and so the applied flow field must drive rearrangements of the microstructure on a much larger scale, where as in the case of the shorter range steeper potential, when only a small deformation is required, at low strain rates, the average change in particle separation corresponds to a relatively small change in the force since the potential will be very flat for most, reasonably small separations. Conversely at high strain rates, where large deformations are required, many more particles encounter the steep region of the potential and thus experience a significantly larger force when the potential is steeper, resulting in a higher value on the viscosity at large strain rates compared with that of the shallower potentials, as one observes in figure 5.13.

It is also worth noting that the strain rate at which the Newtonian region begins to give way to the shear thinning regime occurs at progressively higher values as the interaction potential becomes steeper. This is likely to be due to the fact that a greater deformation is required in order for the flow field's driving of the rearrangement of the microstructure to have a significant effect, whereas with the longer ranged potentials even a small deformation is enough to generate a significant difference in the forces felt by the particles in different regions and so cause a rearrangement in the microstructure that relieves some of the stress. The curve also begins to develop a slightly steeper region before it shallows out. This region becomes more and more pronounced as the potentials become steeper, due to the fact that there are more terms in the parametric equations describing the stress-strain relationship.

Another feature of note is the fact that the viscosity remains Newtonian as the zero strain rate limit is approached ruling out the possibility of this model capturing yield stress like behaviour. This fact is also supported by the parametric equations in table 5.1. While it is clear, as discussed previously, that the viscosity in the Newtonian region increased as the magnitude of the exponent in the interaction potential decreases it remains finite for all potentials for which the model is well defined.

In an attempt to better understand the shear thinning behaviour at high strain rate approximations of the parametric equations describing the stress-strain relationship were taken in the limit of $\kappa \to \infty$, such that the relationship could be written in the form

$$\Sigma_{aa} = a\dot{\epsilon}^{b}, \tag{5.1}$$

where a and b are parameters specific to the form of the interaction potential, in order to ascertain the nature of the shear thinning behaviour and make a more quantitative analysis of the effects of the different power laws and, most importantly of all, obtain values to use in the model described in section 3.1.2.1 in order to integrate these results into the model of the particle-laden fluid. Table 5.2 shows the values of the two free parameters, a and b, for fluids with different power law interactions, while figure 5.14 shows a plot of the corresponding straight lines against the data from the full model.

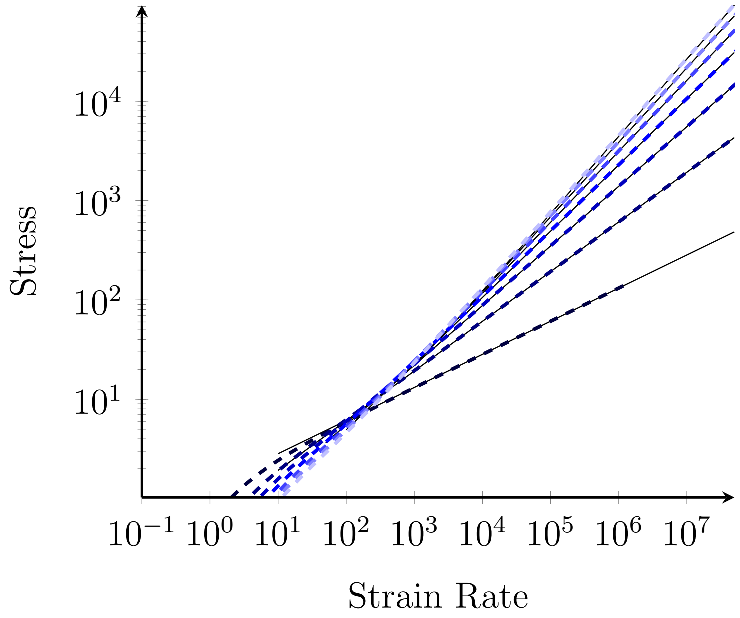

Figure 5.14: Plot showing the normal stress during steady uniaxial extension, like that shown in figure 5.9, as a function of extension rate. The different coloured lines correspond to fluids with different interaction potentials, ranging from $U = r^{-16}$, in palest blue, to $U = r^{-4}$, in darkest blue, in steps of two. The fine back lines show the high strain rate limits of the expressions.

Potential	Constant (a)	Exponent (b)
$U = r^{-4}$	1.31558	$\frac{1}{3}$
$U = r^{-6}$	0.60934	$\frac{1}{2}$
$U = r^{-8}$	0.34933	$\frac{3}{5}$
$U = r^{-10}$	0.22825	$\frac{2}{3}$
$U = r^{-12}$	0.16207	$\frac{5}{7}$
$U = r^{-14}$	0.12181	$\frac{3}{4}$
$U = r^{-16}$	0.09539	$\frac{7}{9}$

Table 5.2: Table of parameters for the function $\Sigma_{aa} = a\dot{\epsilon}^b$ for the stress as a function of strain rate in steady uniaxial extension, at high strain rate.

Here it is clear that these lines are in excellent agreement with the data from the full model where $Pe > 100$. This suggests that even when the Péclet number, and by extension the steady state strain rate, is relatively small the equations are still dominated by the highest order terms and that it is these terms that determine the nature of the shear thinning behaviour. In fact, by taking the limits of the parametric equations one may derive a vernal formula for the exponent

$$b = \frac{p-2}{p+2}, \tag{5.2}$$

for an interaction potential of the form $U = r^{-p}$. In figure 5.14, however, the lines shown forecast further back than this in order to highlight the difference between the predicted, high strain rate, power law behaviour and the more complicated behaviour at lower and intermediate strain rates. This agreement is a strong indication that, at high strain rates, the stress-strain rate relation for this constitutive relation is very well modelled as a power law fluid, and thus is consistent with what one commonly expects for colloids at low concentration and emulsions[64]. Furthermore the fact that it exhibits this behaviour lends some support for equation 3.22 from a microscopic point of view, as well as enabling one to say with much greater precision exactly what the first two parts of the piecewise function are a model of. While the constants of proportionality are perhaps less significant than the exponents it is still worth noting that there is a general trend towards lower values as the interaction potential becomes steeper, as shown in figure 5.15a.

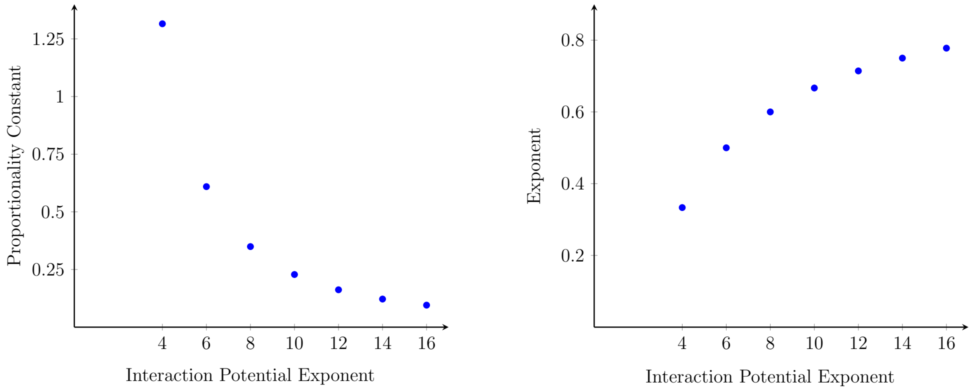

(a) Constant of proportionality. **(b)** Exponent.

Figure 5.15: Plots showing the parameters from equation 5.1 at high strain rate as a function of the power law interaction between the particles.

This is consistent with the fact that the effective viscosity in the Newtonian region is lower in the case of steeper potentials. The first thing to note about the exponents found in this, high strain rate, limit is that they increase with the steepness of the the interaction potential. This is consistent with the lower rate of shear thinning which is apparent from the effective viscosity, shown in figure 5.13, for the steeper potentials. Another important thing to notice about the exponents is the fact that while they are increasing as the potential becomes steeper the rate of increase is falling suggesting that this model will only exhibit Newtonian or shear thinning behaviour regardless of how steep the interaction between the particles becomes. One gets a feel for the origin of this behaviour by looking at equation set 4.70, where it is clear that when a power law with a single term for which the exponent, p_1, is negative is used(7) then, at large strains, the dominant term in equation 4.70a will always be a factor of κ^2 smaller than the dominant term in equation 4.70b, due to the way the integrals scale with κ. Thus by taking the limit of an infinitely steep interaction potential, so as to model hard particles, one may conclude that, based upon this scaling and the data presented here, this constitutive relation predicts Newtonian regions(8) at high and low strain rates separated by a shear thinning region at intermediate strain rates. This is in good agreement with the first three sections of the general form for the viscosity of colloidal dispersions given in reference 64. However, it lacks the shear thickening behaviour commonly observed in concentrated colloidal dispersions at high strain rates[5]. Again this is hardly surprising given the fact that this model is only really valid at low concentrations.

Finally, for completeness and to gain a deeper understanding of how the structure of the fluid is affected by the steady flow field during uniaxial extension, it is worth considering the form of the two particle distribution function at steady state and how it is affected by the interaction between the particles. Figure 5.16 shows the shape of a contour for three fluids with different single power law interactions.

---

(7) Or, in fact, the most negative power in cases where the interaction potential consist of more than one term.

(8) The region at high strain rates will tend towards being Newtonian as the potential becomes steeper since the, constant, difference between the scaling of $\dot{\epsilon}$ and Σ_{aa} will become less and less significant as the exponents of the dominant terms become larger.

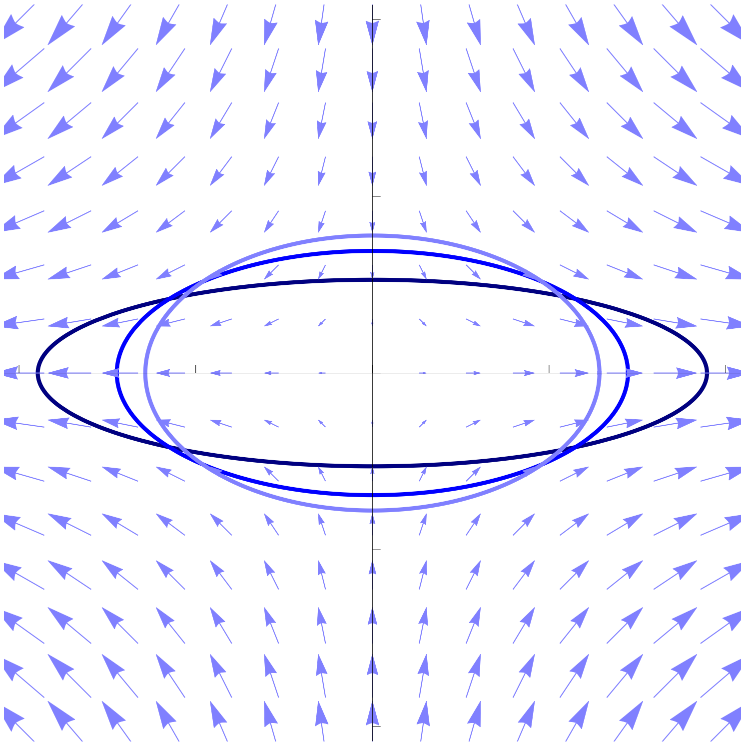

Figure 5.16: Diagram showing a contour of the two particle distribution during steady uniaxial extension. The darkest blue (——) corresponds to an interaction potential of $U = r^{-4}$, the lightest (——) to $U = r^{-8}$ and the intermediate shade (——) to $U = r^{-6}$, while the arrows (→) show the direction of the fluid velocity and their size corresponds to its magnitude, here $\dot{\epsilon} = 50$. All three contours had the same equilibrium radius, integer multiples of which are indicated by the tick marks.

Firstly it is clear from figure 5.16 that, in all cases, the two particle distribution function is compressed, by the flow field, in the normal direction, which is the y direction in figure 5.16, and elongated in the extensional direction, as one might expect, and thus the origin of the restoring force that establishes the steady state. The fact that the two particle distribution function has this form implies that, on average, the separation between the particles in the normal direction is less than it would be at equilibrium and much less than the characteristic separation in the extensional direction, which is greater than the equilibrium value. Thus in the normal direction, on average, there is an increase in the magnitude of the repulsive force between the particles, which counters the force imposed by the flow, which is bringing the particles together. In the direction of extension there is a reduction in this force as the particles are being drawn apart, but because the flow is incompressible, this has the same effect as a net attractive force in the extensional direction, pulling the particles back towards one another, against the flow field. Furthermore the contours are aligned with their semi-major and semi-minor axes along the axes of symmetry of the flow field, hence the reason why the shear components of the stress tensor are zero.

The contours shown in figure 5.16 were chosen such that they all have the same radius at equilibrium to ensure a fair comparison. Thus it is clear, by comparing the three contours shown that the fluids with the shallowest potential undergo the greatest deformation. One can think of this as a manifestation of the fact that the separations between the particles must deviate further from their equilibrium values in order to generate the necessary restoring force to balance the force imposed on them by the flow when the potential is shallow. Or conversely it means that the force exerted by the flow field is sufficient to cause a certain change in the potential energy of the particles and when the interaction potential takes a shallower form this corresponds to a greater change in the characteristic separation of the particles. At low strain rate this is in agreement with what one might expect from the stress, in that the more deformed states, arising from the fluids with the shallowest interaction potentials, have the greatest stress. However this is not the case at higher Péclet numbers, where the situation becomes slightly less intuitive; the deformation remains greater for the fluids with shallower potentials, as one can see in figure 5.17, due to the same reasons as before, but, as figure 5.12 shows, the stress is lower than that experienced by the fluids with steeper potentials, due to the shear thinning nature of this model.

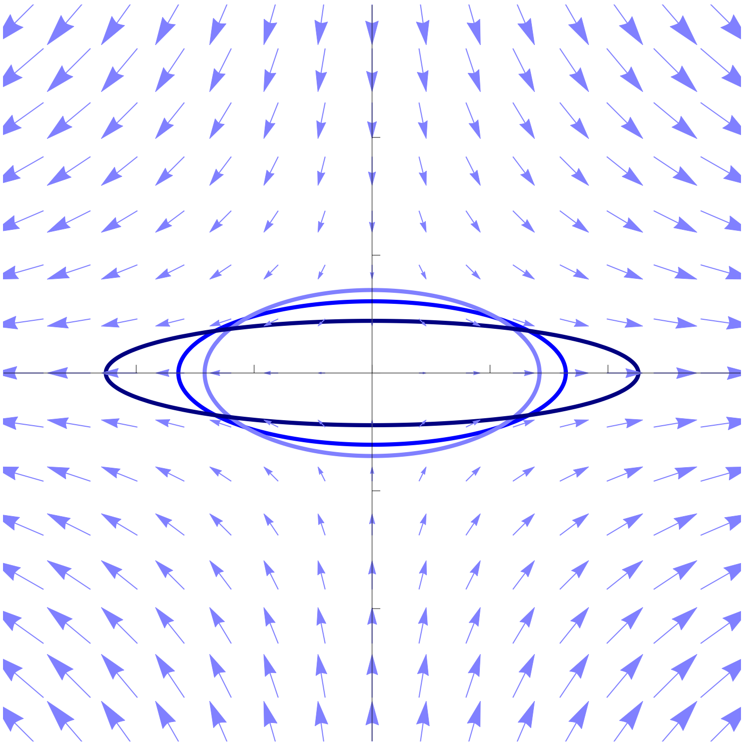

Figure 5.17: Diagram showing a contour of the two particle distribution during steady uniaxial extension. The darkest blue (——) corresponds to an interaction potential of $U = r^{-4}$, the lightest (——) to $U = r^{-8}$ and the intermediate shade (——) to $U = r^{-6}$, while the arrows (⟶) point in the direction of the fluid velocity and their size corresponds to its magnitude, here $\dot{\epsilon} = 150$. All three contours had the same equilibrium radius, integer multiples of which are indicated by the tick marks.

Mathematically the explanation for this is that the expressions for the stress, as shown in table 5.1 have many more, higher order terms, which mean that a greater stress can be produced with only a small deformation. At low strain rates these terms have a much smaller effect, relative to the lower order terms which are present in all of the expressions, and hence the reason why the more deformed states result in the highest stresses when the total deformation is small at low strain rate.

5.1.2.2 Simple Shear

Another case, which is perhaps more relevant to the model of the particle-laden fluid, is that of simple shear, as shown in figure 5.9. Here the situation is slightly more complicated, since there is rotational motion of the flow field in addition to the pure straining flow of uniaxial extension. This means that although the structure is being deformed in one direction it is able to exert some stress in another direction. As far as the analytical solutions to the model in the case of the power law fluids examined thus far go this essentially means that the solution for the parameter that describes the rotation of the two particle distribution function, δ, is non-trivial, though it is still preferable to use knowledge of the geometry of the flow field to eliminate this parameter rather than the parameter describing the magnitude of the deformation, κ, as κ gives more of an impression of the magnitude of the stress and strain in the system and results in the most straightforward form of the parametric equations. Table 5.3 gives the full form of these parametric equations for the shallowest potential considered here(9), $U = r^{-4}$.

Potential	Shear Rate And Normal Stress
$U = r^{-4}$	$\dot{\gamma}=\frac{21\kappa^8-4\kappa^6+4\kappa^2-21}{\pi^{\frac{1}{2}}\kappa^3\sqrt{(3\kappa^2+7)(7\kappa^2+3)}}$ $\Sigma_{aa}=\frac{\pi^{\frac{3}{2}}\left(\kappa^2-1\right)^2}{10\kappa(\kappa^2+1)}$ $\Sigma_{ab}=-\frac{\pi^{\frac{3}{2}}\left(\kappa^2-1\right)\sqrt{(3\kappa^2+7)(7\kappa^2+3)}}{20\kappa(\kappa^2+1)}$

Table 5.3: Table of the parametric equations for the steady state stress and strain rate predicted by the constitutive relation described in section 3.4, for a fluid undergoing simple shear evaluated for an interaction potential of $U = r^{-4}$. Here the parameter κ corresponds to the square of the ratio of the lengths of the semi-minor to semi-minor axis of the, elliptical, two particle distribution function.

As with uniaxial extension the number of terms in the expressions increases with the steepness of the potential, for the same reasons as those outlined in section 5.1.2.1, thus it is not practical to give full expressions for the steeper potentials here. The most striking feature here is the existence of a non-zero stress component in the normal direction, this implies a non-zero normal stress difference which is a clear indication of non-Newtonian behaviour. Here, in agreement with the results in section 5.1.1, the normal stress difference is positive implying that the fluid pulls inwards in the gradient direction, as is common for colloidal dispersions[47,57,58]. Physically this can be thought of as the particles being pulled apart in the flow direction due to the increased magnitude of the interaction forces arising from the fact that the imposed flow field has reduced the characteristic distance between them[57]. This can be seen in figure 5.9 in the images that correspond to the point where the system has reached its steady state(10), where the line through the centre of the ellipse in the flow direction is shorter than the same line in the gradient direction and much shorter than the diameter of the circle that describes the same contour at equilibrium. This along with the fact that the fluid is incompressible means that there must be a force of equal magnitude in the gradient direction pulling the particles together. The existence of this positive normal stress difference may also be of significance to the pattern formation process that results in band patterns as; one may think of the pressure drop in the gradient direction as forcing particles in the sheared fluid, around the end of an obstruction, towards the obstruction itself, as well as one another, while further compacting the existing blockage.

Figure 5.18 shows the stress-strain relationship, for both the shear and normal stress, predicted by this constitutive relation in shear flow for all of the even power law interactions from $U = r^{-4}$ to $U = r^{-16}$, as in section 5.1.2.1.

---

(9) For completeness $\delta = \tan^{-1}\left\{\frac{\sqrt{(7+3\kappa^2)(3+7\kappa^2)}}{2(1+\kappa)(1-\kappa)}\right\}$, though this does not affect the flow curve.

(10) In these plots the tick marks on the axes correspond to the radius of the equilibrium two particle distribution function.

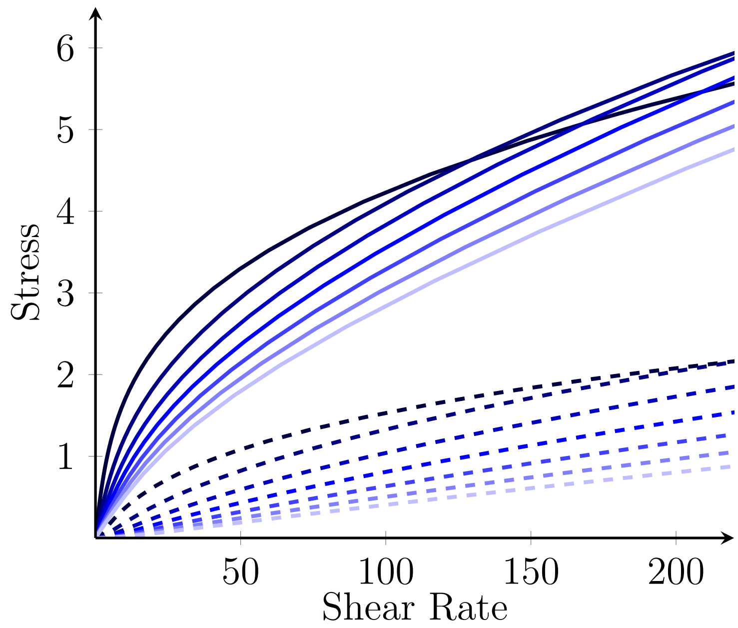

Figure 5.18: Plot showing the magnitudes of the normal and shear stresses in steady shear flow, like that shown in figure 5.9, as a function of shear rate. The different coloured lines show the relationship for fluids with different, repulsive, power law interaction potentials, ranging from $U = r^{-16}$, in palest blue, to $U = r^{-4}$, in darkest blue, in steps of two. The dashed lines show the normal stress while the solid lines show the shear stress.

As with uniaxial extension there is clear evidence of shear thinning behaviour in both the shear and normal stress for all of the interaction potentials at relatively high shear rates. This behaviour can also be seen in the plots of the effective extensional and shear viscosities presented in figures 5.19a and 5.19b respectively.

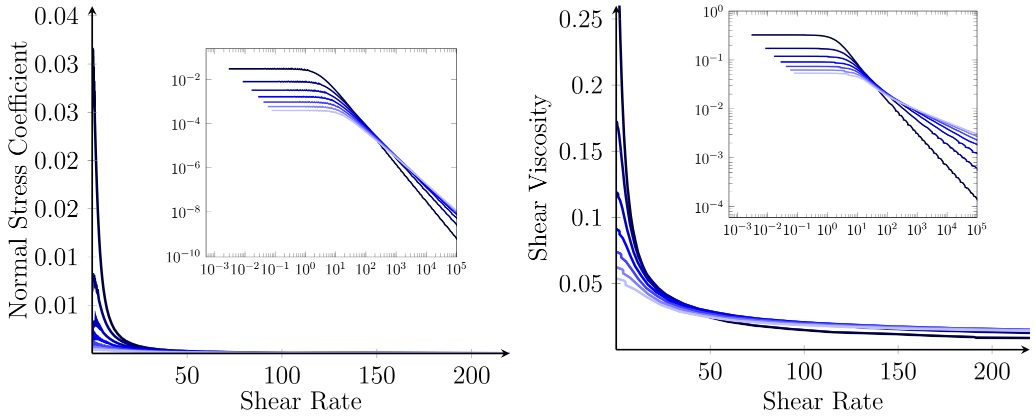

(a) Normal stress coefficient.

(b) Shear viscosity.

Figure 5.19: Plots showing the effective extensional and shear viscosities as a function of shear rate for a system undergoing simple shear flow, like that shown in figure 5.9. The different coloured lines show the relationship for fluids with different, repulsive, power law interaction potentials, ranging from $U = r^{-16}$, in palest blue, to $U = r^{-4}$, in darkest blue, in steps of two. The inserts show the same data on a logarithmic scale.

Also in this flow field, as with the extensional viscosity in uniaxial extension, the shear viscosity exhibits a Newtonian region at low shear rates followed by a shear thinning region at higher shear rates. This can be explained in much the same way, by appealing to the fact that the flow field drives rearrangements in the microstructure. As in section 5.1.2.1 the stress-strain rate relationship was approximated in the limit of $\kappa \to \infty$ to fit a power law approximation,

$$\Sigma = a\dot{\gamma}^b \tag{5.3}$$

where Σ is the shear stress and a and b are free parameters, specific to the interaction potential. The results of this are presented in table 5.4 with their corresponding asymptotes potted alongside the data from the full model in figure 5.20.

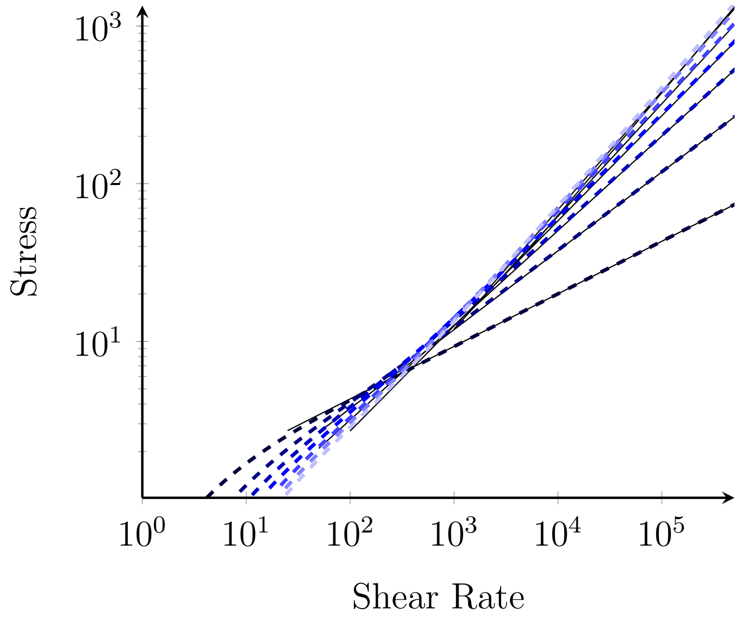

Figure 5.20: Plot showing the shear stress in steady state shear flow, like that shown in figure 5.9, as a function of shear rate. The different coloured lines correspond to fluids with different interaction potentials, ranging from $U = r^{-16}$, in palest blue, to $U = r^{-4}$, in darkest blue, in steps of two. The fine back lines show the approximation in the high shear rate portions of the curves.

Potential	Constant (a)	Exponent (b)
$U = r^{-4}$	0.92959	$\frac{1}{3}$
$U = r^{-6}$	0.37525	$\frac{1}{2}$
$U = r^{-8}$	0.20047	$\frac{3}{5}$
$U = r^{-10}$	0.12529	$\frac{2}{3}$
$U = r^{-12}$	0.08626	$\frac{5}{7}$
$U = r^{-14}$	0.06840	$\frac{3}{4}$
$U = r^{-16}$	0.04875	$\frac{7}{9}$

Table 5.4: Table of parameters for the function $\Sigma_{ab} = a\dot{\gamma}^b$ for the shear stress as a function of shear rate in steady shear flow, at high shear rate.

Perhaps unsurprisingly, despite the more complicated parametric expressions, one sees the same general trend in the results as that observed in the corresponding asymptotes for uniaxial extension. This is unsurprising as one would not expect the rearrangements of the microstructure caused by the flow field to depend strongly on the geometry of the flow field and rather only on the Péclet number, which is merely a measure of the rate of flow in comparison to the rate of diffusion. As before, this is coupled with a general decrease in the magnitudes of the constants of proportionality, consistent with the lower Newtonian viscosity.

What is more interesting are the results for the normal stress coefficient. Figure 5.19a clearly shows an increase at low strain rates followed by a smooth transition to shear thinning around the same region as the shear viscosity becomes non-Newtonian. This low shear rate region, where the Péclet number is less than unity, along with the shear thinning region, was expanded, in the limits of $\kappa \to 1$ and $\kappa \to \infty$, to match the power law function in equation 5.3, where Σ plays the role of the normal stress difference, and the results are given in tables 5.5 and 5.6 respectively, with both sets of asymptotes results plotted alongside the data in figure 5.21.

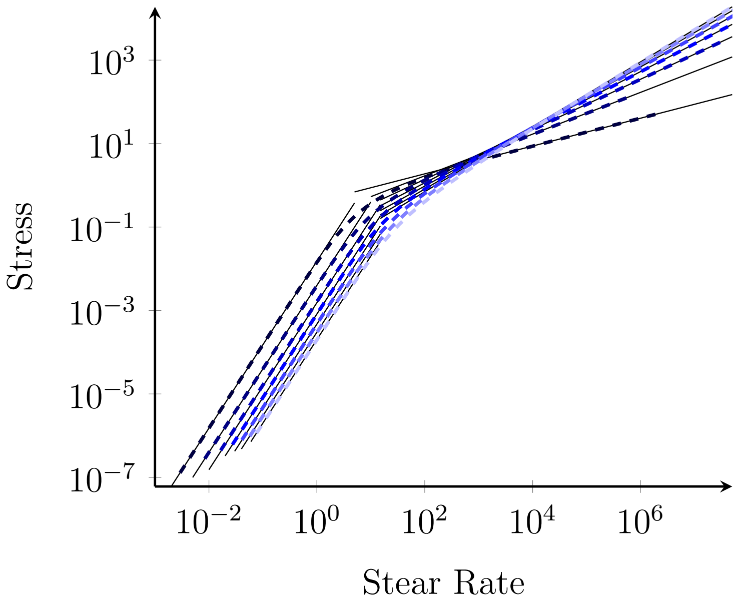

Figure 5.21: Plot showing the normal stress difference in steady state shear flow, like that shown in figure 5.9, as a function of shear rate. The different coloured lines correspond to fluids with different interaction potentials, ranging from $U = r^{-16}$, in palest blue, to $U = r^{-4}$, in darkest blue, in steps of two. The fine back lines show the results of approximations in the low and high shear rate portions of the curves.

Potential	Constant (a)	Exponent (b)
$U = r^{-4}$	0.01514	2
$U = r^{-6}$	0.00399	2
$U = r^{-8}$	0.00153	2
$U = r^{-10}$	0.00082	2
$U = r^{-12}$	0.00047	2
$U = r^{-14}$	0.00030	2
$U = r^{-16}$	0.00020	2

Table 5.5: Table of parameters for the function $\Sigma_N = a\dot{\gamma}^b$ for the normal stress difference as a function of shear rate in steady shear flow, at low shear rate.

Potential	Constant (a)	Exponent (b)
$U = r^{-4}$	0.40571	$\frac{1}{3}$
$U = r^{-6}$	0.16881	$\frac{1}{2}$
$U = r^{-8}$	0.08749	$\frac{3}{5}$
$U = r^{-10}$	0.05310	$\frac{2}{3}$
$U = r^{-12}$	0.03571	$\frac{5}{7}$
$U = r^{-14}$	0.02575	$\frac{3}{4}$
$U = r^{-16}$	0.01952	$\frac{7}{9}$

Table 5.6: Table of parameters for the function $\Sigma_N = a\dot{\gamma}^b$ for the normal stress difference as a function of shear rate in steady shear flow, at high shear rate.

At low strain rates these results show a proportionality of $\Sigma_N \propto \dot{\gamma}^2$, for all interaction potentials, as one expects for colloidal dispersions at low strain rates[58]. Furthermore, as with the shear stress and the normal stress during uniaxial extension, one sees a general decrease in the constants of proportionality, which is consistent with the observation that the fluids with shallower potentials exhibit a greater resistance to flow at low strain rates.

At higher strain rates one sees a similar general trend, in both the constants of proportionality and the exponents, to that observed for the shear stress, in that the constants are reduced as the interaction potential is made steeper while the exponents are enhanced, implying a higher resistance to flow at low strain rates followed by faster shear thinning for the fluids with shallower interaction potentials[11]. These trends are shown in figure 5.22.

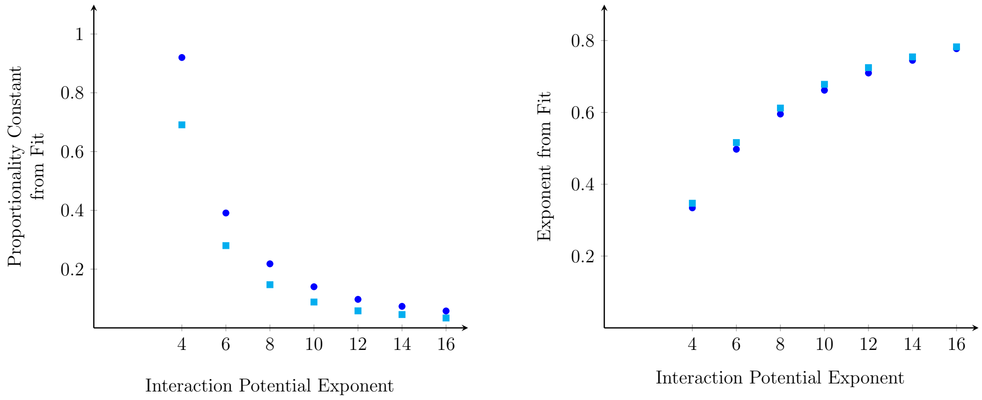

(a) Constant of proportionality. **(b)** Exponent.

Figure 5.22: Plots showing the parameters from equation 5.3 at high shear rate as a function of the power law interaction between the particles. Here the blue circles (●) correspond the the values obtained from the shear component of the stress and the cyan squares (■) correspond to the results obtained from the normal stress difference.

As with uniaxial extension, and in good agreement with what one observes from the plots of the effective viscosity in figure 5.19, these results show a tendency toward Newtonian behaviour with progressively smaller constants of proportionality as the potentials become steeper. Despite the fact that the parametric equations are more complicated in shear flow the reasons behind this tendency are the same as those explained for uniaxial extension.

These results are also in excellent agreement with the results of the theoretical model presented in reference 58 in the absence of hydrodynamic forces, which predicts the same Newtonian and shear thinning behaviour for the shear viscosity and also very similar behaviour for the normal stress difference, with the transition region around a Péclet number of order one to ten, as is the case here. This behaviour is also in good qualitative agreement with experimental results for many colloidal systems[34,49,76,126,164] at low concentration and low strain rates.

In much the same way as described in section 5.1.2.1, in the context of uniaxial extension, the total deformation of the two particle distribution function is reduced as the potential becomes steeper at all values of the Péclet number. An example of the exact form it takes in the case of shear flow is given in figure 5.23.

---

[11] This can also be seen clearly from the plot of the normal stress coefficient as a function of strain rate in figure 5.19a.

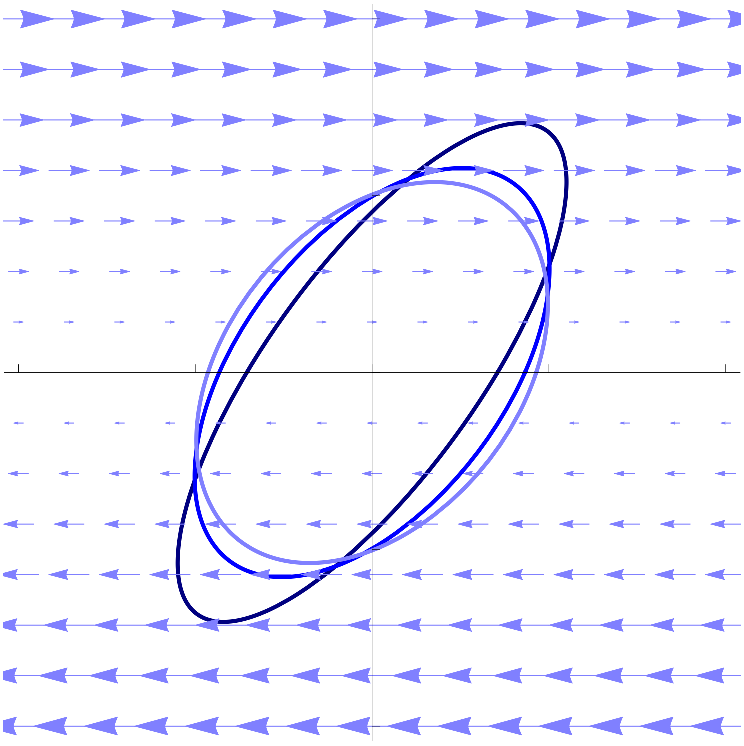

Figure 5.23: Diagram showing a contour of the two particle distribution function during steady shear flow. The darkest blue (—) corresponds to an interaction potential of $U = r^{-4}$, the lightest (—) to $U = r^{-8}$ and the intermediate shade (—) to $U = r^{-6}$, while the arrows (→) show the direction of the fluid velocity and their size corresponds to its magnitude, here $\dot{\gamma} = 50$. All three contours had the same equilibrium radius, integer multiples of which are indicated by the tick marks.

Here one can see that the axes of the two particle distribution function are not aligned with the axes of symmetry in the flow field, in the same way as they are not aligned in figure 5.9, and hence the origin of the normal stress difference.

5.1.3 Solutions to the Low Strain Approximation

Thanks to the linearity of equation 3.116 it was possible to use the time derivative of equation 3.115 to eliminate the rate of change of the stress tensor and solve the resulting linear differential equation,

$$\delta\dot{\mathbf{F}} : \mathbf{A} = \mathbf{E} : \mathbf{B} + \delta\mathbf{F} : \mathbf{C} + \mathbf{E} : \delta\mathbf{F} : \mathbf{D}, \tag{5.4}$$

for the perturbation to the deformation gradient tensor, $\delta\mathbf{F}$, as a function of time having evaluated the four constant matrices, $\mathbf{A}$, $\mathbf{B}$, $\mathbf{C}$ and $\mathbf{D}$. This solution was then substituted back into equation 3.115 to obtain the stress as a function of time. The main advantage to this is that, unlike the full model, which becomes difficult to evaluate when the interaction potential is anything more complicated than a short power series in the separation, the procedure used here is independent of the interaction potential so can be applied in many more situations. That said the bulk of this section will be focused on single power law interaction potentials, as this provides a route for direct comparison with the full model, making it possible to assess the limitations of the low strain approximation.

5.1.3.1 Solutions for Fluids With Single Power Law Interaction Potentials

The first thing to notice about equation 5.4 is that its form suggests that, for any interaction potential, the stress will approach its steady state in an exponential fashion. This is in good agreement with the dynamical behaviour of the full model discussed in section 5.1.1, where it was demonstrated that as the system approaches equilibrium(12) after a prior

---

(12) When the total strain becomes small.

deformation the stress decays exponentially. Figure 5.24 shows the prediction of the low strain approximation for the stress compared to the prediction of the full model as the fluid relaxes after the same initial deformation.

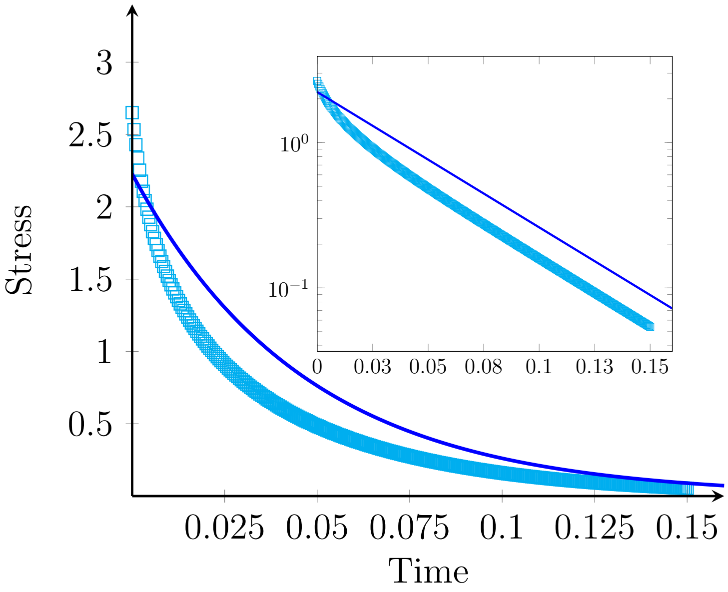

Figure 5.24: Plot comparing the stress predicted by the low strain approximation, indicated by the blue line (—), with that calculated from the full model, marked by the cyan squares (□), as the system relaxes after a step strain. The insert shows the same data plotted on a scale with a logarithmic y axis. This example was generated using an interaction potential of $U = r^{-4}$ and an initial stain of $\kappa = \frac{7}{3}$.

Here it is clear that, as one might expect, the main difference in the dynamics occurs at the start, with the full model predicting a higher initial stress, despite the fact that the deformation is the same, due to the higher order terms. This, initial, stress then decays more rapidly than a single exponential in the case of the full model, as is clear on the logarithmic scale. However, once this initial large deformation has decayed, it is clear that both models predict exponential decay at the same rate. In order to better understand the role that the structure of the fluid plays in determining the stress in the two models one must examine the behaviour of the two particle distribution function. Figure 5.25 shows how the two particle distribution function of the low strain model changes with time compared to that of the full model.

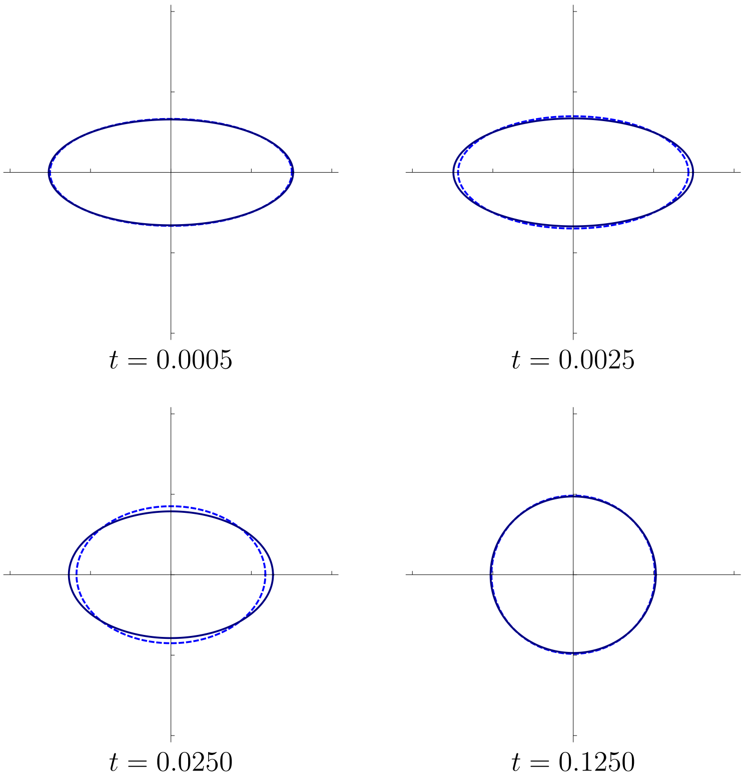

$t = 0.0005$ $t = 0.0025$

$t = 0.0250$ $t = 0.1250$

Figure 5.25: Diagrams showing how a contour of the two particle distribution function, as predicted by the low strain approximation, changes as the system relaxes after an initial step stain. The dark blue solid line (—) shows the prediction of the low strain approximation while the dashed blue line (- - -) shows the full solution. This example was generated using an interaction potential of $U = r^{-4}$.

As with figure 5.24, figure 5.25 clearly shows that the full model predicts a faster initial relaxation of the structure than the low strain approximation does. This is likely to be due to the fact that the contribution of the higher order terms in the equation for the rate of change of the stress is significant when the deformation is large, as it is immediately after the initial strain is released. Somewhat surprisingly, by comparing figures 5.24 and 5.25, one sees that a significant proportion of the difference between the predictions for the stress comes from the equations for the stress at a given deformation, since there is relatively little difference in the shapes of the contours of the two particle distribution functions predicted by the two models given the relatively large differences in the predicted stress shortly after the initial deformation. Clearly this is a result of higher order strain terms in the equation for the stress as a function of strain.

As well as relaxation it is also worth considering what the low strain approximation predicts in terms of the dynamics of the system when in steady flow. To this end its behaviour in both uniaxial extension and simple shear flow was investigated. For uniaxial extension, of a single power law fluid, $U = r^p$, in two dimensions starting from an unstressed state, the stress was found to evolve according to

$$\mathbf{\Sigma}_{ls} = -\frac{(p-1)(2+p)}{p^3(3+p^2)}\pi\Gamma\left\{\frac{2}{p}\right\}\left[1-e^{-\frac{p^2\left(3+p^2\right)}{2(2+p)\Gamma\left\{\frac{2}{p}\right\}}t}\right]\begin{pmatrix}\dot{\epsilon} & 0\\ 0 & -\dot{\epsilon}\end{pmatrix}, \tag{5.5}$$

where p is the exponent of the interaction potential, $p < -2$ or $p > 0^{(13)}$, t is the time since the system was at equilibrium and $\dot{\epsilon}$ is the extension rate, as defined in section 4.4.1. There are two important things to mention here: firstly the stress approaches its steady state value in an exponential fashion, as one would expect given the form of equation 5.4,

---

(13) The model is not defined in the interval $-2 \leq p \leq 0$ because the integrals do not converge, as discussed in appendix B.1.

and secondly that the stress is linear in the strain rate, implying Newtonian behaviour, which is consistent with that observed in the full model at low strain rates. Though the original approximation made here was that the strain, and not the strain rate, was small, one would clearly expect the two to go hand in hand since the steady state strain is lower at lower strain rates and hence it makes good sense that the best agreement between the full model and the low strain approximation should occur at low strain rates. This behaviour is clearly visible in the stress-strain rate relationship shown in figure 5.26, where the two agree very closely until the Péclet number approaches order unity, where the full model begins to exhibit shear thinning behaviour.

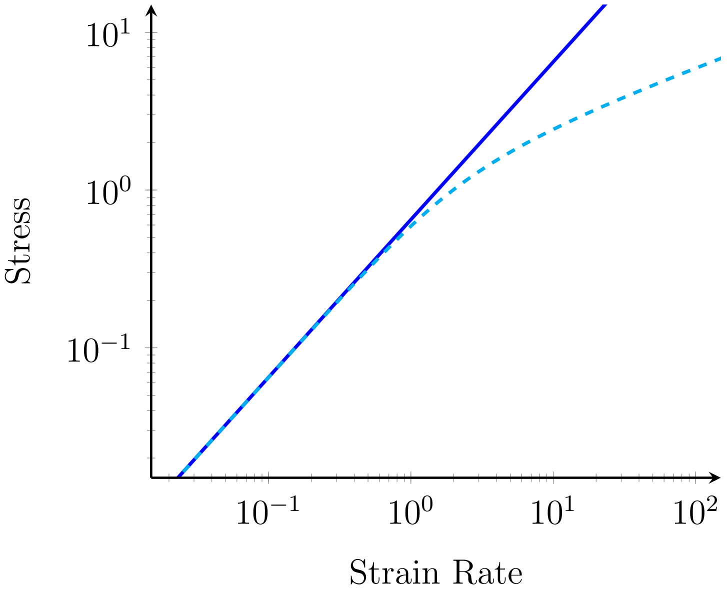

Figure 5.26: Plot comparing the stress-strain rate relationship predicted by the low strain approximation, shown by the solid blue line (—), during uniaxial extension to that of the full model, shown by the dashed cyan line (- - -). This example was generated using an interaction potential of $U = r^{-4}$.

At this point the stress predicted by the low strain model exceeds that predicted by the full model since the effect of the rearrangements caused by the flow field are not present at low order. It is worth pointing out here that, since it is clear from figure 5.26 and the previous argument that the low strain approximation is in excellent agreement with the full model within the Newtonian region, the term in front of the square brackets in equation 5.5 essentially gives the effective viscosity as a function of the exponent of the interaction potential.

Whilst on the topic of the structure it is worth considering what the two models predict for the shape of the two particle distribution function as the system approaches its steady state. Figures 5.27 and 5.28 show this for two different strain rates; one just above unity, where the approximation is still reasonable, and the other at a slightly higher strain rate, where the approximation has begun to break down.

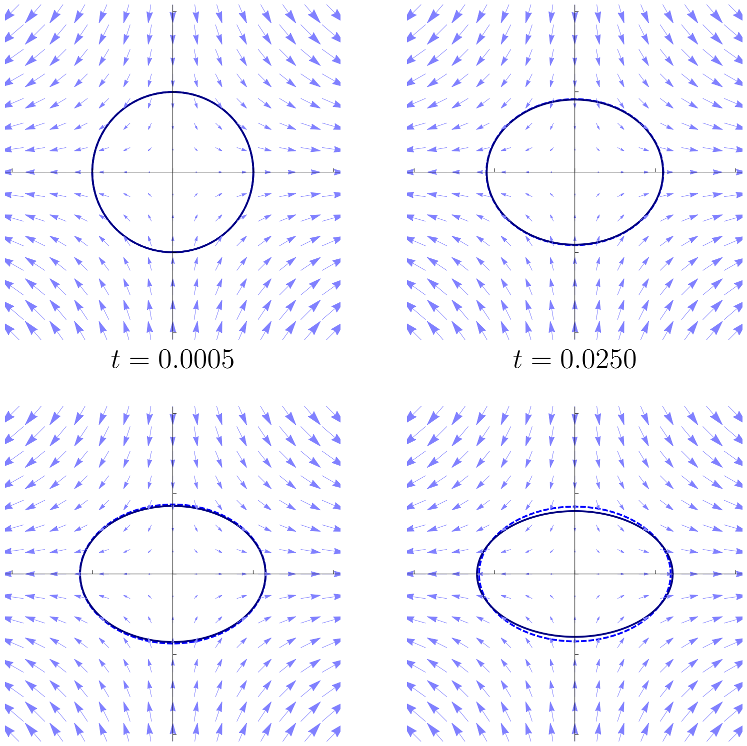

$t = 0.0005$ $t = 0.0250$

$t = 0.0500$ $t = 0.1250$

Figure 5.27: Diagrams showing how a contour of the two particle distribution function, as predicted by the low strain approximation, changes with time at the onset of uniaxial extension. The dark blue solid line (——) shows the prediction of the low strain approximation while the dashed blue line (- - -) shows the full solution. This example was generated using an interaction potential of $U = r^{-4}$ and and strain rate of $\dot{\epsilon} = 2$.

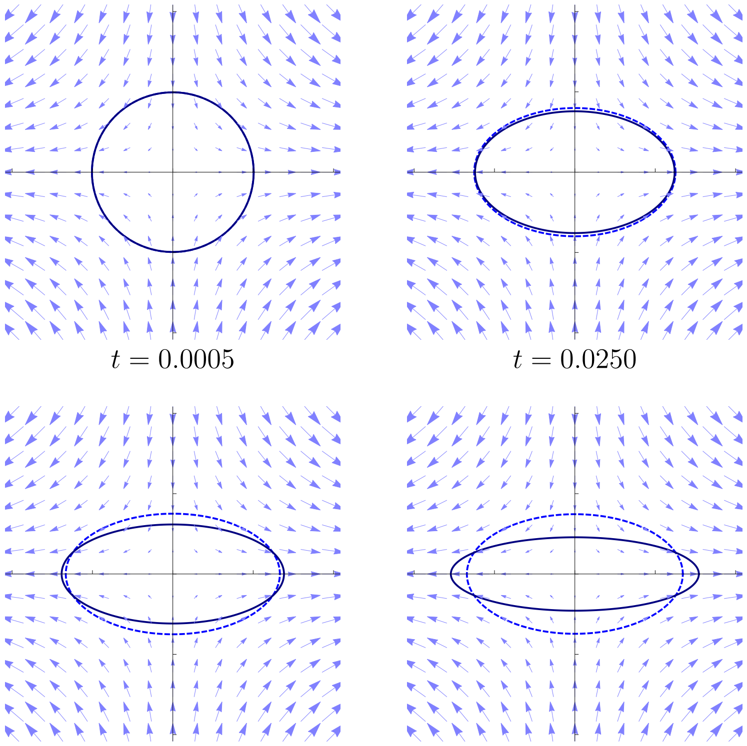

$t = 0.0005$ $t = 0.0250$

$t = 0.0500$ $t = 0.1250$

Figure 5.28: Diagrams showing how a contour of the two particle distribution function, as predicted by the low strain approximation, changes with time at the onset of uniaxial extension. The dark blue solid line (——) shows the prediction of the low strain approximation while the dashed blue line (- - -) shows the full solution. This example was generated using an interaction potential of $U = r^{-4}$ and strain rate of $\dot{\epsilon} = 5$.

In figure 5.27 it is clear that, even though the structure is slightly more deformed in the low strain approximation, there is generally good agreement between the two models as to the shape of the two particle distribution function at all times. By contrast figure 5.28 shows that as time goes on the discrepancies between the two become more and more apparent and it becomes clear that the low strain approximation gives a rather poor estimate of the shape of the two particle distribution function in steady state. Here as with the lower strain rate case the lack of the contribution from the higher order terms means that the structure, in the case of the low strain approximation, has reached a more deformed state before the forces arising from the microstructure match the forces applied by the incident flow field. The difference is that in the latter case, where the strain rate is higher, these higher order terms have a much more significant effect and thus the difference is far more noticeable. It is also worth noting that the deformation of the two particle distribution function predicted by the low strain model at the higher strain rate is relatively large, thus it is unsurprising that the approximation has broken down at this stage, as this is by no means a small strain.

Finally it is worth considering how the stress evolves as a function of time in each case, since this lends itself better to a more quantitative comparison. Plots showing the stress as a function of time for both strain rates are shown in figure 5.29.

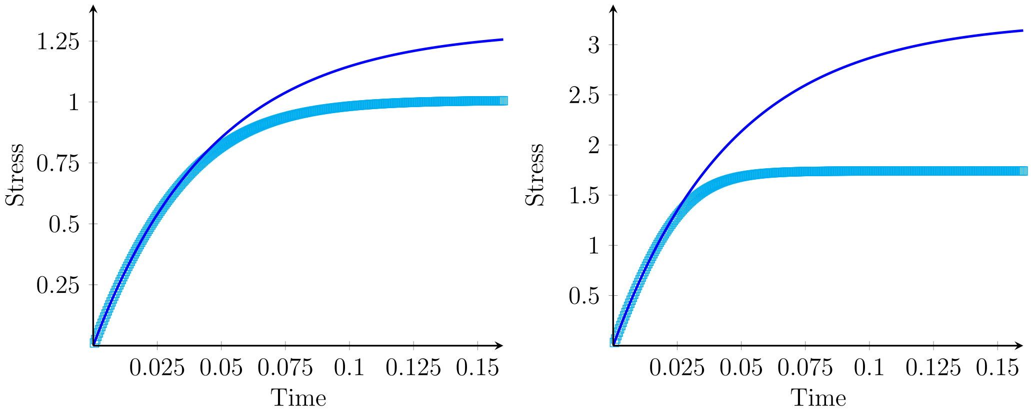

(a) $\dot{\epsilon} = 2$. **(b)** $\dot{\epsilon} = 5$.

Figure 5.29: Plots comparing the stress predicted by the low strain approximation, indicated by the blue line (—), with that calculated from the full model, mark by the cyan squares (□), for a system at the onset of uniaxial extension at two different extension rates, corresponding to the extension rates used to generate figures 5.27 and 5.28 respectively. These examples were generated using an interaction potential of $U = r^{-4}$.

Firstly looking at the plots individually it is clear that the low strain approximation does very well at first, which is to be expected since the overall strain is small. Then at slightly later times the stress, and in a similar way to the results for relaxation at larger strains, in the full model begins to curve more sharply than the exponential of the low strain model. Thus, in agreement with the results shown in figure 5.26, it reaches a lower steady state stress, since the effect of the higher order terms is to cause shear thinning. As well as reducing the steady state stress these higher order terms also allow for the steady state to develop more quickly than a simple exponential. This is most noticeable in figure 5.29b, where their effects are more pronounced. Once again this is in good agreement with the results for relaxation following a step strain, where it was also clear that the low strain approximation yielded slower relaxation. Comparing the values of the steady state stresses in both cases it is clear that, while the low strain approximation over estimates the stress by around 25% of the correct value at $\dot{\epsilon} = 2$, by $\dot{\epsilon} = 5$ it is out by nearly 100%, predicting close to double the value predicted by the full model. While it is difficult to say exactly under what conditions the low strain model fails, since there are no singularities in the full model, it is clear from the original approximation, made in section 3.4.5, that the low strain approximation is no longer valid if any of the terms in the perturbation to the deformation gradient tensor, $\delta\mathbf{F}$, exceed unity. Up to this point it is essentially a matter of how much uncertainty one is willing to accept in order to obtain the simplification to the equations of motion offered by this approximation. In this context it is worth noting that for the fluid used in the examples presented here the largest terms in the deformation gradient tensors were $\frac{5}{38}\sqrt{\pi} \approx 0.233$ and $\frac{25}{76}\sqrt{\pi} \approx 0.583$ for $\dot{\epsilon} = 2$ and $\dot{\epsilon} = 5$, respectively.

In addition to uniaxial extension the response of the low strain approximation in simple shear flow was also investigated. Figure 5.30 compares the time evolution of a contour of the two particle distribution function calculated from the low strain approximation to that of the full model.

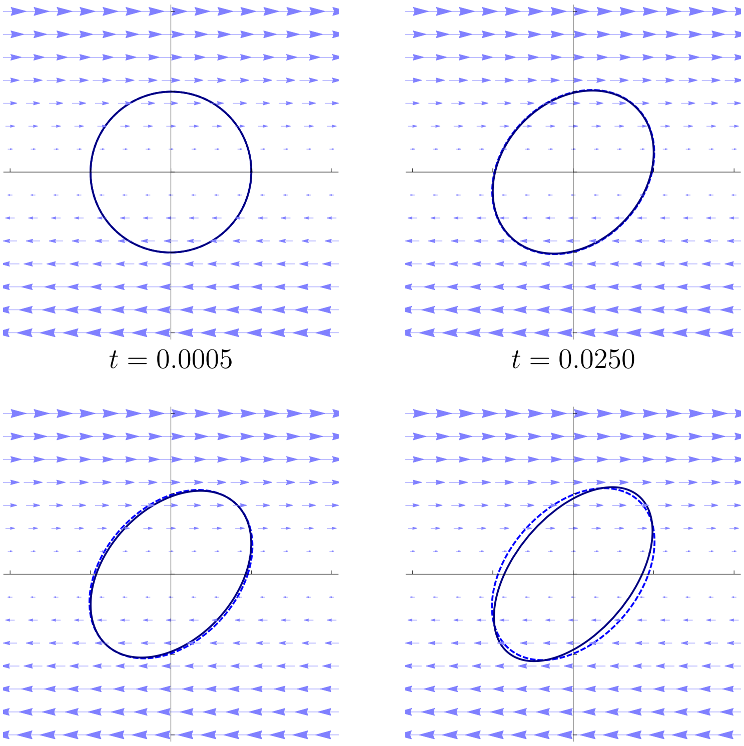

$t = 0.0005$ $t = 0.0250$

$t = 0.0500$ $t = 0.1250$

Figure 5.30: Diagrams showing how a contour of the two particle distribution function, as predicted by the low strain approximation, changes as during simple shear flow, with the system initially at equilibrium. The dark blue solid line (——) shows the prediction of the low strain approximation while the dashed blue line (- - -) shows the full solution. This example was generated using an interaction potential of $U = r^{-4}$ and a shear rate of $\dot{\gamma} = 5$.

This shows a similar kind of behaviour to that demonstrated during uniaxial extension in that the contour for the low strain approximation is more deformed at steady state and takes slightly longer to approach steady state since the higher order terms in the full model enable faster relaxation and result in less deformation, as they allow for the flow field to drive more rearrangements in the microstructure. An important consideration here, which was not relevant in the case of uniaxial extension, is the angle that the axes of the contour make with the axes of symmetry of the flow field. As in figure 5.30, these are the same for both models, suggesting that the stress within the fluid is shared between the different components of the stress tensor in the same way. This is unsurprising given that no approximations have been made about the angle, δ, between these two sets of axes.

As with uniaxial extension the shape of the two particle distribution function in isolation cannot give the whole picture, one must also consider the components of the stress tensor. This is particularly interesting in the case of shear flow since it was shown in sections 5.1.1.1 and 5.1.2.2 that the full model predicts a non-zero normal stress difference. Both components of the stress tensor, for both the full model and the low strain rate approximation, are shown in figure 5.31.

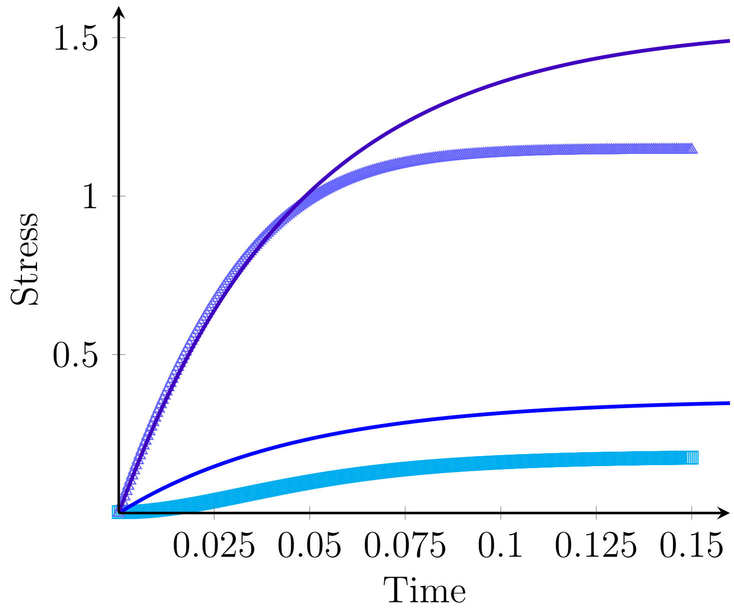

Figure 5.31: Plot comparing the stress predicted by the low strain approximation with the full model during simple shear, as in figure 5.30. The blue (——) and dark purple lines (——) show the normal and shear stresses, respectively, from the approximation, while the cyan squares (□) and light purple triangles (△) show their, respective, values from the full model. In this example $U = r^{-4}$ and $\dot{\gamma} = 5$.

Here as with uniaxial extension the low strain model over estimates the stress. This is true for both the shear and normal component and is to be expected as, once again, it is the higher order terms that are responsible for the shear thinning behaviour. Another property of figure 5.31 worth noting is the fact that, at short times, the low strain model is in good agreement with the full model in terms of the shear stress, which is to be expected since the total strain is still relatively small. Though the low strain model correctly captures the fact that there is a non-zero normal component, it is not well modelled, even at short times. Its shape is more complicated than the term in the low strain model, which is dominated by the exponential, allows for. While the solutions to the low strain model do have some sinusoidal dependence(14), to capture the rotation of the structure by the flow field, these are not strong enough to correctly capture the full complexity of this phenomenon. It is also worth noting that the magnitude of the normal component is much further from the steady state value given by the full model than the shear component is. This is worth remembering since one might argue that, judging by the shear component and the shape of the two particle distribution function, the low strain approximation has not yet broken down at $\dot{\gamma} = 5$, but if one is interested in the magnitude of the normal component then it is probably fair to say that the approximation has failed because the shear rate is too high, since the prediction of the low strain model is almost double that of the full model.

With this in mind it is worth considering the behaviour of the stress components as a function of shear rate. These are shown in figure 5.32.

---

(14) Unfortunately, because the full form of the solution for the stress tensor in simple shear flow is rather more complicated than that for uniaxial extension, it is not practical to show it here.

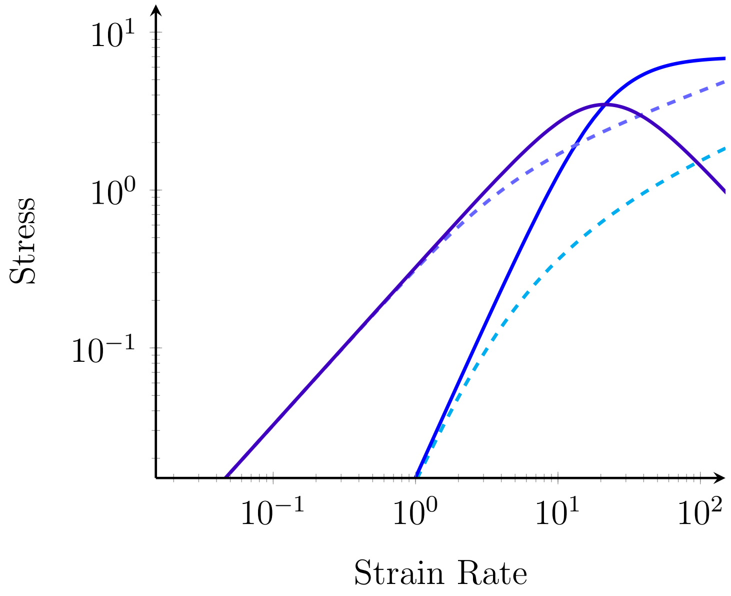

Figure 5.32: Plot comparing the the normal and shear stresses predicted by the low strain approximation, shown by the solid blue (——) and dark purple (——) lines for the normal and shear components respectively, to that of the full model, shown by the dashed cyan (- - -) and light purple (- - -) lines. This example was generated using an interaction potential of $U = r^{-4}$.

In this figure it is clear that, as with uniaxial extension, the low strain model correctly captures the stress-strain relationship at low strain rates and starts to deviate when the strain rate reaches order unity. Furthermore, this means that the shear component exhibits Newtonian behaviour and the normal component exhibits a $\Sigma_N \propto \dot{\gamma}^2$ dependence, as one might expect [58]. However, in contrast to uniaxial extension this does not continue indefinitely and there is a certain amount of curvature, with the shear component even having a turning point. While this is not completely unphysical it does demonstrate that the approximation has completely broken down by this point as the sinusoidal terms, which were present to deal with the rotation, begin to dominate and cause the unexpected behaviour. This is not a serious concern, however, since it occurs in the region far beyond the point where one would expect the model to be reliable.

5.1.3.2 Solutions Using a Potential of Mean Force for Hard Disks

While the simple power law interactions studied in this model so far have provided some interesting insight into its behaviour, there are relatively few physical systems to which they are directly relevant. An interaction potential of much greater physical relevance is that of hard particles, as there are many examples of particles that are well modelled by this interaction and these are very well studied both theoretically [4,5,35,58,133] and experimentally [34,49,76,126,164]. Though the constitutive relation discussed here is implicitly only valid for dilute solutions, since it assumes the inter-particle force is dominated by pair interactions, it is interesting, nevertheless, to examine its behaviour at higher volume fractions, firstly to see how far the model can be pushed and secondly to investigate what effect pairwise interactions have, even when the volume fraction is high. Volume fractions in this region also have relevance to the model of the particle-laden fluid discussed in section 3.1, where one may also be concerned with hard disks, which can jam at relatively high area fractions.

Since hard disks are a natural choice for a two dimensional system, like the particle-laden fluid, described in section 3.1, and all of the discussion involving this constitutive relation up to this point has considered two dimensional systems this section shall be devoted to hard disks, with discussion of hard spheres in the following section.

Since there is no straightforward closed form analytical expression, for the two particle distribution function of hard disks, this was calculated numerically, using a two dimensional variant of the algorithm described in section 4.3.10, for 1000 disks. A range of two particle distribution functions calculated using this method are shown in figure 5.33.

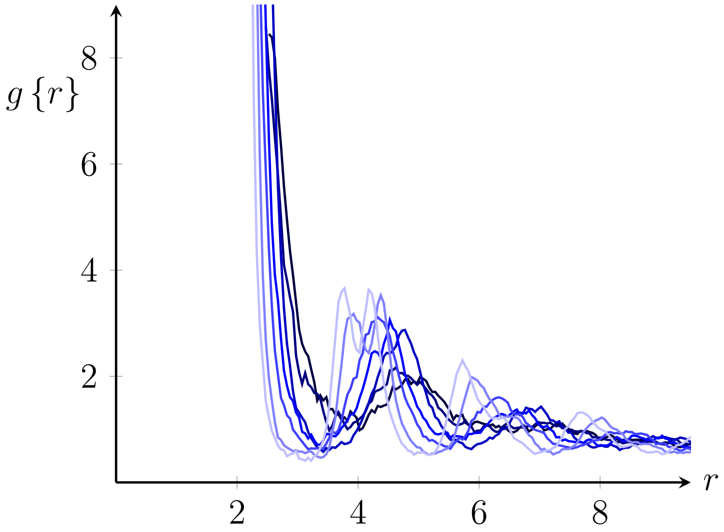

Figure 5.33: Plot of the two particle distribution function for hard disks at a range of different area fractions, as calculated using Monte-Carlo simulations on 1000 particles. Here the volume fractions ranged from 0.45 in the darkest blue to 0.75 in the lightest, in steps of 0.05.

Although this data is a little noisy one can still see the expected form clearly, thus given the fact that this is already an approximation and that the integrations necessary to obtain the constants needed for the low strain model had to be performed numerically this data is good enough to give a good indication of the behaviour predicted by the model. This data was then used to construct the potential of mean force using equation 4.85, such that g_e reproduce the correct shape for the two particle distribution function.

Once the constant matrices had been found at each volume fraction it was then possible to investigate the behaviour of the model in both extensional and shear flow, as in previous sections.

Here, as with the power law interactions, in the case of uniaxial extension the stress behaved in a Newtonian manner as a function of strain rate and evolved in time according to an equation of the form

$$\Sigma = \eta\dot{\epsilon}\left(1 - e^{-\alpha t}\right). \tag{5.6}$$

With this in mind it was possible to extract the effective viscosity, η, and the decay constant, α from the expressions. Figure 5.34 shows the effective viscosity as a function of volume fraction.

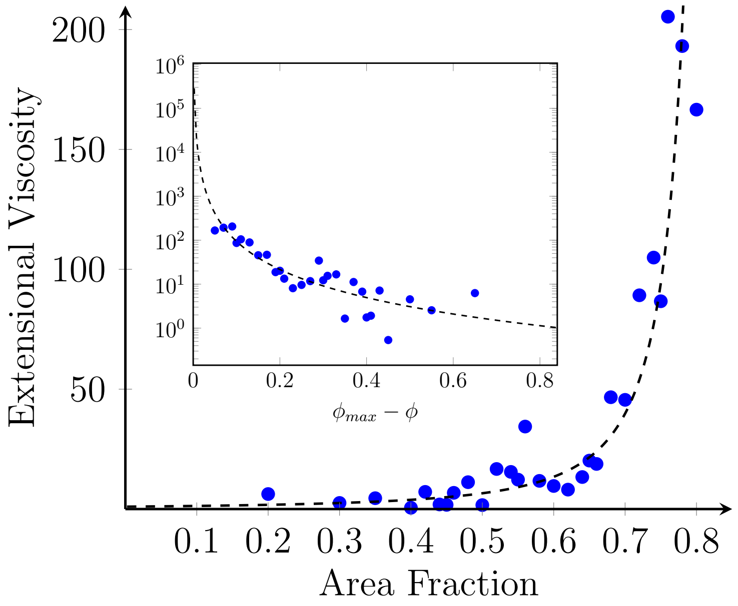

Figure 5.34: Plot showing the effective viscosity, η from equation 5.6, calculated using the low strain approximation for hard disks undergoing uniaxial extension as a function of volume fraction, shown by the blue circles (●). The dashed line (- - -) shows the fit obtained using equation 3.25, resulting in $\phi_{max} = 0.85 \pm 0.03$ and $[\eta] = 2.5 \pm 0.3$. The insert shows the same data with a logarithmic y axis.

Rather surprisingly given the level of approximation and the numerical calculations that have had to be performed to get to this stage, the fitting results(15) obtained from fitting the data in figure 5.34 with equation 3.25 are in remarkably good agreement with what one would expect for hard disks[31,172], having the commonly used $[\eta] = 2.5 \pm 0.3$ and a maximum volume fraction of $\phi_{max} = 0.85 \pm 0.03$ in the correct region for the glass transition[31] and random close packing[172]. Meanwhile the results of fitting the data for the relaxation rate, α, describing the approach to steady state, shown in figure 5.35, suggest a gradual reduction in the speed with which the system reaches its steady state as the volume fraction increases.

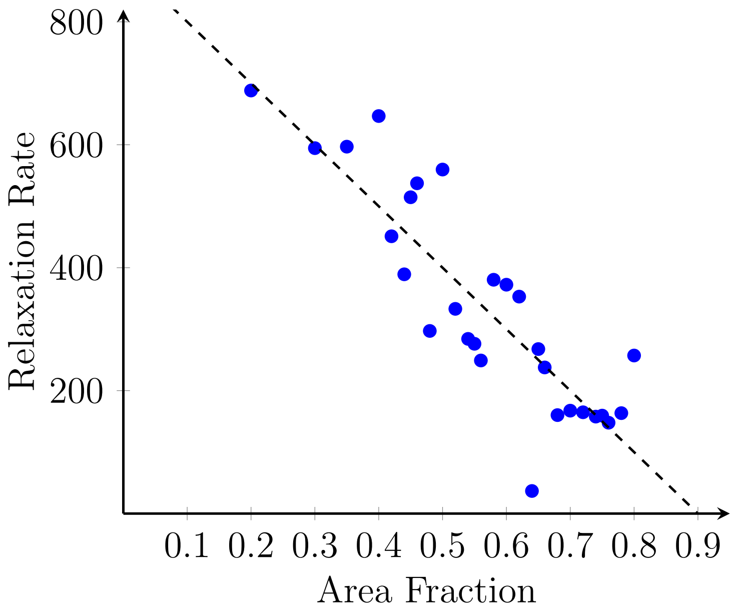

Figure 5.35: Plot showing the effective relaxation rate, α in equation 5.6, during uniaxial extension, according to the low strain approximation. Here the blue circles show the data (●) and the dashed line (- - -) make the line of best fit, $\alpha = -(1000 \pm 100)\,\phi + (900 \pm 60)$.

Here the fact that the relaxation rate is decreasing suggests that the dynamics within the microstructure are slowing down as the volume fraction is increased, which is in good

---

(15) To reduce the number of fit parameters, and produce a better fit, the data was normalised using approximate values for the solvent viscosity calculated from the results obtained in section 5.1.3.1. This was found to produce a better fit to the data than that obtained from simply fitting all three parameters.

agreement with what one would expect, since it becomes more and more difficult for particles to move and relax the structure. Importantly, extrapolation of the line of best fit reveals that, this rate reaches zero at $\phi = 0.9 \pm 0.1$ suggesting that the system is jammed and will not flow regardless of how much stress is applied. The fact that this is within the uncertainty of the value obtained for ϕ_{max}, from fitting of the effective viscosity, and the expected value for random close packing of disks[31,172] is very encouraging, and suggests that the model is computing the correct physical behaviour.

Finally for completeness figure 5.36 shows the behaviour of the viscosity as a function of volume fraction was largely the same in the Newtonian region(16) for simple shear flow(17).

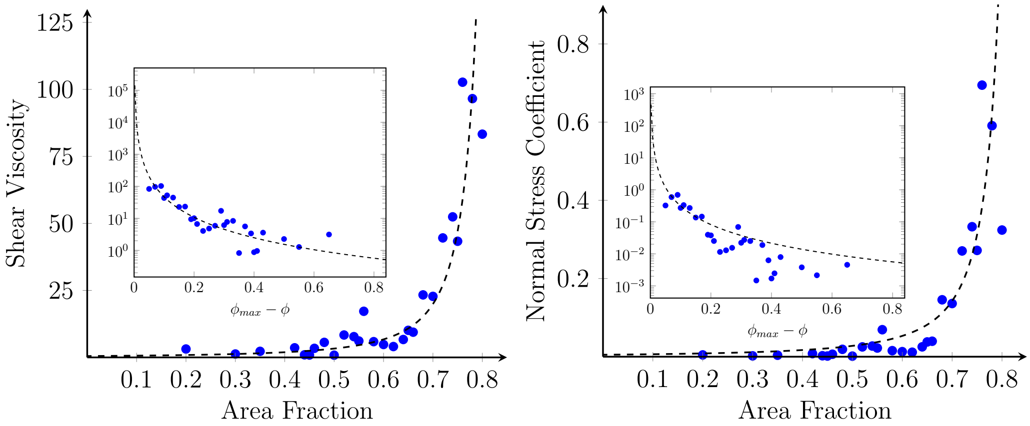

(a) Shear viscosity. **(b)** Normal stress coefficient.

Figure 5.36: Plot showing the effective viscosity, η from equation 5.6, calculated using the low strain approximation for hard disks undergoing simple shear as a function of area fraction, shown by the blue circles (●). The dashed line (- - -) shows the fit obtained using equation 3.25. The results of fitting the shear viscosity were: $\phi_{max} = 0.85 \pm 0.3$ and $[\eta] = 2.5 \pm 0.3$ while the result of fitting the normal stress coefficient, corresponding to the normal component of the stress were: $\phi_{max} = 0.85 \pm 0.03$ and $[\eta] = 2.3 \pm 0.3$. The inserts show the same data with a logarithmic y axis.

Here the fact that the popular Krieger-Dougherty[42] function(18), given by equation 3.25, for the viscosity as a function of volume fraction is such a good fit(19) for the data produced by the low strain approximation, and the fact that the correct constants are obtained, is somewhat surprising when one considers the number of approximations that have been made in the creation of the low strain approximation to the model, and the fact that it is not strictly valid at high volume fraction. One possible physical explanation for this is that when the total strain is small, as a result of low strain rate, or high frequency oscillations in the total strain, the forces arising in the microstructure due to interactions between the particles in fluid, which are well described by equation 5.6 must be dominated by pairwise interactions and thus fall into the remit of this constitutive relation even at high volume fractions.

---

(16) Here a shear rate of $\dot{\gamma} = 1$ was used, which is well below the point at which the low strain approximation breaks down.

(17) It was not possible to calculate the relaxation time in the same way as it was for uniaxial extension, because the time dependence of the stress in the case of shear flow is more complicated, as discussed in section 5.1.3.1.

(18) The choice of this function here is largely based on the fact that several works have shown the Krieger-Dougherty function to be an excellent fit for experimental data[18,49,53,62,76,124]. As such it provides a convenient means of comparing the present results with a number of experiments[18,49,53,62,76,124] on the kinds of fluids that this constitutive relation hopes to model.

(19) Here, as before, the effective solvent viscosity has been approximated using the data in section 5.1.3.1.

5.1.3.3 Solutions in Three Dimensions Using the Percus-Yevick Potential of Mean Force

In order to investigate the effects of volume fraction on the effective viscosity predicted by the low strain approximation, using the potential of mean force produced from the Percus-Yevick approximation for hard spheres[166], equations 3.115 and 3.116 had to be solved in three dimensional space, in order that they be complementary to the Percus-Yevick approximation itself. However, in order to maintain some similarity with the two dimensional model already discussed, as well as the model of the particle-laden fluid described in section 3.1, and to simplify the problem, by removing some of the degrees of freedom in the strain tensor, only situations where the flow was restricted to just two of the dimensions were considered(20).

As with the solutions in two dimensions, for both particles with power law interactions and hard disks, it was found that the stress approached its steady state in a manner dominated by an exponential decay and that at sufficiently low strain rates the stress-strain rate relationship was approximately linear in both planar and shear flow. The region over which this Newtonian flow behaviour was observed, before the low strain approximation failed, was found to be significantly narrower in the case of the three dimensional model of simple shear flow, especially at high volume fractions. This made it rather difficult to obtain reliable data for the effective viscosity at high volume fractions in this flow geometry(21). The normalised(22) viscosity as a function of volume fraction, for planar extension and simple shear, is shown in figure 5.37.

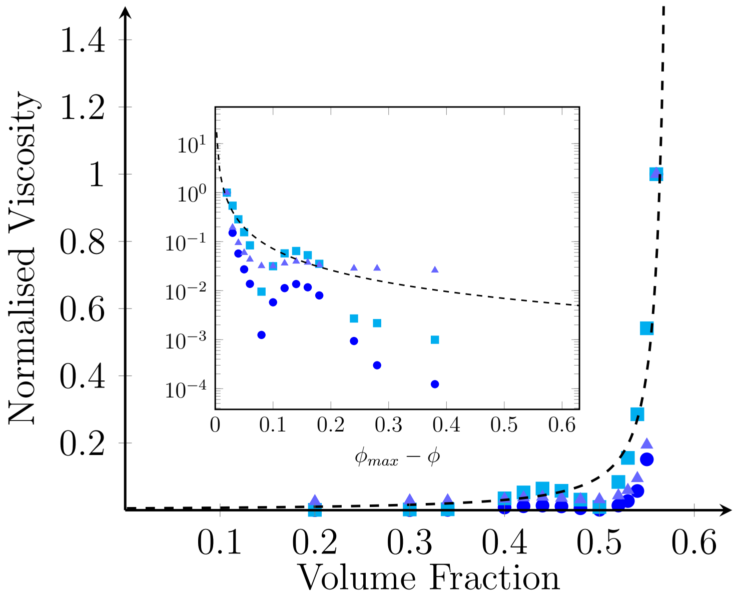

Figure 5.37: Plot comparing data for the normalised viscosity predicted by the low stain approximation applied to hard spheres with equation 3.25 with $[\eta] = 2.5$ and $\phi_{max} = 0.58$. The blue circles (●) correspond the viscosity during planar extension and the cyan squares (■) and light purple triangles (▲) to the shear viscosity and $\frac{\Sigma_N}{\dot{\gamma}}$, in shear flow, respectively. The insert shows the data on a logarithmic y axis.

---

(20) Though, in principle, it would be possible to solve the model for a fully three dimensional system given the appropriate constraints on the flow field.

(21) Thus it was necessary to successively reduce the shear rate to ensure that failure of the approximation was not misinterpreted as a divergence in the viscosity. The data points in figure 5.37 were taken at a Péclet number of 0.0001, where plots of the stress as a function of time confirmed that the approximation did not fail at any of the volume fractions shown.

(22) Here the normalisation is such that the maximum value from each data set is unity, so that the different data sets could be displayed on the same axes for direct comparison.

This shows that all three of the measured viscosities for the two different geometries are in good agreement with the semi-continuum model of the viscosity as a function of volume fraction[42,51], provided that the maximum volume fraction is set to the jamming point[18,31,70,123,127], $\phi_{max} \approx 0.58$, and not the value for random close packing. This is, of course, to be expected since this is a model of the kinetic properties of the system. However, it is clear from the data in figure 5.37 that the viscosity is diverging at the jamming point it is also worth pointing out that this result was re-enforced by the fact that it was not possible to find a stable solution for the stress beyond $\phi \approx 0.57$, no matter how weak the applied flow field was, suggesting that the model was predicting a jammed system, despite the fact that the Percus-Yevick approximation continued to produce reasonable potentials of mean force right up to the random close packing limit[166]. This result is very encouraging and, once again, shows that this relatively simple model does a surprisingly good job of capturing the correct physical behaviour, even at high volume fractions, far beyond what was expected given that only pairwise interactions have been considered.

5.1.4 Numerical Simulations

In order to verify the validity of the approximations made during the analytical evaluation of this constitutive relation a number of numerical simulations were run on the original equations of motion for the particles, as given by equation set 3.74, and described in section 4.4.4. The input parameters for these simulations were chosen to match the parameters used in the non-dimensionalisation of the model such that direct quantitative comparison could be made between the results. Figure 5.38 shows the results of one such simulation and the corresponding analytical results.

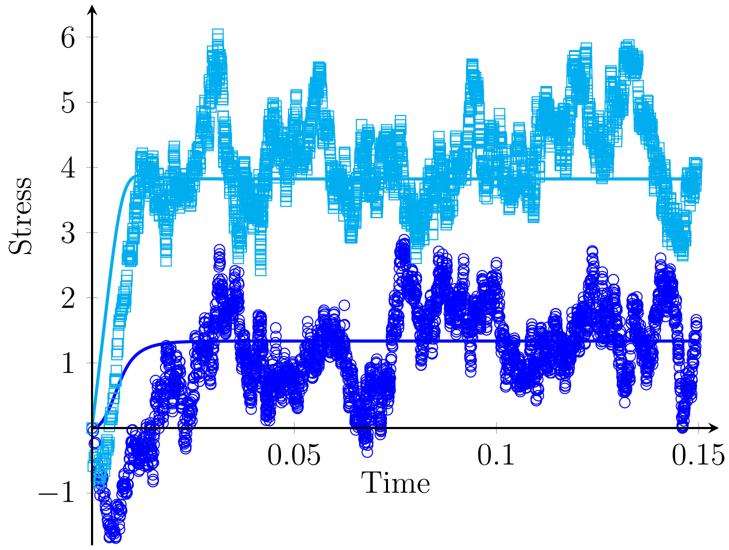

Figure 5.38: Plot comparing the results of a simulation run on the equations of motion of the constitutive relation to its analytical results. The cyan line (—) and cyan squares (□) show the shear stress for the analytical and simulation results respectively, while the blue line (—) and blue circles (○) show the normal component. Here $\dot{\gamma} = 75$ and $U = r^{-4}$ were used.

This shows excellent agreement between the simulation and analytical results in terms of the average values of the steady state stress for both the shear and normal components. Naturally there are very large fluctuations in the stresses obtained from the simulation due to the effects of the Brownian forces and the fact that there is a finite number of particles, meaning that one is able to detect events where two particles pass over one another in the stress. The shapes of the curves are also very similar in terms of how the stress builds up in the fluid. This is most noticeable in the shear stress. However, although the shearing began at the very beginning of the simulation time shown, figure 5.38 shows a significant lag time, between the point at which shearing begins and the point at which the stress begins to build up, with a short period where the stress is negative. One can think of this as being due to the fact that it takes a certain amount of time for the structures in the static particle fluid to break up and allow the particles to begin to move with the solvent. This is merely an artefact of the way in which the simulation was initialised to a state of zero stress.

Although only one example has been given here, it is worth making the point that this kind of strong agreement between the results of the simulation and analytical derivation was seen for a wide range of Péclet numbers, which as well as providing further support for the results in terms of the time evolution of the stress also supports the stress-strain relationship derived for this constitutive relation in steady state.

The fact that there is such a strong agreement between these two sets of results is hardly surprising since they are both based upon the same model. However, it does provide a certain amount of corroboration for the validity of the assumptions and approximations that needed to be made in order to progress with the analytical treatment.

5.2 Simulations of a Particle-Laden Fluid

5.2.1 Linear Stability Analysis

In order to make an analytical assessment of the stability of the particle-laden fluid model, linear stability analysis[3] was performed, using the method outlined in section 4.1.7.

5.2.1.1 Stability of the Basic Model

Upon solving equation set 4.37, for the most basic version of the model, where all of the friction coefficients and the viscosity were held constant, it was found that fluctuations with a wave number $\mathbf{q}$ would, to first order(23), grow exponentially at a rate, R_b, given by

$$R_b = -\frac{q^2\left(1-\phi_0\right)\left.\dfrac{\partial\hat{\pi}}{\partial\phi}\right|_{un}}{1+\left(1-\phi_0\right)\hat{\zeta}_p+\phi_0\hat{\zeta}_s+2\left[\left(1-\phi_0\right)\hat{\eta}+\phi_0\right]q^2}, \tag{5.7}$$

where $\hat{\zeta}_p$ is the non-dimensionalised friction coefficient for the particle-surface interaction, $\hat{\zeta}_s$ if the non-dimensionalised friction coefficient for the solvent-surface interaction, $\hat{\eta}$ is the ratio of the particle fluid viscosity to the solvent viscosity, ϕ_0 is the mean volume fraction of particles and q is the magnitude of the wave vector $\mathbf{q}$. Here the subscript un signifies that the quantities are to be evaluated in the uniform state.

Careful inspection of equation 5.7 reveals that the uniform state is stable as long as the slope of the osmotic pressure, at the average volume fraction is positive, since the rest of the fraction will be positive for all reasonable values of the system parameters. It is clear from figure 3.3 that this is true at both low and high, average, volume fractions for the most basic model, so in these limits one would expect all forms of pattern to be unstable and the system will decay to the uniform state. This was indeed observed to be the case in simulations run on this model in these limits and is discussed further in section 5.2.2.

---

(23) When the system was close to the uniform state.

At intermediate volume fractions, however, the gradient of the osmotic pressure is zero so one would expect neutral stability, where the patterns neither grow nor decay. This scenario will be discussed further in section 5.2.3.

For those patterns that decay, equation 5.7 also makes a prediction about how the rate of decay depends on the magnitude of the wave vector. This dependence is shown in figure 5.39.

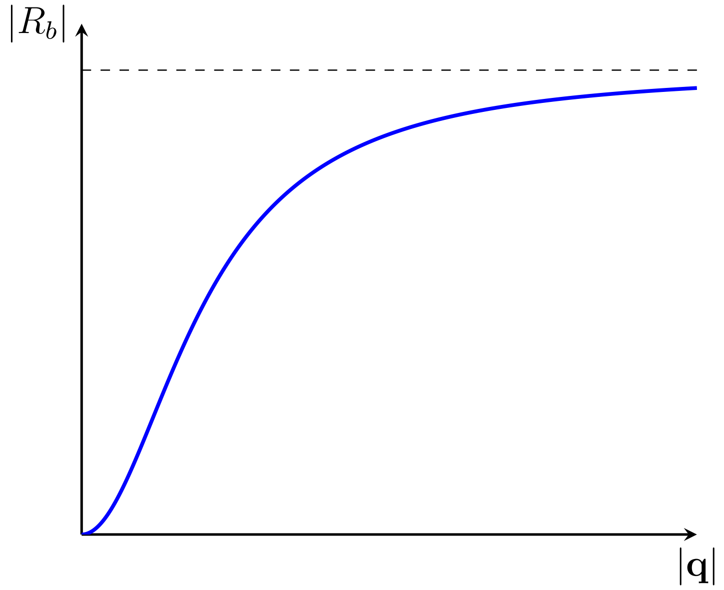

Figure 5.39: Sketch of the form of the decay rate of patterns, when the osmotic pressure has a positive gradient, as a function of the magnitude of the wave vector.

This implies that the patterns on the longest length scales decay the slowest. This is inline with what one might expect since the decay of larger patterns would require the movement of more particles.

For the purposes of completeness it is worth mentioning that the decay constant, R_b, was derived from the real part of equation 4.37d while the imaginary part,

$$\frac{\partial \theta}{\partial \hat{t}} = -\frac{\phi_0 \left(1 + \hat{\zeta}_s + 2q^2\right) \hat{\mathbf{v}}_{sd} \cdot \mathbf{q} - \left(1 - \phi_0\right) \left(1 + \hat{\zeta}_p + 2\hat{\eta} q^2\right) \hat{\mathbf{v}}_{pd} \cdot \mathbf{q}}{1 + \left(1 - \phi_0\right) \hat{\zeta}_p + \phi_0 \hat{\zeta}_s + 2\left[\left(1 - \phi_0\right) \hat{\eta} + \phi_0\right] q^2}, \tag{5.8}$$

corresponding to the argument, θ, of the complex amplitude of the volume fraction fluctuation, where $\mathbf{v}_{pd}$ and $\mathbf{v}_{sd}$ are the drift velocities of the particle fluid and solvent respectively. This can be thought of as the rate at which the pattern travels down the surface, since it converts between the sine and cosine functions as a description of the pattern as the peaks and troughs pass through the origin. Thus it makes sense that it should scale with the drift velocities.

5.2.1.2 The Effects of the Additional Features

In an attempt to make the simple model more physically realistic a number of features, described in section 3.1.2, were added. These included: the addition of non-Newtonian flow behaviour with respect to the shearing of the particle fluid normal to the plain, making the particle fluid's viscosity volume fraction dependent to model the resistance due to crowding and jamming effects, adding velocity dependence to the particle-surface friction coefficient to model the effect static friction at the individual particle level had on the continuum fluid, adding volume fraction dependence to the particle-surface friction coefficient to model the additional resistance that may be caused by the presence of other particles and adjusting the form of the osmotic pressure to account for diffusion and attractive interactions between the particles. In order to assess what effect these additional features had equation set 4.37 was solved once again, for a situation where all of the features, described in section 3.1.2, were implemented. For this model the rate of growth of the fluctuations, R_f, is given by

$$R_f = -\frac{\left.\dfrac{\partial\hat{\pi}}{\partial\phi}\right|_{un} q^2 \left(K + q^2\sqrt{|\hat{\mathbf{v}}_{pd}| - \hat{\mathbf{v}}_{pd}\cdot\hat{\mathbf{q}}}\left[\left.\dfrac{\partial\zeta_p}{\partial\hat{\mathbf{v}}_p}\right|_{un}\cdot\hat{\mathbf{q}}\right]\right)}{KL + q^2\left(L\sqrt{|\hat{\mathbf{v}}_{pd}| - \hat{\mathbf{v}}_{pd}\cdot\hat{\mathbf{q}}} + K\hat{\mathbf{v}}_{pd}\cdot\hat{\mathbf{q}}\right)\left[\left.\dfrac{\partial\zeta_p}{\partial\hat{\mathbf{v}}_p}\right|_{un}\cdot\hat{\mathbf{q}}\right]}, \tag{5.9}$$

where

$$K = \left.\hat{\zeta}_p\right|_{un} + \left.\hat{\eta}\right|_{un} q^2 + \frac{\left(\left.\hat{\zeta}_s\right|_{un} + q^2\right)(1-\phi_0)}{\left.\hat{\zeta}_s\right|_{un} + \phi_0 + q^2} \tag{5.10a}$$

$$L = \left.\hat{\zeta}_p\right|_{un} + 1 + 2\left.\hat{\eta}\right|_{un} q^2 + \frac{\phi_0\left(\left.\hat{\zeta}_s\right|_{un} + 1 + 2q^2\right)}{1-\phi_0} \tag{5.10b}$$

and $\hat{\mathbf{q}}$ is the normalised wave vector.

Close inspection of equations 5.10a and 5.10b reveals that both K and L will be positive for all reasonable values of the system parameters. Thus there are two situations of interest, when considering equation 5.9. The first point worth noting is that it depends on the osmotic pressure in the same way as equation 5.7(24), however, if the particles experience an attractive interaction potential, as described in section 3.1.2.6, there would, potentially, be a region of the osmotic pressure curve where there was a negative gradient and thus the uniform state would be unstable. This alone, however, would not be sufficient for the formation of patterns since, as figure 5.39 shows, the rate of growth increases monotonically with the magnitude of the wave vector so the fastest growing, and hence dominant, fluctuations would be just one particle in size and hence would not constitute a pattern. However, because of the addition of the $\nabla^2\phi$ term in equation 3.31 the wave vector dependence of the growth rate is modified, and takes the form shown in figure 5.40(25), where a dominant fluctuation, of wave vector q^*, will emerge[36] and with it a visible pattern.

---

(24) This is not surprising as equation 5.9 reduces to equation 5.7 if all of the flow dependent coefficients are held constant.

(25) For simplicity the plot shown is for a system were an attractive inter-particle interaction is the only addition to the basic model

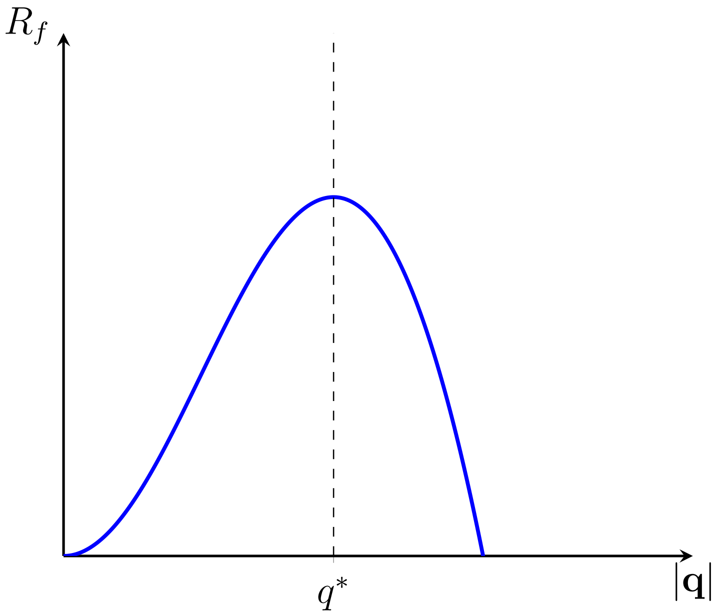

Figure 5.40: Sketch of the form of the growth rate of patterns, when the osmotic pressure has a negative gradient, as a function of the magnitude of the wave vector. Here q^* marks the position of the wave vector of the fluctuation that will grow the fastest.

This kind of behaviour is perhaps unsurprising since equation 3.31 is somewhat reminiscent of the Cahn-Hilliard equation[36,78,118] which is know to form patterns in systems without external flow fields or the presence of the free surface, which one would only expect to affect the shapes of patterns formed. It is not possible to say exactly what the effect of the dynamics will be from the solution of the linearised equations it is clear from equation 5.9 and equation set 5.10 that the surface tension terms do have a significant effect on which fluctuations will grow fastest.

Secondly one might expect that the velocity dependence of the particle-surface friction coefficient would effect the stability of the uniform state since having a negative gradient means that, under certain circumstances, it can make either the top or bottom of the fraction negative. In fact this is not the case, and the velocity dependence of the particle-surface friction coefficient does not affect the stability, though the reasons for this are quite subtle. Clearly for the stability to change one requires that either, but not both, the numerator or denominator of equation 5.9 changes its sign, as $\left.\frac{\partial \zeta_p}{\partial \hat{\mathbf{v}}_p}\right|_{un}$ is always negative, there are two conditions for this:

$$\frac{K}{q^2\sqrt{|\hat{\mathbf{v}}_{pd}| - \hat{\mathbf{v}}_{pd}\cdot\hat{\mathbf{q}}}} < \left|\left.\frac{\partial \zeta_p}{\partial \hat{\mathbf{v}}_p}\right|_{un}\cdot\hat{\mathbf{q}}\right| < \frac{KL}{q^2\left(L\sqrt{|\hat{\mathbf{v}}_{pd}| - \hat{\mathbf{v}}_{pd}\cdot\hat{\mathbf{q}}} + K\hat{\mathbf{v}}_{pd}\cdot\hat{\mathbf{q}}\right)} \tag{5.11a}$$

$$\frac{K}{q^2\sqrt{|\hat{\mathbf{v}}_{pd}| - \hat{\mathbf{v}}_{pd}\cdot\hat{\mathbf{q}}}} > \left|\left.\frac{\partial \zeta_p}{\partial \hat{\mathbf{v}}_p}\right|_{un}\cdot\hat{\mathbf{q}}\right| > \frac{KL}{q^2\left(L\sqrt{|\hat{\mathbf{v}}_{pd}| - \hat{\mathbf{v}}_{pd}\cdot\hat{\mathbf{q}}} + K\hat{\mathbf{v}}_{pd}\cdot\hat{\mathbf{q}}\right)}. \tag{5.11b}$$

Upon multiplying through by $\frac{|\hat{\mathbf{v}}_{pd}|q^2}{KL}$ one immediately sees that equation 5.11a can never be satisfied. While it is possible to satisfy equation 5.11b and thus predict a change in the stability, when one considers the physical meaning behind this condition it becomes clear that the predicted change in sign is an artefact caused by the linearisation of the equations, since it predicts the existence of a wave vector for which the denominator of equation 5.9 is zero, corresponding to an infinite growth rate. This comes about because the linear approximation to the velocity dependence of the particle-surface friction coefficient fails to correctly capture the fact that the friction coefficient, described in equation 3.26, remains finite, and positive, as the particle velocity tends to infinity.

5.2.2 The Decay of Fluctuations to a Uniform Steady State

According to equation 5.7 linear stability analysis predicts that any fluctuations about the uniform state will decay exponentially in time if the gradient of the osmotic pressure with respect to the volume fraction is positive at the mean volume fraction(26). Equation 5.7 also predicts the rate a which this decay will occur based upon the properties of the fluids. In order to investigate the extent to which these predictions, based on the linearised model, agreed with the full model several simulations were run with mean volume fractions in the region of the osmotic pressure curve where its gradient was positive. Figure 5.41 shows how the standard deviation in the volume fraction, which can be thought of as a measure of the magnitude of the volume fraction fluctuations, decays over time in this region for a selection of different parameters.

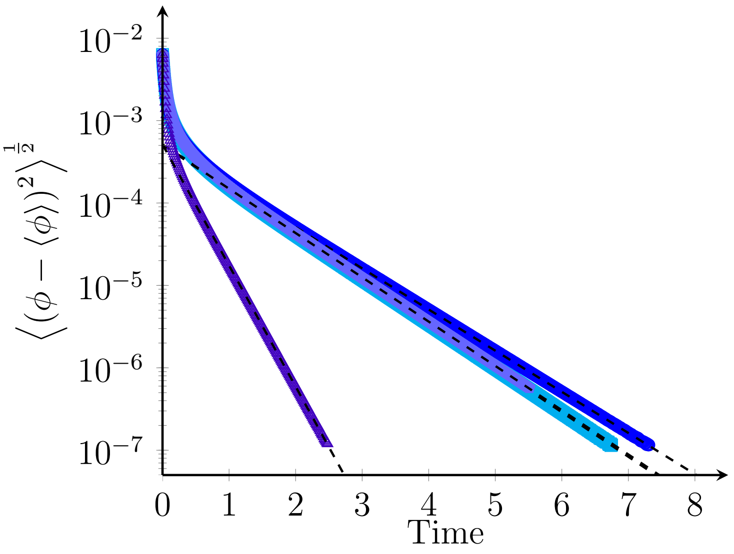

Figure 5.41: Plot showing the decay of the standard deviation in the volume fraction for four different systems. The parameters used here were $\hat{\rho} = 1.2$, $\hat{\mathbf{g}} = 5\hat{\mathbf{y}}$, $\phi_0 = 0.5$, $\phi_{max} = 0.64$, $\phi_l = 0.2$ and $\phi_u = 0.44$ with:

	$\hat{\zeta}_p$	$\hat{\zeta}_s$	$\hat{\eta}$
□	15	1.5	1
○	15	3	1
△	15	1.5	2
⬠	3	1.5	1

The dashed lines (- - -) show the fit results.

The first thing to notice here is that, as predicted by the linear stability analysis of section 5.2.1.1, the magnitudes of the fluctuations decay exponentially at later times when the overall magnitude is small, and this is precisely the region where one would expect equation 5.7 to perform best, since it is based on an expansion about the uniform state. However, the data clearly shows different behaviour very shortly after the simulations began, while the magnitude of the fluctuations is still relatively large. This, faster decay, could easily be misinterpreted as being due to the failure of the linearised model and attributed to higher order terms, but if one takes a closer look at equation 5.7 it is clear that the decay rate predicted by the linear theory depends strongly on the magnitude of the wave vector of the fluctuation in question and in fact what figure 5.41 shows is a superposition of all of these decays. It is the shortest wavelength fluctuations, that decay rapidly, leading to the steep section immediately after initialisation. Since these decay rapidly they soon become negligible and the decay rate tends towards that of progressively longer wavelength fluctuations. Thus the latter part of the plot, which takes the form of a single exponential, is in fact dominated by the decay of the longest wavelength fluctuation in the system, as the amplitudes of all shorter wavelength fluctuations have become negligible by comparison.

---

(26) If the gradient is negative then it predicts fluctuations will grow, but this situation is excluded from the basic model since there are no physical processes within the model that would lead to a negative gradient in the osmotic pressure.

With this interpretation in mind it was possible to fit a single exponential to the later portion of the data and ascertain the decay rate. After inspecting figure 5.41 carefully it was decided that the last 80% of data points should be used for this as the deviation from linearity, on a logarithmic scale, in this region was very small in comparison to the range of values. The results of these fits are given in table 5.7, and indicated by the dashed lines in figure 5.41.

Parameters			Decay Rate	
$\hat{\zeta}_p$	$\hat{\zeta}_s$	$\hat{\eta}$	Theoretical	Fit
15	1.5	1	1.2627	1.2449 ± 0.0002
15	3	1	1.1700	1.1501 ± 0.0002
15	1.5	2	1.2482	1.2376 ± 0.0004
3	1.5	1	3.447	3.383 ± 0.002

Table 5.7: Table comparing the fit results for the decay rate with the rate predicted by equation 5.7 from linear stability analysis. The parameters used for all of the examples shown here were $\hat{\rho} = 1.2$, $\hat{\mathbf{g}} = 5\hat{\mathbf{y}}$, $\phi_0 = 0.5$, $\phi_{max} = 0.64$, $\phi_l = 0.2$ and $\phi_u = 0.44$.

Here, while it is clear that a single exponential is an excellent fit for the data, the decay rates do not agree with the theoretical results, generated by substituting the smallest wave vector the system is able to accommodate into equation 5.7, to within the uncertainty. In fact, as table 5.7 shows the fit values are consistently smaller than the theoretical ones(27). There are a number of possible reasons for this. The first is the fact that the system is closed so that as shorter wavelength fluctuations decay and smooth out they contribute to a slight increase in the amplitude of the longer wavelength fluctuations. Secondly the effect of higher order terms cannot be ruled out, though this is likely to diminish in magnitude as the fluctuations do. Another, more interesting, possibility is that, because the decay of fluctuations depends on the movement of the particles, any additional features that affect their dynamics, locally, may also affect the rate at which the fluctuations decay. For example it is possible for regions which are locally uniform to reduce the rate at which the fluctuations decay globally since there is no driving force acting upon the cells in the centre of such regions since the osmotic pressure here is the same as the surrounding cells. In a finite system, like that used in the simulation, these effects are more noticeable since the population from which an average can be drawn is smaller. The effects of dynamical processes on the decay shall be discussed in more detail in later sections, but before doing so it is worth examining the decay process itself more closely.

The fact that the decay rate of a fluctuation depends on its wavelength has been offered as an explanation for the shape of the plot in figure 5.41 and while this dependence is clear in equation 5.7 the question remains as to whether or not there is any evidence for this in the simulation data. Perhaps the most straightforward way of addressing this question is to examine how the spatial distribution of the relevant quantities in the system changes over time. To this end figure 5.42 shows snapshots of the spatial distribution of the volume fraction at different times during the decay process.

---

(27) This was also found to be the case with several other data sets, not shown here.

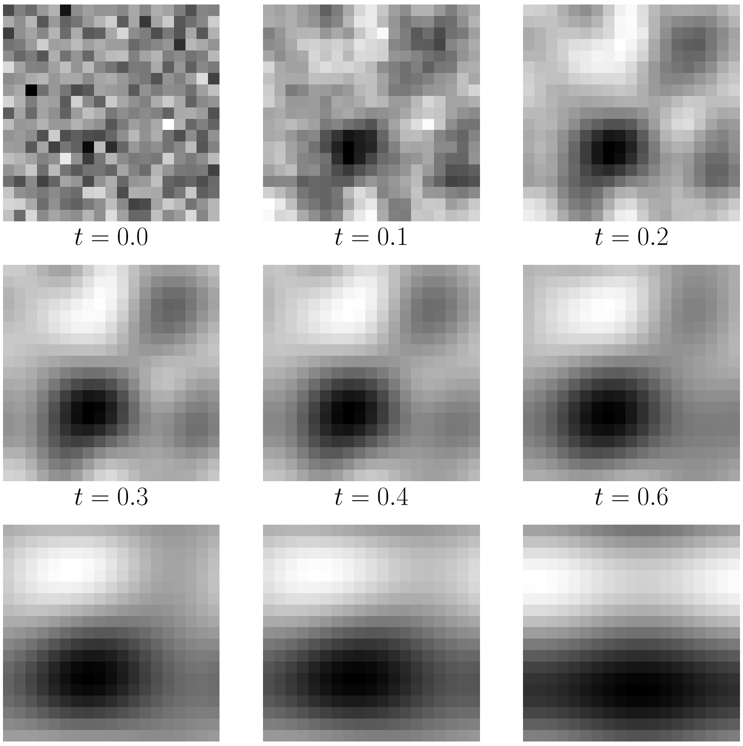

$t = 0.0$ $t = 0.1$ $t = 0.2$

$t = 0.3$ $t = 0.4$ $t = 0.6$

$t = 1.0$ $t = 1.5$ $t = 4.2$

Figure 5.42: Grey scale images showing snapshots in time of the volume fraction in different cells of a system decaying towards a uniform state. Here the volume fraction has been renormalised at every time step such that, at any time, black corresponds to the maximum value and white to the minimum. The parameters used to generate this example were: $\hat{\zeta}_p = 15$, $\hat{\zeta}_s = 1.5$, $\hat{\eta} = 1$, $\hat{\rho} = 1.2$, $\hat{\mathbf{g}} = 5\hat{\mathbf{y}}$, $\phi_0 = 0.5$, $\phi_{max} = 0.64$, $\phi_l = 0.2$ and $\phi_u = 0.44$.

Here the data has been renormalised at each time step such that the fluctuations always appear clearly no matter how small their amplitude. Figure 5.43 shows the same data without this re-normalisation, to give an indication of the "true" distribution as the amplitudes of the fluctuations decay.

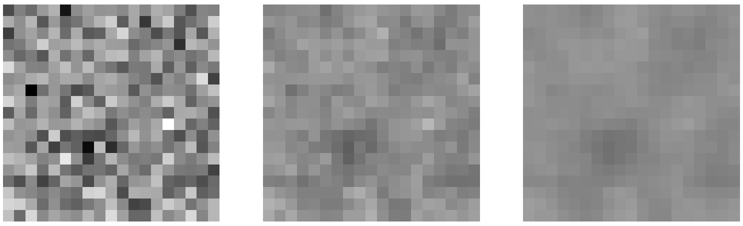

$t = 0.00$ $t = 0.05$ $t = 0.10$

Figure 5.43: Grey scale images showing the same results as figure 5.41, without normalisation. Here the normalisation is based on the initial state only.

Of course the choice of the volume fraction here is a natural one; this is what one observes as a visual pattern, and would be the quantity most easily measured in an experiment, but any of the systems variables: volume fraction, relative velocity or pressure, are equally good representations, and take exactly the same form. The key thing to notice about these figures is that the size of the features one observes becomes progressively larger as time goes on, with the smallest features disappearing very early leaving only features of the order of the system size by the end. Thus this provides clear support for the explanation of the decay rate given earlier and also justification for the decision to use the system size in order to set the wave number for the fits to the latter part of the simulation data. It is also worth noting the striking decay in the amplitude of the fluctuations illustrated by figure 5.43, which shows that even by the second image in figure 5.41 the dense and sparsely populated regions are almost indistinguishable from one another. Thus in this representation one would be unable to observe the slow decay of the longest wavelength fluctuations only seeing the rapid decay of the very shortest wavelengths.

Though figures 5.41 and 5.43 are useful in giving one an impression of what is happening in the system in a way that can be easily related to experimental observables and provide a qualitative justification for the explanation of the decay rate one can go one step further and consider the decay of the fluctuations quantitatively. Because the standard deviation of the volume fraction is insensitive to the different length scales figure 5.41 shows a superposition of the different decay rates. If, however, one makes use of a length scale dependent measure of the amplitude of the fluctuations, such as the structure factor, then the decay of the fluctuations on each length scale becomes apparent. Examples showing how the amplitude of some of the elements of the structure factor of the system shown in figures 5.41 and 5.43 decay over time are given in figure 5.44.

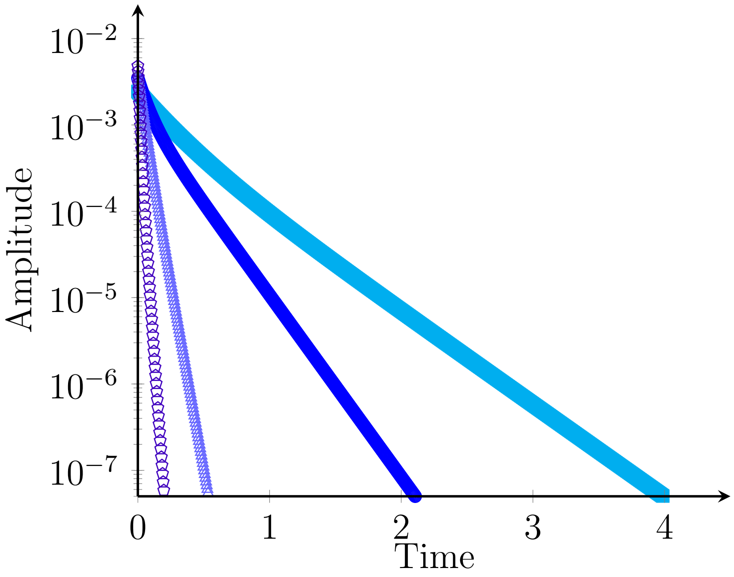

Figure 5.44: Plot showing the decay of elements of the structure factor. The cyan squares (□), blue circles (○), light purple triangles (△) and dark purple pentagons (⬠) correspond to the (9,9), (8,8), (7,7) and (1,1) cells of the structure factor respectively. In this example $\hat{\zeta}_p = 15$, $\hat{\zeta}_s = 1.5$, $\hat{\eta} = 1$, $\hat{\rho} = 1.2$, $\hat{\mathbf{g}} = 5\hat{\mathbf{y}}$, $\phi_0 = 0.5$, $\phi_{max} = 0.64$, $\phi_l = 0.2$ and $\phi_u = 0.44$.

There are two important points to make about this plot; firstly it is clear that, as expected, the fluctuations on the longest length scales decay the slowest and secondly all of the lines are very close to being linear, even at very early times. This suggest that the single exponential decay, predicted by the linear stability analysis performed in section 5.2.1.1, is a very good fit for the data and that the explanation, given earlier, as to why the data for the standard deviation of the volume fraction at early times did not fit into this model is correct.

Finally to conclude the discussion on the decay of fluctuations it is worth commenting on the fact that the decay rate is essentially controlled by three parameters, the drag coefficients, $\hat{\zeta}_p$ and $\hat{\zeta}_s$, and, $\hat{\eta}$, the viscosity ratio. These quantities essentially determine the mobility of the particles. Hence it makes good sense that they determine the rate of decay, as the action of the osmotic pressure means that this process is essentially like a diffusion process, despite the fact that the driving force is not Brownian motion as with a normal diffusion process. Equation 5.7 predicts a decay rate that is independent of both the acceleration of the system, $\hat{\mathbf{g}}$, and the ratio of particle to solvent density $\hat{\rho}$, meaning the decay rate is completely independent of the flow field. Simulations with different values for these variables verify that this is indeed the case, with the fluctuations decaying in exactly the same way even in the absence of any external force. This is not as surprising as it may first appear given the fact that the decay process is driven by the osmotic pressure which depends only on the local volume fraction and not on the flow field.

5.2.3 Neutrally Stable Steady State Patterns

When the osmotic pressure at the mean volume fraction is zero, the linear stability analysis, in section 5.2.1, predicts that the uniform state will be neutrally stable. Thus the behaviour of the system in this region could only really be investigated using numerical simulations.

In fact these simulations revealed a somewhat surprising result in that the system evolves away from its initial state towards a state where vertical channels span the system. Figure 5.45 shows how these channels form from an initially random state.

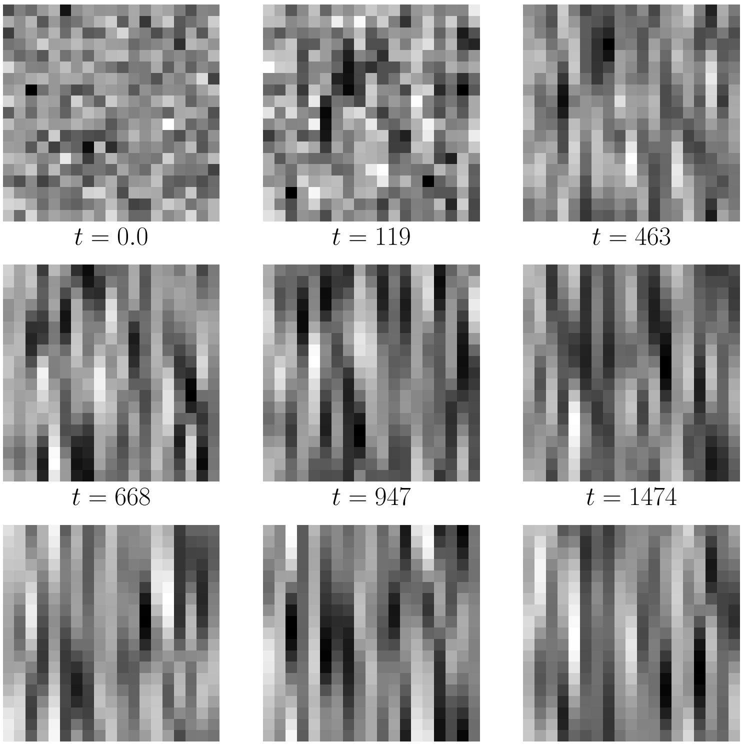

$t = 0.0$ $t = 119$ $t = 463$

$t = 668$ $t = 947$ $t = 1474$

$t = 1710$ $t = 1841$ $t = 2158$

Figure 5.45: Grey scale images showing snapshots of the volume fraction across the simulation cell, for a system in which channel pattens have formed. Here the volume fraction has been re-normalised individually in every snapshot so that the black cells represent the highest volume fraction in the system at that time and white cells the lowest. The parameters used for this example were: $\hat{\zeta}_p = 3$, $\hat{\zeta}_s = 1.5$, $\hat{\eta} = 1$, $\hat{\rho} = 1.2$, $\hat{\mathbf{g}} = 5\hat{\mathbf{y}}$, $\phi_0 = 0.4$, $\phi_{max} = 0.64$, $\phi_l = 0.2$ and $\phi_u = 0.44$.

During this process the variance in the volume fraction across the system initially falls and then stabilises and remains constant once the channels span the whole system. This much is clear from figure 5.46 which shows how the standard deviation in the volume fraction changes with time in a similar system undergoing the same process.

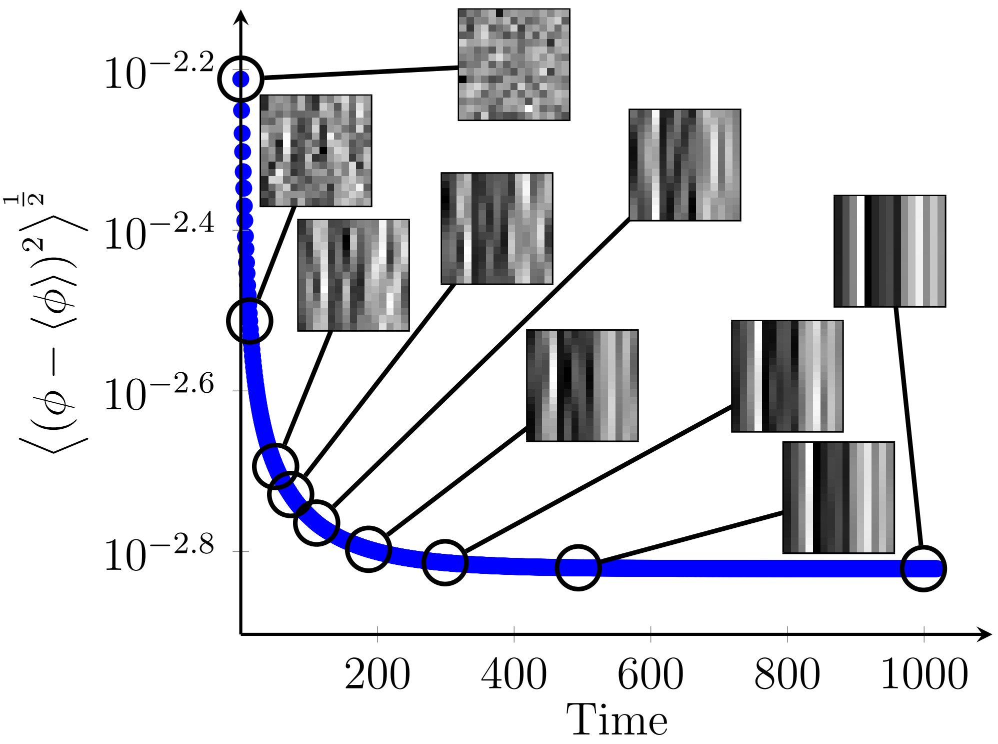

Figure 5.46: Plot showing the variation in the standard deviation of the volume fraction for a system forming a channel pattern. The inserts show snapshots of the spatial distribution of the particles at the times indicated on the plot. In these snapshots the volume fraction is normalised such that black corresponds to the highest volume fraction in the system at that time and white the lowest. The parameters used for this example were: $\hat{\zeta}_p = 2$, $\hat{\zeta}_s = 5$, $\hat{\eta} = 7$, $\hat{\rho} = 1.5$, $\hat{\mathbf{g}} = 15\hat{\mathbf{y}}$, $\phi_0 = 0.45$, $\phi_{max} = 0.64$, $\phi_l = 0.1$ and $\phi_u = 0.54$.

The fact that the linear stability analysis of section 5.2.1 predicts neutral stability implies that, at first order at least, there is no thermodynamic mechanism driving the system into this state, suggesting the transition is simply a result of the dynamics of the flow. This can also be seen in the snapshots shown in figure 5.45, where one sees obstructions, formed by slower moving regions with a high volume fraction of particles, develop randomly in the system. These obstructions then cause other particles to build up behind them leading to a gradual lengthening of the obstruction, from behind. Meanwhile the solvent that is able to pass through the blockage drags some of the particles with it elongating the region of higher than average volume fraction in front of the blockage. This also explains the decay in the variance in the volume fraction. Solvent flowing between these obstructions then acts to clear out a channel. In the absence of diffusion there is a flat plateau in this region of the osmotic pressure curve meaning that there is no driving force encouraging the particles to leave the columns by travelling perpendicular to the flow direction so they simply remain as they are, blocked by the slow moving obstruction. Further support for this hypothesis emerges when one considers the dynamics of the structure factor for such systems. Figure 5.47 shows how the amplitudes of the different wave vectors change over time for the system depicted in figure 5.46.

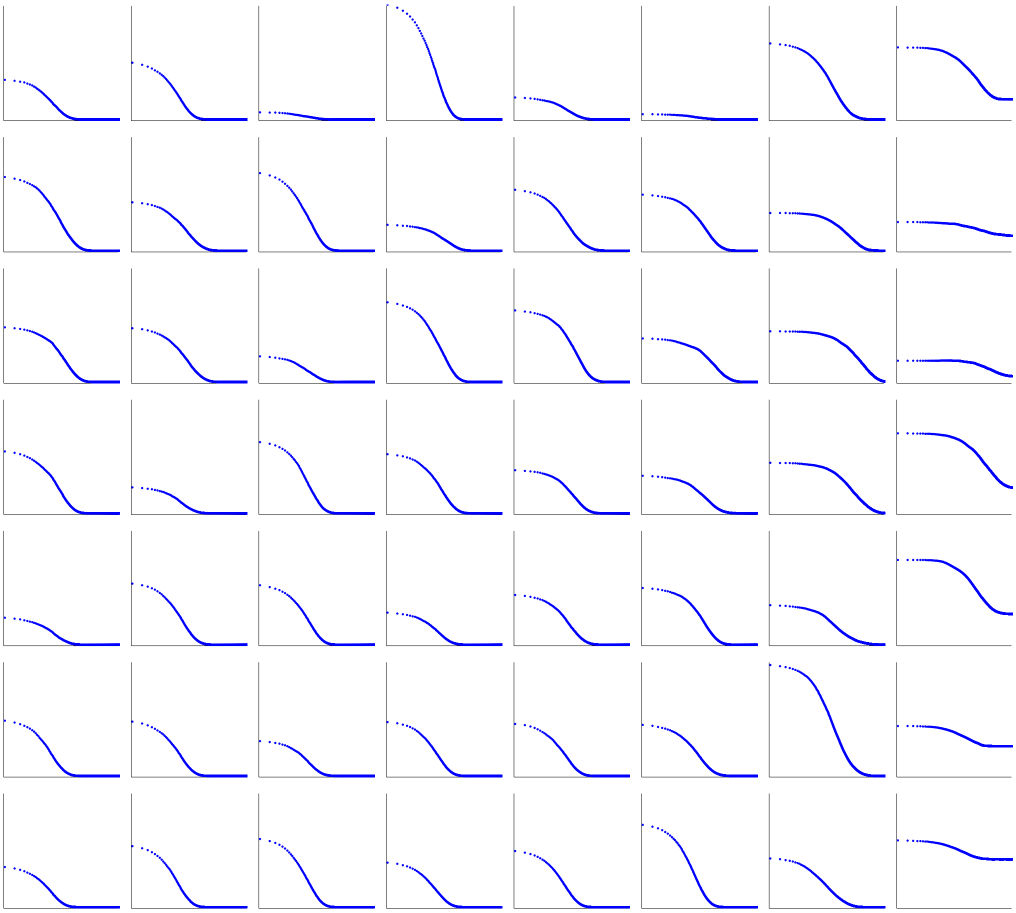

Figure 5.47: Plots showing how the structure factor changes with time for a system forming channel patters. The cells of the grid shown here correspond to the different wave vectors in the system, ranging linearly from $(0, 0)$ in the bottom left to the largest wave vector in the system in the top right, while the plots within them show how the normalised amplitude of that wave vector changes over time. The time here is plotted on a logarithmic scale with $t_{max} = 1019$. The data here is normalised such that the scale is the same on all of the plots, to allow direct comparison. The parameters used to generate this example were: $\hat{\zeta}_p = 2$, $\hat{\zeta}_s = 5$, $\hat{\eta} = 7$, $\hat{\rho} = 1.5$, $\hat{\mathbf{g}} = 15\hat{\mathbf{y}}$, $\phi_0 = 0.45$, $\phi_{max} = 0.64$, $\phi_l = 0.1$ and $\phi_u = 0.54$.

This provides clear evidence that while short wavelength fluctuations in the direction perpendicular to the flow are naturally stable, experiencing very little change in amplitude, longer wavelength fluctuations in this direction decay due to the action of the flow field. In this case it is the shortest wavelength fluctuations that remain due to the fact that the initial blockages, which seed the process are small$^{(28)}$. Meanwhile in the flow direction, because there is nothing to disrupt the structure. Fluctuations on all length scales retain a significant amplitude, despite a slight decay in the long range order, which is to be expected in the early stages as particles flow around the sides of obstructions.

This formation process sets the patterns observed here apart from those most commonly described in the literature[78], in that they do not form as a result of an instability in the equations of motion. Rather coming about purely as a result of the fact that the dynamics of the system cause a decay in the fluctuations in one direction while allowing those in the other to remain. Consequently this potentially represents an entirely novel pattern formation process

---

(28) Later in this section an example will be given where there is a larger blockage in the initial state and it will be demonstrated that this gives way to thicker channels.

In order to better understand how the dynamics of the flow cause this state to come into being it is worth considering how the values of the solvent and particle velocities vary across the system, while the pattern is developing. These are shown, along with the pressure and volume fraction, at two different stages of the process in figure 5.48.

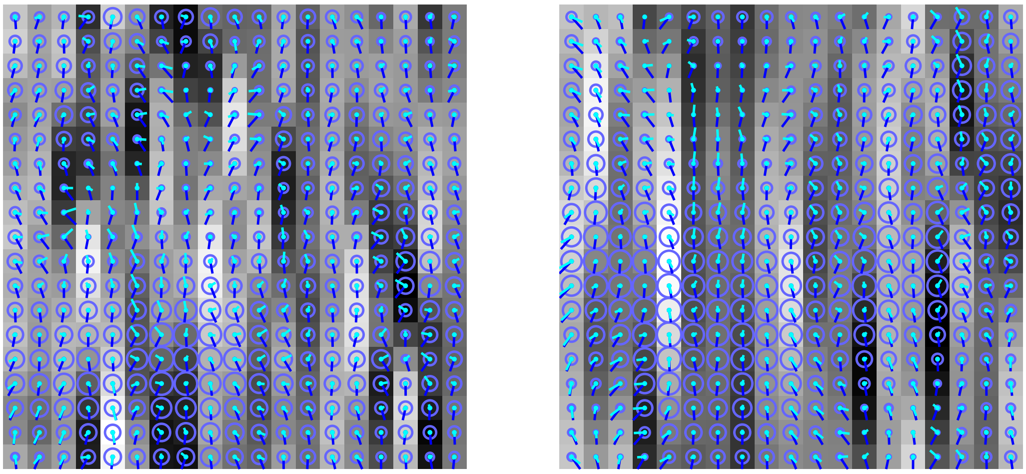

$t = 670$ $t = 2160$

Figure 5.48: Snapshots showing the states of all of the variables in the system shown in figure 5.45 just as the channel pattern begins to emerge, in (a), and when it is well established, in (b). Here the volume fraction is illustrated by the grey scale squares, representing the cells, with black represented the highest volume fraction and white the lowest. The purple circles (○) represent the normalised pressure, with the radius being proportional the pressure in that cell. Finally the blue (•—) and cyan (•—) lines represent the solvent and particle velocities, relative to the particle drift velocity, receptively, the lengths of the lines represent the magnitudes of the vectors and they point in the direction of flow from the centre of each cell. All of the variables are normalised at each time step such that the maximum magnitude of each is one and the minimum is zero.

There are several things to notice here. Firstly it is clear that the solvent travels significantly faster than the particles on average, due to the fact that the friction coefficient mediating the interaction between the solvent and the substrate is lower than that mediating the particle-substrate interaction. Secondly it is also clear that in the early stages, when the obstructions have just begun to spread in the vertical direction, the solvent attempts to flow around the obstruction while the particle fluid must reduce its velocity below the drift velocity in order to avoid encountering the osmotic pressure barrier by allowing the volume fraction in the cell causing the blockage to exceed the threshold. As time goes on and more and more particles arrive at the top of the column this leads to lengthening. It is also clear that the particle fluid travels faster in the regions where the volume fraction is lower, due to the fact that it is being dragged by the faster moving solvent. This process helps to clear out the channels and also enables particles to catch up to the obstructions. The difference in the particle velocity in the two regions is very clear once the channel pattern is well established, since there are long columns of cells where the particle velocity is significantly lower than the drift velocity. This is highlighted in figure 5.49, which shows how the volume fraction and the two relevant velocity components vary throughtout the width of the system when the channel pattern is well established.

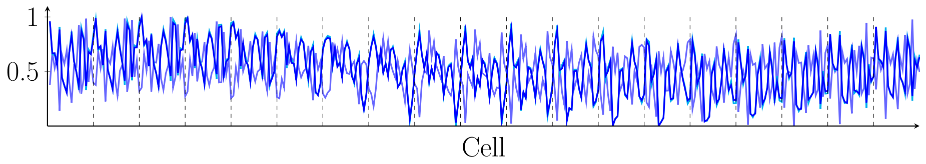

(a) Whole system.

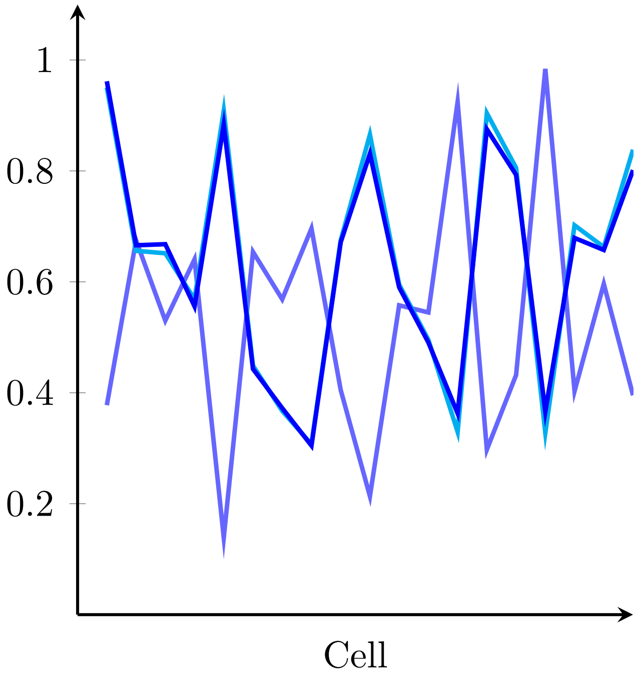

(b) First row.

Figure 5.49: Plots showing the volume fraction, shown by the light purple line (—), and the vertical components of the solvent and particle velocities, show by the cyan (—) and blue (—) lines respectively, across the system shown in figure 5.45. Figure (a) shows the whole system, with the rows separated by dashed lines, while (b) focuses on the first row. All values are normalised to allow for direct comparison.

These plots show very clearly how the channel pattern manifests itself in both the volume fraction and the flow field and the fact that the peaks in the magnitude of the velocities correspond to the troughs in the volume fraction provides strong support for the mechanism outlined above. The anti-correlation between the volume fraction and the magnitudes of the velocities and the correlation between the particle and solvent velocities in the regime where the channels are well established is shown in figures 5.50 and 5.51 respectively, where it is clear that this relationship holds for the entire system.

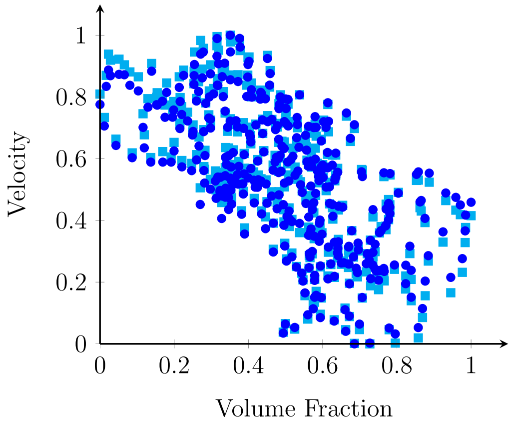

Figure 5.50: Plot showing the vertical component of the normalised particle velocity, marked with blue circles (●), and the solvent velocity, marked by the cyan squares (■), plotted against the volume fraction for the system shown in figure 5.45, in which a channel pattern has formed.

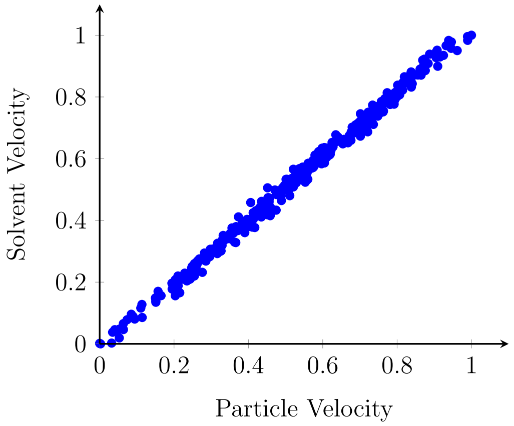

Figure 5.51: Plot showing the y component of the solvent velocity plotted against the y component of the particle velocity, for the system shown in figure 5.45.

Though the correlation between the velocities of the two fluids and the volume fraction is not as strong as that of the correlation between the velocities themselves, this is to be expected since there are many other factors at work here such as the pressure and the other velocity components, and figure 5.50 still provides strong support for the theory that the key to the formation of these channels is an imbalance in the particle velocity in regions of differing volume fraction. Furthermore the strong correlation between vertical components of the particle and solvent velocities confirms that faster flowing solvent in particle deficient regions is in fact speeding up the flow of the particles that are present and clearing them away.

Finally, returning to figure 5.48, another important feature to notice is the long wavelength pressure waves that travel through the system. In the early stages high pressure regions develop just behind the growing obstacles due to that fact that flow is begin restricted, this high pressure then drives the solvent out towards the sides of the obstacles where it can pass by more easily while the low pressure region ahead of the blockage caused by the lack of matter draws it back in. In the established channels these pressure waves continue to pass through the fluid causing the component of the particle and solvent velocities perpendicular to the flow to oscillate as the pressure in the clear channels rises and then falls. However, as conjectured earlier, because the pressure in the particle rich columns does not remain persistently high there is no driving force to make the particles spread out in the direction perpendicular to the flow, provided that the volume fraction in these columns remains below the threshold for the osmotic pressure. In principle this sets the upper limit for the magnitude of the difference in volume fraction between the particle rich and particle deficient regions. However, the fact that these patterns do not increase in intensity means this limit was not reached in practice.

The fact that the patterns do not grow in intensity in this simulation suggests that the physics built into the basic model is not enough to create the patterns seen in experiments. However, the dynamics of this model do provide an interesting insight into the pattern formation process, since the patterns in figure 5.45 are clearly not trivial. Thus one can conclude that while the basic model lacks the ingredients necessary for the patterns to increase in intensity, into something that could be observed visually, it does possess the properties relevant to influence the shape of the patterns. The patterns observed here could in principle seed the channel patterns observed in experiments, perhaps increasing in intensity as a result of the film thinning faster in the particle deficient channels due to the increased flow rate observed here.

Before moving on to discuss the effects of some specific factors and additions to the model it is worth saying something of the phase behaviour of this, most basic, model. A significant number of simulations have been run using this model taking a wide range of different parameters into account, and yet only the two phases, discussed in this and the previous section, have been found. When the gradient of the osmotic pressure is positive the system decays towards the uniform state, whereas when it is zero the channel state discussed in this section acts as an absorbing state appearing as a result of the decay of fluctuations parallel to the flow direction. The only exception to this is, of course, when there is no external flow field, $\hat{\mathbf{g}} = \mathbf{0}$. Naturally as with the decay to the uniform state the rate at which the system reaches the patterned state depends on the mobility of the particles, but unlike the decay to uniformity, also depends on the flow rate and the presence of seeds in the initial state. The locations of these seeds can also affect the structure of the final pattern, as figure 5.52 illustrates.

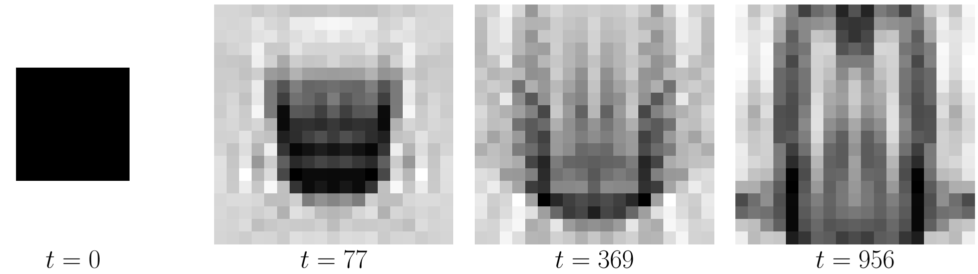

(a) Square.

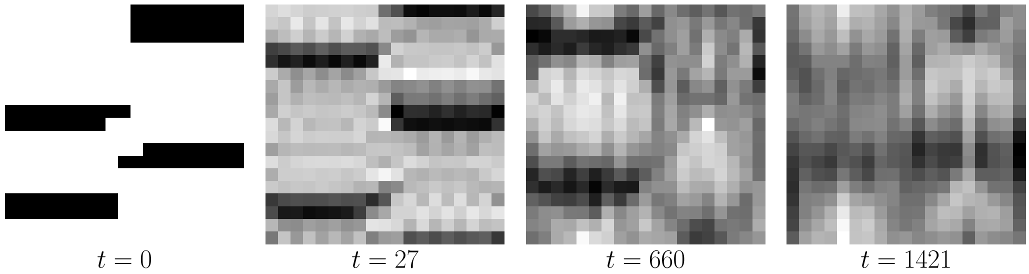

(b) Horizontal stripes.

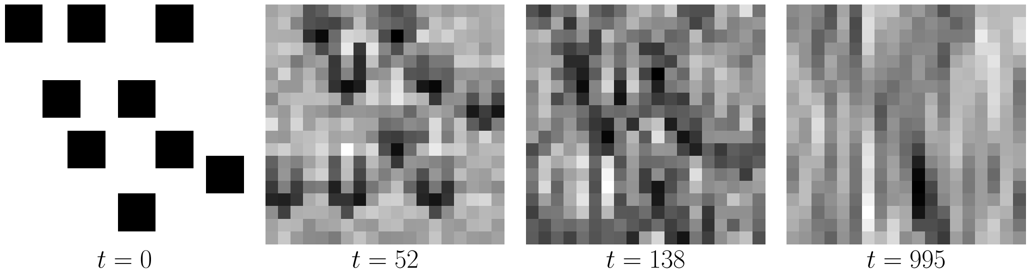

(c) Small squares.

Figure 5.52: Grey scale images showing snapshots of the volume fraction, for three different systems in which channel pattens have formed. The parameters used to generate all three of these examples were the same as those uses to generate figure 5.45, $\hat{\zeta}_p = 3$, $\hat{\zeta}_s = 1.5$, $\hat{\eta} = 1$, $\hat{\rho} = 1.2$, $\hat{\mathbf{g}} = 5\hat{\mathbf{y}}$, $\phi_0 = 0.4$, $\phi_{max} = 0.64$, $\phi_l = 0.2$ and $\phi_u = 0.44$, the only difference being the initial states. Here the volume fraction has been re-normalised individually in every snapshot so that the black cells represent the highest volume fraction in the system at that time and white cells the lowest.

Since many of the steady state structures presented above have at least some structure on the length scale of the gird, owing to the fact that the seeds in the original distribution also had structure on the length scale of the grid, it is worth pointing out that simulations using a purely sinusoidal distribution, with a wavelength equal to the system size, in the direction perpendicular to the flow and a uniform distribution parallel to the flow as an initial state were run to verify that these structures are not simply an artefact of the discretisation. These simulations showed absolutely no change in the structure over time and thus verify that the observed band structure, whatever the scale, is a true steady state of the system, and that the scale is set by the scale of the seeds in the initial state of the system(29).

---

(29) As far as resolution goes it is worth remembering that, while it is not true to say the grid spacing used can portray the structures with accurately at the level of individual cells, it is worth remembering that the spectral method of differentiation used here was shown to provide much better resolution with a limited sample size than a conventional finite differencing method.

Interestingly, however, the amplitude of the initial fluctuations seems to have very little effect on the final pattern, with the ratio of the standard deviation in the volume fraction in the initial and steady states being almost constant regardless of its value in the initial state and there being no noticeable change in the patterns or rate of decay. This fact provides further support for the theory that the patterns are the result of a decay of fluctuations in only one direction, since the standard deviation in the final state can be though of as being that due to the fluctuations in the direction perpendicular to the flow alone.

5.2.3.1 The Effect of Flow Rate

As discussed in section 5.2.2 the rate at which the fluctuations in the volume fraction decay towards the uniform state is independent of the rate at which the fluid is flowing, since this process is driven by the positive gradient of the osmotic pressure, resulting from the steric interactions between the particles. The channel patterns observed in the absence of such an osmotic pressure gradient are a result of the flow and thus one might expect that the rate of flow would have some bearing on how the pattern is formed. Several simulations were performed to investigate this and it was found that, although the flow rate does not affect the steady state of the system, it does have a significant effect on how rapidly the channels form. This much is clear from figure 5.53, which shows how the standard deviation in the volume fraction changes over time in systems which differ only in their gravitational field strengths$^{(30)}$.

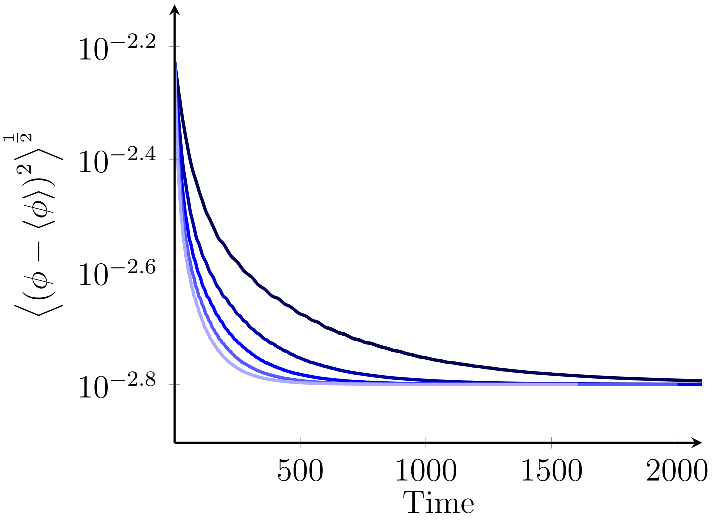

Figure 5.53: Plot comparing the standard deviation of the volume fraction over time for systems with different gravitational field strengths. The darkest blue line corresponds to $\hat{\mathbf{g}} = 5\hat{\mathbf{y}}$ with the magnitude increasing by five for each lighter shade. In these examples: $\hat{\zeta}_p = 2$, $\hat{\zeta}_s = 0.5$, $\hat{\eta} = 2$, $\hat{\rho} = 1.5$, $\phi_{max} = 0.64$, $\phi_l = 0.1$ and $\phi_u = 0.54$.

Its is clear from this plot that the higher flow rates result in the channel pattern forming and stabilising in a much shorter period of time. Of course, this is no great surprise since the formation of the patterns relies on the flow field delivering particles to become trapped behind obstructions, smearing out existing obstructions and clearing channels, all of which are dependent on the flow rate, and would not occur in the absence of flow.

Also worth noting is the fact that the flow rate has no noticeable effect on the standard deviation in the volume fraction at steady state. The reason for this is not as immediately clear, and one might well expect the rate at which the pattern forms to affect its intensity.

---

(30) Since this is directly proportional to both the solvent and particle drift velocities one can think of this as being a synonym for the flow rate, provided all other parameters are held constant.

However, if one refers back to figure 5.47 and recalls that these patterns occur as a result of the fact that fluctuations in the flow direction decay over time while those in the direction perpendicular to the flow remain indefinitely, the explanation for this observation becomes clear: the standard deviation in the volume fraction at steady state is that which is due to the fluctuations in the direction perpendicular to the flow field when all other fluctuations have decayed. Thus since all of the simulations shown in figure 5.53 started from the same initial state one would expect them all to have their same standard deviation in the volume fraction at steady state. With this in mind one may then interpret the rate of decay towards this state as being the rate of decay of the fluctuations in the flow direction, which one would clearly expect to depend on the flow rate.

Finally it is worth pointing out, though images are not shown here, that the patterns formed from the simulations shown in figure 5.53 were all visually very similar once the channels were established.

5.2.4 Additions to the Basic Model

5.2.4.1 The Effect of Attractive Inter-Particle Forces

As discussed in section 3.1.2.6 attractive interactions between particles can arise from a number of sources and result in there being a region of the osmotic pressure curve with a negative gradient. According to the linear stability analysis performed in section 5.2.1 this should result in an instability and the increase in intensity of patterns on certain length scales. Simulations of systems which included attractive forces, verified that this is indeed the case. In the limit of a strong attractive force and weak flow field the patterns produced are what one would expect for conventional spinodal decomposition[36,78,118] and have no preferred direction[36,118], depending only on the osmotic pressure. Some examples(31) of the patterns formed in different regions of the osmotic pressure curve are shown in figure 5.54, while figure 5.55 shows how the standard deviation in the volume fraction changes over time for these patterns.

---

(31) The parameters used here were chosen such that the feature of the pattern were much smaller than the size of the simulation cell so as to avoid problems with the periodic boundary conditions.

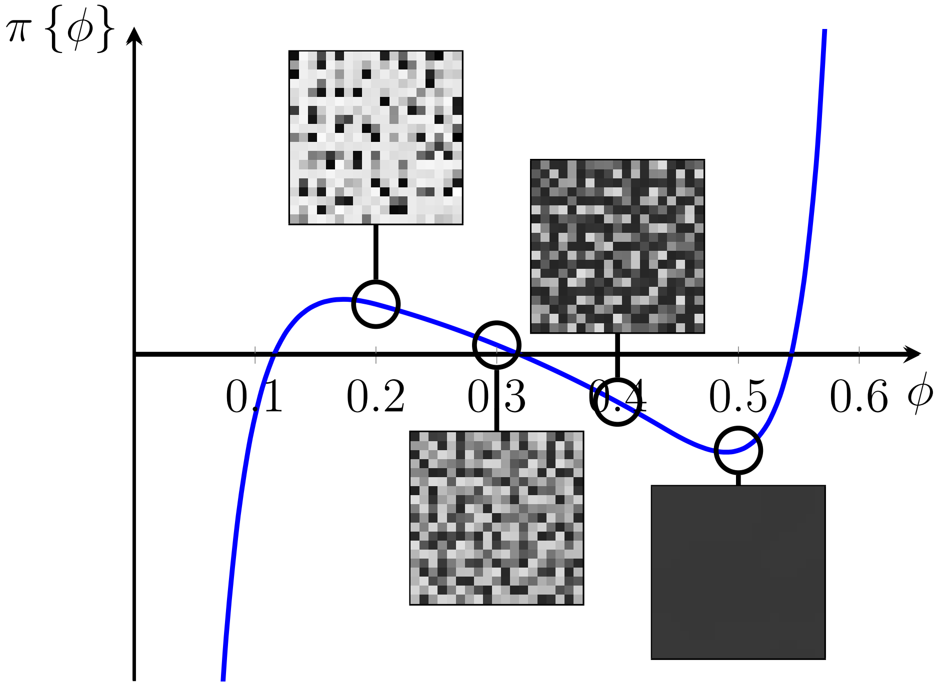

Figure 5.54: Images showing the patterns formed from different initial volume fractions, when the osmotic pressure takes the form shown in the plot. These images were taken at the point where the standard deviation in the volume fraction plateaued. The parameters used in these examples were: $\hat{\zeta}_p = 2$, $\hat{\zeta}_s = 1.5$, $\hat{\eta} = 1$, $\hat{\rho} = 5$, $\hat{\mathbf{g}} = 10\hat{\mathbf{y}}$, $\phi_{max} = 0.64$, $\phi_l = 0.2$ and $\phi_u = 0.44$, $a_{vdW} = 150$ and $\kappa_S = 1$. Here the black in the images corresponds to the maximum possible volume fraction and white to pure solvent.

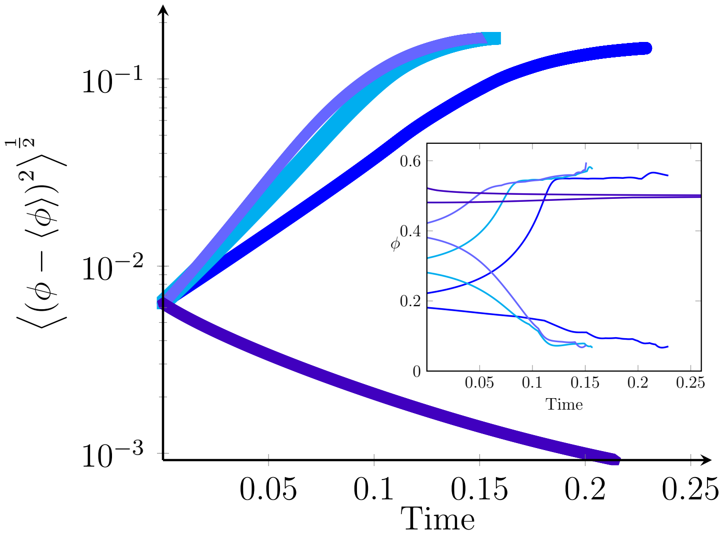

Figure 5.55: Plot showing the standard deviation of the volume fraction over time for the systems shown in figure 5.54. Here the blue circles (●) correspond to $\phi_0 = 0.2$, the cyan squares (■) to $\phi_0 = 0.3$, the light purple triangles (▲) to $\phi_0 = 0.4$ and the dark purple pentagons (⬟) to $\phi_0 = 0.5$. The insert shows the maximum and minimum volume fractions in the system.

The first thing to notice here is just how sensitive the process is to the osmotic pressure; while patterns grow in the region of the curve where the gradient of the osmotic pressure is negative they decay for $\phi_0 = 0.5$, which is just outside this region. Secondly it is worth noting that the patterns initially grow in an exponential fashion, in excellent agreement with the predictions of the linear stability analysis of section 5.2.1. This exponential growth is sustained over a relatively long time in which the pattern becomes reasonably intense, suggesting that even when the fluctuations are large the process is still dominated by the linear order term. Of course once an extreme cell reaches a volume fraction for which the gradient of the osmotic pressure is positive it resist further changes in that direction and as more and more cells reach this point the growth rate of the patterns begins to fall and the system approaches its steady state. This can be seen clearly in figure 5.54 in both the standard deviation and extreme values of the volume fraction. In order to better understand the dynamics of this phase separation it is worth considering how the number of cells at each volume fraction in the system changes over time. Figure 5.56 shows probability distributions for finding cells containing volume fractions within certain ranges at a number of times in the systems evolution for the three systems in the example shown in figure 5.54 that formed patterns.

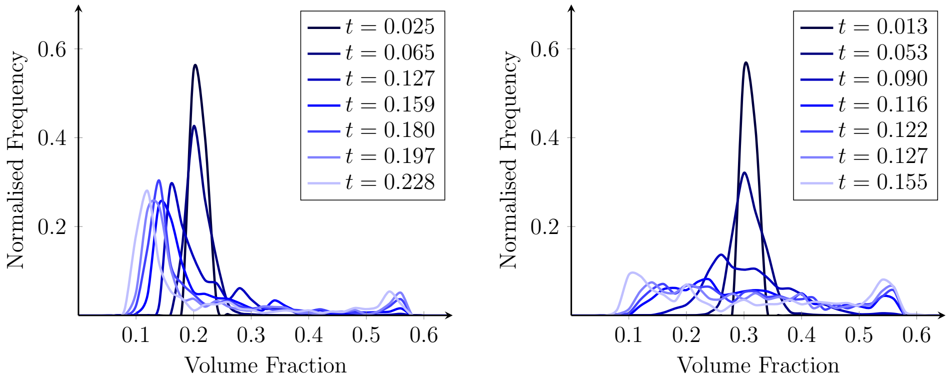

(a) $\phi_0 = 0.2$. **(b)** $\phi_0 = 0.3$.

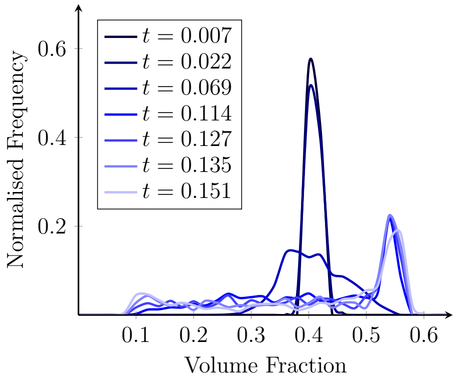

(c) $\phi_0 = 0.4$.

Figure 5.56: Plots showing how the time averaged distribution of the volume fraction in the system changed over time for three of the simulations presented in figure 5.54. Here the plots are normalised so that the probability of finding a cell at a volume fraction between zero and ϕ_{max} is unity and the time avenging used 99 consecutive snapshots in each case, whose average times are shown in the legends of the plots.

These plots show that in all three cases the distribution first widens as the gradient of the osmotic pressure gradient drives particles to move into cells where the volume fraction is higher, creating more cells that have very few particles, in order to conserve particle number. As this process continues the distribution splits into one with two distinct peaks, which results in an overall minimisation of the global free energy. Returning to the patterns themselves it is worth noting that because the interaction is strong and the penalty for creating an interface between the particles and solvent is relatively weak one would expect small features in the pattern, which are indeed evident in figure 5.54.

With the above patterns the fact that the interaction was so strong and the features were small gave the flow field little chance to influence the form of the final pattern, since it formed so quickly and the small size of the features meant that rearrangement after formation was unlikely to occur. However, as figure 5.57 shows, when the attractive interaction between the particles is weaker, the flow field is able to influence the shape of the patterns.

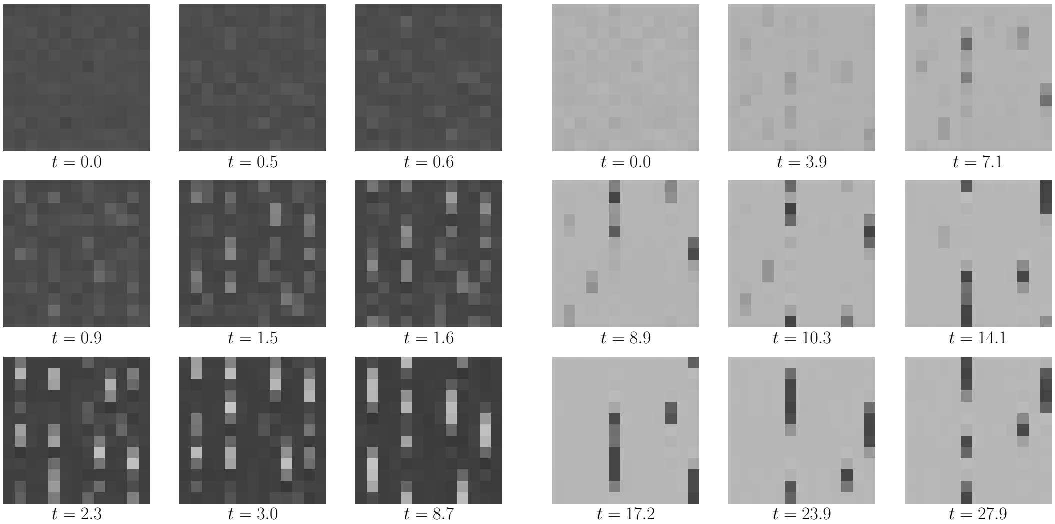

(a) $\phi_0 = 0.445$, $a_{vdW} = 15$, $\hat{\mathbf{g}} = 25\hat{\mathbf{y}}$. **(b)** $\phi_0 = 0.2$, $a_{vdW} = 5$, $\hat{\mathbf{g}} = 5\hat{\mathbf{y}}$.

Figure 5.57: Grey scale images showing snapshots of how the spatial distribution of the volume fraction changes over time for two systems with attractive inter particle forces of different strengths. The images are normalised such that, in each case, black corresponds to the maximum volume fraction and white to pure solvent. The parameters used in both of these examples were: $\hat{\zeta}_p = 2$, $\hat{\zeta}_s = 1.5$, $\hat{\eta} = 1$, $\hat{\rho} = 5$, $\phi_{max} = 0.64$, $\phi_l = 0.2$ and $\phi_u = 0.44$ and $\kappa_S = 1$

Here it is clear that the flow field has the same effect as it did in the case of the neutrally stable fluctuations, in that it stretches out the features in the flow direction forming a channel pattern. The difference here is that the pattern has a much higher intensity, with a much more sharply defined distribution of volume fractions, so as to minimise the global free energy. Key to the formation of this pattern is the fact that while one particular length scale of fluctuation grows fastest all larger scale fluctuations are permitted, and grow. This much is clear from figure 5.40 and means that while the spinodal decomposition[36,78,118] part of the process sets the length scale for the width of the features[36,78,118] , as there is nothing else to influence this in the direction perpendicular to the flow, the flow field is able to drive the elongation of the features in the flow direction[78] , as the solvent washes out clear channels, which remain stable. Thus while an attractive force appears to be necessary for an increase in intensity of patterns the flow field clearly influences their shape significantly.

5.2.4.2 The Effect of Non-Newtonian Viscosity

It is well established that colloidal fluids exhibit non-Newtonian flow behaviour. In order to simulate this behaviour in the model of the particle-laden fluid the very simple piecewise function described in section 3.1.2.1 was used. Although this is very much an empirical expression it was possible to use the results of the constitutive relation detailed in section 5.1 to inform the choice of parameters. While the effects of replicating the qualitative results of this model in the viscosity of the particle fluid will be discussed in more detail later in this section it is perhaps worth considering the effects of shear thinning(32) in the form of a single power law,

$$\hat{\eta} = \hat{\eta}_0 \dot{\gamma}^a, \tag{5.12}$$

where $\hat{\eta}$ is the non-dimensionalised ratio of the viscosity of the particle fluid to the solvent's viscosity, $\dot{\gamma} = \frac{|\hat{\mathbf{v}}_p + \hat{\mathbf{v}}_{pd}|}{\tau}$ is the shear rate, dominated by the contribution in the direction normal to the substrate, $|\hat{\mathbf{v}}_p + \hat{\mathbf{v}}_{pd}|$ being the absolute particle fluid velocity relative to the surface and τ being the film thickness, and $\hat{\eta}_0$ and a are constants describing the particular constitutive relation. Running simulations using this constitutive relation revealed no significant change in the structure of the patterns formed, with the system still tending towards the channel pattern described in section 5.2.3. However slight differences in the rate at which this pattern was formed were observed and differences in the intensity of the fluctuations in the steady state pattern were also apparent. A curve showing how the standard deviation in the volume fraction changed over time for a simulation in which this constitutive relation was used to model a shear thinning fluid is compared to the Newtonian case, with the same initial state, in figure 5.58.

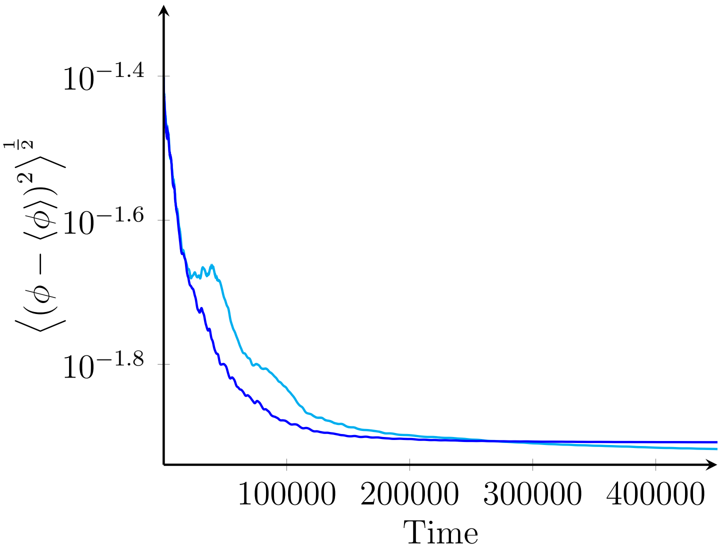

Figure 5.58: Plot comparing the standard deviation in the volume fraction over time of a shear thinning system, in blue (—) to that of a Newtonian system, in cyan (—). Here: $\hat{\zeta}_p = 2$, $\hat{\zeta}_s = 0.9$, $\hat{\eta} = \hat{\eta}_0 \dot{\gamma}^a$, $\hat{\rho} = 1.5$, $\hat{\mathbf{g}} = 0.25\hat{\mathbf{y}}$, $\phi_{max} = 0.64$, $\phi_l = 0.1$ and $\phi_u = 0.54$. Shear thinning was modelled using $a = -25$ and $\tau = 0.275$ and $\hat{\eta}_0$ was tuned so the viscosity at the drift velocity was $\hat{\eta} = 7$, as in the Newtonian case.

In the shear thinning case the constant $\hat{\eta}_0$ was tuned so that the particle fluids in both of the simulations had the same viscosity when travelling at the drift velocity.

The first, and perhaps most important, point worth making about these results is that it was very difficult to find a set of parameters that showed a clear variation in the rate of decay towards the channel pattern when non-Newtonian flow behaviour was added. This is mainly due to the fact that fluctuations about the drift velocity are in general very small in magnitude compared to the drift velocity itself, and decay over time until the pattern is established. Thus in order to translate these into significant viscosity variations within the

---

(32) Shear thickening was also considered for completeness, but detailed results are not presented here since this phenomenon was not observed in the constitutive relation derived to motivate the choice of parameters. Furthermore the results of the hydrodynamics simulations performed as part of the present work, and established results in the literature [5,64,126], suggest that shear thickening, where present, only occurs at high Pélet number in the fluids of interest here, which was not thought to be consistent with the slow draining required for the effects of the viscosity variations to be seen.

system it was necessary to use a very large exponent(33) in equation 5.12 and a relatively low drift velocity. In addition to this the scale factor used needed to be large enough to ensure that the viscous forces played a role in the dynamics and were not subordinate to the frictional forces. Taking all of these factors into account ultimately leads to the realisation that the main conclusion to be drawn from this section is that, in most cases, non-Newtonian flow has no significant effect on the formation of the channel patterns.

Nevertheless, for the purposes of those cases where the fluid is very non-Newtonian and flows very slowly, and for completeness, it is still worth giving some consideration to the effects that are present. From figure 5.58 one notices that the decay towards the patterned state in the Newtonian fluid is not a smooth one, due to the fact that the driving force is very weak so it can take a long time for some of the clusters of particles to break up and smear out in the flow direction. This effect is seen to a far lesser extent in the shear thinning case. Thus one must conclude that the clusters of particles which disrupt the decay in the Newtonian case shear thin and flow past one another more easily when the particle fluid is shear thinning. This certainly makes good physical sense since the particles are of a higher density than the solvent so one would expect these particle rich regions to flow faster in the initial, random, configuration. This also explains why the decay in the Newtonian case is also slightly slower. Further support for this explanation comes from consideration of a shear thickening fluid in the same situation, where results show a much rougher, and slower, decay towards the, patterned, steady state.

The intensity of the final state is also worth noting; the faster smoother decay brought about by the fluid shear thinning results in a slightly higher value of the standard deviation in the volume fraction in the final state. One can think of this as being due to the decay of the fluctuations in the direction perpendicular to the flow, which do not decay once the pattern is established, and only decay during the initial formation process, due to the effect of viscous forces. This is because the force arising from this depends on gradients in the velocity and a higher viscosity penalises these gradients in all directions, but most importantly in the direction perpendicular to the flow. This means that a higher viscosity results in a stronger force, preventing the fluid from splitting into channels of differing flow rates and so less intense channel pattens. As discussed previously the shear thinning fluid has a lower viscosity in the regions where the growth is fastest so this force is reduced within these regions and the fluctuations in the direction perpendicular to the flow field decay more slowly, preserving a greater amplitude for the final state.

Of course many colloidal fluids exhibit a range of different flow behaviours and are not simply shear thinning or shear thickening across the whole range of shear rates. The results given in section 5.1 for the simple constitutive relation derived here are a good example of this, having a Newtonian and shear thinning phase, and of course the model used for the particle fluid's viscosity in the present section admits a whole range of flow behaviours as a function of shear rate; so one may well ask what effect these have on the patterns formed. Naturally one would not expect a significant change in the structure of the pattern since equation 3.22 is nothing more than a combination of the two effects already discussed, neither of which changed the structure of the pattern. However, they

---

(33) In practice this meant that limits needed to be set on the viscosity to prevent numerical instabilities in the early stages of the simulation when fluctuations were large.

do affect the time taken for the system to find its steady state and the amplitude of the fluctuations therein. While equation 3.22 admits a very broad range of behaviours it is somewhat unphysical to assume that all of these would be accessible to the system given that they span a wide range of shear rates in realistic systems and the distribution of likely velocities in this model is very narrow, especially given the fact that the standard deviation in the velocity decays over time. However, it was possible to set the value for the shear rate at which the transition between two of the regimes occurred to be that of the shear rate at the drift velocity, so as to allow the system to explore them both. Since the results of the simple constitutive relation derived in section 3.4 provided a sound microscopic motivation, a Newtonian regime followed by a shear thinning one was used in these simulations, with the transition between them set at the drift velocity. It is difficult, however, to say what exactly constitutes a fair comparison with a constitutive relation of this type. Naturally the viscosity at the drift velocity is equal to the Newtonian viscosity since the fluid is Newtonian up to that point so the average viscosity for the whole system in the Newtonian-shear thinning system would be lower than in the simple Newtonian case so one would trivially expect the decay to be faster and result in more intense patterns, and this is indeed the case. Of course one might argue that finding the average viscosity in the non-Newtonian case and then using this as the viscosity in the simple Newtonian system would yield a better control system, but this quantity changes over time, as the velocity distribution changes, and one is left with the difficult decision of which value to use. The difficulty in finding a good control state meant that it was not possible to make quantitative comparisons, however it is possible to say, based upon qualitative comparison that the effect is much the same as the simple shear thinning case, in that the decay is much smoother than any reasonable Newtonian equivalent as well as being noticeably faster. Furthermore, if one draws the comparison from a system with the same viscosity at the drift velocity, one finds that the decay is faster with the Newtonian to shear thinning cross over than it is in the simple shear thinning case since the viscosity can only decline and not increase with respect to its value at the drift velocity.

5.2.4.3 The Effect of Volume Fraction Dependent Viscosity

As well as expanding upon the basic model to include non-Newtonian flow behaviour in the particle fluid, the effect of the volume fraction on the viscosity was also modelled using the formula proposed by Krieger and Dougherty, and given in equation 3.25. As with the shear dependence this did not cause a noticeable change in the patterns, but did affect the rate at which the system evolved to form the channel patterns, described in section 5.2.3, and in this case also had a slight effect on the magnitude of the standard deviation in the volume fraction of the steady state pattern. The time evolution of the standard deviation in the volume fraction for the same system with and without volume fraction dependent viscosity is shown in figure 5.59.

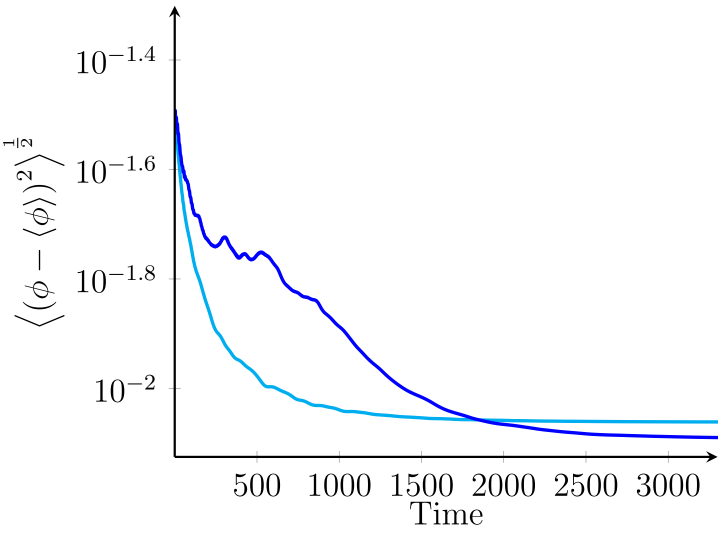

Figure 5.59: Plot comparing the standard deviation of the volume fraction over time for one system with volume fraction dependent viscosity, with $\hat{\eta}_0 = 1$ and $[\eta] = 2.5$, shown by the blue line (——), and one without, having $\hat{\eta} = 6.940$, shown by the cyan line (——). In both examples: $\hat{\zeta}_p = 2$, $\hat{\zeta}_s = 0.9$, $\hat{\rho} = 1.5$, $\hat{\mathbf{g}} = 10\hat{\mathbf{y}}$, $\phi_{max} = 0.64$, $\phi_l = 0.1$ and $\phi_u = 0.54$.

Here the viscosity in the system without volume fraction dependence was tuned to match the value of the viscosity at the mean volume fraction in the other system, thus the two systems may be thought of as being identical when in the uniform state. As figure 5.59 shows adding volume fraction dependence to the viscosity has a significant effect on the path that the system takes toward its steady state, though it is worth noting that this effect is only significant when the standard deviation in the volume fraction is rather high in the initial state. In several simulations, which were started with an initial state in which the system was much closer to uniformity, these effects were barely noticeable. Of course this is to be expected given that the viscosities are identical in the uniform state and the volume fractions at which the channels form lie on a relatively shallow part of the viscosity-volume fraction curve. However, when the volume fraction distribution is significantly heterogeneous for there to be noticeable differences in the viscosity it is clear, from figure 5.59, that adding volume fraction dependence disrupts the smooth decay of the fluctuations towards the patterned state. This is likely to be due to the fact that some parts of the system are flowing significantly faster than others, with those at high volume fractions moving more slowly preventing the flow field from smoothing out inhomogeneities in the flow direction quite so effectively, as a high viscosity penalises gradients in the flow field. Of course as these even out slowly the volume fraction in these regions falls and thus they begin to flow faster and the rate of decay recovers once again. Thus in effect figure 5.59 shows a four stage process: firstly the fluctuations which only involve cells at low volume fraction decay, the rate then falls as only fluctuations involving cells at high volume fraction remain, as the volume fraction in these cells falls the rate begins to recover until the system finally reaches a state where it is completely spanned by channels and decays no further.

One also notices that the standard deviation in the volume fraction of the steady state is slightly lower in the case where the viscosity is volume fraction dependent. This is likely to be due to the fact that the fluctuations in the direction perpendicular to the flow decay more due to fluid flowing around the slow moving high volume fraction regions.

5.2.4.4 The Effect of Static Friction

Another factor which might affect the process of pattern formation in real draining films is the fact that particles, or more specifically the particle fluid as a whole, will resist motion more when initially at rest than it would when moving, due to the fact that the coefficient of static friction between the particles and the surface is higher than the coefficient of dynamic friction. This effect was added to the model of the particle-laden fluid using the simple empirical expression described in section 3.1.2.3. As with the modifications to the viscosity this was not found to make any significant changes to the pattern formed, but did affect the rate of formation.

With this particular property it was unclear exactly what reference system should be used for comparison; one in which the coefficient of friction is the same as the coefficient of dynamic friction used in the variable friction model or one where the coefficient of friction takes the value of equation 3.26 evaluated at the average particle velocity[34]. While the former is arguably more physically relevant since one wishes to model a situation in which the effects of static friction result in an increased resistance to motion, the latter is far more convenient for comparative purposes, as interpretation of the results is not marred by the fact that the average friction coefficient is different in the two simulations. For this reason the time evolution of the standard deviation in the volume fraction for both control simulations is shown alongside that of the simulation that included static fraction in figure 5.58.

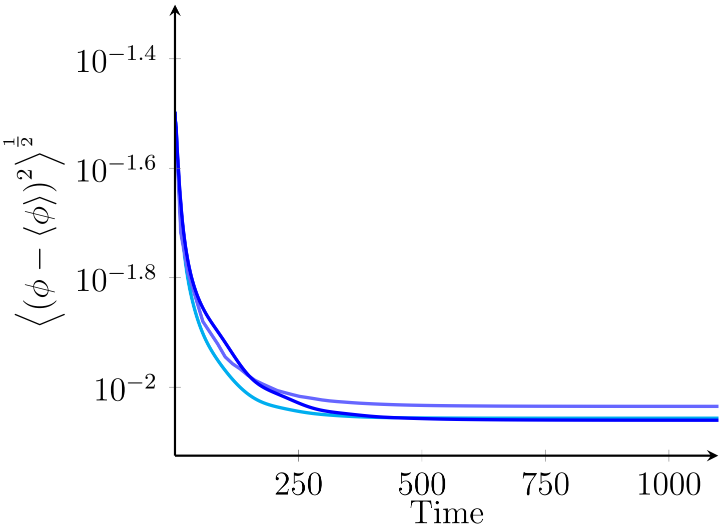

Figure 5.60: Plot comparing the standard deviation over time for a system with static friction, shown by the blue line (—), to two without, shown by the cyan (—) and purple (—) lines. In the first two $\hat{\zeta}_{p\infty} = 2$, the former having $\hat{\zeta}_{p0} = 12$ and $v^* = 3.16$. In the last $\hat{\zeta}_{p\infty} = \hat{\zeta}_p\big|_{v_{pd}}$. In all cases $\hat{\zeta}_s = 0.9$, $\hat{\eta} = 1.2$, $\hat{\rho} = 1.5$, $\hat{\mathbf{g}} = 5\hat{\mathbf{y}}$, $\phi_{max} = 0.64$, $\phi_l = 0.1$ and $\phi_u = 0.54$

The first thing to notice about these results is that they clearly show that the addition of static friction reduces the rate at which the system finds its steady state. When compared with the simulation that has a constant friction coefficient equal to that of the dynamic friction coefficient in equation 3.26 this is hardly surprising, given the fact that the average friction constant is higher. However, close inspection of figure 5.60 reveals that this rate is also lower than that of the system with a constant friction coefficient equal to equation 3.26 evaluated at the drift velocity, proving that there must be other factors at work here beyond a simple increase in the average friction coefficient felt within the fluid. Further evidence of this comes when one inspects the shapes of the curves more closely.

---

(34) Ideally, in this case, the average of the magnitudes of the velocities, not the vector average, in each cell relative to the substrate would have been used, since the friction coefficient in equation 3.26 depends on the magnitude only, but, since this is not guaranteed to remain constant over time, the magnitude of the drift velocity was used instead as an approximation. Fortunately, given the nature of the flow in these kinds of patterns, this provides a relatively good approximation to the former value.

While the two systems with constant friction coefficients produce relatively smooth curves the system with static friction produces a curve that is much more modular in appearance with bumps and sections of differing gradient. These can be thought of as being due to the different regions of the fluid experiencing different values of the particle-surface friction coefficient. This description of the system also explains why the system with static friction included is slowest to decay to its steady state since, by the end, the decay process is dominated by the slowest moving sections of fluid which experience the highest friction.

Also worth noting from figure 5.60 is the fact that, while the two systems with constant friction coefficients differ in terms of the intensity of the fluctuation in their steady states, due to the difference in their friction coefficients, the standard deviation in the volume fraction in the system with static friction is almost identical to that of the system with which it shares a dynamic friction coefficient. This implies that it is the coefficient of dynamic friction and not the average friction that determines the intensity of the patterns in steady state. Intuitively it makes sense that the steady state should not be affected by the coefficient of static friction as this quantity is only relevant for short periods of time during the motion of the fluid, unlike the coefficient of dynamic friction which is intrinsically a property of the fluid, and the substrate, and as such is relevant on all time scales(35).

The fact that the system reaches a steady state in which the patterns are of the same intensity, with and without static friction, sets this effect apart from those involving the viscosity, where the intensity of the final state was altered. The reason for this is that while the viscosity affects the flow in a non-local way, by changing the flow field, the particle-surface friction coefficient is a purely local quantity, which only affects the cell in question, and so fluctuations in this quantity do not increase or reduce the rate of decay of fluctuations in the direction perpendicular to the flow as the variations in the viscosity do. It is this effect that is thought to be responsible for the change in the standard deviation of the volume fraction of the final state noted in sections 5.2.4.2 and 5.2.4.3, and the fact that it is not present here is further evidence in support of this theory.

5.2.4.5 The Effect of Volume Fraction Dependent Friction

As described in section 3.1.2.4 crowding of the particles can affect their motion over the surface and lead to increased resistance. The effect of this on the formation of the channel patterns was investigated by running a number of simulations with and without volume fraction dependence in the particle-surface friction coefficient. Figure 5.61 shows how the standard deviation in the volume fraction changes over time in a pair of example systems.

---

(35) In other words, from a microscopic point of view, after a long time the system would not "remember" a particle briefly coming to rest on the surface and then resuming its motion, but friction between the moving particles and the surface is always present.

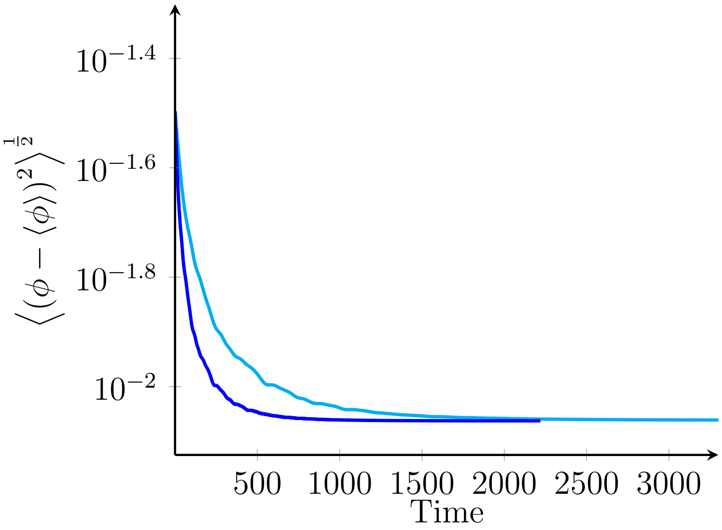

Figure 5.61: Plot comparing the standard deviation of the volume fraction over time for one system with volume fraction dependent friction, where $\hat{\zeta}_{pi} = 2\frac{\phi_i}{\langle\phi\rangle}$, shown by the blue line (—), and one without, where $\hat{\zeta}_p = 2$, shown by the cyan line (—). In both examples: $\hat{\zeta}_s = 0.9$, $\hat{\eta} = 6.940$, $\hat{\rho} = 1.5$, $\hat{\mathbf{g}} = 10\hat{\mathbf{y}}$, $\phi_{max} = 0.64$, $\phi_l = 0.1$ and $\phi_u = 0.54$.

This clearly shows that the addition of volume fraction dependent friction results in a faster decay towards the state where the channels span the system. This is likely to be due to the fact that the lower friction coefficient in regions of lower particle concentration allows the solvent to flow faster while higher friction in concentrated regions results in slow moving blockages causing particles to pile up behind. Although this argument sounds very similar to the argument given in section 5.2.4.3 to explain a slower decay rate, there is one very important difference; while the viscosity penalises gradients in the flow field the friction coefficient is a purely local quantity, thus it does not impede the smoothing out of the inhomogeneities in the volume fraction and instead increases the rate at which the channels form by encouraging the processes responsible.

By contrast with the volume fraction dependent viscosity, once again, the addition of a volume fraction dependent friction does not change the standard deviation in the volume fraction at steady state. This is a further manifestation of the fact that it is local to the cell in question and so does not change the quantities in the surrounding cells, hence there is no change in the amount of decay experienced by the fluctuation in the direction perpendicular to the flow field.

5.2.4.6 The Effect of Diffusion

Because the addition of diffusion to the model only modifies the form of the osmotic pressure curve it could be argued that it is not really an additional feature in its own right as one would not expect it to introduce any new behaviour which is not already present in the model in its other forms. While this is true it is still worth mentioning its effects, for completeness, since it is an important property of real physical systems and relevant to the system which this model hopes to emulate.

In isolation diffusion manifests itself in the model in the form of the addition of a linear term to the existing osmotic pressure curve. This means that the gradient is always positive and thus fluctuations about the uniform state always decay in accordance with the predictions of the linear stability analysis performed in section 5.2.1. However, one nice feature of this is that, in the region where the curve is linear, one can think of the decay rate as being proportional to the temperature, and being independent of the volume fraction(36), which is in line with what one would expect for an ideal gas of particles, and thus makes good sense.

When accompanied by an attractive interaction, as is likely to be the case in a real system, since small particles that are susceptible to Brownian motion typically have attractive van der Waals' forces as well[36], the effect of diffusion is slightly more interesting since, at low temperatures, the change it causes in the shape of the osmotic pressure curve can affect the way the volume fraction is distributed in the steady state system and can also affect the length scale of the dominant fluctuations. At higher temperatures the effects of diffusion can also prevent the phase separation from happening at all and the system returns to a state where all fluctuations decay, as if there were no attractive forces. This is interesting as it provides a physically meaningful control parameter, in the form of the ratio of the strength of the attractive interaction potential and the thermal energy, that allows one to move smoothly between the two different phases of the system, where the patterns either grow or decay. In theory tuning the diffusion coefficient and the volume fraction exactly could produce a neutrally stable state, at a turning point on the osmotic pressure curve. In practice, however, this would manifest itself as an extremely slow growth or decay rate, since it would not be possible to reach the very precise point required for truly neutral stability. Thus in practice the addition of diffusion, and attractive inter-particle forces for that matter, to the model effectively rules out the possibility of channels forming by the process described in section 5.2.3. Hence one can essentially say that this process can only occur in granular materials.

5.2.4.7 Compound Effects

Several simulations, using different combinations of the above effects, were run in order to establish what their compound effect was, but, given the number of different additions considered there are a great deal of potential combinations of different effects, so it would not be practical to consider each one in turn. Fortunately this is unnecessary since all of the effects discussed above fall into two categories: those which change the stability of the uniform state and the structure of the patterns formed and those which only affect the route of the pattern formation process and the time scales involved, without having a significant effect on the structure of the pattern. This makes the results of any combination of effects relatively straightforward to predict. The only two effects that change the structure of the patterns formed are those which affect the osmotic pressure, the addition of attractive forces and diffusion, the result of any combination of these effects can be established simply by examination of the osmotic pressure as a function of the volume fraction of particles. A negative gradient at the mean volume fraction will result in an increase in the intensity of patterns while a positive one will result in decay(37). The only remaining factor at work here, that could change the steady state pattern, is the ratio of the strength of the attraction caused by the osmotic pressure minimum to the strength of the gravitational field and surface tension, which has already been discussed in sec-

---

(36) To the extent that the volume fraction does not lie on the non-linear region of the curve.

(37) Of curse zero gradient results in the formation of the faint channel patterns, but this would be almost impossible to attain with either of these features active, since it would not be possible to set the average volume fraction in a finite system to the precise location of a turning point.

tion 5.2.4. Adding one, or a combination, of the other features to this model would indeed change the time scale over which the pattern forms and may even affects its intensity slightly, but it would not have a significant effect on the structure and while it is difficult to predict quantitatively what effect combinations of such effects might have on this time scale one can make qualitative predictions relatively easily based on the results discussed in sections 5.2.4.3 to 5.2.4.6.

5.3 Complexity Measures

5.3.1 Results for Simple Test Cases

In order to better understand the complexity measures and means of producing probability distributions, they were applied to a number of test patterns, which were specifically designed to test different features of the measures, such as their ability to identify repeat patterns. These patterns were deliberately restricted to just three values for the volume fraction in order to try to ensure that only the shapes of the patterns would affect the complexity value and it would not be affected by small variations in the values of the volume fraction. It is also worth noting at this stage that the complexity values for these patterns were calculated assuming periodic boundary conditions, in order to maintain consistency with the way the complexity of the patterns generated by the particle-laden fluid were measured. The patterns used are shown in figure 5.62 and the complexity values attributed to them by the different measures are given in table 5.8. It should be noted that the correlation function complexity measure used a prior probability distribution based on a checker-board pattern, like the one shown in figure 5.62a. This prior was used throughout, as it was felt that this represented the simplest crystal structure possible on such a grid(38).

---

(38) Although other priors were tested.

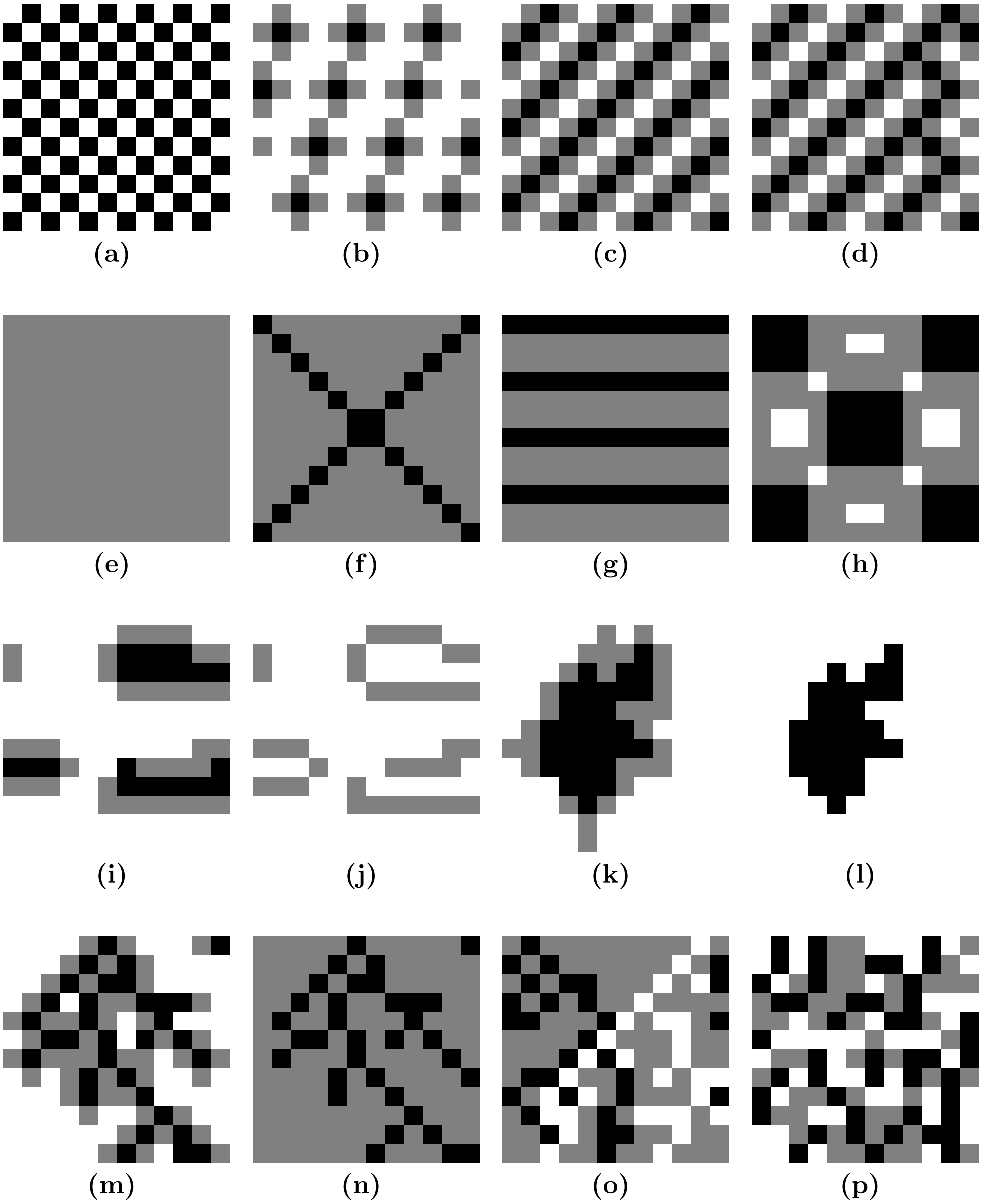

Figure 5.62: Artificially created patterns used to test and calibrate the complexity measures described in sections 3.2 and 4.2.

	Complexity					
	LMC			ICC		
Figure	Gaussian Curvature	Mean Curvature	Correlation Function	Gaussian Curvature	Mean Curvature	Correlation Function
5.62a	0.00000000	0.00000000	0.00000000	0.00000000	0.00000000	0.00000000
5.62b	0.65056707	0.78061204	0.04413500	0.99670882	0.92514700	0.02452229
5.62c	0.62944107	0.24501908	0.44456338	0.67587082	0.38430598	0.37849594
5.62d	0.74958824	0.42054150	0.60415508	0.82840972	0.58543602	0.52636585
5.62e	0.00000000	0.00000000	0.00000000	0.00000000	0.00000000	0.00000000
5.62f	0.70187815	0.21308425	0.34754136	0.86873514	0.61463922	0.27728196
5.62g	0.00000000	1.00000000	0.61035703	0.00000000	0.63456583	0.30811111
5.62h	0.88384311	0.53425133	0.97695983	0.96376948	0.74551419	0.85256911
5.62i	0.85482998	0.41903879	0.83034154	0.79265885	0.79981232	0.58933822
5.62j	0.83960416	0.48683001	0.95101646	0.80890589	0.93589230	0.79077965
5.62k	0.84205615	0.21812666	0.95040273	0.95322478	0.80935738	0.90562354
5.62l	1.00000000	0.07022643	0.96575754	0.94920531	0.65462197	0.85872981
5.62m	0.60186655	0.43861483	0.98192146	0.92337816	1.00000000	0.91224577
5.62n	0.68055689	0.35641835	1.00000000	1.00000000	0.93404430	0.94149939
5.62o	0.56163507	0.64469079	0.90895813	0.89236377	0.99310286	0.79261244
5.62p	0.47216287	0.72182841	0.97408301	0.73834969	0.87709144	1.00000000

Table 5.8: Table showing the normalised complexity values obtained by applying the various complexity measures to the artificially created test patterns shown in figure 5.62. The normalisation of the results is such that the pattern with the highest complexity, of the patterns analysed, was attributed a complexity of one. Here the correlation function measure was used with a checker board pattern, like the one shown in figure 5.62a, as it's prior.

There are several key points to extract from the results in table 5.8. Firstly all of the complexity measures used attributed zero complexity to the checker board pattern and the uniform pattern, this is in good agreement with what one might expect from the arguments given in section 3.2 about what was required of the complexity measures and is a clear indication that the measures chosen do have those desirable properties.

Secondly all of the measures attribute relatively low values to the regular, crystal like structure, shown in figure 5.62c. This is because, while it is a regular repeat structure, it does contain multiple curvatures, for the curvature measures to detect, and multiple length scales detected by the correlation function measure, which are different from those of the prior. These result in a small number of bins being occupied in the probability distributions, and hence a small, but non-zero, value of the complexity. In addition to this comparison of the complexity values for figures 5.62c and 5.62d shows that all of the measures successfully identify the imperfections in the structure in figure 5.62d, as indicated by increased complexity values. Here the increase is due to an increase in the number of occupied bins and a variation in the frequencies in the probability distributions.

Another interesting feature of these results, which goes right to the heart of the discussion about how ill-defined the concept of complexity is, is the fact that the complexity measures disagree significantly as to the complexity of the same patterns and even about which pattern is the most complex. Clearly there is no right or wrong answer here, but, rather more interestingly, the differences between the values here reveal much more about the nature of the measures themselves, or conversely the differences in the values with knowledge of how the measures behave reveals something about the nature of the patterns(39).

In order to better understand why the complexity measures attribute the values they do it is worth considering what happens at the intermediate stage of the calculation by examining the probability distributions which are generated by the different procedures. The probability distributions generated for the test patterns shown in figure 5.62 using the three different approaches are shown in figures 5.63 to 5.65.

---

(39) While this is not of immediate interest here it will form an important part of the discussion in section 5.3.4, where it will be demonstrated that one can, to some extent, determine the key visual features of the pattern from the complexity measures alone.

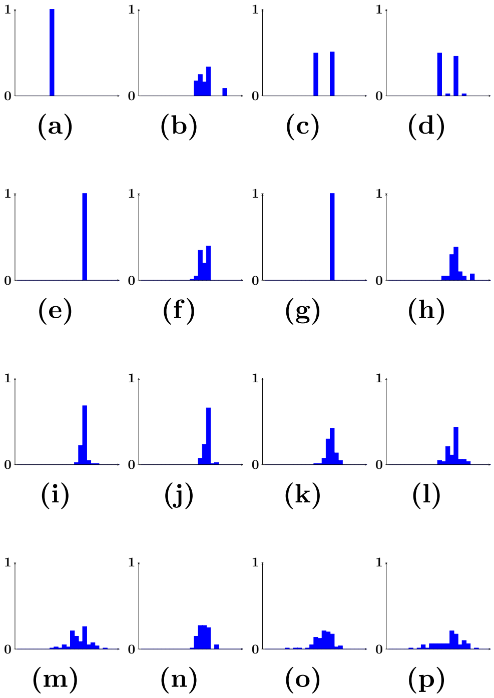

Figure 5.63: Probability distributions for the patterns shown in figure 5.62, biased upon the Gaussian curvature.

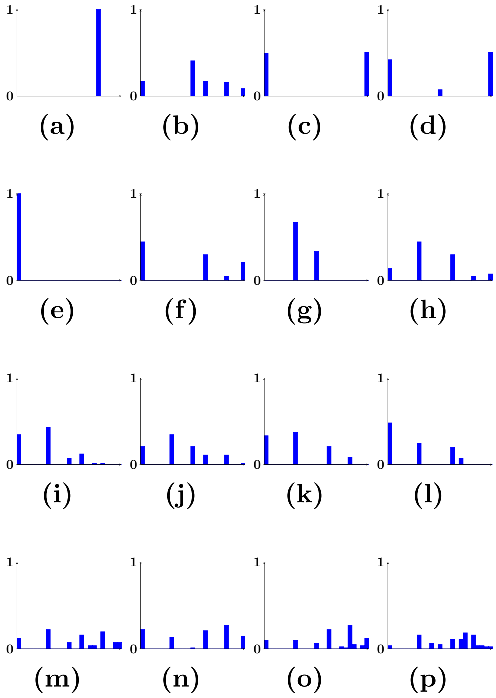

Figure 5.64: Probability distributions for the patterns shown in figure 5.62, biased upon the mean curvature.

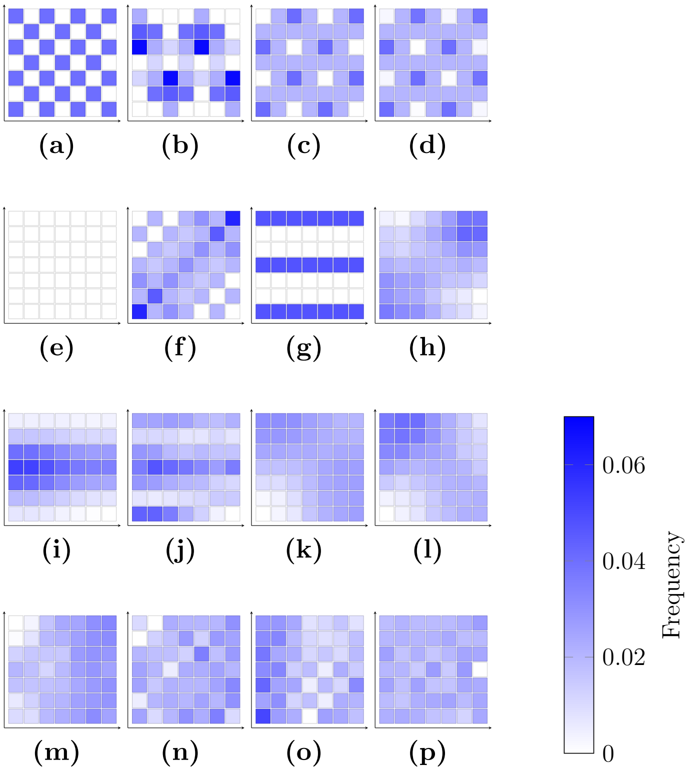

Figure 5.65: Probability distributions for the patterns shown in figure 5.62, biased upon the correlation function.

Using these results one can see much more clearly why the complexity measures respond in the way they do for the patterns shown in figure 5.62. In particular the features of the pattern to which the complexity measure are most sensitive become much more apparent. A good example of this is figure 5.62g which scores highly based on the mean curvature, but is attributed zero complexity by the Gaussian measure. The reason for this is that the Gaussian measure of the curvature is intrinsic and as such is unable to detect the curvature in this particular pattern, this much is clear from figure 5.63g which shows an identical probability distribution to that of the perfectly uniform pattern in figure 5.62e.

By contrast, figure 5.64g shows that there are two different values of the mean curvature present in this pattern at differing frequencies, thus demonstrating the presence of some structure and attaining a high complexity value. Like the mean curvature measure the correlation function detects the presence of some structure in this pattern, but because the intensity of all of the peaks is identical, due to the regular nature of the pattern the complexity value is not quite as high.

By contrast the lack of a regular structure in figure 5.62p leads to a very heterogeneous correlation function, as depicted in figure 5.65p, containing multiple peaks and troughs of differing intensities, which is vastly different to the regular structure of the prior. Hence the correlation function based measures attribute a very high value of complexity to this pattern. However, because this pattern is so heterogeneous, the distribution of curvatures, as measured by both of the curvature measures, is relatively wide as figures 5.63p and 5.64p show, which reduces the complexity values as the pattern is perceived to lie toward the random side of the scale, having a low disequilibrium or redundancy value.

Figure 5.62b is another interesting case of disagreement between the measures. The two curvature measures score this pattern relatively highly as they detect a variety of different curvature values occurring at different frequencies. In contrast the correlation function detects the presence of the regular repeat pattern, which is not so dissimilar to the crystal used as its prior, and thus attributes a low Shannon entropy and therefore a low complexity.

Visually figures 5.62m and 5.62n are very similar, the only real difference being that some of the grey cells further from the structure have been removed in figure 5.62m, hence it is unsurprising that they have been attributed similar complexity values and have similar probability distributions. It is clear, by comparing figures 5.63n, 5.64n and 5.65n with figures 5.63m, 5.64m and 5.65m, that the addition of these new values serves to broaden and soften the probability distributions in all cases. Interestingly, however, the mean curvature based complexity values, which are the smallest of the three, increase going from figure 5.62n to figure 5.62m while the complexity values based on the Gaussian curvature and the correlation function decrease. The reason for this is that there are initially relatively few peaks, of similar size, in the mean curvature probability distribution leading to a relatively low Shannon entropy, thus the increase in the number of peaks, seen in figure 5.64m, leads to a higher complexity value, while the same process occurring to the initially broader probability distributions in figures 5.63n and 5.65n leads to a decrease in the disequilibrium and redundancy.

Similarly, the patterns in figures 5.62i and 5.62j are visually very similar, as are figures 5.62k and 5.62l, with the only difference being the number of volume fraction values used to create them. And, again, it is hardly surprising that the probability distributions generated from them are very similar as well, leading to similar values in the complexity in many cases.

It is also worth pointing out, with regard to these patterns, that the measures based on the mean curvature give much smaller values for the complexity than the other measures, but are able to discriminate between the patterns with much greater precision. This is perhaps most easily seen graphically in figure 5.66.

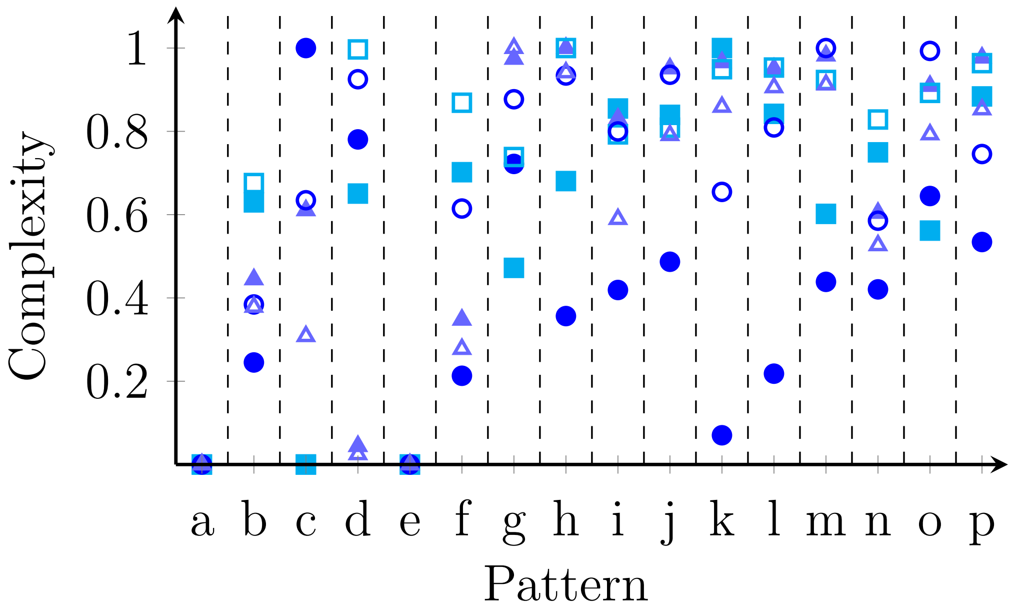

Figure 5.66: Plot showing the normalised complexity values calculated using the different methods for the patterns shown in figure 5.62. Here the cyan squares (■,□) correspond to the measures that use the Gaussian curvature as a means of generating a probability distribution, the blue circles (●,○) to the mean curvature and the light purple triangles (▲,△) to the correlation function. The solid symbols (■,●,▲) correspond to the LMC measure of complexity while the open symbols (□,○,△) correspond the the information based measure.

Figure 5.66 also shows that the Gaussian curvature measure is barely able to distinguish between figures 5.62i and 5.62j, or in the case of the information based measure figures 5.62k and 5.62l, though it does a little better when coupled with the LMC measure in the case of figures 5.62k and 5.62l. Clearly this is down to the fact that the particular probability distributions generated here lie in a region where the information measure is not very sensitive. In the case of figures 5.62k and 5.62l the correlation based measure also struggles to distinguish between the two patterns, though this is perhaps unsurprising since there is little difference in the structure. It is more surprising, however, to discover that coupled with the LMC measure the correlation function approach attributes very similar complexity values to all of the patterns in figures 5.62j to 5.62m, despite clear differences in the probailty distributions shown in figures 5.65j to 5.65m, Once again this is likely to be due to the fact that the complexity measure is simply not sensitive in this region. This is hence part of the reason why it is often better to consider the results of multiple complexity measures when considering the structure of two dimensional patterns.

5.3.2 The Effect of the Probability Distribution on the Complexity

There has been much discussion in section 5.3.1 about the shapes of the probability distributions produced by each of the different means for each of the patterns and these were presented as explanations for how the complexity measures behaved. Clearly from the arguments given in section 3.2, about the nature of the convex measures used here, one would expect that the uniform probability distributions and those where only one of the bins is occupied would yield a complexity of zero, for both of the measures used in this work. However, up until this point nothing has really been said of how the different complexity measures respond to the bin occupancies of intermediate probability distributions.

The first point worth making on this topic is that the complexity measures only depend on the number of bins occupied and their occupation frequency and not on their relative positions. This much is clear from equations 3.34 and 3.36, where it is clear that all of the probabilities are weighted evenly and no information about where they come from in relation to the broader distribution is retained. There is also evidence of this when comparing figures 5.63 and 5.64, in that the probability distributions produced by binning the mean curvature values are much more spread out, with gaps between the occupied bins, than those for the Gaussian curvature, which are usually more centralised around a maximum, yet in some cases there is little difference between the complexity values. Thus, as far as the discussion of these complexity measures goes, one need only be concerned with how many bins are occupied and what the occupancy is, not which bins are occupied.

However, since the occupancy is, in theory, a continuous variable this still leaves an infinite number of possibilities[(40)] so it is not possible to consider the effect that every feature of the probability distribution has on the complexity. One can, however, get a reasonable impression of how the complexity measures work by considering a probability distribution where the probability is restricted to two possible values, such that the occupancy of n of the bins is $\frac{1}{n}$ and the occupancy of all other bins is zero. Since the complexity does not depend on which bins are occupied a convenient mathematical expression for this is

$$p_i = \begin{cases} \frac{1}{n} & 1 \leq i \leq n \\ 0 & n < i \leq N \end{cases}, \tag{5.13}$$

where N is the total number of bins.

Figure 5.67 shows how the complexity, as calculated by the two measures described in section 3.2, responds to the probability distribution described by equation 5.13 as a function of the number of occupied bins, n.

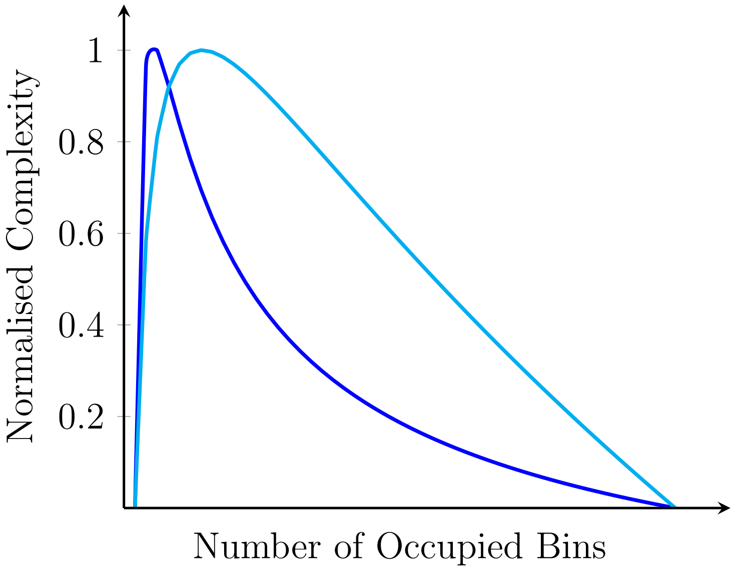

Figure 5.67: Plot of the complexity, as calculated by the two measures described in section 3.2, as a function of the number of occupied bins in a probability distribution where all occupied bins have equal occupancy. Here the blue line (—) corresponds to the LMC measure while the cyan line (—) corresponds to the information based measure.

Here the most striking feature is the fact that the curve for the LMC measure is much narrower than that of the information measure. This has important consequences in

---

(40) Even for a discrete grid, of a reasonable size, the number of possible, unique, arrangements is huge, as the number of unique probability distributions follows a binomial distribution in terms of the total number of bins and the number of grid cells.

terms of the resulting complexity values; while the information measure falls in a roughly linear fashion at high disorder the LMC measure is much steeper just after the peak with a long tail in the highly disordered region. This means that while the information measure offers a wider range of complexity values for relatively disordered states enabling it to discriminate more easily between states of relatively high Shannon entropy the LMC measure can determine, much more precisely, how well ordered the system is in states with a Shannon entropy slightly above the value at maximum complexity.

The positions of the maxima are also important since this gives a clear indication of the types of patterns likely to be deemed the most complex by the different measures. The peak of the LMC measure falls at a lower bin occupancy than that of the information measure suggesting that the LMC measure favours patterns that are slightly more ordered than those which are attributed maximum complexity by the information measure. This is an important consideration when interpreting the complexity values attributed to patterns since it provides another means by which one may draw conclusions about the form of the pattern based purely upon the complexity values it is attributed. One can see a hint of this kind of behaviour in the results presented for the test cases in section 5.3.1, in that the probability distributions in figures 5.63 to 5.65 for the patterns attaining maximum complexity from the LMC measure typically have a smaller number of bins, with higher occupancy, than the probability distributions of those attributed maximum complexity by the information measure.

In addition to this clear difference it is also worth noting that figure 5.67 shows several similarities between the two measures. Not least of these is the fact that both measures give zero complexity when there is only one occupied bin and when the occupancy of all of the bins is equal. This goes right back to the definitions of the measures in section 3.2, where it was argued that a good complexity measure for a two dimensional pattern should attribute zero complexity to both perfectly ordered states, where only one state is occupied, and states of total disorder, where all states are equally likely.

Another important similarity here is that, although the two measures disagree about the exact location of the maximum with respect to the number of occupied bins, the two measures both exhibit a maximum well below the point at which half of the bins are occupied. This implies that both favour systems that are relatively well ordered to those with a very high Shannon entropy. This is likely to be due to the fact that the Shannon entropy rises quickly when only a few states are occupied and then more gradually as the amount of disorder increases. To some extent this agrees well with how one might interpret a pattern visually, in that a small imperfection, or heterogeneous region, would be relatively easy to spot in an otherwise uniform, or perfectly crystalline, system, but it would be much more difficult to detect any order in a system that was highly disordered. Thus it could be argued that there is not only good agreement between the two measures about the positioning of the maxima towards the more ordered end of the spectrum, but that this also agrees with human interpretation of the patterns.

Finally it is worth stressing that although the results presented in figure 5.67 provides a great deal of insight into how the complexity measures behave and acts as a useful tool for interpreting other results, such as those presented in section 5.3.1, one must be careful not to over generalise the points that have been extracted from this data since it is important to remember that these results are only strictly true for the probability distributions descibed by equation 5.13 and variable bin occupancies are an important part of the calculation of the complexity, and can have a significant effect on the final value. In fact it is worth noting at this point, since it complements the results discussed in this section, that a absolute maximum for the LMC measure is known to occur when one of the bins has an occupation probability of two thirds and the remaining one third is spread evenly between the remaining bins[92]. This is worth bearing in mind for two reasons. The first is that it is evidence of the importance of considering the frequency in all of the bins and secondly because it provides further insight into the behaviour of the LMC measure itself, which can be used to aid the understanding of subsequent results.

5.3.3 Maximal Complexity Patterns

To complement the results presented in sections 5.3.1 and 5.3.2, and to further enhance understanding of the complexity measures, Monte-Carlo simulations[3] were run to find the patterns of maximum complexity as defined by the two different complexity measures, described in section 3.2, coupled with the three different methods of converting the pattern into a probability distribution, detailed in section 3.2.1. Figure 5.68 shows the patterns produced.

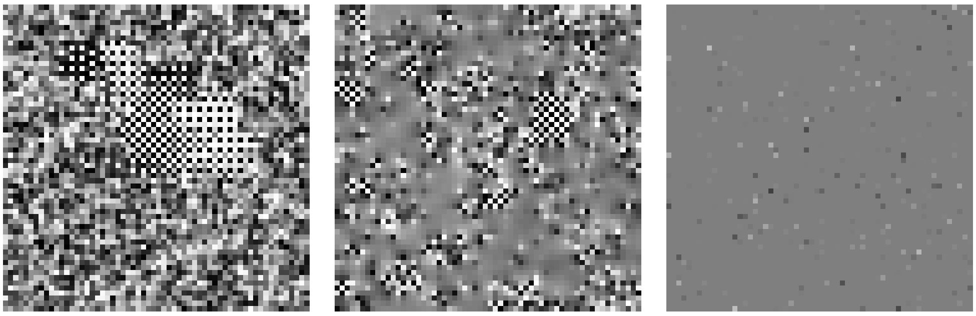

(a) LMC measure using Gaussian curvature.

(b) LMC measure using mean curvature.

(c) LMC measure using the correlation function.

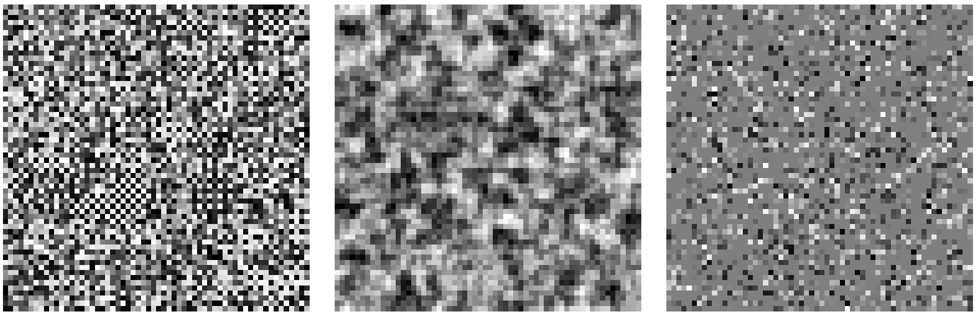

(d) Information measure using Gaussian curvature.

(e) Information measure using mean curvature.

(f) Information measure using the correlation function.

Figure 5.68: Maximum complexity patterns found using the Monte-Carlo method described in section 4.2.2.

Here it is immediately apparent that all of the patterns exhibit a mixture of order and disorder, as is to be expected from the definition of the complexity measures and also what one might, themself, consider a complex pattern. It is interesting, however, to see that this manifests itself in different ways in each of the patterns, some containing regions of ordered structure interspersed between regions of disorder, as in figures 5.68a, 5.68b and 5.68d, with others containing varying amounts of order on different length scales, as in figures 5.68c, 5.68e and 5.68f; while all of the patterns remain, visually, very distinct from one another. Of course in order to understand why the different complexity measures defined these particular patterns as having maximum complexity one must turn to the underlying probability distributions that relate to them. These are shown in figure 5.69.

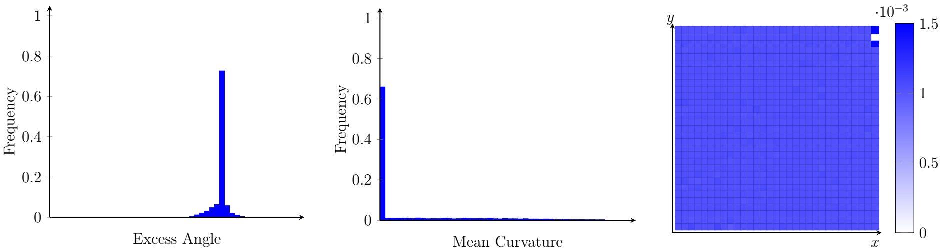

(a) LMC measure using Gaussian curvature.

(b) LMC measure using mean curvature.

(c) LMC measure using the correlation function.

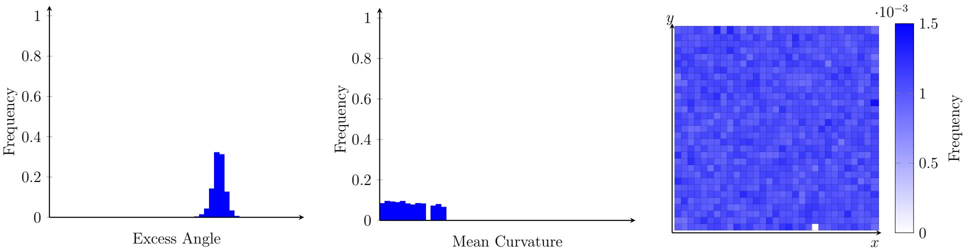

(d) Information measure using Gaussian curvature

(e) Information measure using mean curvature

(f) Information measure using the correlation function.

Figure 5.69: Plots of the underlying probability distributions used to calculate the complexity of the maximum complexity patterns shown in figure 5.68.

Upon examining these probability distributions the same pattern as that noted in sections 5.3.1 and 5.3.2 becomes clear, in that both measures yield a high complexity value when there is a reasonable amount of order in the system. Furthermore there is additional evidence here supporting the results presented in section 5.3.2 that the LMC measure favours narrower probability distributions than the information based measure. This much is clear from the results of all of the different means of generating the probability distributions since the distributions produced by the two curvature measures are clearly wider for the information based measure than their counterparts based on the LMC measure and comparison of figures 5.69a and 5.69d clearly shows that, while the order in the pattern favoured by the LMC measure is restricted to a very narrow range of length scales, order is present on many more length scales in the pattern that maximised the information measure. Clearly the patterns produced using the different means of producing probability distributions have very different visual features and yet the probability distributions themselves bear some striking similarities. This is especially clear among the probability distributions for the patterns that maximised the LMC measure as they are all relatively uniform with one very sharp peak consisting of just a few extreme values. Meanwhile the maximum complexity patterns as judged by the information measure all contain a few bins within which most of the measurements lie, but lack the sharp peak.

It is also important to note that the probability distribution, shown in figure 5.69b, for the maximum complexity pattern as defined by the LMC measure of complexity coupled with the mean curvature is, to a very good approximation, identical to the theoretical complexity maximising distribution for the LMC measure, derived in reference 92. This suggests that the method has indeed found the true maximum. While the probability distributions based on the Gaussian curvature and correlation function are similar they are by no means identical to this theoretical maximum, which poses the question of whether the method has indeed found the maximum in that case. Clearly it has not found the maximum possible complexity, but when one considers what constraints are imposed on the probability distributions by the method used to generate them one can satisfy oneself that the Monte-Carlo method has found the maximum complexity possible, given the particular constraints on the distributions used. For example the correlation function will not show correlations alone, there must also be anti-correlations. This in itself is an important distinction to make, and well worth considering when comparing the complexity values obtained from the different measures.

Another important question to consider here is that of uniqueness; the patterns shown in figure 5.68 are not the only patterns that can maximise the complexity. There are many patterns that could produce the same probability distributions and even many probability distributions that would produce the same complexity values since the complexity measures only depend on the frequencies of the bins and not their relative positions. Thus the probability distributions shown in figure 5.69 have relative frequencies that are unique to the maximum complexity, but the peaks could be positioned anywhere on the x axis and still give the maximum complexity. In terms of the patterns there are clearly an infinite number of patterns that would produce the same probability distributions. However, one would expect to see common features between these patterns since fixing the probability distribution demands that certain features that produce certain curvatures or correlations must be present at certain frequencies. In the case of the two curvature measures, which only use local information about the patterns, they can occur at any location in the system, while the correlation function measure requires order on certain length scales, but this order can come in any form. In fact it was striking how similar patterns generated using different random number seeds, or even different sized grids, become as the complexity approaches its maximum, often with very similar looking features reappearing in different locations or with slightly different shapes. A good example of this is figure 5.68a where the large crystal region remerged every time in different locations, with a slightly different shape.

Turning more to the patterns themselves it is worth noting that in most instances the curvature based measures were maximised by patterns with separate amorphous and crystalline regions, these are most noticeable in figure 5.68a, where there is one large crystal region, but are also clearly present in figures 5.68b and 5.68d. These regions are particularly useful for the purposes of drawing comparisons between the patterns since they have a fixed curvature in the centre and are relatively easy to spot. In the case of the Gaussian curvature the crystalline region occurs in a single region, but the fact that there are different kinds of crystal gives the probability distribution some width. Meanwhile the sharp peak originates from the fairly smoothly varying amorphous region, where the curvature is small. In the case of the information measure the distribution is given even more width by the fact that the crystal regions are spread out and there are more boundaries between regions. This originates from the fact that the information based measure favours broader distributions than the LMC measure. There is also a pronounced difference between figures 5.68a and 5.68b in that, while the Gaussian measure, which is an intrinsic measure of curvature, has a smoothly varying amorphous background the extrinsic, mean curvature results in a uniform background, which gives the peak value at zero curvature. In figure 5.68b there is an example of all possible types of mean curvature, such that all of the bins of the probability distributions are occupied to obtain the maximum complexity, and hence why the crystal regions are relatively small. This would not have been possible with a background like that shown in figure 5.68a because the undulations would have increased the occupancy at low, but non-zero, curvature. This is exactly what has happened in figure 5.68e where a wider distribution was required. The ramifications of this property involving the width of the distribution, which were discussed in section 5.3.2, for the patterns that maximised the two measures are perhaps most clearly observed by comparing the two measures when based on the correlation function, figures 5.68c and 5.68f. Here it is clear that while figure 5.68c is very close to the uniform state, having few features, figure 5.68f has order on many more length scales, giving a broader range of frequencies in the probability distribution, favoured by the information measure.

Before concluding this section it is perhaps worth returning to the issue of uniqueness, especially since some of the patterns such as figure 5.68c are still somewhat reminiscent of the initial, uniform, state. While one can say with a fair amount of confidence, given the previous discussion, that the patterns shown in figures 5.68a to 5.68f are representative of the patterns that maximise the complexity, it is not fair to say that they would not have been different given a different initial condition, for example if the initial state had been random, one would still expect to see some of the same features such as crystal structures in the final states. However, it is unlikely that the background of figure 5.68c would have been quite so uniform as a small amount of short range order set against global disorder would have still produced a correlation function with one prominent peak. There is, however, a good reason, which was touched upon in section 4.2.2, why this avenue was not explored. Even at high effective “temperature”, it is very difficult to get the system out of a random state, since the formation of any kind of regular structure takes not just one, but several, relatively unlikely events. Not only do cells close to each other need to be selected time after time, the amount of material being moved has to be just right, and even though these moves might increase the complexity in the long term it is unlikely that they will each produce a significant increase individually; so there is a good chance of the structure being destroyed in the mean time. Thus the decision to start from the uniform state was simply a matter of practicality, while in principle it should be possible to obtain the maximal complexity patterns from any starting point, starting with a uniform state simply got there faster.

5.3.4 Complexity of Patterns Produced By the Particle-Laden Fluid Model

To conclude this section on the discussion of the various measures of complexity that can be applied to two dimensional patterns it is worth discussing how the complexity changes as patterns evolve in the model of the draining particle-laden fluid, and what can be learnt about these patterns from their complexity.

To begin with it is perhaps most appropriate to consider the channel patterns that form in the basic model in the absence of an osmotic pressure barrier. As discussed in section 5.2.3, these patterns are associated with an overall decay in the amplitude of the fluctuations, rather than the growth in amplitude normally associated with the formation of patterns. Nevertheless there is clearly a pattern present and the complexity measures are only sensitive to the shape of the pattern and not its intensity. It is this feature that makes the complexity measures so useful since they allow one to see the structure of the pattern in a quantitative way despite the decay in its amplitude. Figure 5.70 shows how the complexity, according to the different measures, varies over time.

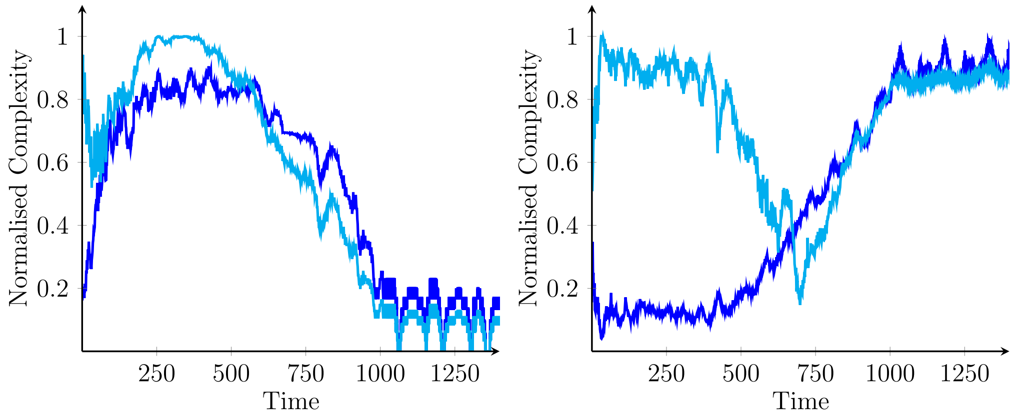

(a) Gaussian curvature. **(b)** Mean curvature.

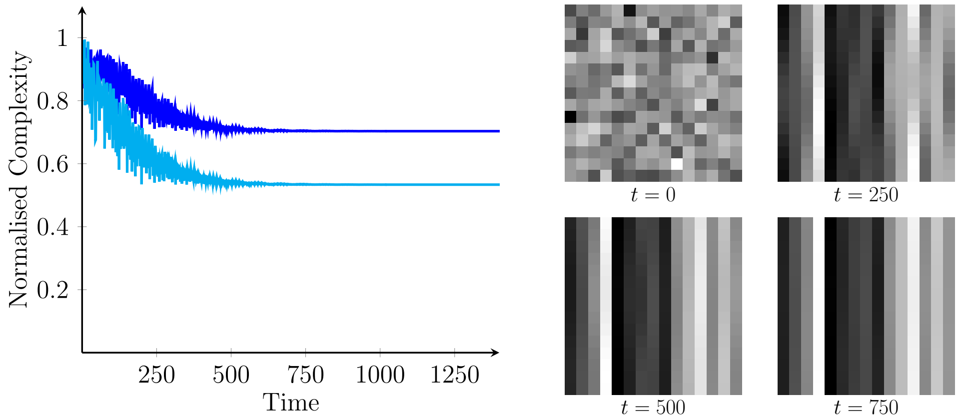

(c) Correlation function. **(d)** Pattern formation process.

Figure 5.70: Plots showing how the LMC and information based measures of complexity change over time, as a channel pattern develops, using different methods for creating a probability distribution. Four snapshots showing the development process are also show. Here the blue line (—) shows the data obtained with the LMC measure and the cyan line (—) that of the information biased measure. The parameters used in this particular simulation were: $\hat{\zeta}_p = 2$, $\hat{\zeta}_s = 5$, $\hat{\eta} = 7$, $\hat{\rho} = 1.5$, $\hat{\mathbf{g}} = 15\hat{\mathbf{y}}$, $\phi_0 = 0.45$, $\phi_{max} = 0.64$, $\phi_l = 0.1$ and $\phi_u = 0.54$.

In these plots as with the test cases presented previously the different measures disagree somewhat as to what the complexity should be. The interesting thing here is that one can infer from this disagreement how the pattern is likely to look without having prior knowledge. Firstly by comparing the two curvature measures one sees that while the Gaussian curvature decays towards the end the mean curvature grows, this is because the Gaussian curvature is unable to detect curvature in situations where the geodesics are parallel, while the mean curvature is. Thus while the mean curvature measure of complexity is approaching the maximum complexity condition, where only a small number of states are occupied with different probabilities the complexity measures based on the Gaussian curvature are decaying as the probability distribution converges on one in which only the zero curvature state is occupied. From this comparison one may glean that the pattern must resemble a corrugated sheet; there must be some undulations and these must come with a range of amplitudes because the mean curvature measures are increasing. This hypothesis is supported further by the drop in complexity for the measures based on the correlation function since the number of different separations over which the system is ordered is falling. These measures do not fall to zero, precluding the possibility of a checkerboard like crystal structure; thus one must conclude that there is either order on some, but not all length scales, or directions, or that the crystal structure is imperfect. However, only the former is consistent with the fall in the Gaussian curvature. Of course from the complexity measures alone one cannot know the orientation of this structure, but it is testament to how effective these comparisons can be that one can tell so much about what structures are present in a way that is non-specific to the pattern in question, and of course one sees all of these features in figure 5.70d.

Of course it makes little sense to stop the discussion there having only considered the complexity of the final, steady state, pattern(41). Arguably the real power of the complexity measures is that, because a single value is produced, they can be plotted as a function of time and so provide a window on the dynamics of the system, which could not have been obtained by looking at the pattern as a whole.

In the first 300, or so, time units the Gaussian curvature measures increase on the whole(42). This can be thought of as being due the initial growth of the channels, before they span the system. Here there are still a range of different mean curvatures, but the number of occupied states is beginning to fall, as the random fluctuations in the flow direction are smoothed out, and the curvature associated with the ends of the growing bands, and the zero curvature associated with the middle begin to dominate the distribution. This phase can also be seen clearly in the correlation function based measures, which fall as the number of features at different separations falls and one feature begins to dominate. The mean curvature based measures remain roughly constant over this period since there is still a fairly wide range of possible curvatures in the system producing a relatively wide distribution. It is precisely this width that leads to the disagreement between the LMC and information based measures that is clearly evident here, but this will be discussed in more detail later. Later on as the channels begin to lengthen the Gaussian curvature begins to level out as it cannot detect the uniform middle sections. At this point the correlation function based measures also level out, and remain level as there is no further change in the length scales over which order is present. The final phase in the development of the channels is the slow smoothing out of inhomogeneities along the length of the channels. This can be seen in figure 5.70d and is associated with a decline in the Gaussian curvature measures as the absence of the ends means that these fluctuations are the only source of variations in the Gaussian curvature. Finally looking at the mean curvature, and returning to the issue of the disagreement between the two different complexity measures, it is clear that while the LMC measure begins to rise the information based measure be-

---

(41) It is worth noting that several simulations on patterns of this type revealed this to be the steady state, in which all the measures remained roughly constant for much longer than the timescale shown on the plots in figure 5.70.

(42) There is an initial fall in the information based measure which will be discussed in more detail in due course.

gins the fall. In this region the number of occupied bins in the probability distribution begins to fall, as the channels emerge and smooth. Because the information based measure tolerates wider distributions the initial complexity is high and falls as the distribution narrows, as shown in figure 5.67. Meanwhile the narrowing of the distribution increases the LMC measure. However, since both measures are maximised by distributions that contain a range of occupation frequencies both measures increase towards the end. This is an example of how knowledge of the underlying probability distributions can be used to make predictions about the patterns formed given their complexity since the comparison of the two measures reveals something of the shape of the probability distribution.

Another case worthy of consideration is the case of the patterns that form as a result of the growth in the amplitude of the fluctuations when an attractive interaction between the particles is included. Examples of these are shown in figures 5.57a and 5.57b; the complexity of these patterns, according to the different measures, is plotted, as a function of time, in figures 5.71 and 5.72 respectively.

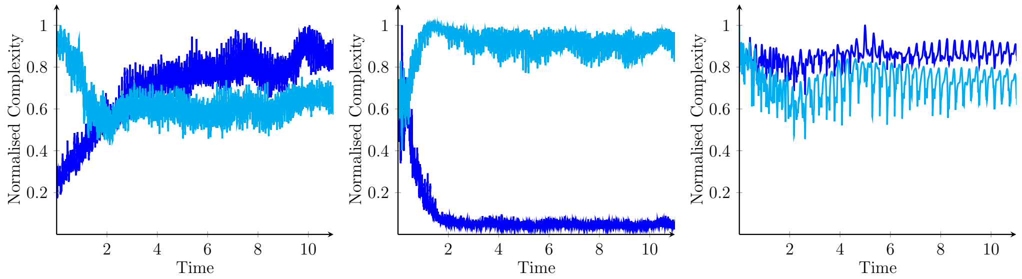

(a) Gaussian curvature. **(b)** Mean curvature. **(c)** Correlation function.

Figure 5.71: Plots showing how the LMC and information based measures of complexity change over time, as fluctuations grow due to attractive forces, using different methods for creating a probability distribution. Here the blue line (—) shows the data obtained with the LMC measure and the cyan line (—) that of the information biased measure. The parameters used to generate this example were the same as those used to generate figure 5.57a: $\hat{\zeta}_p = 2$, $\hat{\zeta}_s = 1.5$, $\hat{\eta} = 1$, $\hat{\rho} = 5$, $\hat{\mathbf{g}} = 25\hat{\mathbf{y}}$, $\phi_0 = 0.4$, $\phi_{max} = 0.64$, $\phi_l = 0.2$ and $\phi_u = 0.44$, $a_{vdW} = 15$ and $\kappa_S = 1$.

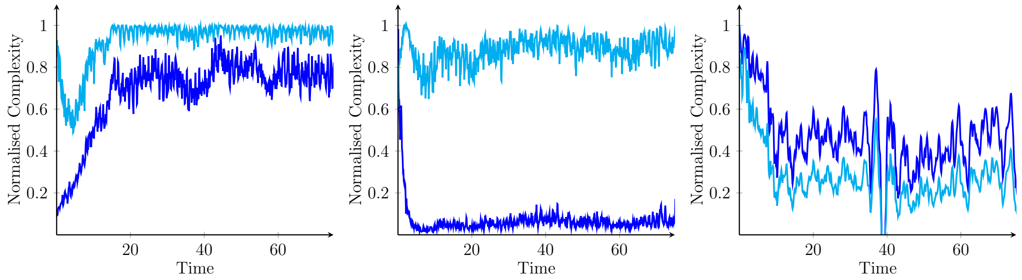

(a) Gaussian curvature. **(b)** Mean curvature. **(c)** Correlation function.

Figure 5.72: Plots showing how the LMC and information based measures of complexity change over time, as fluctuations grow due to attractive forces, using different methods for creating a probability distribution. Here the blue line (—) shows the data obtained with the LMC measure and the cyan line (—) that of the information biased measure. The parameters used to generate this example were the same as those used to generate figure 5.57b: $\hat{\zeta}_p = 2$, $\hat{\zeta}_s = 1.5$, $\hat{\eta} = 1$, $\hat{\rho} = 5$, $\hat{\mathbf{g}} = 5\hat{\mathbf{y}}$, $\phi_0 = 0.2$, $\phi_{max} = 0.64$, $\phi_l = 0.2$ and $\phi_u = 0.44$, $a_{vdW} = 5$ and $\kappa_S = 1$.

As before one can infer a great deal about the structure of the patterns from their complexity values, simply by comparing and contrasting the different measures. The first thing that one notices here is that the evolution of the complexity is very similar for both patterns. Thus upon returning to figure 5.57 it is hardly surprising to see that both of the patterns have common features and undergo a similar formation process. Of course one would expect this to be the case as the underlying Physics is essentially the same. Here, as before, comparing the two measures based on the mean curvature gives some indication as to the shape of the probability distribution for this data since the complexity based on the information measure grows while that based on the LMC measure decays, suggesting that the distribution of mean curvatures becomes broader in the initial growth phase as the stripes begin to emerge. During this same phase it is also clear that in both cases the distribution of Gaussian curvatures narrows, increasing the complexity calculated using the LMC measure while reducing that of the information based measure. In the case of the patterns in figure 5.57a this later recovers due to the fact that the stripes are not as uniform along their length as those in figure 5.57b and hence increase the range of Gaussian curvatures in the distribution. This may also go some way towards explaining why the complexity measures based on the correlation function fall for the patterns in figure 5.57b, but not for those in figure 5.57a.

On the topic of the patterns that form when the particles experience an attractive interaction it is worth, also, considering the patterns formed when the attractive force is very strong, as they are clearly different to those formed when this force is much weaker, as the the flow field has far less influence. An example of a pattern formed under these conditions is given in figure 5.73 along with the time evolution of its associated complexity values.

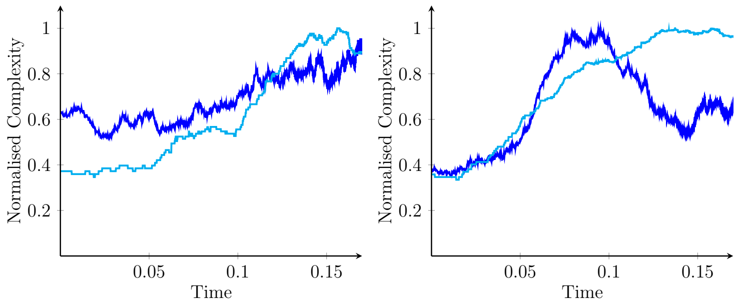

(a) Gaussian curvature. **(b)** Mean curvature.

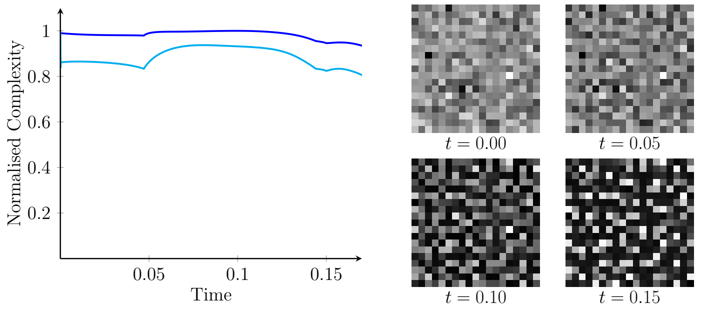

(c) Correlation function. **(d)** Pattern formation process.

Figure 5.73: Plots showing how the LMC measure, indicated by the blue line (—), and information based measure, corresponding to the cyan line (—), change over time, for a system with strong attractive inter-particle forces, using different methods of obtaining a probability distribution. Four snapshots showing the pattern developing are also show .The parameters used here were: $\hat{\zeta}_p = 2$, $\hat{\zeta}_s = 1.5$, $\hat{\eta} = 1$, $\hat{\rho} = 5$, $\hat{\mathbf{g}} = 10\hat{\mathbf{y}}$, $\phi_0 = 0.425$, $\phi_{max} = 0.64$, $\phi_l = 0.2$ and $\phi_u = 0.44$, $a_{vdW} = 150$ and $\kappa_S = 1$.

The first thing to notice here is that the two curvature based measures both increase steadily suggesting that the distribution of curvatures widens, from an initially narrow distribution. As this widening continues the LMC measure that is based on the mean curvature then begins to fall, suggesting that the width of this distribution is beyond the optimum at this stage. The fact that both the mean and Gaussian curvature measures increase suggests the absence of any long thin features like those present in figure 5.70d, since one would expect these to be associated with a decline in the measure based on the Gaussian curvature, for the reasons already outlined. Indeed figure 5.73d reveals that these features are not present in the resulting pattern. One also notices that there is little change in the measures based on the correlation function and this is hardly surprising when one refers to figure 5.73d as there is little change in the shape of the structure. The key difference here is in the amplitude of the fluctuations.

Finally, to conclude this section, it is worth considering how the complexity measures respond to the decay process, by which the system returns to a uniform state under the action of the osmotic pressure. In terms of the amplitude of the fluctuations, there is, of course, no pattern here, but there is still a change in the structure so one would expect the complexity measures to respond to this. The resulting plots of the complexity as a function of time for one such example system are given in figure 5.74 along with snapshots showing the evolution of the pattern itself.

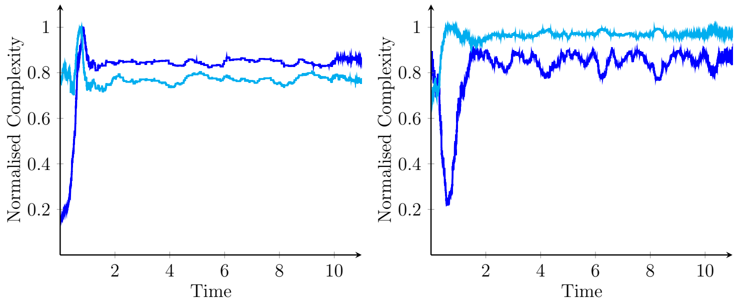

(a) Gaussian curvature. **(b)** Mean curvature.

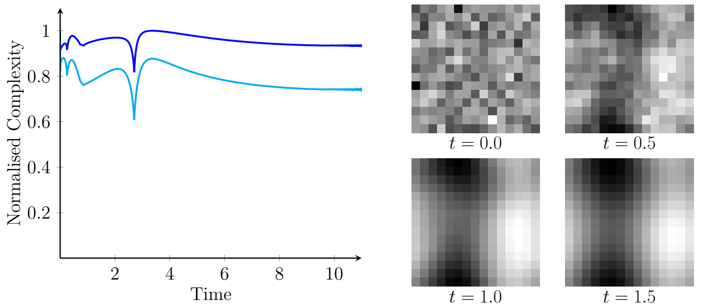

(c) Correlation function. **(d)** Pattern formation process.

Figure 5.74: Plots showing how the LMC measure, indicated by the blue line (——), and information based measure, corresponding to the cyan line (——), change over time, for a system with strong attractive inter-particle forces, using different methods of obtaining a probability distribution. Four snapshots showing the decay process are also show. The parameters used here were: $\hat{\zeta}_p = 2$, $\hat{\zeta}_s = 1.5$, $\hat{\eta} = 1$, $\hat{\rho} = 5$, $\hat{\mathbf{g}} = 10\hat{\mathbf{y}}$, $\phi_0 = 0.425$, $\phi_{max} = 0.64$, $\phi_l = 0.2$ and $\phi_u = 0.44$, $a_{vdW} = 150$ and $\kappa_S = 1$.

In these situations, where the fluctuations in the volume fraction decay, the system quickly reaches a state where only the longest wavelength fluctuations remain. This results in the complexity values levelling out rather quickly. Since the longest wavelength fluctuation is relatively smooth it has a very well defined curvature, which dominates the probability distribution, and so the pattern is attributed a relatively high value of complexity by the curvature based measures. Of course there is some variation in the complexity measures at the start as the shorter wavelength fluctuations in the volume fraction decay, and, naturally, there is significant disagreement between the LMC and information measures as the shape of the distribution changes. The correlation function measures decay slightly as the background fluctuations decay and the system size emerges as the dominant length scale, but this still represents a sharply peaked distribution, vastly different from that of a checker-board, so the complexity does not fall very much.

5.4 Hydrodynamics Simulations

5.4.1 Particles Jamming at a Constriction

Since hydrodynamic forces affect the collective motion of particles it was thought that they may play an important role in the pattern formation process [3], especially for large particles which are not heavily influenced by Brownian motion. Of particular interest, in terms of the processes involved in forming the band patterns observed in draining films [2], is what effect a slow moving, or static, obstruction within the particle flow has on the behaviour of the particles. This is, in many ways, closely related to the formation of fragile solids [26], formed from jammed particles, as the flow passes a constriction [24,26,30,132]. In order to investigate what effect hydrodynamic interactions had on the flow of the particles through a narrow gap in an obstruction a number of simulations with and without hydrodynamic interactions were run so that the results could be compared. In order to simulate two dimensional flow, but remove the effect of the substrate and the solvent-air interface the simulations were run in three dimensional space using infinite boundaries, for the solvent, with the particles initially distributed in a very narrow region in one of the dimensions, which can be thought of as the direction normal to the substrate. Though this came with the distinct disadvantage of allowing the particles near the edge to be surrounded by open solvent, removing the effect of the surfaces meant that it was possible to focus purely on the effect of the inter-particle hydrodynamic forces. Furthermore since it was the behaviour of the particles nearest the gap which was of most interest, it was thought that the artefacts introduced by allowing there to be open solvent around the edges would not have a dramatic effect on the qualitative results(43).

Perhaps the simplest obstruction one can envisage, that causes the stream lines of the flow field to converge, is a gap between two blocks of jammed particles. Figure 5.75 shows simulation results for an amorphous arrangement of neutrally buoyant particles at low volume fraction flowing around this type of constriction, from the frame of reference of the falling particles.

---

(43) Of course this effect could have been removed altogether by using periodic boundary conditions, but this would have introduced difficulties of its own, in the fact that one would no longer be considering one isolated obstruction, but an infinite series of obstructions in all directions, and it was thought that this would have a far more detrimental effect on the results.

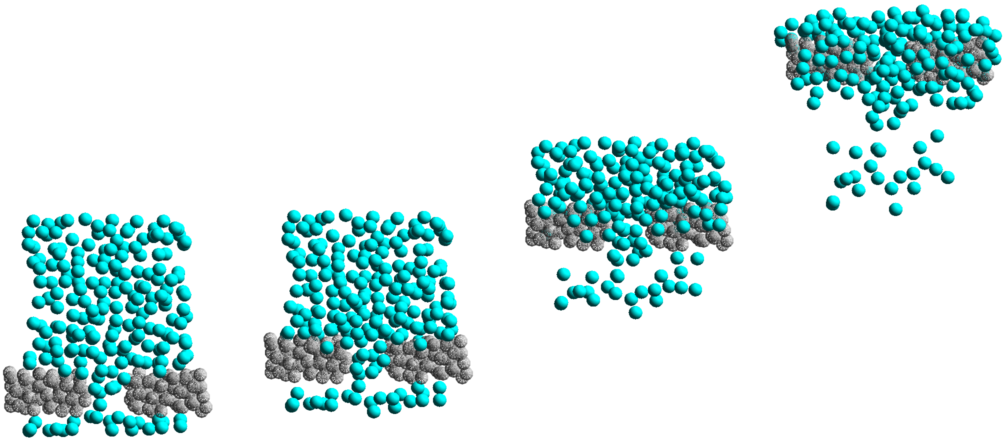

(a) With full hydrodynamic interactions.

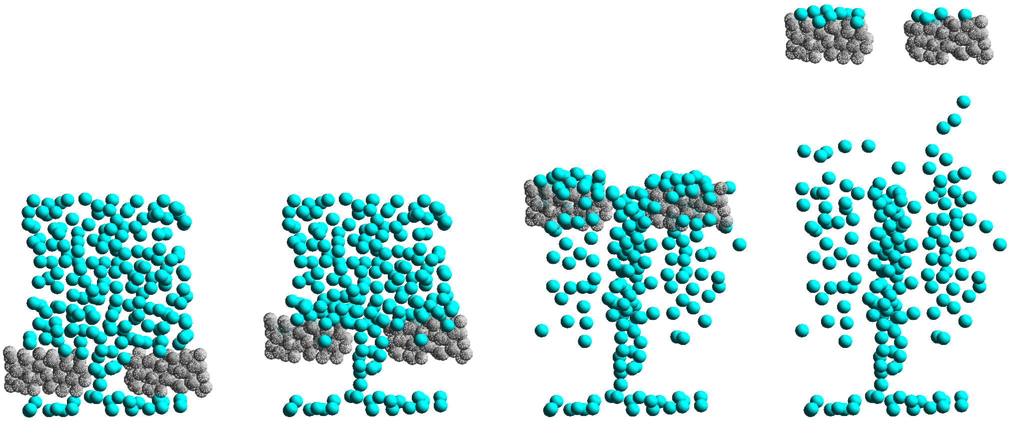

(b) Without hydrodynamic interactions.

Figure 5.75: Snapshots taken of a simulation in which a rigid body with an aperture in it passes an array of neutrally buoyant granular particles in a solvent. The two simulations shown here are identical in every way, except for the fact that the simulation shown in (a) includes the full hydrodynamic interactions while that in (b) does not. Here the free particles are show by the solid cyan spheres (●) and the particles that make up the obstruction by the wire-framed grey spheres (◍). In this example there are 200 free particles and 50 particles in each obstruction and the obstructions moved at one particle radius per time unit.

Here the two simulations are identical in every way except that the one shown in figure 5.75a contains the full hydrodynamic interactions while that shown in figure 5.75b has a constant drag coefficient for a fluid of equivalent viscosity. From this figure it is clear that the hydrodynamic forces have a significant effect on the motion of the particles; while the majority of the particles in the simulation without hydrodynamics fall straight through the gap those in the simulation that includes the full hydrodynamic interactions pass through the gap very slowly, obstructing particles higher up, and, at times jamming and unjamming as described in reference 24. It is also clear that the particles passing in front and behind the obstructions remain with the obstruction for a prolonged period of time in the case where the hydrodynamic interactions are included. This essentially acts to thicken the blockages and further restrict the motion of the particles above. Though there is no penalty for this motion in the simulations presented here, if one were to consider such an event occurring in a thin film there would be a resistive force arising due to particles passing around the blockages in this manner as a result of the surface tension in the solvent-air interface. This thickening of the obstruction would prevent particles from passing around it in this way in the future and also act to pin the obstruction. In the system without hydrodynamic interactions this does not happen and the particles pass easily around the front and back of the obstructions, as they do through the gap. In short the net effect of the hydrodynamic interactions is that they cause the particles to slow down and move with the obstruction, rather than simply moving around it as they do in the absence of hydrodynamic effects. This means that the free particles essentially combine with the blockages forming one larger blockage. It is clear from comparison of figures 5.75a and 5.75b that there are far more particles above and surrounding the obstruction when the hydrodynamic interactions are active than there are when they are not.

In order to examine what effect the width and shape of the gap had, simulations were also run on a range of different gaps. Some of these are shown in figure 5.76.

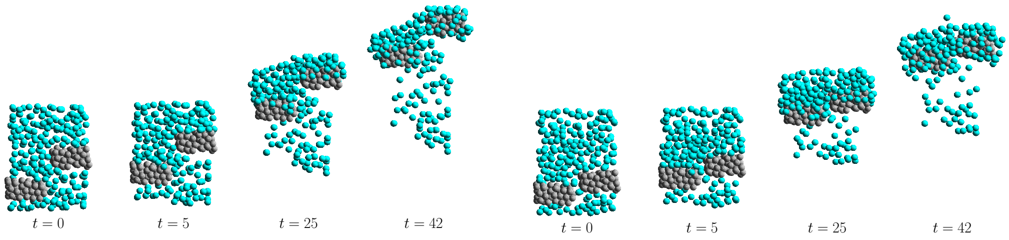

With full hydrodynamic interactions. With full hydrodynamic interactions.

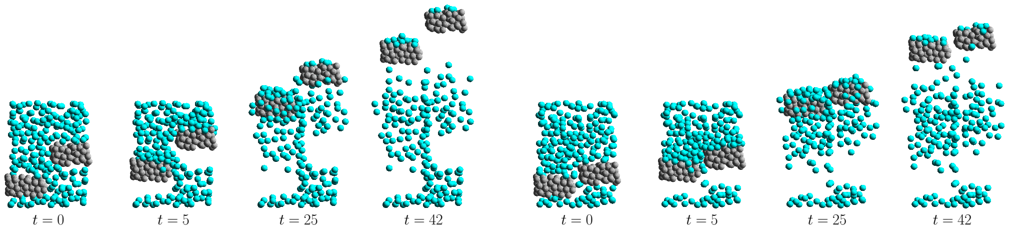

Without hydrodynamic interactions. Without hydrodynamic interactions.

(a) **(b)**

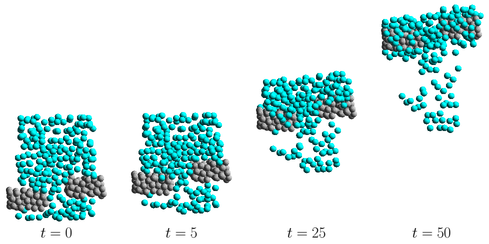

With full hydrodynamic interactions.

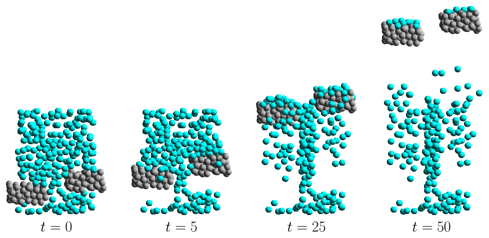

Without hydrodynamic interactions.

(c)

Figure 5.76: Images showing snapshots taken of simulations in which a rigid bodies with three different apertures pass an array of neutrally buoyant granular particles in a solvent. The two simulations shown in each case are identical except for the fact that one includes full hydrodynamic interactions while the other does not. Here the free particles are show by the solid cyan spheres (●) and the particles that make up the obstruction by the wire-framed grey spheres (◍). In these examples there are 200 free particles and 50 particles in each obstruction and the obstructions moved at one particle radius per time unit.

From this figure it is clear that the qualitative results are much the same regardless of the shape of the aperture, the particles still move with the obstructions far more in the simulation that includes the hydrodynamic interactions than they do in the one without. In fact the size of the gap appears to have less of an effect on the simulations with hydrodynamics than it does on those without. This much is clear from comparison of figures 5.76b and 5.76c, where one can see there is very little difference between the two simulations that include hydrodynamic interactions, where as the narrower gap clearly reduces the rate at which particles pass through the obstruction, and increases the number that pass around, in the simulations without the hydrodynamic effects. This is because, although the exact size of the gap is different, the flow field in the solvent has essentially the same features in both cases. The fact that the hydrodynamic interactions reduce the speed of the particles in this way means that they could, in theory, lead to a large gap closing over time.

Also of interest, and particularly relevant to the formation of band patterns, is the behaviour of the particles around the end of a single obstruction. This situation is worth considering for two reasons. Firstly it may be of relevance to the early stages of the process by which band patterns form in draining films of colloidal particles, where it is unlikely that two blockages would occur in close proximity. Secondly making the system simpler by removing the degrees of freedom associated with the relative position of the two blockages means one can gain a deeper understanding of the underlying processes. Figure 5.77 shows simulation results for a system of neutrally buoyant granular particles flowing past an obstruction, while figure 5.78 shows their velocities relative to the solvent as a function of position.

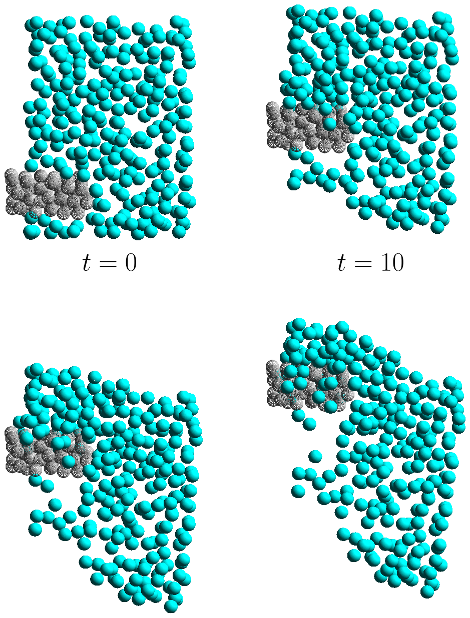

$t = 0$ $t = 10$

$t = 20$ $t = 30$

Figure 5.77: Images showing snapshots taken of a simulation in which a rigid body passes an array of neutrally buoyant granular particles in a solvent. Here the free particles are shown by the solid cyan spheres (●) and the particles that make up the obstruction by the wire-framed grey spheres (◍). In this example there are 200 free particles and 50 particles in the obstruction and the obstruction moved at one particle radius per time unit.

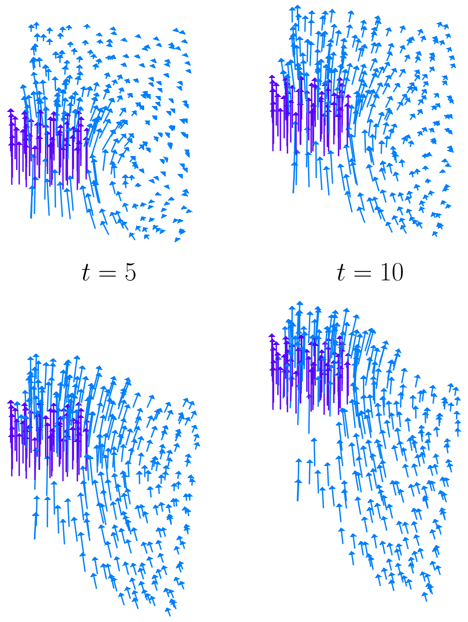

$t = 5$ $t = 10$

$t = 20$ $t = 30$

Figure 5.78: Vector maps showing the velocity of the free particles, and those that make up the obstruction, as a function of position at different points in time for the simulation presented in figure 5.77. The light blue arrows (⟶) show the velocities of the free particles that are centred where the arrows begin, while the dark purple arrows (⟶) show the velocities of the particles which make up the obstruction. Here the arrows indicate the direction in which the particles are travelling and their lengths are proportional to the magnitude of the particle's velocity. The velocities shown are relative to the bulk solvent flow.

There are several key points to take from these figures. Firstly there is the fact that they both clearly show that the particles closest to the obstruction move at a similar speed and spend a prolonged period of time moving beside it, just as the particles did in the gap between the two obstructions. As before this is a result of the collective nature of the hydrodynamic forces and the strong lubrication forces close to the obstruction. It is also worth noting that there are several points during this simulation when rather dense clusters occur close to the end of the obstruction as a result of this behaviour(44). One can think of these as potential sites where jamming could occur causing these clusters to stop and become part of the growing band. Secondly it is worth pointing out what figure 5.78 reveals about the flow behaviour of the particles near the end of the band. There is clear evidence here that while the particles are travelling at roughly the same speed as the obstruction in its direction of motion there is also a non-trivial flow behaviour in the direction perpendicular to this, with particles nearest the obstruction being pushed out to the side so that particles from above can move into their place. One can well imagine how, in the presence of a suitable force to pin the clusters, the combination of these two factors could lead to the growth of the band in the horizontal direction. In addition to this

---

(44) Some of these can be seen in figure 5.77.

figure 5.78 clearly illustrates the wake left behind by the obstruction as it moves through the solvent, the particles below are dragged along with the block, but never attain the same speed, slowing down as they fall further and further behind, leaving a region devoid of particles, below the obstruction, while particles pile up on top, just as they do in the experiments described in reference 2. Finally the images in figure 5.78 provide a clear indication of the long range, many body nature of the hydrodynamic interactions and give one a very clear impression of what consequences this has for the particle fluid.

Looking at figures 5.75 to 5.78 it is easy to see how this kind of collective behaviour could, in principle, lead to the formation of band patterns[2] in a draining film since the hydrodynamic interactions cause the particles to slow down much more as they pass through the constriction, as well as causing the particles behind to bunch up and reach a much higher volume fraction, where they are far more likely to jam and thus close the gap forming a band. Also the pure solvent passing through the gaps in the amorphous blockage also acts to accelerate particles that are below the band away from it, leaving a region deficient of particles as observed in experiments[2]. Furthermore the particles flowing over the obstructions, to the front and back of the figures, act to thicken the bands in this direction. In the presence of the substrate and solvent-air interface this thickening would lead to an increase in the pinning force[2,3] restricting the band's motion, slowing it down even more or enabling it to support a greater force from the falling particles. As the particles behind the band thicken this phenomenon would also act to pin them. This phenomenon is very similar to the explanation proposed in reference 2 for the formation of band patterns, except that it does not require the volume fraction to reach a value close to the jamming point, even locally, since the hydrodynamic forces are long range[68].

5.4.2 Sheared Particle Suspensions

On larger length scales(45) one is typically less interested in the behaviour of individual particles and more concerned with the properties of the continuum[3] particle fluid, such as its viscosity. Much of the present work has been based on models that treat the particles collectively as a continuous fluid. Thus in order to discuss the results of the hydrodynamic simulations presented in this section in the context of these models it was necessary to calculate the properties of the continuum particle fluid. In essence the aim of this section is to address the question of what the consequences of the microscopic behaviour of the particles simulated here are for the properties of the macroscopic particle fluid. In particular what effect the inclusion of many body hydrodynamic forces, on the micro-scale, has on the particle fluid's stress-strain relationship.

In order to investigate the stress-strain relationship a simple shear experiment, in which two plates made up of particles rigidly joined together were moved in opposite directions past a fluid of free particles, was performed. Figure 5.79 shows how a typical simulation was set up.

---

(45) More than a few particle diameters.

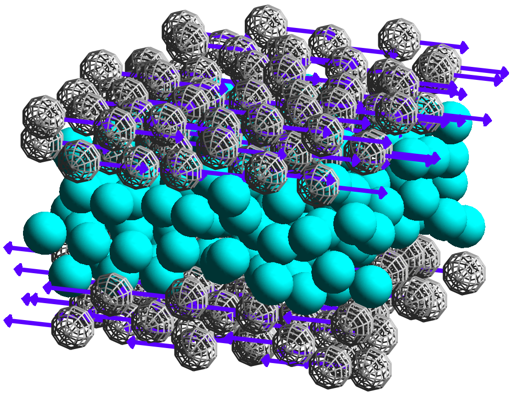

Figure 5.79: Image showing the set up of the shearing simulation at the onset of shear. Here the free particles are shown by the solid cyan spheres (●) and the particles that make up the plates by the wire-framed grey spheres (◍). The purple arrows (⟶) indicate the direction in which the particles forming the plates are about to move.

Here the plates are made up of an amorphous arrangement of particles at the same volume fraction as the free particles. In order to simulate bulk flow in the shear and null directions periodic boundary conditions were used, unfortunately the nature of the calculation performed by HYDROLIB meant that the boundaries in the gradient direction also had to be periodic. This meant that a layer of empty solvent had to be left between the plates and the top and bottom of the simulation cell to limit any unphysical effects caused by the plates passing each other too closely[3,68]. Though it is not possible to say that these effects were eliminated altogether every attempt was made to ensure they were limited and simulations with different plate separations suggest that, for the separation used, these effects were small in magnitude relative to the quantities being measured. Though this method is not without its flaws it does have one distinct advantage over the use of Lees-Edwards[115] type boundary conditions commonly used to simulate bulk shear[115] in that it was possible to include the shearing plates explicitly and thus prevent particles from diffusing further than the plate separation in the gradient direction. This is particularly important for the present work as it means that the simulation results are more relevant to the kinds of confined geometries that occur in thin films[2,73,78,101] and those that occur as the flow field passes around, or between two growing bands[3], or down a narrow channel as a pattern, like those described in reference 2, evolves.

To begin with it is worth considering the motion of the particles, on the microscopic scale, during steady state shear. To this end figure 5.80 shows how the flow component of the velocities of the particles is distributed as a function of their position in the gradient direction at an instant in time, long after the onset of shear, as well as projections of the velocity vectors in the same instant along the null direction.

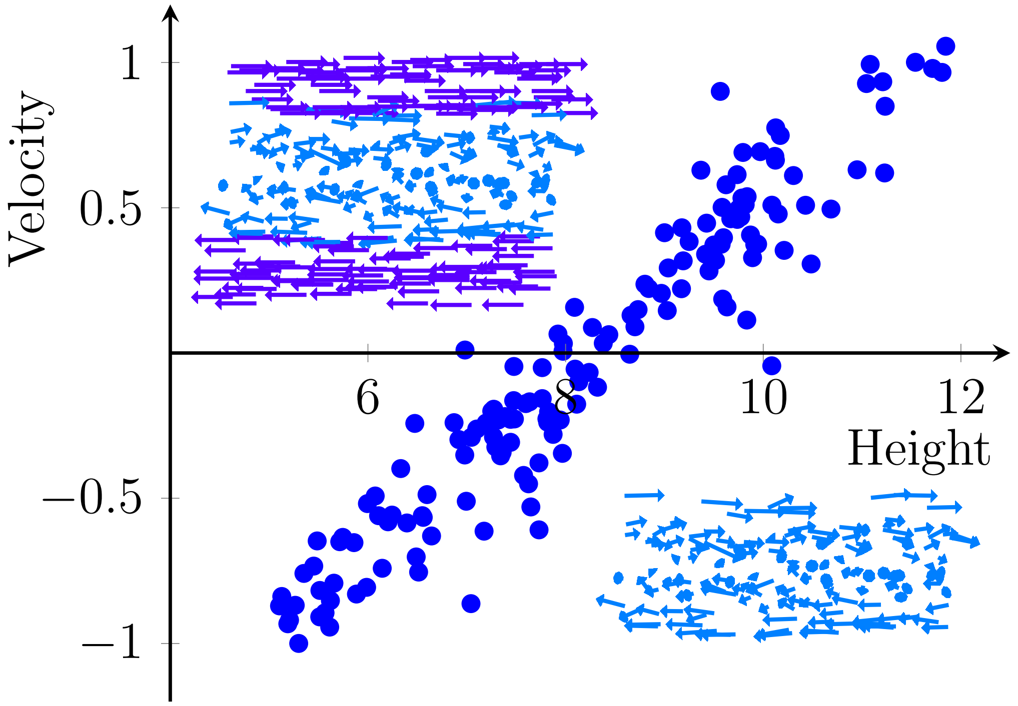

Figure 5.80: Plot showing the component of the particle velocity parallel to the flow direction as a function of position in the gradient direction at an instant in time, long after the system has reached its steady state. The inserts show a front view of the particle velocities in the system at this instant. In both inserts the light blue arrows (→) show the velocities of the free particles that are centred where the arrows begin. In the top insert the dark purple arrows (→) show the velocities of the particles that make up the plates. Here the arrows indicate the direction in which the particles are travelling and their lengths are proportional to the magnitude of the particle's velocity. Here the cubic cell has an edge length of 16, the volume fraction of the particles is $\phi \approx 0.351$, they are being sheared at $Pe = 16.7$ and the separation of the plates is 12 particle radii.

From this plot it is clear that the motion of the plates has resulted in the kind of macroscopic flow field one would expect between two plates. Though this result may not appear to be particularly significant it is worth stressing that this is purely a result of the hydrodynamic interactions, there is no imposed flow field in the solvent other than that created by the plates. If the particles had been treated individually with a constant drag coefficient the moving plates would have exerted no force at all on the free particles between and thus there would be no correlation between the shear component of their velocity and their position. Thus this result demonstrates the importance of the hydrodynamic interactions in this situation.

Since figure 5.80 clearly shows that the motion of the particles is correlated the next question one may wish to address is how this motion changes due to the microstructure of the fluid when viewed from the continuum perspective. For this one requires information about average length scales in the system and thus it is useful to consider the two particle distribution function. Figure 5.81 shows snapshots of how the two particle distribution function changes over time.

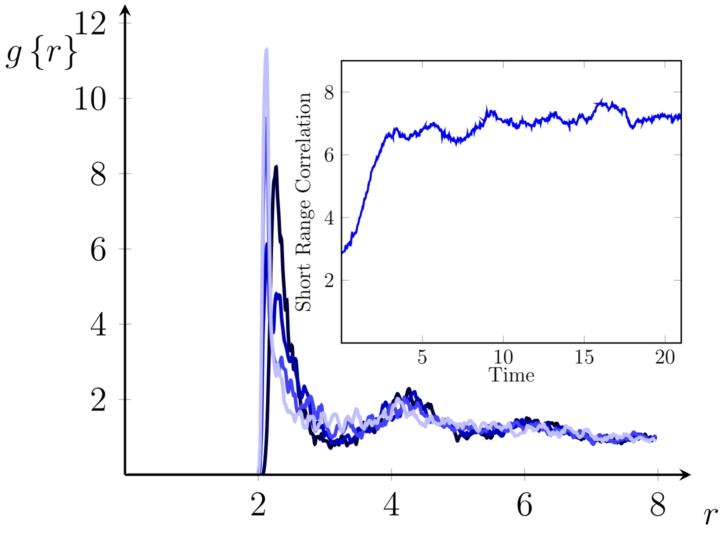

Figure 5.81: Plot of the two particle distribution function, at intervals during shear flow. From darkest to lightest blue: $t = 0.00$ (—), $t = 1.31$ (—), $t = 2.18$ (—) and $t = 9.95$ (—). The insert shows how the strength of the correlation, in the interval $2.0 < r < 2.2$, changed over time. In this example $Pe \approx 16.7$ and $\phi \approx 0.407$ in a cubic cell of length $16a$ and plates separated by $12a$.

From this it is clear that while one initially sees the expected form for an isotropic arrangement of particles the effect of the shear flow is to force more particles into close contact with other particles. This much is made clear in the insert which shows that the strength of the correlation in the region of the curve just after contact increases dramatically at the onset of shear flow and then levels out, at an enhanced value, once the flow is established. As this increase occurs much of the long range order(46) is lost. This is due to the fact that while the shear is forcing particles together it also breaks the symmetry of the isotropic system meaning that the typical separation between particles depends on the direction in which one measures it. This can be seen more clearly in figure 5.82, which shows the time averaged correlation function projected onto the shear-shear gradient plane(47).

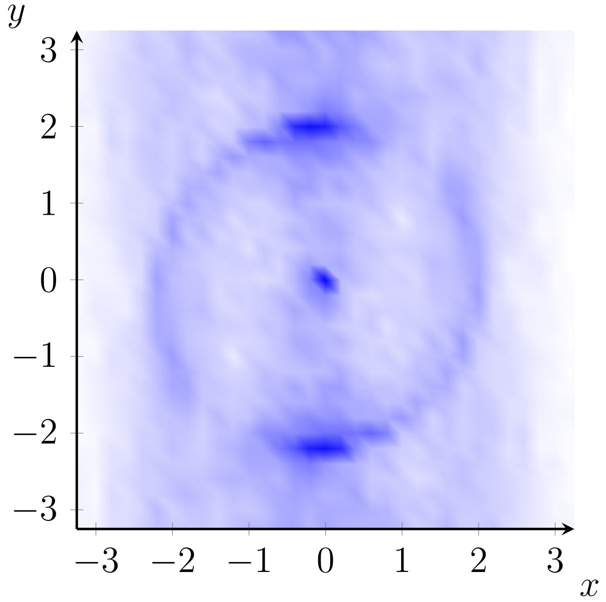

Figure 5.82: Plot showing the time average of the full three dimensional correlation function projected onto the x-y plane, where x is the flow direction and y is the shear gradient direction, taken during steady state shear. Here the darkest blues correspond to the strongest correlations. This example was generated using $Pe \approx 16.7$ and $\phi \approx 0.407$ in a cubic cell with an edge length of 16 particle radii and plates separated by 12 particle radii.

Here one can see the anisotropy clearly given the fact that there is a strong angular dependence to the intensity of the correlations and also evidence of the kind of symmetry one expects to see when simple shear is applied[5,47,58,75,173]. This provides clear support

---

(46) Beyond one particle diameter.

(47) With $\hat{\mathbf{x}}$ being the flow direction, $\hat{\mathbf{y}}$ the gradient direction and the average been taken over the $\hat{\mathbf{z}}$ direction.

for the assumptions made about the deformation of the two particle distribution function in the constitutive model derived in section 3.4 and is also in reasonably good qualitative agreement with the results obtained from it in shear flow, when one compares this result with those in figures 5.9 and 5.23, for example.

Of course the main purpose of this section is to examine how hydrodynamic interactions affect the stress-strain relationship of the suspension. As discussed in section 2.3, previous works[5] on the rheology of Brownian spheres with hydrodynamic interactions in the bulk found shear thinning behaviour at low Péclet number, where the Brownian forces dominate, followed by a Newtonian region and then a shear thickening region, caused by the hydrodynamic forces[5]. Here the situation is slightly different owing to the presence of the plates, though one would expect to see very similar qualitative behaviour in terms of the phases that appear and this is indeed the case as demonstrated by figure 5.83, which shows the steady state viscosity calculated from a number of different simulations with a range of volume fractions(48) and Péclet numbers.

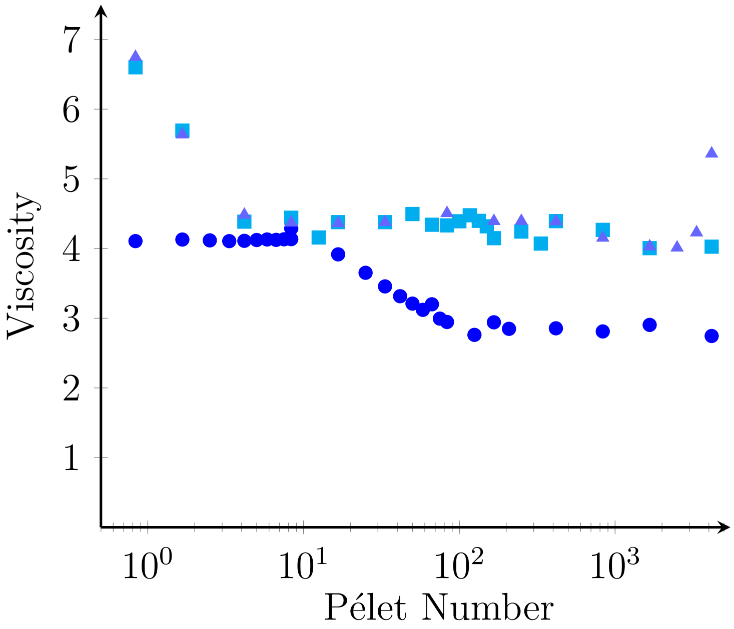

Figure 5.83: Plot showing how the viscosity of suspensions of hydrodynamically interacting particles changed with Pélet number, at three different particle concentrations. The blue circles (●) correspond to a particle volume fraction of 0.351, the cyan squares (■) to 0.407 and the light purple triangles (▲) to 0.421. Here a cubic cell with an edge length of 16 particle radii and plates separated by 12 particle radii were used.

There are several features of note here. Firstly it is clear that the magnitude of the viscosity at equal Péclet numbers increases as the volume fraction increases, as one would expect given the discussion in section 2.4. In this context at low Péclet number one can think of this as being a result of the fact that the particles have less space to move and rearrange the microstructure to reduce stress. In the high Péclet number limit, where the hydrodynamic forces dominate one can view this as a manifestation of the fact that the lubrication forces increase rapidly[68] as particles are forced into closer and closer proximity. This also explains the fact that the features of the plot, namely the shear thinning and shear thickening regions, where they are present, become more pronounced as the volume fraction increases and the particles begin to have a much more significant

---

(48) The estimates of the volume fractions quoted in figure 5.83 are based upon the hydrodynamic radii of the particles and not any of the other quantities used in the simulation to deal with collisions. Though these were, of course, taken into account when initialising the simulation. This value was deemed the most appropriate since it is the hydrodynamic effects rather than the crowding effects that dominate the stress within the range of volume fractions used here, and these are the effects to which this section is devoted.

effect on the suspension's rheological behaviour as a whole. It is also worth noting that in addition to the Newtonian region in between the two non-Newtonian phases, there is also a Newtonian region at very low Péclet number when the particle volume fraction is relatively low. Again this is to be expected given the fact that the solvent is Newtonian and one does not expect to see the effects of rearrangements of the microstructure caused by the flow field when the flow rate is small compared with the diffusion rate. Naturally this region persists to higher Pélet numbers when the volume fraction is low and there are very few particles in close enough proximity for lubrication forces to play a significant role or for caging effects to reduce the diffusion coefficient. This is why this region is only seen in the simulations run at the lowest volume fraction for the range of Péclet numbers shown in figure 5.83. One also notices that only the simulations run at high volume fraction show evidence of shear thickening in this range. This is for the same reason, that one requires a significant number of particles to be within a close proximity for the effects of the lubrication forces to be seen.

The fact that the low Péclet number low volume fraction results are in good qualitative agreement with the results obtained in section 5.1 for the constitutive relation derived in section 3.4 provides further validation of the results obtained and support for their use in extending the model of the particle-laden fluid. Of course, one would expect the results obtained in section 5.1 to fall into this low volume fraction low Péclet number, region since the constitutive relation only takes account of pairwise interactions and thus is only valid at low concentrations and does not attempt to take account of the hydrodynamic interactions, which, according to reference 5, are responsible for the shear thickening behaviour that is observed in these simulations, and indeed in the simulations presented in reference 5 as well as in experiments[20,126,174]. Furthermore the fact that the constitutive relation contains only Brownian forces and agrees with the results of these simulations at low Péclet number provides further support for the theory that the rheological behaviour in this region is dominated by the effects of Brownian motion.

Finally it is worth noting that all of these properties are in good agreement with the experimental[20,126,174] and theoretical[5] data presented in the literature, suggesting that the confinement, imposed by the plates, here has little effect on the flow behaviour in steady state. Of course, this comes as no real surprise as the gap between the plates is still several particle diameters and the plates used here have a similar structure to the free particles, thus they appear as part of the bulk fluid. However, the key to the similarities here is the fact that the viscosity measurements have been taken after the system has been allowed to reach its steady state. In section 5.4.2.1 it shall be shown that the fact that the particles are confined between the plates can have a profound effect on their flow response at the on set of the shear motion.

5.4.2.1 Shear Flow Following Compression

One particular situation of interest here, as in section 5.1.1.1, is what effect a prior compression has on the stress experienced at the onset of shearing flow[3]. As already discussed in section 5.1.1.1, this situation is of particular interest in relation to the formation of band patterns by granular suspensions in thin draining films[2,3], where it is thought that an increased resistance to flow caused by compression in a convergent flow field leads to particles jamming and causes the band to grow[3]. In the case of this investigation a uniaxial, osmotic, compression, using the plates of fixed particles, was performed. This was assumed to model the compression caused in bulk flow as the particles and solvent approach a narrowing. Of course the situation here is far from identical since the plates inevitably contain gaps, through which the solvent could flow freely, however the key feature here, as in a realistic flow scenario, is that the particles are forced together in a non-isotropic way, with the characteristic inter-particle separation in the gradient direction being less than that in the shear and null directions and less than it would be in an isotropic arrangement at the same volume fraction. Once compressed the free particles were then, immediately, sheared, in the same manner as before. Figure 5.84 gives an indication of the process used.

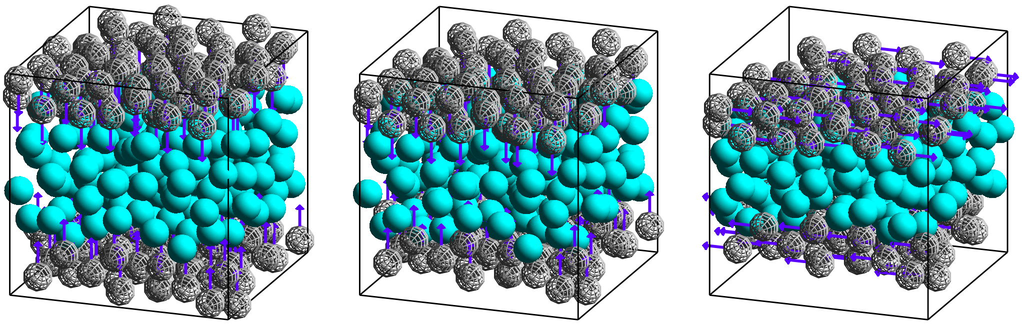

$t = 0$ $t = 1$ $t = 2$

Figure 5.84: Image showing the set up of the shearing simulation at the onset of shear. Here the free particles are shown by the solid cyan spheres (●) and the particles that make up the the plates by the wire-framed grey spheres (○). The purple arrows (→) indicate the direction in which the particles forming the plates are about to move. During the compression step the plates moved relative to one another at a rate of one particle diameter per time unit. The cubic cell has an edge length of 16 and the final volume fraction of the particles is $\phi \approx 0.351$.

Of course the rate of compression is an important feature in this procedure, as one does not want to allow the particles to remain in quasi-static equilibrium during the compression, but without taking the un-physical step of removing Brownian motion from the compression step and then reinstating it in the shearing step. Typically compressions were preformed at a Péclet number in the region of 20 as this was thought sufficiently fast to make sure the final state was not isotropic, but still of a comparable order to the Péclet number of the shearing motion. For comparative purposes the process was also performed with the thermal energy set to zero, to simulate purely granular particles.

In order to establish what effect the compression has it is worth considering the force exerted by the particles on each of the plates during shear flow. Figures 5.85 and 5.86 show the forces measured on each plate and stress, respectively, in two different simulations of identical gap width, volume fraction and shear rate; the only difference being that one followed a compression step, in order to reach the specified gap width, and the other was initialised at that gap width in an isotropic state.

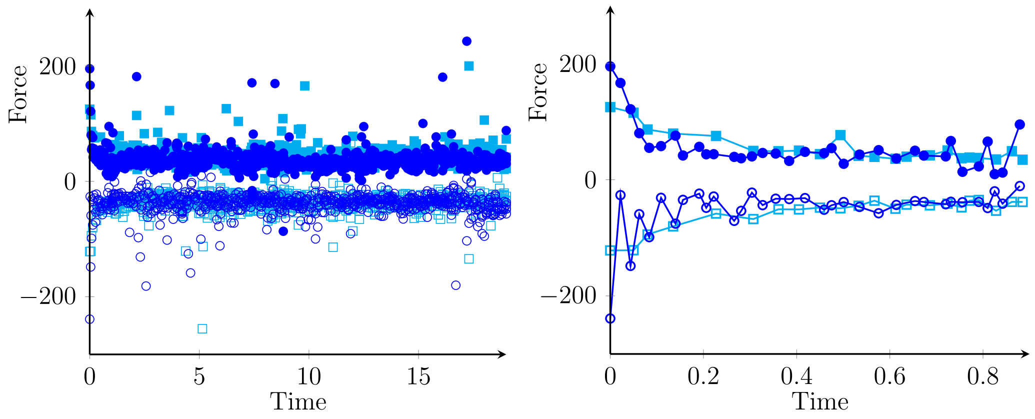

(a) Long time behaviour. **(b)** Short time behaviour.

Figure 5.85: Plots showing how the force exerted by the colloidal solution on the shearing plates varies as a function of the time after the onset of shear flow. In the system used to generate these examples the particles were assumed granular, and the temperature set to zero, the plates moved relative to one another at a rate of one particle diameter per time unit, and the volume fraction was $\phi \approx 0.351$. Here the blue circles (● —●— ○ —○—) correspond to the system which experienced a uniaxial compression prior to shear while the cyan squares (■ —■— □ —□—) correspond to a system initially at equilibrium. The open symbols (○ —○— □ —□—) show the force for the top plate, moving in the positive x direction, while the solid symbols (● —●— ■ —■—) show the force for the bottom plate moving in the negative x direction. A cubic cell with an edge length of 16 particle radii was used and shearing began when the plates were separated by 12 particle radii.

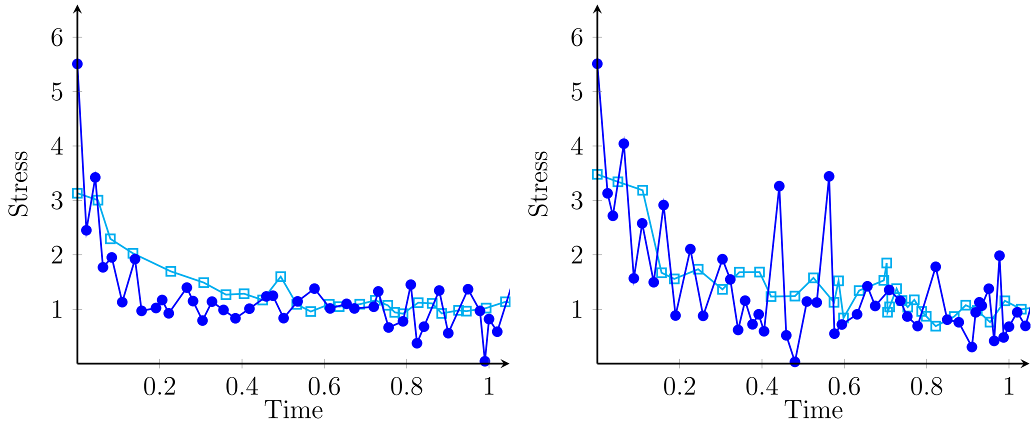

(a) Zero temperature. **(b)** Finite temperature.

Figure 5.86: Plots comparing how the shear stress evolves with time at the onset of simple shear flow in systems of the same volume fraction with and without prior compression. The time scale used here is set such that $t = 0$ corresponds to the point at which the shear flow began. Here the data has been normalised relative to the steady state stress. In the plots the open cyan squares (—□—) show the data for the system which started from an equilibrium configuration while the blue circles (—●—) mark the data for the simulation where shear began following a compression, to achieve an equivalent volume fraction. In these example systems the volume fraction of particles at the onset of shear was $\phi \approx 0.351$, in the finite temperature case a Péclet number of $Pe \approx 16.7$ was used. In both cases during the compression step the plates moved relative to one another at a rate of one particle diameter per time unit. A cubic cell with an edge length of 16 particle radii was used and shearing began when the plates were separated by 12 particle radii.

From these plots it is clear that in both situations the stress on the plates is higher at the onset of shear than it is in steady state(49). One can think of this as being due to

---

(49) Several other simulations were run at a range of Pélet numbers and this was found to be the case in all.

the fact that the new flow field must rearrange the pre-existing structure. Whether the system has been compressed before the onset of shear flow or not there is still ample opportunity for particles to be in close contact in the initial configuration due to the fact that the volume fraction is reasonably high. These close contacts lead to very strong lubrication forces[68] which impede the relative motion of the particles making structural rearrangements difficult and hence make a contribution to the stress regardless of their orientation, but their contribution to the shear stress is most appreciable when the particle separation is smallest in the gradient direction. Clearly this is more likely to occur in the situation where the particles have been compressed in this direction prior to the shearing motion and hence one possible reason why figures 5.85 and 5.86 indicate a higher stress at the onset of the shear when it follows a compression, in both the thermal and zero temperature cases. Another, related, phenomenon that is likely to play a roll in this scenario, and may also go some way towards explaining why the initial stress is greatest following a compression, is steric hindrance. As well as the lubrication forces, caging effects will also reduce the ability of the imposed flow field to rearrange the structure by preventing the particles moving in a certain direction, in particular the flow direction, or rolling over one another when they are travelling at different velocities. These collisions undoubtedly occur between free particles, but the particles making up the plates are by no means immune from this and could easily collide with, or have a slower moving free particle roll over them adding to the resistive force. As the flow proceeds and the motion of the particles begins to resemble that shown in figure 5.80 collisions in the flow direction become less and less common and thus the stress decays. Once again this phenomenon is more likely to occur following compression because the structure has not been given time to relax.

The key issue in the above discussion is that of typical particle separations, which influences both the steric and lubrication forces. Thus it is perhaps worthwhile to consider what effect the compression has on the two particle distribution function. Several snapshots taken during its evolution are shown in figure 5.87.

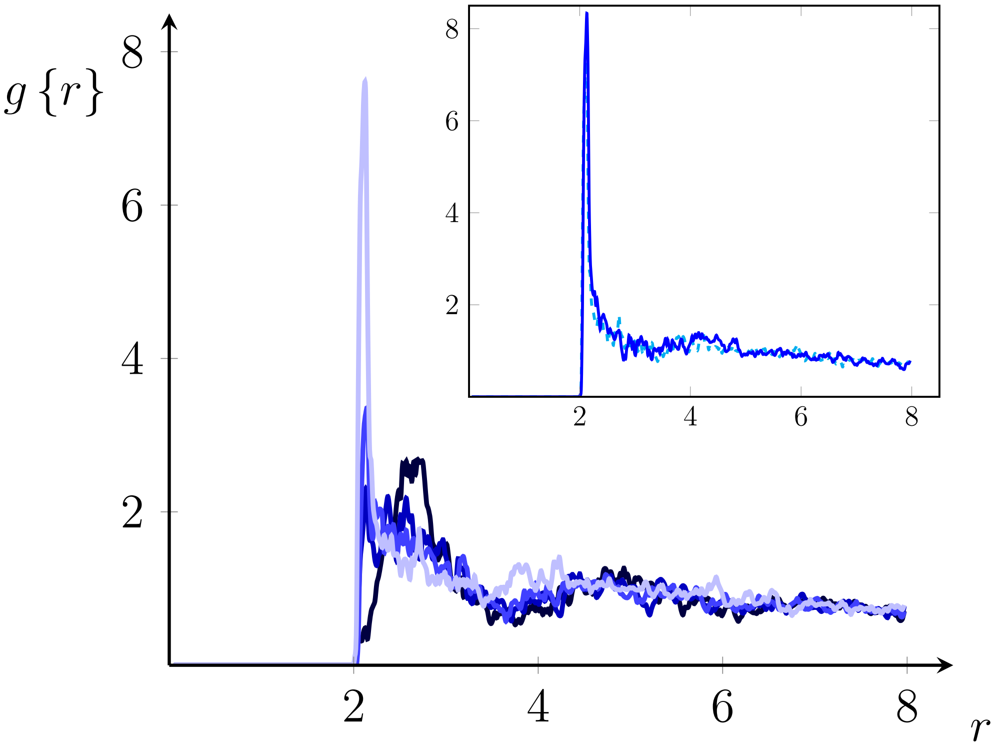

Figure 5.87: Plot showing the two particle distribution function at different stages during the compression step. From darkest to lightest blue the lines correspond to: $t = 0.00$ (—), $t = 1.19$ (—), $t = 1.40$ (—) and $t = 2.00$ (—), when the compression ended. The insert compares the two particle distribution function at the end of the compression step, shown by the dashed cyan line (- - -) with that in steady state shear for the same system, shown by the solid blue line (—). This example was generated using $\phi \approx 0.351$ at zero temperature. During the compression step the plates moved relative to one another at a rate of one particle diameter per time unit. A cubic cell with an edge length of 16 particle radii was used and shearing began when the plates were separated by 12 particle radii

Here it is clear that as the compression proceeds the typical separation between the particles does indeed decrease, and more and more particles are pushed to the point where they are almost touching. This seems to occur in two stages; firstly the peak in the initial distribution moves back towards the minimum possible centre to centre distance, and then the number of particles at that separation begins to increase, as more and more are forced together(50). As with the two particle distribution function shown in figure 5.81, for shear flow, the long range order decays due to the fact that the motion of the plates breaks the symmetry of the initially isotropic system. It is also interesting to note that as the insert reveals the two particle distribution function at the end of the compression step is very similar to the two particle distribution function in steady state shear. This is not to say, however, that the structure is the same, it is merely a result of the fact that both of the flow fields break the symmetry of the system and drive particles together in a particular direction. The key point to take from this figure is that it clearly shows a reduction in the typical inter-particle separation and an increase in the number of particles at the smallest possible separations, thus supporting the proposed explanation that it is these close contacts, and particularly those in the gradient direction that result in the increased start up stress when shear flow follows a uniaxial compression.

---

(50) It is worth remembering that while this process is going on the volume fraction is effectively increasing as the space available to the particles is reduced, while the solvent is escaping through the gaps in the plates.

Briefly returning to figures 5.85 and 5.86 it is worth pointing out that as well as being coupled to an increase in the initial stress required to move the plates, compressing the fluid before shearing it also increases the amplitude of the fluctuations in the stress as a function of time. This may be considered further evidence of an increase in the number of collisions between the particles as the peaks and troughs can be thought of as being due to regions of the system jamming, as two particles collide, and unjamming, when the contact is released. This is clear in both of the example systems shown, but is particularly prevalent in figure 5.86b, where the Brownian forces also play a role. This may be due to the fact that the particles involved are more energetic and thus have a greater influence on the stress or that the addition of Brownian motion simply causes more collisions to occur.

It is also worth pausing to explain the origin of that fact that the forces on the plates do not cancel exactly in the short term, though they do in the long term. This is potentially due to the fact that there are only a relatively small number of particles, so the average is not large enough for exact cancellation within a short period of time. Another important factor in this may be the flow of the solvent through the gaps in the plates which allows for volume conservation without necessarily pressuring the systems one normally expects.

Chapter 6

Conclusion

The main aim of the present work has been to better understand the physical processes involved in the formation of patterns by a thin film of a particle-laden fluid flowing down a surface [2]. In addition to the fact that these patterns occur in many everyday situations [2], the physical processes which underpin their formation go right to the heart of some of the most important concepts in condensed matter physics [2,4–81].

While several factors relating to the interfaces between the fluid and the substrate and the fluid and the air are known to lead to the creation of certain types of patterns in some fluids [2,73,78,101], this work has been devoted to how several factors pertaining to the interactions between the solvent and the particles it carries can lead to pattern formation in the non-equilibrium setting created by the flow down the substrate [2].

One of the central themes of this investigation has been the creation of a simplified model [3] of the draining film of particle-laden fluid. This took the form of a two fluid model, described in section 3.1 [3], which treated the particles and solvent as two distinct, but interacting, continuum fluids, which together conserved both matter and volume. In the most basic form of the model the interactions of the two fluids with the substrate and with each other were mediated by constant friction coefficients and the steric interactions between the particles by a simple empirical osmotic pressure function [3]. The stability of this model was assessed analytically by examining whether or not fluctuations about the uniform state would grow or decay, assuming that the fluctuations were initially small and approximating the equations of motion to first order [3]. This analysis revealed that the model system possessed two phases: one in which fluctuations of all wavelengths were stable, and the system decayed towards its uniform state, due to the action of a positive gradient in the osmotic pressure with respect to the volume fraction of particles, and one in which all fluctuations were neutrally stable, to first order. Numerical simulations of the full equations of motion describing the model confirmed the decay process when the system was initialised to an average volume fraction where the derivative of the osmotic pressure was negative, showing excellent agreement with the predicted decay rate for the longest, and most enduring, wavelength fluctuation. Outside of this region however, where the osmotic pressure was zero the numerical simulations revealed much more interesting behaviour. In this region a slight initial decay was observed in the standard deviation of the volume fraction across the system as a whole, followed by a region of neutral stability, which was observed to persist over an extremely long period of time(1). Inspection of how the volume fraction of the particles varied over space revealed that, in all cases, for all sets of parameters used, the system formed a very faint pattern of vertical channels, somewhat similar in shape to the channels observed in reference 2, but lacking their intensity. Although these patterns do not arise in the conventional manner, as the result of an instability, there is nevertheless clear evidence of a non-trivial structure, detectable in the complexity values obtained here. Since the linear stability analysis showed neutral stability for the first order term in the expansion then one must conclude that these patterns are the result of the contributions made by higher order terms, accessible only through numerical simulation. In fact all of the evidence gathered over the course of this investigation suggests that the origin of the patterns lies in the fact that this system is driven out of equilibrium by the imposition of a flow field. Indeed these patterns do not appear in the absence of an external driving force. The most reasonable explanation, consistent with all of the analysis performed on numerous simulations, is that the flow field rather quickly smooths out any inhomogeneities in the volume fraction that occur in the flow direction and in doing so reduces the standard deviation over the system as a whole, but does not smooth out inhomogeneities in the volume fraction in the direction perpendicular to the flow, as there is no net force in this direction to move the particles. Thus the patterns are a result of the fact that while some fluctuations decay others do not, rather than being generated by an instability which favours the growth of fluctuations on a particular length scale. Hence this represents an entirely novel class of pattern formation process.

The lack of any kind of increase in the pattern's intensity in this, most basic, model leads on to the important conclusion that the physical processes captured within this model are not sufficient to produce the increase in pattern intensity observed in experiments[2]. Since the patterns observed in this model did not increase in intensity, and the horizontal band patterns observed in the experiments presented in reference 2 were not seen, several features were added in an attempt to make the model more realistic, in the hope of reproducing patterns that matched reality more closely. These features included: a non-Newtonian stress-strain relationship[64] in the particle fluid, static friction between the particles and the substrate[79], volume fraction dependence in the viscosity[51] and particle-substrate friction coefficient and attractive interaction between the particles with a term to penalise the creation of an interface between particle rich and particle deficient regions[118]. While adjusting the friction coefficient and viscosity had some significant effects on the way in which the system arrived at it steady state, in the case of the channel patterns, and the time taken to get there, it had little effect on the steady state itself. Further linear stability analysis on the full model concurred with these findings and suggested that the only way to produce an instability at first order was to include an attractive inter-particle interaction to create a region of negative gradient in the osmotic pressure curve. However, it was also apparent that this effect alone would not be sufficient to produce macroscopic patterns as it would not lead to the selection of a finite wavelength for the fastest growing fluctuation, this could only be achieved when the attractive forces were included in conjunction with

---

(1) For at least as long as the longest simulation ran, and several hundred times longer than the time taken to reach this state.

a term to penalise the creation of an interface between particle rich and particle deficient regions[118]. With this addition fluctuations were indeed observed to grow, as one would expect given the similarity with spinodal decomposition[78,118], and in the cases where the attractive interaction was relatively weak, allowing the flow field to influence the structure, channel-like patterns emerged. Once again this suggests a predisposition within the system to form structures of this shape. In terms of the physical motivation for the addition of this attractive force one could simply argue that the particles themselves experience an attractive force, such as van der Waals' interactions, as many colloidal systems do. Or, perhaps more interestingly, one could make the case that this force should be present, to some extent, even in the granular particle-laden fluid since it merely represents a simple model of the effect that surface tension in the solvent-air interface, neglected up to this point, has on the particles. Since clustering the particles together leads to the deformation of a much smaller proportion of this interface than would be the case if the particles were positioned randomly.

In addition to this, two fluid, model, which has been the central theme of this project, investigations have been performed into two other, complementary, models, which focus on specific aspects of colloidal flow that are missing from the simple, two fluid model, but may be responsible for the patterns observed in experiments on such fluids. While it would be impossible to add these features to the two fluid model without destroying the simplicity that makes it so appealing, considering them in detail sheds light on how they may lead to pattern formation, and in particular the formation of band patterns perpendicular to the flow direction, in real fluids.

In order to investigate how the microstructure of the fluid may lead to history dependent flow and non-Newtonian behaviour a simple, first principles, constitutive relation was derived, based on the virial theorem[98]. This yielded several interesting results relevant to the pattern formation process. Firstly the stress-strain relationship predicted by the model could be used in the two fluid simulation to model the non-Newtonian viscosity. Specifically this stress-strain relationship contained two distinct regions: a Newtonian region at low strain rates and a shear thinning region at higher strain rates. Comparison of these results with the literature on the topic[5,34,35,49,61,64,76,126,164], as well as hydrodynamic simulations which were performed as part of the present work, revealed that this was in good agreement with what is expected for this type of fluid. Since the model only included Brownian motion and not hydrodynamic interactions one would only expect to see Newtonian and shear thinning behaviour and not the shear thickening seen at high strain rates in models that include hydrodynamic lubrication forces[5].

Secondly coupling a low strain variant of the model with potentials of mean force for hard spheres and hard disks also provided support from a microscopic point of view for the choice of function used to model the volume fraction dependence of the viscosity, showing excellent agreement with equation 3.25 in both two and three dimensions[18,31,49,53,62,76,124,172]. To some extent this agreement is surprising given the fact that the constitutive relation was derived using only pairwise interactions between the particles, an approximation which is strictly only valid at low concentrations, and yet the data fits the commonly used Krieger-Dougherty[51] function even at high volume fraction and diverges in the correct region. This suggests that the divergence of the viscosity is reasonably well modelled by considering only pairwise interactions.

This constitutive relation also yielded a positive normal stress difference in two dimensional shear flow, which varied in a non-trivial way as a function of shear rate. Such normal stress differences are common in colloidal fluids[47,57,58] and form yet another aspect of their flow behaviour in which they differ from simple Newtonian fluids. This is also an example of a feature of colloidal flow that is missing from the simplified two fluid model of the particle-laden fluid. Physically one can understand the origin of this force by thinking of the tension in the stream lines of the fluid arising from the fact that particles are being drawn apart in the flow direction[57].

The main contribution of this model, however, was that it demonstrates a feature that is missing from the simple two fluid model in that it was possible to show that because the microstructure results in history dependent flow, compression of the fluid in the gradient direction prior to shear leads to an increased shear stress at the onset. This is important since it means that fluid that has to flow around the end of an obstacle is likely to experience a greater resistance as it passes the end and thus this may seed a jamming process which is thought to be responsible for the formation of band patterns[3] observed in experiments. This also adds significance to the existence of the positive normal stress difference since one can think of this pulling particles from the shearing fluid around the edge of an obstruction towards the obstruction itself. The physical origin of the observed increase in the stress at the onset of shear flow lies in the fact that the prior compression means that the typical separation of particles in the gradient direction is less than it would be at equilibrium, resulting in particles travelling at different velocities, due to the shear flow, being brought in to closer contact than they otherwise would be, thus causing them to move further up the repulsive interaction potential and in doing so produce a higher stress.

In addition to this the effect of hydrodynamic interactions in the same situation, and where particles flowed through a constriction, have also been investigated, by creating a simulation at the particle level, which included full, many body, hydrodynamic interactions. An inter-particle interaction potential was added to this simulation to make it possible to simulate particles with interactions and also so that interactions could be added artificially to try to prevent the simulation from getting stuck when the volume fraction was high.

Several hydrodynamics simulations were run on systems of particles being sheared between two plates. Analysis of the steady state flow in these simulations revealed the existence of shear thinning and shear thickening regimes as well as Newtonian behaviour. It was found that at low shear rates and low volume fractions the stress-strain relationship was fairly Newtonian, while shear thinning was observed at higher shear rates, for these relatively low volume fractions. This is in excellent agreement with the predictions of the constitutive relation derived in section 3.4, suggesting strong support for this model. When the volume fraction remains low the system then returns to Newtonian flow at higher shear rates, once again in agreement with the limiting case of the constitutive relation. At higher volume fractions the shear thinning and second Newtonian regime were observed to move to lower shear rates and a relatively weak shear thickening regime emerged. Unsurprisingly, given the high volume fraction required, this regime was not captured within the constitutive relation, which is only strictly valid at low volume fractions. However, all of these results, including those at low volume fractions, were found to be in very good, qualitative, agreement with the results published in the literature for hydrodynamically interacting spheres in bulk flow [5,126]. This suggests that the confinement modelled here, through the use of the plates, did not have a significant effect on the steady state flow curve. Comparing these results with the literature further also helped to explain the origin of the disagreement between these simulations and the constitutive relation at high volume fractions, since the explanation given for the shear thickening regime in reference 5 relates specifically to the lubrication forces, which are not present in the constitutive relation, while the shear thinning regime is thought to be dominated by Brownian effects which are present in both models.

In addition to this the results of hydrodynamics simulations provided further support for the results of the constitutive relation in that simulations of shear following compression in the gradient direction result in a higher initial shear stress than those with an identical shear rate applied to a suspension initially at equilibrium. This was thought to be the result of two factors both related to the fact that, following the compression, the typical inter-particle separation in the gradient direction was lower than in other directions and, more importantly, less than it would be in an equilibrium sample at the same volume fraction. Firstly this meant that there was a greater likelihood of collisions between particles traveling at different velocities in the shear field, an effect also captured in the simple constitutive relation, and secondly due to the fact that the hydrodynamic lubrication forces are incredibly strong when the particles are in close proximity [68]. Naturally the latter effect is only present in the simulation containing the full hydrodynamic interactions, and hence explains the shear thickening observed in figure 5.83.

This is of potential importance to the pattern formation process for the same reasons as the results of the constitutive relation in this flow scenario. However, in this case the hydrodynamic lubrication forces provide another intriguing possibility since they do not require the particles to be at a sufficiently high concentration for jamming to occur, but still yield an increase in the shear stress when shearing follows a compression. This could go some way toward explaining how band patterns can come into being even at relatively low concentrations, well below the jamming point, as in reference 2.

Analysis of the structure within the sheared system also provided support for the way in which deformations were modelled in the derivation of the constitutive relation, in section 3.4, in that the two particle correlation function showed clear evidence of symmetry breaking and a change in the typical inter-particle separation during both shear flow and uniaxial compression. It was also possible to use the hydrodynamics simulation to investigate the process by which bands formed on the particle scale. This was done by creating fixed obstructions, made out of particles, to simulate the effect of a small group of particles becoming stuck on the surface, and then allowing other free particles to drain past them along with the solvent. Although the limitations of the hydrodynamics library used meant that this could only be done in bulk solvent, the results still provided a very good insight into how hydrodynamic effects may play an important role in this situation. Comparing these simulations to others that were identical in every way except for the lack of hydrodynamic interactions revealed that the hydrodynamic interactions cause the free particles to gather around the obstructions and virtually come to rest there, on the large scale this would mean that the obstructions themselves appeared to grow in a direction roughly perpendicular to the flow of the particles as new particles came to rest at the ends. Particles piling up on top of and behind the obstructions would also give the impression of the pattern coarsening. Naturally both of these features are in excellent agreement with the results of reference 2. Of course another feature which is present in real systems is a region devoid of particles in front of the band, one can easily see how this could also arise in the hydrodynamic simulations presented here, as solvent drains through the gaps in the amorphous structure, however care must be taken not to place too much significance on this aspect of the results presented here as the limitation of the bulk solvent means that this could also come from the sides, an effect which is not possible in realistic systems. Nevertheless these results do give a clear indication that the hydrodynamic forces have the potential to lead to the formation of the observed band patterns at the particle scale, and given the results of the compression and shear experiments, it is no great stretch of the imagination to believe that these may expand into macroscopic features by the same physical process. Furthermore as the many body hydrodynamic forces, responsible for this behaviour, are long range, the effects seen here can occur at relatively low volume fractions, and, since they cause particles to gather, can increase the volume fraction locally, within the band, to the point where short range lubrication forces and even jamming effects come into play to further stabilise the band, and perhaps form the kind of fragile solid discussed in reference 30. Staying with this point it is also worth noting that in simulations where there were two obstructions with a gap in between very few particles were able to pass though the gap when the hydrodynamic force were present, suggesting that these forces might have a similar effect at low concentration as that attributed to steric hindrance and jamming, in reference 30, at high concentration.

Another important aspect of the present work has been to develop methods of characterising and analysing the two dimensional patterns produced by these [2] draining films. In order to do this several different complexity measures found in the literature [63,83,85,88,91,99] were considered. Of the measures considered it was felt that class of measures which involved convex functions of the amount of order or disorder [91] in the system were the most appropriate for this task as they attributed zero complexity to both perfectly ordered and completely random systems, in good agreement with intuition about the patterns. Two measures [83,91,99] of this type have been considered here, the popular LMC [83] measure and one based entirely on the information [91,99] contained within the system. Since both of these measures require probability distributions [90] to work from, different methods of obtaining a probability distribution representative of the patterns were also investigated. Since the aim of this exercise was to characterise the shape of the patterns, these probability distributions needed to capture some feature of the shape of the patterns. For this reason two curvature measures and the correlation function were used, each capturing different aspects of the shapes within the patterns.

Several test cases were considered in an attempt to better understand how the measures worked and what kind of features each of them responded to. To further this investigation Monte-Carlo simulations were run to find the patterns that maximised each of the measures [3]. Although these patterns were not unique it was possible to see particular features that were clearly favoured by the measures and some interesting comparisons between the measures were made. With this understanding of how the different probability distribution-complexity measure pairings worked it was possible to apply the complexity measures to the patterns that had been observed to form in the particle-laden fluid. Two important results came out of this exercise. Firstly it became clear that one could discover a great deal about the structures within the patterns simply by comparing and contrasting the complexity values calculated using the different methods. This is a very useful feature of the complexity measures since they make it possible to extract some general features without needing to see the patterns as a whole, which is especially useful in situations where the patterns evolve over time, as they do here, since the complexity provides a single value which can be plotted as a function of time, allowing one to assess, in a qualitative way, how the shapes of the features change over time. This property also makes comparisons between patterns produced in different simulations much more convenient since patterns with similar features can be identified from their complexity values even though the patterns as a whole may not be identical. The second useful feature of the complexity measures is that, because they are only sensitive to the structures and shapes within the patterns, they can be used to identify non-trivial structures even in situations where the amplitude of the fluctuations in the volume fraction is relatively low or decaying, and thus identify patterns in systems which do not have the conventional pattern forming instabilities, or growth in fluctuations, usually associated with the pattern formation process. The combination of these effects made it possible to detect and examine structures and evolution processes within the patterns reported in section 5.2 which may have otherwise been missed.

Although the results presented here complement each other well there are several areas that merit further investigation, not least of which is isolating the origin of the band patterns perpendicular to the flow field in the draining thin film. These are plainly visible in the results of experiments presented in the literature[2] and in many everyday situations. Yet despite the number of additional features added to the model of this situation presented in this work, no evidence of any such patterns was found. Of course this is an important result in its own right, but the theoretical picture remains somewhat incomplete without knowledge of exactly what the missing ingredient is. Both the constitutive model and the hydrodynamics simulations presented alongside the model of the draining thin film indicate the potential importance of flow history dependence in the particle fluid and there are certainly sound physical reasons[3] why this is an excellent candidate as the crucial piece of physics missing from the simple model. However, incorporating of this complex physical behaviour into the simple model whilst retaining the simplicity that makes it so powerful would be no small task. While the hydrodynamics simulations presented here have served an important purpose in providing useful comparisons with the other models making up this work this is an area where considerable improvements could be made. One obvious potential improvement here would simply be to increase the number of particles in the system in order to produce much cleaner data that is less susceptible to the noise caused by individual particles jamming and unjamming. Of course this would represent a huge workload computationally and thus is not practical with current equipment. If this were possible it would also naturally pave the way towards a secondary major improvement in the form of being able to run simulations at high volume fraction with a significantly number of particles for a physically significant amout of time. Arguably the most important result to come out of the hydrodynamics simulations was the observation that prior compression before the onset of shear increases the initial shear stress. This is of potential importance to a broad range of practical applications, not just pattern formation, and certainly warrants further investigation, ideally with a hydrodynamics library specifically designed with this complex protocol in mind, which is able to correctly deal with mixed boundary conditions and volume conserving compressions.

Appendix A

Additional Investigations

A.1 Testing of Hydrodynamics Simulation

In order to make sure that the Brownian forces were being calculated correctly and that the simulation algorithm was maintaining detailed balance, given the adaptive time step, a number of simple test simulations were run.

The first of which was a simple test of diffusion in an infinite solvent. This was used to make sure the correct thermal energy was recovered for each degree of freedom and that the diffusion coefficient was as expected. A number of different initial configurations were tested and it was found that both quantities behaved as expected; with the mean squared displacement of the particles being proportional to the time after initialisation and the thermal energy being equal to the mean squared particle velocity. Figure A.1 shows these two quantities as a function of time for an example system, in which the particles are initially thermalised and well separated.

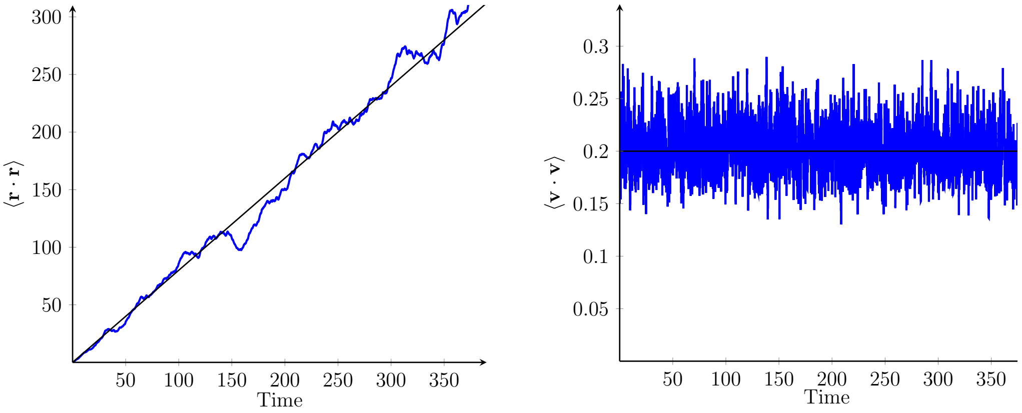

(a) Mean squared separation. **(b)** Mean squared velocity.

Figure A.1: Plots showing how the typical mean squared separation and mean squared velocity change over time during a hydrodynamics simulation with Brownian forces. Here the blue lines (━) show the data and the black lines (━) show the results expected from theory, $\frac{\partial}{\partial t}\langle \mathbf{r}\cdot\mathbf{r}\rangle = \frac{6k_BT}{\zeta}$ for (a) and $\langle \mathbf{v}\cdot\mathbf{v}\rangle = k_BT$ for (b). In this example the thermal energy was set at $k_BT = 0.2$ and the 27 particles used were initially distributed randomly, far away from one another, with velocities chosen from a Maxwell-Boltzmann distribution corresponding to the prescribed thermal energy.

In systems where the particles were not thermalised prior to the start of the simulation one can clearly see that their thermal energy increases relatively quickly to reach the expected level and similarly in systems where the particles were arranged in close proximity at the beginning of the simulation one finds that the effective diffusion coefficient is slightly reduced at the start of the simulation due to caging effects and the strength of the lubrication forces. In both cases this is in good agreement with what one might expect[36].

Another, slightly more sophisticated, test was used to probe how the Brownian forces were distributed. This involved connecting the particles, in pairs, using a Hookean spring potential, of spring constant k; so as to make a hydrodynamic version of the dumbbell model. Since this provided a very well defined distribution against which the simulations could be measured. From theory one would expect the particle centre to centre lengths of the dumbbells to obey a Maxwell-Boltzmann distribution, who's shape is controlled by the ratio of the spring constant to the thermal energy. This was indeed found to be the case, for both strong and weak spring constants, as shown in figure A.2 suggesting that the algorithm was indeed producing Brownian forces with the correct distribution of magnitudes.

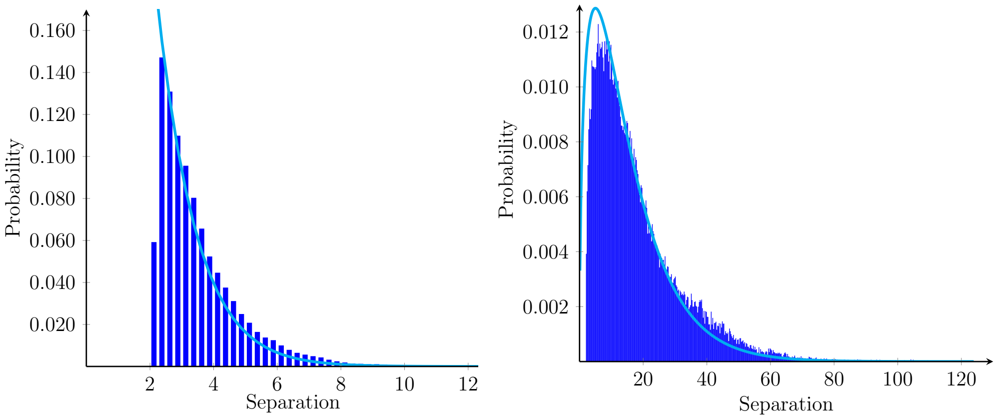

(a) Strong interaction. **(b)** Weak interaction.

Figure A.2: Plots showing how the typical mean squared separation and mean squared velocity change over time during a hydrodynamics simulation with Brownian forces. Here the blue lines (■) show the data and the cyan lines (■) show the results expected from theory, $\frac{k_B T}{k} = 1$ for (a) and $\frac{k_B T}{k} = 10$ for (b).

A.2 Gel Formation With Hydrodynamic Interactions

As mentioned in section 4.3.6 there are may physical systems where both hydrodynamic and pair interactions play a role in the behaviour of the system. One such example is that of the gel phase of interacting colloids[6,135]. Due to the nature of the calculation involved in determining the many body hydrodynamic interactions correctly they are often ignored or approximated[6], in order to allow for the simulation of a significantly larger number of particles. However, these forces are thought to be important in determining the nature of the gel phase[135].

The process of gel formation was investigated, for a small number of particles(1) using the simulation described in sections 3.3 and 4.3, for particles with a Lennard-Jones interaction potential, summarised by[115,175]

$$U = -4\epsilon \left[\left(\frac{\sigma}{r}\right)^6 - \left(\frac{\sigma}{r}\right)^{12} \right], \tag{A.1}$$

---

(1) 300 particles were used in the simulations performed here.

where r is the centre to centre separation of the particles and ϵ and σ are constants, which can be used to tune the shape and strength of the potential.

Figure A.3 shows snapshots of the formation process for two simulations with and without hydrodynamic interactions.

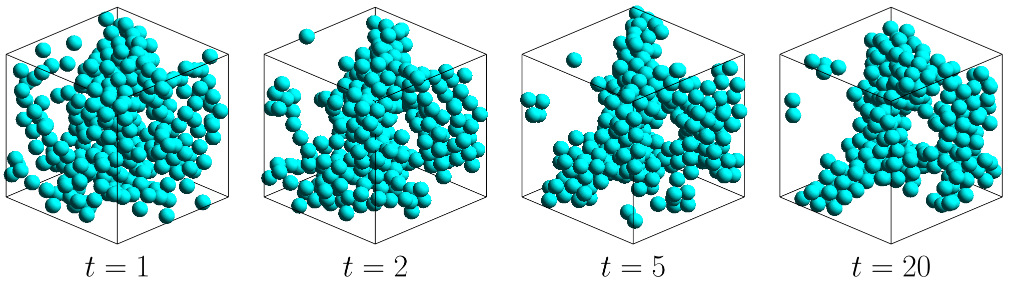

(a) With full hydrodynamic interactions.

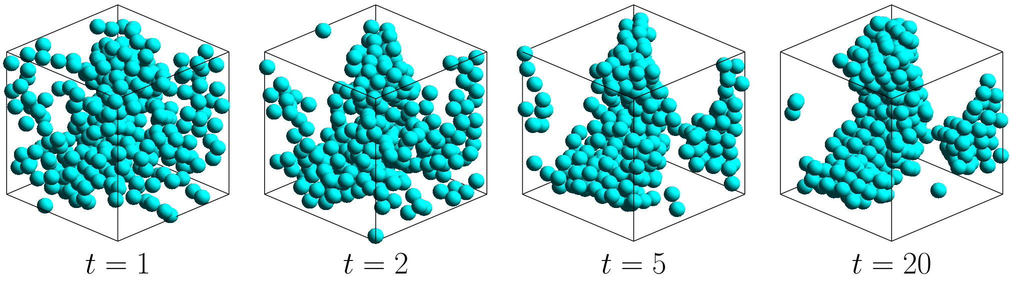

(b) Without hydrodynamic interactions.

Figure A.3: Snapshots taken of a fluid of particles, interacting through a Lennard-Jones interaction, forming a gel structure, with and without hydrodynamic interactions. In this particular example 300 particles at a volume fraction of $\phi = 0.157$, with a thermal energy of $k_B T = 0.1$, were used. The parameters describing the interaction potential used here were $\epsilon = 83.33$ and $\sigma = 1.308$.

Here the two simulations are were identical in every way(2) except for the presence of the hydrodynamic interactions.

It is clear form these snapshots that, although the early stages of the formation process appear to be similar, the presence of the hydrodynamic interactions does have a significant effect on the structure formed, with the simulation lacking hydrodynamic interactions producing a much coarser network. By way of explanation one can think of the flow field generated in the solvent by the long range hydrodynamic interactions as preventing the clusters of particles from coming together quite so readily under the action of the potential, since the flow being set up from one cluster of particles as it move in the direction of another will act to push that cluster away. Furthermore the strength of the sort range lubrication forces will inhibit the rotation of sections of the fractal structure, meaning that it will take longer for them to move into contact with other parts and so slows the coarsening process[44].

A.3 The Effect Of Topology On Sheared Polymers With Hydrodynamic Interactions

Another investigation performed using the hydrodynamics simulation involved the topology of two polymers[3], made out of hydrodynamically interacting spheres with a Hookean

---

(2) Even starting with the same initial particle configuration.

spring potential. In the absence of hydrodynamic effects one would expect two crossed[3] polymers to resist shear more than two that were simply placed next to one another, due to the fact that elastic potential energy would build up as the polymers, unable to separate, stretched in the shearing flow. Unsurprisingly this stretching behaviour was also seen in the hydrodynamics simulations, as figure A.4 shows.

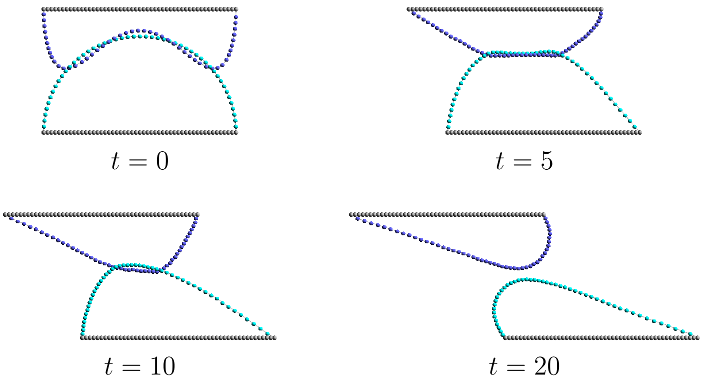

(a) Uncrossed.

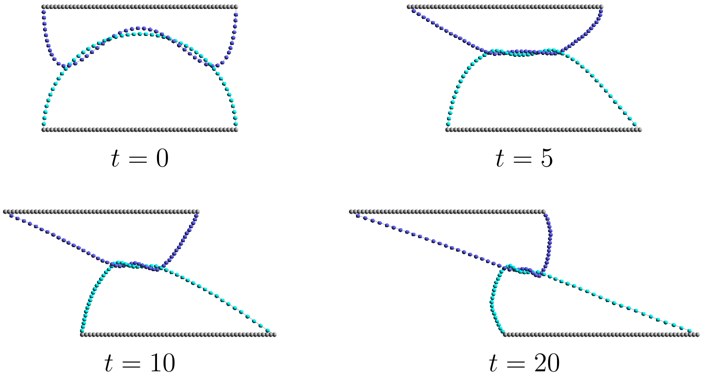

(b) Crossed.

Figure A.4: Snapshots taken of two hydrodynamics simulations in which a string of particles, held together by Hookean springs, model polymers in shear flow. The simulations were identical except for the topology of the polymers. To make the distinction between the two polymers clearer, the particles fastened to the top plate are shown purple (●) while those fastened to the bottom are shown in cyan (●). The particles of the plates are shown by wire frames (◌). In both examples the shear rate was 0.0625, the thermal energy was 0.1 and the spring constant was 10, in dimensionless units.

However, if one pots the force required to maintain the shear rate of the plates as a function of time for both the crossed and uncrossed cases, as in figure A.5, one sees very little difference.

---

[3] To be a little more precise, the term crossed here means that they can only be separated by breaking one of the polymers as, together, the polymer chains and the shearing plates, to which they are fastened, form two closed shapes.

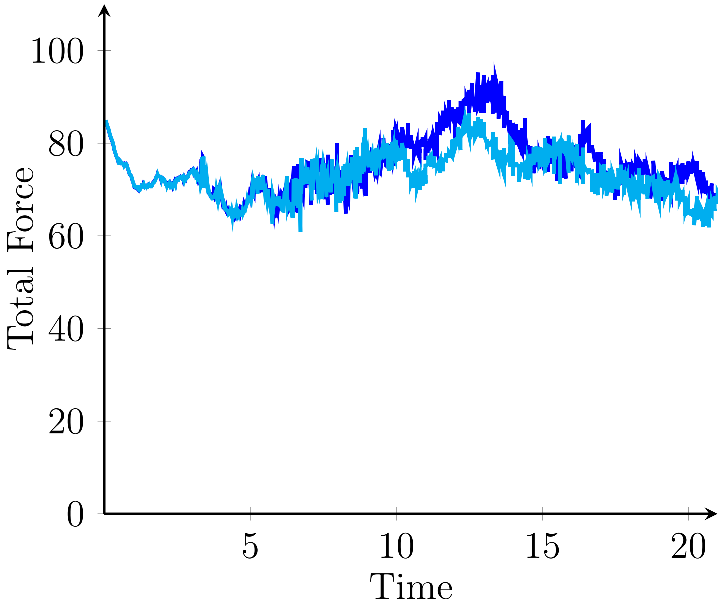

Figure A.5: Plot comparing the force required to move the plates to which two polymers are attached in different topological arrangements. The blue line (—) shows the force in the simulation where the two polymers cross while the cyan line (—) shows the force where they do not. In both simulations the shear rate was 0.0625, the thermal energy was 0.1 and the spring constant was 10, in dimensionless units.

This pattern was repeated for simulations run at a number of different Péclet numbers.

The most likely explanation for the fact that the force on the plates is insensitive to the topology of the chains is that the hydrodynamic forces are masking its effect. Strong lubrication forces for particles which are close to one another mean that there is a strong force resisting the relative motion of the two middle sections of the polymers, in both simulations. This much is clear from figure A.4a, where one can see that it takes a large amount of shear strain for the spring forces to overcome this resistance. As a result, from the point of view of the force measured at the plates, it would appear that these two polymers are joined together, even though they are not.

A.4 Complexity of Experimentally Observed Patterns

As a further investigation, to complement the work presented in section 5.3 on what one can learn about the features of patterns form their complexity, the complexity of some of the patterns observed in the experiments of reference 2 was calculated as a function of time. Figures A.6 and A.7 show how the complexity changed over time during the formation of horizontal band patterns and channel patterns respectively in two videos of real experiments[176].

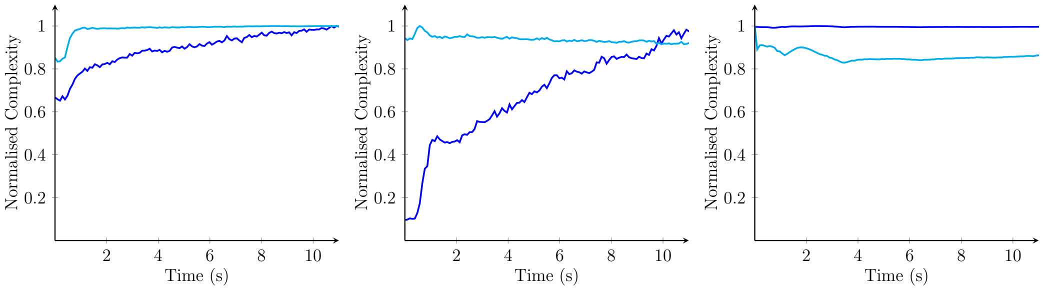

(a) Gaussian curvature. **(b)** Mean curvature. **(c)** Correlation function.

Figure A.6: Plots of the complexity as a function time calculated from a video[176] of horizontal band patterns forming during one of the experiments in reference 2. In these plots the complexity calculated using the LMC measure is shown by the blue lines (—) while that of the information based measure is shown by the cyan lines (—).

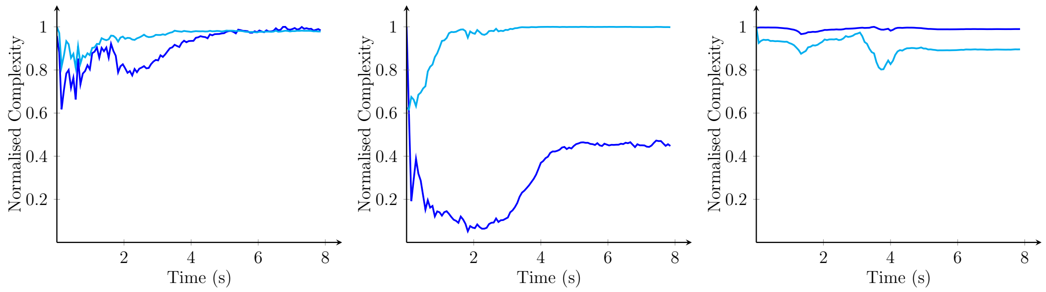

(a) Gaussian curvature. **(b)** Mean curvature. **(c)** Correlation function.

Figure A.7: Plots of the complexity as a function time calculated from a video[176] of vertical channel patterns forming during one of the experiments in reference 2. In these plots the complexity calculated using the LMC measure is shown by the blue lines (—) while that of the information based measure is shown by the cyan lines (—).

Here one sees little change in the measures related to the correlation function as the patterns are not periodic in nature so, in terms of the order on different length scales, their is little to distinguish them from the uniform state. The curvature measures are, however, much more sensitive to the kinds of patterns formed in this case. In all cases, for both patterns, the most noticeable activity, in terms of the complexity, comes at the start, where the pattern is emerging. Then, in most cases, there is little change in the complexity as the pattern increases in intensity. This is likely to be due to the fact that the shape of the pattern is not changing very much by this stage and thus the complexity does not change either. It is worth noting, however, that the LMC measures appears to be somewhat more sensitive to the increase in intensity in the early stages, which is likely to be due to the fact that favouring a narrower distribution makes it more sensitive to small changes in the occupancies of the bins. In figure A.6b one sees a very slight decrease in the information based measure coupled with a significant increase in the LMC measure during this increase in intensity, suggesting that the probability distribution is becoming narrower as the pattern's intensity increases, as one would expect. This also serves to further highlight the superior sensitivity of the LMC measure in this region, where the probability distribution is relatively narrow.

A.5 Generalisation of Complexity Measures

As part of the investigation into the behaviour of the two complexity measures used to analyse patterns in the present work a possible means of adjusting what value of complexity was attributed to different probability distributions was also investigated. While the two measures clearly differ, in terms of how they treat the probability distribution, they both consist of two terms combined in a multiplicative manner. One of these terms, the Shannon entropy, increases with the amount of disorder in the system while the other falls. It was found that raising these terms to different powers, α and β, provides one with a means of controlling how the complexity measures respond, both in terms of which state is attributed maximum complexity and the measure's tolerance to variations around this state. To generalise the measures in a formal manner, one must rewrite equations 3.34

and 3.36 as[91]

$$C^*_{ICC} = \left| \left(1 + \frac{1}{\log\{N\}} \sum_{i=1}^{N} p_i \log\{p_i\}\right)^{\alpha} \left(\sum_{i=1}^{N} p_i \log\{p_i\}\right)^{\beta} \right| \tag{A.2}$$

and

$$C^*_{LMC} = \left| \left(\sum_{i=1}^{N} \left[p_i - \frac{1}{N}\right]^2\right)^{\alpha} \left(\sum_{i=1}^{N} p_i \log\{p_i\}\right)^{\beta} \right|, \tag{A.3}$$

for the information and LMC measures respectively, where p_i is the normalised occupancy of bin i of the probability distribution and N is the number of bins(4).

As with the investigation into how the shape of the probability distribution influenced the standard complexity measures in section 5.3.2 a probability distribution in which all of the occupied bins had the same probability was used to examine the effects the parameters α and β had on the shapes of the curves, like those in figure 5.67, relating the number of occupied bins to the complexity.

Mathematically speaking the two properties one wishes to adjust in order to control the selection of the maximal complexity probability distribution and tolerance to other distributions are the position of the maximum and width of the curves relating the complexity and the number of occupied bins. Returning to equations A.2 and A.3, one notices, from the form of the equations, that the position of the maximum must only depend on the ratio of the two factors, α and β, since raising the whole equation to a fixed power will not change the position of the turning point. This fact is rather convenient since it means the position of the maximum can be plotted as a function of only one control parameter, $\frac{\alpha}{\beta}$. This data is plotted in figure A.8.

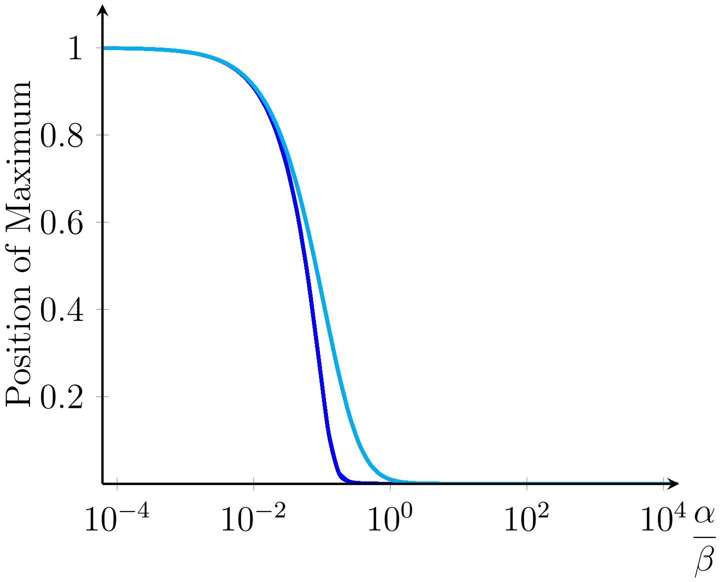

Figure A.8: Plot showing the bin occupancy with maximum complexity as a function of the ratio of the exponents on the order and disorder terms, when all occupied bins have equal occupancy. The blue line (—) corresponds to the LMC measure and the cyan line (—) to the information based measure. The data is normalised such that unity corresponds to all bins being occupied.

It is clear from this figure that in both cases when the Shannon entropy term dominates the maximum complexity state is one in which nearly all of the bins in the probability distribution are occupied, corresponding to a very disordered system, while the opposite is true when the other term dominates. This is, of course, to be expected from the very

---

(4) Here the constant of proportionality in the Shannon entropy has been dropped to limit the number of free parameters.

definition of the Shannon entropy and from the definitions of the complexity measures. More interesting is the behaviour in the centre of the plot, where the two parameters are of comparable magnitude, This shows a relatively sharp drop in the number of bins required to maximise the complexity measures suggesting one would have to tune the measures very carefully to set the maximum complexity at the point where roughly half of the bins are occupied. Also interesting is the fact that the LMC measure and the information measure differ significantly in this region with the LMC measure favouring narrower distributions at a lower ratio and falling more steeply than the information measure. This is in good agreement with figure 5.67, which clearly shows the peak of the LMC measure is positioned to the left of that of the information measure, for the special case of $\alpha = \beta = 1$.

In order to characterise the width of the curves the full width at half maximum was used, and since this depended on both parameters, α and β, in equations A.2 and A.3, it was decided that it would be most convenient to represent the data in two dimensional colour maps. These are shown in figure A.9.

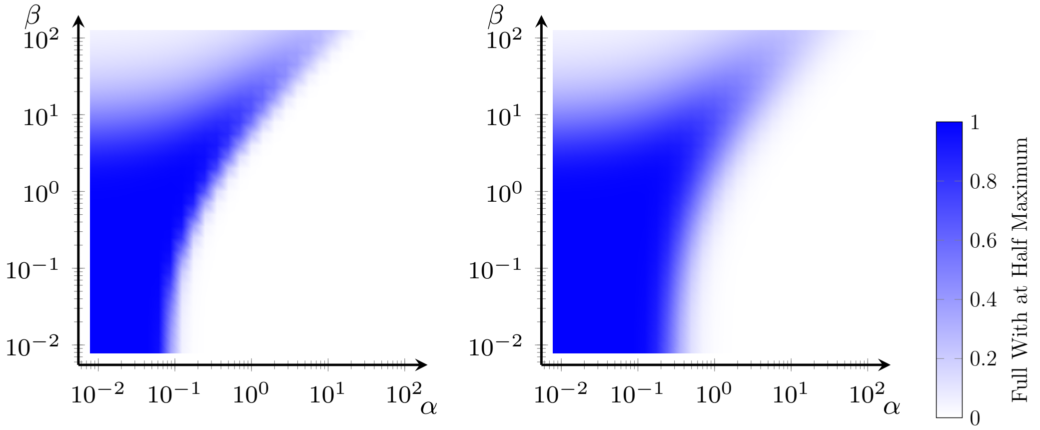

(a) LMC complexity measure. **(b)** Information complexity measure.

Figure A.9: Plots of the full width at half maximum of the curves relating the complexity to the number of occupied bins in a probability distribution where all occupied bins are occupied with the same probability. Here the data has been normalised such that unity corresponds to all bins being occupied.

As these plots show the curves are widest when both parameters are small. This increased width means the measures select the maximum complexity state with less precision and attribute large complexity values to a wide range of states. In order to obtain a very narrow curve, which attributes maximum complexity to only a very narrow range of states immediately surrounding the maximum one requires a large value of α and a small value of β, corresponding to weighting the measures in favour of the term corresponding to the amount of order in the system. This, in turn, means that such precision can only be achieved when the maximum is towards the low occupancy end of the spectrum. However, one can still narrow the curves significantly by choosing a high value of β and low value of α, but interestingly having comparable values generally gives a relatively wide curve. As with so many things in this area the choice of curve shape depends entirely on what one expects from a measure of complexity. Finally it is worth pointing out that these results demonstrate that the curve for the LMC measure narrows at lower values of α. Once again this is in good agreement with figure 5.67, where the LMC measure clearly has a narrower curve.

To conclude this section it is worth pointing out that while this generalisation provides a potentially useful means of creating customised complexity measures as well as an interesting insight into how the measures work, it was not applied to the patterns assessed in the present work as it was felt that it introduced too many free parameters and would have detracted from the understanding gained with regard to the two measures in their standard state.

Appendix B

Proofs

B.1 Proof That the Integrand in the Microstructural Stress Model is Zero on the Bounding Surface

In section 3.4.2 it is asserted that the integrand in equation 3.100,

$$\dot{\mathbf{\Sigma}} = \int_{-\infty}^{\infty} \mathbf{N}\boldsymbol{\nabla} \cdot \left[\left(\mathcal{D}\boldsymbol{\nabla} + \mathcal{M}\boldsymbol{\nabla}U - \mathbf{K}\cdot\mathbf{r} \right) g \right] \mathbf{r}\cdot\boldsymbol{\nabla}U dV, \tag{B.1}$$

is zero on the boundary for all of the interaction potentials presented in this work. In the context of the other approximations and constraints presented in section 3.4 it can be shown that the integrand is indeed zero on the boundary surface in all, but a very limited number of cases. The two relevant approximations for this proof are: the fact that any arbitrary potential can be written as a sum of power law potentials and the assumption that the deformation is affine and as such the two particle distribution function, g, can be replaced with its equilibrium form given an appropriate change of coordinates, this also means that the deformation will serve only to scale the coordinate axes and so will not affect the integrand's value on the boundary surface.

As this proof is not concerned with the value of the integrand at any particular point on the bounding surface and only with its value at an infinite distance from the origin, and U is a function of $|\mathbf{r}|$ only, then it makes sense to write equation B.1 in spherical polar coordinates and only consider the radial integral, which is

$$\int_{0}^{\infty} \left[\mathcal{D}\left(\frac{\partial^2 g_e}{\partial r^2} + \frac{1}{r}\frac{\partial g_e}{\partial r} \right) + \mathcal{M}\left(\frac{\partial g_e}{\partial r}\frac{\partial U}{\partial r} + g_e \frac{\partial^2 U}{\partial r^2} \right) - \left(\mathbf{K}\cdot\hat{\mathbf{r}} \right) \left(r\frac{\partial g_e}{\partial r} + g_e \right) \right] r^d \frac{\partial U}{\partial r} dr, \tag{B.2}$$

where d is the number of spatial dimensions. Here the fact that U and g_e are functions of r only and that the coordinate transformation, that accounts for the affine deformation, is not a function of r has been used. Now using the fact that

$$g_e = e^{-\beta U}, \tag{B.3}$$

from equation 3.91, equation B.2 becomes

$$\int_0^\infty \left[(\mathcal{M} - \mathcal{D}\beta) \frac{\partial^2 U}{\partial r^2} + \beta \left[\left(\frac{\partial U}{\partial r} \right) (\mathcal{D}\beta - \mathcal{M}) - \frac{\mathcal{D}}{r} - \mathbf{K} \cdot \hat{\mathbf{r}} r \right] \frac{\partial U}{\partial r} - \mathbf{K} \cdot \hat{\mathbf{r}} \right] g_e r^d \frac{\partial U}{\partial r} dr. \tag{B.4}$$

At this stage one must give careful consideration to the interaction potential. As was mentioned in section 3.4 any interaction potential can be expressed as the sum of a series of power law interaction potentials,

$$U = \sum_{i=1}^{N} U_i r^{p_i}. \tag{B.5}$$

This means that in order to establish the behaviour of the integrand of equation B.2 one must consider the behaviour of a power law multiplied by an exponential of a power law. In this limit the fact that U may contain more than one power law is irrelevant as a single dominant power will always emerge, however one must be careful in this case since the presence of products in the equation B.2 means that this dominant power does not necessarily relate to any exponent, p_i in equation B.5 in any simple way. Thus one is left with

$$\lim_{r \to \infty} g_e r^q. \tag{B.6}$$

There are two situations of interest here: Firstly if the dominant term in the interaction potential has $p_i > 0$ and is attractive$^{(1)}$ then $g_e \to 0$ as $r \to \infty$, and because g_e is exponential it will reach zero before any power of r reaches infinity. Secondly if the dominant term has $p_i < 0^{(2)}$ then the situation is slightly more complicated as $g_e \to 1$ at infinite separations. So for the integrand of equation B.4 to be zero one requires $q \leq -1$. To discover what this means in terms of the original potential one must substitute equation B.5 into equation B.4 to obtain

$$\int_0^\infty \left[\sum_{j=1}^{N} a_j r^{p_j - 2} + \left[\sum_{k=1}^{N} b_k r^{p_k - 1} - \frac{\mathcal{D}}{r} - \mathbf{K} \cdot \hat{\mathbf{r}} r \right] \sum_{j=1}^{N} c_j r^{p_j - 1} - \mathbf{K} \cdot \hat{\mathbf{r}} \right] \sum_{i=1}^{N} d_i r^{p_i + d - 1} dr, \tag{B.7}$$

where $a_i = (\mathcal{M} - \mathcal{D}\beta) U_i p_i (p_i - 1)$, $b_i = (\mathcal{D}\beta - \mathcal{M}) U_i p_i$, $c_i = \beta U_i p_i$, $d_i = U_i p_i$ and g_e has been assumed to be unity since it will tend to one faster than any power of r tends to its final value as r tends to infinity. Noticing that the first and third terms in equation B.7

---

(1) A repulsive potential that increases with separation over an infinite range, as would be the case with $p_i > 0$, is un-physical.

(2) Since the force only depends on gradients of the potential $p_i = 0$ is not relevant.

have the same dependence on r leaves four terms with distinct r dependence:

$$\sum_{i=1}^{N}\sum_{j=1}^{N} r^{p_i+p_j+d-3}, \tag{B.8a}$$

$$\sum_{i=1}^{N}\sum_{j=1}^{N}\sum_{k=1}^{N} r^{p_i+p_j+p_k+d-3}, \tag{B.8b}$$

$$\sum_{i=1}^{N}\sum_{j=1}^{N} r^{p_i+p_j+d-1}, \tag{B.8c}$$

$$\sum_{i=1}^{N} r^{p_i+d-1}. \tag{B.8d}$$

These in turn, combined with the earlier result that the total exponent on any power of r in an attractive potential must be less than -1, give three conditions(3):

$$p_i < -d, \tag{B.9a}$$

$$p_i + p_j < -d, \tag{B.9b}$$

$$p_i + p_j + p_k < 2 - d, \tag{B.9c}$$

that the exponents in the interaction potential must meet for all i, j and k. The nature of the potential will ultimately determine which of the conditions in equation set B.9 need to be fulfilled and which are automatically fulfilled by the others. For instance if all of the exponents in the interaction potential are negative then one only requires the largest to be smaller than the negative of the number of spatial dimensions.

B.2 Reduction Formulae Used in the Microstructural Stress Model

While the integrals over the radial coordinate in equation set 4.67 are relatively simple to evaluate in terms of gamma functions the integrals over the angular coordinate must be evaluated by reduction formulae. Essentially one wishes to evaluate an integral of the form

$$\mathcal{I}_{2n}^{m} = \int_{0}^{2\pi} \sin^{2n}\{\theta\}\left[1 + C\sin^{2}\{\theta\}\right]^{\frac{1}{2}m} d\theta, \tag{B.10}$$

where n and m are integers and C is an arbitrary constant, which in practice absorbs all of the terms that account for the elongation and rotation(4). It is relatively straightforward to convince oneself that all of the non-zero components of the integrals required by the two dimensional Cartesian representation of the constitutive relation presented here can be represented in this form.

Starting from equation B.10 one requires reduction formulae for both n and m. Firstly

---

(3) Fulfilling the condition $p_i + p_j + d - 1 < -1$ automatically fulfils $p_i + p_j + d - 3 < -1$.

(4) Any difficulties in dealing with the angular dependence can be resolved by a change of the angular coordinate, $\theta \to \theta - \delta$.

consider reducing n by one to give

$$\mathcal{I}_{2n}^{m} = \int_0^{2\pi} \sin\{\theta\} \left(\sin^{2n-1}\{\theta\} \left[1 + C\sin^2\{\theta\}\right]^{\frac{1}{2}m}\right) d\theta, \tag{B.11}$$

which can be integrated by parts to give

$$\begin{aligned} \mathcal{I}_{2n}^{m} = (2n-1) &\int_0^{2\pi} \cos^2\{\theta\} \sin^{2n-2}\{\theta\} \left[1 + C\sin^2\{\theta\}\right]^{\frac{1}{2}m} d\theta \\ + mC &\int_0^{2\pi} \cos^2\{\theta\} \sin^{2n}\{\theta\} \left[1 + C\sin^2\{\theta\}\right]^{\frac{1}{2}(m-2)} d\theta. \end{aligned} \tag{B.12}$$

Equation B.12 can then be rearranged using trigonometric identities to give

$$\mathcal{I}_{2n}^{m} = \frac{2n-1}{2n}\mathcal{I}_{2n-2}^{m} + \frac{mC}{2n}\left[\mathcal{I}_{2n}^{m-2} - \mathcal{I}_{2n+2}^{m-2}\right]. \tag{B.13}$$

Similarly if n is reduced by two one obtains

$$\mathcal{I}_{2n}^{m} = \int_0^{2\pi} \sin^2\{\theta\} \sin^{2n-2}\{\theta\} \left[1 + C\sin^2\{\theta\}\right]^{\frac{1}{2}m} d\theta, \tag{B.14}$$

which can be written as

$$\mathcal{I}_{2n}^{m} = \frac{1}{C}\int_0^{2\pi} \sqrt{1+C\sin^2\{\theta\}} \left[\sqrt{1+C\sin^2\{\theta\}} - \frac{1}{\sqrt{1+C\sin^2\{\theta\}}}\right] \sin^{2n-2}\{\theta\} \left[1+C\sin^2\{\theta\}\right]^{\frac{1}{2}m} d\theta. \tag{B.15}$$

This further reduces to

$$\mathcal{I}_{2n}^{m} = \frac{1}{C}\int_0^{2\pi} \sin^{2n-2}\{\theta\}\left[1+C\sin^2\{\theta\}\right]^{\frac{1}{2}(m+2)} d\theta - \frac{1}{C}\int_0^{2\pi} \sin^{2n-2}\{\theta\}\left[1+C\sin^2\{\theta\}\right]^{\frac{1}{2}m} d\theta \tag{B.16}$$

or

$$\mathcal{I}_{2n}^{m} = \frac{1}{C}\left(\mathcal{I}_{2n-2}^{m+2} - \mathcal{I}_{2n-2}^{m}\right) \tag{B.17}$$

It was then possible to calculate all of the necessary integrals using a combination of equations B.13 and B.17 and the three most basic integrals;

$$\mathcal{I}_0^{1} = 4E\left\{\mathrm{i}\sqrt{C}\right\} \tag{B.18a}$$

$$\mathcal{I}_0^{0} = 2\pi \tag{B.18b}$$

$$\mathcal{I}_0^{-1} = 4K\left\{\mathrm{i}\sqrt{C}\right\}, \tag{B.18c}$$

where K and E are elliptic integrals of the first and second kind respectively,

$$K\{x\} \equiv \int_0^{\frac{\pi}{2}} \left[1 - x\sin^2\{\theta\}\right]^{-\frac{1}{2}} d\theta \tag{B.19a}$$

$$E\{x\} \equiv \int_0^{\frac{\pi}{2}} \left[1 - x\sin^2\{\theta\}\right]^{\frac{1}{2}} d\theta. \tag{B.19b}$$

Appendix C

Source Code

This appendix contains some snippets of the source code of the major simulations performed as part of the present work. These snippets were selected to give a more detailed impression of how some of the key components of each of the algorithms worked in practice; they are not verbatim copies of the original source code, which is far longer than it would have been practical to include in this section, and rather a selection of isolated functions(1). For the purposes of readability some sections of code have been removed and replaced by comments detailing their role.

C.1 Simulation of a Particle-Laden Fluid

As described in section 4.1 the simulation of the particle-laden fluid is based upon a two fluid model, which treats both the solvent and particles as two separate fluids, that together conserve both volume and particle number. In essence the purpose of the simulation algorithm is simply to solve equation set 4.12 at each time step, using a Newton-Raphson iteration scheme. Thus much of the code was devoted to creating the various matrices making up the components of the Jacobian and the equations themselves. From a processing point of view these fall into two classes: those that needed to be updated at every iteration and those that remained constant throughout. The code snippet below shows the function used to make all of the variables that needed to be updated at each iteration.

```
void makeall(){//Make all the variables for a given time step
  int i,j;
  INVDIAG(PhiInv,Phi);//Get inverse of the diagonal matrix of phi values
  VPABS();//Get the absolute square values of the particle velocity
  SHEAR();//Get the shear rate
  EXPV2();//Work out the exponential of vp^2
  VISCOSITY();//Calculate the viscosity
  OSMOTIC();//Calculate the osmotic pressure
  FRICTION();//Calculate the friction constant for the particles
  dH();//Viscosity derivatives
  dPI();//Osmotic pressure derivative
```

---

(1) These functions are not intended to form "light weight" versions of the full simulations and are unlikely to compile or run in the state in which they are presented here. The real simulation codes rely on other functionality, which is not presented here, to perform their role. The full source code for all of the simulations, data analysis programs and scripts can be downloaded from `https://bitbucket.org/Craig_Hall/phd-project-source-code`.

```
  dZetap();//Friction derivatives
  #include "Equations/Matrix.c"//Do all matrix operations that are needed.
  #include "Equations/Jaccobian.c"//Make Jacobian from the matrices
  #include "Equations/Functions.c"//Evaluate the equations of the model
  for(i=0;i<sNN;++i){//Correct Jacobian for cell where pressure is zero
    J_sp->x[map[Z_row][i]]=double0;
  }
  J_sp->x[map[Z_row][Z_row]]=double1;
  f[Z_row]=double0;
}
```

Here the ordering is very important since the calculation of many of the matrices required depended on prior knowledge of various system parameters, such as the viscosity and friction coefficients, and naturally the Jacobian and vector of evaluated equations could not be formed until all of the necessary matrix combinations had been made. The ordering of the matrix multiplications was also very important with the simplest combinations having to be created first and built on at each level until all of the required matrices had been calculated. For example to form the combination $\mathbf{v} = (\mathbf{A} \cdot \mathbf{B}) \cdot \mathbf{c}$, where $\mathbf{A}$ and $\mathbf{B}$ are both matrices and $\mathbf{c}$ is a vector, the bracketed term would need to be evaluated and stored first. The intermediate results in these calculations were all saved in memory as many of them appeared in multiple combinations and doing so greatly reduced the number of, time consuming, matrix multiplications that needed to be performed. Returning to the example; naturally reordering and calculating $\mathbf{A} \cdot (\mathbf{B} \cdot \mathbf{c})$ would be faster in this case, however, if the combination $\mathbf{A} \cdot \mathbf{B}$ occurs elsewhere in the calculation it makes sense to calculate it once and save it. Thus decisions on the ordering of such calculations had to be made on a case by case basis(2). The final part of this function replaces the final equation for one of the cells with a condition setting the pressure scale, to prevent the set of equations from being degenerate.

As well as the variables there are also a number of quantities in the system that remain constant throughout the simulation. These include the matrices used to perform the spectral derivatives, and the templates describing the structure of the matrices used. Although the values in many of the matrices change at each iteration all of the matrices in the system have a constant zero pattern so it makes sense to calculate and store the templates at the beginning. The code snippet below shows the operations involved in calculating the constants, and is only called once at the beginning of each simulation.

```
void makeconstants(){//Make all constant needed (only called at beginning)
  int i,j,k;
  Diag=makeD(NN);//Dummy diagonal matrix to be used for creating templates
  Dx=makeDx(N,M);Dy=makeDy(N,M);Dx2=makeDx2(N,M);Dy2=makeDy2(N,M);DxDy=
    makeDxDy(Dx,Dy,N,M);//Make derivatives
  DxIT=makeDx_T(N,M);DyIT=makeDy_T(N,M);//Dummies to make templates
  DxT=makeT(DxIT,NN);DyT=makeT(DyIT,NN);DxT2=tempmult(DxT,DxT,NN);DyT2=
    tempmult(DyT,DyT,NN);DxDyT=tempmult(DxT,DyT,NN);DxDyIT=makeA(DxDyT,NN);
    //Make templates
  for(i=0;i<NN;++i){//Make identity matrix
    IIT[i][i]=1;
    I[i]=double1;
```

---

(2) The file containing these calculations has not been included as it is too large to make a meaningful contribution to this section.

```
}
#include "Equations/Templates.c"//Include all the templates
#include "Equations/Jtemplate.c"//Include all template for Jacobian
freeMI(DxIT,NN);//Free templates for Dx, Dy and the identity matrix
freeMI(DyIT,NN);
freeMI(IIT,NN);
J_sp=(cs*)malloc(sizeof(cs)); //Compressed column version of Jacobian
J_sp->m=sNN;//Number of rows will be 6 time the number of cells
J_sp->n=sNN;//Number of columns will be 6 time the number of cells
J_sp->nz=-1;//Let sparse matrix solver know it's in compressed column
  format
J_sp->p=(csi*)malloc((sNN+1)*sizeof(csi));//Create list of column indices
master_p=(csi*)malloc((sNN+1)*sizeof(csi));//Master version. Normal
  version will change during calculation so needs to be reset for next
  iteration
k=0;
for(i=0;i<sNN;++i){
  J_sp->p[i]=k;//Running total of non-zero elements
  master_p[i]=k;
  for(j=0;j<sNN;++j){//Count number of non-zero elements in each column
    k+=JIT[j][i];
  }
}
J_sp->p[sNN]=k;//Record beginning of last column
master_p[sNN]=k;
J_sp->nzmax=k;
J_sp->i=(csi*)malloc(k*sizeof(csi));//Create array to hold the row
  induces
master_i=(csi*)malloc(k*sizeof(csi));
J_sp->x=(double*)malloc((k+1)*sizeof(double));//Array for non-zero
  elements
k=0;
for(i=0;i<sNN;++i){
  for(j=0;j<sNN;++j){
    if(JIT[j][i]==1){//Go though the whole Jacobian recording row indices
      J_sp->i[k]=j;
      master_i[k]=j;
      ++k;
    }
  }
}
map=(int**)malloc(sNN*sizeof(int*));//Contains index of the compressed
  column array where value at the location i,j appears
for(i=0;i<sNN;++i){
  map[i]=(int*)malloc(sNN*sizeof(int));
  for(j=0;j<sNN;++j){
    map[i][j]=J_sp->nzmax;//All entries set to nzmax so zeros at end
  }
}
for(i=0;i<J_sp->n-1;++i){//For each column except the last one
  for(j=J_sp->p[i];j<J_sp->p[i+1];++j){//All indices that correspond to
  column
    map[J_sp->i[j]][i]=j;//Set the value at the position in the mapping
  matrix
```

```
    }
  }
  for(j=J_sp->p[i];j<J_sp->nzmax;++j){//All indices in compressed array
   corresponding to last column
    map[J_sp->i[j]][i]=j;//Set the value at position in the mapping matrix
  }
  freeMI(JIT,sNN);//Free the template of the Jacobian
}
```

A major part of this piece of code is devoted to the calculation of the compressed column form of the Jacobian and a mapping between this and its natural, matrix, form. Establishing this relationship here saves a great deal of time later on as it allows for efficient copying of the values into the compressed column form of the Jacobian, without requiring the creation of the full matrix.

Since many of the matrices dealt with by this simulation were sparse, and had constant zero patterns, it made sense to write a function to perform multiplications in a manner that avoided the zeros. The function below shows how this was done for matrices with non-trivial zero patterns.

```
void MatrixMatrix(double **C,double **A,double **B,templateP *M){
  int i,j,k=(*M).s,l;
  for(i=0;i<k;++i){//For all the elements in C that will be non-zero
    C[(*M).T[i].r][(*M).T[i].c]=A[(*M).T[i].r][(*M).P[i].x[0]]*B[(*M).P[i].
   x[0]][(*M).T[i].c];//Set that element to the value of the first product
    l=(*M).P[i].xn;//Get number of contributing products for this element
    for(j=1;j<l;++j){//For all other contributions add product to C
      C[(*M).T[i].r][(*M).T[i].c]+=A[(*M).T[i].r][(*M).P[i].x[j]]*B[(*M).P[
   i].x[j]][(*M).T[i].c];
    }
  }
}
```

When one of the matrices was diagonal separate functions were used, but these are not shown here.

In a similar way the LU-decomposition step was also done using a sparse method. In this case the function provided by the CSparse library[152] was used. The code below shows the steps involved in preparing the Jacobian for this function.

```
void ludcomp(cs *A,double *x){//Solve the linear system given the right
   hand sides x and a compressed column version of the Jacobian A
  int i;
  i=A->nzmax;//Record the number of non-zero entries
  cs_dropzeros(A);//Call CSparce routine to drop any remaining zeros
  cs_droptol(A,tol);//Call CSparce routine to drop any values with a
   magnitude less than tol
  cs_dfree(cs_dmperm(A,1));//Call CSparce routine to permute the matrix
  cs_lusol(1,A,x,0.01);//Call CSparce routine to solve the linear system
  A->nzmax=i;//Reset the number of non-zero entries
  A->x=(double*)realloc(A->x,(i+1)*sizeof(double));
  A->i=(csi*)realloc(A->i,i*sizeof(csi));
  A->p=(csi*)realloc(A->p,(sNN+1)*sizeof(csi));
  for(i=0;i<A->nzmax;++i){//Reset the indexing array for next iteration
    A->i[i]=master_i[i];
  }
```

```
  for(i=0;i<A->n+1;++i){
    A->p[i]=master_p[i];
  }
}
```

Here the functions called before the main `cs_lusol`[152] function are used to drop any quantities, that are included as potential non-zeros in the template, but are zero or very small at the current iteration, in order to reduce the number of elements in the non-zero pattern[152] and in doing so speed up the function. Early on in the iteration process, when very few of the equations were satisfied the tolerance used for removing these elements was set quite high, to try to save as much time as possible in the processing of a Jacobian that was unlikely to produce solutions that satisfied all of the equations. This was then lowered to obtain greater accuracy as the solution was approached.

As a final note on this simulation it is worth discussing the distinction between the first step and all subsequent steps. At the beginning of the simulation the initial volume fraction in each of the simulation cells was read from a file, but none of the other quantities were known. This meant that the equations being solved had to be modified slightly so that the standard Newton-Raphson method used for the rest of the simulation steps could be applied to discover the values of the other unknowns. Essentially this meant removing equation 4.12f from equation set 4.12 and replacing it with $\phi - \phi_{old} = 0$ such that the values of the other five unknowns could be found, without changing the sizes of any of the matrices(3). One can see how this was achieved in practice by comparing the `solveteq0` function, used to find the initial state, to the `solve` function, used at all subsequent time steps.

```
int solve(){//Solve the set of equations for the next time step
  makeall();//Make all matrix and matrix vector combinations needed
  if(compare()){//Check to see if the equations have been satisfied
    return 0;
  }
  ludcomp(J_sp,f);//LU decomposition to find increments
  return 1;
}

int solveteq0(){//Solve equations for the initial setting
  int i,j;
  makeall();//Make all matrix and matrix vector combinations needed
  for(i=0;i<NN;++i){
    for(j=0;j<NN;++j){//Delete last equation and replace with phi-phi0=0
      J_sp->x[map[i+5*NN][j]]=double0;
      J_sp->x[map[i+5*NN][j+NN]]=double0;
      J_sp->x[map[i+5*NN][j+2*NN]]=double0;
      J_sp->x[map[i+5*NN][j+3*NN]]=double0;
      J_sp->x[map[i+5*NN][j+4*NN]]=double0;
      J_sp->x[map[i+5*NN][j+5*NN]]=double0;
    }
    J_sp->x[map[i+5*NN][i+5*NN]]=double1;
    f[i+5*NN]=double0;//Phi is already the solution so f(6) is satisfied
```

---

(3) Using a smaller Jacobian would have improved efficiency slightly, but since the sparse solver ignored the zeros anyway it was felt that this improvement was not worth the additional complexity it would have added to the algorithm, especially since this step typically took just one iteration.

```
  }
  if(compare()){//See if equations have been satisfied on this iteration
    return 0;
  }
  ludcomp(J_sp,f);//LU decomposition to find increments
  return 1;
}
```

C.2 Hydrodynamics Simulation

Although the hydrodynamic forces were calculated using the HYDROLIB library[12], this only returned an array, the friction matrix, for a given array of particle positions, the calculation of the other forces and the evolution of the system in time had to be dealt with separately. The theory behind all aspects of this simulation is discussed in sections 3.3 and 4.3, suffice to say here that the simulation was centred around the modified velocity Verlet algorithm of reference 113. The code snippet below shows the algorithm used to evolve the state of the system(4).

```
      do while(run)!Run until stop signal is received (code elsewhere)
        do 1 i=1,n,1!Test if particles are close enough to collide
          do 2 j=i+1,n,1!Consider particles with higher index than i
            rr(1)=c(0,i)-c(0,j)
            rr(2)=c(1,i)-c(1,j)
            rr(3)=c(2,i)-c(2,j)
            !Do periodic boundary conditions for rr
            vv(1)=vt(i,1)-vt(j,1)
            vv(2)=vt(i,2)-vt(j,2)
            vv(3)=vt(i,3)-vt(j,3)
            temp=dsqrt(rr(1)*rr(1)+rr(2)*rr(2)+rr(3)*rr(3))!Separation
            temp2=rr(1)*vv(1)+rr(2)*vv(2)+rr(3)*vv(3)
            if(temp.LT.collideS.AND.temp2.LT.0) then!If particles within
  set distance and heading towards each other collision will occur
              rr(1)=rr(1)/temp!Normalise separation to get contact normal
              rr(2)=rr(2)/temp
              rr(3)=rr(3)/temp
              impulse=temp2/temp!Calculate magnitude of impulse (I=R.V)
              !Update velocities for an perfect elastic collision
              vt(i,1)=vt(i,1)-impulse*rr(1)!Particle 1
              vt(i,2)=vt(i,2)-impulse*rr(2)
              vt(i,3)=vt(i,3)-impulse*rr(3)
              vt(j,1)=vt(j,1)+impulse*rr(1)!Particle 2
              vt(j,2)=vt(j,2)+impulse*rr(2)
              vt(j,3)=vt(j,3)+impulse*rr(3)
            end if
2         continue
1       continue
        !Treat collisions with rigid particles
        vmax=0.0
```

---

(4) In order to reduce the size of the snippet this code relates only to the free particles and is designed to run in series. It also assumes infinite boundary conditions, though the positions in the code where one would need to deal with periodic boundaries and driven particles are marked by comments.

```
       do 3 i=1,nt,1!Find the maximum velocity in any direction
         temp=dabs(v(i))
         if(temp.GT.vmax) vmax=temp
         temp=dabs(v(i+n))
         if(temp.GT.vmax) vmax=temp
         temp=dabs(v(i+2*n))
         if(temp.GT.vmax) vmax=temp
3      continue
       if(vmax.GT.1.0) then
         dt=dtmax/vmax!Set dt for fastest particle in the system
       else
         dt=dtmax
       end if
       do 4 i=1,n,1!Find out when the next collision is likely to occur
         do 5 j=i+1,n,1
           rr(1)=c(0,i)-c(0,j)
           rr(2)=c(1,i)-c(1,j)
           rr(3)=c(2,i)-c(2,j)
           !Do periodic boundary conditions for rr
           vv(1)=vt(i,1)-vt(j,1)
           vv(2)=vt(i,2)-vt(j,2)
           vv(3)=vt(i,3)-vt(j,3)
           temp=rr(1)*vv(1)+rr(2)*vv(2)+rr(3)*vv(3)
           if(temp.GT.0) then!Only real roots when particles are moving
  towards each other
             temp2=vv(1)*vv(1)+vv(2)*vv(2)+vv(3)*vv(3)
             temp=(collide*dsqrt(temp2)+temp)/temp2
             if(temp.LT.dt) dt=temp!If the next collision occurs before
  the end of the time step change the time step size
           end if
5        continue
4      continue
       !For rigid particles
       if(dt.LT.dtmin) dt=dtmin!Stop freezing on repeated collisions
1111   continue
       normaldt=dsqrt(dtold/dt)-1.0!To renormalise the random force
       do 6 i=1,n,1
         a(i,1)=a(i,1)+xi(6*i-5)*normaldt!Correct noise for new time step
         a(i,2)=a(i,2)+xi(6*i-4)*normaldt
         a(i,3)=a(i,3)+xi(6*i-3)*normaldt
         al(i,1)=al(i,1)+xi(6*i-2)*normaldt
         al(i,2)=al(i,2)+xi(6*i-1)*normaldt
         al(i,3)=al(i,3)+xi(6*i)*normaldt
6    continue
       do 7 i=1,n,1!Velocity Verlet algorithm (Part 1)
         c(0,i)=c(0,i)+(vt(i,1)+0.5*a(i,1)*dt)*dt!Update positions
         c(1,i)=c(1,i)+(vt(i,2)+0.5*a(i,2)*dt)*dt
         c(2,i)=c(2,i)+(vt(i,3)+0.5*a(i,3)*dt)*dt
         !Do periodic boundary conditions for c
         v(6*i-5)=vt(i,1)+0.5*a(i,1)*dt!Update velocity
         v(6*i-4)=vt(i,2)+0.5*a(i,2)*dt
         v(6*i-3)=vt(i,3)+0.5*a(i,3)*dt
         v(6*i-2)=omt(i,1)+0.5*al(i,1)*dt
         v(6*i-1)=omt(i,2)+0.5*al(i,2)*dt
```

```
         v(6*i)=omt(i,3)+0.5*al(i,3)*dt
7      continue
       !Update positions for rigid particles
       minr=collide
       do 8 i=1,n,1!Find the minimum particle separation
         do 9 j=i+1,n,1
           rr(1)=c(0,i)-c(0,j)
           rr(2)=c(1,i)-c(1,j)
           rr(3)=c(2,i)-c(2,j)
           !Do periodic boundary conditions for
           temp=dsqrt(rr(1)*rr(1)+rr(2)*rr(2)+rr(3)*rr(3))!Separation
           if(temp.LT.minr) minr=temp
9       continue
8     continue
       !Treat collisions with rigid particles
       if(minr.LT.collide)then
         do 10 i=1,n,1!Undo position update
           c(0,i)=c(0,i)-(vt(i,1)+0.5*a(i,1)*dt)*dt
           c(1,i)=c(1,i)-(vt(i,2)+0.5*a(i,2)*dt)*dt
           c(2,i)=c(2,i)-(vt(i,3)+0.5*a(i,3)*dt)*dt
           !Do periodic boundary conditions for c
           v(6*i-5)=vt(i,1)
           v(6*i-4)=vt(i,2)
           v(6*i-3)=vt(i,3)
           v(6*i-2)=omt(i,1)
           v(6*i-1)=omt(i,2)
           v(6*i)=omt(i,3)
10       continue
         !Undo update of positions for rigid particles
         dtold=dt
         dt=dt*0.5
         if(dt.LT.dtmin) then
           write(*,*) ’Particles are jammed. No time step is possible’
           goto 2222
         end if
         goto 1111
       endif
       do 11 i=1,nt,1!Set forces to zero initially
         f2(i,1)=0.0
         f2(i,2)=0.0
         f2(i,3)=0.0
11     continue
       do 12 i=1,nt,1!Nested loops go through particle pairs
         do 13 j=i+1,nt,1
           if(interact(i,j).EQ.1) then!Particles are interacting
             if(cnct(i,j).EQ.’.’) then!Particles are not rigidly joined
               rr(1)=c(0,i)-c(0,j)
               rr(2)=c(1,i)-c(1,j)
               rr(3)=c(2,i)-c(2,j)
               !Do periodic boundary conditions for
               ft=forceor(rr(1),rr(2),rr(3),FORCE_CONSTANTS)
               rr(1)=ft*rr(1)
               rr(2)=ft*rr(2)
               rr(3)=ft*rr(3)
```

```
                  f2(i,1)=f2(i,1)-rr(1)
                  f2(i,2)=f2(i,2)-rr(2)
                  f2(i,3)=f2(i,3)-rr(3)
                  f2(j,1)=f2(j,1)+rr(1)!By Newtons 3rd law
                  f2(j,2)=f2(j,2)+rr(2)
                  f2(j,3)=f2(j,3)+rr(3)
                end if
              end if
13          continue
12        continue
          call eval!Use HYDROLIB to evaluate the friction matrix
          do 14 i=1,6*n,1
            f(i)=0
            do 15 j=1,6*nt,1
              f(i)=f(i)+fr(i,j)*v(j)!Apply drag force F=Zeta*v
15          continue
14        continue
          do 16 i=n+1,6*nt,1!Do the same for rigid body particles
            f(i)=0
            do 17 j=1,6*nt,1
              f(i)=f(i)+fr(i,j)*v(j)!Apply drag force F=Zeta*v
17          continue
16        continue
          call dpotrf('L',6*nt,fr,6*nt,i)!Perform Cholesky decomposition
          do 18 i=1,6*n,1
            psi(i)=ZBQLNOR()!Generate a vector of Gaussian noise
18        continue
          sigma=dsqrt(kBT2/dt)
          do 19 i=1,6*n,1
            xi(i)=0
            do 20 j=1,i,1
              xi(i)=xi(i)+fr(i,j)*psi(j)!Multiply noise by the correct factor
20          continue
            xi(i)=xi(i)*sigma!Multiply to preserve detailed balance
            xi(i)=zeta*psi(i)*sigma
19        continue
          do 21 i=1,n,1!Velocity Verlet algorithm (Part 2)
            a(i,1)=xi(6*i-5)-f(6*i-5)+f2(i,1)!Update accelerations
            a(i,2)=xi(6*i-4)-f(6*i-4)+f2(i,2)-g
            a(i,3)=xi(6*i-3)-f(6*i-3)+f2(i,3)
            al(i,1)=oneoverMOI*(xi(6*i-2)-f(6*i-2))
            al(i,2)=oneoverMOI*(xi(6*i-1)-f(6*i-1))
            al(i,3)=oneoverMOI*(xi(6*i)-f(6*i))
            vt(i,1)=v(6*i-5)+0.5*a(i,1)*dt!Correct velocity
            vt(i,2)=v(6*i-4)+0.5*a(i,2)*dt
            vt(i,3)=v(6*i-3)+0.5*a(i,3)*dt
            omt(i,1)=v(6*i-2)+0.5*al(i,1)*dt
            omt(i,2)=v(6*i-1)+0.5*al(i,2)*dt
            omt(i,3)=v(6*i)+0.5*al(i,3)*dt
21        continue
          !Work out forces on rigid body particles
          Time=Time+dt!Increment time
          dtold=dt!Record the old time step so for re-normalising force
        end do
```

```
 2222 write (*,*) 'Simulation ended at t=',Time
      stop
      end
```

One of the key features of this algorithm is the way in which it deals with collisions between the particles. This is incredibly important as the hydrodynamic forces diverge when particles touch, so the algorithm must ensure that this never happens. The first test for collisions is performed at the beginning of each time step to see if any particles are ready to collide before the positions are updated. The time of the next collision is then calculated and used to set the size of the time step, provided that it does not result in the fastest particle in the system traversing more than a set distance. Finally after the positions have been updated, but before the calculation of the hydrodynamic forces, a test is performed to make sure no particles are touching, or overlapping, as a result of the acceleration terms in the equation, that are not accounted for in the prediction of the time of the next collision. If the arrangement fails this test the movement of the particles is undone and another attempt is made with a smaller time step. This method ensures that the simulation never attempts to evaluate the hydrodynamic friction matrix with a system of particles that would result in divergence of the force, whilst maximising the time step(5).

C.3 Constitutive Relation for Interacting Colloidal Dispersions

Although, in theory, it is possible to evaluate the constitutive relation derived here using analytical means, for a power law potential, it was far more practical to evaluate the functions using Mathematica as this allowed them to be used directly in the numerical calculations used to reproduce the dynamics of the system.

Before the calculation could commence a number of functions and constants needed to be defined, including the function used to treat the deformations and the velocity gradient tensor. These are shown in the code snippet below.

```
\[ScriptCapitalK]={{kxx,kxy},{kyx,kyy}};(*Velocity gradient tensor*)
kT=Transpose[\[ScriptCapitalK]];
p=-4;(*Exponent of single power law interaction potential*)
U[r_]=r^p;(*Interaction potential*)
g=Exp[-U[r]];(*Two particle distribution function*)
f=Sqrt[(1/\[Kappa])*(1+(\[Kappa]^2-1)*(Sin[\[Theta]-\[Delta]])^2)];(*
   Function for correct change of variables*)
M={{Cos[\[Theta]],-Sin[\[Theta]]},{Sin[\[Theta]],Cos[\[Theta]]}};(*Rotation
    matrix to rotate Cartesian velocity gradient tensor with polar frame*)
MT=Transpose[M];
kTp=Simplify[Expand[M.kT.MT]];
rkTr=Expand[{1,0}.kTp.{1,0}];(*Relevant components for the integrals*)
rkT\[Theta]=Expand[{1,0}.kTp.{0,1}];
(*Specific constants of the fluid and flow being modelled*)
\[ScriptCapitalD]=1;(*Diffusion constant*)
\[ScriptCapitalM]=1;(*Mobility constant*)
```

---

(5) It is worth spending time obtaining the most advanced arrangement possible as the calculation of the hydrodynamic forces is by far the most time consuming part of the simulation.

```
Clear[\[Gamma]];
kxx=\[Gamma];(*Components of velocity gradient tensor for flow field*)
kxy=0;
kyx=0;
kyy=-\[Gamma];
```

With these in place it was then possible to evaluate the necessary integrals for the stress and its rate of change. These are shown below.

```
\[CapitalSigma]aa=Simplify[(1/2)*Integrate[Integrate[g*(U'[r]*r^2/.r->r/f)
    ,{r,0,Infinity}]*Cos[2*\[Theta]]/f,{\[Theta],0,2*Pi}]](*Diagonal
    component of the stress*)
\[CapitalSigma]ab=Simplify[(1/2)*Integrate[Integrate[g*(U'[r]*r^2/.r->r/f)
    ,{r,0,Infinity}]*Sin[2*\[Theta]]/f,{\[Theta],0,2*Pi}]](*Off diagonal
    component of the stress*)
\[CapitalSigma]aad=(*Rate of change of the diagonal component*)
Simplify[(1/2)*\[ScriptCapitalD]*Integrate[Cos[2*\[Theta]]*Integrate[g*((5*
    U''[r]*r+U'''[r]*r^2)/.r->r/f),{r,0,Infinity}]/f,{\[Theta],0,2*Pi}]]-
    Simplify[(1/2)*\[ScriptCapitalM]*Integrate[Cos[2*\[Theta]]*Integrate[g
    *(((2*U'[r]*r+U''[r]*r^2)*U'[r])/.r->r/f),{r,0,Infinity}]/f,{\[Theta],0
    ,2*Pi}]]+(*Diffusive and interaction term*)
Simplify[(1/2)*Integrate[Cos[2*\[Theta]]*Integrate[g*(((2*U'[r]*r^2+U''[r]*
    r^3)*rkTr)/.r->r/f),{r,0,Infinity}]/f,{\[Theta],0,2*Pi}]]-
Simplify[Integrate[Sin[2*\[Theta]]*Integrate[g*(((U'[r]*r^2)*rkT\[Theta])/.
    r->r/f),{r,0,Infinity}]/f,{\[Theta],0,2*Pi}]](*Advection term*)
\[CapitalSigma]abd=(*rate of change of off diagonal component of stress*)
Simplify[(1/2)*\[ScriptCapitalD]*Integrate[Sin[2*\[Theta]]*Integrate[g*((5*
    U''[r]*r+U'''[r]*r^2)/.r->r/f),{r,0,Infinity}]/f,{\[Theta],0,2*Pi}]]-
    Simplify[(1/2)*\[ScriptCapitalM]*Integrate[Sin[2*\[Theta]]*Integrate[g
    *(((2*U'[r]*r+U''[r]*r^2)*U'[r])/.r->r/f),{r,0,Infinity}]/f,{\[Theta],0
    ,2*Pi}]]+(*Diffusive and interaction term*)
Simplify[(1/2)*Integrate[Sin[2*\[Theta]]*Integrate[g*(((2*U'[r]*r^2+U''[r]*
    r^3)*rkTr)/.r->r/f),{r,0,Infinity}]/f,{\[Theta],0,2*Pi}]]+
Simplify[Integrate[Cos[2*\[Theta]]*Integrate[g*(((U'[r]*r^2)*rkT\[Theta])/.
    r->r/f),{r,0,Infinity}]/f,{\[Theta],0,2*Pi}]](*Advection term*)
```

Once the integrals had been evaluated it was possible to set the rate of change of the two independent components of the stress tensor to zero and solve for the two parameters describing the deformation in order to obtain the stress as a function of strain rate, for the velocity gradient tensor give in the previous definitions. The following code shows how this was implemented.

```
sol=FullSimplify[(Solve[{\[CapitalSigma]aad==0,\[CapitalSigma]abd==0},{\[
    Gamma],\[Delta]}]/.C[1]->0)[[1]]];(*Solve for shear rate*)
SR=FullSimplify[\[Gamma]/.sol](*Shear rate in terms of deformation*)
SS=FullSimplify[\[CapitalSigma]ab/.sol](*Stress in terms of deformation*)
NS=FullSimplify[-\[CapitalSigma]aa/.sol]
\[Eta]=FullSimplify[D[SS,\[Kappa]]/D[SR,\[Kappa]]](*Viscosities*)
\[Mu]=FullSimplify[D[NS,\[Kappa]]/D[SR,\[Kappa]]]
graph1=ParametricPlot[{{SR,NS},{SR,SS}},{\[Kappa],0.01,1}](*Stress vs
    strain rate*)
graph2=ParametricPlot[{{Log[Abs[SR]],Log[Abs[NS]]},{Log[Abs[SR]],Log[Abs[SS
    ]]}},{\[Kappa],0.01,1}](*Stress vs strain rate*)
graph3=ParametricPlot[{{Log[Abs[SR]],Log[Abs[\[Mu]]]},{Log[Abs[SR]],Log[Abs
    [\[Eta]]]}},{\[Kappa],0.01,1}](*Viscosity vs strain rate*)
```

Unlike the steady state stress-strain relationship, the dynamics of the deformation and by extension the dynamics of the stress had to be calculated numerically. This was done using a very simple static time step Euler approach(6). This procedure is shown in the following code snippet.

```
loops=250;
\[Kappa]0=0.999;(*Parameters for initial state*)
\[Delta]0=Pi/2;
\[Gamma]=0.1;(*Constant strain rate*)
\[CapitalSigma]AA=\[CapitalSigma]aa/.{\[Kappa]->\[Kappa]0,\[Delta]->\[Pi]/2
    -\[Delta]0};
\[CapitalSigma]AB=\[CapitalSigma]ab/.{\[Kappa]->\[Kappa]0,\[Delta]->\[Pi]/2
    -\[Delta]0};
dt=0.0005;(*Static time step*)
range=2;(*Range of plots*)
t=0;
s=FindRoot[{\[CapitalSigma]aa==\[CapitalSigma]AA,\[CapitalSigma]ab==\[
    CapitalSigma]AB},{{\[Kappa],0.999},{\[Delta],0.001}},PrecisionGoal->5,
    AccuracyGoal->5];(*Solve numerically*)
kk=\[Kappa];(*Temporary variables*)
dd=\[Delta];
k=kk/.s;
d=dd/.s;
G:=PolarPlot[Sqrt[k/(1+(k^2-1)*(Sin[\[Theta]+d])^2)],{\[Theta],0,2*Pi},
    PlotRange->range];
P=Show[G,V];
plot={P};
\[CapitalSigma]aaT={{t,\[CapitalSigma]aa/.{\[Kappa]-> k,\[Delta]->\[Pi]/2-d
    }}};(*List of stresses at all time steps to make a plot of stress vs
    time*)
\[CapitalSigma]abT={{t,\[CapitalSigma]ab/.{\[Kappa]-> k,\[Delta]->\[Pi]/2-d
    }}};
\[Kappa]T={{t,k}};
\[Delta]T={{t,d}};
For[i=0,i<loops,i++;(*Loop for specified number of steps*)
\[CapitalSigma]AA=N[Re[\[CapitalSigma]AA+(\[CapitalSigma]aad/.s)*dt]];(*
    update the stress using the rate of change of stress*)
\[CapitalSigma]AB=N[Re[\[CapitalSigma]AB+(\[CapitalSigma]abd/.s)*dt]];
t=t+dt;(*update the time*)
s=FindRoot[{\[CapitalSigma]aa==\[CapitalSigma]AA,\[CapitalSigma]ab==\[
    CapitalSigma]AB},{{\[Kappa],k},{\[Delta],d}},PrecisionGoal->5,
    AccuracyGoal->5];(*Solve for the values of the parameters at the new
    stress*)
k=kk/.s;(*Store numerical values for this time step*)
d=dd/.s;
G:=PolarPlot[Sqrt[k/(1+(k^2-1)*(Sin[\[Theta]+d])^2)],{\[Theta],0,2*Pi},
    PlotRange->range];
V:=VectorPlot[{kxx*x+kxy*y,kyy*y+kyx*x},{x,-range,range},{y,-range,range}];
P=Show[G,V];
plot=Append[plot,P];
\[CapitalSigma]aaT=Append[\[CapitalSigma]aaT,{t,(\[CapitalSigma]aa/.{\[
    Kappa]-> k,\[Delta]->\[Pi]/2-d})}];
```

---

(6) Since the analytical relationships could be evaluated very rapidly, and only a few hundred time steps were required to obtain the necessary level of detail, this scheme was thought adequate.

```
\[CapitalSigma]abT=Append[\[CapitalSigma]abT,{t,(\[CapitalSigma]ab/.{\[
    Kappa]-> k,\[Delta]->\[Pi]/2-d})}];
]
graph4=ListPlot[{\[CapitalSigma]aaT,\[CapitalSigma]abT},PlotStyle->{Lighter
    [Blue,0.5],Darker[Blue,0.5]},AxesLabel->{"t","\[CapitalSigma]"}];(*plot
     stresses as a function of time*)
L=ListAnimate[plot](*Animation of two particle distribution function*)
```

This code allowed for the calculation of both the stress and the shape of the equiprobability contours of the two particle distribution function as functions of time.

As discussed in section 3.4.5 a low strain approximation to the model was also created, in addition to the full model. This was used to deal with interaction potentials that were too complicated for full model, such as the solution to the Percus-Yevick approximation. The code below shows how the matrices of equation 3.117d were calculated and equation 3.116 solved.

```
(*Matrices*)
J=r;(*Jacobian determinant for two dimensional polar coordinates is r*)
n1={Cos[\[Theta]],Sin[\[Theta]]};(*Cartesian unit vectors*)
n2={Cos[\[Theta]],Sin[\[Theta]]};
n1n2mhI=FullSimplify[Outer[Times,n1,n2]-1/2*{{1,0},{0,1}}];(*x/y-component
    *)
gradU=Grad[U[r],{r,\[Theta]},"Polar"];(*Gradient of the interaction
    potential*)
gradg=Grad[g,{r,\[Theta]},"Polar"];(*Gradient of the correlation function*)
rr={r,0};(*Vector r (needed in dot products)*)
MMT=FullSimplify[Outer[Times,M,MT]];(*Rotation matrix*)
rMMTgradg=FullSimplify[rr.MMT.gradg];
rMMTgradgn1n2mhI=FullSimplify[Outer[Times,rMMTgradg,n1n2mhI]];
rgradU=rr.gradU;
dAA=rMMTgradgn1n2mhI*rgradU*J;(*Strain to the stress (integrand)*)
AA=Integrate[Integrate[dAA,{r,0,Infinity}],{\[Theta],0,2*Pi}];
n1n2mhIJrgradU=n1n2mhI*J*rgradU;
gradn1n2mhIrgradUJ=Map[Grad[#,{r,\[Theta]},"Polar"]&,n1n2mhIJrgradU,{2}];
rrMMTgradn1n2mhIrgradUJ=FullSimplify[gradn1n2mhIrgradUJ.MMT.rr];
dBB=g*rrMMTgradn1n2mhIrgradUJ;(*Velocity gradient tensor (integrand)*)
BB=Integrate[Integrate[dBB,{r,0,Infinity}],{\[Theta],0,2*Pi}];
laplaciann1n2mhIrgradUJ=FullSimplify[Map[Laplacian[#,{r,\[Theta]},"Polar"
    ]&,n1n2mhIJrgradU,{2}]];
dCC1=FullSimplify[\[ScriptCapitalM]*Outer[Times,rMMTgradg,(gradn1n2
    mhIrgradUJ.gradU)]];
dCC2=FullSimplify[\[ScriptCapitalD]*Outer[Times,rMMTgradg,laplaciann1n2
    mhIrgradUJ]];
dCC=dCC2-dCC1;(*Flow independent strain tensor (integrand)*)
CC=Integrate[Integrate[dCC,{r,0,Infinity}],{\[Theta],0,2*Pi}];
dDD=Outer[Times,rMMTgradg,rrMMTgradn1n2mhIrgradUJ];(*Strain-Velocity
    gradient (integrand)*)
DD=Integrate[Integrate[dDD,{r,0,Infinity}],{\[Theta],0,2*Pi}];
(*Solution of equations of motion for low strain approximation*)
dF={{dFxx[T],dFxy[T]},{dFxy[T],-dFxx[T]}};(*Deformation tensor*)
dFdA=FullSimplify[(D[dF,T].AA)[[1]][[1]]+(D[dF,T].AA)[[2]][[2]]];
dFC=FullSimplify[(dF.CC)[[1]][[1]]+(dF.CC)[[2]][[2]]];
dFD=FullSimplify[(dF.DD)[[1]][[1]]+(dF.DD)[[2]][[2]]];
KBpdFD=FullSimplify[(kT.Transpose[(BB+dFD),{3,4,1,2}])[[1]][[1]]+(kT.
```

```
    Transpose[(BB+dFD),{3,4,1,2}])[[2]][[2]]];(*Term that depends on the
    strain rate*)
eq=FullSimplify[KBpdFD+dFC-dFdA];(*Full matrix equation to be solved*)
Sol=FullSimplify[DSolve[{eq[[1]][[1]]==0,eq[[1]][[2]]==0},{dFxx[T],dFxy[T
    ]},T]];(*Solve the two coupled scalar equations*)
c1=(Solve[(Sol[[1]][[1]][[2]]/.T->0)==0,C[1]])[[1]][[1]][[2]];(*Use
    condition that system is initially isotropic to determine constants of
    integration*)
c2=(Solve[(Sol[[1]][[2]][[2]]/.T->0)==0,C[2]])[[1]][[1]][[2]];
dFsolaa=Sol[[1]][[1]][[2]]/.{C[1]->c1,C[2]->c2};
dFsolab=Sol[[1]][[2]][[2]]/.{C[1]->c1,C[2]->c2};
dFsol={{dFsolaa,dFsolab},{dFsolab,-dFsolaa}};(*Time dependent strain*)
dFsolT=Transpose[dFsol];
Stress=Simplify[(dFsolT.AA)[[1]][[1]]+(dFsolT.AA)[[2]][[2]]];(*Stress*)
steadyStress=Limit[Stress,T->Infinity];(*Infinite time for steady state*)
Stress//MatrixForm
steadyStress//MatrixForm
Manipulate[Plot[{Stress[[1]][[1]]/.\[Gamma]->\[Gamma]0,Stress[[1]][[2]]/.\[
    Gamma]->\[Gamma]0},{T,0,1}](*Plot two components*)
```

References

[1] R. Standish. On complexity and emergence. *Complexity International*, 9:0101005v1, 2001.

[2] M. Buchanan, D. Molenaar, S. de Villiers, and R. M. L. Evans. Pattern formation in draining thin film suspensions. *Langmuir*, 23(7):3732–3736, Mar 27 2007.

[3] R. M. L. Evans, 2011-2015. Private Communication.

[4] Adolfo J. Banchio and John F. Brady. Accelerated Stokesian dynamics: Brownian motion. *The Journal of Chemical Physics*, 118(22):10323–10332, 2003.

[5] David R. Foss and John F. Brady. Structure, diffusion and rheology of Brownian suspensions by Stokesian Dynamics simulation. *J. Fluid Mech*, 407:167–200, 2000.

[6] Eric Dickinson. Brownian dynamic with hydrodynamic interactions: the application to protein diffusional problems. *Chem. Soc. Rev.*, 14:421–455, 1985.

[7] Geoffrey C. Ansell, Eric Dickinson, and Malcolm Ludvigsen. Brownian dynamics of colloidal-aggregate rotation and dissociation in shear flow. *J. Chem. Soc., Faraday Trans. 2*, 81:1269–1284, 1985.

[8] Donald L. Ermak and J. A. McCammon. Brownian dynamics with hydrodynamic interactions. *The Journal of Chemical Physics*, 69(4):1352–1360, 1978.

[9] W. Hess and R. Klein. Generalized hydrodynamics of systems of Brownian particles. *Advances in Physics*, 32(2):173–283, 1983.

[10] Frank Snijkers, Rossana Pasquino, and Jan Vermant. Hydrodynamic Interactions between Two Equally Sized Spheres in Viscoelastic Fluids in Shear Flow. *Langmuir*, 29(19):5701–5713, 2013. PMID: 23600865.

[11] M. Reichert. *Hydrodynamic Interactions in Colloidal and Biological Systems.* PhD thesis, Physics, 2006.

[12] K. Hinsen. HYDROLIB: a library for the evaluation of hydrodynamic interactions in colloidal suspensions. *Computer Physics Communications*, 88(2-3):327–340, 1995.

[13] R.C. Ball and J.R. Melrose. Lubrication breakdown in hydrodynamic simulations of concentrated colloids. *Advances in Colloid and Interface Science*, 59(0):19–30, 1995.

[14] Kengo Ichiki and John F. Brady. Many-body effects and matrix inversion in low-Reynolds-number hydrodynamics. *Physics of Fluids*, 13(1):350–353, 2001.

[15] S. Kim and S.J. Karrila. *Microhydrodynamics: Principles and Selected Applications.* Dover Civil and Mechanical Engineering. Dover Publications, 2013.

[16] Veronique Trappe and Peter Sandkühler. Colloidal gels-low-density disordered solid-like states. *Current Opinion in Colloid & Interface Science*, 8(6):494–500, 2004.

[17] Ning Xu and Emily S. C. Ching. Effects of particle-size ratio on jamming of binary mixtures at zero temperature. *Soft Matter*, 6:2944–2948, 2010.

[18] Denis S. Grebenkov, Massimo Pica Ciamarra, Mario Nicodemi, and Antonio Coniglio. Flow, Ordering, and Jamming of Sheared Granular Suspensions. *Phys. Rev. Lett.*, 100:078001, Feb 2008.

[19] G. Lois and J. M. Carlson. Force networks and the dynamic approach to jamming in sheared granular media. *EPL (Europhysics Letters)*, 80(5):58001, 2007.

[20] Emanuel Bertrand, Jerome Bibette, and Véronique Schmitt. From shear thickening to shear-induced jamming. *Phys. Rev. E*, 66:060401, Dec 2002.

[21] Didier Lootens, Henri Van Damme, and Pascal Hébraud. Giant Stress Fluctuations at the Jamming Transition. *Phys. Rev. Lett.*, 90:178301, Apr 2003.

[22] G. Katgert and M. van Hecke. Jamming and geometry of two-dimensional foams. *EPL (Europhysics Letters)*, 92(3):34002, 2010.

[23] ME Cates, JP Wittmer, JP Bouchaud, and P Claudin. Jamming and stress propagation in particulate matter. *Physica A*, 263(1-4):354–361, Feb 1 1999. 20th International Conference On Statistical Physics (statphys 20), Paris, France, Jul 20-24, 1998.

[24] Andrew I. Campbell and Mark D. Haw. Jamming and unjamming of concentrated colloidal dispersions in channel flows. *Soft Matter*, 6:4688–4693, 2010.

[25] Dapeng Bi, Jie Zhang, Bulbul Chakraborty, and R. P. Behringer. Jamming by shear. *Nature*, 480(7377):355–358, 2011.

[26] M. E. Cates, J. P. Wittmer, J.-P. Bouchaud, and P. Claudin. Jamming, Force Chains, and Fragile Matter. *Phys. Rev. Lett.*, 81:1841–1844, Aug 1998.

[27] D. A. Head, A. Ajdari, and M. E. Cates. Jamming, hysteresis, and oscillation in scalar models for shear thickening. *Phys. Rev. E*, 64:061509, Nov 2001.

[28] Andrea J. Liu and Sidney R. Nagel. Jamming is not just cool any more. *Nature*, 396(6706):21–22, 1998.

[29] C. B. Holmes, M. Fuchs, and M. E. Cates. Jamming transitions in a schematic model of suspension rheology. *EPL (Europhysics Letters)*, 63(2):240, 2003.

[30] MD Haw. Jamming, two-fluid behavior, and “self-filtration” in concentrated particulate suspensions. *Phys. Rev. Lett.*, 92(18):185506, May 7 2004.

[31] J. A. Drocco, M. B. Hastings, C. J. Olson Reichhardt, and C. Reichhardt. Multiscaling at Point J: Jamming is a Critical Phenomenon. *Phys. Rev. Lett.*, 95:088001, Aug 2005.

[32] Cristian Mankoc, Angel Garcimartin, Iker Zuriguel, Diego Maza, and Luis A. Pugnaloni. Role of vibrations in the jamming and unjamming of grains discharging from a silo. *Phys. Rev. E*, 80:011309, Jul 2009.

[33] M. E. Cates, C. B. Holmes, M. Fuchs, and O. Henrich. *Schematic mode coupling theories for shear thinning, shear thickening, and jamming*, chapter 17, pages 203–216. Elsevier, 2003.

[34] Abdoulaye Fall, N. Huang, F. Bertrand, G. Ovarlez, and Daniel Bonn. Shear Thickening of Cornstarch Suspensions as a Reentrant Jamming Transition. *Phys. Rev. Lett.*, 100:018301, Jan 2008.

[35] J. M. Brader, M. E. Cates, and M. Fuchs. First-Principles Constitutive Equation for Suspension Rheology. *Phys. Rev. Lett.*, 101:138301, Sep 2008.

[36] R.A.L. Jones. *Soft Condensed Matter.* Oxford Master Series in Condensed Matter Physics. Oxford University Press, 2002.

[37] R.G. Larson. *Constitutive Equations for Polymer Melts and Solutions.* Butterworths Series in Chemical Engineering. Butterworths, 1988.

[38] R.G. Larson. *The Structure and Rheology of Complex Fluids*. Topics in Chemical Engineering. Oxford University Press, USA, 1998.

[39] Y.H. Lin. *Polymer Viscoelasticity: Basics, Molecular Theories, and Experiments*. World Scientific, 2003.

[40] Zhengdong Cheng, Jixiang Zhu, Paul M. Chaikin, See-Eng Phan, and William B. Russel. Nature of the divergence in low shear viscosity of colloidal hard-sphere dispersions. *Phys. Rev. E*, 65:041405, Apr 2002.

[41] john F. Brady, aditya S. Khair, and manuj Swaroop. On The Bulk Viscosity Of Suspensions. *Journal of Fluid Mechanics*, 554:109–123, 2006.

[42] Irvin M. Krieger and Thomas J. Dougherty. A Mechanism for Non-Newtonian Flow in Suspensions of Rigid Spheres. *Transactions of the Society of Rheology*, 3(1):137–152, 1959.

[43] J. Mewis and N.J. Wagner. *Colloidal Suspension Rheology*. Cambridge Series in Chemical Engineering. Cambridge University Press, 2012.

[44] W. C. K. Poon, L. Starrs, S. P. Meeker, A. Moussaid, R. M. L. Evans, P. N. Pusey, and M. M. Robins. Delayed sedimentation of transient gels in colloid-polymer mixtures: dark-field observation, rheology and dynamic light scattering studies. *Faraday Discuss.*, 112:143–154, 1999.

[45] J. C. van der Werff and C. G. de Kruif. Hard-sphere Colloidal Dispersions: The Scaling of Rheological Properties with Particle Size, Volume Fraction, and Shear Rate. *Journal of Rheology*, 33(3):421–454, 1989.

[46] Jamie Fletcher. Making the connection - particle size, size distribution and rheology, 2011.

[47] John F. Brady and Michael Vicic. Normal stresses in colloidal dispersions. *Journal of Rheology (1978-present)*, 39(3):545–566, 1995.

[48] Meheboob Alam and Stefan Luding. Rheology of bidisperse granular mixtures via event-driven simulations. *Journal of Fluid Mechanics*, 476:69–103, 2003.

[49] F. Chu, J. Guillot, and A. Guyot. Rheology of concentrated multi-sized poly(St/BA/MMA) latices. *Colloid and Polymer Science*, 276(4):305–312, 1998.

[50] A. Rao. *Rheology of Fluid and Semisolid Foods: Principles and Applications*. Chapman & Hall Food Science Book. Aspen Publishers, 1999.

[51] Irvin M. Krieger. Rheology of monodisperse latices. *Advances in Colloid and Interface Science*, 3(2):111–136, 1972.

[52] Diego B. Genovese. Shear rheology of hard-sphere, dispersed, and aggregated suspensions, and filler-matrix composites. *Advances in Colloid and Interface Science*, 171–172(0):1–16, 2012.

[53] William J. Frith, P. d'Haene, R. Buscall, and J. Mewis. Shear thickening in model suspensions of sterically stabilized particles. *Journal of Rheology*, 40(4):531–548, 1996.

[54] H. A. Barnes. Shear-Thickening ("Dilatancy") in Suspensions of Nonaggregating Solid Particles Dispersed in Newtonian Liquids. *Journal of Rheology*, 33(2):329–366, 1989.

[55] Eric Dickinson. Structure and rheology of colloidal particle gels: Insight from computer simulation. *Advances in Colloid and Interface Science*, 199-200(0):114–127, 2013.

[56] J. Bławzdziewicz and Grzegorz Szamel. Structure and rheology of semidilute suspension under shear. *Phys. Rev. E*, 48:4632–4636, Dec 1993.

[57] EJ Hinch. The measurement of suspension rheology. *Journal of Fluid Mechanics*, 686:1–4, 2011.

[58] J Bergenholtz, JF Brady, and M Vicic. The non-Newtonian rheology of dilute colloidal suspensions. *Journal of Fluid Mechanics*, 456:239–275, 2002.

[59] J. F. Brady and G. Bossis. The rheology of concentrated suspensions of spheres in simple shear flow by numerical simulation. *Journal of Fluid Mechanics*, 155:105–129, June 1985.

[60] Matthias Fuchs and Michael E. Cates. Theory of Nonlinear Rheology and Yielding of Dense Colloidal Suspensions. *Phys. Rev. Lett.*, 89:248304, Nov 2002.

[61] Johan Bergenholtz. Theory of rheology of colloidal dispersions. *Current Opinion in Colloid & Interface Science*, 6:484–488, 2001.

[62] Fran çois Boyer, Élisabeth Guazzelli, and Olivier Pouliquen. Unifying Suspension and Granular Rheology. *Phys. Rev. Lett.*, 107:188301, Oct 2011.

[63] DP Feldman and JP Crutchfield. Measures of statistical complexity: Why? *Phys. Lett. A*, 238(4-5):244–252, Feb 9 1998.

[64] J.V. Koleske. *Paint and Coating Testing Manual: Fourteenth Edition of the Gardner-Sward Handbook*. Gardner-Sward handbook. ASTM, 1995.

[65] Geoffrey C Ansell and Eric Dickinson. Brownian dynamics simulation of the fragmentation of a large colloidal floc in simple shear flow. *Journal of Colloid and Interface Science*, 110(1):73–81, 1986.

[66] Antonio M. Puertas, Matthias Fuchs, and Michael E. Cates. Comparative Simulation Study of Colloidal Gels And Glasses. *Phys. Rev. Lett.*, 88:098301, Feb 2002.

[67] F. Alonso-Marroquin, I. Vardoulakis, H. J. Herrmann, D. Weatherley, and P. Mora. Effect of rolling on dissipation in fault gouges. *Phys. Rev. E*, 74:031306, Sep 2006.

[68] B. Cichocki, B. U. Felderhof, K. Hinsen, E. Wajnryb, and J. Bl/awzdziewicz. Friction and mobility of many spheres in Stokes flow. *The Journal of Chemical Physics*, 100(5):3780–3790, 1994.

[69] Eric Brown, Nicole A. Forman, Carlos S. Orellana, Hanjun Zhang, Benjamin W. Maynor, Douglas E. Betts, Joseph M. DeSimone, and Heinrich M. Jaeger. Generality of shear thickening in dense suspensions. *Nat Mater*, 9(3):Nature Publishing Group—224, January 2010.

[70] P. N. Segrè, V. Prasad, A. B. Schofield, and D. A. Weitz. Glasslike Kinetic Arrest at the Colloidal-Gelation Transition. *Phys. Rev. Lett.*, 86:6042–6045, Jun 2001.

[71] Andrea J. Liu and Sidney R. Nagel. Granular and jammed materials. *Soft Matter*, 6:2869–2870, 2010.

[72] R Brannon. Kinematics: The Mathemaics Of Deformation. Online Course notes, December 2008.

[73] Alexander Oron, Stephen H. Davis, and S. George Bankoff. Long-scale evolution of thin liquid films. *Rev. Mod. Phys.*, 69:931–980, Jul 1997.

[74] David R Reichman and Patrick Charbonneau. Mode-coupling theory. *Journal of Statistical Mechanics: Theory and Experiment*, 2005(05):P05013, 2005.

[75] John F Brady. Model hard-sphere dispersions: statistical mechanical theory, simulations, and experiments. *Current Opinion in Colloid & Interface Science*, 1(4):472–480, 1996.

[76] Koichi Takamura and Theo G. M. van de Ven. Shear Thinning Behavior of Concentrated Latex Dispersions. *Macromolecular Symposia*, 288(1):78–86, 2010.

[77] P. Ballesta, R. Besseling, L. Isa, G. Petekidis, and W. C. K. Poon. Slip and Flow of Hard-Sphere Colloidal Glasses. *Phys. Rev. Lett.*, 101:258301, Dec 2008.

[78] Justin C. T. Kao and A. E. Hosoi. Spinodal decomposition in particle-laden Landau-Levich flow. *Physics of Fluids*, 24(4):041701, 2012.

[79] A Baule, H Touchette, and E G D Cohen. Stick-slip motion of solids with dry friction subject to random vibrations and an external field. *Nonlinearity*, 24(2):351, 2011.

[80] Jacinta C. Conrad and Jennifer A. Lewis. Structure of Colloidal Gels during Microchannel Flow. *Langmuir*, 24(15):7628–7634, 2008. PMID: 18582141.

[81] M. Mooney. The viscosity of a concentrated suspension of spherical particles. *Journal of Colloid Science*, 6(2):162–170, 1951.

[82] Maurizio Cardaci, Vito Di Gesù, Maria Petrou, and Marco Elio Tabacchi. A fuzzy approach to the evaluation of image complexity. *Fuzzy Sets and Systems*, 160(10):1474–1484, 2009.

[83] R López-Ruiz, HL Mancini, and X Calbet. A statistical measure of complexity. *Phys. Lett. A*, 209(5-6):321–326, Dec 25 1995.

[84] Yu.A. Andrienko, N.V. Brilliantov, and J. Kurths. Complexity of two-dimensional patterns. *The European Physical Journal B - Condensed Matter and Complex Systems*, 15:539–546, 2000. 10.1007/s100510051157.

[85] F. Kaspar and H. G. Schuster. Easily calculable measure for the complexity of spatiotemporal patterns. *Phys. Rev. A*, 36:842–848, Jul 1987.

[86] Y. Chen and Hari Sundaram. Estimating Complexity of 2D Shapes. In *Multimedia Signal Processing, 2005 IEEE 7th Workshop on*, pages 1–4, 30 2005-nov. 2 2005.

[87] José Roberto C. Piqueira and Sérgio Henrique V.L. de Mattos. Note on LMC complexity measure. *Ecological Modelling*, 222(19):3603–3604, 2011.

[88] A. Lempel and J. Ziv. On the Complexity of Finite Sequences. *Information Theory, IEEE Transactions on*, 22(1):75–81, Jan 1976.

[89] Wentian Li. On the relationship between complexity and entropy for Markov chains and regular languages. *Complex Systems*, 5:5–4, 1991.

[90] H. Su, A. Bouridane, and D. Crookes. Scale Adaptive Complexity Measure of 2D Shapes. *Pattern Recognition, International Conference on*, 2:134–137, 2006.

[91] J. S. Shiner, Matt Davison, and P. T. Landsberg. Simple measure for complexity. *Phys. Rev. E*, 59:1459–1464, Feb 1999.

[92] C Anteneodo and A.R Plastino. Some features of the López-Ruiz-Mancini-Calbet (LMC) statistical measure of complexity. *Phys. Lett. A*, 223(5):348–354, 1996.

[93] James P. Crutchfield and David P. Feldman. Statistical complexity of simple one-dimensional spin systems. *Phys. Rev. E*, 55:R1239–R1242, Feb 1997.

[94] Karl Young, Yue Chen, John Kornak, Gerald B. Matson, and Norbert Schuff. Summarizing Complexity in High Dimensions. *Phys. Rev. Lett.*, 94:098701, Mar 2005.

[95] Antoinette Tordesillas, David Kirszenblat, and Christine Mangelsdorf. Taming the Complexity of Granular Materials with Vector Calculus. *Australasian Journal of Engineering Education*, 15(2):85–94, October 2009.

[96] Xavier Calbet and Ricardo López-Ruiz. Tendency towards maximum complexity in a nonequilibrium isolated system. *Phys. Rev. E*, 63:066116, May 2001.

[97] B. Chazelle and J. Incerpi. Triangulation and shape-complexity. *ACM Trans. Graph.*, 3:135–152, April 1984.

[98] L.E. Reichl. *A Modern Course in Statistical Physics.* University of Texas Press, 1988.

[99] C. E. Shannon. A mathematical theory of communication. *SIGMOBILE Mob. Comput. Commun. Rev.*, 5(1):3–55, October 1948.

[100] James P. and Crutchfield. The calculi of emergence: computation, dynamics and induction. *Physica D: Nonlinear Phenomena*, 75(1-3):11–54, 1994.

[101] Junjie Zhou, B. Dupuy, A. L. Bertozzi, and A. E. Hosoi. Theory for Shock Dynamics in Particle-Laden Thin Films. *Phys. Rev. Lett.*, 94:117803, Mar 2005.

[102] C.W Hirt, J.L Cook, and T.D Butler. A lagrangian method for calculating the dynamics of an incompressible fluid with free surface. *Journal of Computational Physics*, 5(1):103–124, 1970.

[103] William Kizner. A Numerical Method for Finding Solutions of Nonlinear Equations. *Journal of the Society for Industrial and Applied Mathematics*, 12(2):pp. 424–428, 1964.

[104] Deborah Sulsky and J.U Brackbill. A numerical method for suspension flow. *Journal of Computational Physics*, 96(2):339–368, 1991.

[105] J. G. P. Barnes. An Algorithm for Solving Non-Linear Equations Based on the Secant Method. *The Computer Journal*, 8(1):66–72, 1965.

[106] T.A. Davis. *Direct Methods for Sparse Linear Systems.* Fundamentals of Algorithms. Society for Industrial and Applied Mathematics, 2006.

[107] K.F. Riley, M.P. Hobson, and S.J. Bence. *Mathematical Methods for Physics and Engineering.* Cambridge University Press, 2006.

[108] Marc Spiegelman. *Myths & Methods in Modeling.* Columbia University, 2004.

[109] Shirley Black, Noel & Moore. Successive Overrelaxation Method. Web, March 2012.

[110] Volker Strassen. Gaussian elimination is not optimal. *Numerische Mathematik*, 13:354–356, 1969. 10.1007/BF02165411.

[111] Eric W Weisstein. Strassen Formulas. MathWorld–A Wolfram Web Resource.

[112] H. R. P. Bailey, D. H. & Gerguson. A Strassen-Newton algorithm for high-speed parallelizable matrix inversion. In *Proceedings of the 1988 ACM/IEEE conference on Supercomputing*, Supercomputing '88, pages 419–424, Los Alamitos, CA, USA, 1988. IEEE Computer Society Press.

[113] Robert D. Groot and Patrick B. Warren. Dissipative particle dynamics: Bridging the gap between atomistic and mesoscopic simulation. *The Journal of Chemical Physics*, 107(11):4423–4435, 1997.

[114] Jos Stam. Stable fluids. In *Proceedings of the 26th annual conference on Computer graphics and interactive techniques*, Siggraph '99, pages 121–128, New York, NY, USA, 1999. ACM Press/Addison-Wesley Publishing Co.

[115] P. Allen and D.J. Tildesley. *Computer Simulation of Liquids.* Oxford Science Publ. Clarendon Press, 1989.

[116] P.B.Sunil Kumar. Numerical Methods and Programing, October 2008.

[117] Am Turing. The Chemical Basis Of Morphogenesis. *Philosophical Transactions Of The Royal Society Of London Series B-Biological Sciences*, 237(641):37–72, 1952.

[118] John W. Cahn and John E. Hilliard. Free Energy of a Nonuniform System. I. Interfacial Free Energy. *The Journal of Chemical Physics*, 28(2):258–267, 1958.

[119] R. Besseling, L. Isa, P. Ballesta, G. Petekidis, M. E. Cates, and W. C. K. Poon. Shear Banding and Flow-Concentration Coupling in Colloidal Glasses. *Phys. Rev. Lett.*, 105:268301, Dec 2010.

[120] H. Hinrichsen and D.E. Wolf. *The Physics of Granular Media.* Wiley, 2006.

[121] Mark R. Wilson. Determination of order parameters in realistic atom-based models of liquid crystal systems. *Journal of Molecular Liquids*, 68(1):23–31, 1996.

[122] J. Bergenholtz, W. C. K. Poon, and M. Fuchs. Gelation in Model Colloid-Polymer Mixtures. *Langmuir*, 19(10):4493–4503, 2003.

[123] Ran Ni, Martien A Cohen Stuart, and Marjolein Dijkstra. Pushing the glass transition towards random close packing using self-propelled hard spheres. *Nat Commun*, 4:2704, 2013.

[124] Allen P. Minton. Hard Quasispherical Particle Models for the Viscosity of Solutions of Protein Mixtures. *The Journal of Physical Chemistry B*, 116(31):9310–9315, 2012.

[125] P. D'Haene, J. Mewis, and G.G. Fuller. Scattering Dichroism Measurements of Flow-Induced Structure of a Shear Thickening Suspension. *Journal of Colloid and Interface Science*, 156(2):350–358, 1993.

[126] Hans Martin Laun. Rheological properties of aqueous polymer dispersions. *Die Angewandte Makromolekulare Chemie*, 123(1):335–359, 1984.

[127] K. N. Pham, A. M. Puertas, J. Bergenholtz, S. U. Egelhaaf, A. Moussaid, P. N. Pusey, A. B. Schofield, M. E. Cates, M. Fuchs, and W. C. K. Poon. Multiple Glassy States in a Simple Model System. *Science*, 296(5565):104–106, 2002.

[128] R. M. L. Evans and M. D. Haw. Correlation length by measuring empty space in simulated aggregates. *EPL (Europhysics Letters)*, 60(3):404, 2002.

[129] Raffaele Mezzenga, Peter Schurtenberger, Adam Burbidge, and Martin Michel. Understanding foods as soft materials. *Nature Materials*, 4:729–740, 2005.

[130] Gary L Hunter and Eric R Weeks. The physics of the colloidal glass transition. *Reports on Progress in Physics*, 75(6):066501, 2012.

[131] C. H. Mak. Large-scale simulations of the two-dimensional melting of hard disks. *Phys. Rev. E*, 73:065104, Jun 2006.

[132] M. D. Haw. Volume fraction variations and dilation in colloids and granulars. *Philosophical Transactions of the Royal Society A: Mathematical,Physical and Engineering Sciences*, 367(1909):5167–5170, 2009.

[133] J F Brady and G Bossis. Stokesian Dynamics. *Annual Review of Fluid Mechanics*, 20(1):111–157, 1988.

[134] K. Hinsen, 2007. HYDROLIB documentation.

[135] Rammile Ettelaie, 2013. Private Communication.

[136] Ivan Malcevic and Omar Ghattas. Dynamic-mesh finite element method for Lagrangian computational fluid dynamics. *Finite Elements in Analysis and Design*, 38(10):965–982, 2002.

[137] Milan Kucharik, Richard Liska, Pavel Vachal, and Mikhail Shashkov. Arbitrary Lagrangian-Eulerian (ALE) methods in compressible fluid dynamics. In *Programs and Algorithms of Numerical Mathematics 13*, pages 178–183, 2006.

[138] Addison-Wesley. *GPU gems*. Nvidia Corporation, 2005.

[139] A.F. Bennett. *Lagrangian fluid dynamics*. Cambridge monographs on mechanics and applied mathematics. Cambridge University Press, 2006.

[140] S. Biringen and C. Cook. On Pressure Boundary Conditions For The Incompressible Navier-stokes Equations Using Nonstaggered Grids. *Numerical Heat Transfer*, 13(2):241–252, 1988.

[141] Henning Braess and Peter Wriggers. Arbitrary Lagrangian Eulerian finite element analysis of free surface flow. *Computer Methods in Applied Mechanics and Engineering*, 190(1-2):95–109, 2000.

[142] Nuttapong Chentanez and Matthias Müller. Real-time Eulerian water simulation using a restricted tall cell grid. *ACM Trans. Graph.*, 30:82:1–82:10, Aug 2011.

[143] Wu Chun-Liang and Zhan Jie-Min. Eulerian simulation of sedimentation flows in vertical and inclined vessels. *Chinese Physics*, 14(3):620, 2005.

[144] Jean Donea, Antonio Huerta, J.-Ph. Ponthot, and A. Rodríguez-Ferran. *Arbitrary Lagrangian-Eulerian Methods*, volume 1, chapter 14, pages 1–25. John Wiley & Sons, Ltd, 2004.

[145] M. Griebel, T. Dornseifer, and T. Neunhoeffer. *Numerical simulation in fluid dynamics: a practical introduction*. SIAM monographs on mathematical modeling and computation. Society for Industrial and Applied Mathematics, 1998.

[146] Micky Kelager. Lagrangian Fluid Dynamics Using Smoothed Particle Hydrodynamics, 2006.

[147] Maciej Matyka. Solution to two-dimensional Incompressible Navier-Stokes Equations with SIMPLE, SIMPLER and Vorticity-Stream Function Approaches. Driven-Lid Cavity Problem: Solution and Visualization. *arXiv preprint physics/0407002*, 1:0407002, 2004.

[148] Ronald P. and Fedkiw. Coupling an Eulerian Fluid Calculation to a Lagrangian Solid Calculation with the Ghost Fluid Method. *Journal of Computational Physics*, 175(1):200–224, 2002.

[149] C. Pozrikidis. *Introduction to Theoretical and Computational Fluid Dynamics*. Oxford University Press, 1997.

[150] Jamie Price. Lagrangian and Eulerian Representations of Fluid Flow: Kinematics and the Equations of Motion, 2006.

[151] W.H. Press, S.A. Teukolsky, W.T. Vetterling, and B.P. Flannery. *Numerical recipes in C: the art of scientific computing*. Cambridge University Press, 1999.

[152] JA Scott. Sparse direct methods: An introduction. In *Electronic Structure and Physical Properies of Solids*, pages 401–415. Springer, 2000.

[153] Julian D. Laderman. A noncommutative algorithm for multiplying 3 × 3 matrices using 23 multiplications. *Bull. Amer. Math. Soc.*, 82(1):126–128, 01 1976.

[154] G. Schachtel. A noncommutative algorithm for multiplying 55 matrices using 103 multiplications. *Information Processing Letters*, 7(4):180–182, 6 1978.

[155] Larson. Iterative Methods For Solving Linear Systems. Web.

[156] J. Nickolls and W.J. Dally. The GPU Computing Era. *Micro, IEEE*, 30(2):56–69, March 2010.

[157] Tesla Workstation Solutions. Web, 2012.

[158] Michael Zeltkevic. Forward and Backward Euler Methods. Web, 1998.

[159] S.H. Chen, J.S. Huang, and P. Tartaglia. *Structure and Dynamics of Strongly Interacting Colloids and Supramolecular Aggregates in Solution*. Nato Science Series C:. Springer Netherlands, 2012.

[160] L. D. Landau and E. M. Lifshitz. *Fluid Mechanics*, volume 6 of *Course of Theoretical Physics*. Butterworth Heinemann, 2 edition, 1987.

[161] Dan Liu and Guoliang Xu. Angle deficit approximation of Gaussian curvature and its convergence over quadrilateral meshes. *Computer-Aided Design*, 39(6):506–517, 2007.

[162] Eric W. Weisstein. Gaussian Curvature. MathWorld–A Wolfram Web Resource.

[163] G.D.J. Phillies. *Elementary Lectures in Statistical Mechanics.* Graduate Texts in Contemporary Physics. Springer New York, 2000.

[164] A. M. Philippe, C. Baravian, V. Bezuglyy, J. R. Angilella, F. Meneau, I. Bihannic, and L. J. Michot. Rheological Study of Two-Dimensional Very Anisometric Colloidal Particle Suspensions: From Shear-Induced Orientation to Viscous Dissipation. *Langmuir*, 29(17):5315–5324, 2013. PMID: 23544905.

[165] Otis R Walton. Numerical simulation of inelastic, frictional particle-particle interactions, 1993.

[166] W.B. Russel, D.A. Saville, and W.R. Schowalter. *Colloidal Dispersions.* Cambridge Monographs on Mechanics. Cambridge University Press, 1992.

[167] Richard Chandler and Paul Northrop. randgen.f. web, 2003.

[168] Kitty van Gruijthuijsen, Marc Obiols-Rabasa, Marco Heinen, Gerhard Nägele, and Anna Stradner. Sterically Stabilized Colloids with Tunable Repulsions. *Langmuir*, 29(36):11199–11207, 2013. PMID: 23937718.

[169] Zhang Xianyi, Wang Qian, Werner Saar, Zaheer Chothia, Chen Shaohu, and Luo Wen. OpenBLAS. Web.

[170] W Wolthers, MHG Duits, D Van Den Ende, and J Mellema. Shear history dependence of the viscosity of aggregated colloidal dispersions. *Journal of Rheology (1978-present)*, 40(5):799–811, 1996.

[171] Jorrit Mellema. Experimental rheology of model colloidal dispersions. *Current opinion in colloid & interface science*, 2(4):411–419, 1997.

[172] James G. Berryman. Random close packing of hard spheres and disks. *Phys. Rev. A*, 27:1053–1061, Feb 1983.

[173] Thanh N. Phung, John F. Brady, and Georges Bossis. Stokesian Dynamics simulation of Brownian suspensions. *Journal of Fluid Mechanics*, 313:181–207, 4 1996.

[174] Norman J Wagner and John F Brady. Shear thickening in colloidal dispersions. *Physics Today*, 62(10):27–32, 2009.

[175] B.P. Cowan. *Topics in statistical mechanics.* Imperial College Press Advanced Physics Texts Series. ICP, Imperial College Press, 2005.

[176] Taken from the supplementary information associated with reference 2.